COPY 1

FAA-RD-76-76-I

FAA WJH Technical Center
00093053

AIRCRAFT CONFIGURATION NOISE REDUCTION

VOLUME I
Engineering Analysis

NAFEC
LIBRARY
SEP 20 '76

D6-42849-1
June 1976

FINAL REPORT

Document is available to the public through the
National Technical Information Service,
Springfield, Virginia 22151.

FAA WJH Technical Center
Tech Center Library
Atlantic City, NJ 08405

Prepared for

U.S. DEPARTMENT OF TRANSPORTATION
FEDERAL AVIATION ADMINISTRATION
Systems Research & Development Service
Washington, D.C. 20590

NOTICE

This document is disseminated under the sponsorship of the Department of Transportation in the interest of information exchange. The United States Government assumes no liability for its contents or use thereof.

TECHNICAL REPORT STANDARD TITLE PAGE

1. Report No. FAA-RD-76-76-I	2. Government Accession No.	3. Recipient's Catalog No.
4. Title and Subtitle AIRCRAFT CONFIGURATION NOISE REDUCTION Vol. I: Engineering Analysis		5. Report Date June 1976
		6. Performing Organization Code
7. Author(s) D. G. Dunn, L. M. Butzel, A. DiBlasi, L. Filler, and L. D. Jacobs		8. Performing Organization Report No. D6-42849-1
9. Performing Organization Name and Address Boeing Commercial Airplane Company P.O. Box 3707 Seattle, Washington 98124		10. Work Unit No.
		11. Contract or Grant No. DOT-FA74WA-3497
12. Sponsoring Agency Name and Address Federal Aviation Administration 800 Independence Avenue S.W. Washington, D.C. 20591		13. Type of Report and Period Covered Contractor Final Report (August 1974–June 1976)
		14. Sponsoring Agency Code

15. Supplementary Notes
H. C. True, DOT/FAA Technical Monitor
A. DiBlasi, coauthor from Aeritalia S.P.A.

16. Abstract

This report discusses use of wing and fuselage structures as noise barriers for shielding aircraft engine noise from the community. The report concerns use of favorable aircraft configurations for community noise reduction of turbojet and turbofan powered aircraft. Significant noise reduction potential is illustrated on a hypothetical engine-over-wing (EOW) configuration using high-bypass-ratio turbofan engines. Noise shielding estimation procedures are developed for two types of configuration noise reduction concepts; i.e., the EOW and the engine-over-fuselage (EOF).

Results are described for a theoretical analysis, a major Boeing/Aeritalia test program, and an empirical analysis of test data. As a result, analytical prediction procedures are defined, computerized, and added to the software previously developed under NASA contract NAS2-6969. The shielding prediction procedures consider individual noise components: inlet fan, compressor, exit fan, core, turbine, and jet noise. A new source, jet/edge interaction noise, can also be predicted using the procedures. The collective software, incorporating the shielding package of this report, can be used to estimate community noise levels of wing and fuselage shielded turbofan or turbojet noise.

This report is presented in three volumes. Volume I contains the engineering analysis. Volume II contains a User's Guide for computer programs and other appendices. Volume III contains the complete computer program listing.

17. Key Words Noise reduction, Noise suppression, Wing shielding, Fuselage shielding, Diffraction, Refraction, Scattering, Community noise, Fan noise, Core noise, Turbine noise, Jet noise, Jet/edge noise		18. Distribution Statement Document is available to the public through the National Technical Information Service, Springfield, Virginia 22151.

19. Security Classif. (of this report) Unclassified	20. Security Classif. (of this page) Unclassified	21. No. of Pages 414	22. Price

Form DOT F 1700.7 (8-69)

METRIC CONVERSION FACTORS

Approximate Conversions to Metric Measures

Symbol	When You Know	Multiply by	To Find	Symbol
		LENGTH		
in	inches	*2.5	centimeters	cm
ft	feet	30	centimeters	cm
yd	yards	0.9	meters	m
mi	miles	1.6	kilometers	km
		AREA		
in^2	square inches	6.5	square centimeters	cm^2
ft^2	square feet	0.09	square meters	m^2
yd^2	square yards	0.8	square meters	m^2
mi^2	square miles	2.6	square kilometers	km^2
	acres	0.4	hectares	ha
		MASS (weight)		
oz	ounces	28	grams	g
lb	pounds	0.45	kilograms	kg
	short tons (2000 lb)	0.9	tonnes	t
		VOLUME		
tsp	teaspoons	5	milliliters	ml
Tbsp	tablespoons	15	milliliters	ml
fl oz	fluid ounces	30	milliliters	ml
c	cups	0.24	liters	l
pt	pints	0.47	liters	l
qt	quarts	0.95	liters	l
gal	gallons	3.8	liters	l
ft^3	cubic feet	0.03	cubic meters	m^3
yd^3	cubic yards	0.76	cubic meters	m^3
		TEMPERATURE (exact)		
°F	Fahrenheit temperature	5/9 (after subtracting 32)	Celsius temperature	°C

*1 in = 2.54 (exactly). For other exact conversions and more detailed tables, see NBS Misc. Publ. 286, Units of Weights and Measures, Price $2.25, SD Catalog No. C13.10:286.

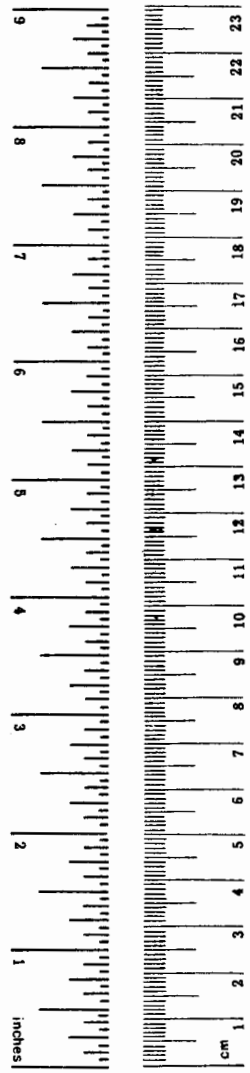

Approximate Conversions from Metric Measures

Symbol	When You Know	Multiply by	To Find	Symbol
		LENGTH		
mm	millimeters	0.04	inches	in
cm	centimeters	0.4	inches	in
m	meters	3.3	feet	ft
m	meters	1.1	yards	yd
km	kilometers	0.6	miles	mi
		AREA		
cm^2	square centimeters	0.16	square inches	in^2
m^2	square meters	1.2	square yards	yd^2
km^2	square kilometers	0.4	square miles	mi^2
ha	hectares (10,000 m^2)	2.5	acres	
		MASS (weight)		
g	grams	0.035	ounces	oz
kg	kilograms	2.2	pounds	lb
t	tonnes (1000 kg)	1.1	short tons	
		VOLUME		
ml	milliliters	0.03	fluid ounces	fl oz
l	liters	2.1	pints	pt
l	liters	1.06	quarts	qt
l	liters	0.26	gallons	gal
m^3	cubic meters	35	cubic feet	ft^3
m^3	cubic meters	1.3	cubic yards	yd^3
		TEMPERATURE (exact)		
°C	Celsius temperature	9/5 (then add 32)	Fahrenheit temperature	°F

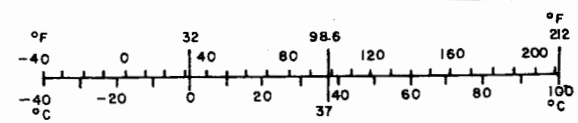

PREFACE

This is one of three volumes of the final report on "Aircraft Configuration Noise Reduction" submitted by the Boeing Commercial Airplane Company, Seattle, Washington, 98124, in fulfillment of Department of Transportation contract DOT-FA74WA-3497, dated 1 August 1974. This work was completed for the ATC Airport Facilities section of the Federal Aviation Administration (DOT). Mr. H. C. True was the Contract Technical Monitor.

The report is divided into three volumes for easy use as shown below:

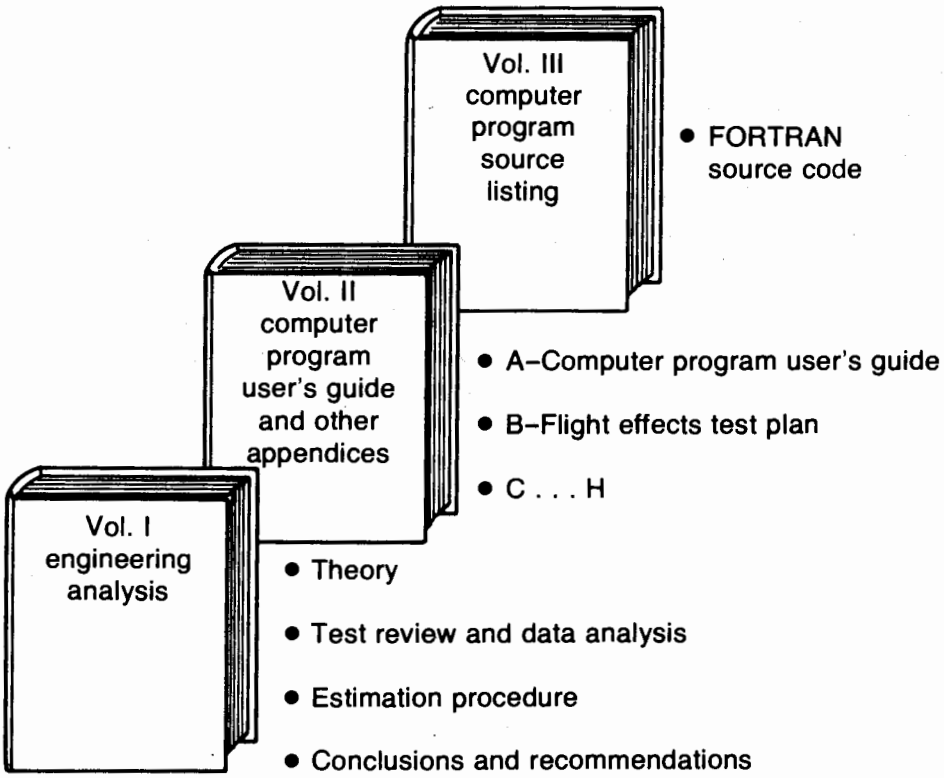

This report is volume I of the series and was prepared by the Noise Technology Staff of the Boeing Commercial Airplane Company. It contains an extensive evaluation of a relatively new technology: aircraft configuration noise reduction. The report, for the first time, collectively presents a large amount of noise shielding data and analysis, develops estimation methods, and assesses the potential for use of configuration shielding in community noise reduction.

Loan copies of volumes II and III are available from the FAA, Safety and Noise Abatement Division, Systems Research and Development Service, Washington, D.C.

ACKNOWLEDGMENT

The achievements of this report are the result of many individuals' efforts besides the authors. The following contributions are gratefully acknowledged.

	Contribution	Individual(s)
1.	Empirical Analysis and Data Base Support	C. F. Wintermeyer
2.	Computer Programming	J. S. Westall
3.	Preliminary Flight Effects Test Planning	E. F. Small
4.	Parametric Jet Shielding and Jet/Edge Interaction Test Data	R. Gulati
5.	Theoretical Shielding Support	T. L. Clark
6.	Boeing/Aeritalia Data Base Support	S. C. Oas, W. V. Bhat, and A. J. Bohn
7.	Illustrations and Equations	M. S. Johns, J. Grimes, D. J. Goudie, and J. R. Sutter
8.	Typing	M. E. Garcia

TABLE OF CONTENTS

Page

SUMMARY xxxi

1.0 INTRODUCTION 1

2.0 INFLUENCE OF WING AND FUSELAGE STRUCTURES ON TURBOMACHINERY NOISE COMPONENTS 7
- 2.1 Scope and Previous Work 7
  - 2.1.1 Diffraction 8
  - 2.1.2 Refraction 9
  - 2.1.3 Scattering 10
- 2.2 Some Basic Theoretical Elements 10
  - 2.2.1 Half-Plane Diffraction 11
  - 2.2.2 Infinite Cylinder Diffraction 37
  - 2.2.3 Jet Refraction (Ray Acoustic Model) 49
  - 2.2.4 Wing Wake Effects 63
- 2.3 Turbomachinery Noise Shielding Test Program 88
  - 2.3.1 Static Experiments 88
  - 2.3.2 Ambient Flow Experiments 160
- 2.4 Development of Shielding Estimation Method 176
  - 2.4.1 Shielding of Noise From Compact Sources 184
  - 2.4.2 Wing Shielding of Exhaust Turbomachinery Noise Components 217
  - 2.4.3 Flight and Forward Velocity Effects on Wing Shielding 245

3.0 INFLUENCE OF WING ON JET EXHAUST NOISE 257
- 3.1 Jet Noise Shielding and Jet/Edge Interaction Noise 257
  - 3.1.1 Jet Exhaust Noise Shielding 257
  - 3.1.2 Jet/Edge Interaction Noise 259
- 3.2 Experiments 259
  - 3.2.1 Cold Pipe Flow Shielding/Interaction Test 259
  - 3.2.2 Wall Isolation Facility Shielding Test 265
  - 3.2.3 SST Model Jet Shielding Test 272
  - 3.2.4 Wall Isolation Facility Test (Jet/Edge Interaction Noise) 272
  - 3.2.5 Quiet Air Facility Test (Jet/Edge Interaction) 272
- 3.3 Jet Noise Shielding Estimation 290
  - 3.3.1 Empirical Estimation Equations 290
  - 3.3.2 Data/Estimation Equation Comparison 291
- 3.4 Jet/Edge Interaction Noise Estimation 295
  - 3.4.1 Theoretical Basis 295
  - 3.4.2 Effect of Forward Velocity 296
  - 3.4.3 Semiempirical Estimation Procedure 298
  - 3.4.4 Correction for Nozzle Placement 304
  - 3.4.5 Strouhal Number 311
  - 3.4.6 Summary of Estimation Equation 312
  - 3.4.7 Data/Estimation Equation Comparison 315
  - 3.4.8 Conclusions 315

TABLE OF CONTENTS–(Concluded)

4.0 SUMMARY OF ESTIMATION PROCEDURES 318
- 4.1 Scope of Estimation Procedures 318
- 4.2 Computerized Procedures 322
  - 4.2.1 Wing Shielding of Discharge Turbomachinery Noise Components . 324
  - 4.2.2 Wing Shielding of Inlet Turbomachinery Noise Components 332
  - 4.2.3 Wing Shielding of Jet Noise 333
  - 4.2.4 Jet/Edge Interaction Noise 336
- 4.3 Manual Procedures 340
  - 4.3.1 Fuselage Shielding 340
  - 4.3.2 Wing Wake Scattering 344
- 4.4 Example Case 348
  - 4.4.1 Statement of Problem 348
  - 4.4.2 Input Data 348
  - 4.4.3 Results 349

5.0 CONCLUSIONS 353
- 5.1 Noise Reduction Potential for the Engine-Over-Wing Configuration 353
- 5.2 Computerized Model for Turbomachinery Noise Shielding 353
- 5.3 Observations From Full-Scale Engine Noise Shielding Test 355
- 5.4 Apparent Turbomachinery Noise Location in Jet Flow 355
- 5.5 Possible Importance of Flanking Radiation 356
- 5.6 Jet Noise Shielding Model 356
- 5.7 Jet/Edge Interaction Noise Model 356

6.0 RECOMMENDATIONS 358

REFERENCES 361

BIBLIOGRAPHY 365

FIGURES

No.		Page
1	Aircraft Configuration Noise Reduction Factors Influencing Predictions	xxxiii
2	Wing Shielding of Exhaust Turbomachinery Noise	xxxv
3	Shielding Estimation Procedure for Exhaust Turbomachinery Noise Components	xxxviii
4	Potential for Typical EOW Shielding Noise Reduction	xl
5	Example Noise Estimation Capability (Takeoff)	xli
6	Concepts for Evaluation of Aircraft Configuration Effects	3
7	Geometry for Half-Plane Diffraction	12
8	Theoretical Attenuation Trends for Half-Plane Shielding	15
9	Theoretical Diffraction Pattern for a Half-Plane in the Far Field	16
10	Half-Plane Diffraction (Ray Acoustics)	18
11	Amplitude of Fresnel Integral for Incident and Image Signals	19
12	Geometry for Directional/Compact Source Diffraction	21
13	Theoretical Half-Plane Diffraction Pattern for Directional/Compact Source (Flyover, $\eta = 0^0$)	23
14	Theoretical Half-Plane Diffraction Pattern for Directional/Compact Source (Sideline, $\eta = 75^0$)	24
15	Major Elements in Half-Plane Diffraction (Source Location and Directivity)	25
16	Uniform Flow Transformation for Half-Plane Diffraction	28
17	Physics of Flow Transform for Half-Plane Diffraction	30
18	Theoretical Diffraction Pattern for a Half-Plane in the Far Field With Uniform Flow	31
19	Filter Bandwidth Effect on Half-Plane Diffraction Pattern	34
20	Half-Plane Diffraction Comparison for Single-Point, Random-Phased-Ring, and Linear-Phased-Ring Sources	36
21	Effect of Source Size on Half-Plane Diffraction	38
22	Comparison of Single-Point-Source Model With Line-Source Model	39
23	Cylinder Diffraction Variables	41
24	Convergence of Cylinder Diffraction Solution	42
25	Effect of Ambient Flow on Cylinder Shielding	44
26	Two-Dimensional Equivalent Model for Cylinder Diffraction	46
27	Point-Source Noise Shielding From an Infinite Cylinder	47
28	Noise Diffraction About a Fuselage	48
29	Jet Flow Effects	50
30	Implications of Jet Refraction Effects on Half-Plane Shielding	54
31	Impact of Jet Refraction on Maximum Wing Shielding Attenuation (Theoretical Estimate)	57
32	Impact of Jet Refraction on Wing Shielding Shadow Zone Boundary (Theoretical Estimate)	58
33	Three-Dimensional Jet Flow Refraction Solution	60
34	Idealization for Wing Shielding of Turbomachinery Noise Components	62
35	Model for Sound Refraction Through Wing Wake	65
36	Noise Attenuation of a Wing Trailing Wake	68
37	Sound Scattered by Turbulent Wake of an Airfoil	71

FIGURES–(Continued)

No.		Page
38	Scattered Intensity Relative to Unscattered Intensity (1 kHz)	72
39	Scattered Intensity Relative to Unscattered Intensity (3 kHz)	73
40	Scattered Intensity Relative to Unscattered Intensity (10 kHz)	74
41	Differential Scattering Cross Section as a Function of Scattering Angle	81
42	Differential Scattering Cross Section as a Function of Strouhal Number	82
43	Scattering Cross Section as a Function of Scattering Angle	83
44	Scattering Cross Section as a Function of Strouhal Number	84
45	Range of Test Conditions for an EOW Configuration	91
46	Compact-Source Shielding Test Setup (Group 1) With Simulated Single-Edged, Semi-Infinite Half-Plane Barrier	93
47	Compact-Source Shielding Test Setup (Group 1) With Simple, Multiedged, "Flat Board" Barrier	94
48	Compact-Source Shielding Test Setup (Group 1) With Typical Jet Transport Wing-Shaped Barrier	95
49	Schematic of Compact-Source Shielding Test Setup	96
50	Dimensions of Jet Transport Wing-Shaped Barrier	97
51	Compact-Source Shielding Test Setup (Group 1) With Cylindrical Barrier	99
52	Compact-Source Shielding Test Setup (Group 2) in Large Test Chamber (LTC)	100
53	Sketch of LTC Layout (Overhead View)	101
54	Detailed Sketch of Shield/Speaker Arrangement	102
55	Effect of Source Orientation on Shielding of Simulated Semi-Infinite Half-Plane Barrier	103
56	Effect of Source Frequency on Shielding of Simulated Semi-Infinite Half-Plane Barrier	104
57	Comparison of Shielding Behavior of "Flat Board" and Simulated Semi-Infinite Half-Plane Barriers	105
58	Apparent Diffraction Contributions of Leading and Trailing Edges of Wing Barrier	106
59	Effect of Source Position on Shielding Effectiveness of Scale-Model Transport Wing	107
60	Unshielded and Shielded Behavior of Altec Source as Tested in LTC	109
61	Comparison of Semi-Infinite Half-Plane Barrier Performance as Tested in Fan Rig Room and LTC	112
62	Model Fan Rig Test Setup, "Flyover" Configuration	114
63	Model Fan Rig Test Setup, "25° Sideline" Configuration	115
64	Schematic of Model Fan Rig Test Setup	116
65	Position of the Shield With Respect to the Nozzle Exit	117
66	Geometry of Winglike Shield	118
67	Fan-Tone Behavior With and Without 90° Shield	120
68	Fan-Tone Behavior With and Without 25° Shield	121
69	Overview of WIF Test Facility	122
70	WIF Test Facility Schematic	123
71	WIF Test Nozzles	125

FIGURES–(Continued)

No. Page

72 Wing/Nozzle Geometric Relations (WIF Test) 127
73 Shadow Boundary Definitions for WIF Tests 129
74 Closeup View With Wing in "Flyover" Position 130
75 Setup With Wing in "25° Sideline" Configuration 131
76 Typical Narrowband Spectral Behavior of Data From WIF Test 132
77 Radiated Unshielded and Flyover Wing-Shielded 9.6-kHz Tone Noise From Nozzles 8-14 134
78 Radiated Unshielded and Flyover Wing-Shielded 19.3-kHz Tone Noise From Nozzles 8-14 135
79 Radiated Unshielded and Flyover Wing-Shielded 29-kHz Tone Noise From Nozzles 8-14 136
80 Unshielded and Shielded Flyover Polar Distributions of Tone Noise From Nozzle 11 (With Thrusting Flow) 137
81 Unshielded and Shielded 25° Sideline Wing-Shield Configuration Polar Distributions of Tone Noise From Nozzle 11 (With Thrusting Flow) 138
82 Unshielded and Shielded Flyover Polar Distributions of Tone Noise From Nozzle 11 (Without Thrusting Flow) 139
83 Comparison of Tone Noise Polar Distribution for Nozzle 11 (With and Without Thrusting Flow) 140
84 Mounted Engine With Inlet Tube and Barriers–Full-Scale JT9D Tulalip Shielding Tests 142
85 View of Inlet Tube and Engine From Behind 90° Wing–Full-Scale JT9D Tulalip Shielding Tests 143
86 Flyover (90° Wing) Configuration Setup–Full-Scale JT9D Tulalip Shielding Tests 144
87 Wing/Engine Geometry for Tulalip Shielding Tests 145
88 Overall Arrangement for Tulalip Test Setup 146
89 Tulalip Shielding Test Wing Configuration 147
90 Typical Narrowband Spectra From JT9D Tulalip Shielding Test 150
91 Example of Recorded and Shifted Turbine (T6) Tone Data for 90° Wing Configurations 151
92 Full-Scale JT9D Tulalip Shielding Test Results: Mean Shielding Effect of 90° Wing on Turbine Tone at Mean Frequency of 4.60 kHz 153
93 Full-Scale JT9D Tulalip Shielding Test Results: Mean Shielding Effect of 25° Wing on Turbine Tone at Mean Frequency of 4.60 kHz 154
94 Full-Scale JT9D Tulalip Shielding Test Results: Mean Shielding Effect of 90° Wing on Discharge Fan Tone at Mean Frequency of 1.66 kHz 155
95 Typical Full-Scale JT9D Tulalip Test Results: Broadband Core and Jet Noise 156
96 Measured Average Baseline (No Wing) Directivity for Tulalip Shielding Tests 157
97 Full-Scale JT9D Tulalip Shielding Test Results: Shielding Attenuation of Broadband Engine Exhaust Noise 158
98 Schematic of UARL Test Area 161

FIGURES–(Continued)

No.		Page
99	Nacelle and Wing for UARL Tunnel Shielding Tests	162
100	Microphone Array for UARL Tunnel Shielding Tests	163
101	Average Unshielded and Shielded Tone Noise Results at 0 m/s Tunnel Velocity (UARL Test)	167
102	Effect of Tunnel Velocity on Reduction of Tone Noise Due to Wing Shielding	168
103	Powered Nacelle Noise Spectra With and Without Wing	169
104	Airplane With Horn Mounted Below Wing	170
105	Detail of Horn Mounted Above Wing	171
106	Horn-Over-Wing Flight Test Layout	172
107	Typical Results for Horn-On-Wing Shielding Test for X = 17 cm	173
108	Typical Results for Horn-On-Wing Shielding Test for X = 52 cm	174
109	Light Airplane Static Wing Shielding Test Setup	175
110	Comparison of 727-100 and -200 Level Flyover Noise Levels at Approach Power and 25° Flaps	177
111	Comparison of 727-100 and -200 Level Flyby Data at 25° Flaps	178
112	727-100 and -200 Geometry Comparison	179
113	Comparative Average of 4-kHz 1/3-Octave-Band Level Flyby Data for 727-100 and -200 at 25° Flaps	181
114	Estimated and Observed Fan-Tone Flyby Noise Levels of 727-100 and -200 at 25° Flaps	182
115	Sound Field of Directional Source With and Without Acoustical Sound Barrier (Test Data, Blue Room Facility)	186
116	Effect of Source Directivity on Sound Diffraction (Test Data, Blue Room Facility)	187
117	Directional Source Shielding Test Results in LTC Facility	188
118	Compact-Source Simulation of Typical Turbomachinery Noise Source	189
119	Comparison of Predicted and Measured Diffraction Far Field of Directional Source (f = 20 kHz and ψ_p = 135°)	191
120	Comparison of Predicted and Measured Diffraction Far Field of Directional Source (f = 20 kHz and ψ_p = 90°)	192
121	Comparison of Predicted and Measured Diffraction Far Field of Directional Source (f = 10 kHz and ψ_p = 120°)	193
122	Comparison of Predicted and Measured Diffraction Far Field of Directional Source (f = 10 kHz and ψ_p = 90°)	194
123	Comparison of Predicted and Measured Diffraction Far Field of Directional Source	195
124	Superposition of Diffraction Components (Test Data, Blue Room Facility)	196
125	Configuration Tested to Evaluate Diffraction Around Multiple Edges	198
126	Theoretical Half-Plane Evaluation Configurations	200
127	Evaluation of Half-Plane Approximations, f = 20 kHz	201
128	Evaluation of Half-Plane Approximations, f = 10 kHz	202
129	Evaluation of Half-Plane Approximations, f = 5 kHz	203
130	Sound Diffraction About Model Wing, X = 53.4 cm, f = 20 kHz	204
131	Sound Diffraction About Model Wing, X = 26.7 cm, f = 20 kHz	205

FIGURES–(Continued)

No. Page

132 Sound Diffraction About Model Wing, X = 53.4 cm, f = 10 kHz 206
133 Sound Diffraction About Model Wing, X = 53.4 cm, f = 5 kHz 207
134 Application of Half-Plane Diffraction Theory for a Directional Source Near a Wing/Flap System 208
135 Sample Sound Diffraction About Wing/Flap System 209
136 Source/Wing Test Geometry 211
137 Comparison of Broadband and Tone Sound Diffraction Field (Test Data, Blue Room Facility) 212
138 Free-Field Sound Source Directivity and Cylinder Diffraction Test Geometry 213
139 Cylinder Diffraction Theory Versus Measurement (Quasi-Anechoic Chamber Test), f = 2.5 and 5 kHz 214
140 Cylinder Diffraction Theory Versus Measurement (Quasi-Anechoic Chamber Test), f = 10 and 20 kHz 215
141 Point-Source Noise Shielding From an Infinite Cylinder 216
142 Major Elements Considered Exhaust in Turbomachinery Noise Shielding Data Analysis 218
143 Schematic of Optimization Computer Program for Determining Apparent Source Locations for Exhaust Turbomachinery Noise-Shielding Test Data 221
144 Engine/Wing Geometry 222
145 Decomposition of Wing Shielding Data Into Leading and Trailing Edge Diffraction Components 224
146 Comparison of Optimization Prediction With Shielding Model Test (WIF) 226
147 D-Nozzle Wing Shielding Results and Optimized Prediction 227
148 Apparent Source Location in Exhaust Flow (Trailing Edge) 228
149 Wing Shielding Optimization Results for Apparent Source Position (Directional/Point-Source Analysis) 229
150 Correlation of Apparent Source Location With Refraction Model (No Empiricisms) 231
151 Apparent Source Location for Wing Trailing Edge (Flyover Case) 233
152 Empirical Adjustments to Jet Refraction Theory for Apparent Source Position 235
153 Correlation of Apparent Source Location With Refraction Model (Empiricisms Included) 236
154 Turbomachinery Noise Shielding Model Performance (Flyover Wing Geometry) 238
155 Turbomachinery Noise Shielding Model Performance (25° Wing Geometry) 239
156 Turbomachinery Noise Shielding: Prediction Versus Measurement 240
157 Comparison of Estimated and Actual Shielding as Measured in Model Fan Rig Room 241
158 Comparison of Estimated and Actual Shielding as Measured in LTC 243

FIGURES–(Continued)

No.		Page
159	Predicted Effect of UARL Tunnel Velocity on Shielding Effectiveness of Model Wing Barrier	248
160	Effect of Tunnel Flow on Wing Shielding Attenuation	249
161	727-100 and -200 Aircraft Engine/Wing Geometry	251
162	Flight Test Results and Estimates	251
163	Schematic of Turbomachinery Noise Estimation Methods	252
164	Estimated Turbomachinery Noise Shielding in Flight	256
165	Jet Exhaust Flow Shielding and Interaction	258
166	Cold Pipe Flow Test Setup	260
167	Cold Pipe Flow Test–Closeup View	261
168	Schematic of Cold Pipe Flow Test	262
169	Typical Cold Pipe Flow Test Results	263
170	Nozzle Types and Dimensions	266
171	Wall Isolation Facility (WIF) Jet Shielding Test Setup	267
172	Nozzle/Shield Closeup (WIF Jet Shielding Test)	268
173	Nozzle/Shield Schematic (WIF Jet Shielding Test)	269
174	WIF Jet Shielding Test Results	270
175	SST Jet Shielding Exhaust Nozzles	273
176	Test Setup With Standard C-6 Nozzle (SST Jet Shielding Test)	274
177	Test Setup With 21-Tube Nozzle (SST Jet Shielding Test)	275
178	SST Jet Shielding Test Setup Schematic	276
179	Effect of Rectangular Panel Shields on Far-Field Radiated Noise of Hot, Single-Flow, 21-Tube Nozzle	277
180	WIF Jet/Edge Interaction Test Schematic–Elevation	278
181	D-Nozzle Forward Velocity Test (WIF Jet/Edge Interaction Test)	279
182	Wing/Body Shield (WIF Jet/Edge Interaction Test)	280
183	Wing/Body Shield Schematic (WIF Jet/Edge Interaction Test)	281
184	Far-Field Noise of D-Nozzle Rig	282
185	Slot Nozzle With 30.4-cm Plate (QAF Jet/Edge Interaction Test)	283
186	D-Nozzle With 30.4-cm Plate (QAF Jet/Edge Interaction Test)	284
187	Variable Divergent Rectangular Nozzle (QAF Jet/Edge Interaction Test)	285
188	Slot Nozzle With 30.5-cm Plate	286
189	D-Nozzle for Jet/Edge Noise Test	287
190	Variable Divergent Rectangular Nozzle–Side Plates and Hinged Top Plate	288
191	Edge Noise Spectra as a Function of Radiation Angle	289
192	Estimation Equation Comparison	292
193	Model Jet Noise Shielding Configurations	293
194	Jet Noise Shielding Data Correlation	294
195	Jet/Edge Interaction Geometry and Coordinates	297
196	Jet/Edge Interaction Normalized Sound Pressure Level (Ref. 49)	300
197	Jet/Edge Interaction 1/3-Octave-Band Peak SPL Scaling (Ref. 49)	302

FIGURES–(Concluded)

No.		Page
198	Jet/Edge Interaction Schematic Showing Effect of Nozzle Placement	305
199	Effect of Nozzle Placement (Incomplete Interaction) on Jet/Edge Interaction Noise	307
200	Effect of Nozzle Placement (Trailing Edge Position Relative to Potential Core Length) on Jet/Edge Interaction Overall SPL	310
201	Characteristic Frequency, f_0, as a Function of Shield Length, L, for Jet/Edge Interaction Noise	313
202	Jet/Edge Interaction Noise (Estimation Versus NASA Data)(Ref. 50)	316
203	Computation Sequence	320
204	Interface Between New and Old Software	321
205	Airframe Shielding Model Development	323
206	Unshielded SPL Directivity Curves for High-Bypass-Ratio Turbofans	325
207	Wing Shielding Package (Subroutine SHLDSP)	327
208	Wing Shielding Calculation Module (Subroutine SHATTN)	329
209	Effect of h/L Geometry Variation on Jet/Edge Interaction Noise	337
210	Nomograph of Noise Reduction Underneath the Airplane Flightpath ($\phi = \pm 180^0$)	343
211	Interpolated Noise Diffraction About a Fuselage	345
212	Example Noise Estimation Capability (Takeoff)	351
213	Example of Aircraft Configuration Noise Reduction	352

TABLES

No.		Page
1	Shielding Test Summary	4
2	Summary of Static Turbomachinery Noise Shielding Tests	89
3	Summary of Ambient Flow Turbomachinery Noise Shielding Tests	90
4	Typical Model Fan Rig Test Conditions	119
5	Nozzle Flow Conditions (WIF Test)	126
6	Typical JT9D Tulalip Test Conditions	149
7	UARL Tunnel Shielding Test Configurations	164
8	Tunnel and Nacelle Operating Conditions for UARL Tunnel Shielding Tests	165
9	Mean Flyover Test Conditions for 727 Airplanes	180
10	Range of Parameters for Cold Pipe Flow Test	259
11	Nozzle Operating Conditions	265
12	"Observed" Jet/Edge Interaction Noise (ΔSPL) as a Function of Nozzle/Shield Geometry	306
13	Estimated Flyover Test Results	350
14	Typical Estimated Community Noise Reduction for EOW Versus EUW Configured Airplane	354

ABBREVIATIONS AND SYMBOLS

Abbreviation or symbol	Description	Section reference*
A	Nozzle discharge area (m^2)	4.2.3
A or a	Effective cylinder radius (dimensionless)	2.2.2
A_J	Nozzle area (m^2)	3.0
A/P	Airplane	
a_0	Standard speed of sound (340 m/s)	3.0
a_∞	Ambient speed of sound (m/s)	3.0
(a, b, c, d)	Dimensionless variables for simplification of far-field, half-plane diffraction solution	2.2.1
(a′, b′, c′, d′)	Same as above, except transformed to account for uniform flow effects	2.2.1
B or b	Effective source distance from cylinder center (dimensionless)	2.2.2
BPR	Engine bypass ratio	
BW	Filter bandwidth (decades)	
b	Source distance upstream from wing's trailing edge (m)	2.2.4
b	Shield span wetted by jet (m)	3.0
C	Chord of airfoil (m)	2.2.4
C	Constant for nozzle placement effect, eq. (95) (dB)	3.0
C_D	Wing profile drag coefficient	
C_{Do}	Reference wing profile drag coefficient	
C_P	Specific heat of air at constant pressure	
CPA	Closest point of approach (m)	
C_V	Specific heat of air at constant volume	

*Unless noted otherwise by section reference, the definition applies everywhere in this report.

Abbreviation or symbol	Description	Section reference
C_z	Ambient speed of sound at aircraft altitude at visual overhead position (m/s)	
C_o	Ambient speed of sound (m/s)	
D	Nozzle diameter (m)	
D	Partial differential operator (m^{-1})	2.2.4.1
D	Diameter of cylinder producing far-wake turbulence (m)	2.2.4.2
DC	Directivity correction (dB)	
D_H	Nozzle hydraulic diameter, $4A_J/P$ (m)	
DSPL	Relative sound pressure level (dB)	
D_1	Hydraulic diameter of primary-exhaust nozzle (m)	
D_2	Hydraulic diameter of secondary-exhaust nozzle (m)	
d	Turbulence half-width of wing wake (m)	2.2.4.2
d	Jet/edge interaction height (m)	3.0
$d\sigma/d\Omega$	Differential scattering cross section (m^2)	
$d\sigma_s/d\Omega$	Characteristic differential scattering cross section	
E	Energy-wave number spectrum of turbulent velocity fluctuations (m/s^2)	
EBB	Engine-beside-body	
EOF	Engine-over-fuselage	
EOW	Engine-over-wing	
EPNL	Effective perceived noise level (EPNdB)	
EPR	Engine pressure ratio	
EUW	Engine-under-wing	
E_o	Reference energy-wave number velocity spectrum normalizing constant (m/s^2)	

Abbreviation or symbol	Description	Section reference
F	Dimensionless characteristic scattering intensity	2.2.4.2
F	Spectrum shape factor, eq. (78) for jet/edge interaction noise	3.0
$F(a, b, \phi)$	Cylinder diffraction series expansion	2.2.2
$F(z)$	Complex Fresnel integral	2.2.1
FPR	Fan pressure ratio	
F_0	Relative overall scattered intensity	
F_1	Fundamental fan tone frequency (Hz)	
f	Frequency (Hz)	
f_L	Filter band lower "cutoff" frequency (Hz)	
f_N	Normalized Doppler-shifted frequency (Hz)	
f_U	Filter band upper "cutoff" frequency (Hz)	
f_0	Characteristic frequency often corresponding to the frequency where the spectrum level is maximum (Hz)	
$G(\bar{r}\|\bar{r}_0)$	Green's function	
GRAD	Aircraft climb gradient	
H	Height of nozzle centerline above the shield surface (m)	
$H(K\, r_0, \theta - \theta_0)$	Sound pressure level shielding attenuation function for a point source (dB)	
$H(\psi)$	Far-field, unshielded sound pressure field directivity function	
H.P.	Half-plane	
$H_N^{(1)}$	Nth order Bessel function of the third kind, i.e., Hankel function	
h	Source height above wing (m)	2.2.4.2

Abbreviation or symbol	Description	Section reference
h	Height of nozzle lip above shield surface (m)	
i	Imaginary number, $(-1)^{.5}$	
I, J	Indices	
J_N	Nth order Bessel function of the first kind	
K	Wave number (m^{-1})	
K	Nozzle placement effect correction for jet/edge interaction noise (dB)	3.0
K′	Wave number transformed to include uniform flow effects (m^{-1})	
$\overline{K}$	Wave number vector (m^{-1})	
K_o	Reference wave number (m^{-1})	
Kr_o, Kr_1, Kr_2, Kr_3	Dimensionless barrier heights	
$\underset{\sim}{k}$	Surface pressure wave vector (m^{-1})	
k_1	Streamwise component of surface pressure wave vector (m^{-1})	
L	Shield length (m)	3.0
L	Overall length of engine, i.e., inlet plane to nozzle exit plane (m)	2.4.2
$\hat{L}$	Unit vector parallel to vector $\overline{\ell}$	
L_c	Jet potential-core length (m)	
L_{co}	Jet potential-core length at static test conditions (m)	
LTC	Large Test Chamber	
L_o	Characteristic differential scattering cross-section level (dB)	
$\hat{L}_o$	Unit vector parallel to vector $\overline{\ell}_o$	
L_1	Shield length from primary-nozzle exit plane to wing/flap system's trailing edge (m)	
L_2	Same as above, except for secondary nozzle (m)	
ℓ	Characteristic eddy scale (m)	

Abbreviation or symbol	Description	Section reference
$\bar{\ell}$	Modification of observer position vector $\bar{r}$ (m). Modified vector $\bar{\ell}$ equals vector $\bar{r}$ with components parallel to vector $\hat{M}$ removed.	
ℓ_0	Reference characteristic eddy scale (m)	
$\bar{\ell}_0$	Modification of source position vector $\bar{r}_0$ (m). Modified vector $\bar{\ell}_0$ equals vector $\bar{r}_0$ with components parallel to vector $\hat{M}$ removed.	
M	Local flow Mach number	
$\hat{M}$	Unit vector for uniform flow direction parallel to equivalent half-plane representing wing edge	
M_J	Jet Mach number	
M_0	Ambient flow Mach number	
$\bar{M}_0$	Uniform flow Mach number vector parallel to equivalent half-plane representing wing edge	
$\dot{M}_1$	Primary-nozzle mass flow (kg/s)	
$\dot{M}_2$	Secondary-nozzle mass flow (kg/s)	
M_2	Nominal flow Mach number in wing wake	
N	Number of jet engines	
N	Empirical constant in jet/edge interaction noise formulation (dB)	3.0
NPR	Nozzle pressure ratio	
NR	Noise reduction (dB)	
N_1	Rotational speed (RPM)	
P	Nozzle perimeter (m)	
$P(\underset{\sim}{k}, \omega)$	Surface pressure wave number/frequency power spectral density	
$P(\bar{r}_0)$	Sound source distribution function	
P_I	Incident acoustic field	
$\hat{P}_N$	Unit vector for sound propagation direction to the observer	

FAA WJH Technical Center
00093053

Abbreviation or symbol	Description	Section reference
PNL	Tone-corrected perceived noise level (PNdB)	
P_{ref}	Reference RMS pressure (20 $\mu N/m^2$)	
PR_P	Primary-nozzle pressure ratio	
PR_S	Secondary-nozzle pressure ratio	
P_S	Complex shielded pressure field diffracting about a wing edge	
P_S	Scattered acoustic field	2.2.4.2
P_{SJ}	Complex shielded pressure field for Jth point source	
P_T	Complex total shielded pressure field	
P_T	Total acoustic field	2.2.4.2
P_z	Ambient pressure at aircraft altitude at visual overhead (atm)	
P_{oJ}	Unshielded pressure field for Jth point source	
p	Dimensionless acoustic pressure	
p_I	Observed sound pressure without wing wake	
p_R	Observed refracted sound pressure with wing wake	
$\dot{q}$	Source strength (Hz)	
q_I	Incident sound intensity (W/m^2)	
q_S	Scattered sound intensity (W/m^2)	
R	Distance between sound source and observer (m)	
R′	Distance between image sound source and observer (m)	
RMS	Root mean square	
RPS	Revolutions per second	
R_1	Minimum distance for sound propagation from source to shielding barrier edge to observer (m)	
r	Distance from edge to observer (m)	
r	Radial displacement normal to cylinder wall (m)	2.2.2.1

Abbreviation or symbol	Description	Section reference
Z	Incomplete interaction parameter for jet/edge interaction noise	3.4
Z_0	Reference correlation term for jet noise shielding	4.2.3
Z_0	Aircraft height above the ground at visual overhead, figure 6 of reference 2 (m)	
α	Source orientation angle relative to half-plane barrier (deg)	
α	Slope of curve for jet refraction theory correlation with shielding measurements of apparent shadow zone boundary change (deg)	2.4.2
α	Airplane angle of attack (deg)	3.0
α_{F1}, α_{F2}	Flap angles (deg)	
α_N	Engine inclination angle relative to tunnel flow (deg)	2.2.3, 2.4.2, and 4.2
α_W	Wing chord angle of attack (deg)	
α_1	Wing/flap system's trailing edge sweep angle (deg)	2.2.4.1
α_2	Wing's leading edge sweep angle (deg)	3.0 2.3
α_3	Wing's dihedral angle (deg)	3.0
β	Empirical adjustment constant in jet refraction theory formula	
β	Sound propagation direction angle (deg)	
β	Jet spreading angle (deg)	
β_0	Elevation angle (deg)	
β_0	Jet spreading angle for static tests (deg)	
Γ	Normalizing constant (dB)	
γ	Apparent offset of shadow zone boundary not accounted for in jet refraction theory except by inclusion of induced ambient flow (deg)	

Abbreviation or symbol	Description	Section reference
γ	Uniform flow transform factor for wave number	2.2.1 and 2.2.2
γ	Ratio of specific heats (C_P/C_V)	2.2.4.1
γ	Source orientation angle relative to half-plane barrier (deg)	2.3.1
$\Delta(L)$	Transverse jet mixing layer scale (m)	
ΔSPL	Sound pressure level change from a reference condition, i.e., attenuation spectra, relative scattered intensity, etc. (dB)	
ΔSPL_{edge}	Change in jet/edge interaction noise due to nozzle/edge geometry changes (dB)	
Δu	Maximum mean velocity deficit in a wing wake (m/s)	
$\Delta x\ \Delta z$	Differential surface area of a wing wake (m^2)	
$\Delta\psi$	Shadow zone boundary change (deg)	
$\Delta\psi_P$	Predicted shadow zone boundary change using jet refraction theory (deg)	
$\Delta\psi_S$	Apparent unshielded directivity curve shift due to presence of shielding barrier (deg)	
δ	Engine inlet axis orientation angle relative to half-plane barrier (deg)	2.2.1
δ	Wing wake thickness (m)	2.2.4.1
$\delta(x, y, z)$	Three-dimensional Dirac delta function	
δ_E	Engine inclination angle relative to the horizon (deg)	
ϵ	Tolerable fractional error constant	
η	Azimuth direction angle relative to shielding half-plane for observer coordinate (deg)	

Abbreviation or symbol	Description	Section reference
η'	Same as above, except transformed to account for uniform flow effects (deg)	
θ	Elevation direction angle relative to shielding half-plane for observer coordinate (deg)	
θ	Cylinder diffraction shadow angle (deg)	2.2.2
θ	Scattering angle (deg)	2.2.4.2
θ	Polar microphone angle (deg)	2.3.1.1
θ'	Elevation direction angle relative to shielding barrier half-plane for observer coordinate except transformed to account for uniform flow effects (deg)	
θ_0	Source coordinate direction angle relative to shielding half-plane (deg)	
θ_0	Shadow boundary angle relative to jet exhaust (deg)	2.2.3
θ_0	Reference direction angle for jet/edge interaction noise (deg)	4.2.4
θ_0'	Apparent source coordinate direction angle relative to shielding half-plane (deg). This angle is different from θ_0 for the nozzle coordinate due to jet flow, uniform flow, scattering, and/or flanking radiation.	
θ_0'	Same as above, except relative to jet exhaust axis (deg). This angle defines the direction of acoustic energy propagation from a source inside the jet as observed outside the jet.	2.2.3
$\theta_1, \theta_2, \theta_3$	Shadow boundary angles (deg)	
θ_1	Angle between the direction of acoustic energy propagation and the jet exhaust axis for acoustic waves inside the jet (deg)	2.2.3.2

Abbreviation or symbol	Description	Section reference
θ_2	Angle between line drawn from assumed source position inside the nozzle to the barrier edge and the equivalent half-plane for the barrier (deg)	2.2.3.2
λ	Wavelength (m)	
μ	Micro-; i.e., 10^{-6}	
μ, ν	Empirical exponents for jet/edge interaction noise spectrum shape formula	3.0
ξ	Angle between vectors $\bar{r}$ and $\hat{M}$ (deg)	2.2.1.2
ξ	Direction angle for observer relative to cylinder shielding barrier axis (deg)	2.2.2
ξ	Angle between airplane's flightpath and sound propagation path to observer (deg)	4.2
ξ'	Angle between vectors $\bar{r}'$ and $\hat{M}$ (deg). This angle is the same as ξ (sec. 2.2.1.2) except transformed to account for uniform flow effects.	
ξ_0	Angle between vectors $\bar{r}_0$ and $-\hat{M}$ (deg)	
ξ_0'	Angle between vectors $\bar{S}'$ and $-\hat{M}$ (deg). This angle is the same as ξ_0 except transformed to account for uniform flow effects.	
ρ_J	Jet density (kg/m^3)	
ρ_0	Standard density (1.225 kg/m^3)	
Σ	Summation	
σ	Scattering cross section (m^2)	
$\bar{\sigma}$	Root-mean-square decibel error incurred in fitting diffraction theory to wing shielding test data (dB)	
σ_{min}	Modified total scattering cross-section function (m^2)	

Abbreviation or symbol	Description	Section reference
σ_N	Dimensionless scattering cross section	
σ_s	Characteristic scattering function (m^2)	
$\sigma_{s\ min}$	Modified characteristic scattering function (m^2)	
σ_T	Total scattering cross section (m^2)	
Φ_T	Energy-wave number spectrum of turbulent temperature fluctuations (m^3 - $^oK^2$)	
ϕ	Observer angle for cylinder diffraction measured in plane normal to cylinder axis (deg)	
ϕ	Wing tilt angle (deg)	2.3.1.2
ϕ_o'	Angle relative to jet exhaust axis or equivalent half-plane barrier for normal direction to acoustic wavefronts as observed outside the jet (deg)	
ϕ_1	Same as above except as observed inside the jet (deg)	
φ	Direction angle relative to normal to wing wake plane (deg)	
ψ	Direction angle for sound emission relative to the noise source's symmetry axis; i.e., usually the engine's inlet axis (deg)	
ψ'	Same as above, except for image source due to presence of half-plane shielding barrier (deg)	
ψ_P	Direction angle for maximum sound intensity (deg)	
$\psi_P(\underset{\sim}{r}, \omega)$	Power spectral density of radiated pressure	
ψ_o	Direction angle for sound emission grazing the shielding barrier's edge for shortest propagation path (R_1) from source to edge to observer (deg)	

Abbreviation or symbol	Description	Section reference
ψ_0'	Same as ψ_0 except for image or apparent sources (deg)	
Ω	Solid angle into which sound is scattered (steradian)	
ω	Circular frequency (sec^{-1})	
ω_0	Characteristic circular frequency (sec^{-1})	
∇^2	Laplacian operator (m^{-2})	

SUMMARY

Introduction

The Boeing Commercial Airplane Company (BCAC) under contract to the Department of Transportation/Federal Aviation Administration (DOT/FAA) has conducted a study to reduce aircraft community noise using wing and fuselage structures as acoustical barriers. This is the final report for this study contract covering the period of August 1974 through June 1976.

Airframe shielding of jet engine noise appears to offer a viable alternative to more nacelle lining treatment to achieve lower community noise levels for future aircraft. The study shows that the engine-over-wing (EOW) and the engine-over-fuselage (EOF) airplane configurations have significant noise reduction potential. The EOW configuration, with high-bypass-ratio (BPR = 5) engines, can reduce noise levels about 7 EPNdB at conditions specified in FAR Part 36 (ref. 1).

Estimation procedures are the result of the study to quantify the noise reduction possible by favorable engine placement in the proximity of shielding aircraft structures. The estimation procedures consider engine component noise (inlet fan, compressor, exit fan, turbine, core, and jet) sources, the generation of jet/edge interaction noise, and the influence of jet flow, ambient flow, and the wing wake on shielded noise levels.

The estimation procedures applicable to the EOW concept are computerized and added to the community noise estimation software previously developed under NASA contract NAS2-6969 (refs. 2 and 3). The new computer software is currently implemented on the CDC6600 NOS computer system at the Aircraft Noise Prediction Office, NASA Langley Research Center, Hampton, Virginia. Appendix A of the volume II report contains the user's guide for the new software. The revised software provides a tool for conducting trade studies to evaluate aircraft configuration noise reduction concepts.

Objective

This study fulfills the following objectives:

- Define a generalized airframe shielding estimation procedure for turbofan engine noise.
- Specify an analytical model for the effect of flight on shielded noise.
- Develop a test plan to validate the analytical flight effects model (see app. B of the vol. II report).
- Computerize the shielding estimation procedure.
- Determine if airframe structure shielding is a viable concept relative to engine/nacelle design for community noise suppression.

Theoretical/Empirical Approach

Figure 1 shows that engine noise enters the region (shadow zone) on the opposite side of shielding structures (wings, fuselages, etc.) largely by:

- Diffraction – wave propagation about barriers
- Refraction – wave propagation through shear flows
- Scattering – wave propagation through turbulent flows

Each of the phenomena is present for wing shielding of exhaust turbomachinery noise.

Theory was available for describing diffraction, refraction, and scattering phenomena as independent processes for relatively simple geometries, but not as simultaneously occurring processes for wing/flap geometries. Test data were used to validate, empirically adjust, and integrate theoretical "building blocks" into a shielding estimation package. The concept of an apparent compact source, i.e., the apparent noise emission point, was used to simplify and to describe the joint effects of refraction and diffraction on wing shielding of exhaust turbomachinery noise.

For the engine-over-wing (EOW) concept, available theory and test data were extensive enough to develop an analytical model. The resulting estimation procedure that evolved included three major divisions:

- Shielding of turbomachinery noise (inlet fan, compressor, exit fan, turbine, and core noise)
- Shielding of jet noise
- Generation of jet/edge interaction noise

For the engine-over-fuselage (EOF) concept, available test data tended to support cylinder diffraction theory but were too limited to define an estimation procedure having general application for all turbofan engine noise components. The theoretical diffraction solution also had numerical evaluation problems associated with it. Hence, a preliminary manual estimation procedure was defined based on the theory. Further test and study are required before improvements can be made to estimate the noise reductions associated with the EOF concept.

Test Data Base

An extensive Boeing/Aeritalia test data base was available to guide the development and empirical adjustment of the theoretical building blocks noted previously. Most of the tests concerned wing shielding; however, one model test was conducted on cylinder shielding of a compact noise source. The wing shielding tests dealt mainly with high-bypass-ratio turbofan engine noise, although significant portions of the results directly carry over to turbojet applications, i.e., jet noise shielding. Acoustic measurements were taken in the far field with and without the shielding barriers in

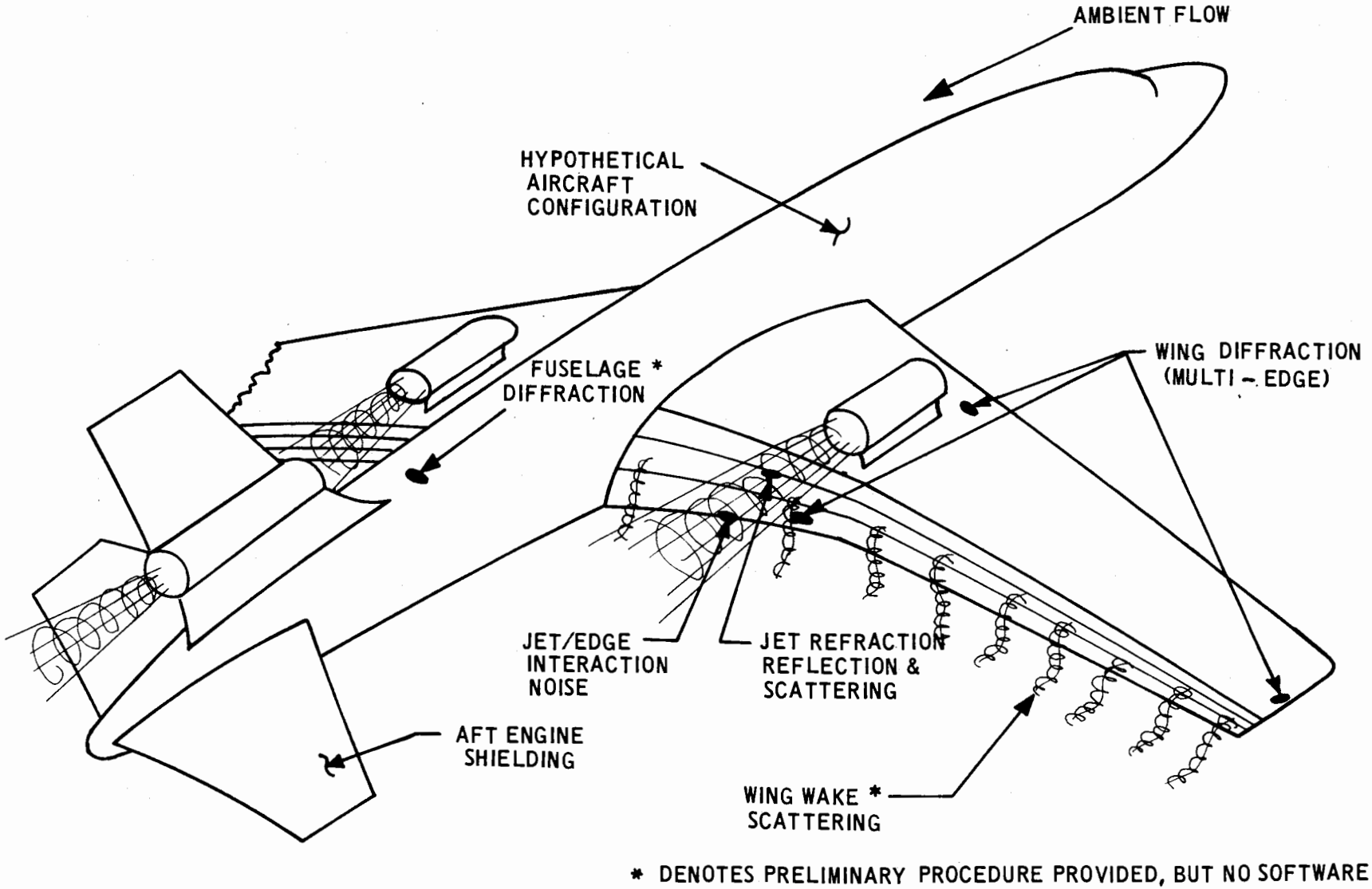

Figure 1.—Aircraft Configuration Noise Reduction Factors Influencing Predictions

place. The tests ranged from model-scale to full-scale engine ground tests and from static to flight tests. The types of noise sources simulated ranged from compact to distributed sources for noise emanating from exhaust jets. Barrier geometries tested encompassed the flat board, model, and full-scale wing/flap systems, as well as a cylinder. Three types of flow conditions were simulated in the static tests: no flow, single-exhaust flow (hot and cold), and dual-exhaust flow with a hot primary and cold secondary. In conjunction with the numerous static tests, four different types of tests were conducted to investigate flight effects on shielded noise. These involved a powered nacelle wind tunnel test, an open throat/open cycle tunnel test for jet/edge interaction noise, an airborne/horn-on-wing flight test, and 727-100 and -200 airplane flight tests.

Wing Shielding of Turbomachinery Noise

A wing is very effective at shielding turbomachinery (TM) noise because the noise emanates from locations close to the engine's inlet or exit. Figure 2 illustrates the idealizations that describe wing shielding of exhaust TM noise including core noise. An EOW configuration is represented by a noise source placed at the nozzle exhaust centerline above a set of equivalent half-planes. With jet exhaust flow, this source appears axially distributed and the radiated acoustic field becomes very directional. This distributed source can be represented as a set of apparent directive/compact sources, one for each wing edge. Each of these apparent sources is assumed to have the same far-field radiation characteristics of an actual engine's discharge TM noise component. Using diffraction theory, the apparent source location becomes the key variable that determines how much sound propagates around the edge. Jet refraction theory for wave propagation through shear flow is used to specify the location of these apparent source(s). Empirical terms are introduced to modify the refraction theory estimates so they agree with shielding test data observations. After the apparent sources are located for each wing edge, diffraction theory is used to calculate the sound emanating from the edges to the observer in the shadow zone beneath the wing. A random-phase superposition of edge solutions is used to calculate the total observed sound field.

Wing Shielding of Jet Noise

A wing is much less effective at shielding jet noise (compared to TM noise) because the noise source extends a large distance downstream of the engine. Since a compact noise source model is not possible for jet noise, a strictly empirical approach is used. An empirical procedure is defined based on methods and data from von Glahn and Boeing/Aeritalia data. These data show qualitative agreement with theoretical considerations. In addition, the shielded jet noise appears to follow the same relative velocity scaling relationships as unshielded jet noise. Hence, flight effects are automatically included in the jet noise shielding estimation procedure by referencing sound attenuation to the unshielded flight jet noise.

Jet/Edge Interaction Noise

The interaction of engine exhaust with the edge of a shielding structure generates additional noise that is otherwise absent. This noise is termed jet/edge interaction noise. The method used to estimate this new source combines both theory and test data.

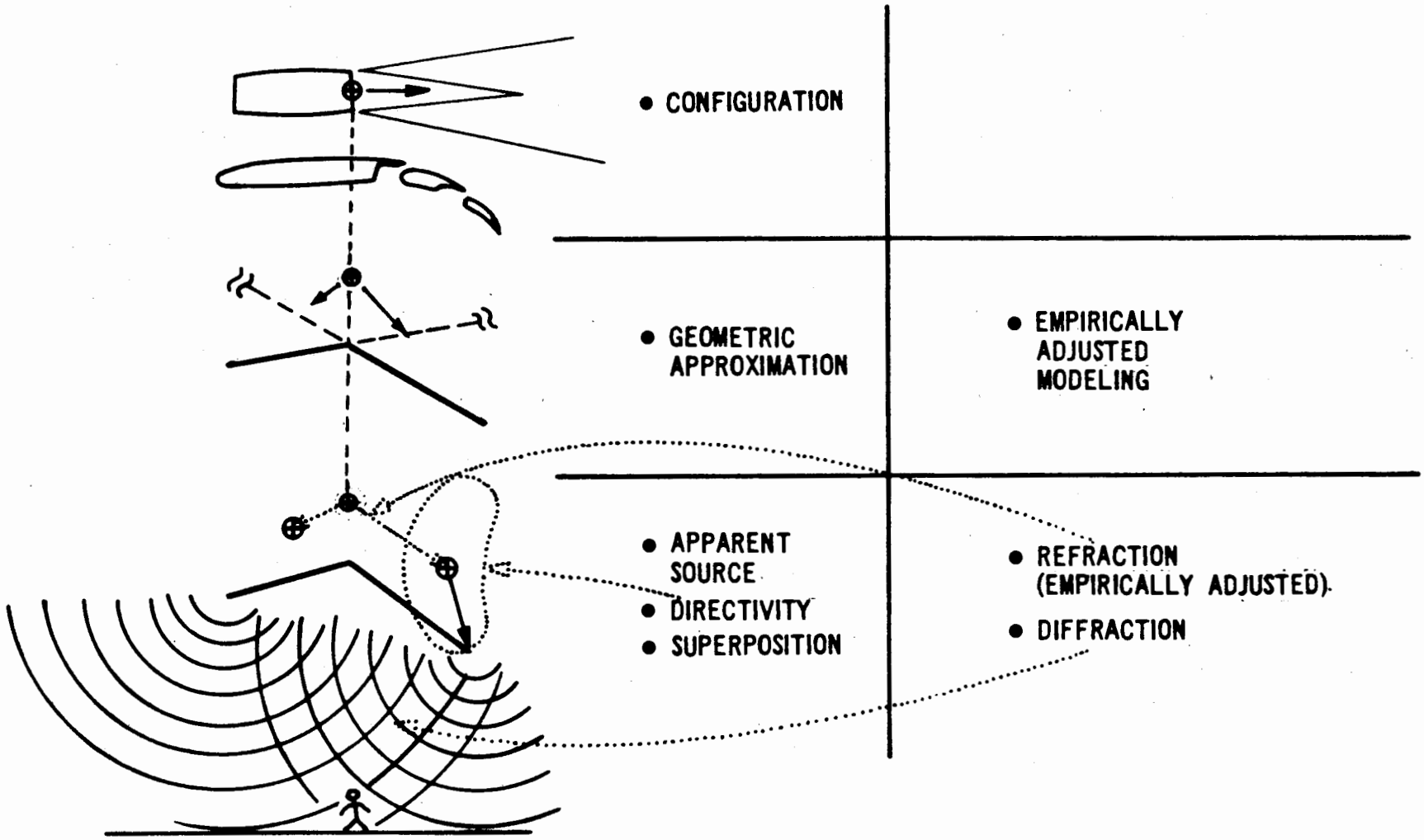

Figure 2.—Wing Shielding of Exhaust Turbomachinery Noise

Diffraction theory for hydrodynamic pressure fluctuations near an edge is used to estimate noise radiation from turbulent jet flow over the wing's trailing edge. The theory provides the general form of the estimation equation. Boeing/Aeritalia test data are used to define empirical adjustments to this equation. This enables development of relationships describing the effect of varying shield length and nozzle height above the shield surface. Ambient flow effects on jet/edge interaction noise generation are considered theoretically and verified for shield lengths shorter than the jet potential core (approximately five nozzle hydraulic diameters long). The jet/edge interaction noise for shields of this type follows a relative velocity to the fifth power scaling relationship for the overall sound pressure level. The resulting procedure is compared with independent NASA test data. The comparisons are favorable.

Flight Effects on TM Noise Shielding

The effects of flight on wing shielding are uncertain. Flight influences four processes important to wing shielding of exhaust TM noise:

- Jet refraction
- Wing diffraction
- Wing wake refraction
- Wing wake scattering

In the first two processes (jet refraction and wing diffraction), flight effects are handled by coordinate transformations for wave propagation in flow. The net effect on the noise observed in the zone on the opposite side of the barrier is estimated to be:

- A large decrease in noise propagation about the wing's trailing edge
- A small increase in noise propagation about the wing's leading edge

The third process (wing wake refraction) appears to have negligible effect on the noise observed under an airplane's flightpath, except possibly lowering the noise observed at extreme sideline positions where there is no community noise problem. The last process (wing wake scattering) indicates additional sound can enter a wing's shadow zone and can set a limit on the noise reduction provided by the wing. This limit or noise floor set by scattering increases with flight speed. Considering all the processes above for the trailing edge, opposing effects theoretically occur due to flight. The opposing factors can tend to be equal, giving a net result of no change or a slight increase in shielding effectiveness. As noted above, theory predicts the leading edge case will have a moderate loss in shielding effectiveness associated with ambient flow.

Available test data simulating flight for TM noise shielding show, on the average, small changes in sound attenuation relative to static test data. This tends to substantiate the theory above in part, but it is believed the data are too incomplete to verify the theory. This uncertainty is associated with known test problems, i.e., failure to isolate the phenomena of interest, contamination of data by unwanted noise sources, reverberation,

etc. For the present it is recommended that the effects of flight on shielding attenuations be assumed negligible.

Estimation Method

Both computer software and manual methods are provided for airframe noise shielding estimation. Figure 3 gives an overview of major elements considered to estimate wing shielded exhaust TM noise components. The sketches show the engine/wing configuration and the typical perceived noise level (PNL) time history of a noise component. A similar estimation method is used for inlet noise, except the center of the inlet plane is chosen for the apparent source location. The final estimation procedure actually encompasses more applications than shown in figure 3; i.e.,

- Wing/flap system or lifting surface shielding of inlet fan or compressor, exit fan, turbine, core, and jet noise components
- Jet/edge interaction noise generation
- Wing wake scattering
- Fuselage shielding and reflection for compact and distributed noise sources

The first two capabilities merit computer programming based on test substantiation and are included in the new community noise estimation software. Coordinate transformations accounting for ambient flow effects in the jet refraction and wing diffraction processes are included in the software for optional use. The last two capabilities (wing wake scattering and fuselage shielding) are preliminary and are defined herein as manual estimation procedures. The results from the manual estimation procedures can be input to the new computer software to evaluate the impact of wing wakes and/or an aircraft fuselage on the airplane's community noise.

The new computer software can be used by an aircraft designer to conduct noise trade studies. Used in conjunction with a test program, an airplane configuration can be optimized for maximum noise shielding reductions. Configuration optimization without a corresponding test program entails unreasonable risk. Using this "tool," the designer can consider the following factors:

- Engine/wing/fuselage geometry
- Engine exhaust flow conditions
- Directivity and spectrum shape of individual noise sources
- Flight speed
- Flyover or sideline observer geometries

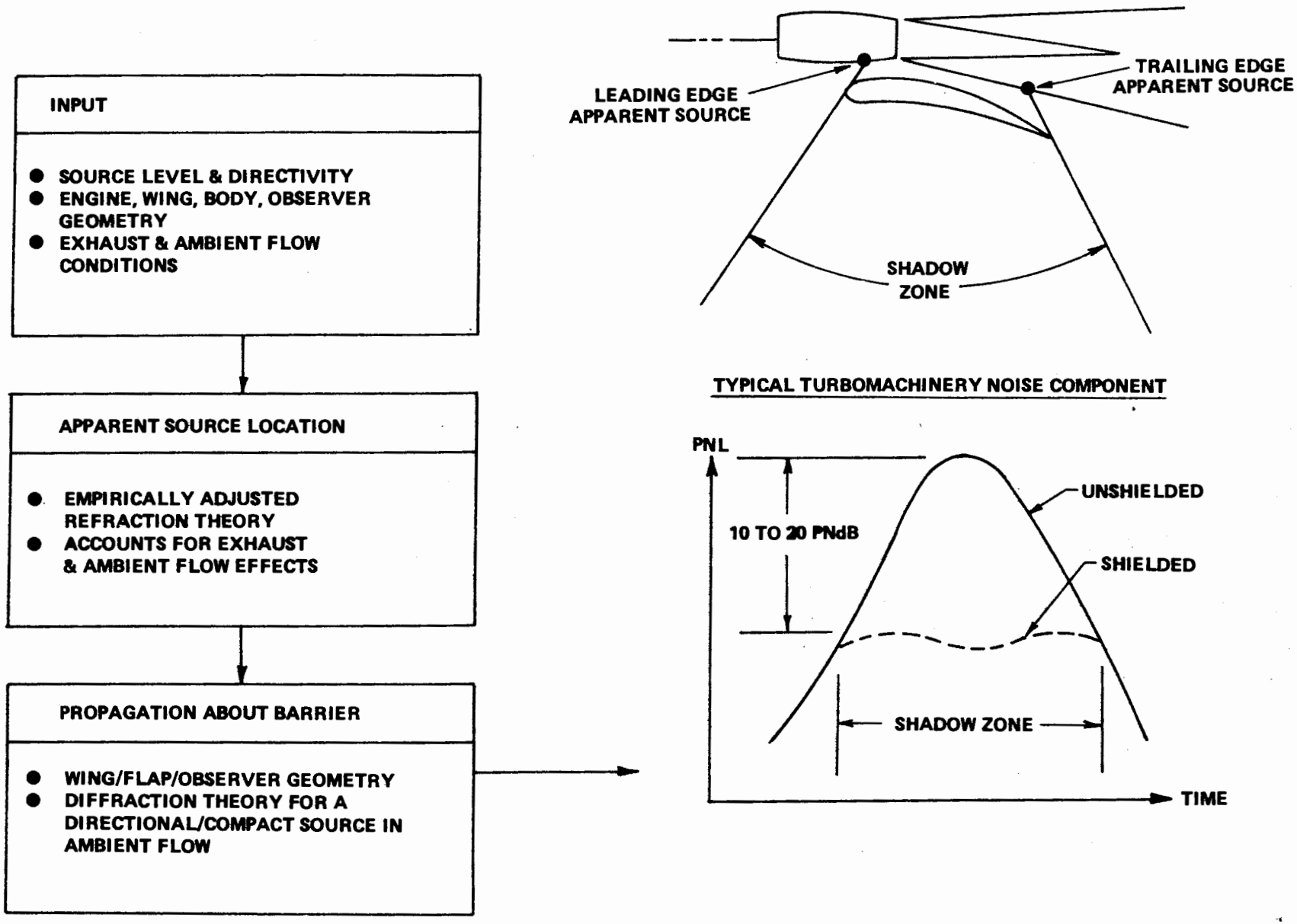

Figure 3.—Shielding Estimation Procedure for Exhaust Turbomachinery Noise Components

Typical Results

A realistic example is provided to illustrate results calculated by the computer program and noise reduction features attributed to shielding. Figures 4 and 5 show the estimated community noise levels of an EOW configuration in comparison to an engine-under-wing (EUW) configuration. The results are typical of current high-bypass-ratio (BPR = 5) turbofan engines. For this example, the inlets of the two configurations are different. The EUW has a short hardwall inlet whereas the EOW's inlet has peripheral lining treatment and extended length so that the benefit of aft arc noise reduction by shielding is partially balanced by noise reductions in the forward arc. The estimated results for the EUW configuration would not change significantly even if it had the same inlet as that selected for the EOW configuration. Hence, it appears that the EOW configuration with high-bypass-ratio engines offers additional noise reduction potential of 8, 5, and 6 EPNdB for takeoff, sideline, and approach conditions, respectively.

The relative importance of individual noise source components is shown in figure 4. The estimated EOW noise sources in the order of importance are inlet fan, exit fan, core, jet, turbine, and jet/edge interaction noise. This indicates that further noise reduction might be realized by additional inlet duct and fan exhaust duct lining. Also, jet/edge interaction noise doesn't appear to be a community noise problem. However, since jet/edge noise is primarily low-frequency sound and the high-frequency sound is shielded, an EOW configuration might be discernible from conventional EUW aircraft by subjectively appearing to have more "rumble" (see spectra shown in fig. 5).

For takeoff, figure 5 shows typical perceived noise level (PNL) time histories for both the EOW and EUW configurations. Noise reductions in excess of 15 PNdB are possible by use of the EOW concept. However, in units for effective perceived noise level (EPNL), the reductions are less because the time history is "double peaked" and appears longer in duration. The noise level reductions may actually be somewhat larger (about 1.5 EPNdB theoretically) due to favorable flight effects.

Estimates using the computer program are compared with the limited test data base simulating flight. The comparison indicates that there are weaknesses in the flight effects theory (uniform flow and wing wake scattering) and uncertainties in the test data. Hence, the flight effects option incorporated in the program is too preliminary to justify general use. A tentative test program is defined to better evaluate the influence of flight on airframe shielding (app. B of the vol. II report). For the interim period, the computer program should be used without flight effects in the shielding calculations.

Further Research Needed

This work reveals areas requiring additional study and test. These areas deal with the effect of flow on shadow zone noise levels. There are three important flow regions: jet, ambient, and wing wake. Each region needs independent examination. The available data base deals largely with high-bypass-ratio turbofans. Additional research needs to consider the changes in shielding due to engine cycle variations with bypass ratio. There is also a strong need to carefully control reverberation and stray flanking path radiation in future shielding tests.

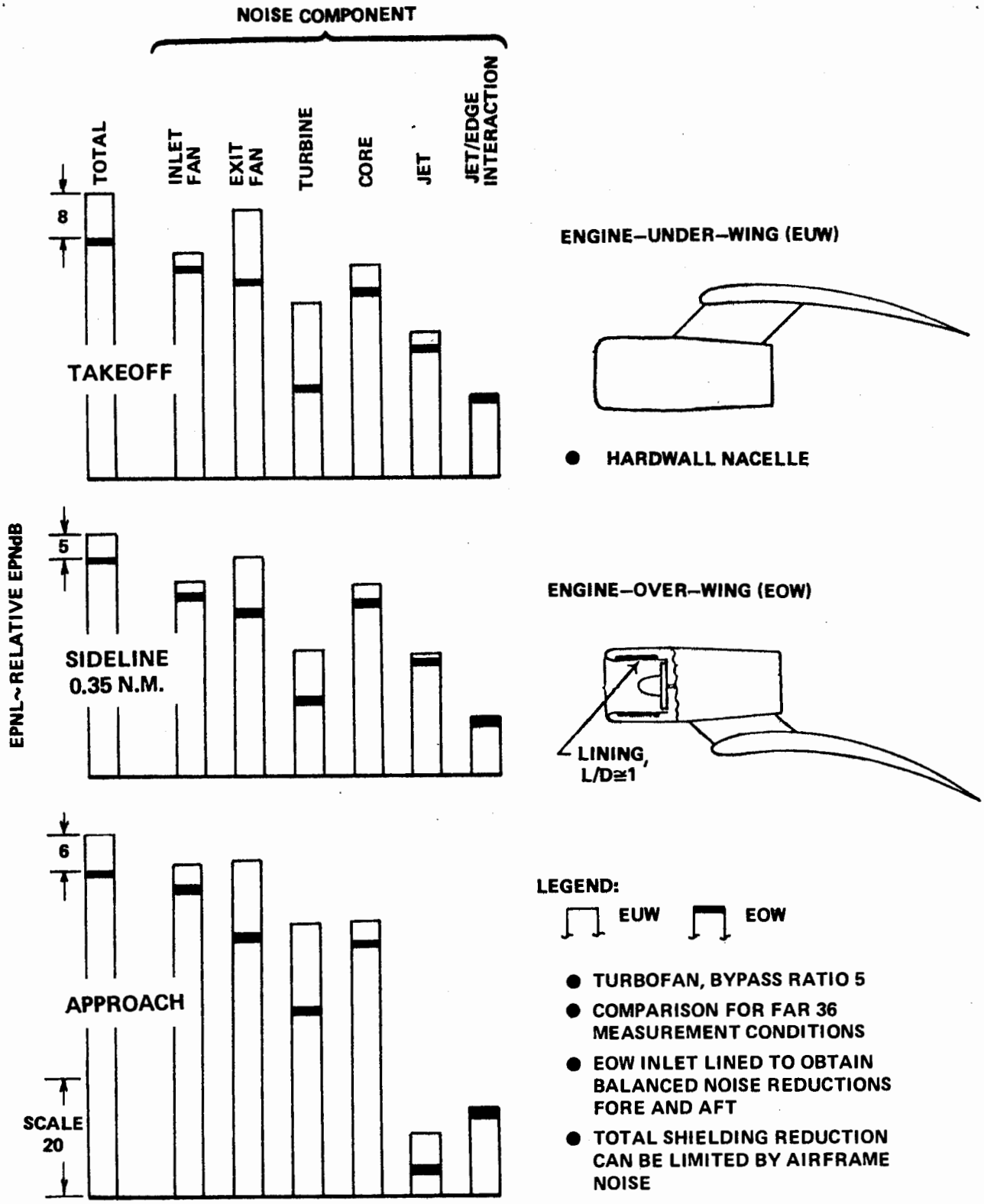

Figure 4.—Potential for Typical EOW Shielding Noise Reduction

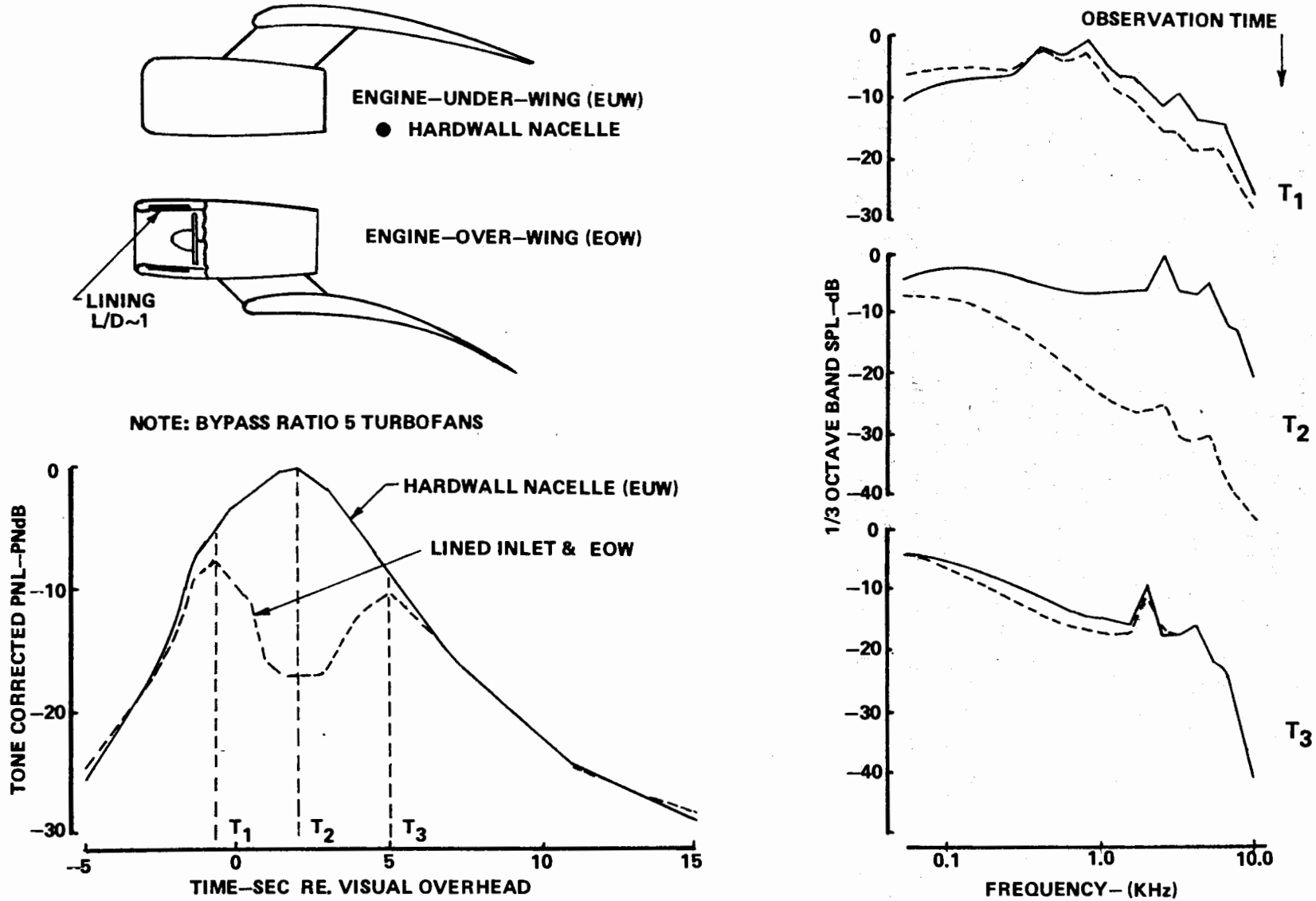

Figure 5.—Example Noise Estimation Capability (Takeoff)

Concluding Remarks

In conclusion, aircraft configurations using surfaces as acoustical barriers offer significant noise reduction potential. The engine-over-wing and engine-over-fuselage configurations use the positive aspects of engine installation effects for community noise reduction. The estimation procedures herein apply for these configurations. For high-bypass-ratio turbofan-powered aircraft, the EOW concept provides an average noise reduction potential of about 7 EPNdB compared to the EUW concept. Important results of the study are the determination of engine installation effects and how these effects change with an engine/airframe configuration, exhaust flow conditions, and flight speed. The flight test simulation and fuselage shielding data bases are inadequate. Otherwise, the data base for wing/flap shielding geometries is fairly extensive. From this data base and available theory, an analytical shielding estimation procedure is defined for community noise predictions. The procedure is, in part, programmed for the computer and can be used for trade studies. The estimation procedure can be used to determine wing shielding attenuation to an accuracy of about ±2 EPNdB. Many aerodynamic and structural design aspects of engine-over-wing aircraft need to be further developed before commercial transports can realize the potential noise reduction benefits of airframe shielding. This study clearly shows that configuration shielding has noise reduction potential that needs to be developed further.

1.0 INTRODUCTION

This report presents a study of community noise reduction from favorable jet engine placement with respect to aircraft structures. Current engine-under-wing (EUW) airplanes are configured without regard to use of the wings and/or fuselage as acoustical barriers. However, use of these aircraft elements as "noise shields" appears to provide significantly lower community noise levels relative to EUW placement. Hence, estimation methods to quantify these shielding benefits are needed.

The purpose of this effort is to develop an aircraft noise shielding estimation method. Shielding of aircraft engine noise has previously been considered by DiBlasi et al. and Hellstrom (refs. 4 and 5). These works showed that, by proper selection of apparent source locations, diffraction theory estimates agree reasonably well with static engine shielding test data. However, these efforts were not done in sufficient generality for estimation of aircraft noise shielding flybys. This effort extends the previous efforts by including jet flow and flight effects in the estimation procedure and implements the method in an integrated computer program for community noise source and contour estimation.

The present study is concerned with jet aircraft engine noise. This noise can be grouped as

- Turbomachinery (TM) noise generated within the engine and escaping via inlet and exhaust ducts

- Jet exhaust noise generated outside the engine (aft of exhaust nozzles) in the region of intense jet temperature and velocity gradients, and turbulent activity

Turbomachinery noise includes compressor, inlet fan, exit fan, turbine, and core noise. Jet exhaust noise includes jet and jet/edge interaction noise. Jet noise arises from the interaction of the exhaust fluid with the ambient air. Jet/edge interaction noise arises from the interaction of the exhaust fluid with any nearby surfaces.

The biggest payoff for shielding is in the reduction of turbomachinery noise components observed in the community. This is because these noise components appear near the engine in contrast to the extended locations of jet noise generation. Hence, wing shielding from engine-over-wing (EOW) configurations is particularly applicable to high-bypass-ratio turbofan engines with their relatively lower jet noise and higher turbomachinery noise. Potentially significant aircraft engine noise reductions can be achieved in the community by the joint use of shielding and the more conventional engine lining and jet suppression. However, two additional factors need to be considered before the full shielding potential can be realized.

The aerodynamic viability of EOW configurations is not fully demonstrated. In addition, the full effectiveness of EOW shielding used in combination with other more conventional noise reduction methods will be limited by airframe noise. This more recently detected noise is caused by the interaction of the moving airframe with ambient air. Airframe noise levels are only 8 to 10 dB below current FAR 36

certification requirements and represent a noise floor. Both aerodynamic performance and the airframe noise floor are practical aspects of realizing both high performance and reduced community noise from EOW configurations. Neither performance nor airframe noise were considered in this effort. However, this is required before EOW commercial transports will be developed.

This study emphasized configurations expected to provide effective perceived noise level reduction in the community. Hopefully this can be achieved without sacrificing economics. Note that airframe structures can act as shields for observers in certain regions called shadow zones and as reflectors in other regions. Figure 6 shows classes of aircraft configuration concepts for which one might envision significant shielding and reflection effects:

- Engine-under-wing (EUW)
- Engine-beside-body (EBB)
- Engine-over-fuselage (EOF)
- Engine-over-wing (EOW)

All these concepts are in current use, although not necessarily for the benefit of community noise. For airframe structures to act beneficially (as shields), the engine(s) must be placed so the structures are between the engine and the observer. Figure 6 gives a brief evaluation of different configuration concepts. The EOW and EOF are logical choices for reducing community noise.

Available data are much more extensive for the EOW than for the EOF configurations. This is a result of the EOF concept being generally viewed as less practical for multiengined airplanes. Hence, both past shielding efforts and this effort deal mainly with the EOW concept, although the EOF case is considered to the extent available theory and data permit. Table 1 shows an overview of the type of data available for use during this study. Sound from a source on one side of a barrier such as a wing can penetrate into the "shadow zone" on the opposite side of the barrier by four modes:

- Transmission through the barrier
- Refraction by any steady-state velocity and/or temperature gradients
- Scattering from turbulence and/or vortices
- Diffraction about the barrier in an otherwise homogeneous medium

Additional sound can also be generated when the engine exhaust interacts with the barrier. This additional sound also penetrates into the shadow zone. Hence, these five mechanisms are important to understanding shielding and to formulate a shielding estimation method.

CONFIG. (TYPICAL AIRCRAFT)	PRINCIPAL REDUCTION MECHANISM	PRINCIPAL ENHANCEMENT MECHANISM
EUW (737,747,....)	NONE IDENTIFIED	JET/EDGE INTERACTION
EOF (727, DC-10,..)	BODY SHIELDING	NONE IDENTIFIED
EBB (727, DC-9, ..)	NONE IDENTIFIED	NONE IDENTIFIED
EOW (YC-14, VFW-614)	WING (TAIL) SHIELDING	JET/EDGE INTERACTION

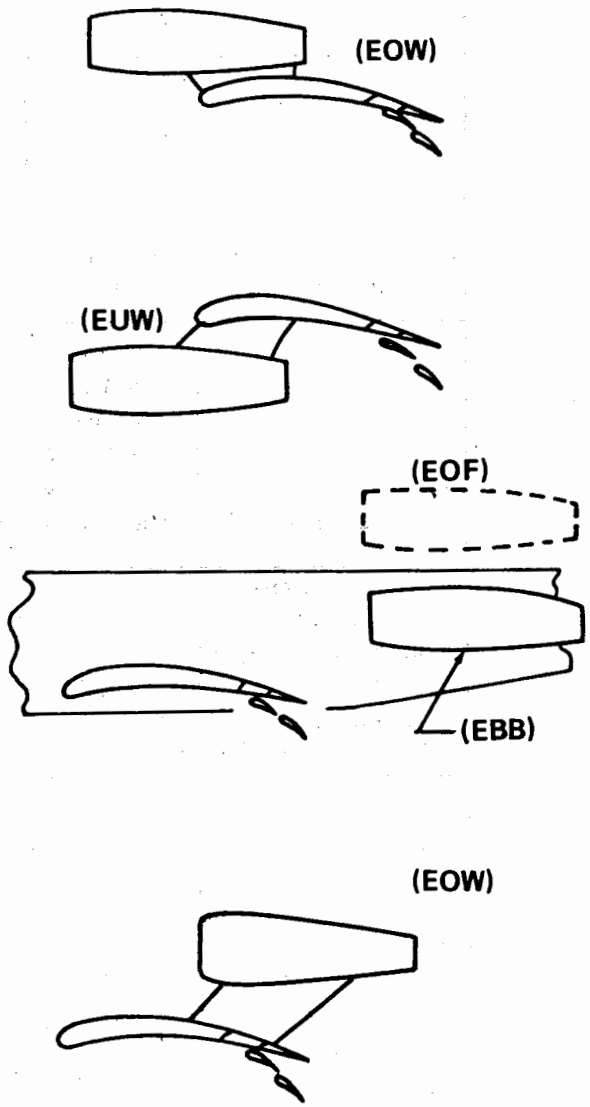

Figure 6.—Concepts for Evaluation of Aircraft Configuration Effects

Table 1.—Shielding Test Summary

Type of test		Type of noise source			
			Distributed source		
		Compact source	Fan, turbine, and core simulation	Jet	Jet/edge interaction
STATIC	No efflux	*Directional source with a) Flat board b) Wing c) Cylinder	● Whistle in nozzle placed over wing with double-slotted flap		
STATIC	Cold efflux (single flow)		● Model fan rig (0.3 m dia) with a) Flat board b) Wing/flap system with and without gaps	*2.5-cm-dia pipe (parametric model) with wing/flap system (EOW and EUW)	● D- and slot nozzle on wing/flap system
STATIC	Hot efflux (single and dual flow)		● Whistle in secondary flow (coannular/coplanar and D-nozzle) wing with double-slotted flap ● JT9D engine ground rig with and without wing shielding	● SST model jet with flat plate barrier	
Flight simulation		*Airborne horn-on-wing flight test	● Powered nacelle with wing/flap system (UARL tunnel) ● Inlet fan noise shielding by wing and fuselage (727-100 and -200 flight test)	● Single round and D-nozzle on wing in jet simulated wind tunnel	

● Shielding only

* Shielding and reflection

Briefly, sections 2.0 and 3.0 jointly contain a discussion of theory, a review of test information, and an analysis of theory and test, resulting in development of an estimation method that is compared against measurements. Section 4.0 summarizes the estimation method and the associated computerized and manual estimation procedures. Sections 5.0 and 6.0 present conclusions and recommendations, respectively. More detail on sections 2.0, 3.0, and 4.0 is presented in the paragraphs that follow.

Section 2.0 discusses the influence of wing and fuselage structures on turbomachinery noise components. Theory is discussed in sections 2.1 and 2.2. First, the available theory of sound diffraction from compact sources about semi-infinite half-planes and infinite cylinders is discussed and developed further. Both the diffraction theory for directional/compact sources and the influence of uniform flow are discussed. However, exhaust turbomachinery noise components may not appear compact, but rather might appear distributed because noise propagates from the nozzle out through jet flow gradients. Hence, modeling of extended sources by a compact/directional source is examined and shown applicable. This leads to introduction of the equivalent apparent source (location) and methods of determining these locations by examining shielded noise in far-field shadow zones. Hence, the theory of sound refraction through a jet is also discussed in terms of its relation to the shielding of exhaust turbomachinery noise. Next, theoretical consideration is given to flight effects on shielding, including the theory of wing wake refraction due to velocity deficits and the theory of sound scattering due to wake inhomogeneities.

In section 2.3 the discussion turns to the presentation of an extensive TM noise shielding test program completed jointly by the Boeing/Aeritalia companies. This test program deals with static and flight experiments ranging from scale models to full-scale engines and airplanes in flight. Experience gained from this broad background of test data served to focus the effort on practical key issues in addition to those noted for the theory above.

Section 2.4 compares the results of test with theory and shows the development of an estimation method for wing shielding of TM noise. Test results using small loudspeakers simulating compact/directional sources near simple shielding geometries and model wing/flap systems compare favorably with simple compact-source diffraction theory. Analysis of tests on both model- and full-scale turbofans with jet exhaust flow results in empirical determination of apparent compact-source locations for exhaust TM noise. Similarity is observed between apparent point-source locations implied by the shielded test data examined using compact-source diffraction theory and source locations predicted by jet refraction theory. Hence, apparent exhaust turbomachinery noise source locations are estimated with an empirically corrected jet refraction theory. Resulting estimated shielded noise levels compare favorably with test. Theoretical changes in shielding due to flight and test data are compared. Comparisons are not favorable, which could in part be due to insufficient information to accurately evaluate scattering and uniform flow effects.

Section 3.0 deals with wing shielding of the two jet exhaust noise components, i.e., jet and jet/edge interaction noise. Results are presented from tests completed independently by Boeing and jointly by Boeing/Aeritalia companies. An estimation

equation for jet noise shielding is developed based on these test data and an empirical procedure by von Glahn. A new noise source, jet/edge interaction noise, is discussed next and the effect of ambient flow (flight effects) is evaluated. Evaluation of measured jet/edge interaction noise and comparison with theory results in development of a semiempirical estimation method for jet/edge interaction noise. Favorable comparisons of estimates for jet/edge interaction noise with independent tests conclude section 3.0.

Section 4.0 is a summary of the shielding estimation method. Both computerized and manual estimation procedures are presented. The computer software for shielding has been incorporated into existing community noise estimation software developed earlier under contract NAS2-6969. A requirement for use of the new software is a working knowledge of results obtained under the previous contract, as reported in references 2 and 3.

The computerized procedures deal with the shielding influence of a wing on TM and jet exhaust noise components and have a substantial backup of static test data and/or firm theory. The manual estimation methods not computerized because of limited test data and/or limited theory are those dealing with fuselage shielding and wing wake effects. Estimations using the manual methods can be input to the new computer software for community noise estimations. A realistic example problem is discussed to illustrate the computerized prediction capability.

The introduction above refers to the contents of volume I, *Engineering Analysis*. The complete effort is reported in three volumes. The remaining two are

- Volume II, *Computer Program User's Guide and Other Appendices*
- Volume III, *Computer Program Listing*

Appendices to material discussed in volume I are grouped in the volume II report.

2.0 INFLUENCE OF WING AND FUSELAGE STRUCTURES ON TURBOMACHINERY NOISE COMPONENTS

This section discusses the influence of the aircraft wing and fuselage on the noise radiation of turbomachinery noise components of turbofan engines. Emphasis is placed on shielding provided by these structures. First, previous work in the three areas of diffraction, refraction, and scattering is briefly reviewed in section 2.1. Available theory for these three areas is applied in section 2.2 to describe characteristics of turbomachinery noise sources emanating from turbofan engines and propagating around wing and fuselage structures in motion. The effect of jet exhaust noise in the close presence of wing shielding surfaces is discussed later in section 3.0. Extensive Boeing/Aeritalia and other Boeing noise shield data for turbomachinery noise components are thoroughly reviewed in section 2.3. Section 2.4 concludes with an evaluation of this test program, resulting in a semiempirical analytical estimation procedure for turbomachinery noise shielding by wing/flap systems.

2.1 SCOPE AND PREVIOUS WORK

In this section, the problem of airframe shielding is first discussed in specifics. The applicability and shortcomings of previous work are summarized. The approach used in this study is briefly summarized. This is followed by a review of previous work in the areas of diffraction, refraction, and scattering.

An extensive literature survey was made at the onset of this study. The material considered to be within the scope of the study is listed in the bibliography. Considerable research has been done in the theories of diffraction, refraction, and scattering, but not in the complete context of airframe shielding of turbofan engine noise. All previous works (secs. 2.1.1 through 2.1.3) consider only one or two idealized aspects of the problem, and none of the following:

- The sound source can be imbedded in a hot turbulent jet flow.
- Ambient flow can surround the jet flow.
- Jet flow may not be completely attached to the shielding surface.
- The spatial distributions of the noise source(s) are unknown.
- The shielding barrier may have a strong wake behind it that can refract and scatter sound.

An attempt has been made in this report to consider these factors in addition to the theory already available. We have attacked the problem using theoretical Green's function solutions in conjunction with the concept of a directive/compact source. We have incorporated some empiricisms to make the theoretical formulations fit experimental data. This approach, though approximate, contains the essential trends

implied by theory and the quantitative results observed in tests. It permits some cautious interpolation and extrapolation into regions where information is presently lacking.

Consideration of the shielding of turbomachinery noise components required the combined use of two relatively independent phenomena: (1) jet refraction and (2) diffraction of sound about a barrier. These fundamentally differing wave propagation mechanisms were used jointly in determining the apparent sound emission point between the engine's nozzle exit and the barrier's edge. We have used a ray acoustic refraction model to determine the preferential noise emission angle relative to the jet axis. This direction angle is then used to specify an apparent source position that permits a diffraction formula to fit experimental shielding data. It should be recognized that the apparent point-source concept violates a physical reality–the noise source has a spatial distribution. Hence, near-field implications that result from this modeling should not be taken too seriously. The concept has merit because it reduces the complexity of the problem to consideration of simple wave theory and includes a minimum number of empiricisms. It also avoids complicated integrations that a more detailed source model would require.

The possibility of strong flow wakes behind the barrier required the study of two additional phenomena:

- Wing wake refraction
- Wing wake scattering

We have considered both aspects of the wing wake using theoretical refraction and scattering models. In the first case, noise attenuation appeared possible; in the second, a wing shielding attenuation limit was implied. Unfortunately, the paucity of experimental data did not permit the development of reliable estimation methods for these two phenomena. However, preliminary estimates using the theory indicate that the wing wake can have a significant impact on airframe shielding.

2.1.1 DIFFRACTION

Prior to about 1900, the diffraction of light and sound was treated theoretically by approximate methods developed by Huygens, Kirchhoff, and Fresnel (ref. 6). At the turn of the century, Sommerfeld (ref. 6) solved exactly the diffraction problem for plane waves incident to the straight edge of a thin, flat, semi-infinite half-plane. When radar scattering problems became important during the Second World War, further significant advances in diffraction theory were made. Copson, Schwinger, Clemmow, and others (ref. 7) introduced integral formulations based on the application of the Fourier transform to partial differential equations for which exact solutions could be found using the Weiner-Hopf technique (ref. 8). Closed-form solutions were found for the diffraction of plane (refs. 9 and 10), cylindrical (refs. 7 and 8), and spherical waves (refs. 6 and 10) about a straight-edge half-plane. A uniformly convergent series solution was also found for the diffraction of spherical waves about a cylindrical body (ref. 10).

Diffraction of sound about a barrier in a moving media has been addressed within the recent 20 years by Adamczyk, Candel, Chase, Crighton and Leppington, Ffowcs-Williams and Hall, Jones, and others (refs. 11 through 22). Adamczyk, Candel, and Jones considered the case of uniform flow about the half-plane. Chase, Crighton and Leppington, and Ffowcs-Williams and Hall considered the case of turbulent flow attached to one side of the half-plane and the determination of the sound field in the stationary medium.

It was found for the uniform flow case that the solution could be expressed in the same mathematical form as the case without flow. The solution confirmed the intuitively expected result that the radiation pattern for the diffracted sound field is "skewed" toward the direction of flow. On the other hand, the case of turbulent flow interacting with the barrier generated additional sound due to a fluctuating pressure field near the edge. Ffowcs-Williams and Hall, and Crighton and Leppington, treated the problem within Lighthill's formulation of aerodynamic sound by dealing with a volume distribution of quadrupoles near the edge. They found that the dominant contributors to the radiated sound in the stationary medium were due to sources within a characteristic eddy scale distance from the edge. Chase took their results one step further by reducing the volume integral solution to a surface integral. He explicitly related the quadrupole source model for subsonic turbulent flow to a wave-vector/frequency spectral density model of hydrodynamic pressure. This treatment circumvented the difficulty of not having detailed knowledge about Lighthill's volume source distribution by replacing the distribution with a measurable quantity–hydrodynamic pressure on the barrier.

2.1.2 REFRACTION

The effects of flow about an acoustical barrier require the consideration of refraction in addition to diffraction. The principles of sound refraction have been known for quite some time (1878), i.e., Lord Rayleigh (ref. 23). Initial applications of these principles to practical situations occurred with the advent of sonar. Only recently has refraction theory been applied to problems of sound propagation in air.

In the 1950's, Miles (ref. 24) and Ribner (ref. 25) addressed the effects of sound refraction at the interface between fluids at different velocity and temperature. Ribner pointed out that three fundamentally different phenomena can occur:

- Ordinary reflection and transmission
- Total reflection with an exponentially decaying disturbance in the other medium
- Amplified reflection and transmission

He also examined the energy balance and concluded that the moving fluid is the source of energy for the amplified waves. Recently, C. Yeh (ref. 26) solved the problem of two surfaces of discontinuity that represent a layer of fluid between two semi-infinite regions. Yeh's solution was quite general in the sense that the fluid properties and velocities of all three regions could be arbitrarily assigned. Schubert (ref. 27) considered the refraction effects of the sound radiated from a free round jet with both a ray and

wave acoustic model. He illustrated that a ray acoustic model alone was inadequate for specifying the refraction effects on the far-field sound radiation pattern emanating from the jet. H. Y. Lu (ref. 28) considered the refraction of sound for a source imbedded in a jet but attenuated by a thin hot jet surrounding the inner jet. Butler et al. (ref. 29) examined the refraction effects due to a vortex set up by flow about a delta wing. He found good *qualitative* agreement between ray acoustic theory and experimental data at high frequencies, i.e., greater than 4 kHz. His opinion was that *quantitative* agreement between experimental data and a wave acoustic theory would likely result provided the detailed velocity field was known.

2.1.3 SCATTERING

There are inhomogeneities in the wake behind a wing shielding barrier for an aircraft in flight. This necessitates consideration of scattering in addition to diffraction and refraction.

Scattering theory has been a recent development; early works first appeared in Russian literature around 1940. All the investigators on this subject have based their theories on a small-perturbation analysis of the equations of fluid motion. In the mid-1950's, Lighthill (ref. 30) and Batchelor (ref. 31) studied scattering by jet turbulence. Tatarski (ref. 32) completed a major work in 1961. However, an omission by Tatarski was corrected by Monin (ref. 33) in 1962.

Monin's formulation treats scattering by both velocity and temperature fluctuations, but it necessitates that the mean flow is uniform and that multiple scattering effects are negligible. A necessary input to this model is the specification of the properties of the turbulent fluctuations.

Wake turbulence has been studied experimentally by Townsend (ref. 34) and Uberoi and Freymuth (ref. 35) far downstream of circular cylinders. Unfortunately, the most important turbulence information, i.e., that applying to the wake close behind an airfoil, is almost nonexistent. Some data was published by Clark (ref. 36) for the near wake of an airfoil. We have combined this turbulence information with Monin's theory to permit the impact of wing wake scattering on airframe shielding to be determined within an order of magnitude.

2.2 SOME BASIC THEORETICAL ELEMENTS

Diffraction, refraction, and scattering theories are considered logical methods for describing noise shielding provided by acoustical barriers such as a wing or fuselage. In this section, the available theoretical solutions are examined to explore their use to characterize airframe shielding of turbofan engine noise components. Existing far-field compact-source diffraction solutions are illustrated and discussed for the following barrier types:

- Semi-infinite half-plane
- Infinite cylinder

For the half-plane, the compact-source solution is extended in this section to include a directive sound source. The effect of noise source spatial distribution is addressed in general, and examples are given for certain idealized source models. The effect of finite bandwidth sound detection equipment is also approximated. Attention then turns to the impact of flow on propagation of sound around a barrier. Consideration of flow is broken down into three categories:

- Uniform flow
- Jet flow
- Wing wake

A modified Lorentz coordinate transformation is used to describe the effects of uniform flow. The jet flow case is idealized by simple ray acoustic refraction theory, ignoring the scattering and ducting effects that can be present. These latter effects are then included by the introduction of empirical parameters determined from test data. The discussion of wing wake refraction and scattering concludes this theoretical section. These basic theoretical elements have helped interpret the data acquired in an extensive test program and are basic building blocks for our final prediction procedure.

2.2.1 HALF-PLANE DIFFRACTION

2.2.1.1 Compact Source

Uniform Radiator.–Consider the situation illustrated in figure 7, where a compact source is placed in the vicinity of a thin, semi-infinite half-plane. The acoustic field, p_T, can be found by solving the following boundary value problem:

$$\nabla^2 p_S + K^2 p_S = 0 \tag{1}$$

$$\frac{\partial}{\partial y} p_T = 0 \qquad \text{on the half-plane} \tag{2}$$

where the time (t) variation, exp (i 2π f t), has been suppressed, and

p_S = scattered field

p_T = total field = $p_I + p_S$

p_I = incident field = $\exp\left[i\,\overline{K}\cdot(\overline{r}-\overline{r}_0)\right]\Big/\left[\overline{K}\cdot(\overline{r}-\overline{r}_0)\right]$

r_0 = vector to source coordinate

$\overline{r}$ = vector to observer coordinate

$\overline{K}$ = wave number vector of magnitude $K = 2\pi\, f/C_0$ in direction $\overline{r}$

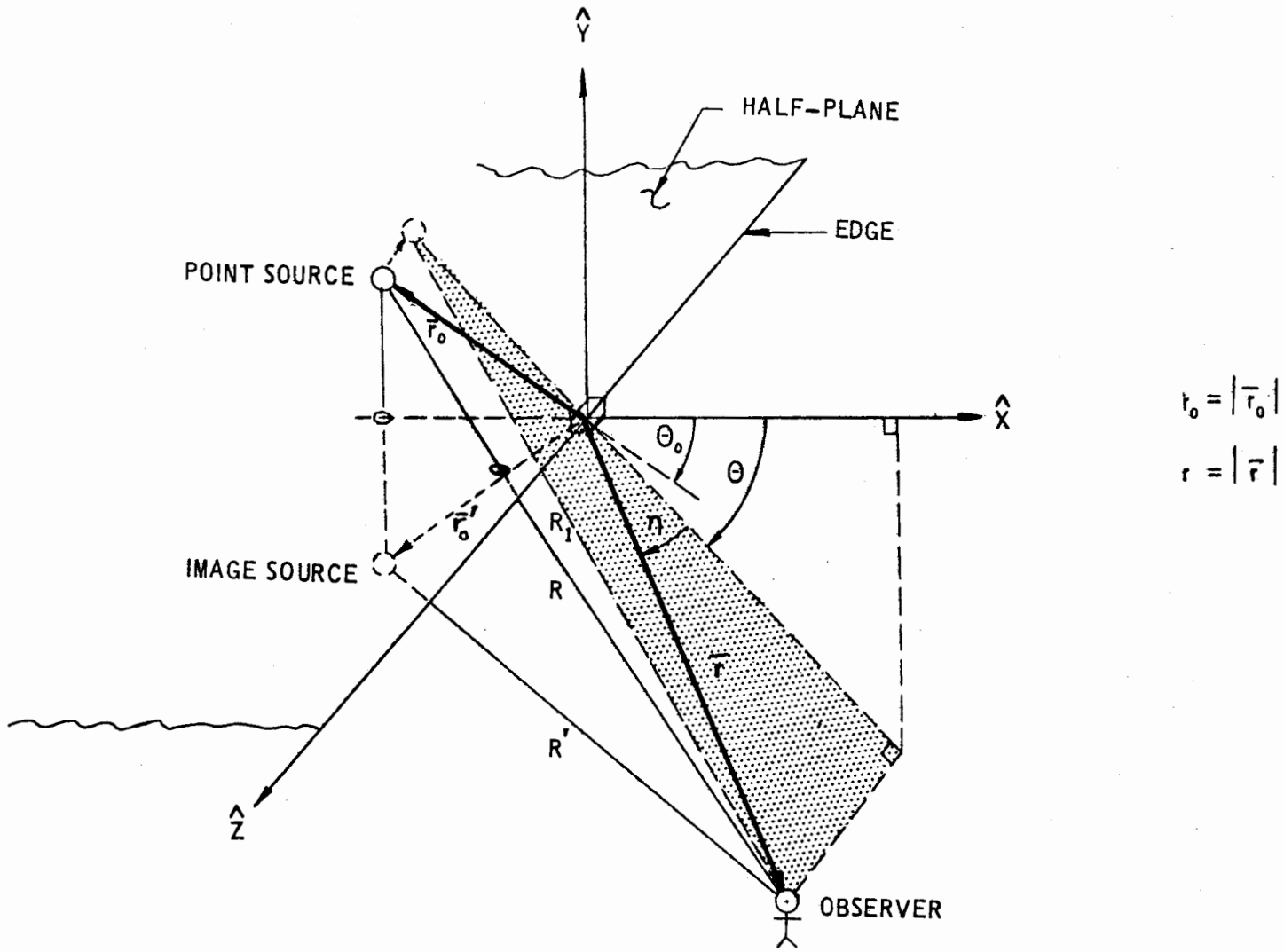

Figure 7.—Geometry for Half-Plane Diffraction

$[\bar{K} \cdot (\bar{r} - \bar{r}_o)]$ = is assumed to be large, i.e., greater than 10

f = frequency (Hz)

This problem has been solved by numerous investigators, as discussed in section 2.1.1. The solution is given by

$$p_T = p_I \, G(\bar{r}|\bar{r}_o) \tag{3}$$

where G is the Green's function solution of the problem in the asymptotic limit; i.e.,

$$G(\bar{r}|\bar{r}_o) = \frac{R}{\sqrt{R_1 (R_1 + R)/2}} F[\sqrt{K (R_1 - R)}] + \frac{R}{\sqrt{R_1 (R_1 + R')/2}} \exp[-i K (R - R')] \, F[\sqrt{K (R_1 - R')}] \tag{4}$$

with (R_1, R, R') being defined in figure 7 and

F(z) = complex Fresnel integral (ref. 37)

$$= \frac{1}{\sqrt{i\pi}} \int_Z^{\infty} \exp(i x^2) \, dx \tag{5}$$

In the acoustic far field, i.e, $r >> r_o$, this solution simplifies to

$$G(\bar{r}|\bar{r}_o) = F(a\,b) + F(a\,c) \exp(-i\,a^2\,d) \tag{6}$$

where the terms (a, b, c, d) are defined in terms of the variables $(K\,r_o, \eta, \theta, \theta_o)$ in figure 7 as follows:

$a^2 = 2\,K\,r_o \cos\eta$

$b = \sin[(\theta - \theta_o)/2]$

$c = \sin[(\theta + \theta_o)/2]$

$d = \sin\theta \sin\theta_o = [\cos(\theta - \theta_o) - \cos(\theta + \theta_o)]/2$

The total sound field given by equation (6) equals the diffracted incident field, plus the diffracted image field delayed in phase to account for the difference in path length between the source/observer and an image source/observer. This interpretation will be useful when we address the directive radiator.

Another observation about equation (6) is that the sound field for a discrete tone source is a function of only three dimensionless variables: $(K\,r_o \cos\eta, \theta - \theta_o, \theta + \theta_o)$. In the

shadow zone ($\theta > \theta_0$), the last variable ($\theta + \theta_0$) is not very important and the sound pressure level attenuation in dB can be written as

$$\Delta SPL = -10 \log_{10} |G|^2$$

$$\simeq H(K\, r_0 \cos\eta,\ \theta - \theta_0) \tag{7}$$

where

$(\theta - \theta_0)$ = shadow angle

$K\, r_0 \cos\eta$ = dimensionless effective barrier height

Typical trend charts for this attenuation are shown in figure 8. It appears that large attenuations are possible and that this attenuation is proportional to $10 \log_{10}(K\, r_0 \cos\eta)$ in the deep shadow zone of the half-plane. Figure 9 illustrates the complete radiation pattern about the half-plane. Three zones may be defined:

- Shadow zone for $\theta > \theta_0$
- Light zone for $-\theta_0 < \theta < \theta_0$
- Reflection zone for $\theta < \theta_0$

In the shadow zone, the sound field is dominated by a diffracted field emanating from the edge. In the light zone, the sound field is dominated by the incident field. In the reflection zone, the sound field is dominated by both the incident and the image fields, and a strong interference phenomenon results. The transition between each of these zones is accompanied by ripples in the radiation pattern that have been often called "diffraction rings."

A most significant result of this section is the reduction (grouping) of the variables for the far-field formula (eq. 6). Since community noise estimates apply strictly to the far field and the case for a real jet engine mounted over a wing is more complicated than a single half-plane diffraction problem, any simplification at the start is indeed convenient and desirable. We will make use of equation (6) in further discussion on wing shielding.

Directive Radiator.–The solution for the diffraction of sound emitted from a directive radiator in the presence of a simple barrier geometry (half-plane) without flow has never been addressed in the literature except for idealized sources: monopole, dipole, and quadrupole. Here a representative approximation is postulated based on the unshielded source's radiation pattern and a ray acoustic interpretation of diffraction. This choice of approximation is considerably less complex than an equally valid approach wherein simple sources are superimposed in such a manner to have a similar unshielded radiation pattern and the total diffracted field is calculated by integrating the contributions of each individual source via equation (6).

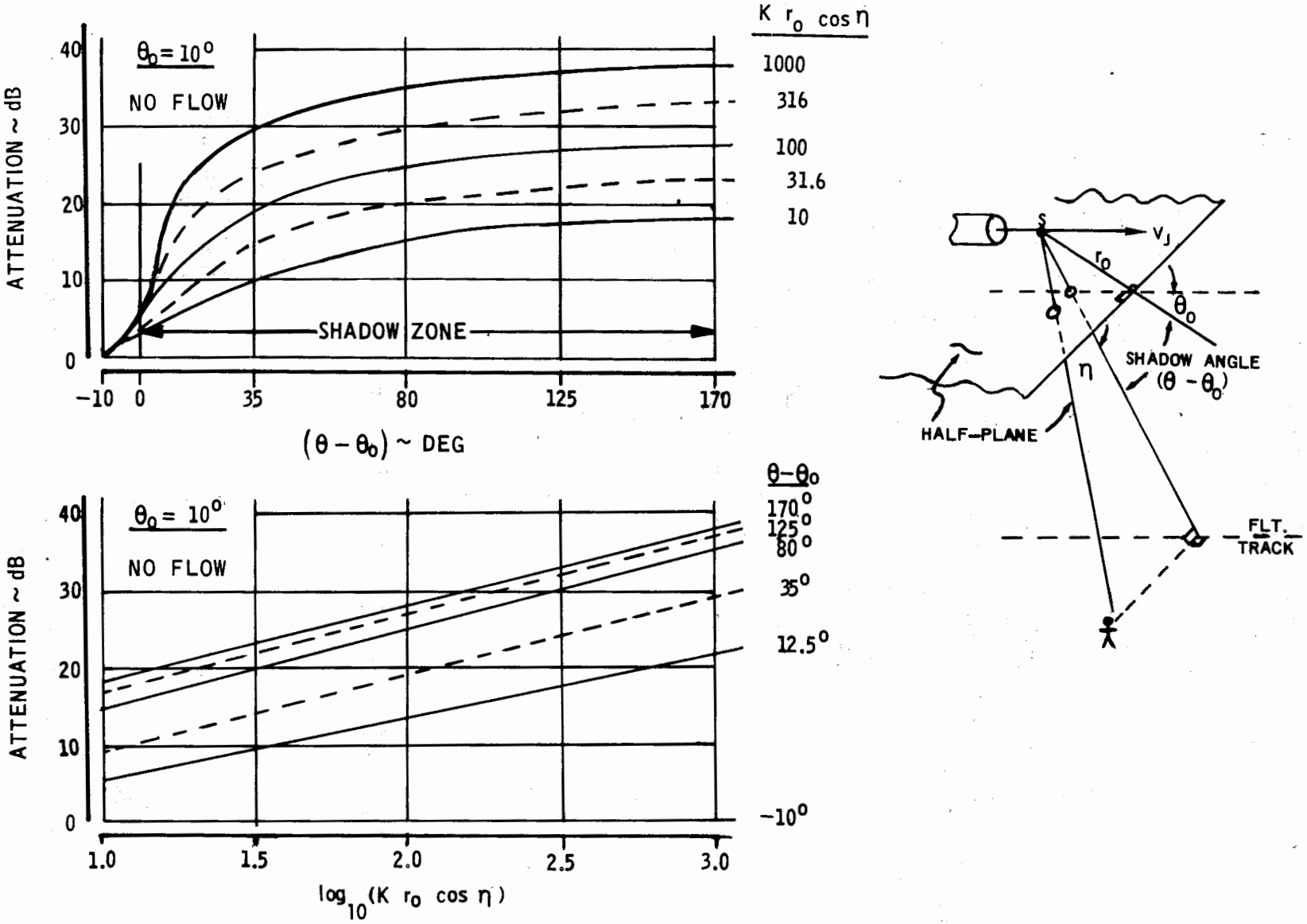

Figure 8.—Theoretical Attenuation Trends for Half-Plane Shielding

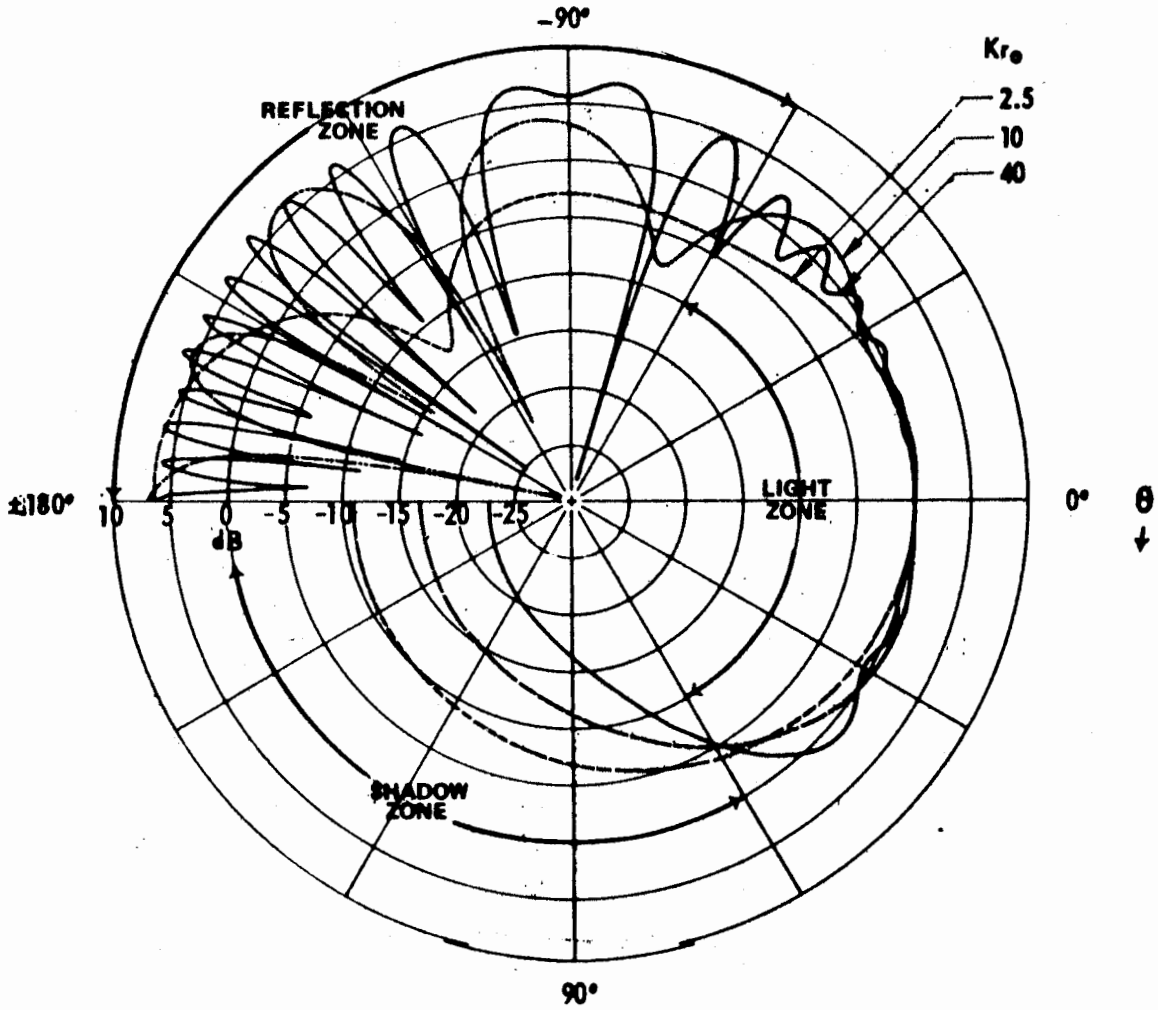

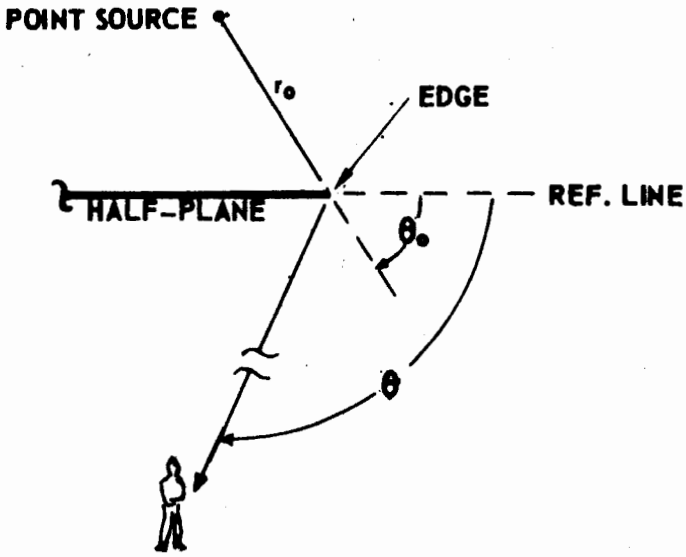

NOTES:

1) NO FLOW
2) DISCRETE TONES
3) $K r_0 = 2.5, 10, 40$
4) $\theta_0 = 60°$

Figure 9.—Theoretical Diffraction Pattern for a Half-Plane in the Far Field

We have extended Keller's (ref. 38) interpretation of diffraction for a monopole to include a directional/compact source. Keller says for the case of the half-plane that any incident sound ray upon the edge will be scattered (diffracted) in a cone about the edge as illustrated in figure 10. Specification of an observer position, i.e., vector $\bar{r}$, limits the number of cones to be considered to just one. A unique point A on the edge can be defined where an incident sound ray is scattered and a portion of the ray's acoustic energy reaches the observer in the shadow zone as a diffracted ray.

The point A can be located by:

1. Rotating the vector $\bar{r}_0$ in the X-Y plane until it lines up with the projection of the vector $\bar{r}$ in the X-Y plane. This defines the line C-D shown in the figure.

2. Drawing a line from point D to the observer point B. The intersection of line B-D with the edge gives point A.

The ray path for sound propagation from source to edge to observer is that defined by the lines S-A and A-B. This path length is the minimum distance for sound to reach the observer. Sound rays incident upon any other portion of the edge are not diffracted to this particular observer position. This last statement was questioned; however, it has been experimentally verified (see sec. 2.4.1.1).

We now turn our attention to how the sound field varies as the observer position is rotated about the Z-axis. For the case of an omnidirectional point source–a monopole–the required field can be calculated using equation (6) given previously for the uniform radiator. Figure 11 shows the amplitude of the two parts of this equation for a hypothetical case. It is evident that the total sound field is the superposition of two diffraction fields, one related to an incident field and the other to a virtual image field. Each of these fields can be divided into a light zone where $|F|^2$ is of the order unity, and a shadow zone where $|F|^2$ is significantly less than 1.

The solution for the case of a directional/compact source must in the limit reduce to that for the monopole and must be continuous. These requirements and the above interpretations for the monopole point-source solution lead to the following three postulations:

- The sound received in the shadow zone for the incident (image) field is directly related to the acoustic energy radiated toward the edge via the shortest path from the incident (image) source to edge to observer.

- The sound received in the light zone for the incident (image) field is a function of the incident (image) source's free-field radiation pattern.

- In the far field for the half-plane, the Fresnel integral in equation (6) results in a "diffraction coefficient" that relates the incident (image) source's free-field radiation pattern with the incident (image) diffraction pattern.

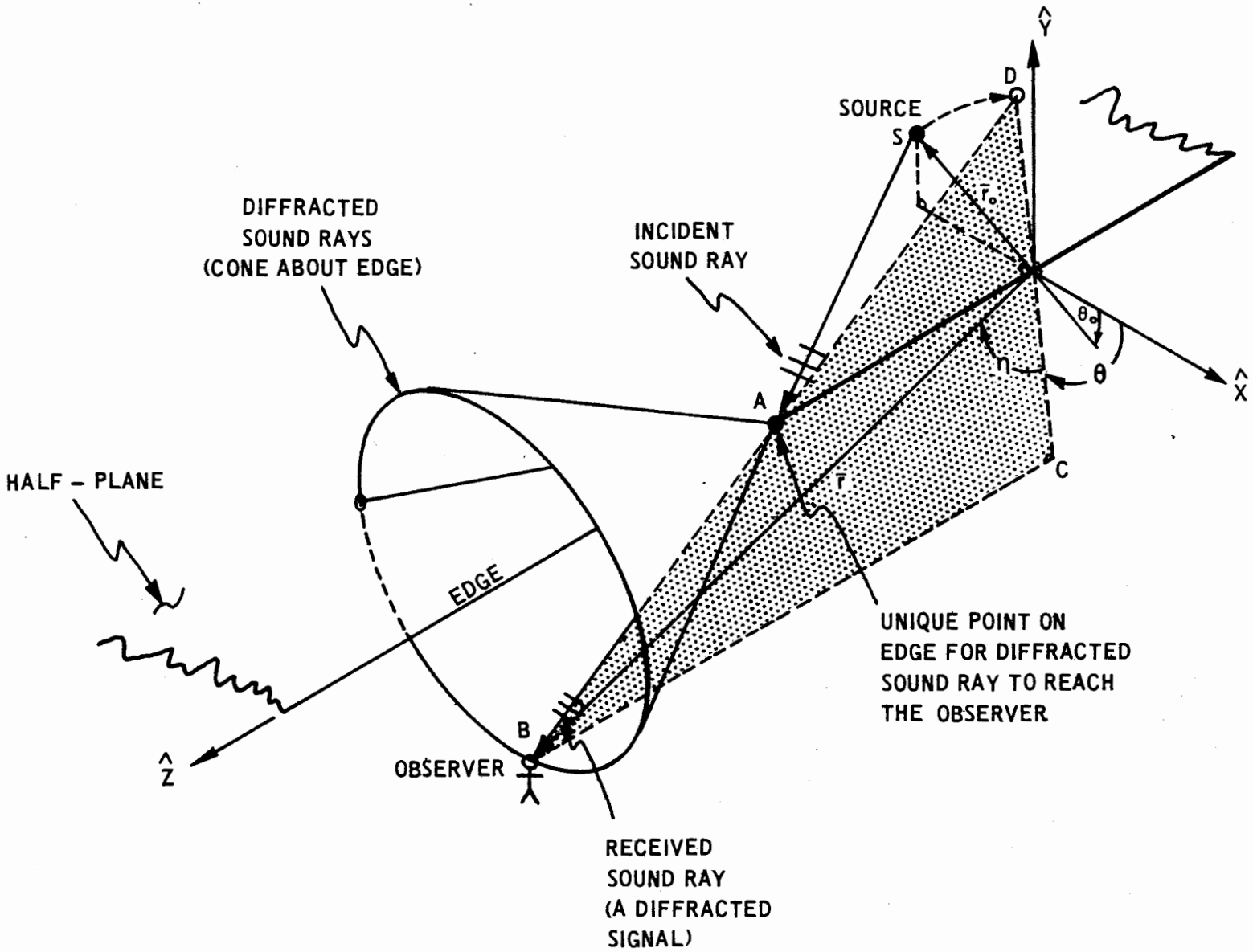

Figure 10.—Half-Plane Diffraction (Ray Acoustics)

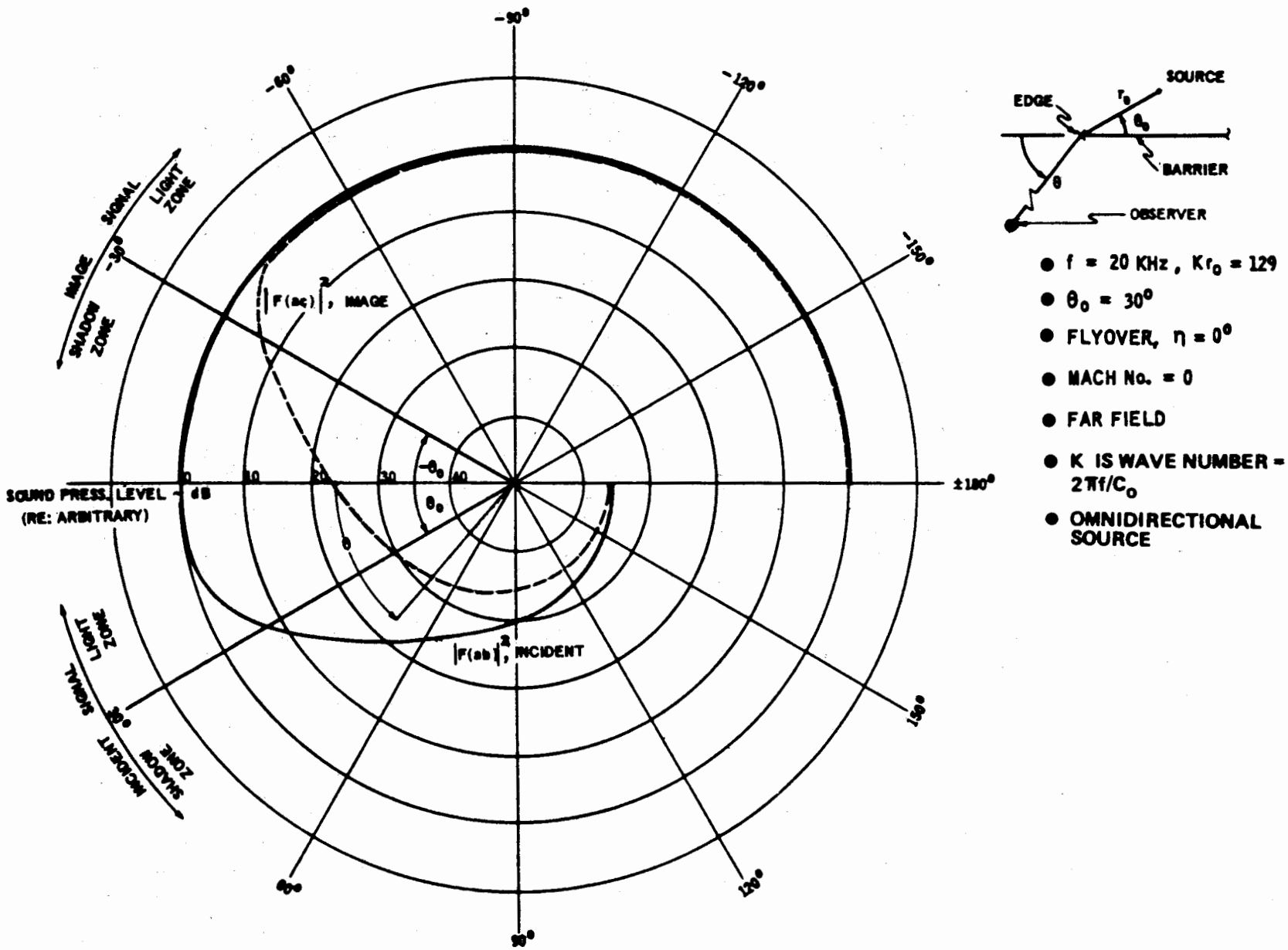

Figure 11.—Amplitude of Fresnel Integral for Incident and Image Signals

Combining these three postulations into one results in a formula similar to that for the monopole point source; i.e.,

Monopole Point Source

$$p_T = p_I\, F(a\, b) + p_I\, F(a\, c) \exp(-\, i\, a^2\, d) \tag{8}$$

where P_I is constant.

Directional/Compact Source

$$p_T = H(\psi)\, F(a\, b) + H(\psi')\, F(a\, c) \exp(-\, i\, a^2\, d) \tag{9}$$

where

(ψ, ψ')	=	directivity angles for the incident and image signals relative to the noise source reference vectors $\hat{S}$ and $\hat{S}'$ shown in figure 12
$H(\psi)$	=	$p_I(\psi)$ for the light zone of the incident field, e.g., $\theta \leq \theta_0$
	=	$p_I(\psi_0)$ for the shadow zone of the incident field, e.g., $\theta > \theta_0$
$H(\psi')$	=	$p_I(\psi')$ for the light zone of the image field, e.g., $\theta \leq -\theta_0$
	=	$p_I(\psi_0')$ for the shadow zone of the image field, e.g., $\theta > -\theta_0$
(ψ_0, ψ_0')	=	directivity angles for the direction grazing the barrier's edge along the shortest path around the edge to the observer in the shadow zone for the incident and image fields
$p_I(\psi)$	=	the far-field unshielded sound pressure directivity function

It should be noted that the second derivative of equation (9) with respect to angle ψ becomes impulsive in the transition between light and shadow zones; i.e., $\theta = \theta_0$ and $\theta = -\theta_0$. This impulsive character makes the rigor of the solution suspect; i.e., it doesn't satisfy the original wave equation (1). The impulsiveness is due to the simple form chosen to represent the function $H(\psi)$. More complicated expressions can be found that do not have this character, but it is doubtful that they would be significantly more accurate in estimating the sound pressure levels observed in experimental data. Equation (9) provides a simple means to calculate the total far-field sound pressure for a directional/compact source placed near a half-plane in the absence of flow. It represents a generalization of the monopole point-source solution and reduces to this solution when $p_I(\psi)$ is constant. Further, it can also be applied to the case of an infinite barrier by taking the limit as r_0 approaches infinity and θ_0 approaches zero. The requirements of energy conservation are also satisfied; i.e., the half-plane doesn't cause any change in the total radiated energy. The barrier changes only the spatial distribution of energy in the far-field radiation pattern.

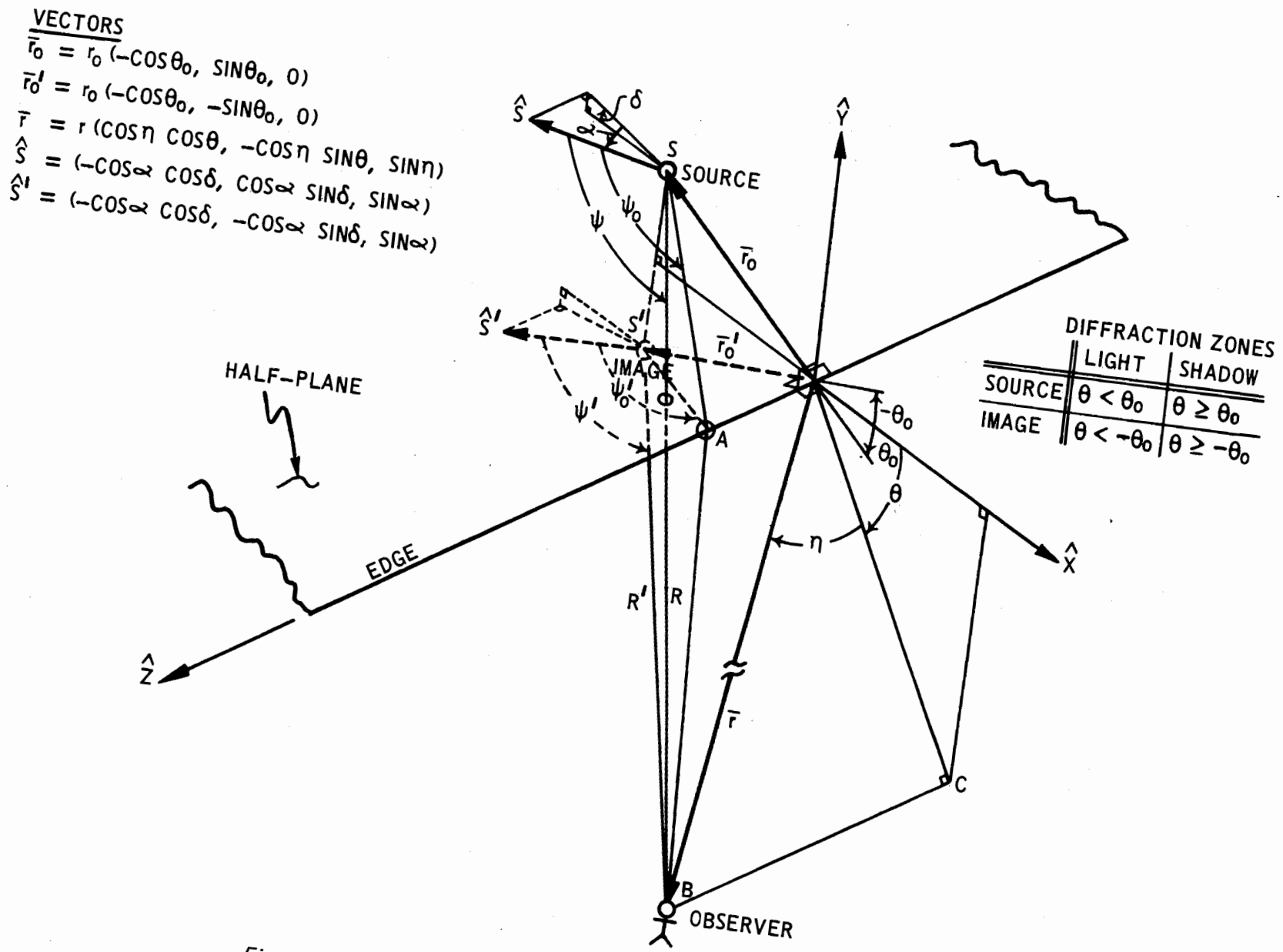

Figure 12.—Geometry for Directional/Compact Source Diffraction

Sample calculations using equation (9) have been made for a compact source having the radiation characteristics typical of those for discharge turbomachinery noise. Figure 13 shows the case for a flyover situation, $\eta = 0^0$. For comparison, the curve for a monopole source of equal total energy has been added. For both shielded curves (directional and monopole sources), a large portion of the acoustic energy is redirected to the upper side of the half-plane. However, the sound in the shadow zone (θ greater than θ_0) for the directional source is higher by 6 dB than that for the omnidirectional point source (monopole) because the sound intensity illuminating the edge is 6 dB higher. Figure 14 shows the case for the observer placed off to the side of the X-Y plane, $\eta = 75^0$, for the same two sources as in figure 13. In this case, the sound in the shadow zone for the directional source collapses into the line for the monopole because the sound strength incident upon the edge point A is approximately the same for the two sources.

Summary of the Characteristics of Compact-Source Diffraction About a Half-Plane.–This subsection discusses the effects of compact-source location and directivity changes on shielding provided by half-plane barriers. A clear understanding of corresponding shadow zone noise level changes is needed before the effects of jet efflux on the propagation of sound out of a nozzle (jet refraction theory) can be discussed.

Figure 15 illustrates the effects of source location and directivity changes of sound pressure levels (SPL) observed in the far field on the opposite side of the barrier. Results shown are for the two-dimensional case where $\eta = 0^0$.

The effect of a change in barrier height r_0 is shown in figure 15a. The sketch at the right shows the movement of the sound source that produced changes in shadow zone SPL indicated by the shielded curves. At the shadow zone boundary ($\psi = \psi_0$), the curves for the two source positions intersect. The intersection point is 6 dB below the level observed without the barrier, i.e., unshielded SPL. As the observer moves into the deep shadow zone (ψ less than ψ_0), the sound level decreases. The slopes of the two curves become shallower as the observer moves deeper into the shadow zone. The difference between the curves asymptotically approaches a limit denoted by $\Delta_1 = -10 \log_{10} (r_0'/r_0)$.

The effect of a change in shadow boundary ψ_0 is illustrated in figure 15b. The sketch to the right shows the angular movement of the source that produced the shielded SPL changes indicated to the left. The shielded SPL curve is simply shifted to the left by an angle $\Delta\psi$ equal to the rotation angle of the source about the edge. Some overshoot is noticed in the shielded curve for the source location at S′. This overshoot is part of the diffraction "rings" or oscillations noted previously in the discussion of figure 8 as one moves from the shadow zone into the light zone. The 6-dB difference between the unshielded and shielded SPL still occurs at the shadow boundaries ψ_0 and ψ_0' noted in the figure with circled points on the shielded SPL curves. In the deep shadow zone, circled points on each shielded curve show that one curve is just shifted by the angle $\Delta\psi$ relative to the other curve.

The effect of a change in the unshielded sound source's directivity curve is given in figure 15c. At the shadow zone boundary ($\psi = \psi_0$), two circled points on the unshielded SPL curves, $S(\psi)$ and $S'(\psi)$, are noted. These circled points are reference levels for the

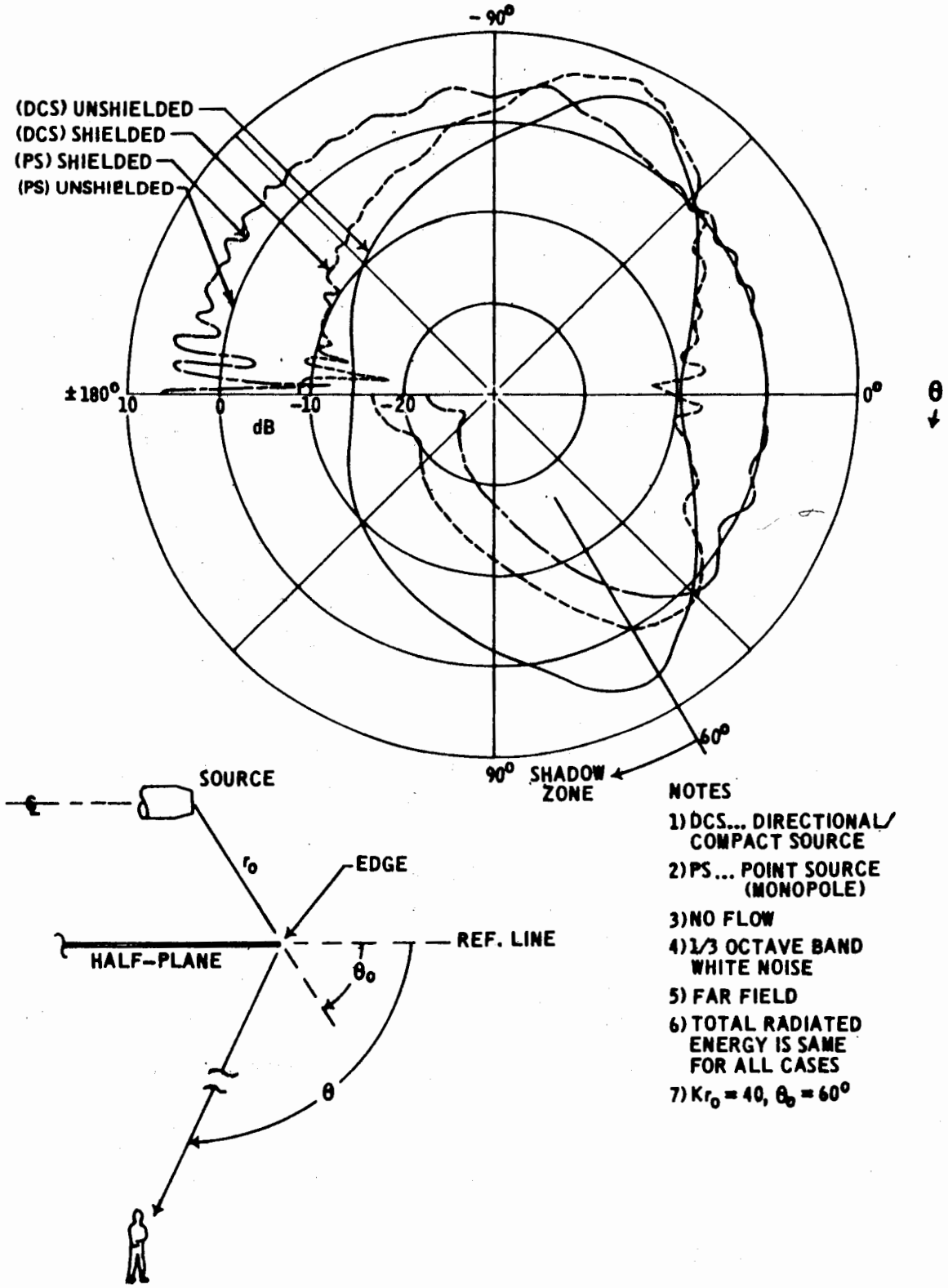

Figure 13.—Theoretical Half-Plane Diffraction Pattern for Directional/Compact Source (Flyover, $\eta = 0°$)

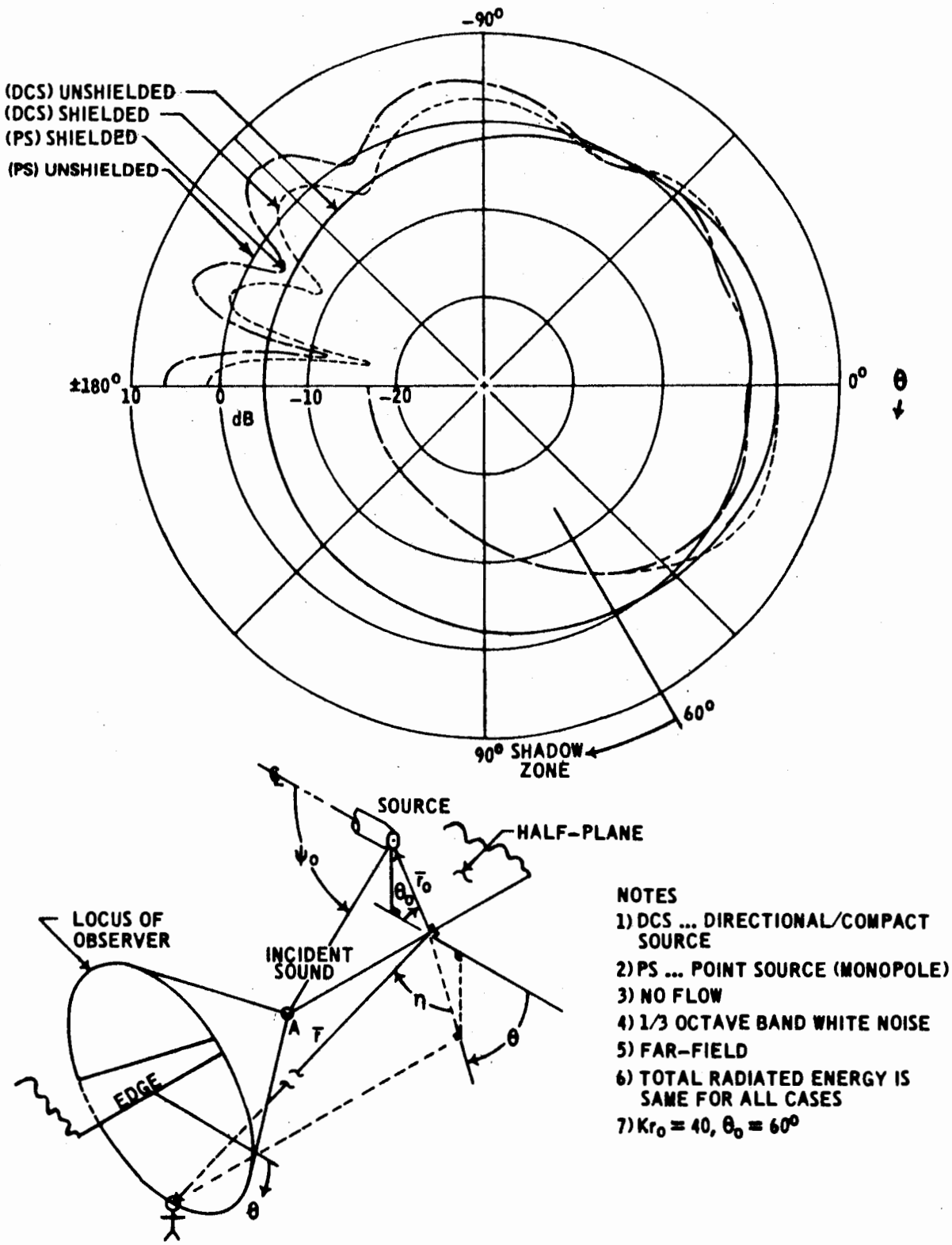

Figure 14.—Theoretical Half-Plane Diffraction Pattern for Directional/Compact Source (Sideline, $\eta = 75°$)

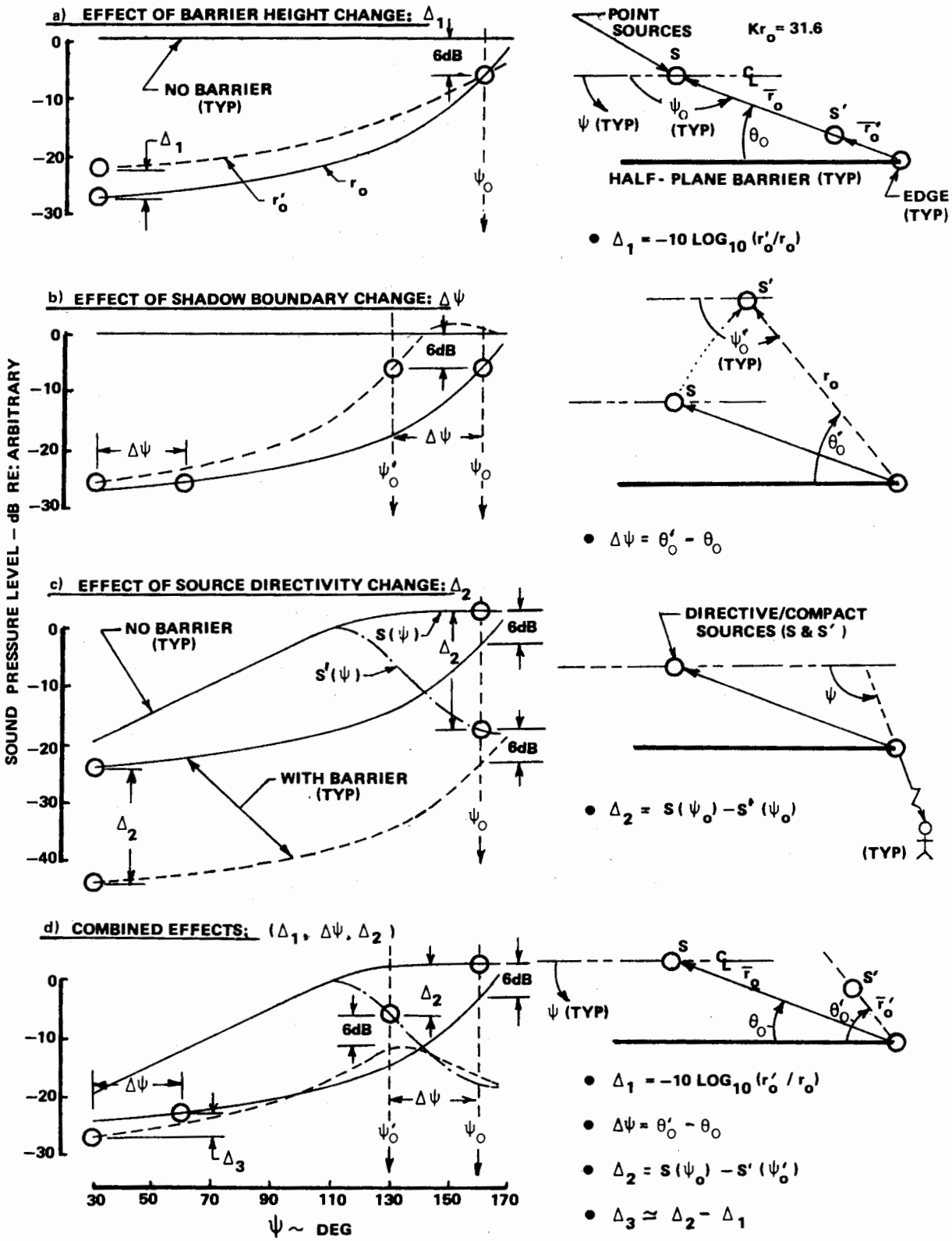

Figure 15.—Major Elements in Half-Plane Diffraction (Source Location and Directivity)

shielded curves directly below. The difference between the level of these points is denoted as Δ_2. Directly below these points the two shielded curves are also separated by the level difference Δ_2 and each shielded curve is 6 dB below its corresponding unshielded curve. As the observer moves into the shadow zone, the difference Δ_2 is maintained between the two shielded SPL curves. However, the shape of the shielded curves has no resemblence to that of the unshielded curves in the shadow zone. As the observer moves into the light zone, each shielded SPL curve fairs into the corresponding unshielded curve.

In figure 15d, all the previous effects are combined to form a representative example that we will refer to when we discuss jet refraction, test program results, and empirical analysis as related to exhaust TM noise shielding. The two different directive/compact sources from figure 15c are now placed at different locations relative to the barrier edge. The sketch at the right shows sources S and S′ at locations (r_0, θ_0) and (r_0', θ_0'), respectively. On the left are shown the predicted results. Some key points are noted by the circled points. The level difference (Δ_2) is between reference unshielded SPL's for the pertinent shadow zone boundary angles (ψ_0 and ψ_0'). For the same angular displacement of an observer into the shadow zone, a level difference (Δ_3) between the two shielded curves is noted. This difference can be estimated by the formulas given to the right, directly under the sketch.

The major points of this figure are the following.

- A change in the barrier height causes a change in the slope of the shielded SPL curve near the shadow boundary. At the shadow boundary, the shielded curve is approximately 6 dB below the unshielded level and shows little if any variation with a change in barrier height. In the deep shadow zone, the difference between shielded curves is approximately proportional to the logarithm of the ratio of barrier height.

- A change in the shadow zone boundary is caused by an angular movement of the source relative to the edge. The shielded SPL curves will shift in the same direction and same angular amount as the angular rotation of the source.

- The far-field unshielded SPL in the direction grazing the barrier edge is the reference level for sound diffracting into the shadow zone. Whatever change is made to this level will be reflected in the shielded sound level in the shadow zone. The shape of the shielded SPL radiation pattern in the shadow zone is relatively independent of the unshielded SPL, except for the dependence noted at the shadow zone boundary. As the observer moves into the light zone, the shielded SPL fairs into the unshielded SPL with the possibility of some oscillations occurring.

- Source location (r_0', θ_0') and directivity $S'(\psi)$ are key variables that determine shadow zones and the shielded sound pressure level distribution $SPL(\psi)$. These three variables can then be used to synthesize different shielded SPL data trends. One constant is discernible, however. The shielded SPL is usually 6 dB below the unshielded SPL at the shadow zone boundary.

2.2.1.2 Uniform Flow Effects

Presented here is a three-dimensional generalization of a coordinate transformation that commonly appears in sound theory (refs. 9, 11, 12, 19, 21, and 22) to handle acoustic problems involving uniform flow. In essence, the problem of diffraction about a half-plane *with flow* is transformed mathematically into a problem *without flow*. Some detail on the derivation of the transform is given in appendix C of the volume II report for a two-dimensional case of an omnidirectional compact source placed near a half-plane. The three-dimensional transform was generalized a posteriori by comparing the works of Adamczyk (ref. 11) and Candel (ref. 12).

The half-plane diffraction solutions for pressure given in section 2.2.1.1, equation (9), are equally valid for velocity potential for the case without flow. However, with flow, the interpretation of the solutions in the transformed coordinates depends upon whether the flow is incident or away from the edge of the half-plane, i.e., the solution represents pressure for a trailing edge as well as velocity potential for a leading edge. The resulting expression for pressure for the leading edge case requires differentiation of the velocity potential in the streamwise direction. This differentiation gives rise to a term that represents additional acoustic intensity radiating from the proximity of the leading edge.

The unprimed system with flow is transformed to an equivalent primed system without flow. The transformation in three dimensions is illustrated in figure 16. Vectorially, the transform steps are as follows:

$$\gamma^2 = 1/[1 - (\bar{M}_o \cdot \hat{x})^2] \tag{10}$$

$$\bar{\ell}_o = \bar{r}_o - (\bar{r}_o \cdot \hat{M})\,\hat{M} \tag{11}$$

$$\hat{L}_o = \bar{\ell}_o/|\bar{\ell}_o| \tag{12}$$

$$\bar{t}'_o = \bar{r}_o + (\gamma - 1)\,(\bar{r}_o \cdot \hat{M})\,\hat{M} \tag{13}$$

$$\cos \xi'_o = (\cos \xi_o + M_o)/(1 + M_o \cos \xi_o) \tag{14}$$

$$\bar{s}' = |\bar{t}'_o|\,(\sin \xi'_o\ \hat{L}_o - \cos \xi'_o\ \hat{M}) \tag{15}$$

$$\bar{r}'_o = \bar{s}' - (\bar{s}' \cdot \hat{z})\,\hat{z} \tag{16}$$

$$\bar{\ell} = \bar{r} - (\bar{r} \cdot \hat{M})\,\hat{M} \tag{17}$$

$$\hat{L} = \bar{\ell}/|\bar{\ell}| \tag{18}$$

$$\bar{t}' = \bar{r} + (\gamma - 1)\,(\bar{r} \cdot \hat{M})\,\hat{M} \tag{19}$$

$$\cos \xi' = (\cos \xi - M_o)/(1 - M_o \cos \xi) \tag{20}$$

$$\bar{r}' = |\bar{t}'|\,(\sin \xi'\,\hat{L} + \cos \xi'\,\hat{M}) \tag{21}$$

$$K' = \gamma K \tag{22}$$

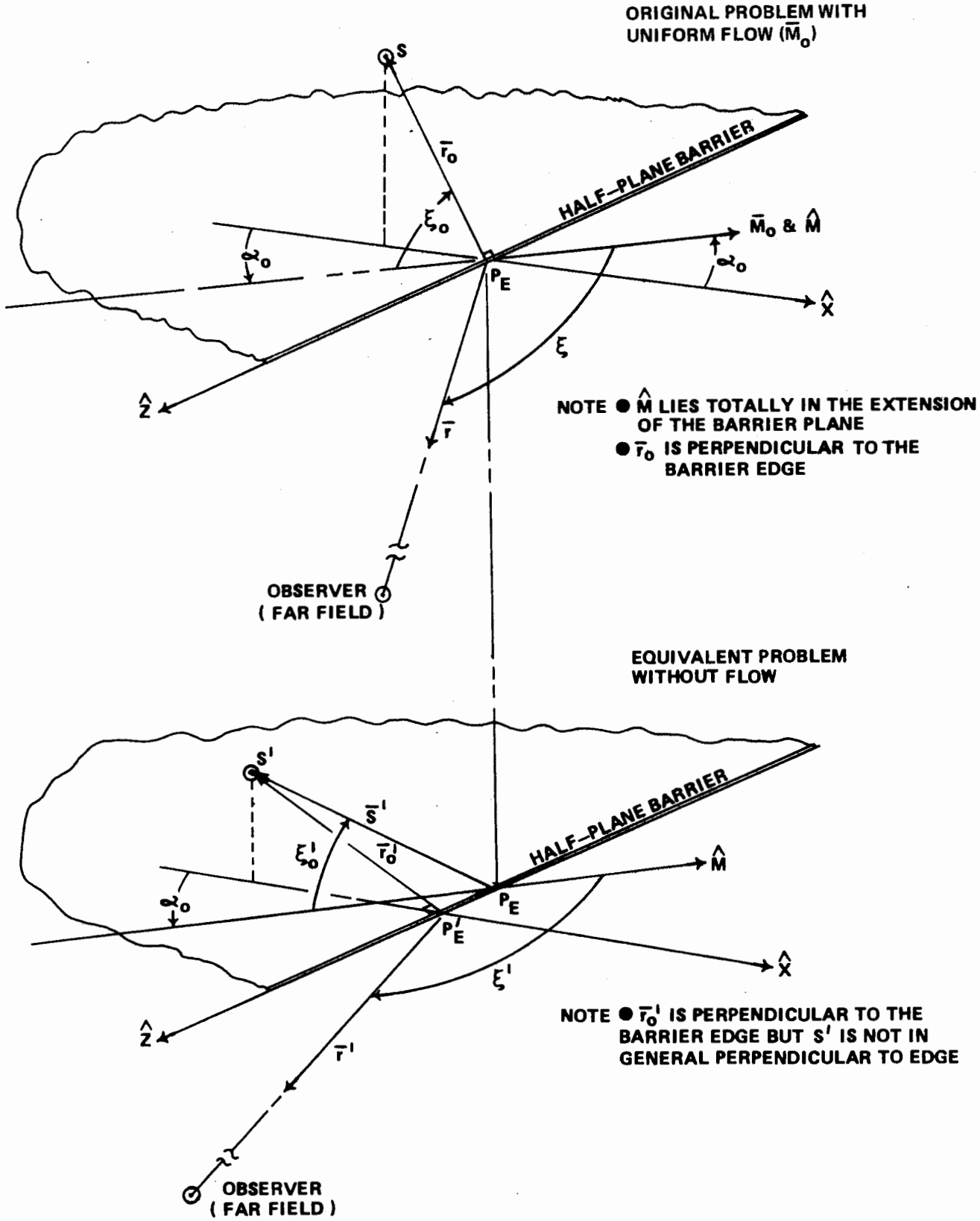

Figure 16.—Uniform Flow Transformation for Half-Plane Diffraction

where

$\overline{M}_0$ = flow Mach number vector parallel to the half-plane

M_0 = $|\overline{M}_0|$

$\hat{M}$ = $\overline{M}_0/M_0$

The angles $(\theta', \theta_0', \eta')$ are then defined in terms of the new vectors $(\overline{r}', \overline{r}_0')$ relative to the half-plane coordinate system (X, Y, Z). The directivity angles in the functions $H(\psi)$ and $H(\psi')$ are still defined, however, in terms of the unprimed coordinate variables (θ, θ_0, η). Figure 17 illustrates the interpretation associated with this last result. Using the above change in variables in equation (9) results in the solution for the case with flow. Depending on the continuity condition at the edge, the solution represents either pressure or velocity potential.

When the quantity $(\overline{M}_0 \cdot \hat{X})$ is positive, the flow is away from the edge. Hence, we have a trailing edge case and equation (9) represents pressure. When the quantity $(\overline{M}_0 \cdot \hat{X})$ is negative, we have a leading edge case and equation (9) represents velocity potential. Differentiation in the streamwise direction in a similar manner, as indicated in appendix C in the volume II report, results in the solution for pressure. The result for the leading edge case is

$$p_T = H(\psi)\, F(a'\, b') + H(\psi')\, F(a'\, c') \exp[-i\,(a')^2\, d']$$

$$+ T_{LE}\sqrt{\frac{i}{\pi}}\,\frac{[b'\, H(\psi) + c'\, H(\psi')]}{a'} \exp[i\,(a')^2/2] \tag{23}$$

where

T_{LE} = $(\overline{M}_0 \cdot \hat{X})/(1 + M_0 \cos \xi')$

a', b', c', d' = a, b, c, d as defined in section 2.2.1.1, except using the transformed variables

This completes the mathematics necessary to specify the diffraction solution for uniform flow parallel to a "thin" half-plane shield. We now turn our attention to illustration of the results. Figure 18 shows diffraction for three flow cases about a half-plane for an omnidirectional compact source, i.e.,

- Flow over a trailing edge
- No flow
- Flow over a leading edge

WIND TUNNEL SITUATION

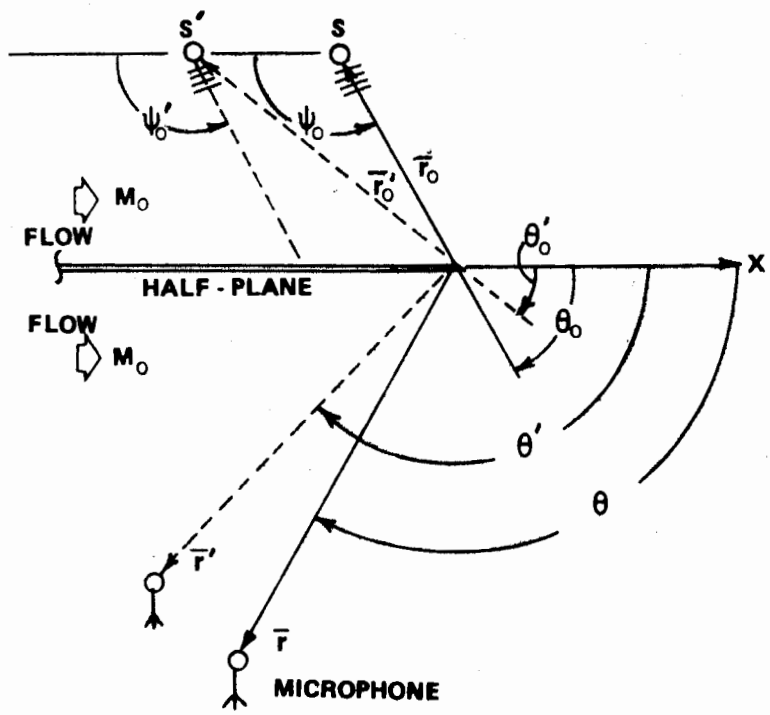

NOTES

1) WITHOUT FLOW, SOURCE (S) EMITS WAVE PACKET IN DIRECTION ψ_0. THE EDGE RECEIVES THE ENERGY AT DIRECTION θ_0 AND DIFFRACTS A PORTION OF THE RECEIVED ENERGY TO MICROPHONE AT DIRECTION θ.
2) WITH FLOW, SOURCE (S') EMITS WAVE PACKET IN DIRECTION $\bar{\psi}_0'$, WHICH HAPPENS TO EQUAL ψ_0 IN THIS CASE. THE EDGE RECEIVES THE ENERGY AT DIRECTION θ_0' AND DIFFRACTS A PORTION OF THE RECEIVED ENERGY IN DIRECTION θ'. CONVECTION OF THE SOUND WAVES CAUSES THE ANGLES (Θ, Θ_0) AND (Θ', Θ_0') TO DIFFER.
3) VECTOR LENGTHS ($\bar{r}_0'$, $\bar{r}'$) RELATIVE TO ($\bar{r}_0$, $\bar{r}$) ARE INTENTIONALLY DRAWN NOT TO SCALE TO ILLUSTRATE ANGULAR RELATIONSHIPS MORE CLEARLY.

Figure 17.—Physics of Flow Transform for Half-Plane Diffraction

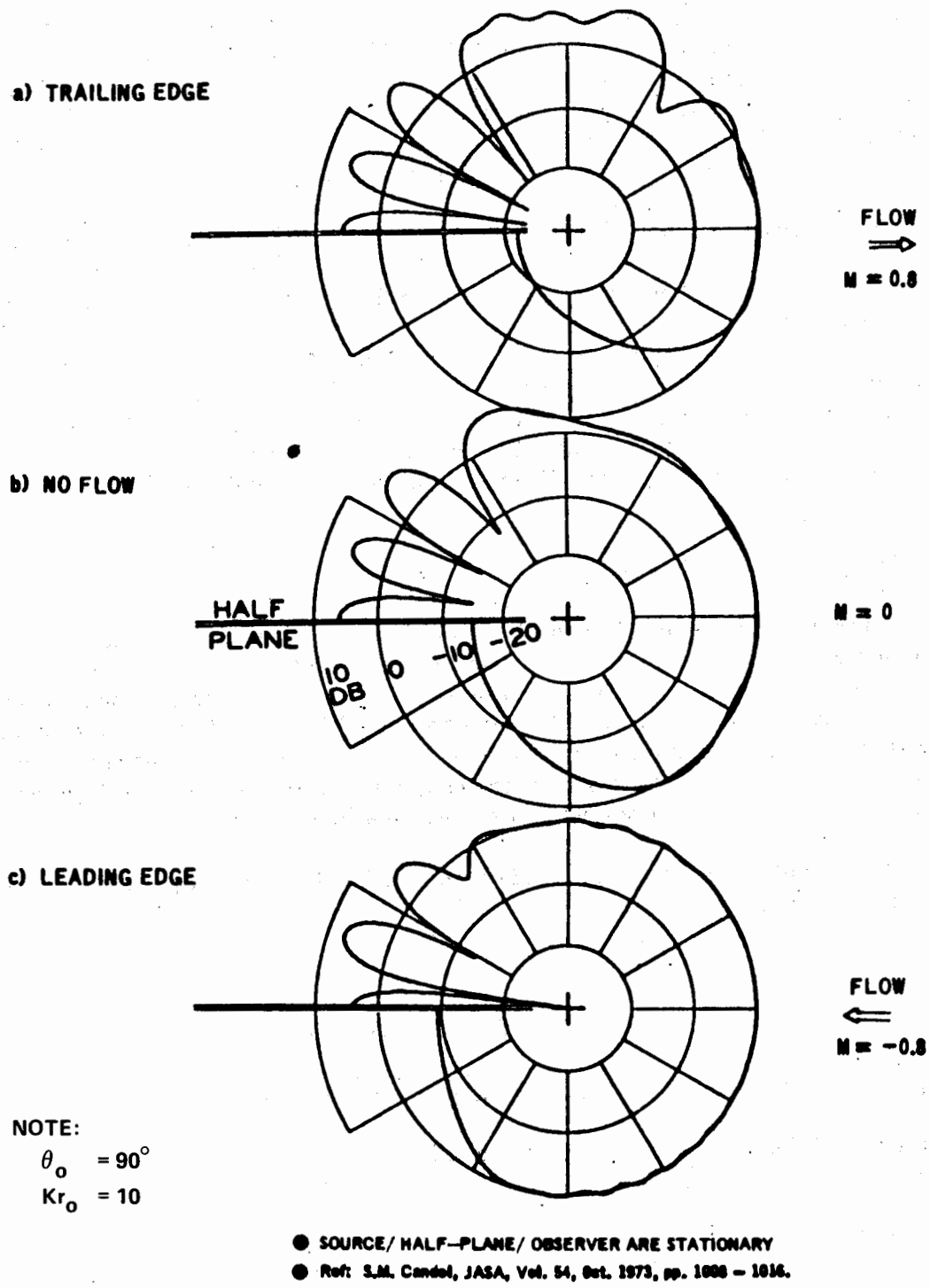

Figure 18.—Theoretical Diffraction Pattern for a Half-Plane in the Far Field With Uniform Flow

The source is oriented at an angle $\theta_0 = 90^0$ with respect to the vector $\hat{X}$ and the observer lies in the plane normal to the half-plane. From these results, it appears that the transformation accounts for the convection of the sound field in the direction of flow, which was intuitively expected. In the shadow zone, there is a gain in shielding effectiveness when there is flow over the trailing edge. On the other hand, with flow over the leading edge, there is a loss in shielding effectiveness.

So far in this discussion it has been assumed that the source, edge, and observer are stationary relative to each other. When the source and edge are in motion relative to the observer, another effect must be added. This effect is the familiar Doppler effect, which causes a frequency and level change. The Doppler effect is a function of the type of source (monopole, dipole, quadrupole, etc.), the flight Mach number, and the angle between the flightpath and the sound propagation path. This last effect is already included in the source estimation procedures and documentation from NASA contract NAS2-6969. Hence, we will not discuss the details of it further, and only note that it must be accounted for in noise predictions along with the ambient flow effects on diffraction.

2.2.1.3 Filter Bandwidth Effects

If one compares the point-source (monopole) curve for $K\,r_0$ equal to 40 in figure 9 with the point-source curve in figure 13 of section 2.2.1.1, a difference in the diffraction patterns is discerned, e.g., figure 19. This difference can be interpreted as a noise source effect, i.e., discrete tone versus 1/3-octave-band "white noise" measured using 1/3-octave-band analysis equipment, or as a bandwidth effect where the diffracted noise is measured using a 1-Hz bandwidth filter instead of a 1/3-octave-band filter. The latter interpretation is chosen here to represent the effects mathematically.

It can be shown that the relative amplitude spectrum for the shielded pressure may be expressed in the form:

$$|\bar{p}_T|^2 = p_T \cdot p_T^*$$

$$= A(f) + B(f)\cos[f\,C(f) - D(f)] \tag{24}$$

where p_T^* denotes the complex conjugate of the total pressure field.

During the sound detection process, a physical filter introduces a frequency averaging effect, i.e.,

$$|\bar{p}_T|^2 \simeq \frac{1}{(f_U - f_L)} \int_{f_L}^{f_U} (p_T \cdot p_T^*)\, df \tag{25}$$

where (f_L, f_U) are the filter's "cutoff" frequencies and the filter's frequency response is assumed to be an ideal flat response. If the terms A(f) and B(f) are slowly varying

compared to the function, $\cos\left[f\ C(f) - D(f)\right]$, over the limits of integration, then equation (25) may be further approximated by

$$|\bar{p}_T|^2 \simeq A(f) + B(f)\cos[q_1\ f\ C(f) - D(f)]\ \frac{\sin[q_2\ f\ C(f)]}{[q_2\ f\ C(f)]} \tag{26}$$

where

f	=	center frequency for the filter (Hz)
q_1	=	$0.5\ (\epsilon + 1/\epsilon)$
q_2	=	$0.5\ (\epsilon - 1/\epsilon)$
ϵ	=	$10^{.05W}$
W	=	the filter's bandwidth in decades, i.e., $10\ \log_{10}(f_U/f_L)$

Equation (26) was used to calculate the curves shown in figures 13 and 19. In the reflection zone ($\theta < -60^0$) of figure 19, the oscillations due to interference between the incident and image fields are smoothed due to the averaging effect of the sound detection process. As one moves into the shadow zone (θ greater than θ_0), more noise reduction appears for the 1/3-octave-band curve relative to the discrete tone curve. However, this additional reduction is inconsistent because it usually disappears when the sound frequency is changed. Perhaps an interference phenomenon occurs when signals within a filter's bandwidth are averaged. On the other hand, the approximation given by equation (26) may be somewhat in error for the example chosen.

A more careful evaluation of equation (25) in the deep shadow zone is required to explain this apparent interference effect. However, we have not pursued this further because:

- The error, if real, will not seriously impact community noise estimates.
- A closed-form solution has not been found, necessitating numerical integration in equation (25).
- Numerical integration is computationally expensive for community noise predictions.

2.2.1.4 Distributed Sources

In this section we examine the half-plane diffraction patterns of three noise source distributions. The purpose is to find the simplest source representation that closely simulates the diffracted field of spatially extended and phased noise sources, i.e., turbofan engine noise components. The three models are the coherent-phased ring, the

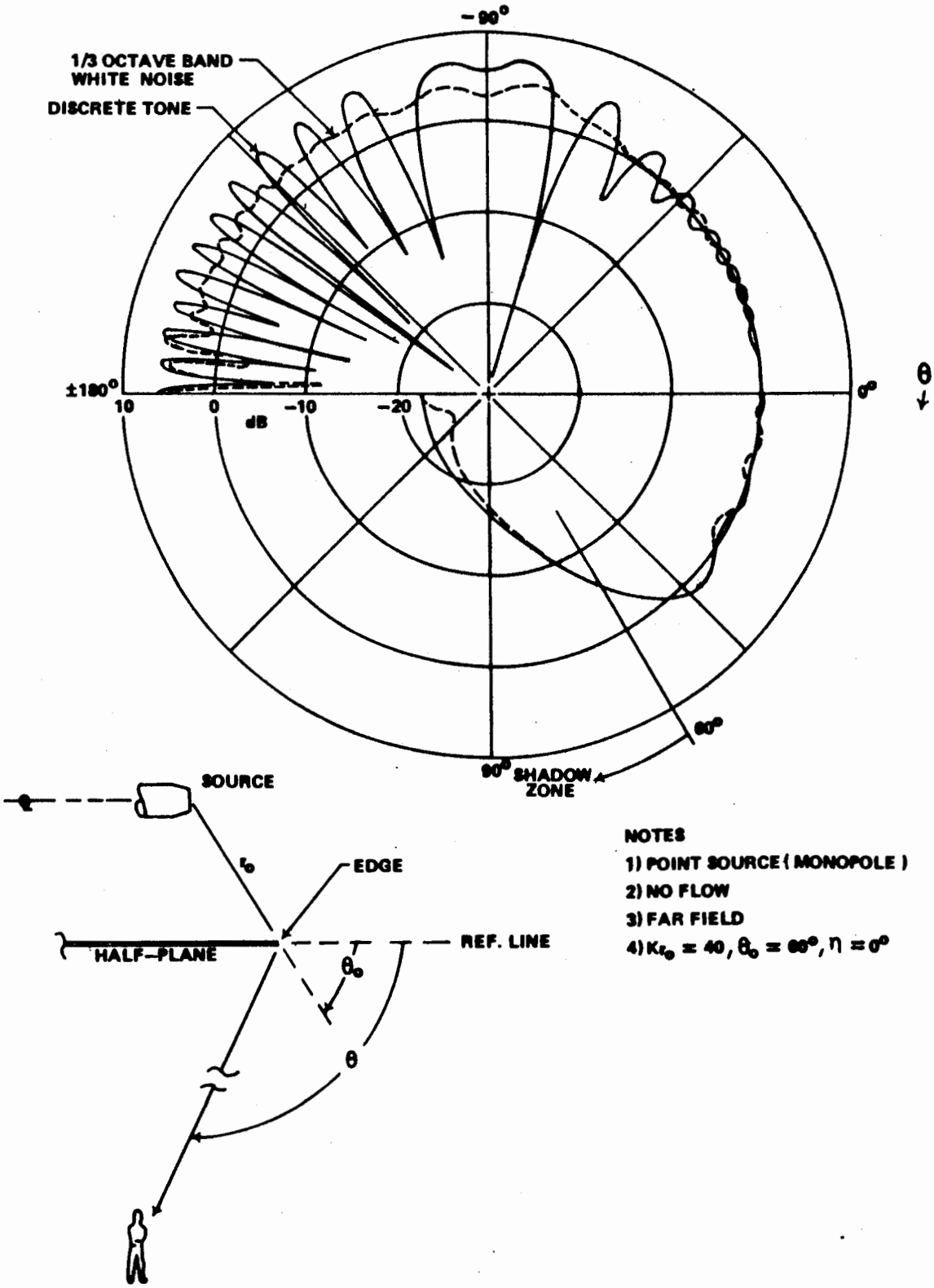

Figure 19.—Filter Bandwidth Effect on Half-Plane Diffraction Pattern

random-phased ring, and the random-phased line. Noise shielding comparisons are made for the following idealized types of noise sources:

- Single point
- A single point with a linear-phased ring of points superimposed about it. This is done to simulate the fan tones emitted from an engine's inlet where the actual source is spinning in time.
- A single point with a random-phased ring of points superimposed about it. This is done to approximate the case where flow turbulence makes the noise emitted from the nozzle exit appear completely uncorrelated.
- A line of random-phased points. This is done to simulate the effect of an axial source distribution.

The formula that can be used to approximate the effects of a noise source spatial distribution on sound diffraction is as follows:

$$p_T/p_I = \int_V p(\bar{r}_o)\, G(\bar{r} \mid \bar{r}_o)\, dv \Big/ \int_V p(\bar{r}_o)\, dv \tag{27}$$

where

V	=	source volume
$p(\bar{r}_o)$	=	source distribution function
$G(\bar{r}\,\vert\,\bar{r}_o)$	=	Green's function for the half-plane, equation (6)

If a system of point sources (p_{IJ}) is used to represent $p(\bar{r}_o)$, then this integral may be approximated by the following equations for the source distribution listed:

Coherent-Phased Distribution

$$\bar{p}_T/\bar{p}_I \cong \Big[\sum_{J=1}^{N} p_{IJ}\, G(\bar{r}\,|\,\bar{r}_{oJ})\Big] \Big/ \Big[\sum_{J=1}^{N} p_{IJ}\Big] \tag{28}$$

Random-Phased Distribution

$$|p_T/p_I|^2 \cong \Big[\sum_{J=1}^{N} |\, p_{IJ}\, G(\bar{r}\,|\,\bar{r}_{oJ})|^2\Big] \Big/ \Big[\sum_{J=1}^{N} |p_{IJ}|^2\Big] \tag{29}$$

Figure 20 shows typical results using these approximations for the first three source models noted above. Comparison of the curves for the random phased and the single point show that the maximum sound pressure level reductions are identical in the deep shadow zone directly under the half-plane. Differences between these curves occur only in the transition between the light zone and the shadow zone. The curves for the

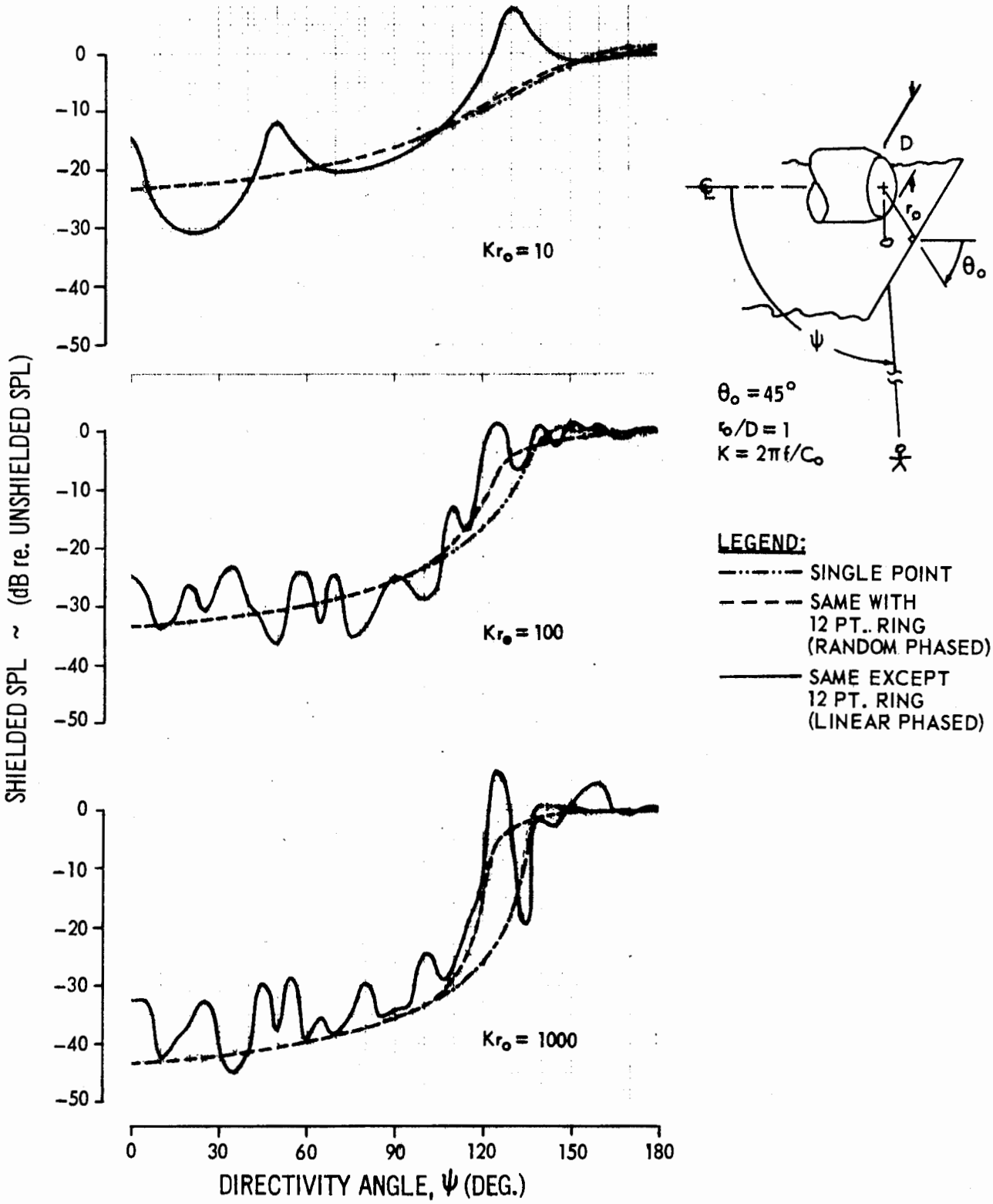

Figure 20.—Half-Plane Diffraction Comparison for Single-Point, Random-Phased-Ring, and Linear-Phased-Ring Sources

linear-phased ring are complicated by an interference phenomenon. Available wing shielding data for fan turbine and core noise have not shown this degree of interference. Hence, the linear-phased-ring model will not be considered further.

Figure 21 shows the effect of varying the random-phased-ring source diameter. As the diameter, D, of the ring approaches one-quarter the barrier height, r_0, the curves for the random-phased ring are almost identical to those for the single-point source. Hence, the spatial effect on diffraction of a radial distribution of random sources is not very significant.

Figure 22 shows a similar comparison for the random-phased-line source. In this case, we have optimized the position for the single point resulting in an "apparent source" that gives the least-square-dB error fit to the line source estimate. The curve for the single-point–source model is an excellent fit, but the apparent source is not at the actual center of the line source. This serves to emphasize the statement made previously in section 2.1, i.e., "... the apparent point-source concept violates a physical reality ... near-field implications that result from this modeling should not be taken too seriously."

Nevertheless, the apparent point-source concept does contain the essential trends of the more complicated source models and it is more efficient in terms of computational expense. Through use of equation (9) in section 2.2.1.1, the effect of the noise source's directivity can be incorporated in predictions. What needs to be determined is where to put the source. This determination has comprised the major effort of this report. Discussion of this determination for wing shielding will be deferred until sections 2.2.3 and 2.4.

2.2.2 INFINITE CYLINDER DIFFRACTION

Described here is a fuselage noise shielding estimation procedure as modeled by diffraction about an infinite cylinder. It appears likely that fuselage shielding could be effective in reducing engine noise components for engine over-the-fuselage installations provided that diffraction is the most significant transmission mode by which sound reaches the community under the aircraft's flightpath.

Noise reduction as large as 15 dB at 1 kHz has been theoretically estimated for the inlet noise from the 727 aircraft during flyovers. Unfortunately, complete substantiation of the theory by test is lacking. The mathematical solution described below is proposed as an interim procedure until adequate test data become available.

Further, it has been found that the mathematical solution is computationally expensive and unstable in certain regions. Therefore, it has not been incorporated in the computerized procedures of this report. To make trade studies, a nomogram and a table look-up approach have been developed. Use is limited to the region where the mathematical solution does not oscillate wildly.

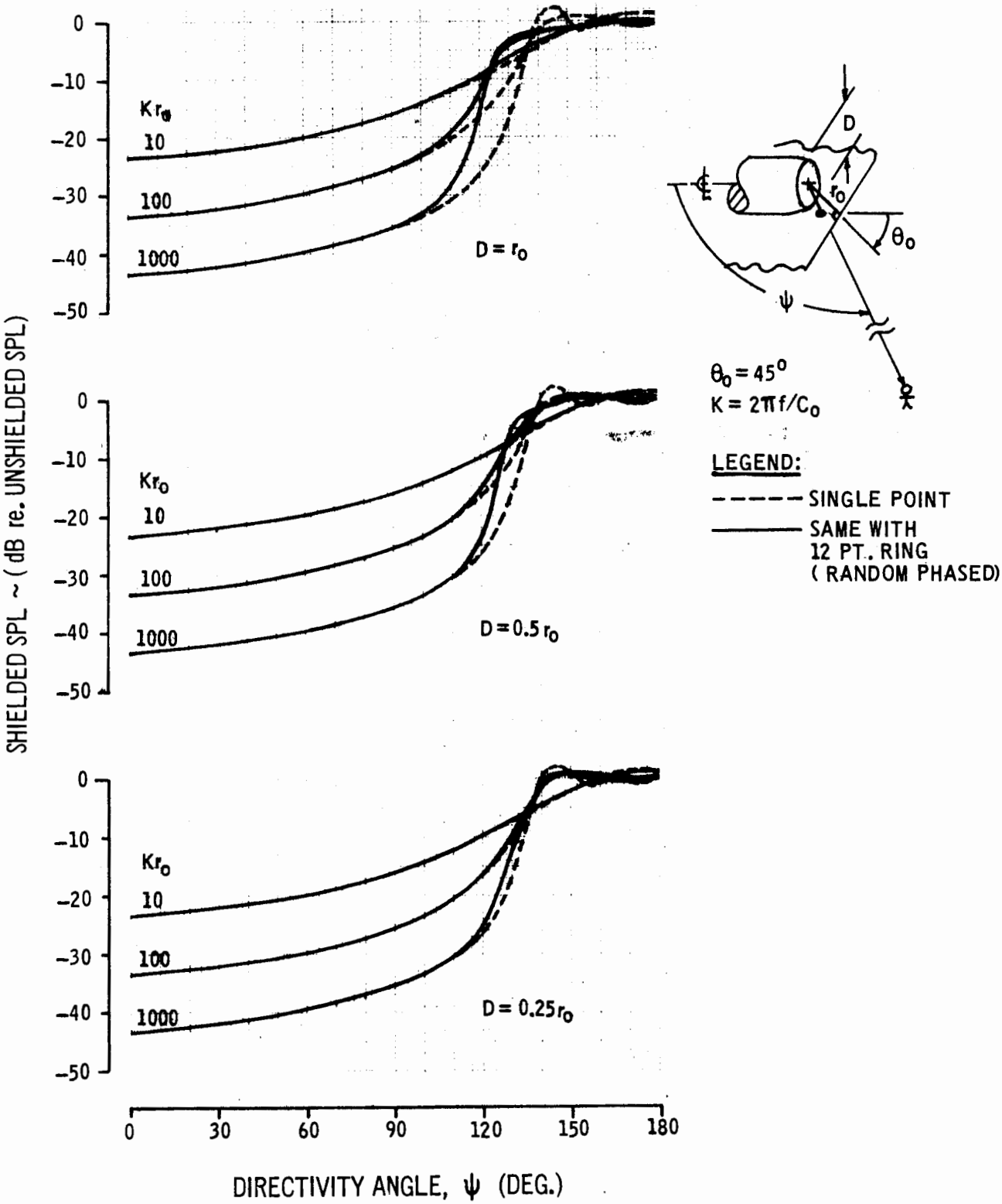

Figure 21.—Effect of Source Size on Half-Plane Diffraction

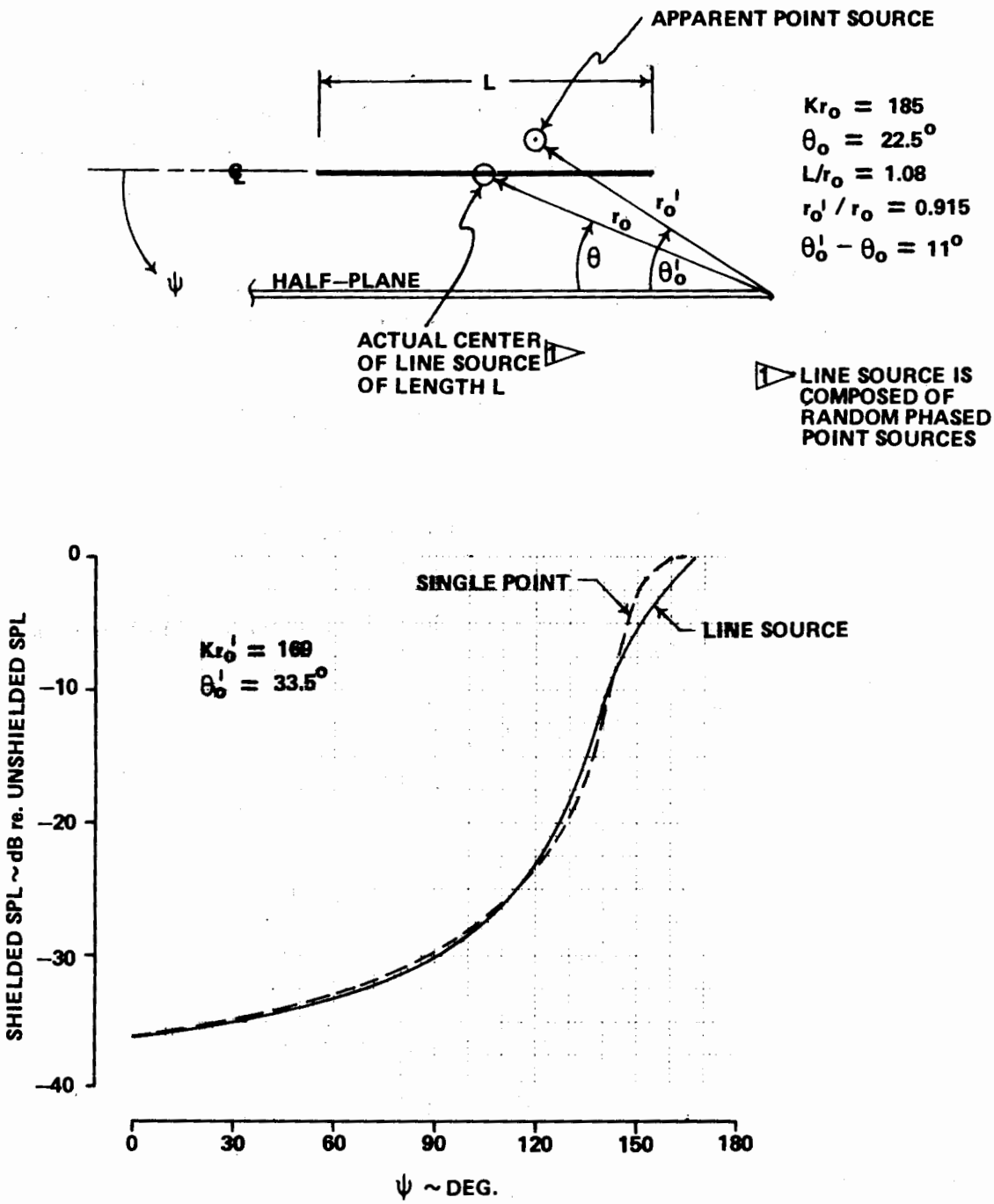

Figure 22.—Comparison of Single-Point-Source Model With Line-Source Model

2.2.2.1 Compact Source

Consider a simple monopole sound source in the vicinity of a reflecting cylinder of infinite length with no flow. The acoustic pressure field can be found by solving a boundary value problem similar to that for the half-plane (eqs. 1 and 2) except the boundary condition, equation (2), is replaced by

$$\frac{\partial}{\partial r} p_T \doteq 0 \text{ at the cylinder wall} \tag{30}$$

where r is the displacement coordinate normal to the cylinder wall. The solution to this problem is given in reference 10 as a Fourier series involving Bessel functions of the first through third kind (ref. 37), i.e.,

$$p_T/p_I = G(\bar{r}\,|\,\bar{r}_o) = 1 - F(a,b,\phi)\exp(i\,b\cos\phi) \tag{31}$$

where (see fig. 23 for notation and geometry)

a = effective cylinder radius (dimensionless)
$= K\,r\sin\xi$

b = effective source distance from cylinder center (dimensionless)
$= K\,R\sin\xi$

$$F(a,b,\phi) = \sum_{n=0}^{\infty} q_n(a,b)\cos(n\,\phi)$$

$$q_o(a,b) = H_o^{(1)}(b)\,J_o'(a)/H_o^{(1)\prime}(a)$$

$$= [J_o(b) + i\,Y_o(b)]\;J_1(a)/[J_1(a) + i\,Y_1(a)]$$

$$q_n(a,b) = 2(-i)^n\,H_n^{(1)}(b)\,J_n'(a)/H_n^{(1)\prime}(a)$$

$$= 2(-i)^n\,[J_n(b) + i\,Y_n(b)]\;[n\,J_n(a) - a\,J_{n+1}(a)]\,/$$

$$\left\{[n\,J_n(a) - a\,J_{n+1}(a)] + i\;[n\,Y_n(a) - a\,Y_{n+1}(a)]\right\}$$

$[J_n, Y_n, H_n^{(1)}]$ = n^{th} order Bessel functions of the first through third kind, respectively

The series, $F(a, b, \phi)$, is uniformly convergent; however, the number of terms required in the summation can be large depending on the value of "a" (see fig. 24). The ratio p_T/p_I is of prime interest for calculating the diffraction pattern of a discrete tone written in sound pressure level (SPL) form:

$$\Delta SPL = 10\log_{10}|p_T/p_I|^2 \tag{32}$$

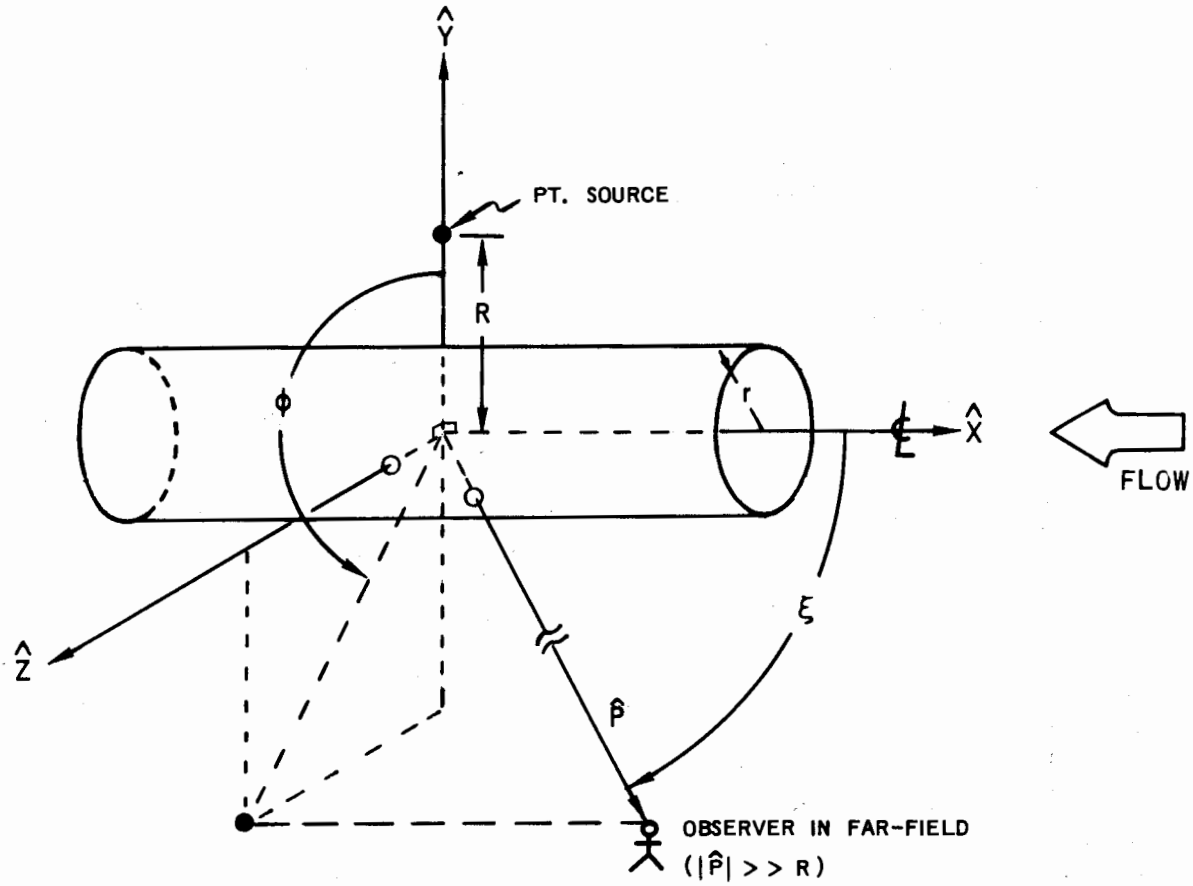

VARIABLES:

- f SOURCE FREQUENCY (Hz)
- C_0 AMBIENT SPEED OF SOUND (m/s or fps)
- r CYLINDER RADIUS (m or ft)
- R RADIAL DISTANCE FROM CYLINDER CENTER TO POINT SOURCE (m or ft)
- ξ OBSERVER ANGLE WITH RESPECT TO CYLINDER AXIS
- ϕ ANGLE BETWEEN SOURCE AND OBSERVER LINES WHERE THE TWO LINES FORM THE ANGLE AT THE CENTER OF THE CYLINDER. THE ANGLE IS IN THE PLANE NORMAL TO THE CYLINDER AXIS
- M_0 FLOW MACH NUMBER
- B FILTER BANDWIDTH IN DECADES, i.e. $\Delta f = f(\eta - 1/\eta)$ WITH $\eta^2 = 10^B$

  * NOTE * $B = 0$ FOR POWER SPECTRAL DENSITY
  $= 0.1$ FOR 1/3 OCTAVE BANDS
  $= 0.3$ FOR FULL OCTAVE BANDS

Figure 23.—Cylinder Diffraction Variables

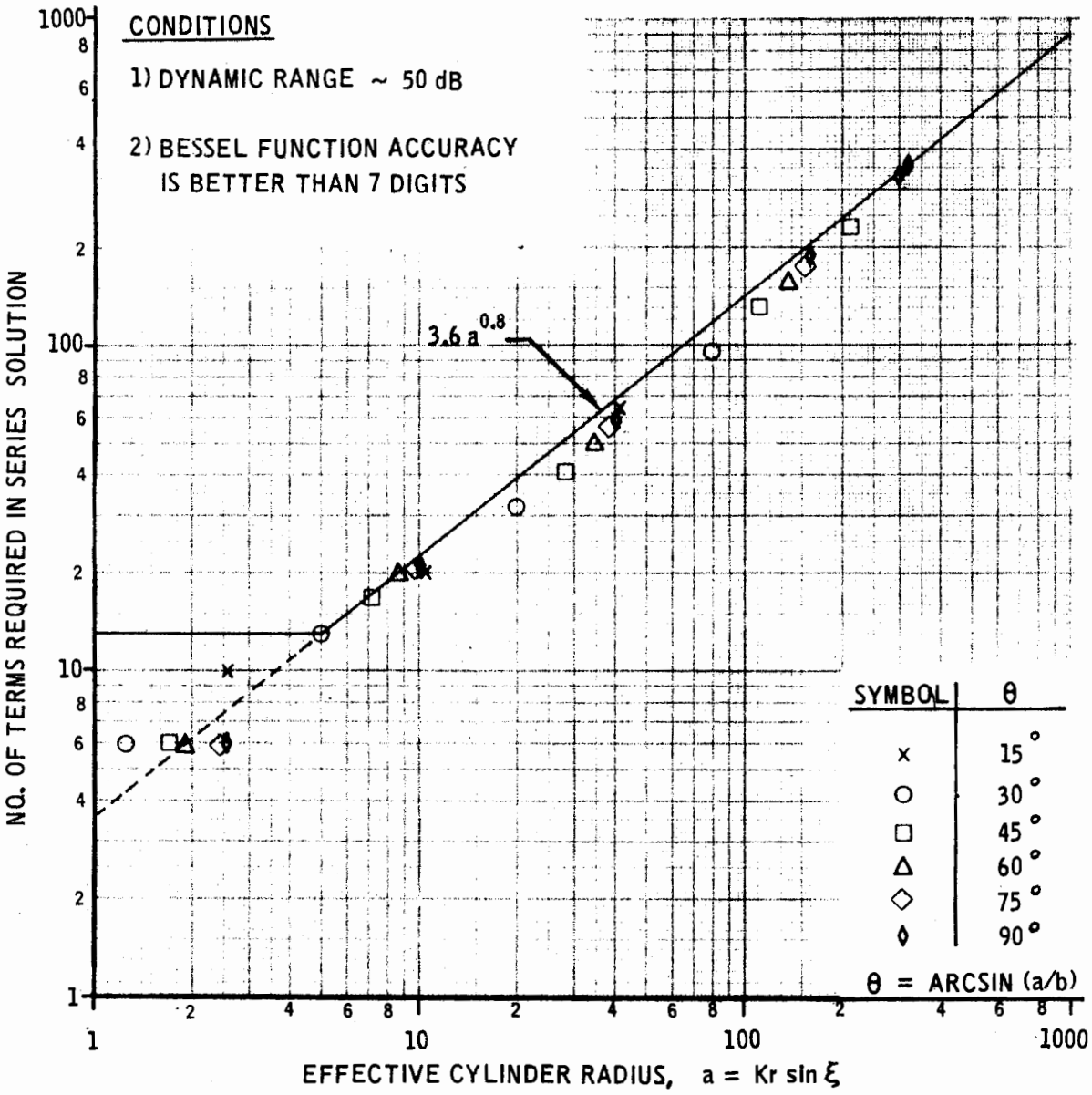

Figure 24.—Convergence of Cylinder Diffraction Solution

Assuming that a 50-dB dynamic range is sufficient in the final answer for ΔSPL, then the following constraints apply:

- Values for the term "a" must be limited to absolute values less than 160, approximately.
- The number of terms required in the summation is given by the maximum of $(13, 3.6\,a^{.8})$, approximately.
- The Bessel functions need to be calculated to an accuracy of seven significant digits or better.

2.2.2.2 Uniform Flow Effects

The effect of uniform flow can be included in the solution, equation (31), to account for aircraft motion through the air. Three flow regions in the vicinity of an aircraft's fuselage are

- Turbulent boundary layer
- Wing wake
- Uniform flow medium surrounding the boundary layer and wing wake

It is not clear what effect the first two flow regions will have on cylinder diffraction. Refraction theory, to be discussed in section 2.2.4.1, would predict that a slight gain in shielding effectiveness is possible. On the other hand, flow scattering theory (sec. 2.2.4.2) would predict a shielding limit to occur depending on the level of the scattered sound field. The effect of the third flow region can be quantified in a manner similar to that used for the half-plane, section 2.2.1.2. However, only two variables are involved for cylinder diffraction, i.e.,

$$K' = K/\sqrt{1 - M_o^2} \tag{33}$$

$$\cos \xi' = (\cos \xi + M_o)/(1 + M_o \cos \xi) \tag{34}$$

where, again, unprimed variables refer to the system with flow and the prime refers to these variables transformed to an equivalent system without flow. These transformed variables (K', ξ') are to be substituted in place of (K, ξ) in equation (31). Figure 25 shows an example calculation of the effect of ambient flow on the diffraction of sound about a long cylinder. Flow causes the attenuation distribution to be skewed about $\xi = 90^o$ in comparison to the symmetric static attenuation. Reversal of the flow direction also causes a reversal of attenuation distribution about the 90° angle. Symmetry with respect to flow Mach number, M_o, is evident for the two cases shown.

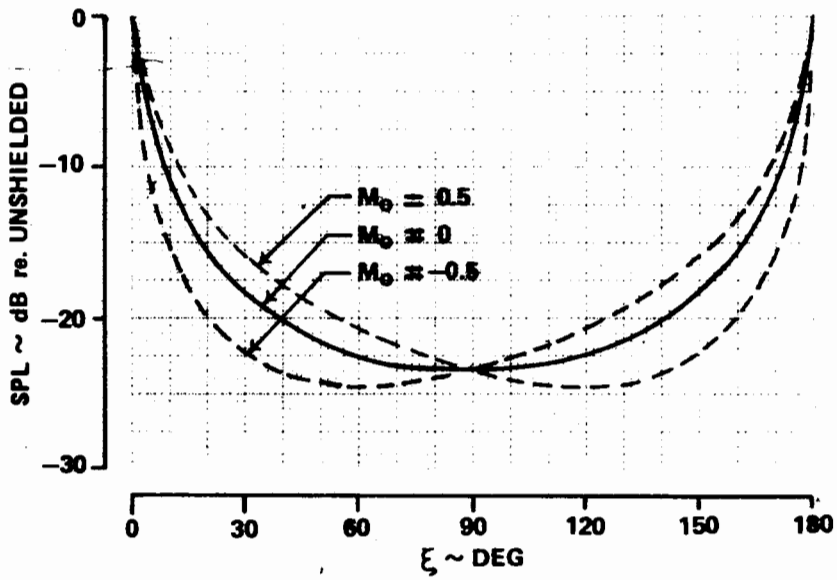

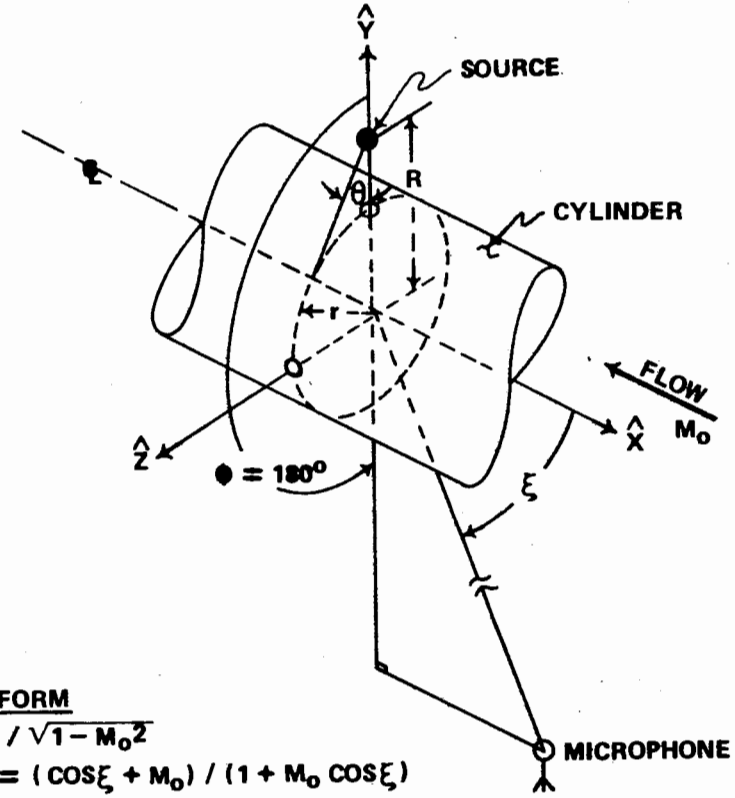

NOTES

a) POINT SOURCE (MONOPOLE)

b) KR = 100

c) $\theta = \sin^{-1}(r/R) = 45^\circ$

d) THEORETICAL ESTIMATE

TRANSFORM

$K' = K / \sqrt{1 - M_o^2}$

$\cos\xi' = (\cos\xi + M_o) / (1 + M_o \cos\xi)$

Figure 25.—Effect of Ambient Flow on Cylinder Shielding

From equations (31) through (34) presented above, it is possible to transform the three-dimensional cylinder diffraction problem with flow into an equivalent two-dimensional model. Figure 26 illustrates the equivalence. It is evident from the figure and the mathematics that the theoretical results can be considered as a function of only three independent variables: (a, b, ϕ) or (b, θ, ϕ). The latter variables have been chosen to develop predicted trends from the theory. Figure 27 shows sample results for an observer placed directly opposite the sound source on the other side of a shielding cylinder. Figure 28 shows a representative variation in the diffraction pattern as the observer moves to other angular positions, ϕ.

In the first part of section 2.2.2, it was noted that the solution is computationally expensive and unstable in certain regions. To circumvent this difficulty, a series of trend curves has been developed in appendix D of the volume II report for the range of conditions:

$$\left.\begin{array}{l} b = 2.5, 10, 40, 160, 320, 640 \\ \theta = 15^\circ, 30^\circ, 45^\circ, 60^\circ, 75^\circ \\ \phi = 0^\circ \text{ to } \pm 180^\circ \end{array}\right\} \text{See cross-reference table D-1, appendix D, volume II}$$

Large values of θ correspond to the sound source being relatively close to the fuselage and small values of b correspond to a low-frequency condition. The predicted trends for large θ and small b are slowly varying. Interpolation with respect to (log b, θ, ϕ) is permissible. However, when b is increased or θ is decreased, the curves show oscillations corresponding to constructive and destructive interference between the incident and scattered (diffracted) pressure fields. In the shadow zone of the cylinder, i.e., $|\phi|$ greater than ($180^\circ - \theta$), the oscillations are more pronounced. This is due to a strong interference phenomenon occurring between two signals diffracting around each side of the cylinder.

2.2.2.3 Filter Bandwidth Effects

The effect of finite bandwidth on the diffraction pattern for the cylinder is similar to that discussed previously for the half-plane in section 2.2.1.3. However, the approximation, equation (26), cannot be applied because the terms A(f) and B(f) are not slowly varying compared to $\cos\left[f\,C(f) - D(f)\right]$ when equation (31) is put in the form of equation (24) of section 2.2.1.3. Digital integration of equation (31) is required for a detailed evaluation of the filter bandwidth effect on the sound detection process of cylinder diffraction. Unfortunately, this calculation is discouraged by the computational difficulties associated with equation (31).

To illustrate the expected effects, we have relied on experience gained from the half-plane and studies on ground reflection (ref. 2) to make a manual "eyeball" estimate of the filter bandwidth effect. Such an estimate has been added to the discrete tone curves shown in figures D-1 through D-13 of appendix D in the volume II report. Due to the frequency averaging that a physical filter introduces to the detection process, the amplitude of the oscillations in the diffraction curves is reduced. In the high-frequency

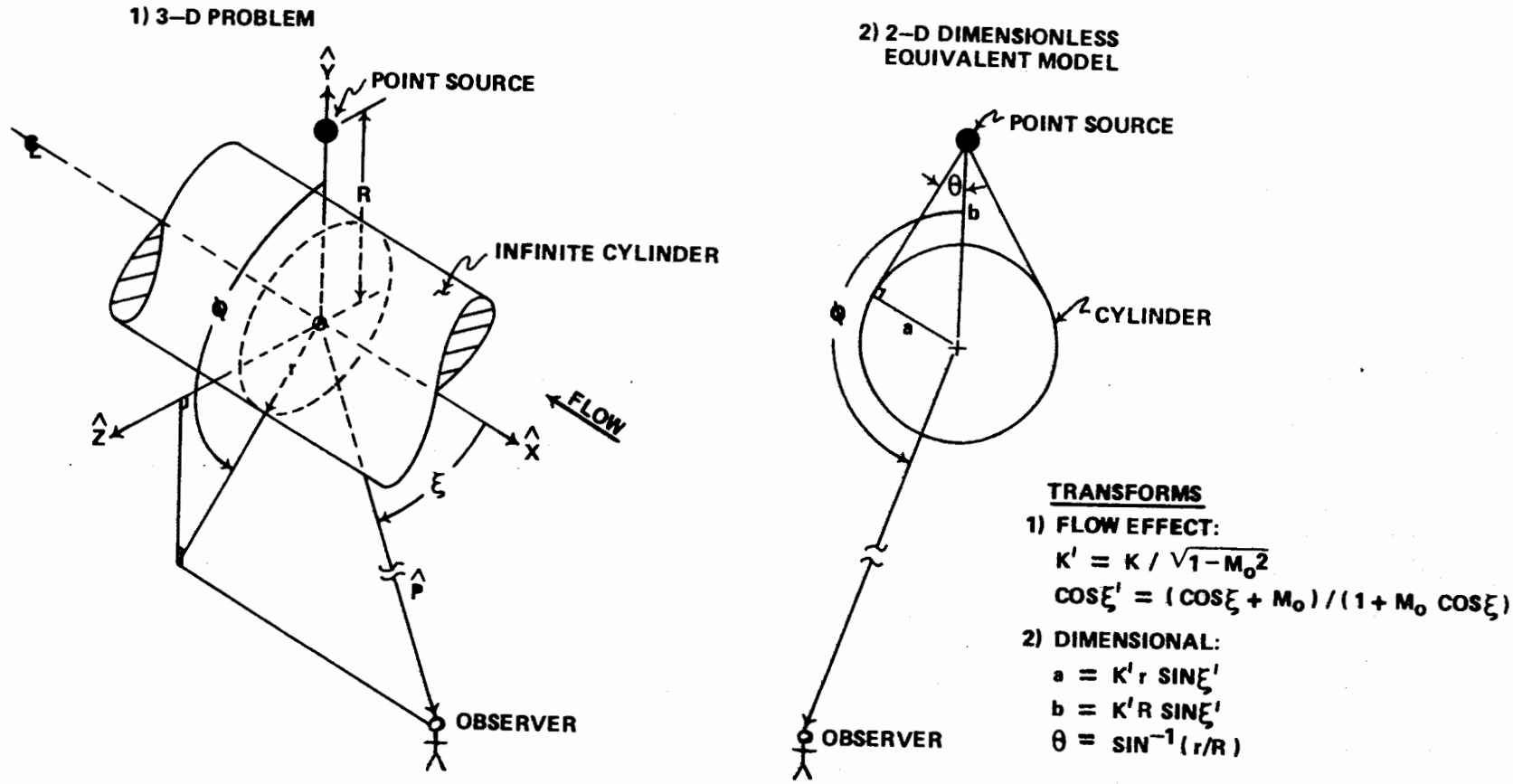

Figure 26.—Two-Dimensional Equivalent Model for Cylinder Diffraction

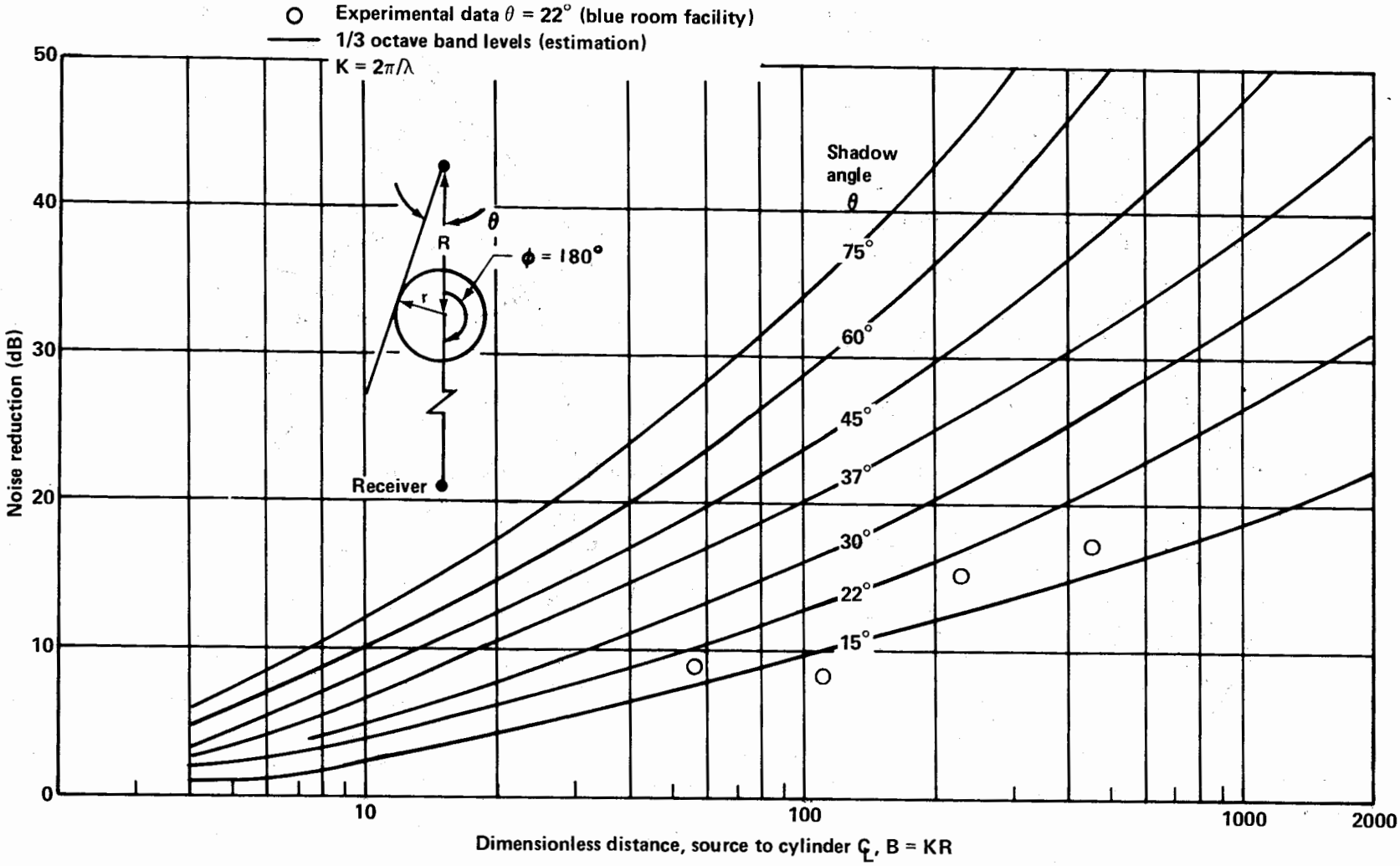

Figure 27.—Point-Source Noise Shielding From an Infinite Cylinder

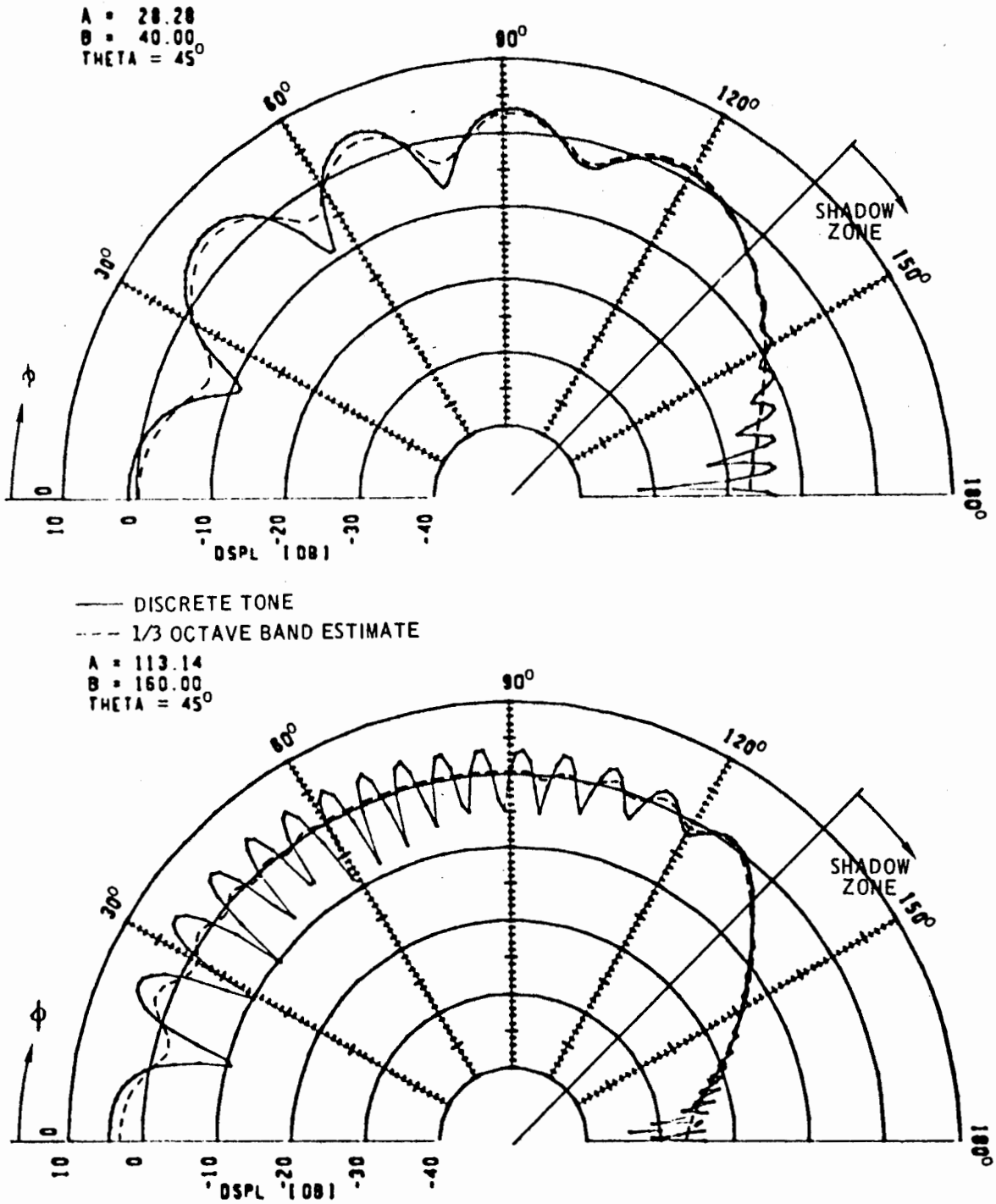

Figure 28.—Noise Diffraction About a Fuselage

limit in the light zone, i.e., $|\phi|$ less than $(180^o - \theta)$, the oscillations average toward a limit value of zero. In the shadow zone, i.e., $|\phi|$ greater than $(180^o - \theta)$, the strong interference phenomenon occurring for the signals diffracting around each side of the cylinder is smoothed out. In the low-frequency limit (b is small), the curves for discrete tones and 1/3-octave-band levels become identical. At intermediate frequencies, our best guess is shown. We feel this is representative of what a numerical evaluation would show.

2.2.2.4 Distributed Sources

The effect of a distributed source on diffraction about a cylinder can be calculated using the same formulas (eqs. 27, 28, and 29), presented in section 2.2.1.4 for the half-plane, except the Green's function in this case is given by equation (31). We have not made any detailed calculations to illustrate this effect because of problems noted previously in the solution and because of experience already gained from the half-plane samples. We believe that the effects of a distributed source on the shielding of a cylindrical body would be similar to that observed for the half-plane; i.e.,

- Additional complicated interference should occur in the diffraction patterns for coherent-phased source distributions.

- Less interference (a smoothing out of the curves) should occur in the diffraction patterns for random-phased source distributions.

- The source's spatial distribution should not have a significant effect on noise reductions in the deep shadow zone of the shielding barrier when the source's size is less than approximately one-quarter the characteristic dimension of the shielding barrier.

2.2.3 JET REFRACTION (RAY ACOUSTIC MODEL)

The theory of the refraction of sound as it propagates through velocity and temperature gradients in a jet is a relatively new development (refs. 26, 27, and 28). For a free jet, the theory is quite a complex subject in itself, and more so when coupled with the concept of shielding. To our knowledge no one has attempted to describe theoretically the phenomena when shielding barriers are placed near a jet. A rigorous theory for this problem would likely require detailed knowledge about the distribution of noise sources embedded in the jet flow and about the jet structure. This knowledge is lacking. However, the impact of jet flow on wing shielding of turbomachinery noise is significant and requires some type of model that considers refraction effects.

Figure 29a shows a typical observation of the effect as determined from fitting the directional/compact-source diffraction theory to wing shielding test data for exhaust turbomachinery noise (section 2.4.2). In this determination of the apparent source location, the problem is worked backwards using the far-field diffracted sound levels to determine the apparent location of a compact/directional noise source relative to a shielding barrier such as a wing. This solution has the apparent sound emission point downstream from the nozzle exit plane, often near the lower portion of the jet flow.

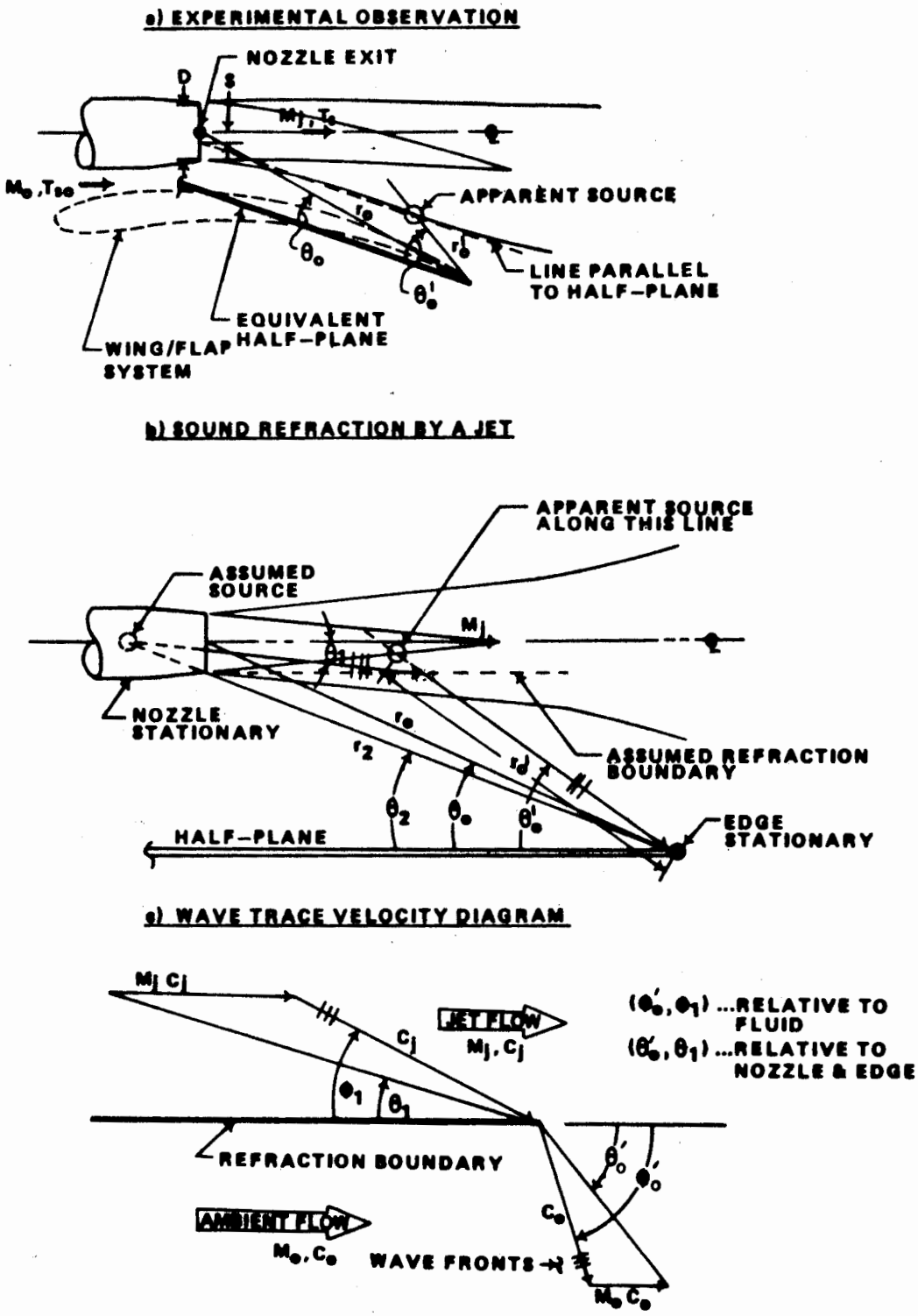

Figure 29.—Jet Flow Effects

When the engine is in close proximity to a wing/flap system and as the flaps are extended, the apparent sound source location appears to move further downward and aft toward the flap trailing edge. It is hypothesized that a refraction model can be used to determine the location of this apparent source and the location changes as engine performance and nozzle/wing geometry are varied.

2.2.3.1 Assumptions

Figure 29b shows a simplification of the problem initially given in figure 29a. The half-plane and engine centerline are now shown parallel. In order to use plane-wave approximations and to avoid complications of rigorous spherical wave refraction theory, we propose the following assumptions.

- The actual turbomachinery noise source is upstream inside the nozzle at the intersection of the jet centerline and the line defined by (r_2, θ_2).

- The distance (r_2) between the source and the barrier edge is greater than 10 wavelengths.

- The barrier edge is outside the jet efflux.

- The control surface for the refraction boundary is a cylinder about the engine centerline with a radius equal to one-half the nozzle diameter. Hence, the boundary is assumed to lie at the median of the shear zone between the jet potential core and the ambient flow. The finite thickness of this zone is assumed to have a negligible effect on the direction that acoustic waves leave the jet relative to the engine centerline.

- The product of the jet Mach number and $\sin(\theta_1)$ is not greater than unity .

- The apparent source coordinate is within the jet on the line defined by θ_0'. The distance r_0' from the edge to the apparent source is to be determined empirically inasmuch as this dimension is sensitive to other phenomena that might also be occurring, i.e., ducting and scattering.

- "Tilting" the equivalent half-plane as in figure 29a versus that shown in figure 29b has a negligible effect on the direction that acoustic waves leave the jet flow.

2.2.3.2 Two-Dimensional Solution

Analysis.–With the assumptions above, the following equations must be solved for the emission angle θ_0'. (The term $\cot \theta_0'$ is underlined in the equations to note that this is an iteration quantity whose value we must guess initially.) It is at this angle that the predominant acoustic energy leaves the jet flow.

Geometry (fig. 29b) requires:

$$\cot \theta_1 = 2(r_0/D) \sin \theta_0 \cot \theta_2 + [1 - 2(r_0/D) \sin \theta_0] \underline{\cot \theta_0'} \tag{35}$$

where

$$\cot \theta_2 = 2(r_o/D) \cos \theta_o/[2(r_o/D) \sin \theta_o - 1]$$

Wave propagation inside the jet (fig. 29c) requires:

$$\cot \theta_1 = (M_J + \cos \phi_1)/\sin \phi_1 \quad \text{or}$$

$$\cot \phi_1 = -M_J \sin^2 \theta_1 + \cos \theta_1 \sqrt{1-(M_J \sin \theta_1)^2} \tag{36}$$

From continuity of wave number and phase velocity at the hypothetical refraction boundary:

$$\cos \phi'_o = \cos \phi_1/[(M_J - M_o) \cos \phi_1 + (C_J/C_o)] \tag{37}$$

where (M_J, C_J) and (M_o, C_o) are the Mach number and speed of sound inside and outside the jet, respectively.

Finally, wave convection outside the jet gives the relationship for the geometric angle θ_o':

$$\underline{\cot \theta'_o} = (M_o + \cos \phi'_o)/\sin \phi'_o \tag{38}$$

Equations (35) through (38) can be considered as a nonlinear function $y = f(\cot \theta_o')$ for which the solution, θ_o', is found by finding the intersection between the curves $y = x$ and $y = f(x)$. Wegstein's secant modification iteration scheme is proposed for solution (ref. 39) since it converges rapidly for this problem; i.e., usually five iterations are required for five significant digit answers. The iteration steps are:

Let $x_o = 0, \quad y_o = f(x_o)$

$x_1 = y_o, \quad y_1 = f(x_1)$

Iterate the following calculations for $i = 1, 2, \ldots$

$$x_{i+1} = x_i - (x_i - x_{i-1})/[1 - (x_{i-1} - y_{i-1})/(x_i - y_i)]$$

$$y_{i+1} = f(x_{i+1})$$

until both the following conditions are satisfied:

$$|x_i - x_{i-1}| < 0.1\, \epsilon\, |x_i|$$

and

$$|x_i - y_i| < \epsilon\, |x_i|$$

with the unspecified tolerance constant, ϵ, to be set to the tolerable relative error, i.e., $\epsilon = 10^{-N}$ where N is the number of significant digits desired in the result.

After the iteration has converged, the angles ϕ_0' and θ_0' specify the direction of propagation of the acoustic waves leaving the jet (fig. 29c). The angle ϕ_0' corresponds to the direction normal to the wave fronts, whereas the angle θ_0' corresponds to the direction that acoustic energy is leaving the jet. Without ambient flow, these two angles are identical.

To put the problem in the context of diffraction about the half-plane with uniform flow, ϕ_0' is the angular displacement of the apparent source relative to the half-plane. Attention now turns to the determination of the "effective barrier height," r_0'. If the apparent source is assumed to be on the engine centerline,

$$r_0'/r_0 = \sin\theta_0/\sin\phi_0'$$

Experimental observations show that the apparent source usually appears near the lower side of the jet boundary when the engine is placed quite close to a wing. We introduce an empirical term in the preceding equation to account for this observation, i.e.,

$$r_0'/r_0 = [\sin\theta_0/\sin\phi_0']\,[1 - 0.5\,\beta\,D/(r_0\sin\theta_0)] \tag{39}$$

where β is a dimensionless term to be determined. For the apparent source confined within the jet, the permissible values of β range from -1 to +1. (This restricts apparent source location to within a nozzle radius of the jet flow centerline.) It is expected that β is dependent on the nozzle/wing geometry and possibly the exhaust flow conditions. When the nozzle is close to the wing, the value of β approaches +1.

Implications of Jet Refraction on Shielding.–The significant result from the above analysis is the ability to calculate apparent source locations (r_0', θ_0') based on a jet refraction model reflecting both nozzle-to-edge (observer) geometry (r_0/D, θ_0) and efflux flow properties (M_0, M_J, T_s/T_{s0}). As discussed previously in the theory of sound diffraction of directive/compact sources, the far-field directivity is an important element in establishing the reference incident level and hence the apparent shielding. Jet refraction appears to play an important role in shaping this far-field directivity for exhaust turbomachinery noise components. Experiments have shown that omnidirectional sources placed in nozzles became directional in the far field with efflux flow. Schubert (ref. 27) presents a theory on the effects of a free jet on the radiation of noise sources embedded in jet flow. However, the computations are complex and impractical for community noise applications. This presents no problem here, however, because we rely on a firm test data base for definition of far-field directivity of exhaust fan, turbine, and core noise. With this directivity information, and the ability to calculate apparent source locations using jet refraction theory, we are ready to combine the theories of jet refraction and directive/compact-source diffraction in a model for wing shielding estimation of exhaust turbomachinery noise.

Figure 30 illustrates the key shadow zone effects of source location changes on sound diffraction about a wing edge and the possible corresponding cause due to location and directivity changes expected from refraction of sound through jet efflux flow. First, figure 30a reviews the far-field shadow zone sound pressure level changes (see graph) as

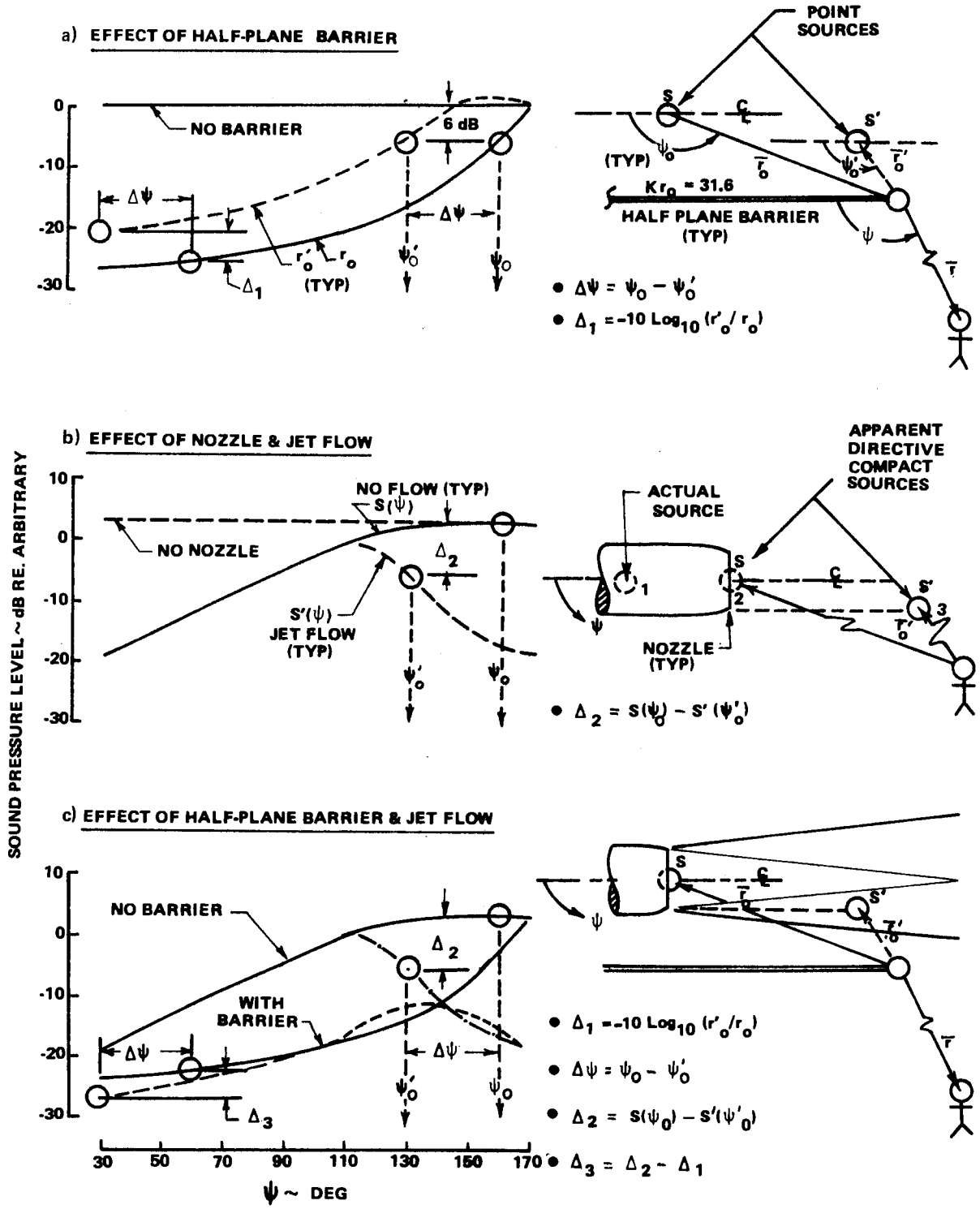

Figure 30.—Implications of Jet Refraction Effects on Half-Plane Shielding

a point source is moved from one location to another nearer the barrier edge and closer to the half plane (see sketch). Here, an actual source S located at (r_0, ψ_0) is moved to (r_0', ψ_0') and labeled S′. (Angles θ_0 and ψ_0 are used interchangeably since in this example $\psi_0 = 180^0 - \theta_0$). These locations are conveniently chosen to respectively correspond to the apparent source locations S and S′ when an actual compact source is placed inside a nozzle without jet flow and then with jet flow as shown in the sketch for figure 30b. The refraction equations (35) through (39) were used to calculate the change in location for apparent source locations S and S′ using the following geometric and flow properties:

$\psi_0 = 160^0$	$r_0/D = 4$	$M_J = 0.6$
$\theta_0 = 20^0$	$\beta = 1$	$T_s/T_{so} = 1$
	$M_0 = 0$	

The circles in figure 30a, as in our previous discussion on diffraction, call out the shadow boundaries ψ_0 and ψ_0' for sources S and S′.

The effect of the nozzle and jet flow on the far-field unshielded sound pressure level of the simple source is shown in figure 30b. The sketch for these trends is shown at the right. Imagine an observer placed at the hypothetical near-field location shown. This observer location corresponds to where the edge of the half-plane will eventually be. With no jet flow, the observer detects sound as though it is generated by the whole nozzle exit (location 2), not by the actual source inside the nozzle (location l). The center of this apparent source at location 2 is noted by S in the sketch. With jet flow, the observer no longer detects the apparent source to be at the nozzle exit. The center of sound appears to be downstream from the nozzle exit near the lower side of the jet (location 3). This point is labeled apparent source S′ in the sketch of figure 30b. These apparent source positions correspond to those chosen in the sketch of figure 30a.

Imagine that the observer moves into the far field. Based on test data, the typical far-field unshielded SPL directivity observed is shown by the curves in figure 30b. He observes three sound fields due to three placements of the simple source:

- Source by itself
- Source inside the nozzle without exhaust flow (apparent source S)
- Source inside the nozzle with exhaust flow (apparent source S′)

Although an omnidirectional source was placed inside the nozzle, apparent sources S and S′ are no longer omnidirectional due to the effect of the nozzle and the flow. Reference unshielded SPL's, $S(\psi_0)$ and $S'(\psi_0')$, are noted by circles in the graph of figure 30b when the source is placed inside the nozzle. These reference levels correspond to the shadow boundary angles (ψ_0' and ψ_0) when the half-plane barrier is put next to

the nozzle for the conditions with and without jet flow, respectively. The difference between these two reference levels is noted by Δ_2 similar to that previously called out in figures 15c and 15d in the discussion on diffraction.

The two effects of diffraction (fig. 30a) and jet refraction (fig. 30b) can possibly be combined. Necessary physical conditions for coupling the idealizations are:

- The barrier does not alter the noise radiation characteristics of the jet significantly.

- There is a one-to-one correspondence between sound levels observed in the near field (outside the jet) and the far field at least for direction angles ψ near ψ_0' and ψ_0, respectively, for the cases with and without jet flow.

It is tacitly assumed that these conditions are met. Hence, in figure 30c, the two effects of figure 30a and 30b are coupled together. The sketch at the right shows conceptually the physics of turning on the jet flow. The curves plotted to the left are simply a repeat of those given previously in figure 15d. This example strongly suggests that the theories of combined diffraction and jet refraction could be used to model observed wing shielding trends for turbomachinery noise components. This example provides insight on what to expect when experimental TM noise shielding data is examined.

Figure 31 shows the impact that jet refraction could have on the term Δ_1 in figure 30a for sound diffraction about the trailing edge of a wing/flap system for flyover conditions using the solution formulas (eqs. 35 through 39) given above. We have plotted the results as $10 \log_{10}(r_0'/r_0)$ versus the cotangent of the direction angle, ψ_0, that grazes the trailing edge. This angle appears to be a controlling parameter for both diffraction (sec. 2.2.1) and jet refraction, i.e., $\psi_0 = 180^0 - \theta_0$ in figure 29b. Figure 31 illustrates the sensitivity of the refraction effects due to changes in the following variables:

- Exhaust flow Mach number, M_J

- Exhaust flow temperature, T_s/T_{so}

- Ambient flow Mach number, M_0

- Nozzle size, r_0/D

It can be seen that as the nozzle is placed close to the wing surface (ψ_0 approaches 180^0), the maximum wing shielding attenuation should be less than that predicted by diffraction with the source located at the nozzle. This loss becomes smaller as the nozzle is withdrawn from the surface. This implies that the most shielding attenuation might be realized with the nozzle placed off of the wing's surface. Unfortunately, these curves do not include the effect of the noise sources' directivity with the movement of the apparent source. Hence, the implication needs further study.

Figure 32 similarly shows the change in the shadow zone boundary ($\Delta\psi$ in fig. 30a) corresponding to a downstream shift in the apparent source position relative to the

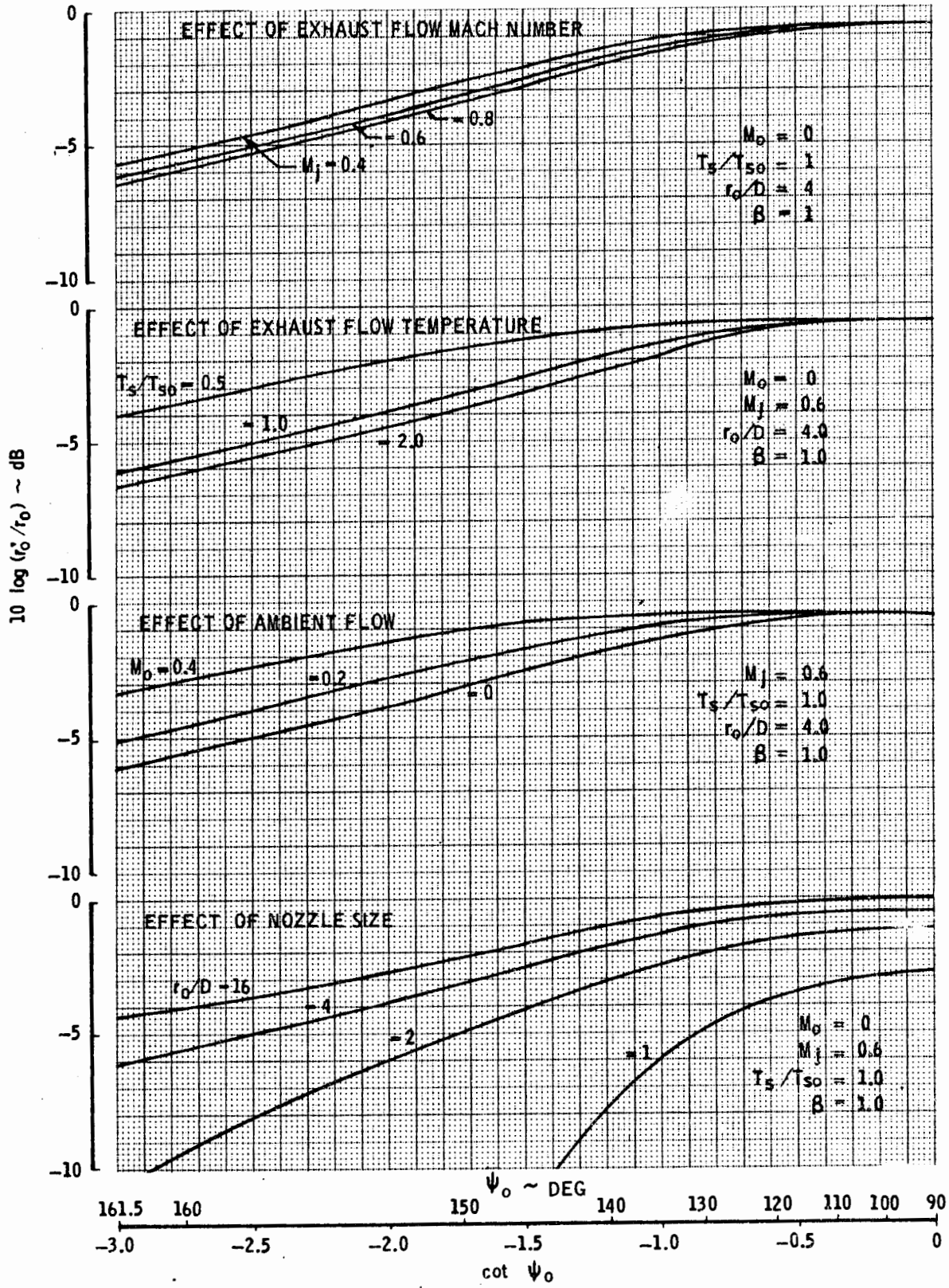

Figure 31.—Impact of Jet Refraction on Maximum Wing Shielding Attenuation (Theoretical Estimate)

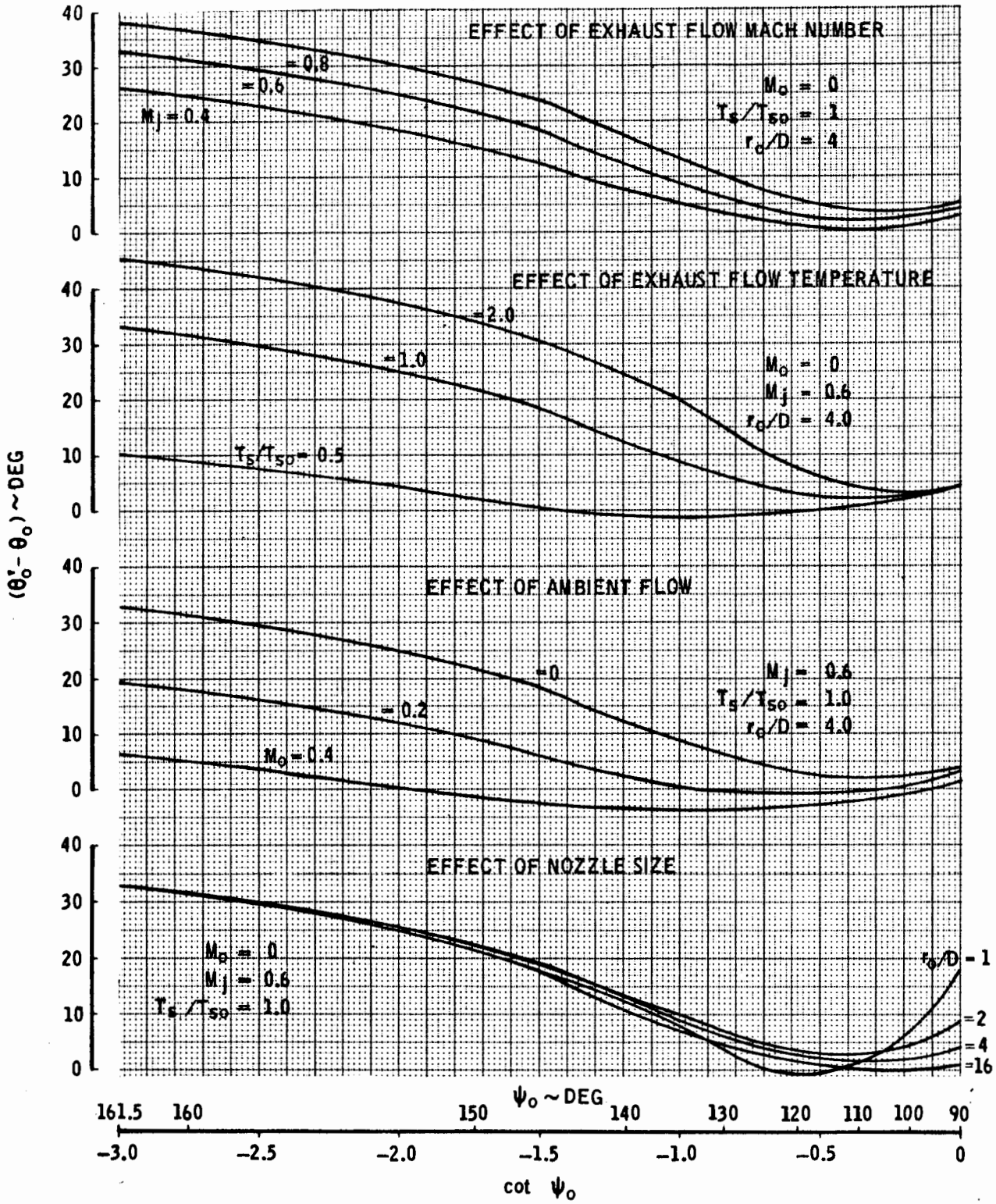

Figure 32.—Impact of Jet Refraction on Wing Shielding Shadow Zone Boundary (Theoretical Estimate)

nozzle exit plane. A decrease in the angular size of the shadow zone should occur due to refraction. Qualitatively, the trends shown in figures 30 through 32 have been observed in our wing shielding experiments using apparent source locations that make a directional/compact-source diffraction model agree with the actual far-field shielded SPL test data.

2.2.3.3 Three-Dimensional Approximation

We have generalized the previous two-dimensional solution to approximate the three-dimensional case. This approximation is necessary for shielding predictions when the observer is placed off to the side of the aircraft's flight track projection on the ground plane. The approximation is somewhat crude because the nature of the jet flow field is uncertain; i.e., the flow field can be significantly altered due to the presence of the wing. The result accounts for the redirection of acoustic waves as they leave the jet and the apparent concentration of acoustic energy in the lower portion of the jet nearest the shielding surface.

In figure 33a, the nozzle and observer are shown oriented arbitrarily with respect to the equivalent half-plane of the wing's trailing edge. The convention used for the discussion of the directional/compact-source diffraction theory (fig. 12) is shown in this figure as it relates to the refraction of sound by a jet. The angular change, $\Delta\psi$, in the sound propagation direction is likened to a downstream movement of an emission point P_1 to point P_2. The angular change, $\Delta\psi$, is related to the aforementioned two-dimensional refraction problem by substituting:

- $(180^0 - \psi_0)$ for θ_0 in equation (35)
- $|\bar{a}|$ for r_0 in equation (35)
- $[(180^0 - \psi_0) + \Delta\psi]$ for ϕ_0' in equation (37)

With these substitutions, the point P_2 may be located.

Figure 33b shows the case where the equivalent half-plane is not parallel to the engine centerline, which might result when the flaps are extended. The vectors $\bar{b}$ and $\bar{b}'$ shown in this figure represent the vectors $\bar{a}$ and $\bar{a}'$ of figure 33a projected into a plane that is normal to the half-plane barrier and contains the engine's centerline. The apparent source is located at the intercept, P_3, of two lines:

- A line parallel to vector $\bar{b}'$ drawn from the edge to point P_2
- A line parallel to the half-plane that is displaced a distance S from the nozzle centerline

The distance S is defined as the nozzle radius times the dimensionless empirical parameter β discussed previously for the two-dimensional problem.

Figure 33c shows the manner in which the polar coordinates (r_0', ϕ_0') for the apparent source are calculated relative to the wing edge. A vector $\bar{C}$ is drawn from the point A on

a) ANGULAR SHIFT OF SOURCE ($\Delta\psi$)

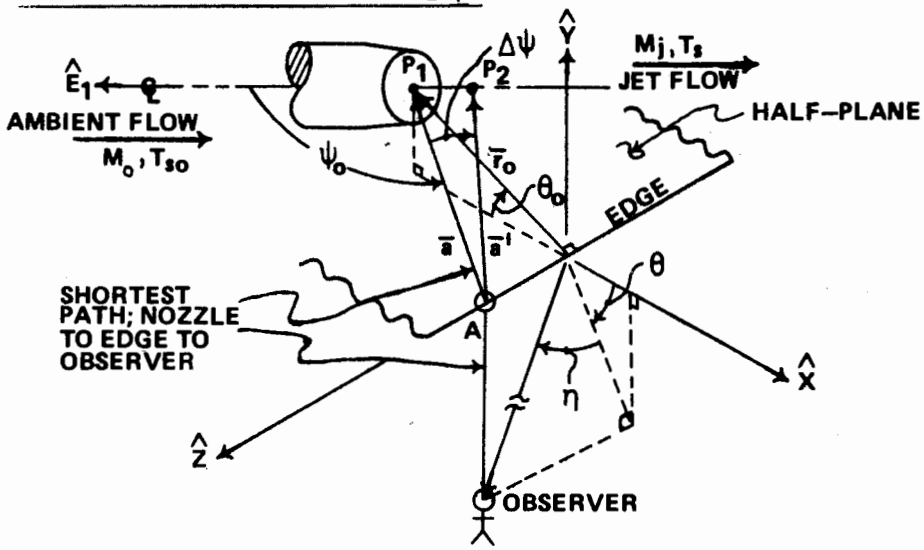

b) SHIFT TOWARDS HALF–PLANE (P_2 TO P_3)

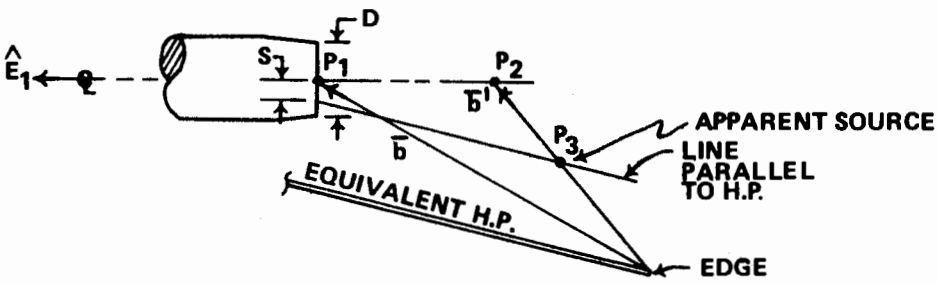

NOTES

1) VECTORS $\bar{b}$ & $\bar{b}'$ ARE VECTORS $\bar{a}$ & $\bar{a}'$ PROJECTED INTO PLANE NORMAL TO HALF–PLANE THAT CONTAINS THE ENGINE ℄

2) $\beta = 2S/D$

c) RELATING APPARENT SOURCE BACK TO 3–D GEOMETRY

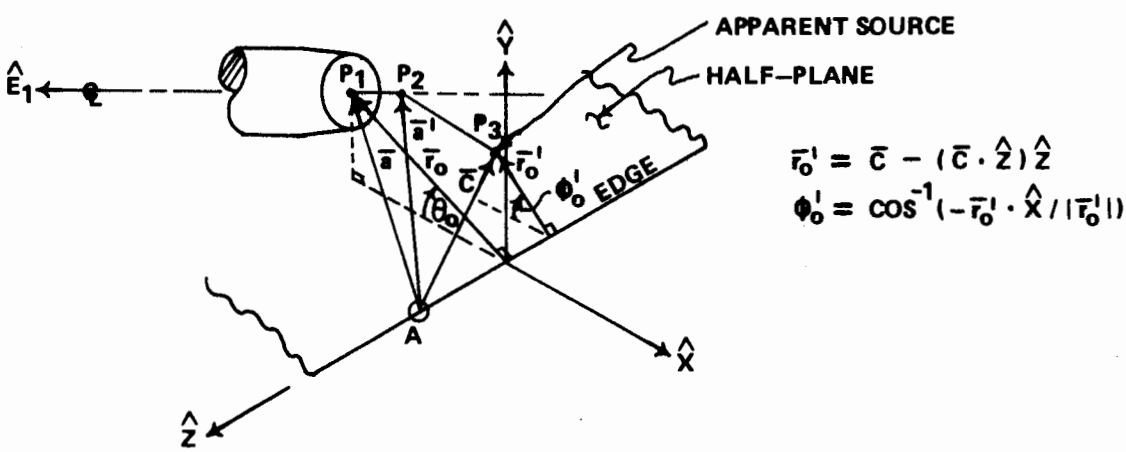

$$\bar{r}_o' = \bar{c} - (\bar{c} \cdot \hat{Z})\hat{Z}$$

$$\phi_o' = \cos^{-1}(-\bar{r}_o' \cdot \hat{X} / |\bar{r}_o'|)$$

Figure 33.—Three-Dimensional Jet Flow Refraction Solution

the edge (same point A as in fig. 33a) to the point P_3 of the apparent source. The components of vector $\bar{C}$ along the edge are then removed to give a vector $\bar{r}_0'$ which is normal to the edge. The coordinates (r_0', ϕ_0') are then calculated from the vector $\bar{r}_0'$ using the formulas shown beside the sketch in figure 33c.

It seems appropriate to stop and to take stock of the material presented so far before proceeding to the next section on wing wake effects. Figure 34 shows the physical situation for which we are trying to develop a noise shielding estimation procedure:

- The jet engine is in close proximity to a wing.
- A sound source is upstream inside the exhaust nozzle.
- Jet flow is present.
- Ambient flow is present.
- A wing wake is present.

Sound emitted from the source gets outside the engine by two possible modes:

- Transmission through the jet
- Transmission through the engine case

The first mode above has been quantified as it relates to propagation of sound out of the jet and about the wing. The second mode, case radiation, is usually unimportant and is mentioned only to denote that situations in shielding can arise where it might need consideration. Once the sound gets outside the engine, the acoustic propagation into the shadow zone of the wing is governed by three transmission modes:

- Edge diffraction
- Wing wake scattering and refraction
- Flanking radiation

The available theory for the first mode has been presented in section 2.2.1. The wing wake will be discussed in the next section. The third mode is mentioned because it represents a noise floor contamination that is usually always present to some degree or less. It results when other scattering or reflecting surfaces are near the exhaust nozzle and the wing, i.e., various test site surfaces such as airplane fuselage, support structures, walls, trees, ground, etc. Currently, there is no means available to quantify the effects of flanking radiation. Qualitatively, it can cause the apparent noise source to appear quite close to the wing edges when diffraction theory is fitted to experimental data. This effect was observed in our data analysis.

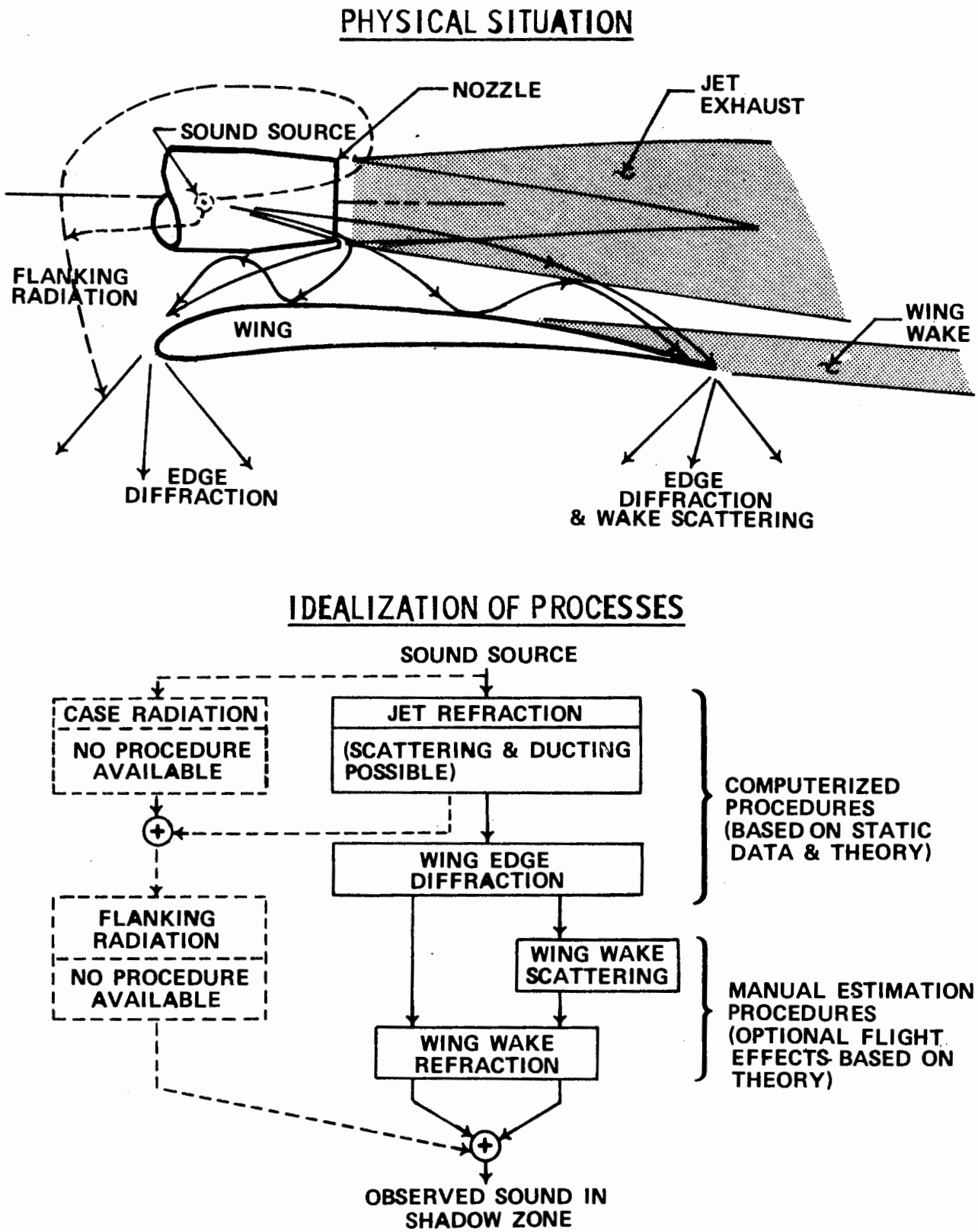

Figure 34.—Idealization for Wing Shielding of Turbomachinery Noise Components

Another physical interpretation in line with jet flow effects can also explain the apparent source being close to the wing edges. Sound is emitted from the source inside the jet and is convected downstream. As the sound waves emerge from the lower side of the jet, they are redirected by the phenomenon called refraction. A large portion of this sound strikes the wing and is reflected upward. That escaping upward or away from the wing's shadow zone is of no interest and is not shown in figure 34. However, a portion of this upward reflected sound can be reflected back toward the wing by the jet flow provided the transmission coefficient for sound passing into the jet is small. This condition is usually always met for jet engines. Hence, it is possible that acoustic energy can be channeled or ducted in the region between the jet and the wing before being diffracted about the trailing edge of the wing.

A similar channeling situation can occur for sound propagating forward toward the wing's leading edge, except the engine case is the surface that can reflect the sound back toward the wing. The net result of the ducting phenomenon is that the sound appears to be emitted from locations quite close to the wing edges as the engine is placed closer and closer to the wing for flyover observer geometries. For the observer positioned to the side of the airplane's flight track, this ducting phenomenon should disappear and the apparent source should be closer to the location of the actual nozzle exit plane.

The jet refraction model presented above contains the effects just noted for turbomachinery noise diffracting about the wing's trailing edge by use of the empirical term β. For the leading edge, the effect of reflections off the engine case is not specifically addressed in the refraction model because of uncertainty about the engine case geometry and mounting. Also, it is not clear which effect could be dominant, i.e., ducting or flanking radiation. Both effects are likely to occur. Further discussion of these effects will be deferred to section 2.4.2 dealing with the data analysis.

2.2.4 WING WAKE EFFECTS

An additional complication arises when the EOW aircraft is in flight. A wake of retarded flow velocity and turbulence exists behind the airplane wing. Both boundary layers and any flow separations contribute to this wake. The wing wake provides a mechanism for sound to be refracted and scattered into the shadow zone. The velocity deficit in the wake causes sound refraction, whereas the inhomogeneities cause the scattering of sound. The processes of wing wake refraction and scattering happen simultaneously with the process of diffraction. It is difficult to decipher the order in which the processes occur. Hence, it is assumed that the phenomena occur in cascade where the order of the processes is immaterial. Figure 34 in the previous section shows the idealization of all the effects from the emission of sound at the source to the reception of sound by an observer in the wing's shadow zone. It is assumed that some of the acoustic energy in the vicinity of the wing's edge is diffracted and some is scattered by inhomogeneities in the wake. Unfortunately, percentages for the energy reaching the observer by edge diffraction versus wake scattering are unknown. It is possible that the wake scattering process could limit the wing shielding potential.

In this section two theoretical models are examined to quantify the effects of a wing wake on sound propagation:

- A refraction model, which considers the wake as a layered velocity medium
- A scattering model, which considers the wake as a medium with imbedded inhomogeneities

First, the refraction model will be discussed. Sound attenuation can possibly result if the aircraft can be configured to take advantage of the wake refraction phenomenon. The scattering model is presented next. The importance of scattering is that it does not provide any noise reduction capability; rather, it limits the attenuation possible by use of aircraft surfaces as acoustical barriers. Also, it is likely that the scattering effects can wipe out the benefits obtained by the refraction process.

2.2.4.1 Wake Refraction

Figure 35 shows the idealization applicable to the modeling of the wing wake as a layered medium. The assumptions for this model include the following.

- The sound source is fixed relative to the airplane and is represented by a compact source.
- A perfect and inviscid gas comprises the medium for sound propagation.
- The wing's trailing wake is constant in velocity and temperature. The velocity is different from the free-stream velocity while the temperature is the same.
- The wake extends to infinity with finite thickness.
- The presence of the wing as a solid body can be included with this model by superimposing the effects of refraction on wing diffraction. This is done by assuming that the two processes, diffraction and refraction, occur in cascade and can be lumped together by the product of the transfer functions for each process.

We seek to find an expression relating the sound that propagates through the wake with that observed to propagate through the same region without the wake. This expression has been found. It was obtained by solving the following time-dependent, convected wave equation:

$$(D^2 - \nabla^2)\, p = (\gamma/C_o)\, D\, \dot{q}\, \delta(x, y, z) \tag{40}$$

where

D = partial differential operator = $(1/C_o)\, \partial/\partial t + M\, \partial/\partial x$

M = local flow Mach number

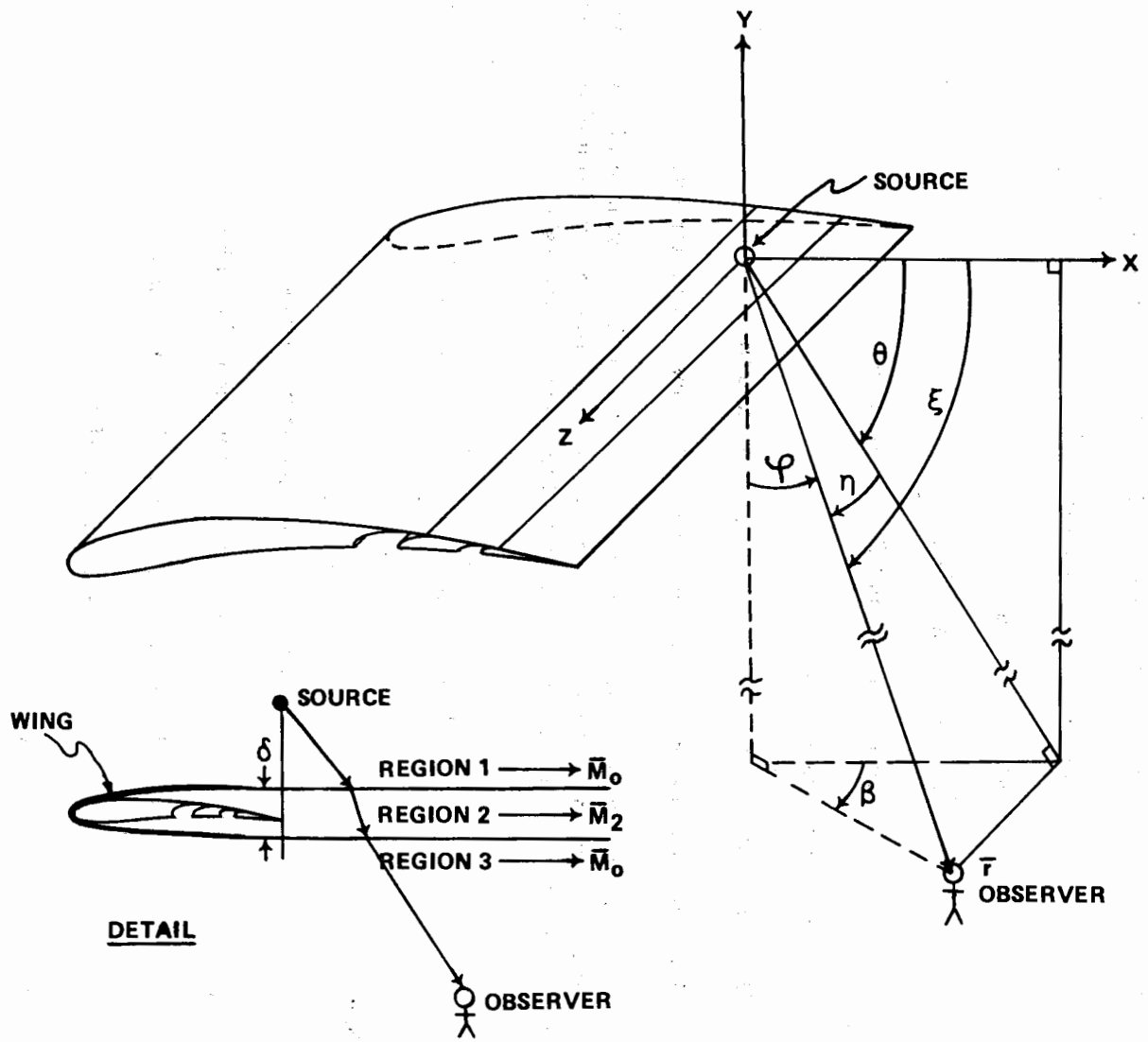

Figure 35.—Model for Sound Refraction Through Wing Wake

∇^2	=	Laplacian operator = $\partial^2/\partial x^2 + \partial^2/\partial y^2 + \partial^2/\partial z^2$
p	=	dimensionless acoustic pressure = $(P - P_o)/P_o$
γ	=	ratio of specific heats = C_P/C_V
C_o	=	speed of sound
$\dot{q}$	=	source strength (Hz)
$\delta(x, y, z)$	=	three-dimensional Dirac delta function

The boundary conditions to be satisfied are:

- Outgoing waves exist only for y being positive and in region 3.
- Acoustic pressure and displacement are continuous at all interfaces.

H. Y. Lu (ref. 28) has solved this problem in the far field. The details of his solution are provided in appendix E of volume II. The magnitude of the observed sound in region 3 relative to that without the wake is given by the following expression.

$$|p_R/p_I|^2 = [(d^2 - 1)\sin^2(\zeta_2 f/f_o) + 1]^{-1} \tag{41}$$

where

p_R	=	observed sound pressure with the wake
p_I	=	observed sound pressure without the wake
f_o	=	characteristic frequency (Hz) = $C_o/(2\pi\,\delta)$
f	=	sound source frequency (Hz)
d	=	$(C + 1/C)/2$
C	=	$[\zeta_2 (1 - a M_o)^2] / [\zeta_o (1 - a M_2)^2]$
ζ_2	=	$[1 - a M_2)^2 - (a^2 + b^2)]^{1/2}$
ζ_o	=	$[(1 - a M_o)^2 - (a^2 + b^2)]^{1/2}$
a	=	$\left[\dfrac{\cos\xi}{(1 - M_o^2 \sin\xi)^{1/2}} - \dfrac{M_o}{(1 - M_o^2)}\right]$

$$b = \left[\frac{1}{1 - M_o^2} - \frac{1 - M_o^2 \cos^2 \xi}{1 - M_o^2 \sin^2 \xi} \right] \frac{\sin \eta}{\sin \xi}$$

(M_o, M_2, δ) = wake properties shown in figure 35

(ξ, η) = direction angles shown in figure 35

Calculations have been made using the above equation to evaluate this refraction model. The implications of the calculated results are:

- Sound propagating through the wake will not be attenuated except in directions nearly perpendicular to the flow direction ($\beta = 90^o$) and approaching grazing incidence ($\psi = 90^o$) with respect to the wake.

- As grazing incidence is approached, a "cutoff effect" occurs suddenly for values of ψ between 70° and 90°. Large sound attenuation is possible in this cutoff zone. Outside this zone, no appreciable attenuation occurs.

- The calculated attenuation scales with respect to the product of the sound source frequency and the wake thickness.

- The attenuation increases with an increase in sound frequency, wake thickness, and wake velocity deficit.

Figures 36a and 36b illustrate the significant results noted above where attenuation is possible. Present aircraft configurations in which this attenuation might be discerned are those with the jet engines mounted in the rear of the airplane, aft and above the main wing chord plane. The sound attenuation should be detectable for inlet noise components with the observer positioned at far sideline distances from the airplane's flight track, i.e., but should not be detectable for observers positioned directly under the flightpath where community noise levels are generally higher. Hence, it seems unlikely that the wing wake can be relied upon to provide any significant community noise reduction.

Another refraction effect for flow about a wing has been studied by G. F. Butler et al. (ref. 29). This refraction is caused by the wing vortex, rather than the trailing wake. Butler has presented a ray acoustic theory and test data to confirm that the refraction phenomenon actually occurs for a delta wing aircraft. Unfortunately, his prediction model requires a detailed velocity field description and this information is either not available or difficult to obtain. We have not pursued further development of Butler's prediction model for this reason. We do feel that the subject deserves more study because the noise reductions shown in Butler's paper were significant; i.e., the strong leading-edge-induced vortex established by the delta wing did tend to redirect the sound emitted from a source placed above the wing away from the zone beneath the airplane. This effect was in addition to the shielding provided by the wing.

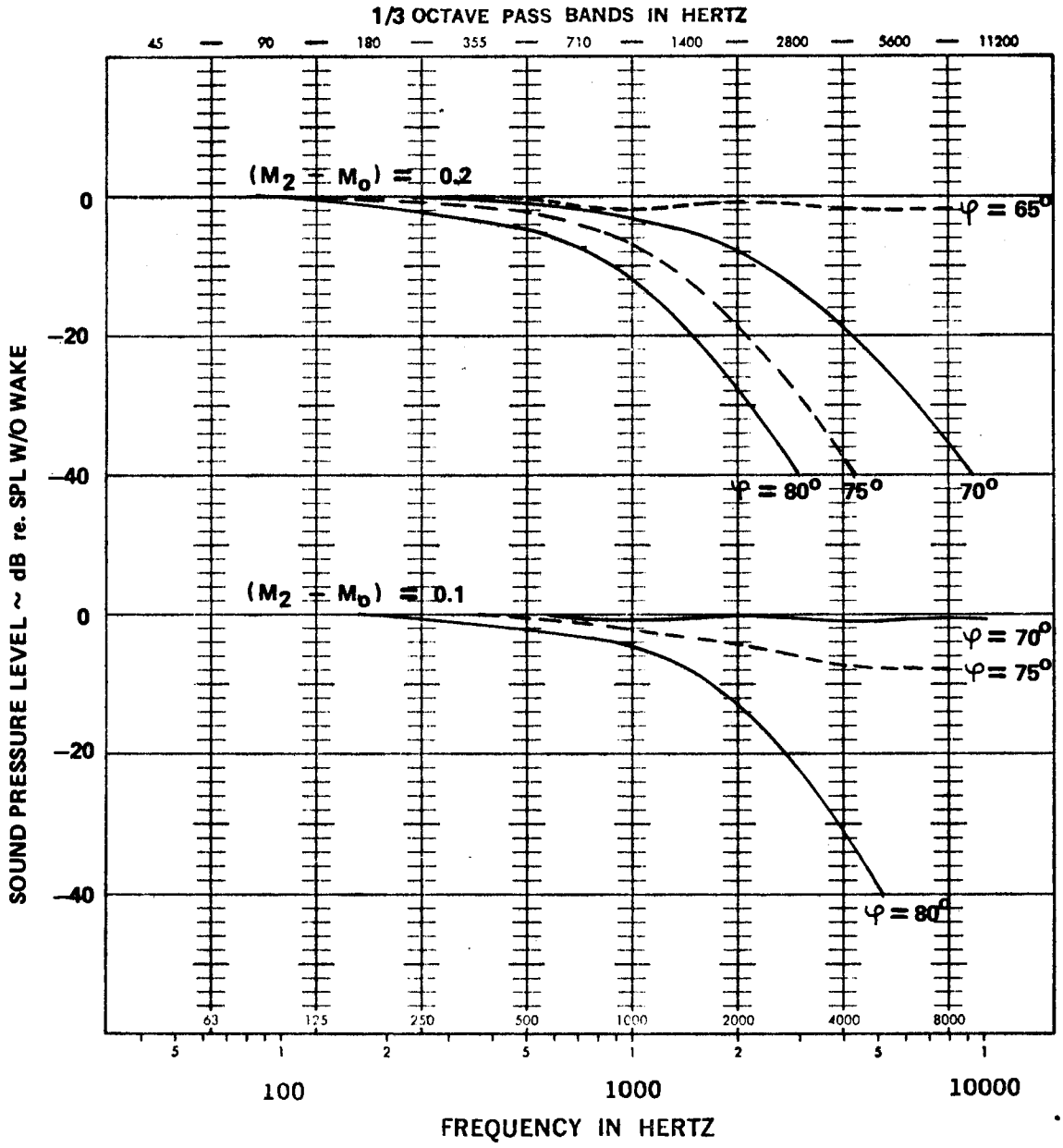

● $M_o = 0.3$

● $\beta = 90°$

● THEORETICAL ESTIMATE

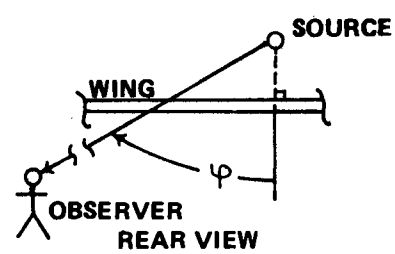

a) WAKE THICKNESS $\delta = 0.3$ m

Figure 36.—Noise Attenuation of a Wing Trailing Wake

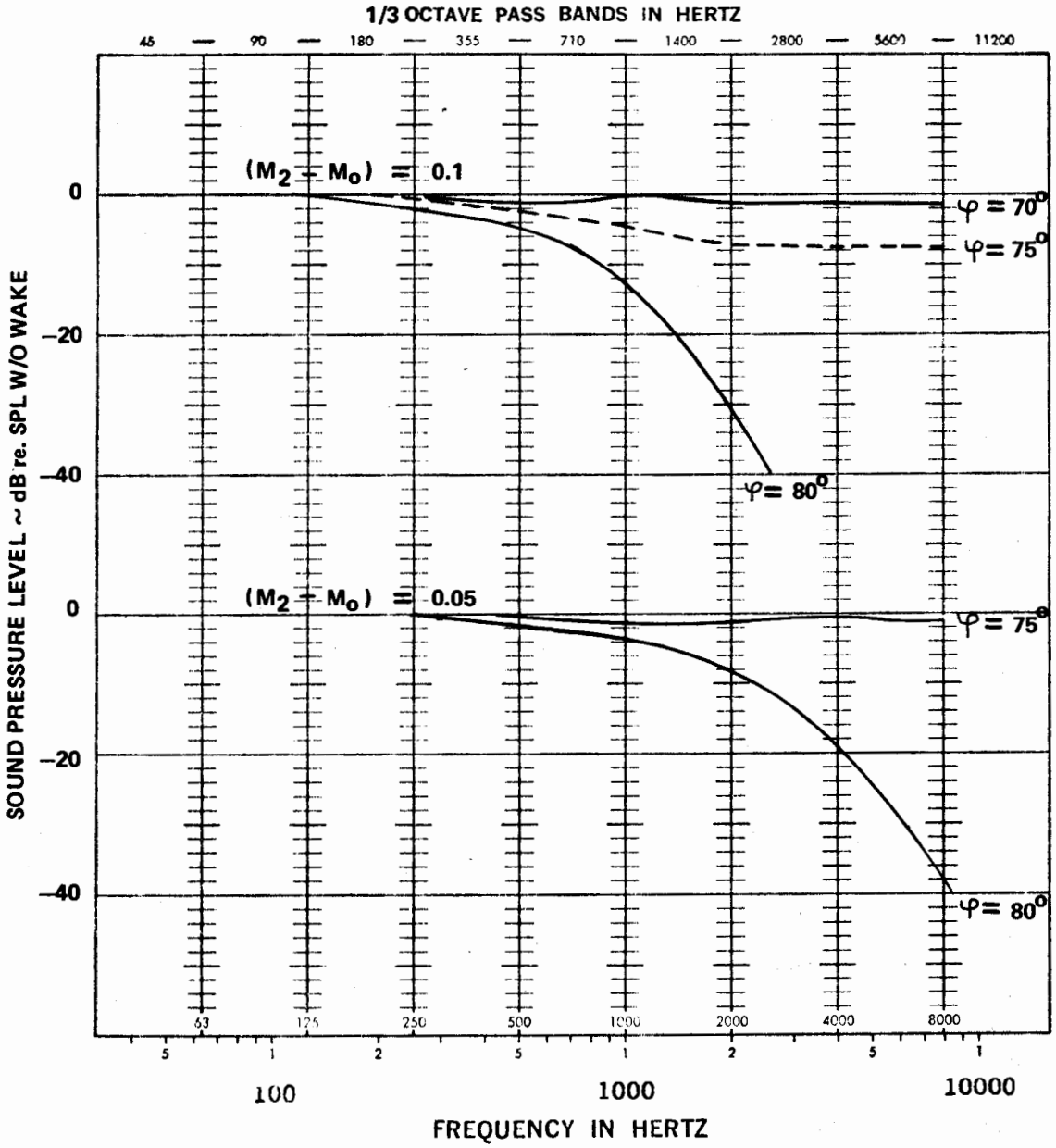

- $M_o = 0.3$
- $\beta = 90^o$
- THEORETICAL ESTIMATE

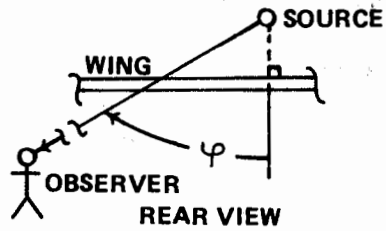

b) WAKE THICKNESS $\delta = 0.61$ m

Figure 36.—(Concluded)

2.2.4.2 Wake Scattering

This section discusses the loss of wing shielding effectiveness of EOW aircraft configurations due to the scattering of sound by the turbulent wing wake when the aircraft is in motion. Figure 37 shows how turbulence in the wing wake can redirect sound into the wing's shadow zone. The objective of this section is to:

- Specify conditions under which scattering is significant
- Estimate the magnitude of the scattered sound field
- Identify weaknesses in the scattering theory where additional information is needed

The material presented here is based on an internal Boeing report prepared by C. H. Berman.

The EOW concept is thought to have the potential of providing in excess of 20 dB reduction in turbomachinery noise. This reduction is limited by other noise sources that can be present and various flanking transmission modes in which sound gets into the wing's shadow zone. Thus, scattered sound fields must be 20 to 30 dB below levels encountered in the absence of the wing in order not to constitute a limit to such a suppression concept.

The present analysis shows that wing wake scattering can potentially prevent shielding attenuation of typical wing flap systems from being as large as 20 dB. Estimates have been made for representative cases. Figures 38 through 40 show calculated results for a flight Mach number of 0.27, a wing with a 6.1-m chord length assuming four different profile drag coefficients ($C_D = 0.004$, 0.01, 0.1, 0.2), and three different frequencies (f = 1, 3, 10 kHz). The ratio of scattered to unscattered sound intensity is shown as a function of the scattering angle (θ). These estimates show that scattering is significant at high frequencies (10 kHz) for both high- and low-drag cases. At 3 kHz, it is significant for all but the lowest drag case. At 1 kHz, scattering is important for only the two highest drag cases. Drag coefficients for typical high-lift systems of commercial transports range from 0.01 to 0.1. Hence, scattering will limit the shielding attenuation potential when flap systems are deployed.

A major deficiency in the preceding estimates is the incomplete knowledge of the wake's turbulent intensity as a function of the wing's profile drag coefficient. This relationship is known for the far wake behind bodies, but little information is available concerning the near wake where the highest turbulence intensities and greatest scattering occur. Some near-wake turbulence data was obtained for the present analysis in order to relate turbulence intensity to wing drag (ref. 36). Unfortunately, the data covered only the highest drag cases and it appeared that the drag coefficients were somewhat high for the airfoil test sections used to obtain the data. Since our estimates are based either directly on this data or on extrapolations to lower values of wing drag, the scattered sound estimates are probably accurate within an order of magnitude, i.e., ±10 dB.

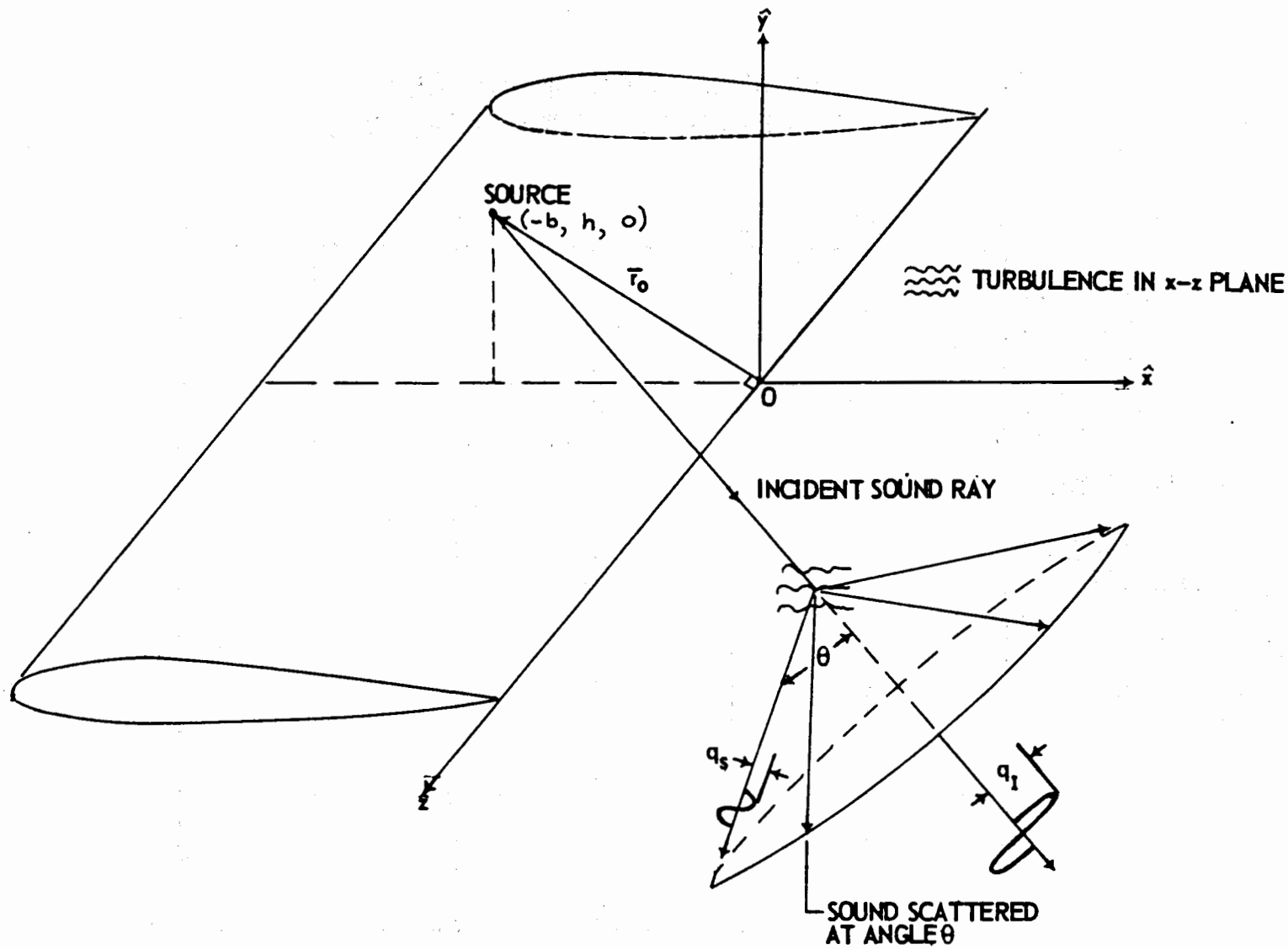

Figure 37.—Sound Scattered by Turbulent Wake of an Airfoil

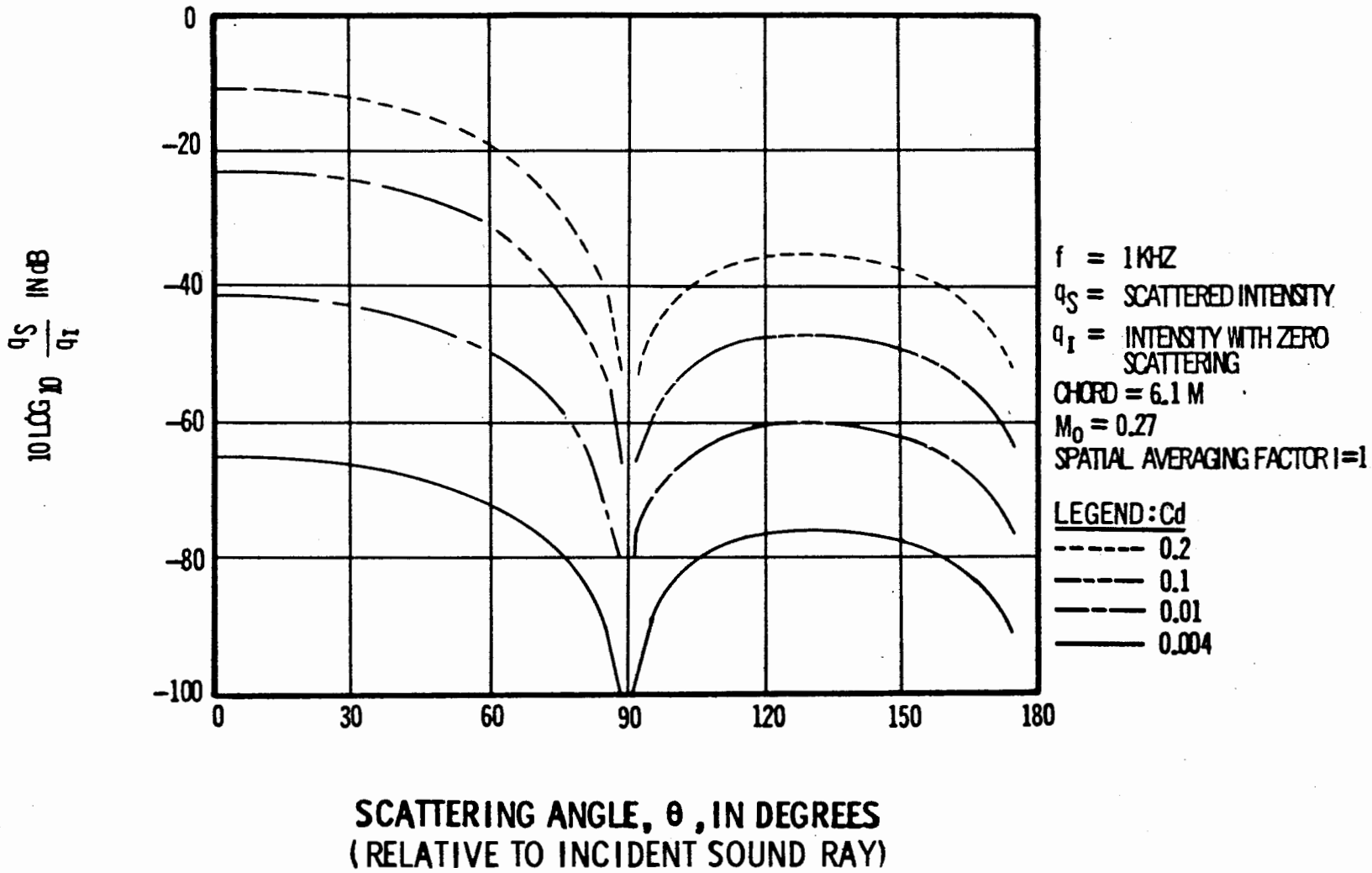

Figure 38.—Scattered Intensity Relative to Unscattered Intensity (1 kHz)

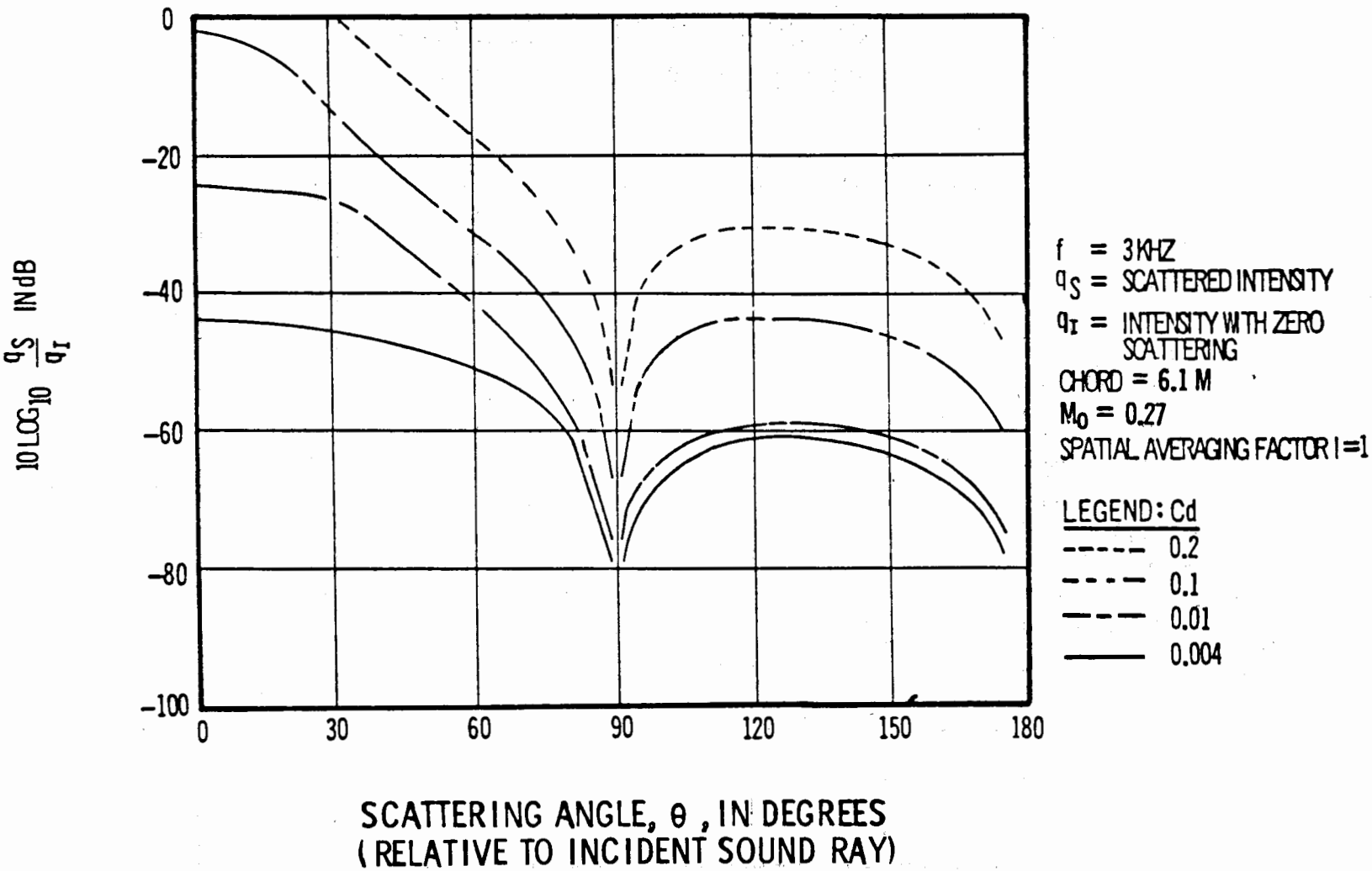

Figure 39.—Scattered Intensity Relative to Unscattered Intensity (3 kHz)

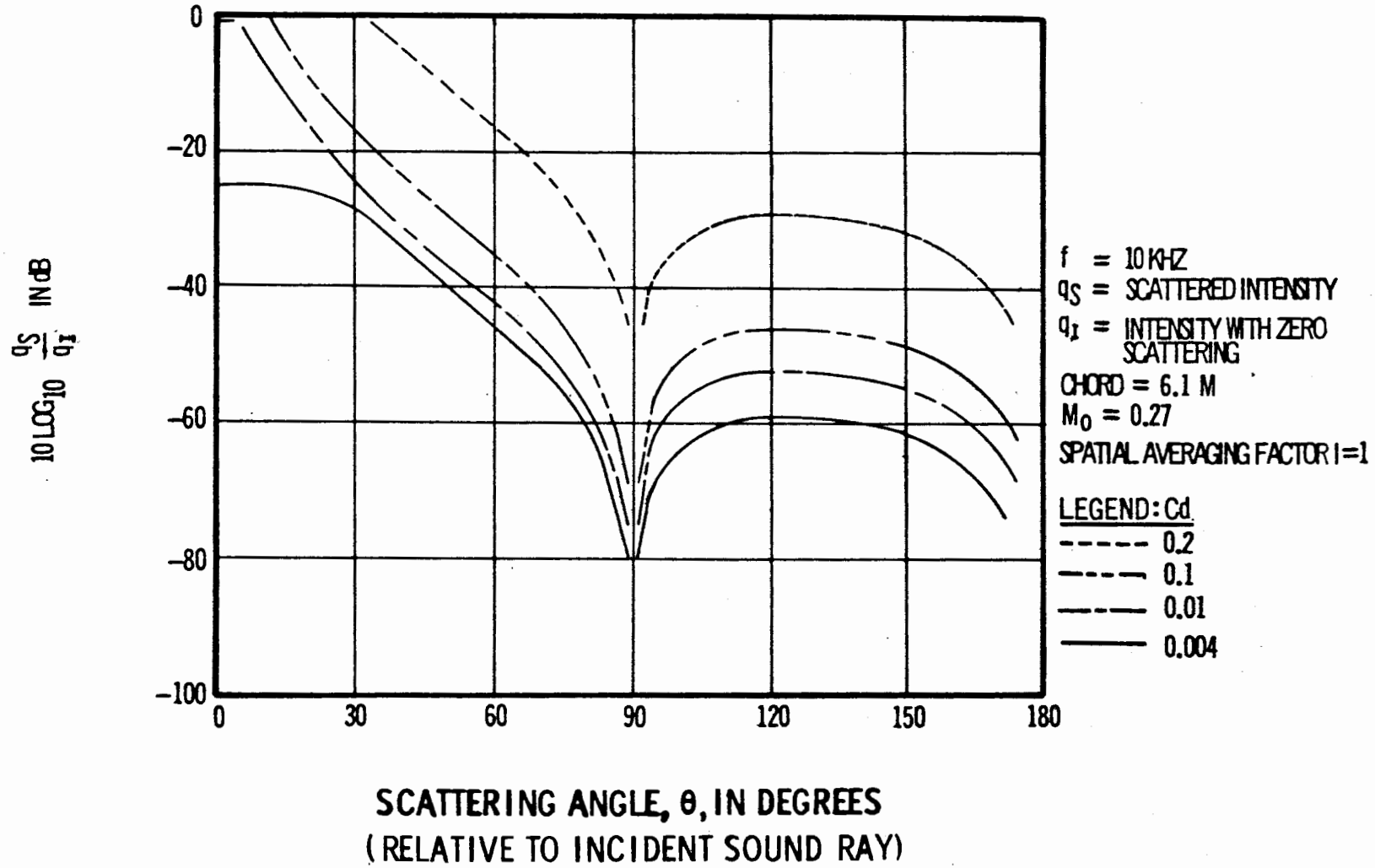

Figure 40.—Scattered Intensity Relative to Unscattered Intensity (10 kHz)

Additional experiments need to be performed to obtain turbulence intensity and scale over a wide range of wing profile drags in the near wake. Due to uncertainty in near-wake properties, the theoretical procedure presented below has not been added to the software of the current contract, but has been simplified for manual calculations (sec. 4.3.2) using trend curves.

Scattering theory has been previously used for acoustic radar detection of an airplane's wing tip vortex wake. It is highly desirable for small airplanes to avoid the vortex wakes of larger aircraft because upsets can occur. However, the present application has not been encountered before to our knowledge. The scattering model presented below might be improved by including the effects of multiple scattering and sheared flow in the analysis, but because of the lack of comprehensive near-wake turbulence data such refinement is not warranted. Use of this model is restricted to preliminary assessment of wing wake effects.

Analysis.–Figure 37 shows the idealization of the scattering process by a wing wake. The noise source is located at a height (h) above and a distance (b) upstream of a wing's trailing edge. The sound incident upon the wing wake is scattered by the turbulence. The scattered sound is to be determined as a function of frequency, angle relative to the incident direction, wing aerodynamic parameters, and flight Mach number. The following assumptions are applied to the process.

- Wake inhomogeneities are characterized by turbulence frozen in time during the scattering process, although the scattered sound is actually modulated by the time variation of the turbulence.

- The scattering process is isotropic.

- The effect of temperature fluctuations in the wake is negligible.

- Wake inhomogeneities are in a stationary fluid although the scattering actually takes place in a sheared flow. The more realistic situation can be approximated by multiplying the transfer functions for scattering by the transfer function for wing wake refraction (sec. 2.2.4.1).

- Sound propagation through the wake inhomogeneities can be described by a single scattering process. Second-order effects of multiple scattering are negligible.

- The majority of sound scattered into the wing's shadow zone occurs in the vicinity of the wing's trailing edge because the turbulence is most intense close to the edge and decreases as one moves downstream.

- The characteristic eddy scale for the wake turbulence is proportional to the wing chord length and the square root of the wing's profile drag coefficient.

- The wake turbulence intensity is proportional to the wing profile drag coefficient and the square of the free-stream velocity.

- The frequency spectrum shape for the wake turbulence is similar to that of jet turbulence, i.e., constant at low frequencies with a high-frequency "rolloff" above a characteristic frequency. The far-wake turbulence is independent of the particular body generating the wake, and depends only on the total profile drag of the body.

With these assumptions, the scattering process is described by methods developed by Monin (ref. 33). The incident sound wave fronts are deformed and thus scattered due to random convection of sound by the velocity fluctuations and random propagation speed variations due to temperature fluctuations. Monin gives the governing equation for the process as:

$$\frac{d\sigma}{d\Omega} = 2\pi K^4 V \{ C_o^{-2} E[2K \sin(\theta/2)] \cos^2(\theta/2) + 0.25 T^{-2} \Phi_T[2K \sin(\theta/2)] \} \cos^2 \theta \tag{42}$$

where

$\frac{d\sigma}{d\Omega}$ = differential scattering cross section

σ = scattering cross section

Ω = solid angle into which sound is scattered

K = magnitude of the sound wave number, i.e., $2\pi f/C_o$

V = volume of turbulence through which sound passes

C = speed of sound

T = static temperature (absolute units)

θ = scattering angle

E = energy-wave number spectrum of the turbulence velocity fluctuations

Φ_T = energy-wave number spectrum of the turbulent temperature fluctuations

One interprets the differential scattering cross section as

$$\frac{d\sigma}{d\Omega} = r^2 (q_s/q_I) \tag{43}$$

where

r = distance of the observer from the scattering volume

q_s = scattered sound intensity

q_I = incident sound intensity

Thus, ($q_I\, d\sigma$) is the total sound power scattered into the differential area ($r^2\, d\Omega$), and ($d\sigma$) has the dimensions of area. For turbulence that is locally uniformly distributed in planes parallel to the incident wave fronts, we write

$$d\Omega = 2\pi \sin\theta\, d\theta \tag{44}$$

For an unheated flow, such as a wing wake, the mean temperature differences occur only because of compressibility effects and the temperature fluctuations will scale with these mean differences. Estimates for the present case show that the scattering due to thermal fluctuations is at least 20 dB less than that due to velocity fluctuations, except in a narrow range of angles near $\theta = 180^0$, i.e., the case of direct backscatter. Sound scattered by velocity fluctuations drops rapidly to zero in this narrow range. Scattering data from a heated jet obtained from Baerg and Schwarz (ref. 40) were used to make these estimates. Hence, we will drop the temperature fluctuation term in equation (42) above and consider that the scattering is due only to velocity fluctuations.

The form for the velocity wave number spectrum, E, is chosen to be similar to that used by Rudd (ref. 41). Thus, E(K) is given approximately by

$$\frac{E(K)}{E_o} = \begin{Bmatrix} 1 & \text{for } K \leqslant K_o \\ (K/K_o)^{-11/3} & \text{for } K > K_o \end{Bmatrix} \tag{45}$$

In order to put equation (42) in dimensionless form, we define a new quantity (σ_N) as

$$\sigma_N = C_o^{\,2}\, \sigma/(2\pi\, K^4\, V\, E_o) \tag{46}$$

Thus, combining equations (42) through (46), we obtain

$$\begin{aligned} \frac{\partial\sigma_N}{\partial\Omega} &= \cos^2\!\left(\frac{\theta}{2}\right)\cos^2\theta && \text{for } 2K\sin\!\left(\frac{\theta}{2}\right) \leqslant K_o \\ &= \left[\frac{2K}{K_o}\sin(\theta/2)\right]^{-11/3}\cos^2\!\left(\frac{\theta}{2}\right)\cos^2\theta && \text{for } 2K\sin\!\left(\frac{\theta}{2}\right) > K_o \end{aligned} \tag{47}$$

Another quantity often computed is the total scattering cross section (σ_T) found by integrating equation (42) over all scattering angles from $\theta = 0^0$ to 180^0. However, this quantity by itself can be deceptive at high frequencies where it is known that the dominant scattering angle is small, i.e., the angle in which the majority of the scattered acoustic energy is scattered. Thus, it is possible that microphone measurements of

average pressure with and without scattering may show little difference, even though considerable sound can be scattered at angles greater than the dominant scattering angle. We will, therefore, define a quantity (σ_{min}) that gives the total sound power scattering at angles θ greater than θ_{min} when multiplied by the incident intensity (q_I). Thus σ_T equals σ_{min} when $\theta_{min} = 0^o$, and σ_{min} equals zero when $\theta_{min} = 180^o$.

We calculate σ_{min} by integrating equation (47) after inserting the expression for $d\Omega$ from equation (44). The technique for this integration is shown in Rudd's paper (ref. 41), except an apparent typographical error occurs in the details presented there. The correct formulation is:

$$\sigma_{min} = A + B \tag{48}$$

where

$$A = \pi \left[(\cos^3 \theta_{min} - \cos^3 \theta_A)/3 + (\cos^4 \theta_{min} - \cos^4 \theta_A)/4\right]$$

$$B = 8\pi \left(\frac{2K}{K_o}\right)^{-11/3} \sum_{J=1}^{4} C_J \left[T^{(6J-11)/3} - 1\right]$$

$$(C_J, J = 1,4) = (3/5, 15, -24/7, 12/13)$$

$$T = \sin(\theta_B/2)$$

and the conditions for evaluation of equation (48) are

$$[B = 0, \theta_A = \pi] \qquad \text{if } 2K < K_o$$

$$\left[\theta_A = \theta_B = 2 \sin^{-1}\left(\frac{K_o}{2K}\right)\right] \qquad \text{if } 2K \sin\left(\frac{\theta_{min}}{2}\right) \leqslant K_o$$

$$[A = 0, \theta_B = \theta_{min}] \qquad \text{if } 2K \sin\left(\frac{\theta_{min}}{2}\right) > K_o$$

Far-Wake Considerations.–The constants K_o and E_o are now evaluated based on turbulence characteristics in the far wake of a cylinder from experimental studies by Townsend (ref. 34) and by Uberoi and Freymuth (ref. 35). The one-dimensional wave number spectrum dependence of Uberoi and Freymuth is transformed into a three-dimensional spectrum by the method of Tatarski (ref. 32) so that

$$E(K) = 0.623 \ \overline{u^2}/(\ell^2 K^{11})^{1/3} \tag{49}$$

for very high frequencies under the assumption of isotropic turbulence. Here $\overline{u^2}$ is the average square of the streamwise component of the turbulence fluctuation. The characteristic eddy scale (ℓ) is obtained by

$$\ell = (x\ D)^{1/2} \tag{50}$$

where D is the diameter of the cylinder and x is the distance behind the cylinder. One relates ℓ to K and E by the condition

$$\frac{3}{2}\overline{u^2} = 4\pi \int_0^\infty K^2 E(K)\, dK \tag{51}$$

in conjunction with equations (45) and (49). One finds that

$$K_o \ell = 11.93 \tag{52}$$

and

$$E_o = (3.83)\, 10^{-5}\, \ell^3\, \overline{u^2} \tag{53}$$

Next, the cylinder diameter D is related to the cylinder drag from experimental Reynolds number data, so that equation (50) becomes

$$\ell = (1.94\, t_M\, x)^{1/2} \tag{54}$$

or

$$\ell = (0.97\, C_D\, C\, x)^{1/2} \tag{55}$$

where

t_M = total momentum thickness of the wake

C_D = section profile drag of an airfoil producing the same amount of drag as the cylinder

C = chord of the equivalent airfoil

The turbulence intensity also varies with distance from the airfoil's trailing edge. From reference 35, it is found that

$$\frac{\overline{u^2}}{u_o^2} = 1.17\, C_D\, (1 + x/C)^{-1} \left[\frac{\overline{u^2}}{(\Delta u)^2}\right] \tag{56}$$

where

u_o = airplane speed

Δu = maximum mean velocity deficit in the wake at a distance x from the trailing edge

In the same reference, the mean square turbulence intensity, $\overline{u^2}$, is found to be approximately 10% of the square of the velocity deficit on the centerline of the far wake; i.e.,

$$\overline{u^2} \cong 0.1\ (\Delta u)^2 \tag{57}$$

At this point we introduce another quantity, σ_s, defined as the characteristic scattering function, in order to develop a set of normalized curves to illustrate the scattered sound's frequency and scattering angle dependence. Let

$$S = \text{Strouhal number} = f\,\ell/C_D \tag{58}$$

$$\sigma_s = S^4\,\sigma \tag{59}$$

so that

$$\sigma_{min} = (2\pi)^5 \frac{E_o}{C_D^2} \frac{V}{\ell^4} \sigma_{s\,min} \tag{60}$$

$$\frac{d\sigma}{d\Omega} = (2\pi)^5 \frac{E_o}{C_D^2} \frac{V}{\ell^4} \left(\frac{d\sigma_s}{d\Omega}\right) \tag{61}$$

Using this definition, the characteristic scattering function, $d\sigma_s/d\Omega$, is shown in figure 41 as a function of θ with S as a parameter and in figure 42 as a function of S with θ as a parameter. Figures 43 and 44 show similar curves for $\sigma_{s\,min}$ as a function of θ_{min} using equations (48), (58), and (59). One then can find the appropriate scattering cross section at a particular frequency, f, scattering angle, θ, and elemental turbulent volume, V, by the following steps.

- Calculate S from equation (58)
- Calculate ℓ from equation (54)
- Compute E_o from equation (53), with $\overline{u^2}$ from equations (56) and (57) or some other specification
- Look up $\sigma_{s\,min}$ or $d\sigma_s/d\Omega$ from the curves, figures 41 through 44
- Calculate σ_{min} or $d\sigma/d\Omega$ from equations (60) and (61), respectively

Near-Wake Considerations.–It is expected that the near-wake characteristics will play a greater role than the far wake in the impact of scattering on noise shielding by an EOW configuration. This is because the near wake is usually much closer to the sound source and the absolute turbulence level is higher at locations closer to the wing. Unfortunately, much less applicable information is known about the near wake.

Before discussing the near wake in detail, we must first set up the scattering equation in a manner more compatible with our wake information. Consider the volume element in equation (17) to be

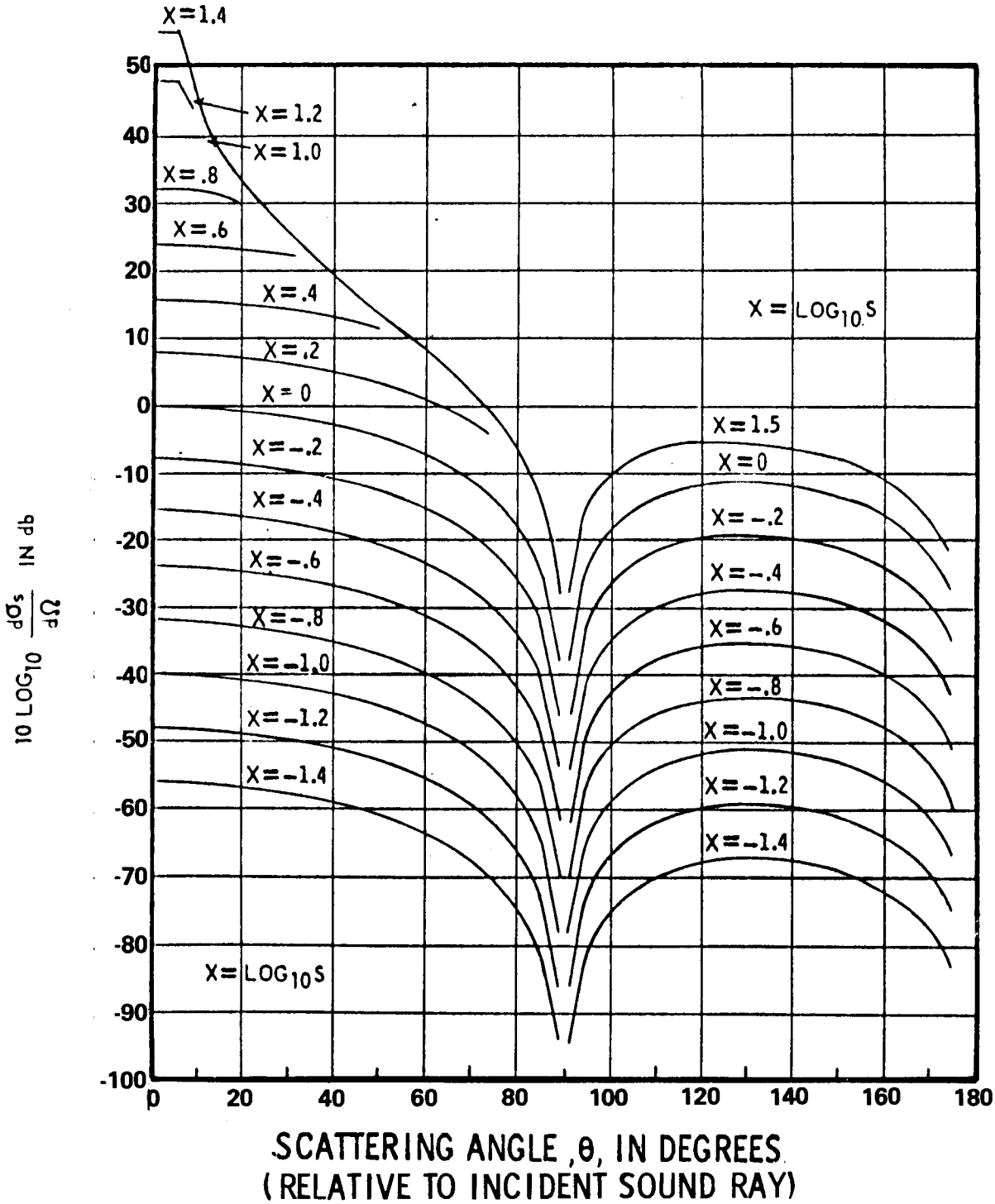

Figure 41.—Differential Scattering Cross Section as a Function of Scattering Angle

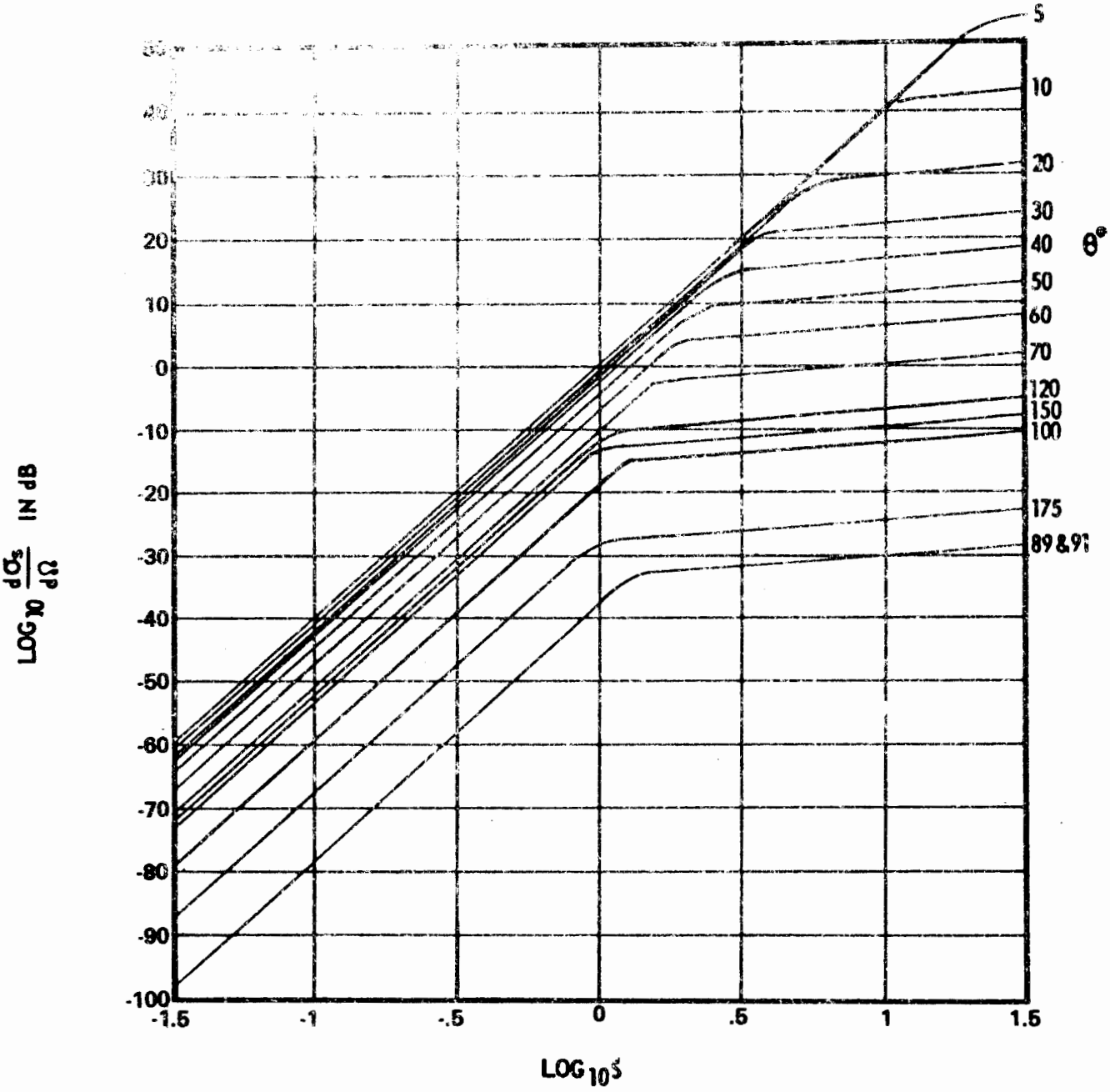

Figure 42.—Differential Scattering Cross Section as a Function of Strouhal Number

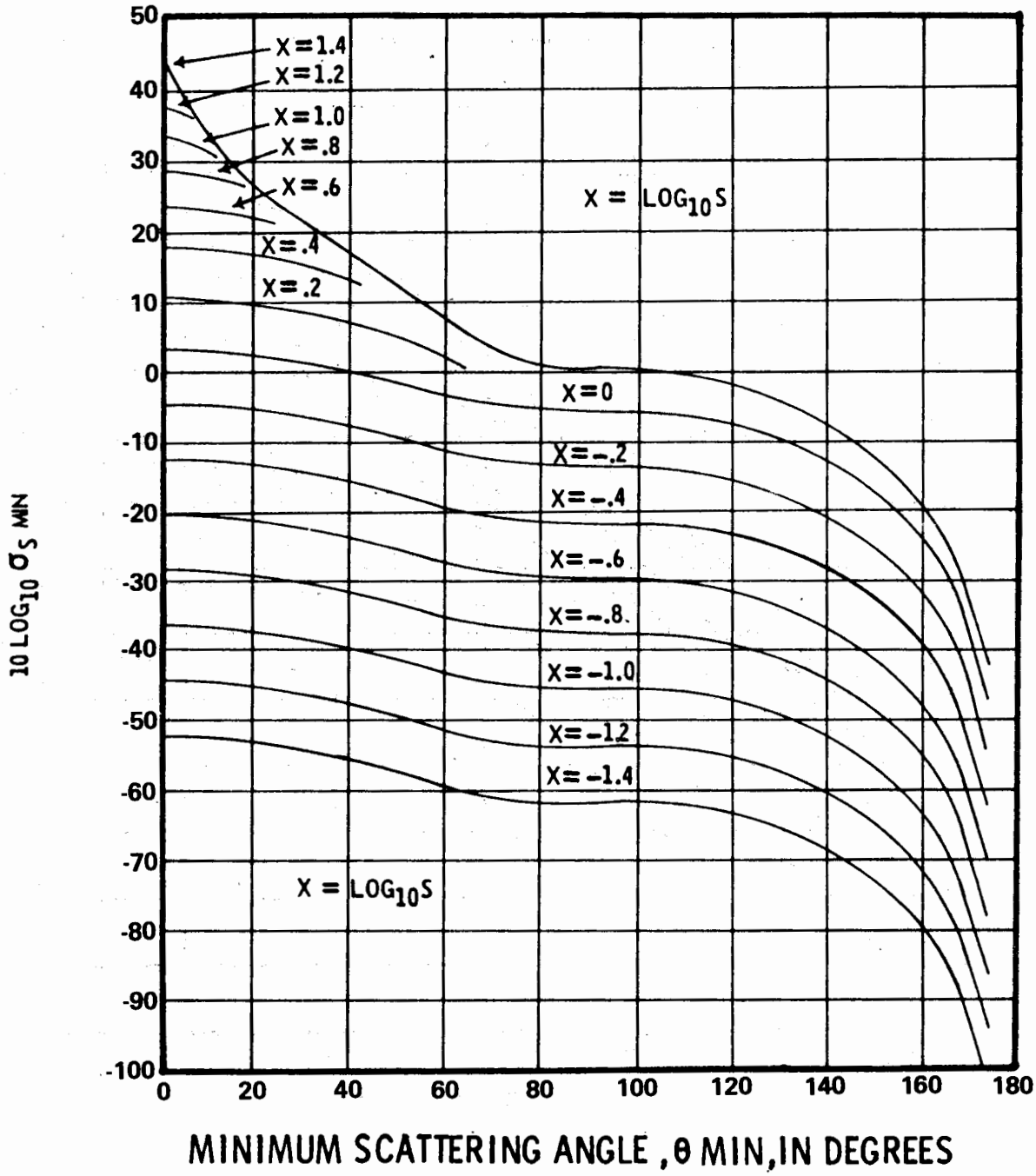

Figure 43.—Scattering Cross Section as a Function of Scattering Angle

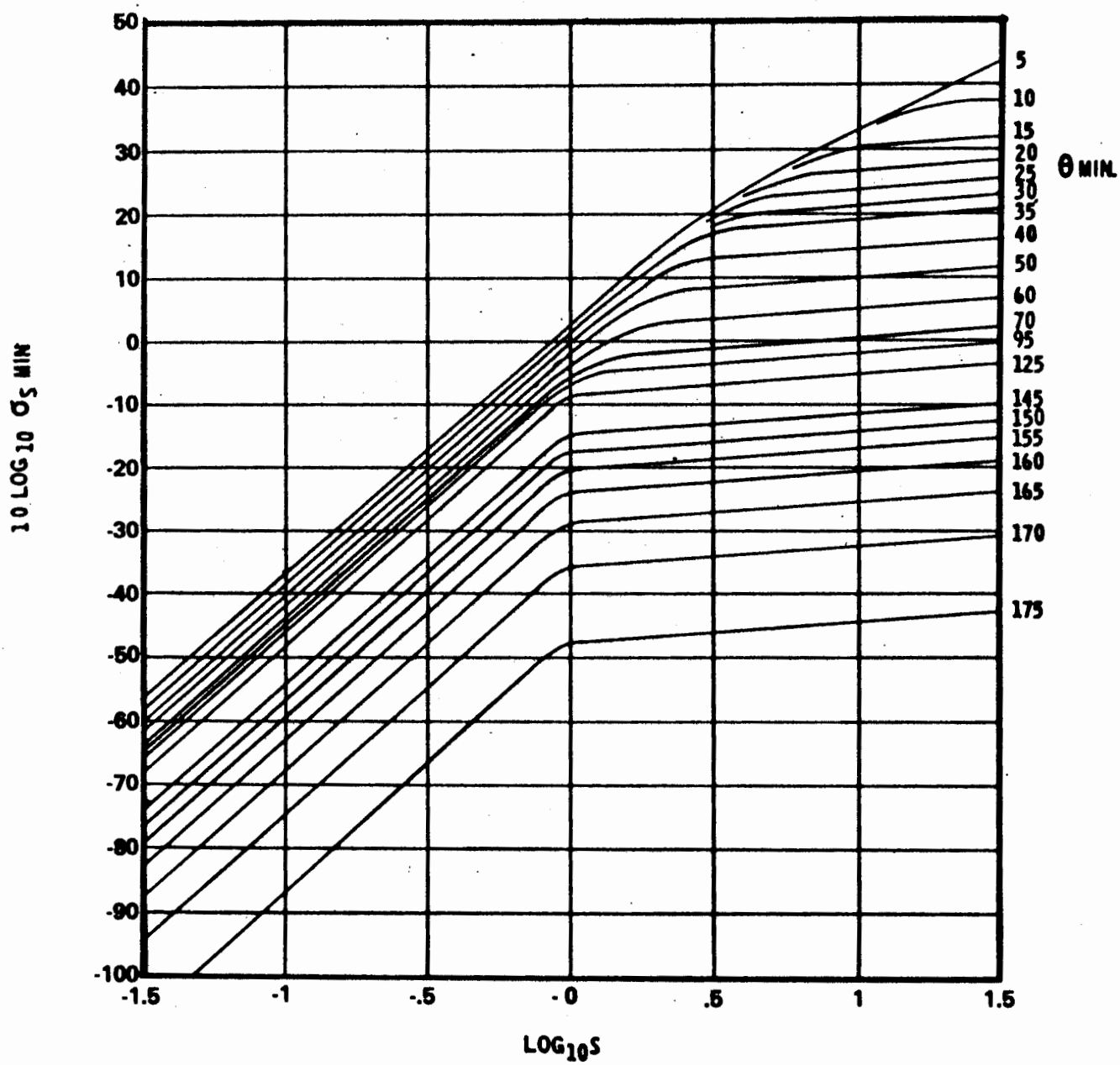

Figure 44.—Scattering Cross Section as a Function of Strouhal Number

$$V = 2d \ \Delta x \ \Delta z \tag{62}$$

where

d = the half-width of the far wake at a distance x from the trailing edge

($\Delta x \ \Delta z$) = a differential surface area of the wake

Townsend (ref. 34) has measured d and by comparing his results with equation (50), one finds ℓ equals approximately 0.59 d for the data examined. Thus, using equations (53) and (59), we obtain

$$\frac{d\sigma}{d\Omega} \cong 1.27 \ M_o^2 \ \left(\frac{\bar{u}^2}{u_o^2}\right) \Delta x \ \Delta z \ \frac{d\sigma_s}{d\Omega} \tag{63}$$

for each elemental area of the wake. Thus, one can use either measured values for $\overline{u^2}$ for the near wake or equations (56) and (57) for the far wake.

We now consider the ratio of the scattered sound intensity to the intensity that would be received along the incident direction in the absence of scattering as measured at the same far-field distance (r). For a source of strength Q located at a distance r_o from the elemental wake area, the intensity (q_I) incident on the wake is proportional to Q/r_o^2 while in the far field this intensity in the case of no scattering is proportional to Q/r^2. Thus, from equation (43)

$$q_s/q_I \sim \frac{1}{r_o^2}$$

and inserting this into equation (63), gives

$$q_s/q_I = 1.27 \ M_o^2 \ \left(\frac{\bar{u}^2}{u_o^2}\right) \frac{\Delta x \ \Delta y}{r_o^2} \ \frac{d\sigma_s}{d\Omega} \tag{64}$$

for each element of wake area. In general, we must integrate over the entire wake surface so that

$$q_s/q_I \cong 1.27 \ \pi \ M_o^2 \ \left[\frac{\bar{u}^2}{u_o^2} \ \frac{d\sigma_s}{d\Omega}\right]_{\text{typical}} I \tag{65}$$

where I represents an averaging factor to account for the evaluation of the integral. It is assumed that I has a value of about unity and the term ($\Delta x \ \Delta y/r_o^2$) equals π from the notation given in equations (64) and (65). A calculation of the averaging factor I is given in appendix F of volume II wherein the value $I \simeq 1$ was found to be good. Hence,

$$q_s/q_I \cong 1.27 \ \pi \ M_o^2 \ \left[\frac{\bar{u}^2}{u_o^2} \ \frac{d\sigma_s}{d\Omega}\right]_{\text{typical}} \tag{66}$$

Near-Wake Data and Sample Estimates.–Clark (ref. 36) obtained near-wake data behind a number of airfoil sections tested in a free jet tunnel. The values of profile drag coefficient C_D seemed rather high, particularly for symmetrical airfoils at 0^0 angle of attack. For example, the lowest C_D measured was 0.12 whereas Abbott and von Doenhoff (ref. 42) show values as low as 0.004 for lift coefficients (C_L) as high as 0.7. Whether Clark's values are high due to the facility, upstream turbulence, the measurement technique, or the fact that his Reynolds number is at least a factor of 10 lower than the range reported in reference 42 is unknown. However, we shall use Clark's data to represent the high-drag case despite the disagreement. For example, reference 42 shows the drag of some simple flap systems to be rising rapidly in the vicinity of $C_D = 0.12$ and $C_L = 2.7$. In addition, the details of the near wake of a high-drag airfoil operating at a lift coefficient of zero can't be expected to match those of a high-lift flap section even if the drags for the two sections are the same. Clark's measured wake turbulence intensity has been used to calibrate our scattering model, equation (66), through use of the scaling relationships given in equation (56), i.e., $\overline{u^2} \sim C_D$. When Clark's turbulence data are scaled to low-drag-coefficient (C_D) values, high turbulence estimates can result because his data show that the turbulence intensity drops off faster than a linear relationship as C_D is reduced.

The estimates given previously in figures 38 through 40 are based on scaling up Clark's near-wake model data to a 6.1-m chord wing. Clark's data show that the ratio of turbulence scale to the wing chord, ℓ/C, is approximately 0.15. Scaling up arbitrarily for the high-drag condition, $C_D = 0.2$, gives $\ell = 0.9$ m. For the low-drag conditions, we have scaled ℓ according to the relationship of equation (55), i.e.; ℓ^2 is proportional to C_D. The turbulence intensity, $\overline{u^2}/u_o^2$, is 9.5×10^{-3} at the condition $C_D = 0.2$ and $M_o = 0.27$. Equation (65) was used for the estimates in the form

$$\frac{q_S}{q_I} = F \frac{d\sigma_S}{d\Omega} \tag{67}$$

where F is a calibration constant for the expression (eq. 65) at different Strouhal number (S in eq. 58) values.

The following chart lists the values of $10 \log_{10}(F)$ and $\log_{10}(S)$ that were used for the estimates given in figures 38 through 40. These reference values were used to calibrate the curves shown in figure 41.

Profile drag, C_D	$10 \log_{10}(F)$, dB	$\text{Log}_{10}(S)$		
0.004	-53.1	-0.27	0.207	0.730
0.01	-49.1	0.179	0.656	1.180
0.1	-39.1	0.429	0.906	1.429
0.2	-25.6	0.429	0.906	1.429
Frequency, kHz		1.0	3.0	10.0

A similar technique can be used to determine the total sound power scattered at angles greater than some minimum angle, θ_{min}, as compared to the total incident power by making use of the curves for $\sigma_{s\ min}$ given in figures 43 and 44.

Remarks.–It should be noted that the scattering angles, θ and θ_{min}, are relative directions normal to the wave fronts and do not take into account the effects of convection by ambient flow. Refraction of sound by the wake causes only a displacement of acoustic rays and produces no angular change in the direction of sound propagation in the far field.

The airfoil has little effect on the strength of the sound field incident to the wake. Ffowcs-Williams and Hall (ref. 17) have implied this in their work on diffraction about a semi-infinite plate with flow; i.e., the diffraction solution is identical to the free-field solution in the plane downstream of the plate edge.

Whenever the ratio of scattered sound to incident sound approaches unity, the assumption of single scattering breaks down and multiple scattering effects must be considered. In the examples given for the high-drag cases, this situation arose. Physically, a significant amount of energy is scattered, but the majority of the total sound is not scattered through large angles, and large fluctuations in the sound amplitude are likely observed. Under the high-drag conditions illustrated, significant scattering occurred at all frequencies considered. Hence, predicted wing shielding attenuations on the order of 20 dB or more by diffraction theory must be questioned whenever flaps may be deployed. When flaps are retracted corresponding to a low-drag condition, the examples show that very little scattering over the full frequency range (1 kHz to 10 kHz) would occur except at small scattering angles.

The single most important quantity controlling the wing wake process and hence limiting wing shielding attenuation is the near-wake turbulence intensity. This intensity is directly related to the airfoil's profile drag coefficient. Additional tests should be conducted to accurately measure this turbulence as a function of the wing's profile drag. Sound scattering tests should be performed to check the above theory using actual turbulence data. Measurements should include:

- Turbulence intensity
- Turbulence scale
- Mean velocity profile behind the airfoil section

A variety of typical airfoil sections including configurations with flaps should be used for the experiment. The experiment should address the effects of variations in the angle of attack and the Reynolds number based on the wing chord. Of particular interest is the range of Reynolds numbers greater than 4×10^6.

To obtain the corresponding acoustic shielding data when turbulent wakes and significant background noise are present, special measurement techniques are required. This is because the scattered signal levels will in general be low compared to the

unscattered signal. The pulse technique, such as that used in references 40 and 43, would allow the desired scattered signal to be extracted, provided the sound source is highly directional.

2.3 TURBOMACHINERY NOISE SHIELDING TEST PROGRAM

Numerous model- and full-scale tests have been conducted by Boeing to develop methods for efficiently achieving and understanding far-field TM noise reductions associated with airframe shielding. The majority of these tests were conducted as a part of the Boeing/Aeritalia 7X7 airplane program. During a phase of this program, configurations with engines over the wing and engines shielded by body/tail appendages were explored as a means of achieving significantly reduced community noise levels with minimum or no loss in airplane performance. (While the EOW configuration is not currently being considered for the 7X7, it is being used in the YC-14. This airplane is being built for the USAF and will fly for the first time in July 1976.) The 7X7 shielding test efforts concentrated on the use of a high-bypass-ratio turbofan propulsion system. However, some test results were obtained applicable to turbojet propulsion systems.

The tests reviewed in this section are summarized in tables 2 and 3. Pertinent variables and their ranges are shown in figure 45. Discussion is limited to examination of test purpose, setup, variables, and typical results. Some discussion of results is given, but in general is deferred to section 2.4. In the case of the cylindrical barrier, all discussion of test variables and results is deferred to section 2.4.1.5.

In reviewing these tests the reader should be aware that when the tests were actually run, demonstration of shielding was usually the main concern. Typically, achievement of a 20-dB noise reduction was then taken as proof of the potential of wing shielding. Hence, reflections in the test arena were controlled only to a level sufficient to demonstrate wing shielding values up to 20 dB. In the present study the assumption is made that the amount of shielding provided by the particular barrier/noise source combination may be treated as a diffraction-controlled process. Hence, assessment of possible situations in which noise reaching shadow zones when controlled by mechanisms other than diffraction becomes potentially important. In general, very little data is available to either qualify or quantify these flanking paths. The possible importance of test arena arrangement on shielding and the estimation of shielding is discussed in section 2.4.2.4.

Tests concerned with the effect of wing surfaces on jet exhaust noise shielding and noise generation are not considered in the present section, but are discussed separately in section 3.2.

2.3.1 STATIC EXPERIMENTS

All of these tests were conducted with stationary barrier and noise source simulation. Hence, in regions beyond the jet efflux, noise propagated through an air medium essentially at rest. These tests did not simulate airplane forward velocity. Such effects are considered in the tests discussed in section 2.3.2.

Table 2.—Summary of Static Turbomachinery Noise Shielding Tests

TEST	EFFECT	BARRIER	PHYSICAL NOISE SOURCE	A/P FLY-BY GEOM. IMPLIED
COMPACT SOURCE SHIELDING TESTS (GROUP 1 - 1972) (GROUP 2 - 1975)	• NOISE REDUCTION BY SHIELDING • FINITE BARRIER SIZE • NOISE LEAKAGE THRU GAPS • LOSS OF SHIELDING DUE TO FLANKING RADIATION • NOISE ENHANCEMENT BY REFLECTION	• SIMULATED SEMI-INFINITE PLANE • SIMPLE MULTI-EDGE BARRIER (FLAT BOARD) • SCALE MODEL WING w/wo FLAP GAPS • CYLINDER	• SMALL, DIRECTIVE HORN SPEAKER	• FLYOVER
MODEL FAN RIG SHIELDING TEST (1972)	• NOISE REDUCTION BY SHIELDING • NOISE LEAKAGE THRU GAPS	• WING TRAILING EDGE BARRIER w/wo FLAP GAPS	• 30 CM DIA COLD FLOW DISCHARGE FAN RIG	• FLYOVER • SIDELINE
WALL ISOLATION FACILITY SHIELDING TEST (WHISTLE IN SECONDARY FLOW) (1972)	• NOISE REDUCTION BY SHIELDING	• SCALE MODEL WING WITH FLAPS AND WITH BODY SEGMENT	• WHISTLE TONE INJECTED INTO SECONDARY FLOW PLENUM OF DUAL FLOW NOZZLE • HOT PRIMARY • COLD SECONDARY • 7 NOZZLE COMBINATIONS	• FLYOVER • SIDELINE
FULL SCALE JT9D TULALIP SHIELDING TESTS (1973)	• NOISE REDUCTION BY SHIELDING	• FULL SCALE TYPICAL COMMERCIAL JET TRANSPORT WING	JT9D ENGINE WITH SUPPRESSED INLET	• FLYOVER • SIDELINE

Table 3.—Summary of Ambient Flow Turbomachinery Noise Shielding Tests

TEST	EFFECT	BARRIER	PHYSICAL NOISE SOURCE	A/P FLY-BY GEOM. IMPLIED
UARL TUNNEL/ POWERED NACELLE SHIELDING TEST (1973)	• DISCHARGE FAN & TURBINE TONE NOISE SHIELDING DEPENDENCE ON FORWARD VELOCITY	• SCALE MODEL JET TRANSPORT WING WITH LEADING & TRAILING EDGE FLAPS	• 10 CM FAN/COLD FLOW DRIVEN TURBINE WITH LINED INLET NACELLE	• FLYOVER
AIRBORNE/HORN-ON-WING-SHIELDING TEST (1973)	• TONE NOISE SHIELDING DEPENDENCE ON FORWARD VELOCITY	• WING OF LIGHT AIRPLANE	• HORN TYPE SPEAKER	• FLYOVER (ACTUAL)
727-100;200 FLYBY INLET SHIELDING TEST COMPARISONS (1971/1972)	• INLET FAN NOISE SHIELDING BY WING AND FUSELAGE	• APPROACH CONFIGURED WINGS OF 727-100 AND 727-200	• JT9D MOUNTED 727 ENGINES	• FLYOVER (ACTUAL)

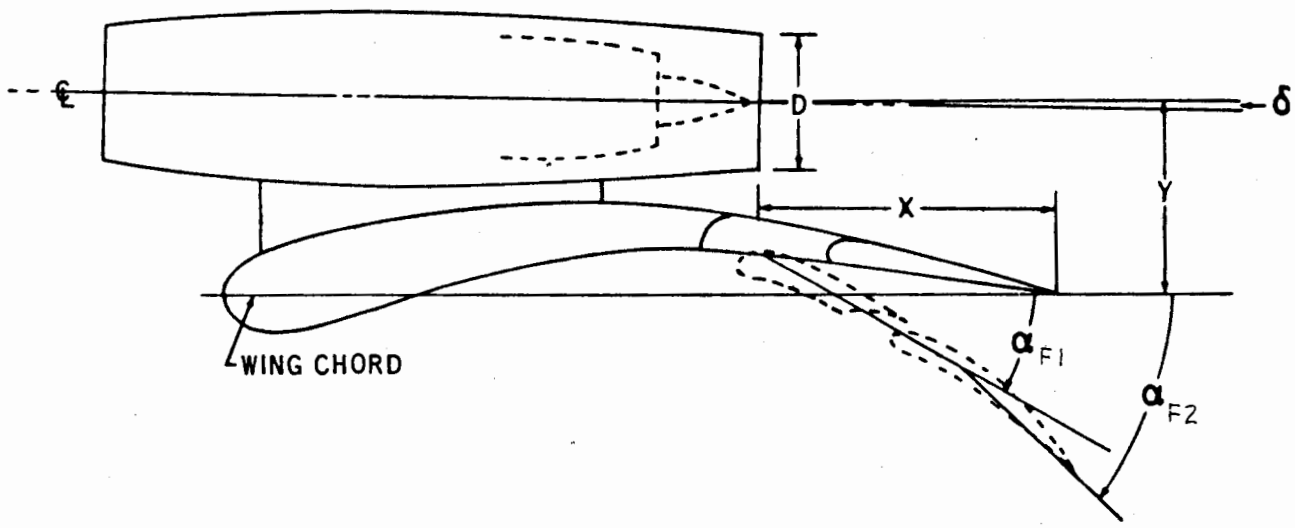

Variables	Range
• Nozzle exit to flap edge distance	$1 < \frac{X}{D} < 10$
• Engine ℄ to wing chord	$0.5 < \frac{Y}{D} < 3.0$
• Flap angles	$5° < \alpha_{F1} < 36°$
	$30° < \alpha_{F2} < 90°$
• Engine bypass ratio	$0 < BPR < 7$
• Engine pressure ratio	$1.1 < EPR < 2.6$
• Fan pressure ratio	$1.05 < FPR < 1.6$
• Primary exhaust total temperature*	$T_{T0} < T_T < 1560°\,R$
• Elevation angle,** β_o	$-90° < \beta_o < 90°$
• Aircraft Mach number	$0 < M_0 < 0.23$

• Nozzle geometry; 1) round secondary vs ⌓ shape secondary,
2) retracted, co-planar, or extended primary nozzle with respect to secondary exit plane.

---

*T_{T0} = ambient total temperature

**Top view corresponds to $\beta_o = -90°$
Bottom view corresponds to $\beta_o = +90°$

Figure 45.—Range of Test Conditions for an EOW Configuration

2.3.1.1 Compact-Source Shielding Tests

This sequence consists of two separate groups of experiments. Group 1 experiments were conducted during 1972 to investigate:

1. The effect of noise source directivity on shielding (and reflection) of (and from) winglike barriers for a no-flow, compact noise source, both broadband and tone

2. The possible treatment of multiedged finite-sized barriers as a collection of independent, semi-infinite, half-plane barriers

3. The reduction in shielding associated with flap gaps

4. Shielding by finite-length cylindrical barriers

Group 2 experiments were conducted during 1975 as an explicit part of the current study. The purpose of these tests was to provide further verification of the effect of source directivity on shielding. In addition, these tests also provided explicit data on the potential importance of test arena arrangement and characteristics on observed shielded noise.

Three winglike barriers were examined as a part of the group 1 experiments:

- A geometrically simple barrier configuration simulating a single-edged, semi-infinite half-plane, per figure 46

- A geometrically simple, multiedged "flat board" barrier, per figure 47

- A typical jet transport wing-shaped barrier with adjustable flaps (gaps), per figure 48

The test setup used for the winglike barriers consisted of a noise source and shield combination mounted on a rotating turntable, as suggested in figures 46, 47, and 48. An Altec type 3000H driver (with the horn removed) was used as a noise source. The behavior of the source/shield combination or source alone was obtained with a single microphone, positioned 1.8 m from the noise source. The noise source "mouth" was always located on the turntable's axis of rotation. Output of the microphone processor was real time recorded on a polar chart plotter slaved to rotate synchronized with the source/shield setup. All group 1 tests were conducted in the "blue room," a controlled quasi-anechoic chamber of floor dimensions 10 by 10 m and 3.4 m in height. A schematic of the test setup is shown in figure 49. Dimensions of the scale-model transport wing are given in figure 50.

The noise source was operated both in broadband and tone modes. Tone frequencies of 2.5, 5, 10, and 20 kHz were used. In general, the axis of symmetry of both the noise source and its directivity pattern coincided. The directivity pattern was symmetric about the noise source centerline. The off-axis 3-dB-down angle was roughly 80° at 2.5 kHz, 60° at 5.0 kHz, 40° at 10 kHz, and 30° at 20 kHz. With the winglike barriers,

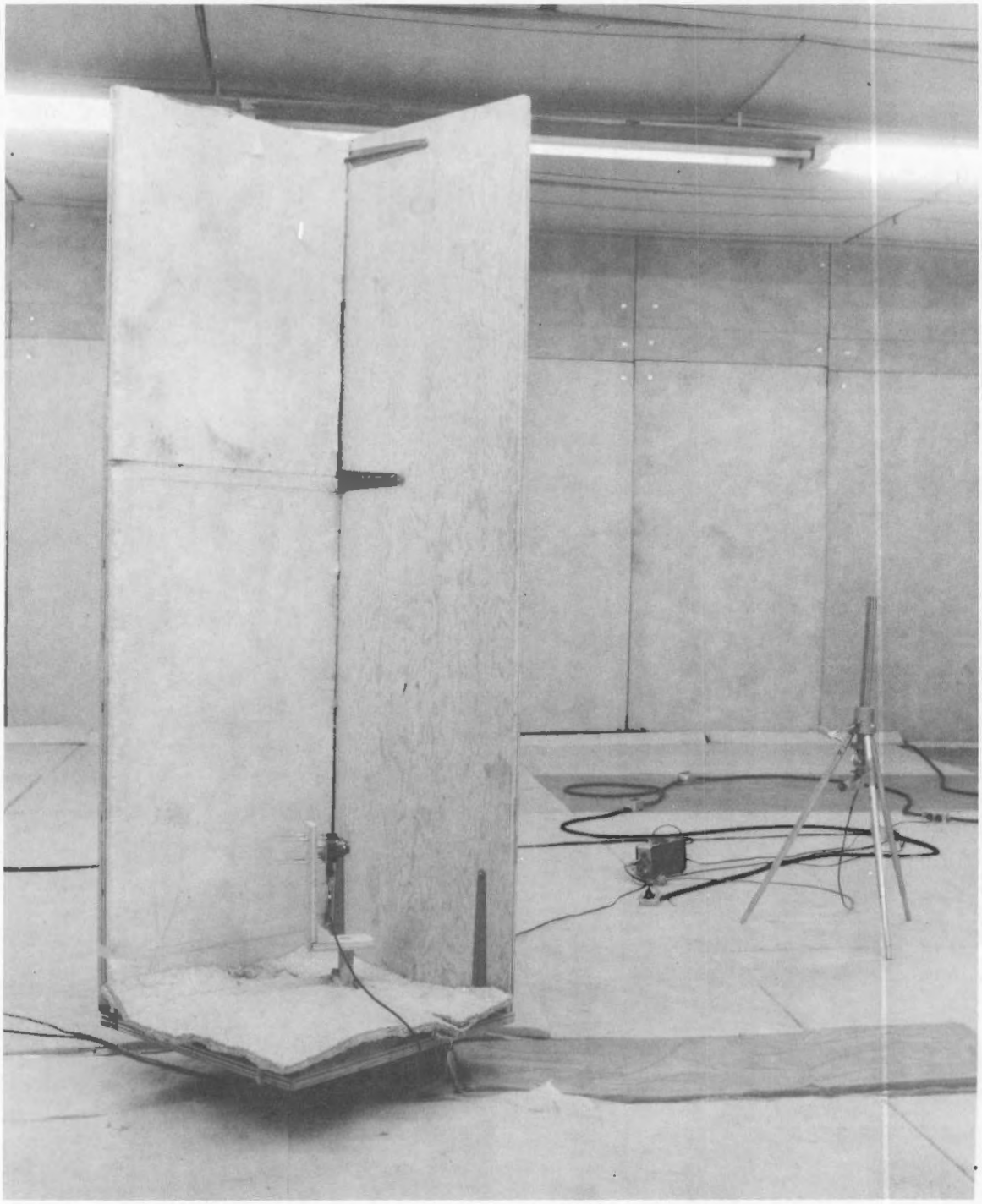

Figure 46.—Compact-Source Shielding Test Setup (Group 1) With Simulated Single-Edged, Semi-Infinite Half-Plane Barrier

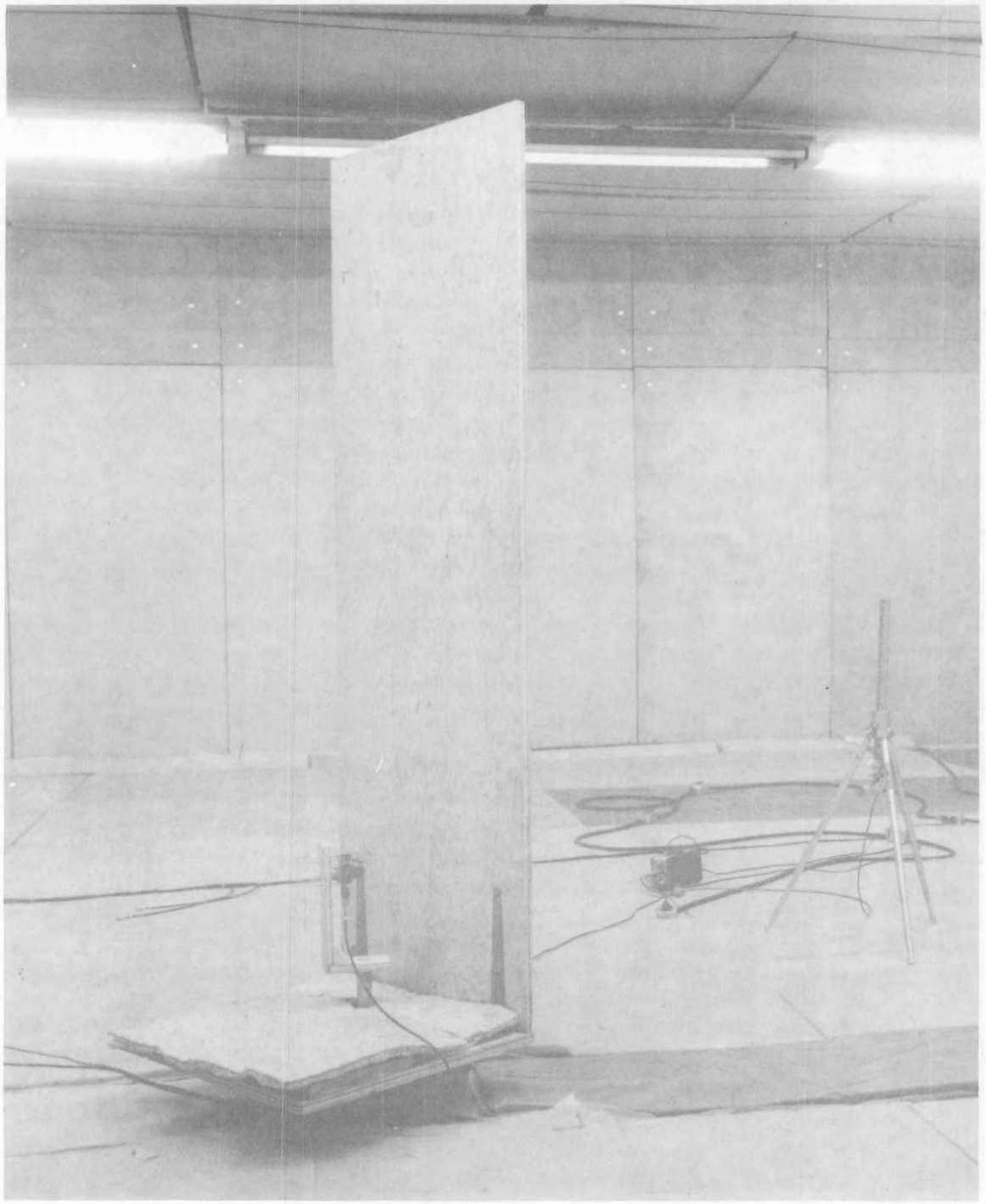

Figure 47.—Compact-Source Shielding Test Setup (Group 1) With Simple, Multiedged, "Flat Board" Barrier

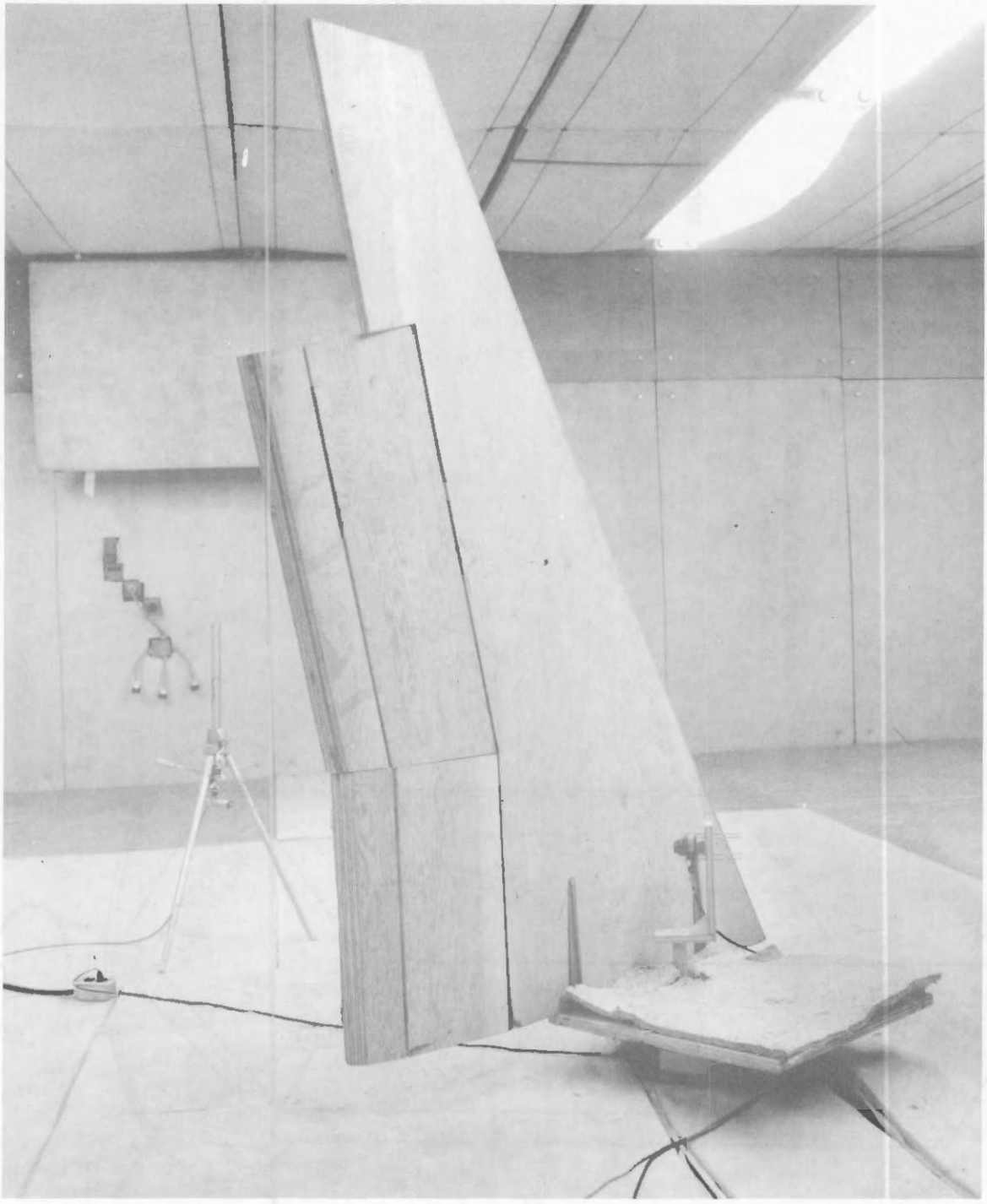

Figure 48.—Compact-Source Shielding Test Setup (Group 1) With Typical Jet Transport Wing-Shaped Barrier

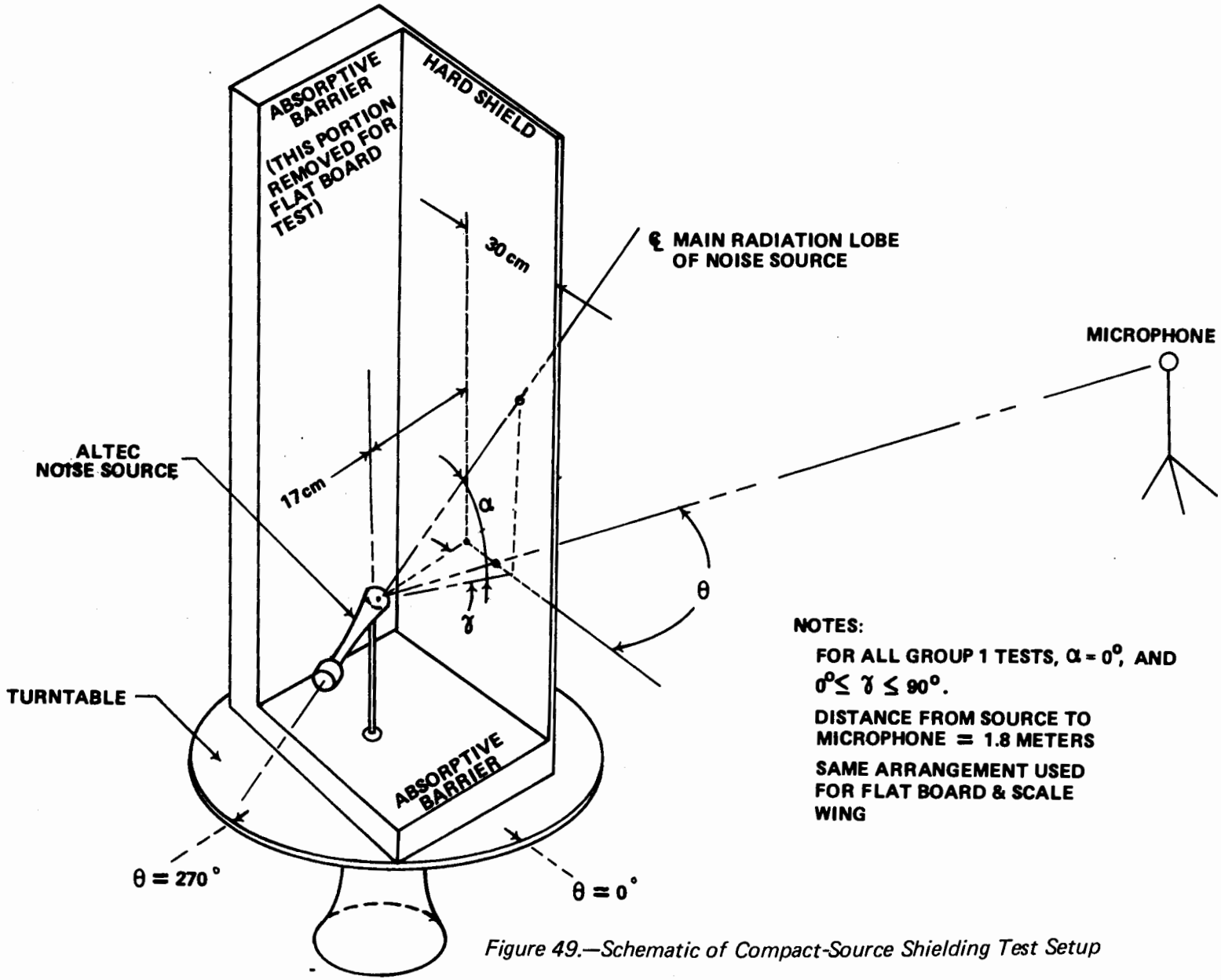

Figure 49.—Schematic of Compact-Source Shielding Test Setup

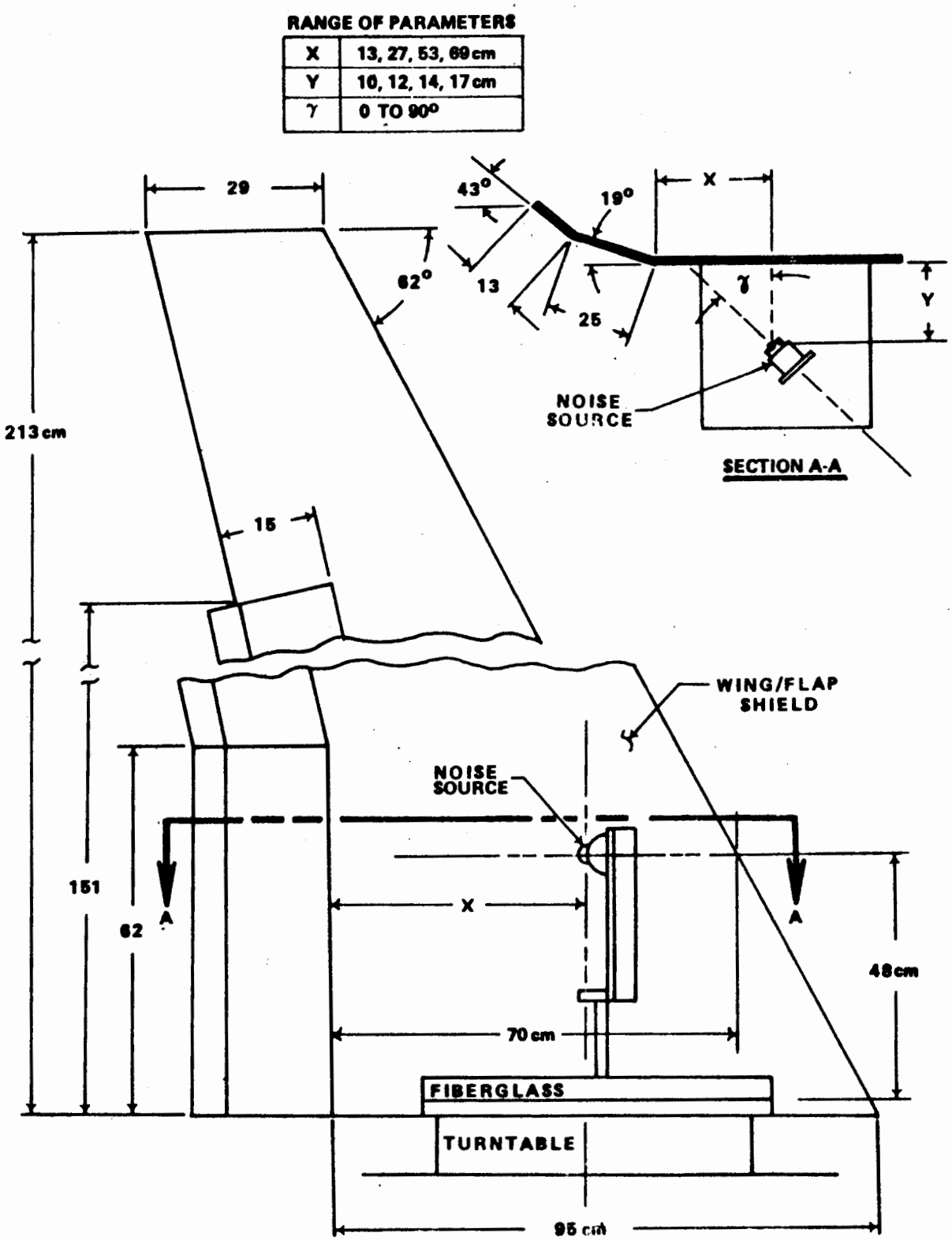

Figure 50.—Dimensions of Jet Transport Wing-Shaped Barrier

the axis of symmetry was set parallel to the plane of the turntable base, i.e., $\alpha = 0^0$ (see fig. 49), and was aimed in various directions in this plane, i.e., $\gamma = 90^0, 45^0, 30^0, 0^0$, etc.

A cylindrical barrier (fig. 51) was also tested as a part of the group 1 experiments. In this case the barrier and source were stationary. A single microphone carried on a movable overhead boom was used. An Altec 3000H driver (with the horn removed) was again used as the noise source with its axis of symmetry aimed at the center of the cylindrical barrier. Shielded and unshielded data were obtained both for broadband and tone modes (at 2.5, 5, 10, and 20 kHz).

Group 2 tests, conducted some 3 years later, used only the simulated semi-infinite half-plane barrier. The Altec 3000H source was again used, but this time with a small horn attached. The horn caused the driver to produce a more directive radiation pattern. The noise source was aimed at various points of the free vertical edge corresponding to elevation angles, α, between $+55^0$ (above the horizontal) to -55^0 (below the horizontal). See figure 49 for a schematic illustration of α.

The first part of the group 2 tests was run in the Boeing Large Test Chamber (LTC), a large highly anechoic facility. The general arrangement of the room and test setup are shown in figures 52, 53, and 54. Control of test arena reflections during this test was probably better than for any previous shielding test programs at Boeing–certainly better than other tests described in this report.

The remainder of the group 2 tests were conducted in the Boeing model fan rig room. The room is described in the next section. The same source/shield/receiver microphone system was used. Hence, the only variable was the test arena itself.

Typical results from the group 1 tests are shown in figures 55 through 59, which all portray polar distributions for tone noise levels taken at 10^0 intervals from measured, smoothed, continuous-distribution charts. Because of the smoothing process, these sampled results are also indicative of the behavior of a 1/3-octave-bandwidth display of broadband noise.

Figure 55 indicates the effect of source directivity upon the shielding effectiveness of the simulated semi-infinite half-plane barrier of figure 46. The data suggests that the shielded noise behavior is dependent upon the unshielded level at the shadow boundary, while within the shadow zone it is independent of the unshielded levels. Figure 56 indicates that the shielding effectiveness of the barrier increases with increasing frequency. This is consistent with the simple point-source theory discussed in section 2.2.

Figure 57 compares the behavior of the simulated semi-infinite half-plane barrier with that of the "flat board" barrier (shown in fig. 47). The data indicates that in the shadow zone of the flat board barrier, the noise appears to behave as the superposition of the shadow zone noise of right- and left-sided simulated semi-infinite half-plane barriers.

Figure 58 shows the overall shielding effectiveness of the scale-model wing (fig. 48). The separate noise contributions coming around the wing leading and trailing edges are also

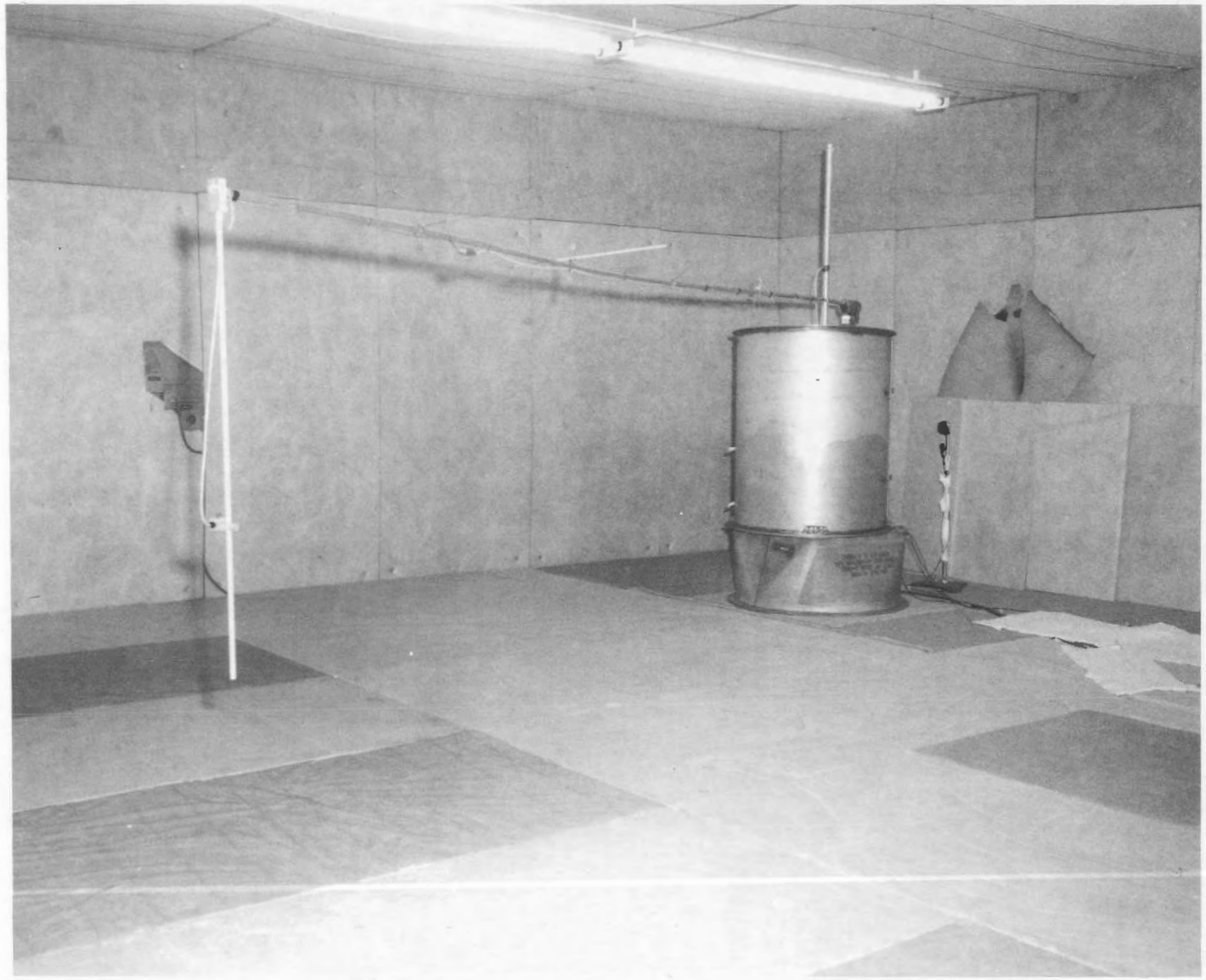

Figure 51.—Compact-Source Shielding Test Setup (Group 1) With Cylindrical Barrier

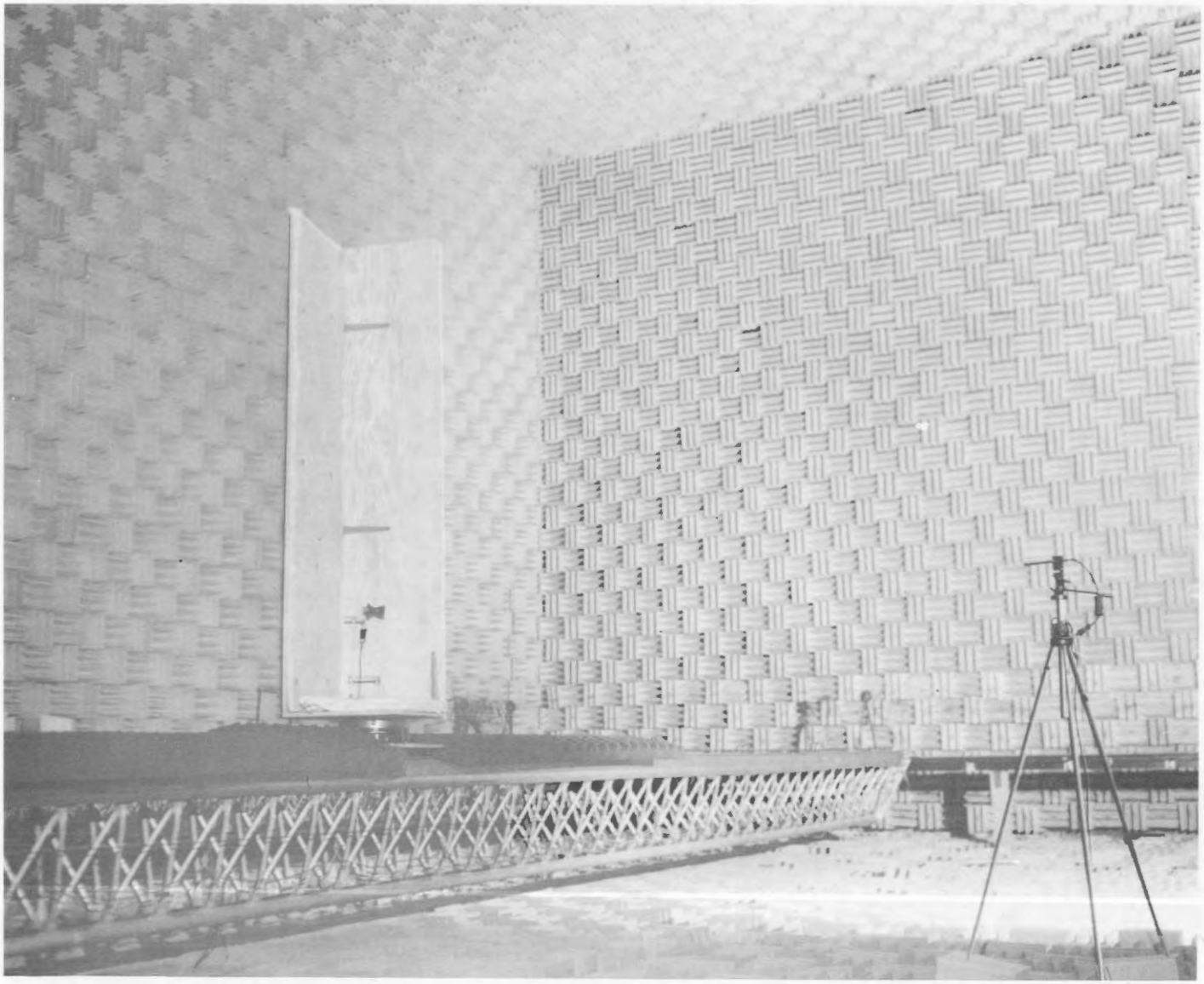

Figure 52.—Compact-Source Shielding Test Setup (Group 2) in Large Test Chamber (LTC)

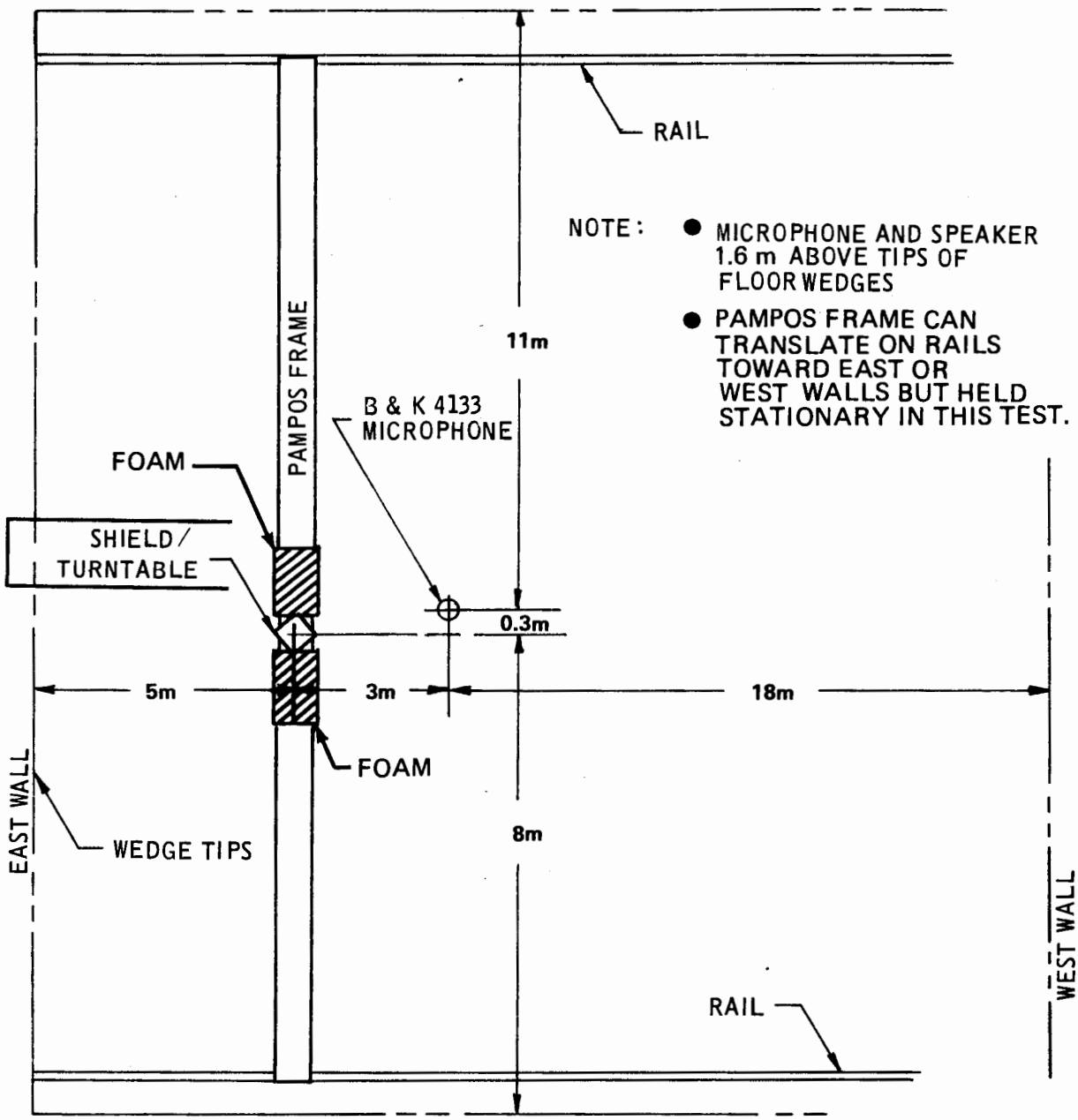

Figure 53.—Sketch of LTC Layout (Overhead View)

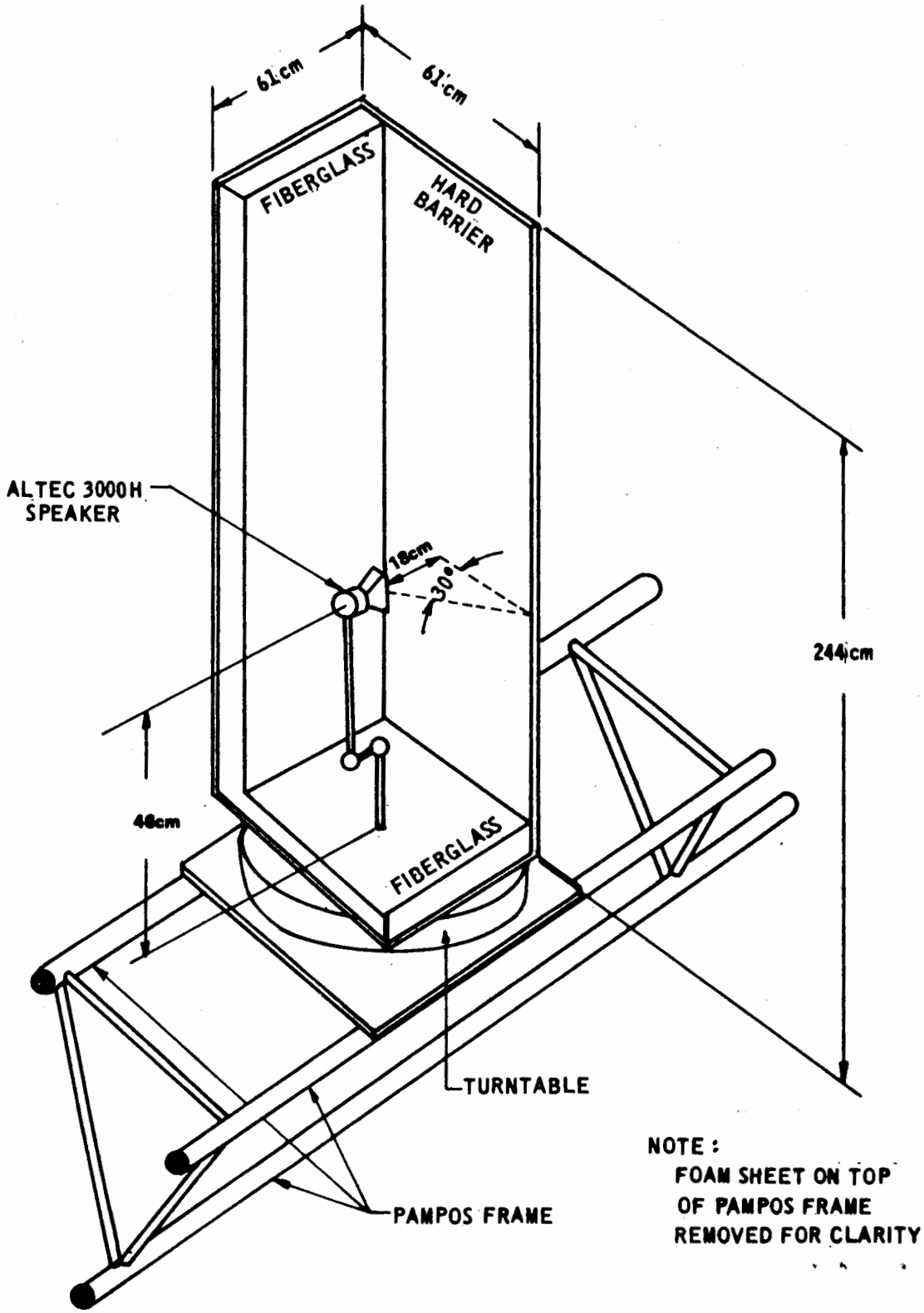

Figure 54.—Detailed Sketch of Shield/Speaker Arrangement

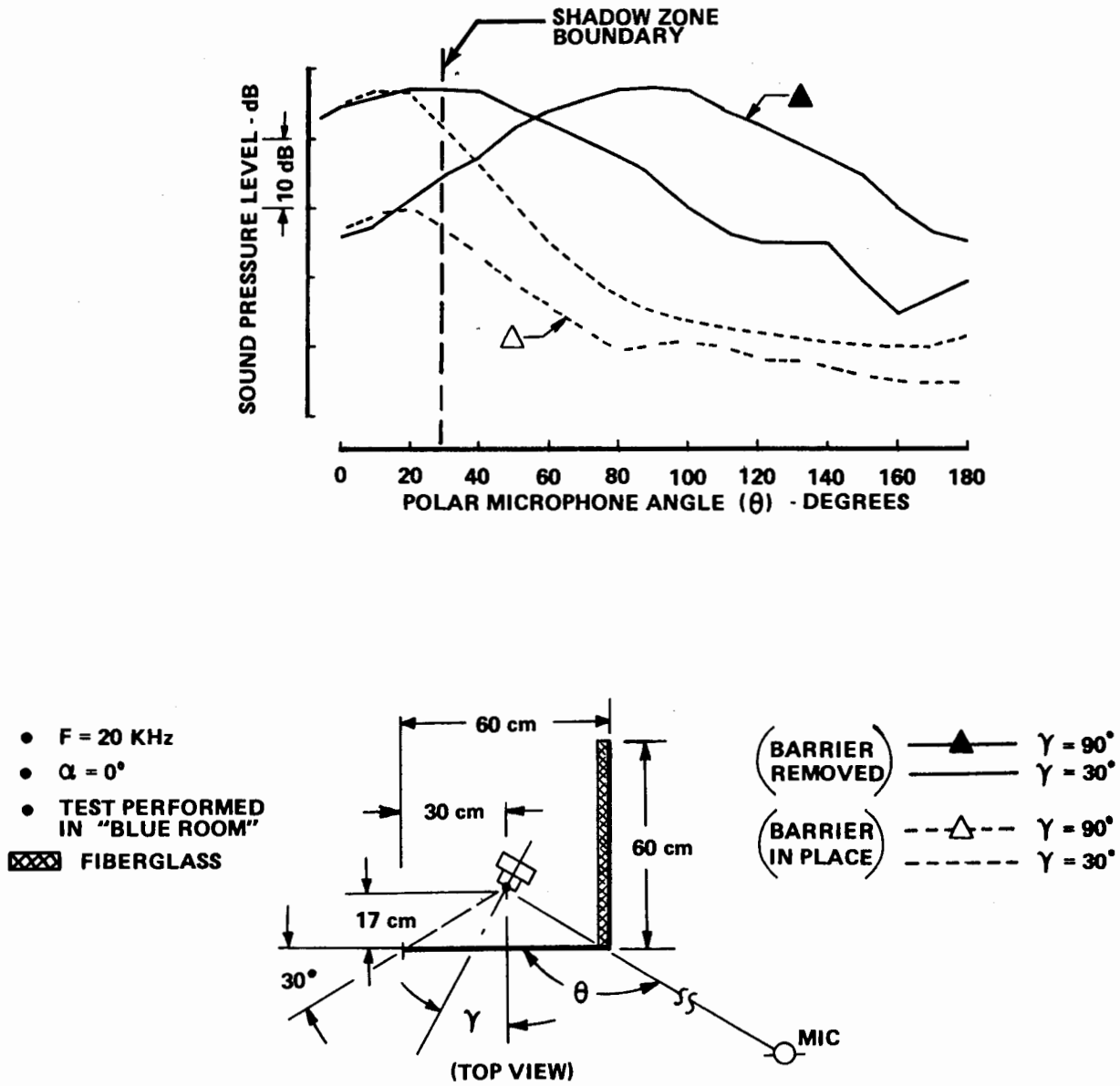

Figure 55.—Effect of Source Orientation on Shielding of Simulated Semi-Infinite Half-Plane Barrier

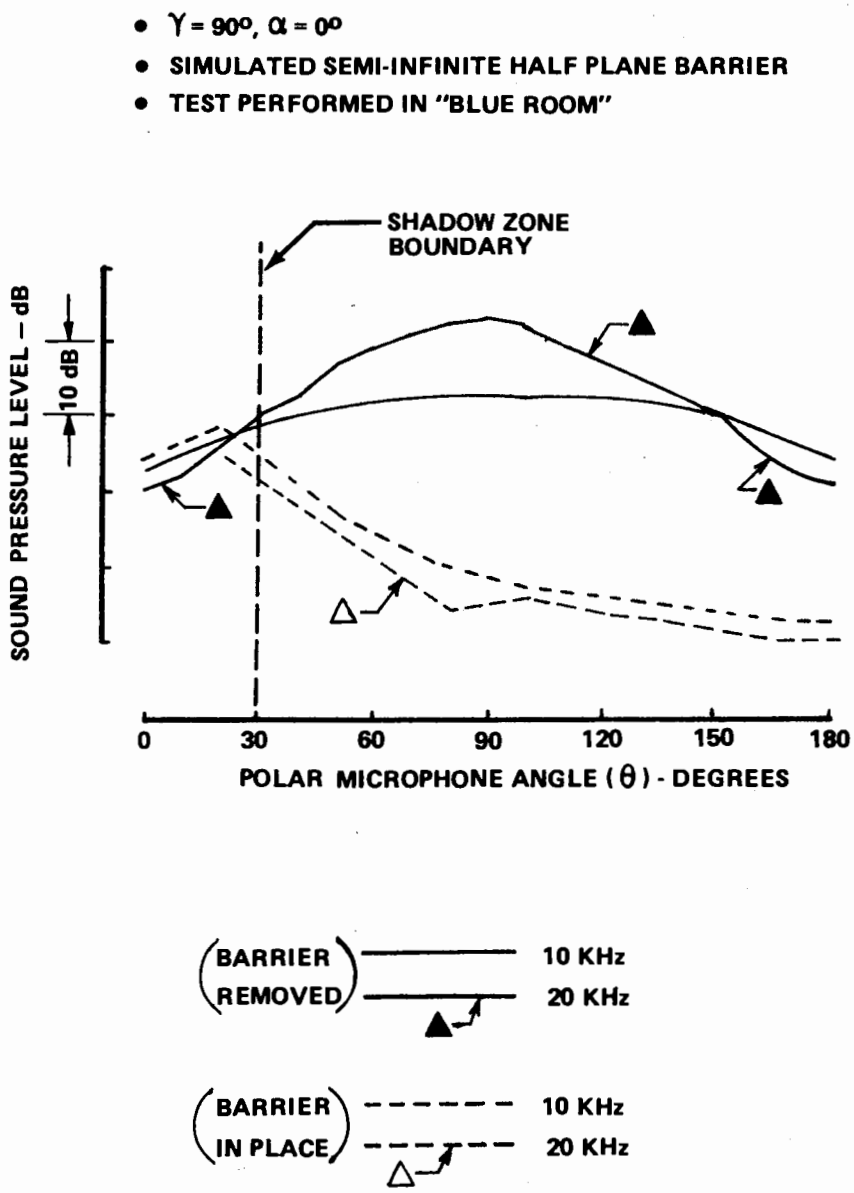

Figure 56.—Effect of Source Frequency on Shielding of Simulated Semi-Infinite Half-Plane Barrier

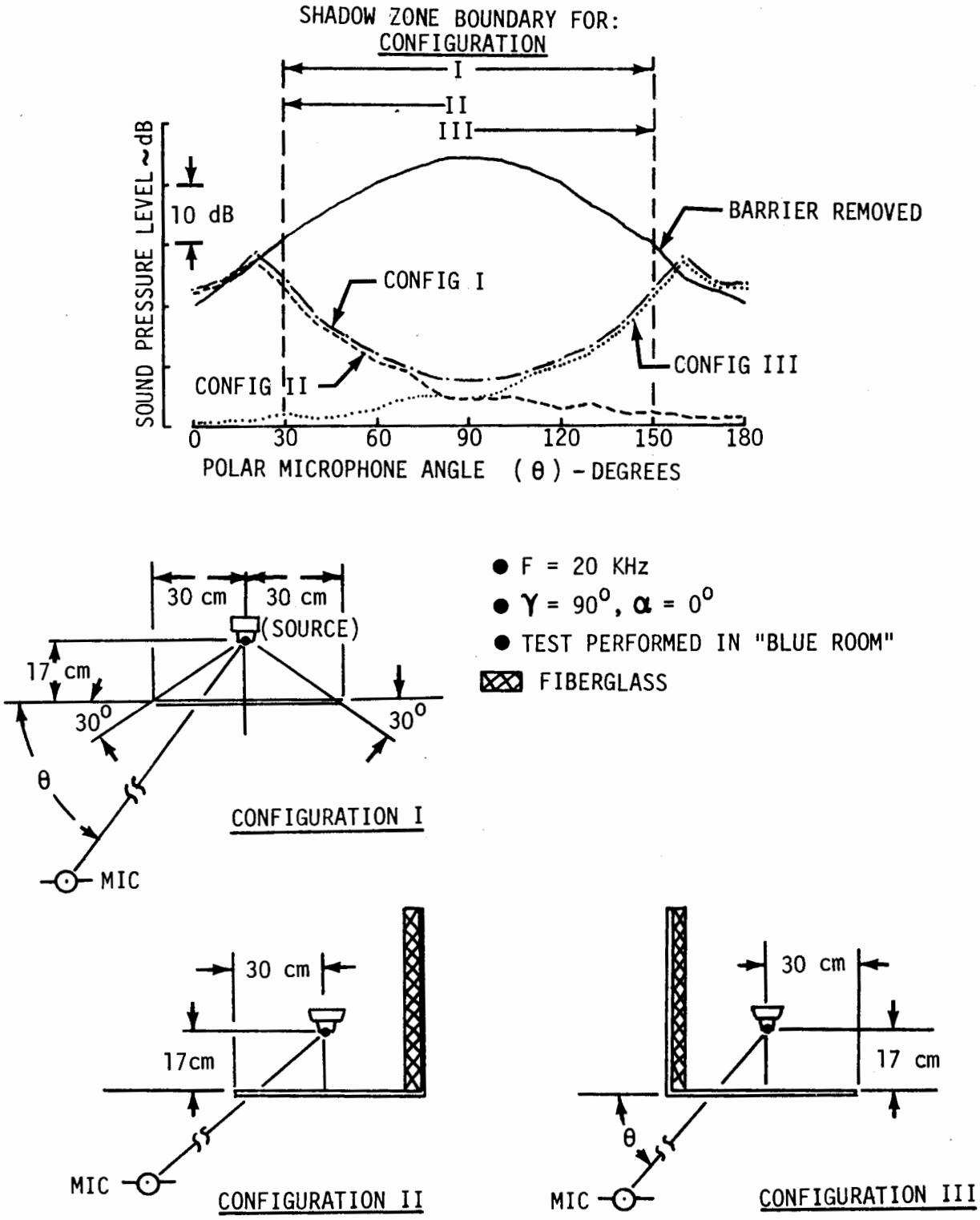

Figure 57.—Comparison of Shielding Behavior of "Flat Board" and Simulated Semi-Infinite Half-Plane Barriers

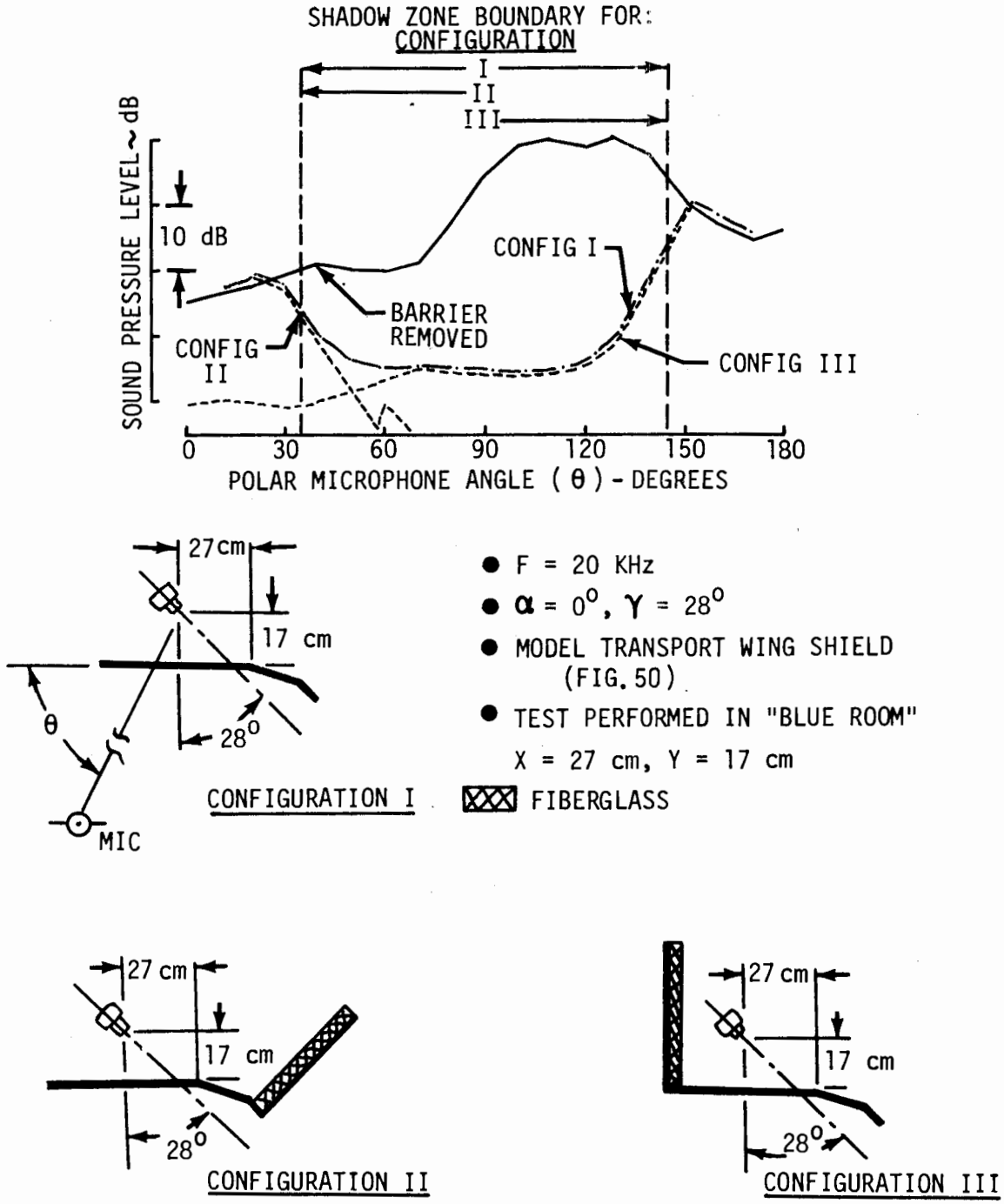

Figure 58.—Apparent Diffraction Contributions of Leading and Trailing Edges of Wing Barrier

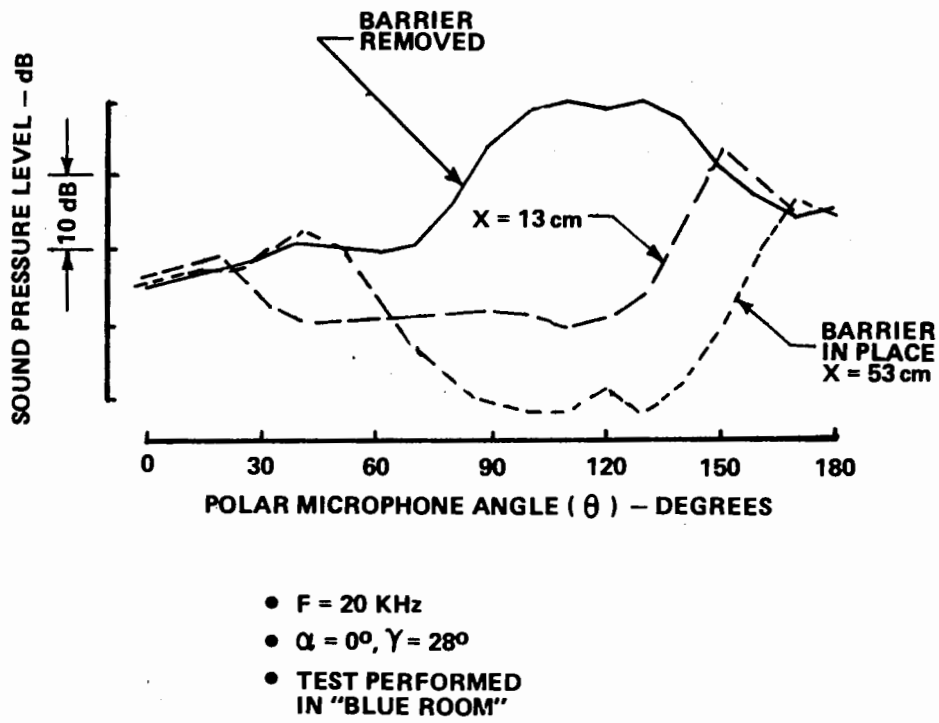

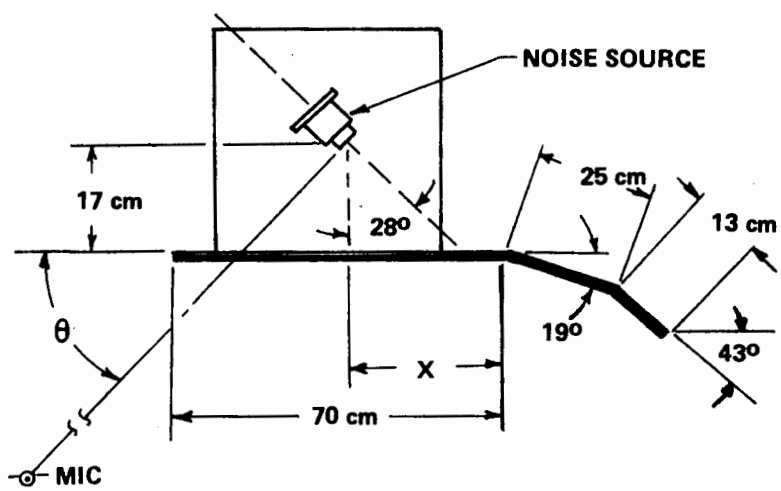

Figure 59.—Effect of Source Position on Shielding Effectiveness of Scale-Model Transport Wing

shown. The leading edge contribution was obtained by placing a lined barrier at the trailing edge, much as was done to simulate the semi-infinite half-plane barrier, and vice versa for the trailing edge contribution. The noise penetrating the shadow zone of the wing appears to be the superposition of contributions from the leading and trailing edges considered separately.

Figure 59 shows the effect on wing shielding of changes in source location. As would be predicted by the simple theory discussed in section 2.2, noise coming around the leading edge is increased while noise coming around the trailing edge is reduced as the source is moved further away from the trailing edge and closer to the leading edge.

Results from the group 2 tests in the LTC are shown in figures 60 and 61. Group 2 test results are also discrete samples from smoothed, continuous charts. Figure 60 shows results for the Altec noise source aimed at three different barrier edge locations, i.e., γ constant at 60^0 with $\alpha = 0^0$, 55^0, and -55^0 (see figs. 49, 52, and 54). For these orientations, the center of the maximum lobe makes a grazing incidence with the barrier edge. With the noise source set at $\alpha = 0^0$, the greatest sound intensity was directed toward the barrier edge point closest to the receiver microphone. For $\alpha = 55^0$ (i.e., toward the open end of the barrier), the greatest sound intensity incident on the barrier edge was about 14 dB higher than that incident on the barrier edge point closest to the receiver microphone. In the case of $\alpha = 0^0$ or 55^0, the shielded noise appears to depend on the unshielded level directed at the barrier edge point closest to the receiver. Also, levels within the shadow zone of the barrier are independent of the corresponding unshielded noise levels as was seen previously in tests of this type in the blue room.

For the case of $\alpha = -55^0$, the fiberglass pad on the base of the barrier (fig. 54) was removed, and hence the noise source was directed at the unlined base. It can be seen that the shielding effectiveness of the barrier for this situation is much reduced compared to the $\alpha = 0^0$ or 55^0 cases. Flanking radiation resulting from scattering/reflection of sound off the barrier base and pampos framework (fig. 54) appears to be a probable cause of the reduced shielding effectiveness.

Figure 61 compares results obtained in the LTC and in the quasi-anechoic room where the model fan rig shielding tests (see sec. 2.3.1.2) were run. The test setups in the two rooms were essentially the same. The noise source used in the LTC was slightly more directive than the noise source used in the model fan rig room. Hence, essentially the only difference in the tests was the difference in the test arenas. As can be seen, the shielding effectiveness of the barrier when tested in the model fan rig room is noticeably less than when tested in the LTC. Flanking radiation produced by reflection off the fan rig room walls is suspected to contribute to the higher noise levels in the fan rig room.

2.3.1.2 Model Fan Rig Test

An objective of this 1972 test program was to investigate the potential shielding of discharge fan tone noise by a winglike barrier. For this purpose, The Boeing Company's 12-in. cold-flow fan facility with its anechoic receiving room was used. The fan was designed to deliver a fan pressure ratio of 1.5 at a fan tip speed of 366 m/s.

- TEST PERFORMED IN LTC
- SIMULATED SEMI– INFINITE HALF PLANE BARRIER
- TONE FREQUENCY = 20 KHz

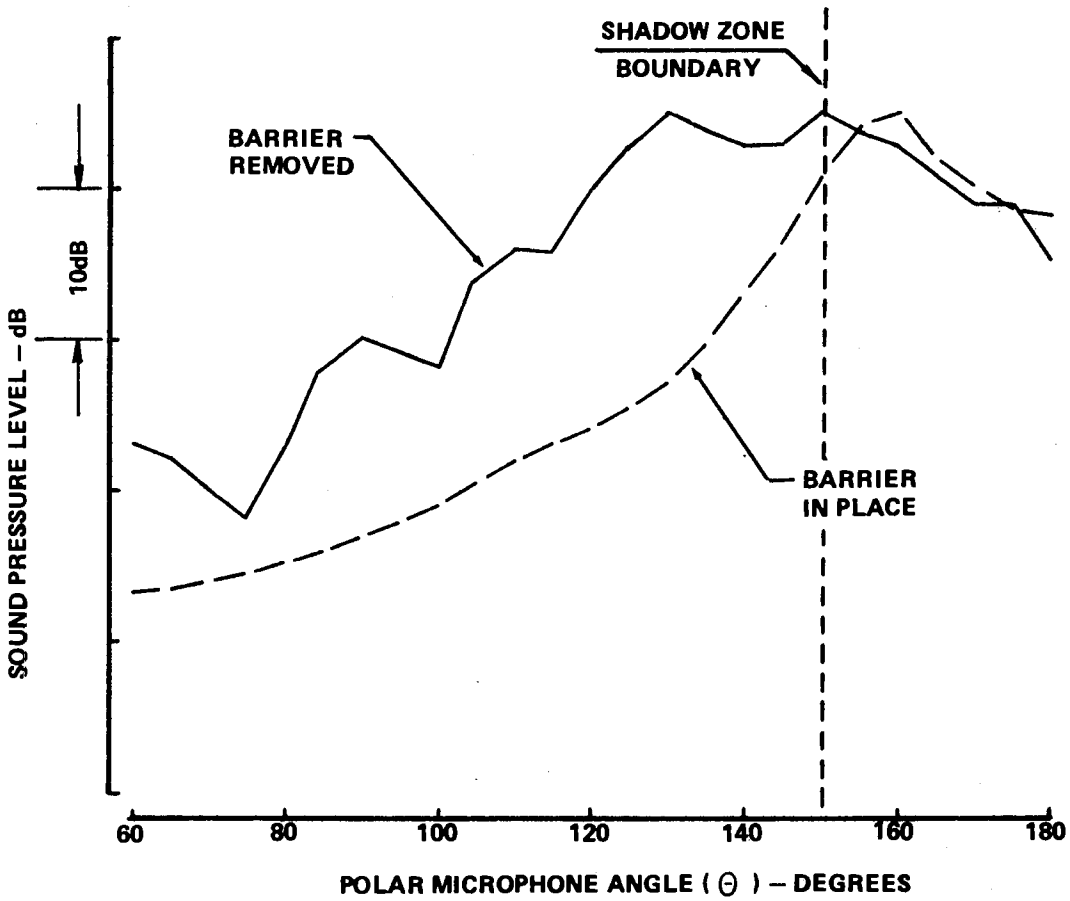

a) SOURCE AT $\alpha = 0^\circ, \gamma = 60^\circ$ (SEE FIG. 49)

Figure 60.—Unshielded and Shielded Behavior of Altec Source as Tested in LTC

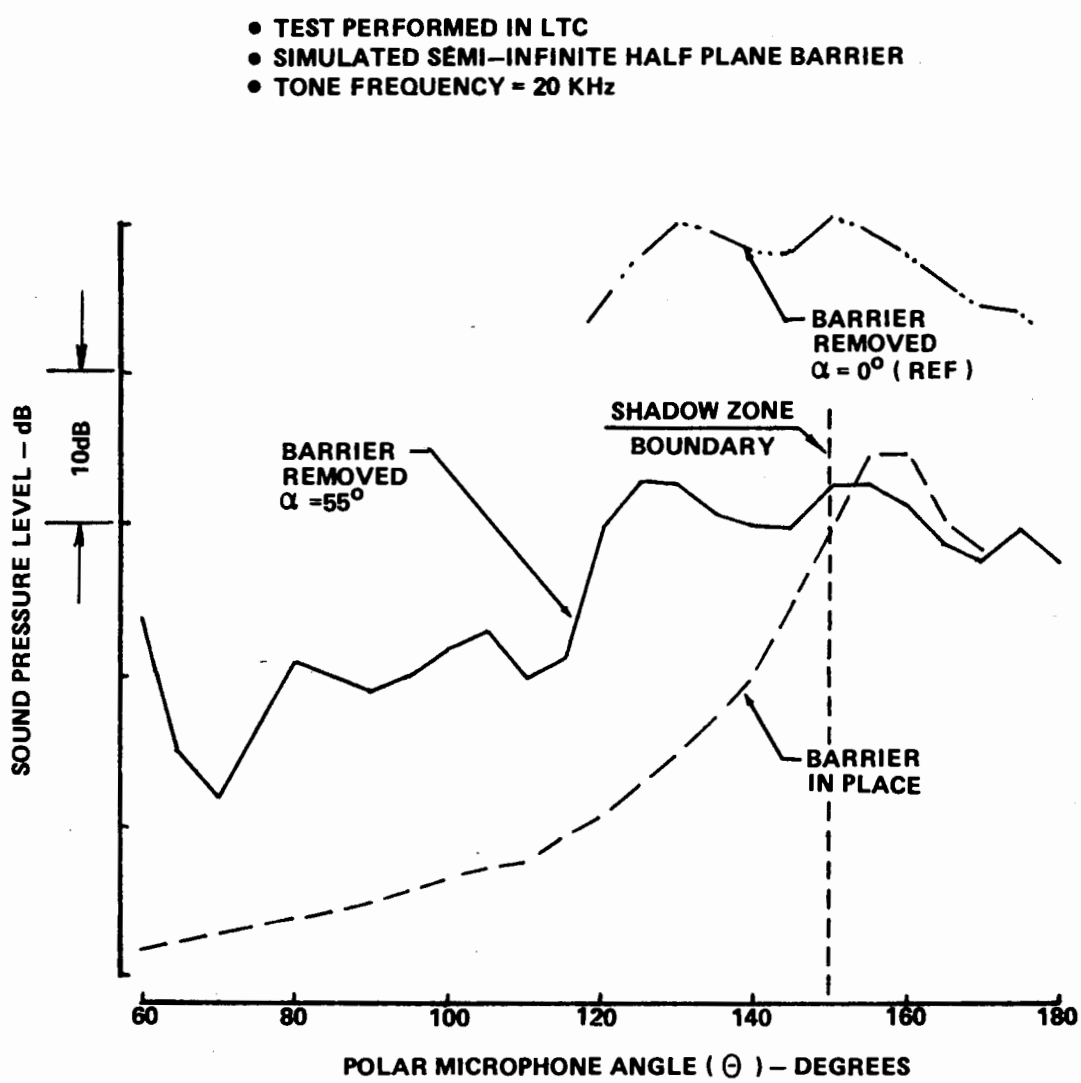

b) SOURCE AT $\alpha = 55^{\circ}$, $\gamma = 60^{\circ}$ (SEE FIG. 49)

Figure 60.—(Continued)

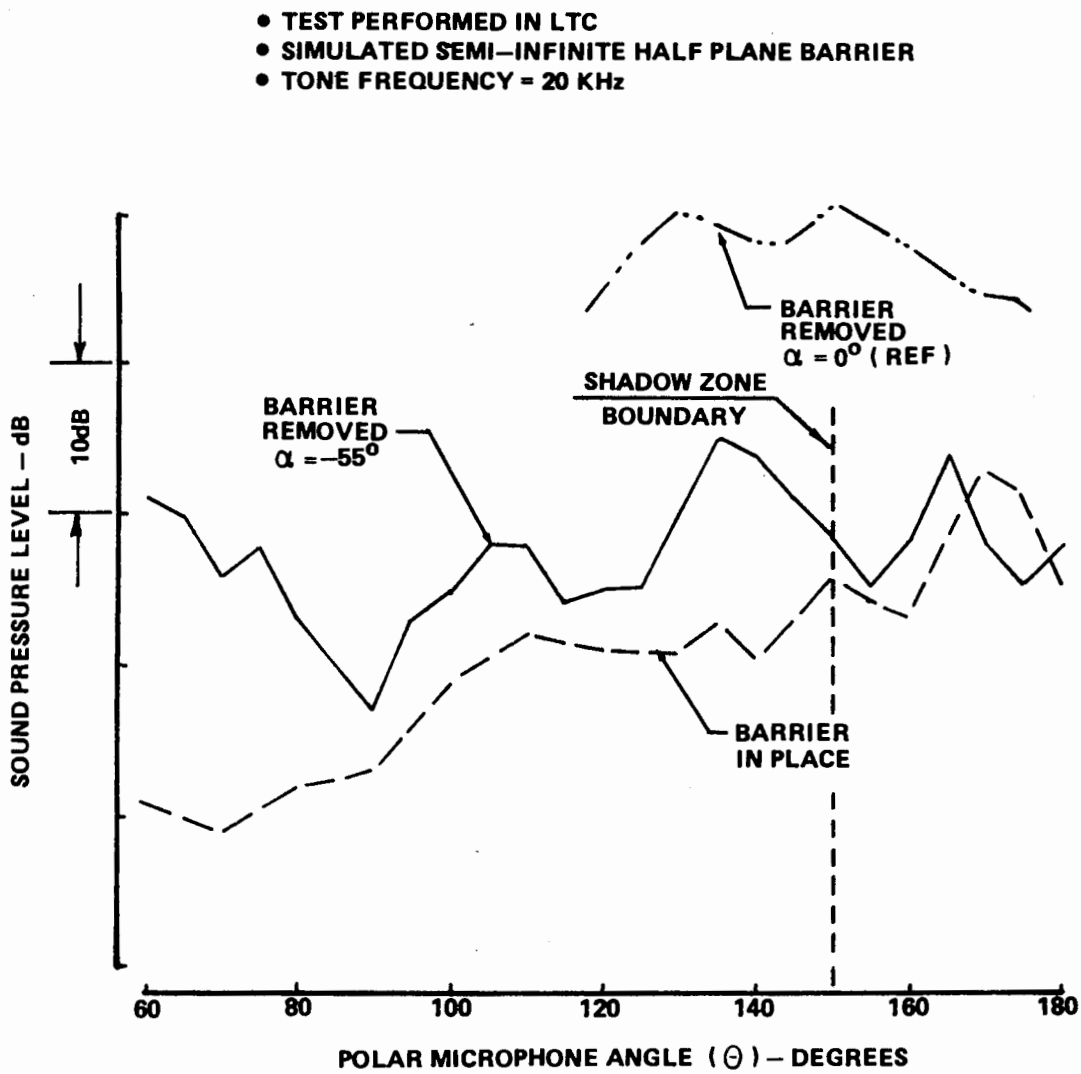

c) SOURCE AT $\alpha = -55^0$, $\gamma = 60^o$ (SEE FIG. 49)

Figure 60.—(Concluded)

- SIMULATED SEMI-INFINITE HALF PLANE BARRIER
- SOURCE ORIENTED AT $\alpha = +55°$, $\gamma = 60°$ (SEE FIG. 49)
- TONE FREQUENCY = 20 KHz

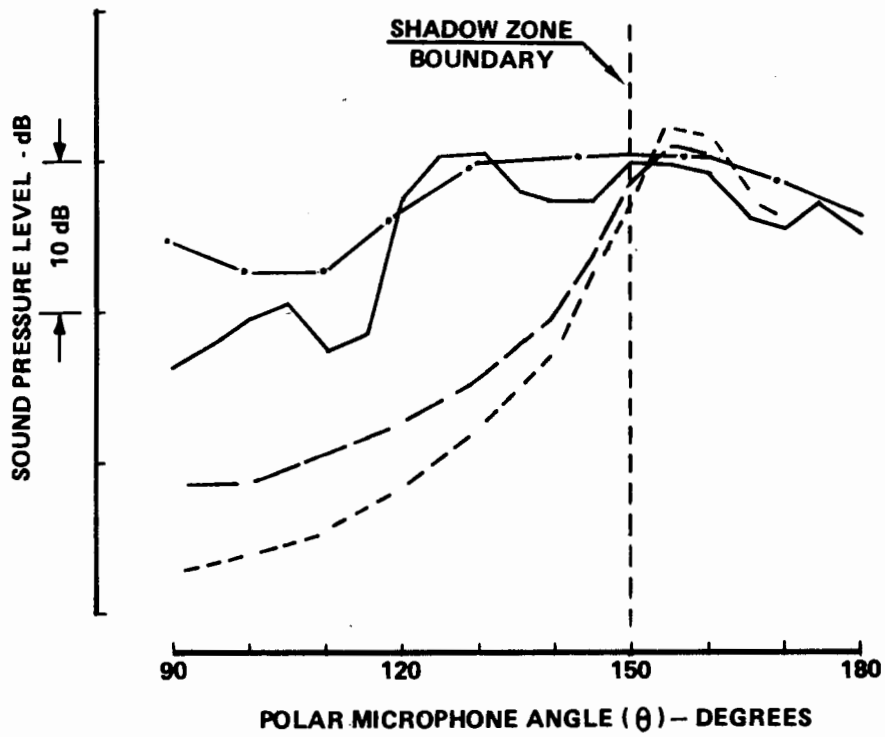

TEST PERFORMED IN MODEL FAN RIG ROOM

—·— BARRIER REMOVED

— — — BARRIER IN PLACE

TEST PERFORMED IN LTC

——— BARRIER REMOVED

– – – – BARRIER IN PLACE

Figure 61.—Comparison of Semi-Infinite Half-Plane Barrier Performance as Tested in Fan Rig Room and LTC

The main dimensions of the anechoic room were 10.8 m by 10.1 m floor space and 3.4 m high. The walls, floor, and ceiling were carefully padded with 10-cm-thick battens of fiberglass covered with heavy weave fiberglass cloth. At 20 kHz, the absorption of these batts was about 95%. It now appears that such an absorption value is not large enough to prevent room wall reflection from influencing the levels detected in the deep shadow zone of the shield used during the test program.

An array of eight microphones was placed on a line parallel to the fan centerline, but offset 3.0 m to the side. Figure 62 shows the test setup with the winglike shield in a "flyover" attitude relative to the receiving microphones (wing tilt angle $\phi = 90^0$). Figure 63 shows the shield in a "25^0 sideline" attitude (wing tilt angle $\phi = 25^0$). A schematic of the room layout for the test is shown in figure 64, and dimensions of the winglike shield in figures 65 and 66.

A typical range of geometric test parameters investigated is shown in table 4. For each configuration, measurements were taken at four different fan speeds: 17,400, 22,500, 24,500, and 26,740 RPM. Typically, acoustic time samples for each of the eight microphones would be recorded on FM tape for approximately 35 sec. Recorded data would then be reduced to 40-Hz bandwidth spectral format from 40 to 20,000 Hz using a Federal Scientific UA-6A narrowband analyzer. The average analyzer sample time was 16 sec.

Typical results are shown in figure 67 for a 90^0 wing. An essentially consistent trend with shield length, X, and fan tone frequency is discernible. Shielding attenuation is seen to increase with increasing shield length and frequency. Both trends are, of course, in agreement with the theory that has been discussed.

Some results for a 25^0 wing are shown in figure 68. Consistent trends as observed above for the 90^0 wing are difficult to discern in this case. An examination of the geometries suggests complicating near-field effects are quite likely important for the 25^0 wing, much less so for the 90^0 wing. It is also apparent that for the 25^0 wing, many of the microphones are in the transition region between bright and shadow zones, further adding to the complexity of the data.

2.3.1.3 Wall Isolation Facility Shielding Test (Whistle in Secondary Flow)

An objective of this test was to investigate wing shielding of fan noise emanating from the secondary of dual-flow, hot-primary, cold-secondary nozzles. For this purpose the Boeing Wall Isolation Facility (WIF) was used.

The WIF is composed of two areas: (1) the interior area where the burner, air supplies, and other associated hardware are located and (2) the outside test arena where the test hardware and microphone boom are located. Figures 69 and 70 depict the facility and microphone boom. The standard microphone positions on the boom are at 10^0 increments between 90^0 and 160^0, with the 90^0 microphone being located directly above the nozzle in the nozzle exit plane. The boom has a radius of 7.6 m as measured from the intersection of the nozzle exit plane and the nozzle centerline. The outdoor arena is surrounded by concrete buildings on two sides, a concrete floor, with various pipes and

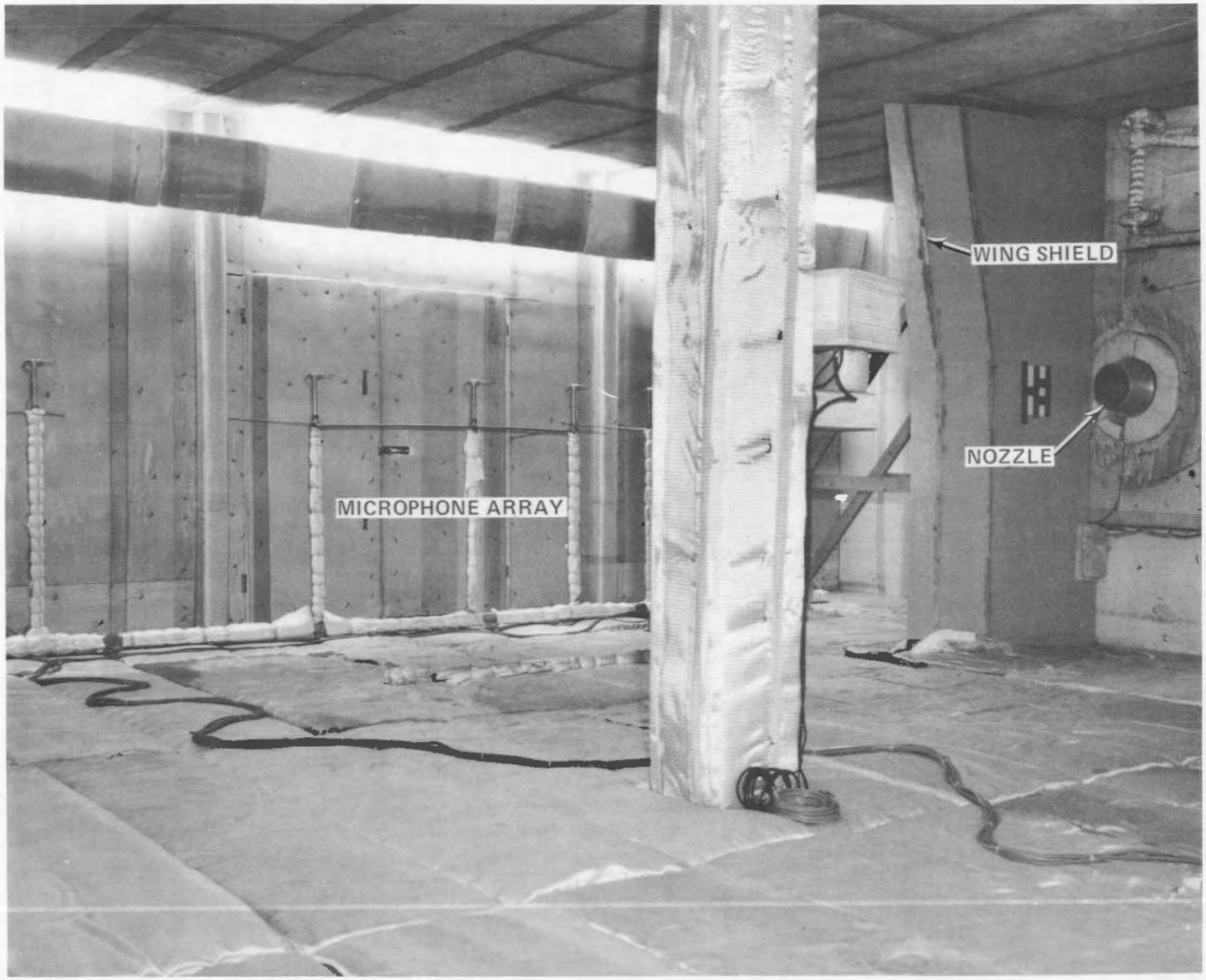

Figure 62.—Model Fan Rig Test Setup, "Flyover" Configuration

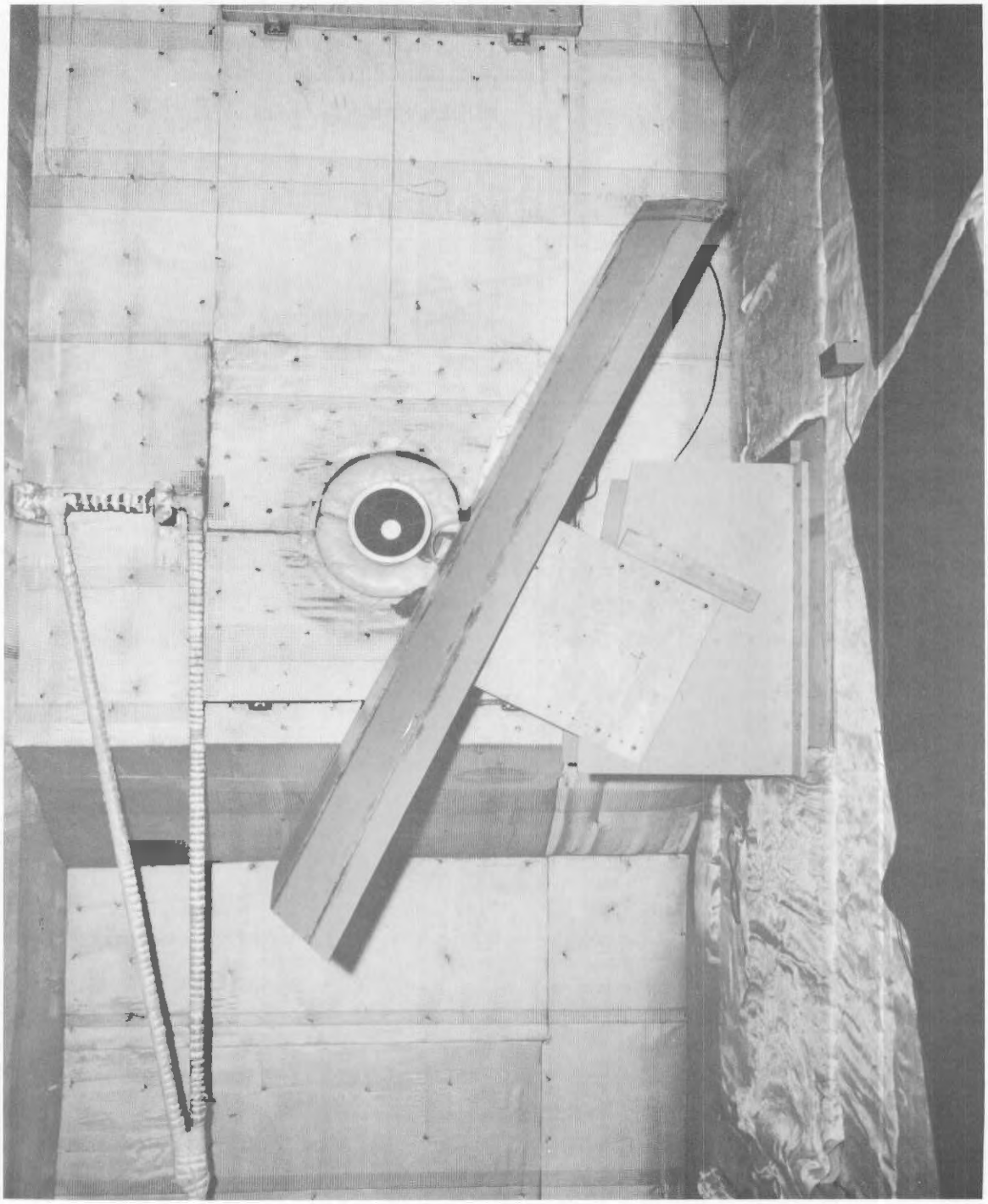

Figure 63.—Model Fan Rig Test Setup, "25° Sideline" Configuration

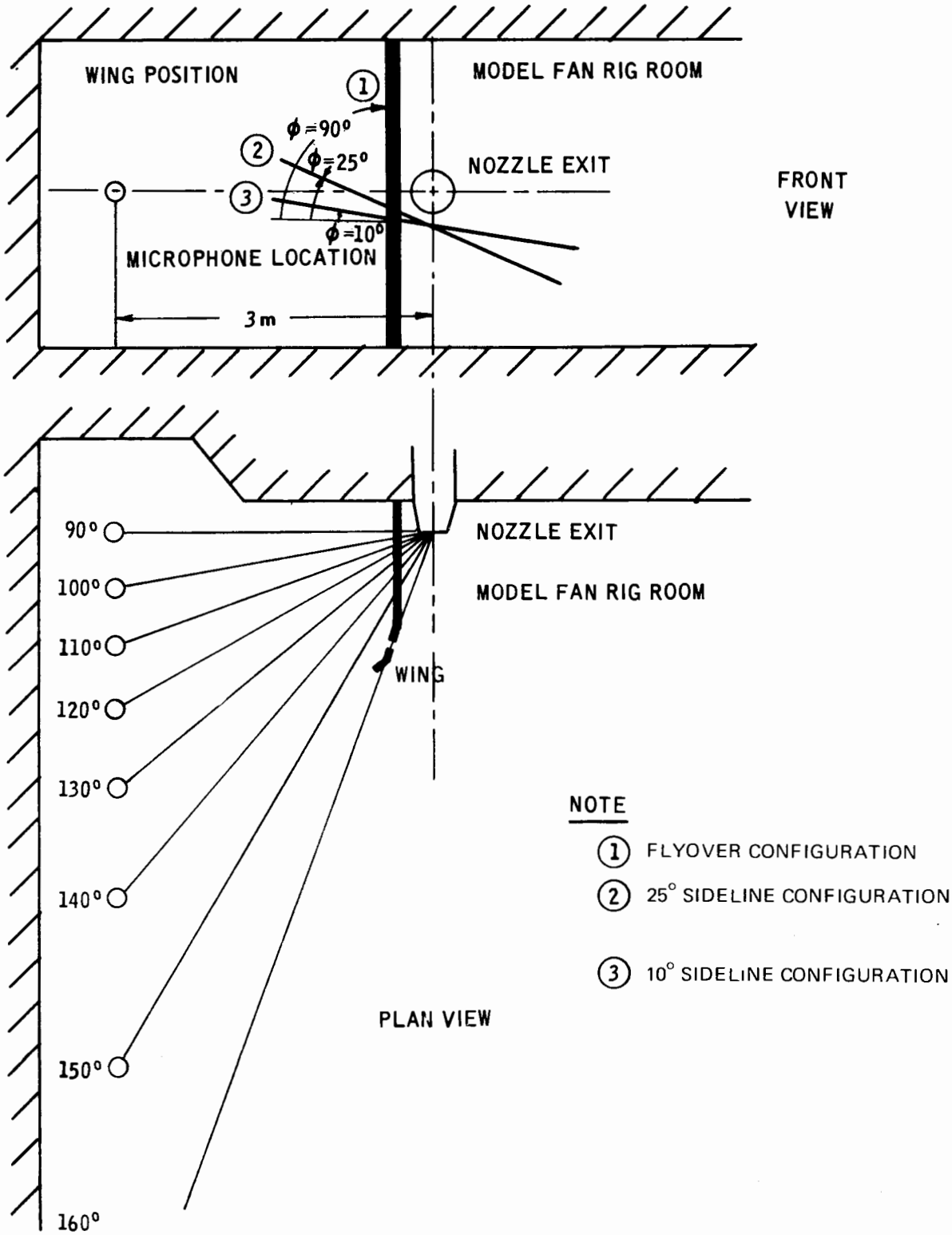

Figure 64.—Schematic of Model Fan Rig Test Setup

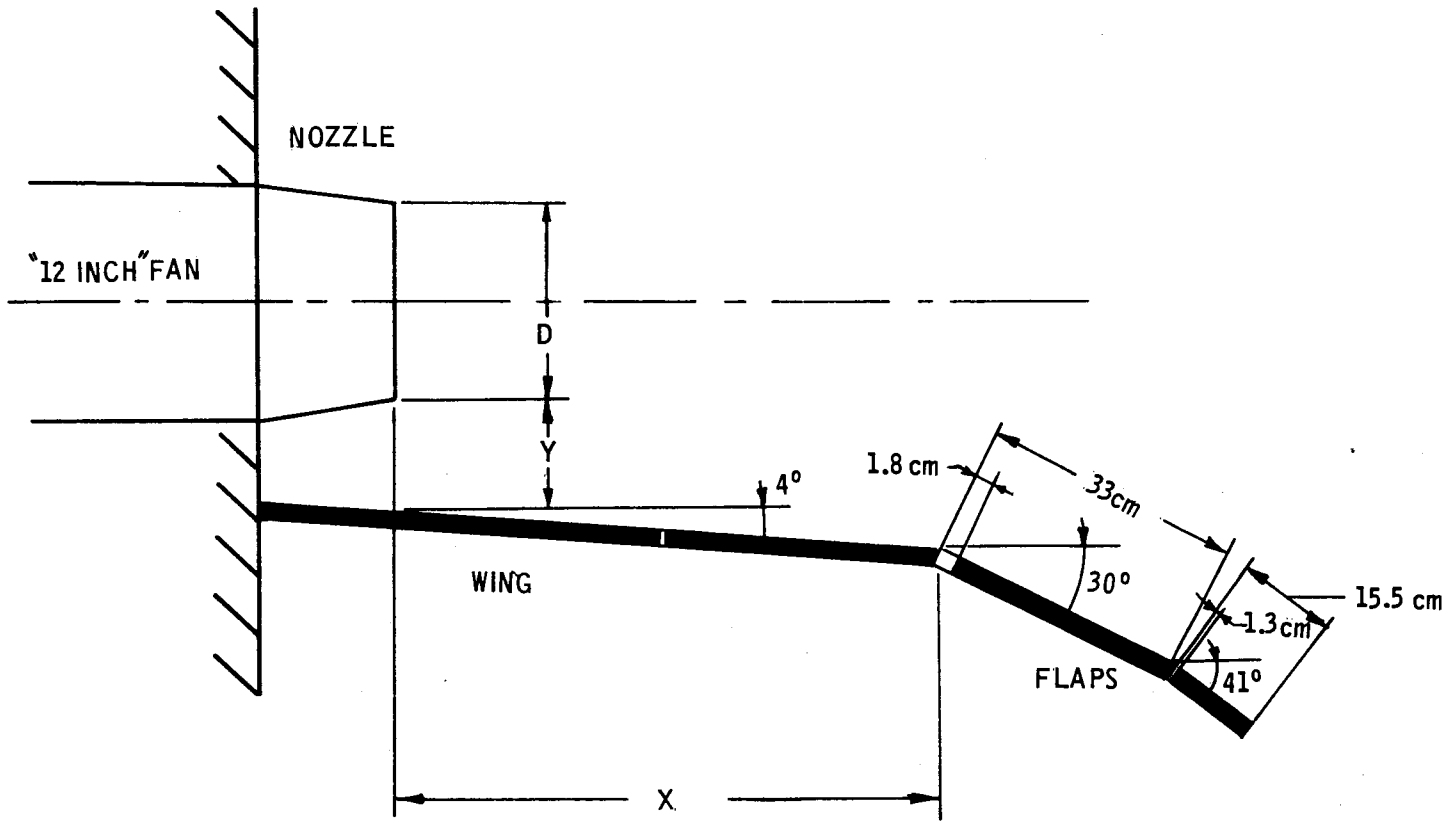

NOTE: WING THICKNESS = 1.3cm PLYWOOD

Figure 65.—Position of the Shield With Respect to the Nozzle Exit

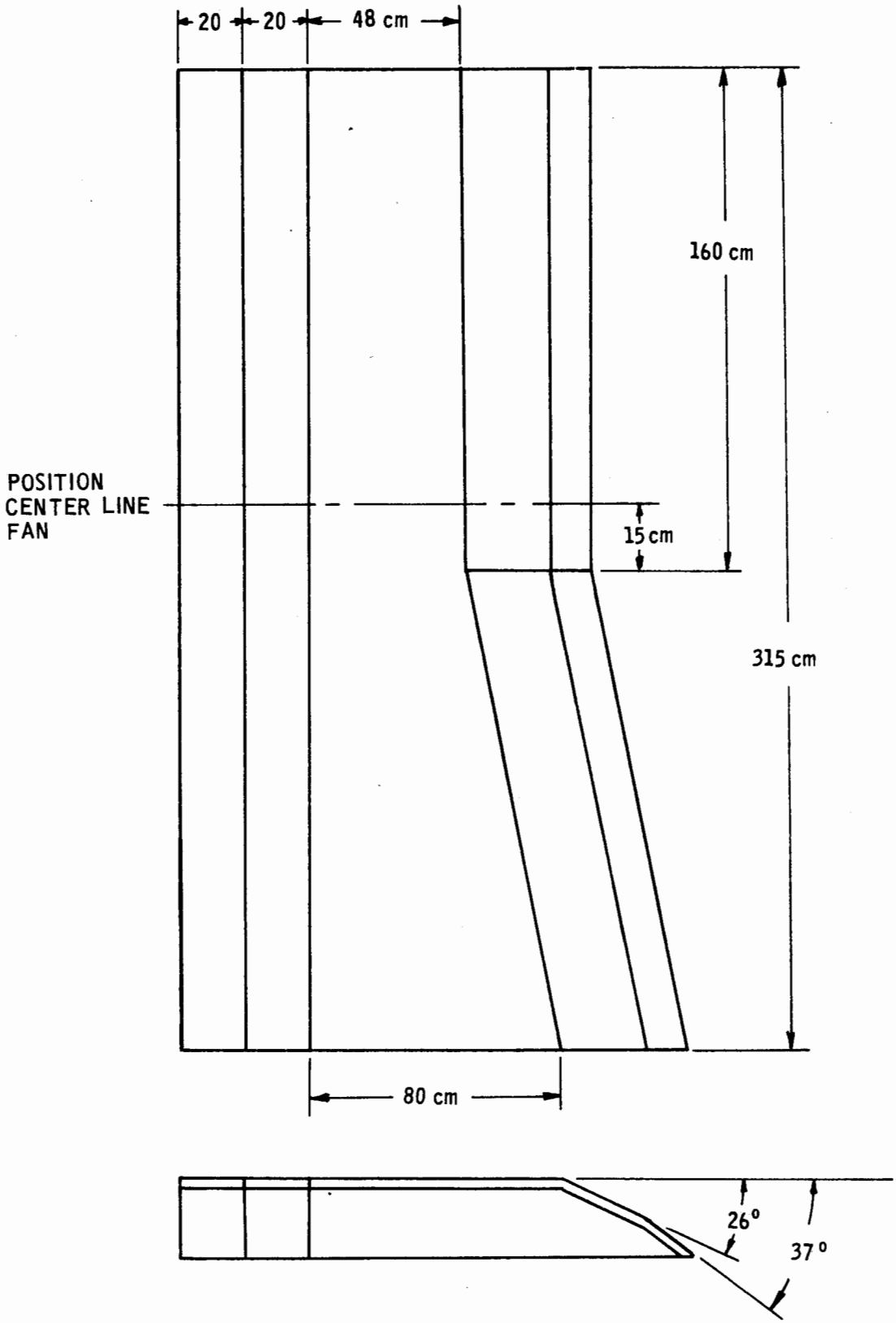

Figure 66.—Geometry of Winglike Shield

Table 4.—Typical Model Fan Rig Test Conditions

RUN	D NOZZLE DIA CENTIMETERS	Φ DEGREES	Y cm	X cm	REMARKS
1C	25.73	—	—	—	BASELINE (SHIELD REMOVED)
2	25.73	90	15	48	SHIELD IN PLACE, GAPS SEALED
3	25.73	90	15	89	SHIELD IN PLACE, GAPS SEALED
4	25.73	90	15	69	SHIELD IN PLACE, GAPS SEALED
1D	30.58	—	—	—	BASELINE (SHIELD REMOVED)
8	30.58	25	15	48	SHIELD IN PLACE, GAPS OPEN
9	30.58	25	15	89	SHIELD IN PLACE, GAPS OPEN
10	30.58	25	15	69	SHIELD IN PLACE, GAPS OPEN

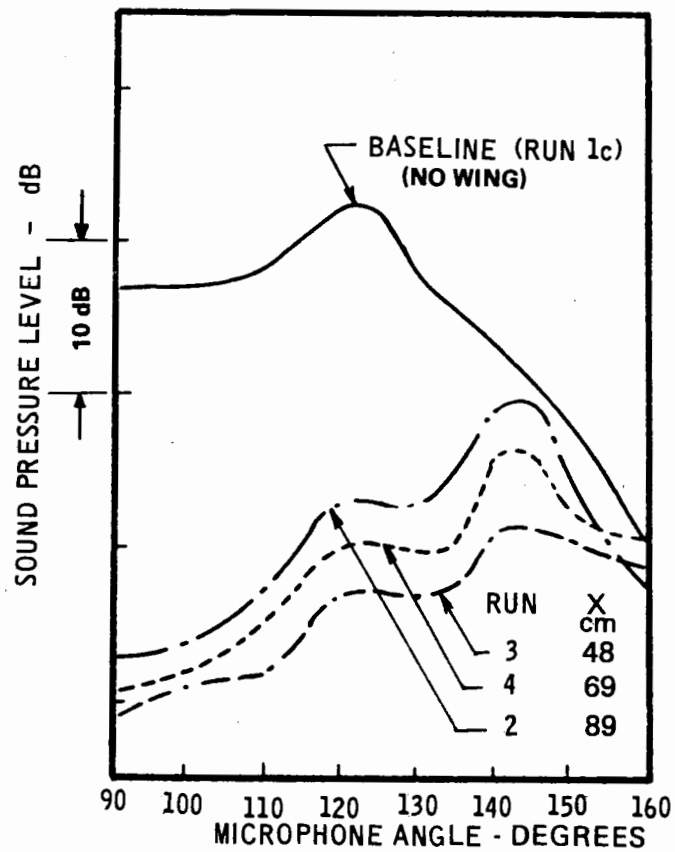

NOTES

- 9.28 KHZ
- 90° SHIELD
- 3m SIDELINE ARRAY OF MICROPHONES

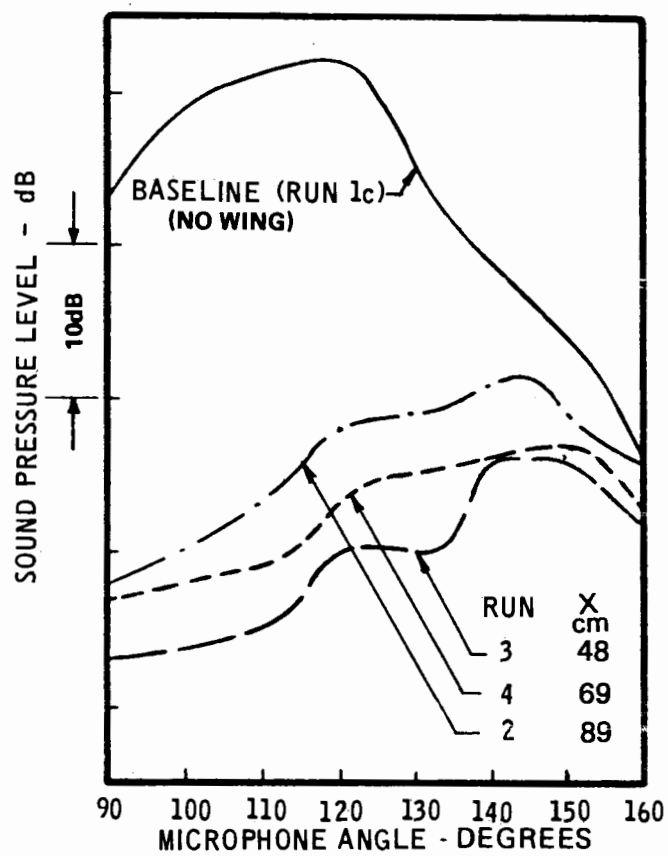

NOTES

- 14.2 KHZ
- 90° SHIELD
- 3m SIDELINE ARRAY OF MICROPHONES

Figure 67.—Fan-Tone Behavior With and Without 90° Shield

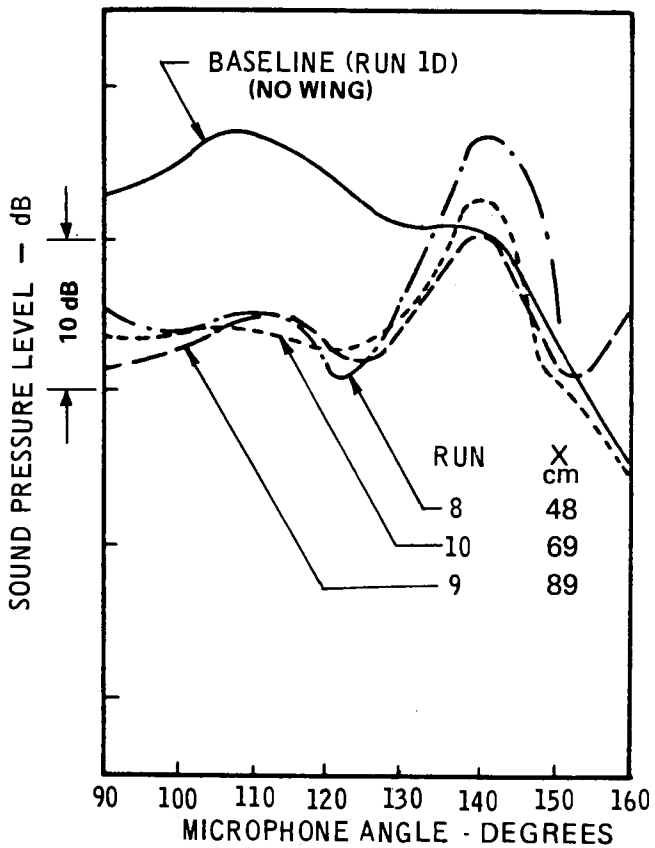

NOTES

- 9.28 KHZ
- 25° SHIELD
- 3m SIDELINE ARRAY OF MICROPHONES

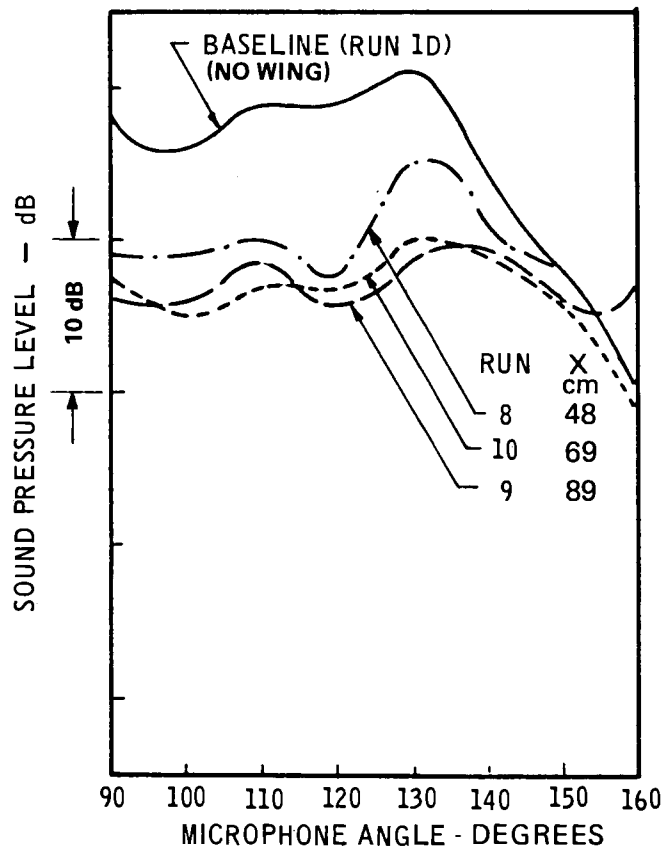

NOTES

- 14.2 KHZ
- 25° SHIELD
- 3m SIDELINE ARRAY OF MICROPHONES

Figure 68.—Fan-Tone Behavior With and Without 25° Shield

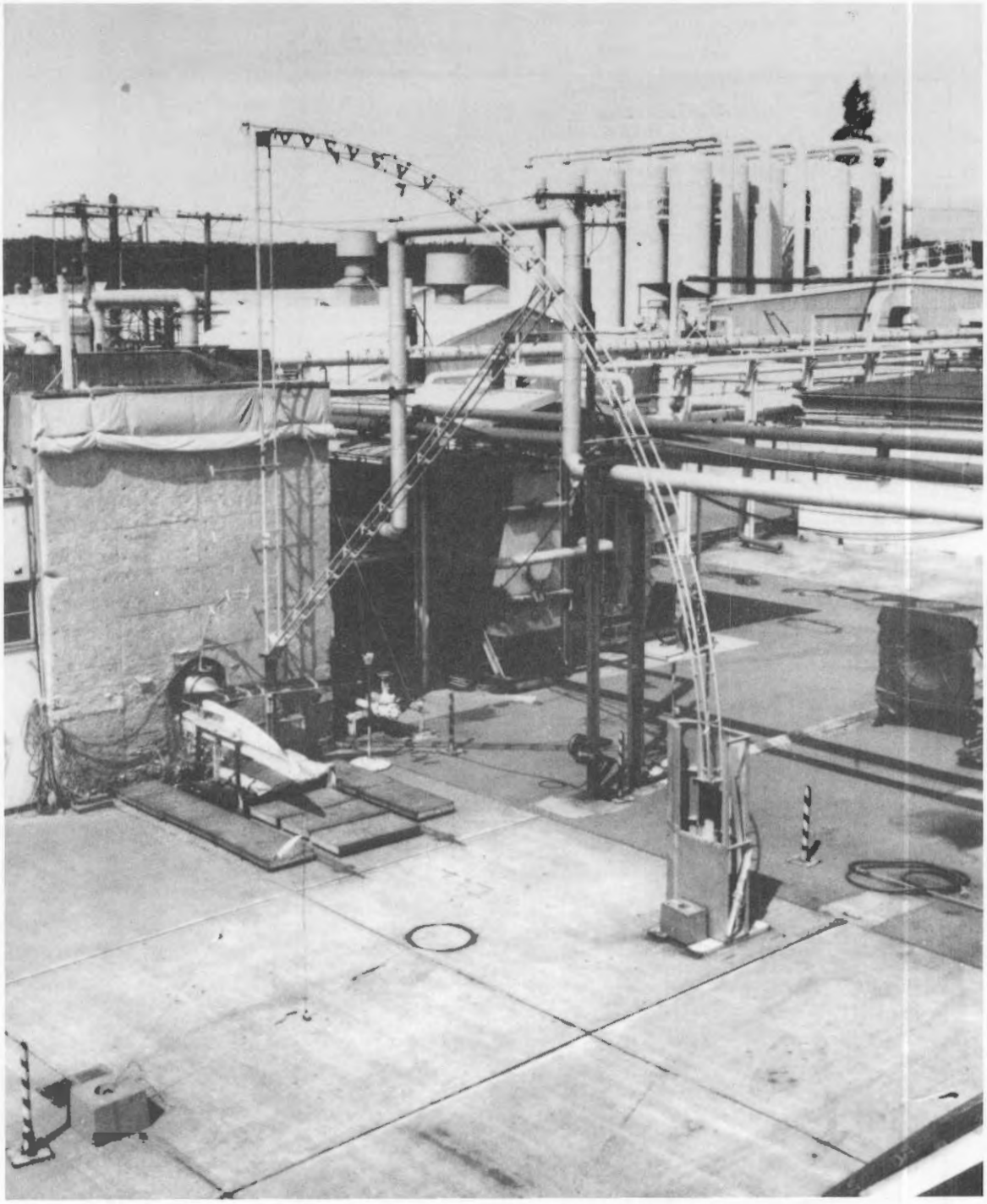

Figure 69.—Overview of WIF Test Facility

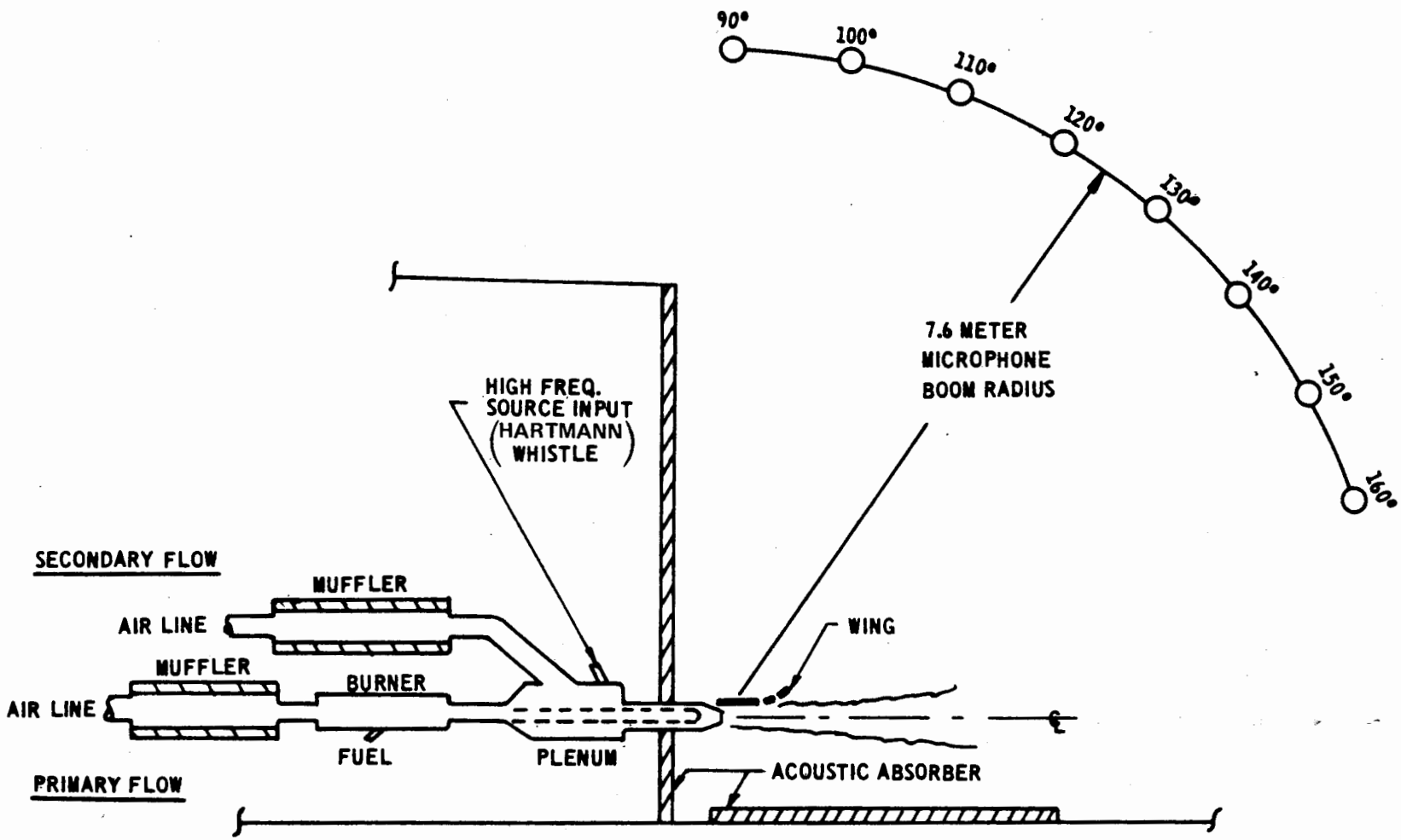

Figure 70.—WIF Test Facility Schematic

other hard surfaces located outside the immediate arena. The wall from which the nozzle extends is covered with fiberglass approximately 8 cm thick. Batts of wire-mesh-covered fiberglass were placed on the ground near the nozzle exit. A 45° ramp covered with 10 cm of fiberglass was located directly opposite the nozzle exit at a distance of 13 m.

A pretest investigation of the facility was conducted to determine its reverberation characteristics. To obtain proper shielding data, it was determined that the reverberant level should be a minimum of 25 dB below the direct signal level. This could not be accomplished using the standard microphone technique or by placing additional fiberglass padding throughout the arena. Directional (parabolic) microphones were therefore developed to reject reverberant off-axis signals and provide the desired minimum signal-to-noise ratio.

Seven nozzles were used in the shielding tests at the WIF. The nozzles tested were as follows:

Nozzle number	Bypass ratio	Description
8	5:1	Extended primary
9	5:1	Coplanar exit
10	5:1	Retracted primary
11	7:1	Small plug
12	7:1	Large plug
13	7:1	18-lobe mixer
14	7:1	D-nozzle exit

Schematics for all nozzles are shown in figure 71. All were axially symmetric, i.e., circular, except nozzle 14 (the D-nozzle). This nozzle is characteristic of the type to be used in the upper surface blowing (USB) propulsion system of the YC-14 aircraft presently under construction by Boeing for the USAF. The nozzles were operated at the four flow conditions listed in table 5.

A scale-model wing and fuselage segment was fabricated. The wing and flaps were constructed from aluminum. The fuselage was also fabricated from aluminum, but backed with dense foam, making a solid construction. Figure 72 shows a dimensioned sketch of the wing. The flaps were positioned at 23°/46°, and the geometry was such that the flap gap was essentially closed.

A Hartmann whistle located in the secondary plenum was used as the high-frequency noise source to simulate fan tones. The whistle fundamental frequency was 9600 Hz, with usable overtones at 19,300 and 29,000 Hz. A Photocon model 752 microphone was located next to the whistle to monitor and attain specific SPL's. The Hartmann whistle was calibrated prior to the test, and a table of SPL versus whistle pressure was obtained for nozzle pressure ratios of 1.1, 1.2, 1.3, and 1.4. This calibration then permitted the whistle fundamental to be reset to the same SPL as nozzle pressure ratio was varied. In addition, the Photocon microphone output was monitored on-line with a B&K meter as a further check of whistle output at the fundamental frequency.

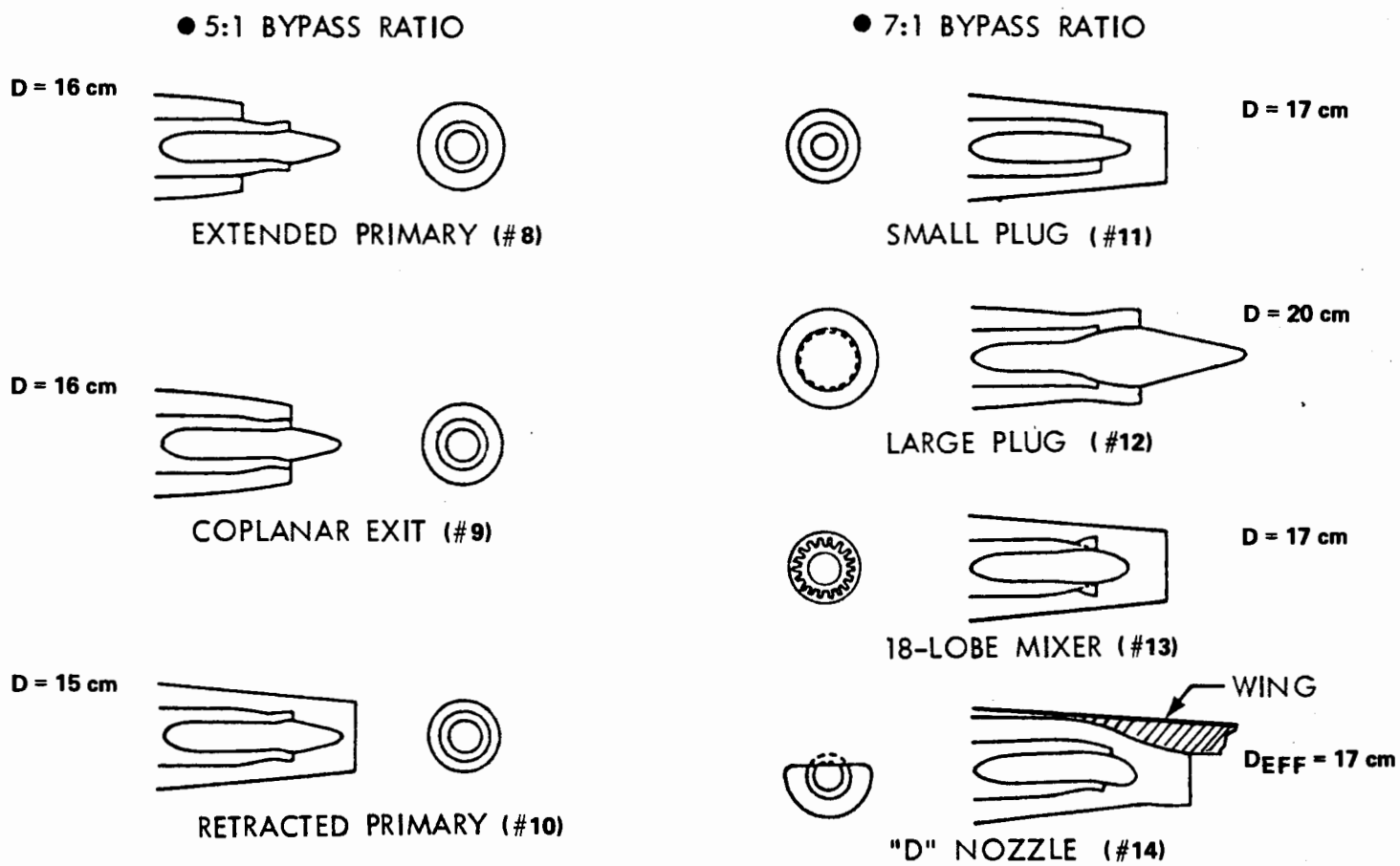

Figure 71.—WIF Test Nozzles

Table 5.—Nozzle Flow Conditions (WIF Test)

PR_P	T_{TP} °K	PR_S	T_{TS} °K	V_P m/s	V_S m/s	V_S/V_P	B.P.R.
1.1	400	1.1	AMB	188	125	.66	5.85
1.2	440	1.2	AMB	267	172	.64	6.03
1.3	480	1.3	AMB	327	205	.63	6.27
1.4	580	1.4	AMB	379	230	.61	6.47

NOTE:

PR_P = PRIMARY PRESSURE RATIO

PR_S = SECONDARY PRESSURE RATIO

T_{TP} = PRIMARY TOTAL TEMPERATURE

T_{TS} = SECONDARY TOTAL TEMPERATURE = AMBIENT

B.P.R. = BYPASS RATIO BASED ON NOMINAL AREA RATIO OF 3.9

V_P = VELOCITY OF PRIMARY FLOW

V_S = VELOCITY OF SECONDARY FLOW

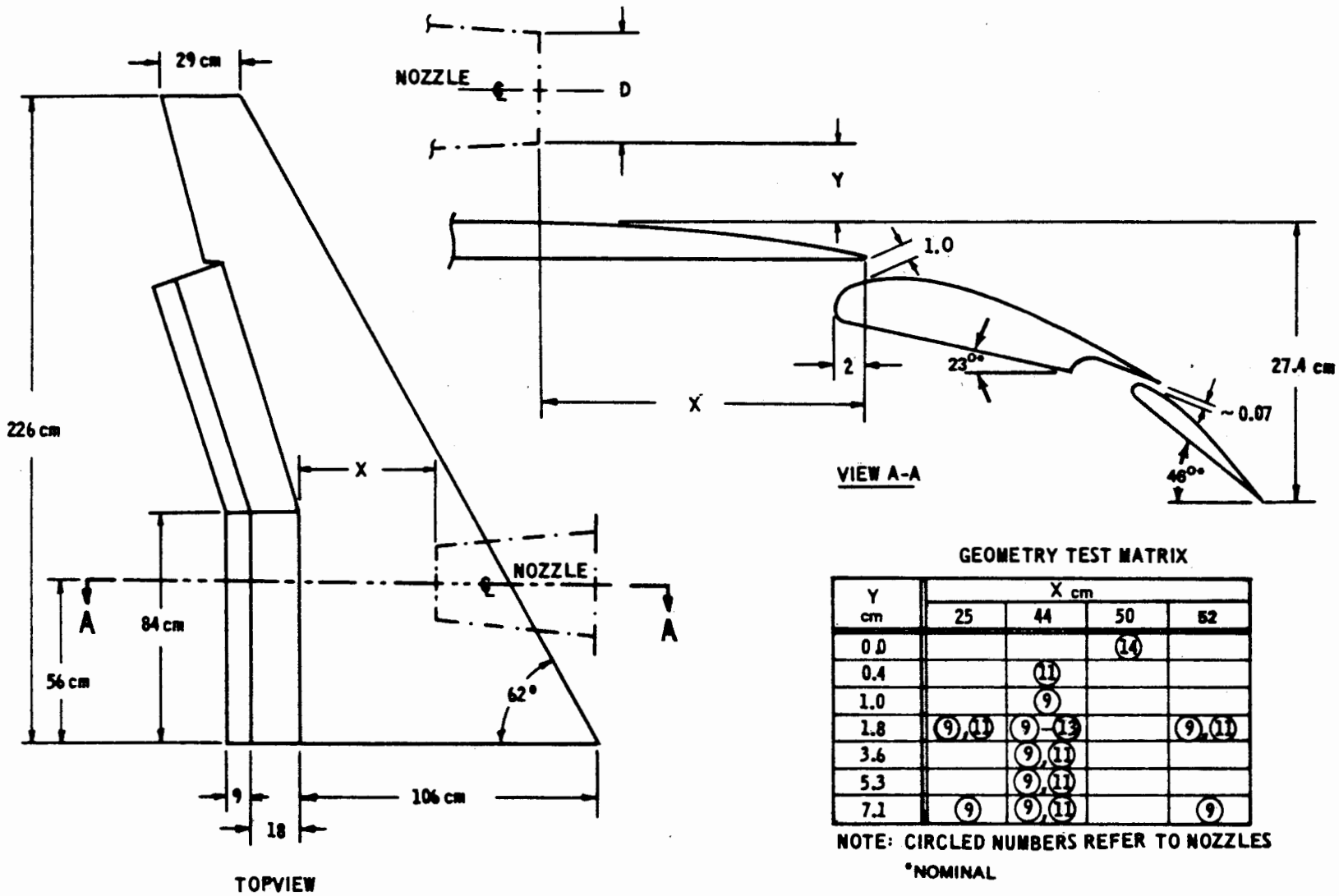

GEOMETRY TEST MATRIX

Y cm	X cm 25	44	50	52
0.0			(14)	
0.4		(11)		
1.0		(9)		
1.8	(9),(11)	(9)-(13)		(9),(11)
3.6		(9),(11)		
5.3		(9),(11)		
7.1	(9)	(9),(11)		(9)

NOTE: CIRCLED NUMBERS REFER TO NOZZLES

*NOMINAL

Figure 72.—Wing/Nozzle Geometric Relations (WIF Test)

Figure 73 shows how the shadow zone boundary is defined for flow nozzles. The shadow zone boundary is defined here based strictly on geometry. This definition implies an equivalent point source at the intersection of the nozzle centerline and exit plane. This is somewhat arbitrary because noise coming from an exhaust nozzle is not expected to be compact for either the flow or no-flow case. Hence, the real effective shadow zone boundaries may differ from this and the apparent source location may be further downstream from the nozzle.

Figures 74 and 69 show the wing mounted in the flyover configuration for a typical nozzle. A matrix of nozzle wing positions was tested per the table shown in figure 72. The nozzle baseline position was at X = 44 cm and Y = 1.8 cm, with the exception of nozzle 14 (D-nozzle), which was tested only at X = 50 cm and Y = 0.0 cm.

Figure 75 shows the 25° sideline configuration for a typical nozzle. The matrix of nozzle wing positions tested is the same as for the flyover configuration. The nozzle baseline positions were as defined above for the flyover case.

Recording instrumentation consisted of the following: (1) eight parabolic reflecting microphones on a 7.6-m-radius boom at 90°, 100°, 110°, 120°, 130°, 140°, 150°, and 160° and (2) one microphone located in the secondary of the plenum and adjacent to the Hartmann whistle. Narrowband plots (80-Hz bandwidth) were made for each microphone measurement as illustrated in figure 76.

Generally, the test sequence was as follows. (1) With a particular nozzle installed, a no-wing test condition was conducted. (2) The no-wing test condition was then followed immediately by a wing shielding sequence consisting of several different X and Y positions. (3) At each test position, nozzle pressure ratios were set at 1.1, 1.2, 1.3, and 1.4. Data recordings were narrow-band analyzed, resulting in a total of 2115 narrow-band flyover plots. Noise data for each set of pressure ratios and for all repeat runs were then averaged and an SPL established for each microphone with and without the wing. The data were averaged over the nozzle pressure ratio range because there was considerable scatter in both shielded and unshielded noise data. Hence, these SPL's represent an intermediate pressure ratio condition between 1.1 and 1.4.

The Hartmann whistle was also operated during a series of "no-flow" runs with certain nozzles. (The only airflow from the nozzle was due to flow from the Hartmann whistle.) The tests encompassed both no-wing and wing-in-place runs. Noise data were again analyzed into narrow bands.

Noise level data with and without the wing in place were examined as a part of this contract effort for the following group of cases:

- All nozzles simulating the flyover configuration and located at one position with respect to the wing, X = 44 cm and Y = 18 cm

- Nozzle 11 simulating both the flyover and 25° sideline configurations for several nozzle locations

- Nozzle 11 with no flow simulating flyover for several nozzle locations

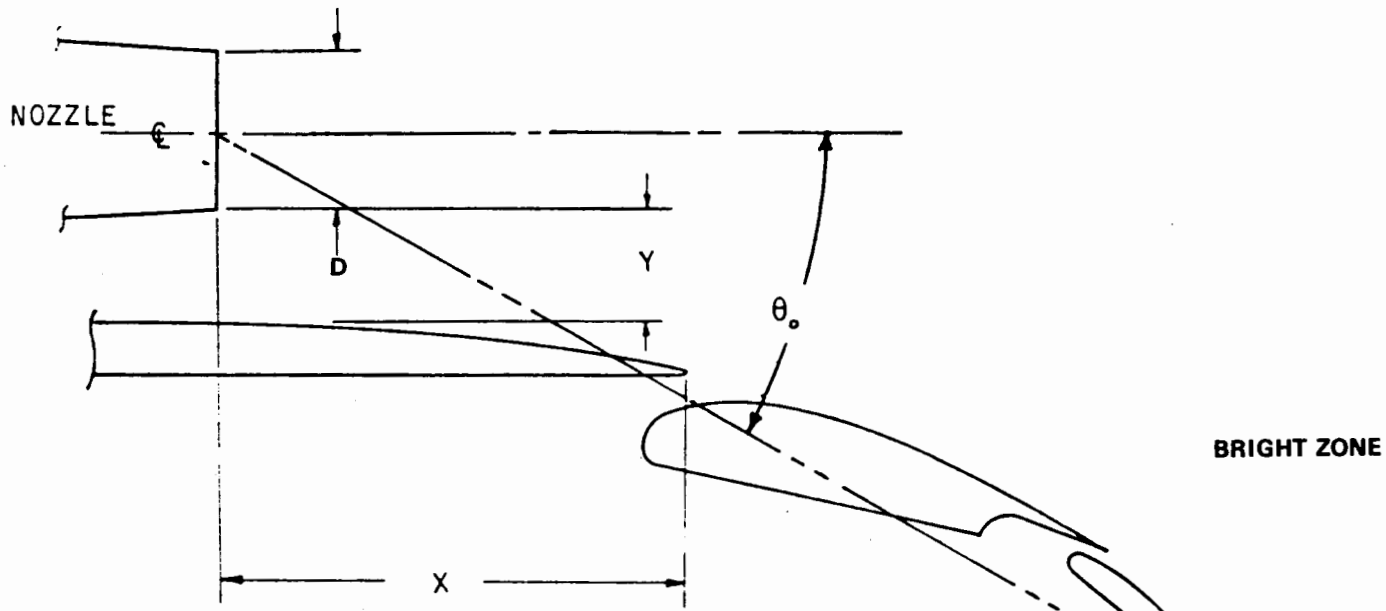

X cm	Y cm	θ_o Degrees
50	0	25
52	1.8	26
44	1.8	28
25	1.8	36

Figure 73.—Shadow Boundary Definitions for WIF Tests

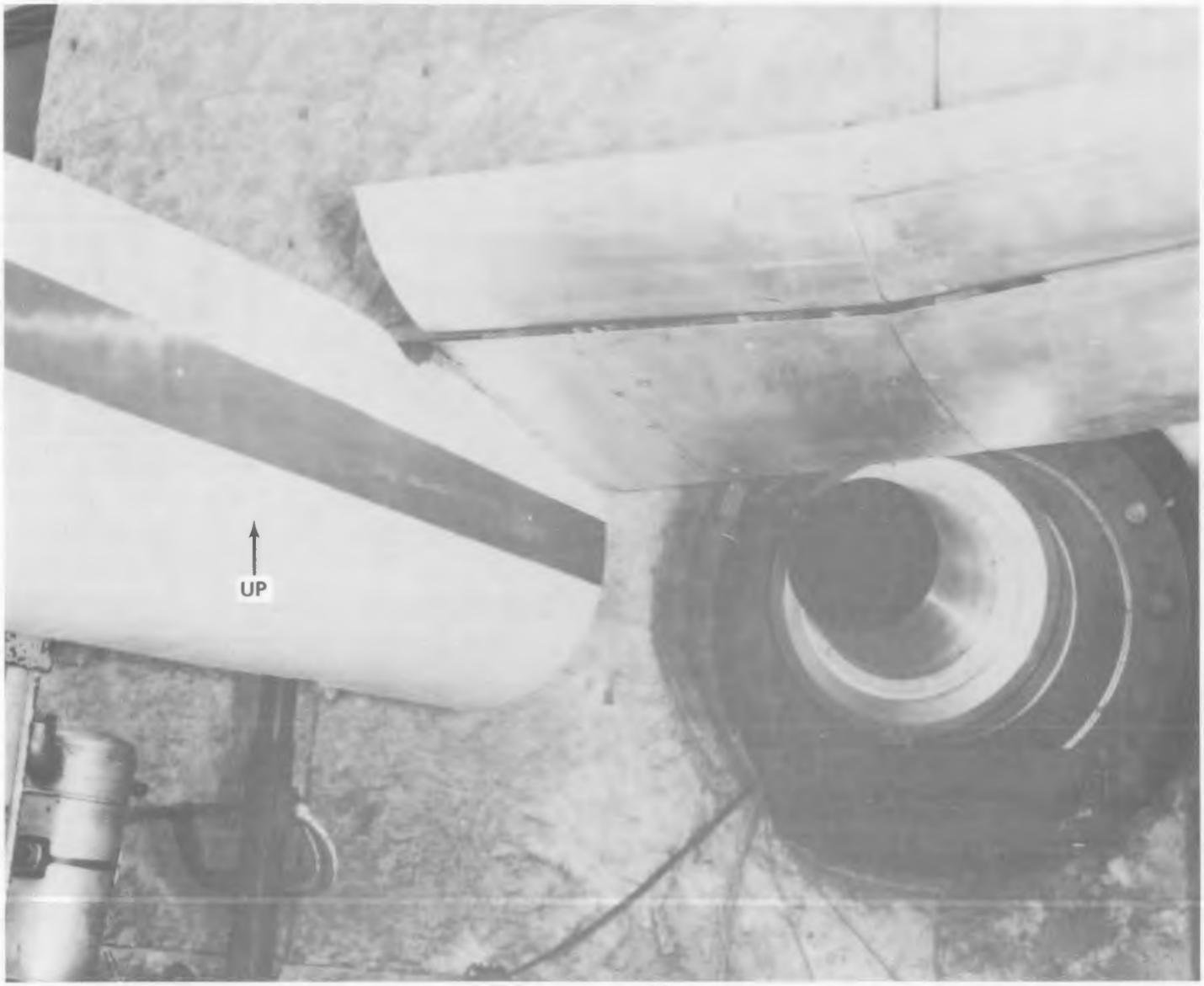

Figure 74.—Closeup View With Wing in "Flyover" Position

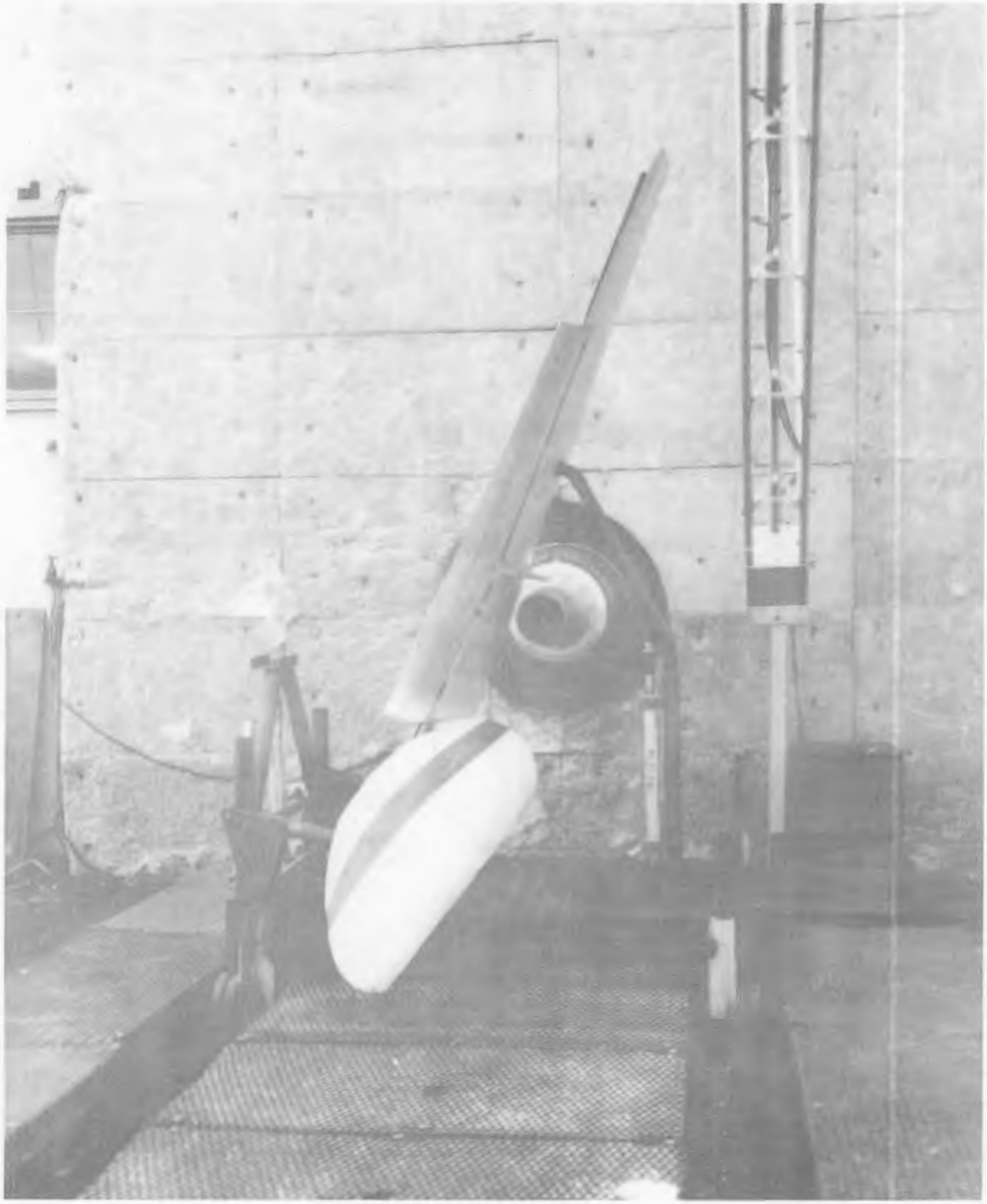

Figure 75.—Setup With Wing in "25° Sideline" Configuration

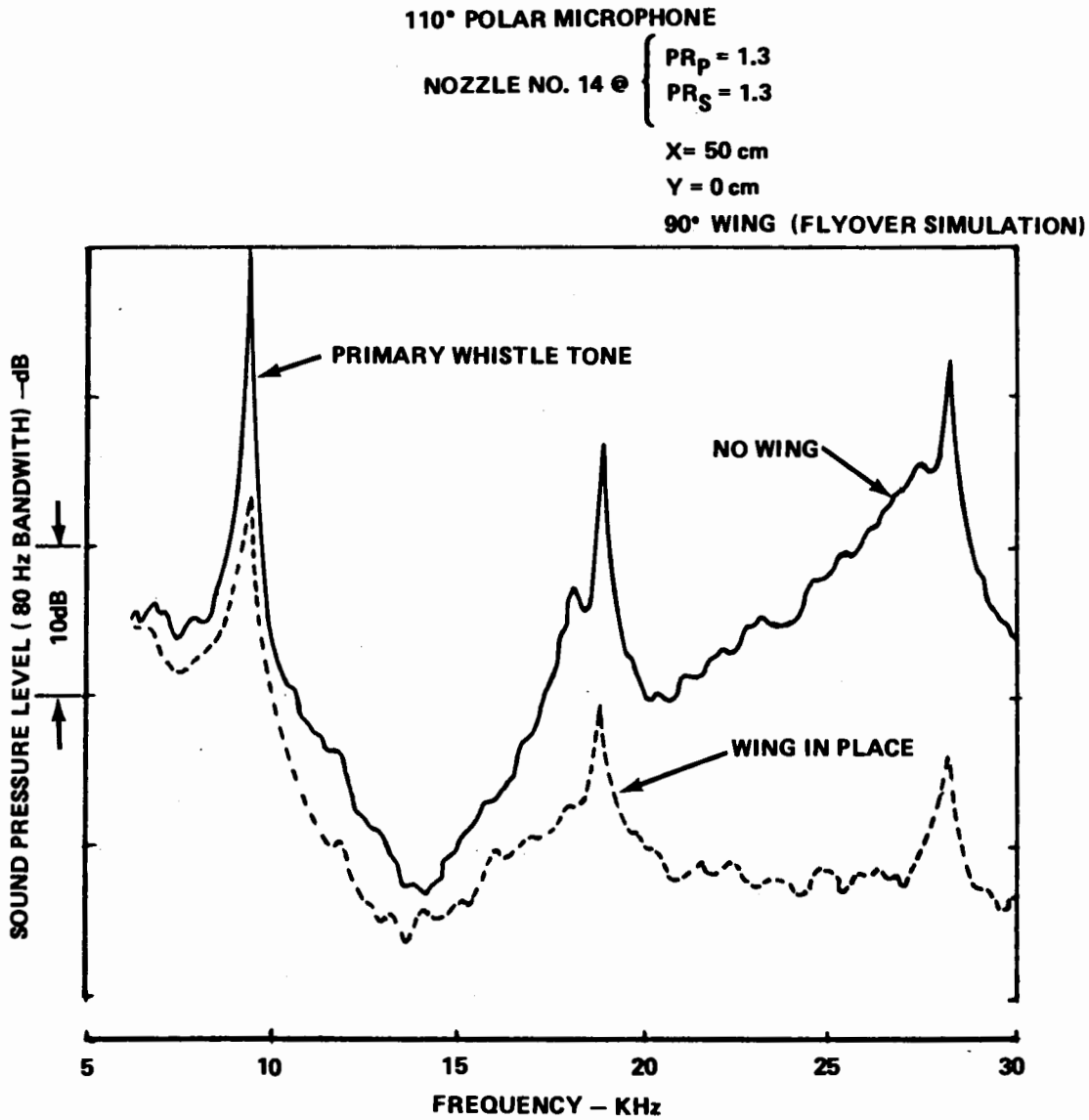

Figure 76.—Typical Narrowband Spectral Behavior of Data From WIF Test

Comparative polar noise level distributions for nozzles 8 through 14 are shown in figures 77, 78, and 79. Each figure shows results for a separate frequency–9.6, 19.3, and 29 kHz, respectively. In each case, the upper graph shows the shielded and unshielded tone noise from these nozzles, and the lower graph shows the shielding attenuation provided by the wing. The nozzle location was constant at X = 44 cm and Y = 1.8 cm.

A consistent trend cannot be identified that relates to differences in nozzle design. The nozzles show identical behavior within about 4 dB with the exception of the D-nozzle, which appears to produce somewhat more shielding attenuation at shallow angles. Generally, there is an increase in shielding attenuation with increasing tone frequency, which is consistent with theory discussed previously.

Figure 80 shows changes in the radiated polar distribution of tone noise with changes in nozzle-to-wing position for nozzle 11 for the flyover configuration at 9.6, 19.3, and 29.0 kHz. Shielding attenuation is seen to increase as the nozzle is moved further forward from the trailing edge of the wing (increasing X), as would be expected from simple theory.

Figure 81 shows corresponding polar distributions for nozzle 11 in the 25° sideline wing shield configuration. Again, shielding attenuation increases with increasing X and also with increasing tone frequency.

All the previous polar distributions of noise have been shown for thrusting flow from the nozzle. Corresponding no-flow distributions are shown for nozzle 11 for a flyover wing shield configuration in figure 82. Again, shielding attenuation increases with increasing tone frequency. Changes in X have a less obvious effect on shielding attenuation for the no-flow case than for the previous case with exhaust flow, i.e., figure 80.

A comparison of noise levels and shielding attenuations measured with and without flow is shown in figure 83. The comparison shows that both shielded and unshielded levels and shielding attenuation are similar through polar angles of 130°. Above this angle there is deviation. With flow, the unshielded noise is fairly directional, with peak levels at 130°. Without flow, noise levels from the nozzle are more omnidirectional, with a broad peak at 160°. Although the geometric shadow boundary angle is 152° as defined in figure 72, apparent shadow zone boundary angles shown in figure 83 are 145° and 155° for flow and no flow, respectively. Here, apparent shadow zone boundary is as defined in the theoretical discussion in section 2.2 on compact noise sources. That is, the apparent shadow zone boundary is defined as the point where 6 dB of shielding attenuation has been achieved as one passes from the bright zone into the shadow zone. This definition has been used in defining the apparent shadow zone boundaries shown in figure 83. Without flow, the apparent shadow zone boundary is further aft–near 155°–as opposed to about 145° with flow. In the deep shadow zone below 130° the shielding attenuations are nearly constant and identical, and shielded levels closely parallel the slope of the unshielded levels up to angle 130°. These observations suggest that levels in the shadow zone below 130° are reverberation (or reflection) controlled. Furthermore, the reflections appear to come from the fiberglass batts placed below the

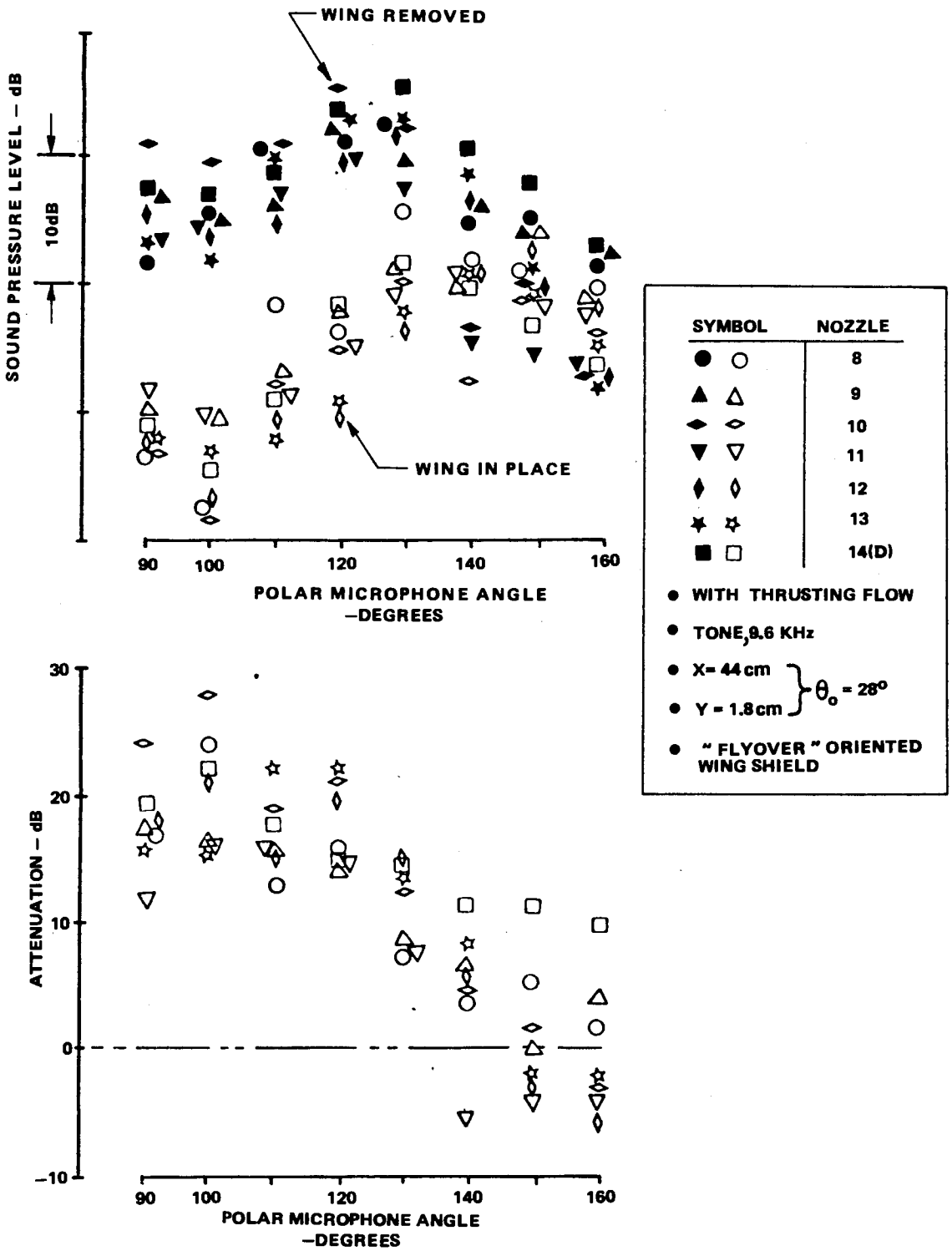

Figure 77.—Radiated Unshielded and Flyover Wing-Shielded 9.6-kHz Tone Noise From Nozzles 8-14

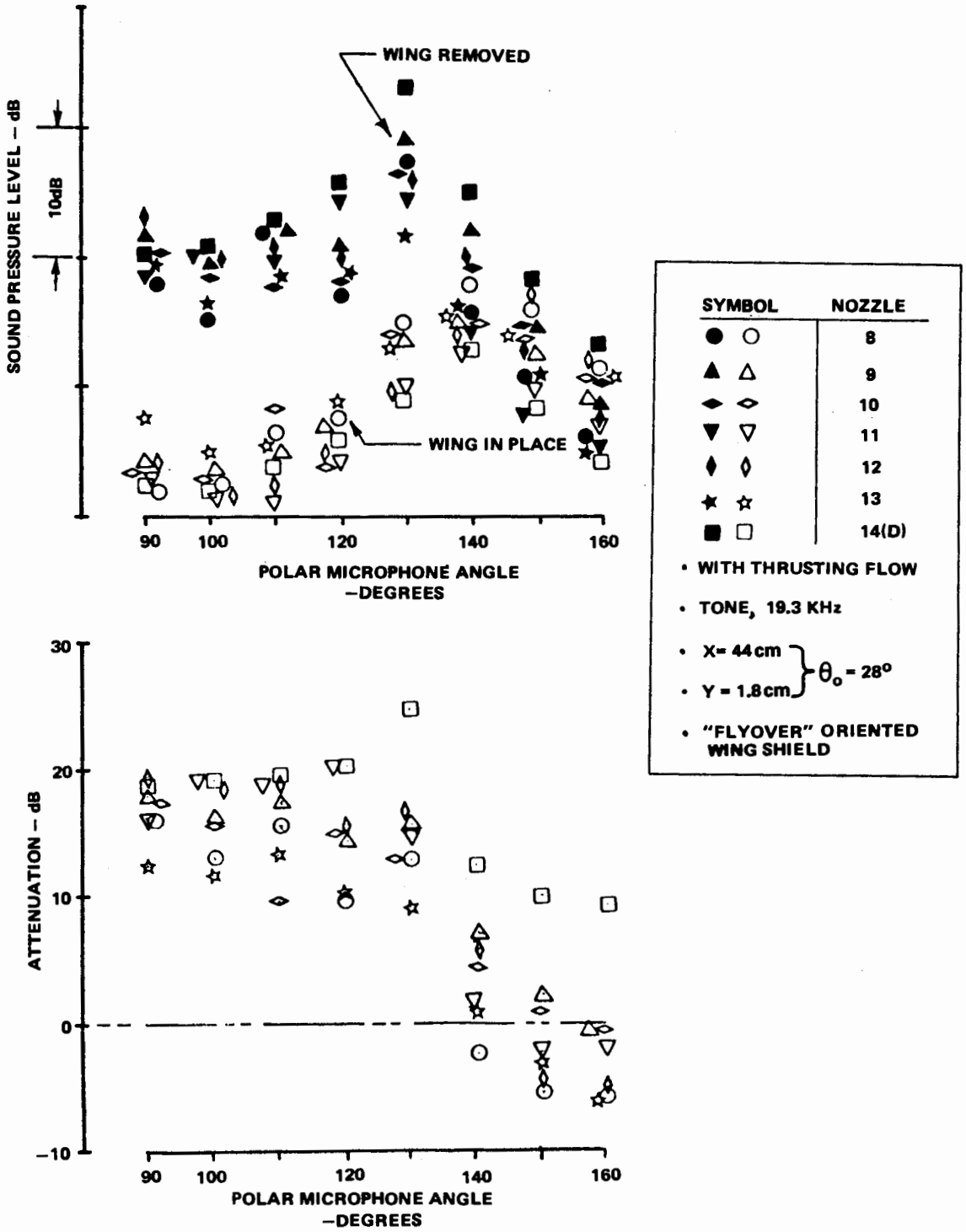

Figure 78.—Radiated Unshielded and Flyover Wing-Shielded 19.3-kHz Tone Noise From Nozzles 8-14

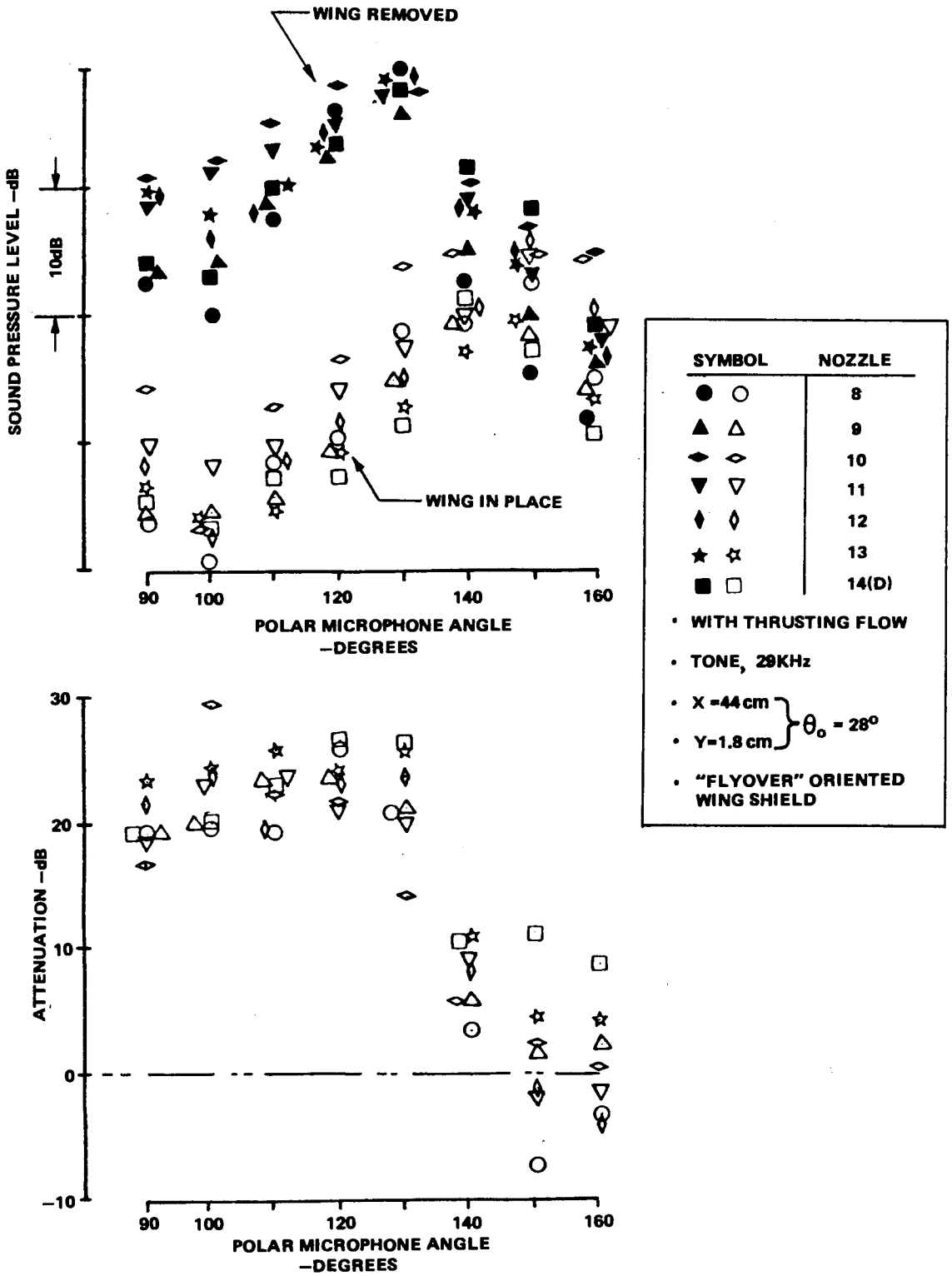

Figure 79.—Radiated Unshielded and Flyover Wing-Shielded 29-kHz Tone Noise From Nozzles 8-14

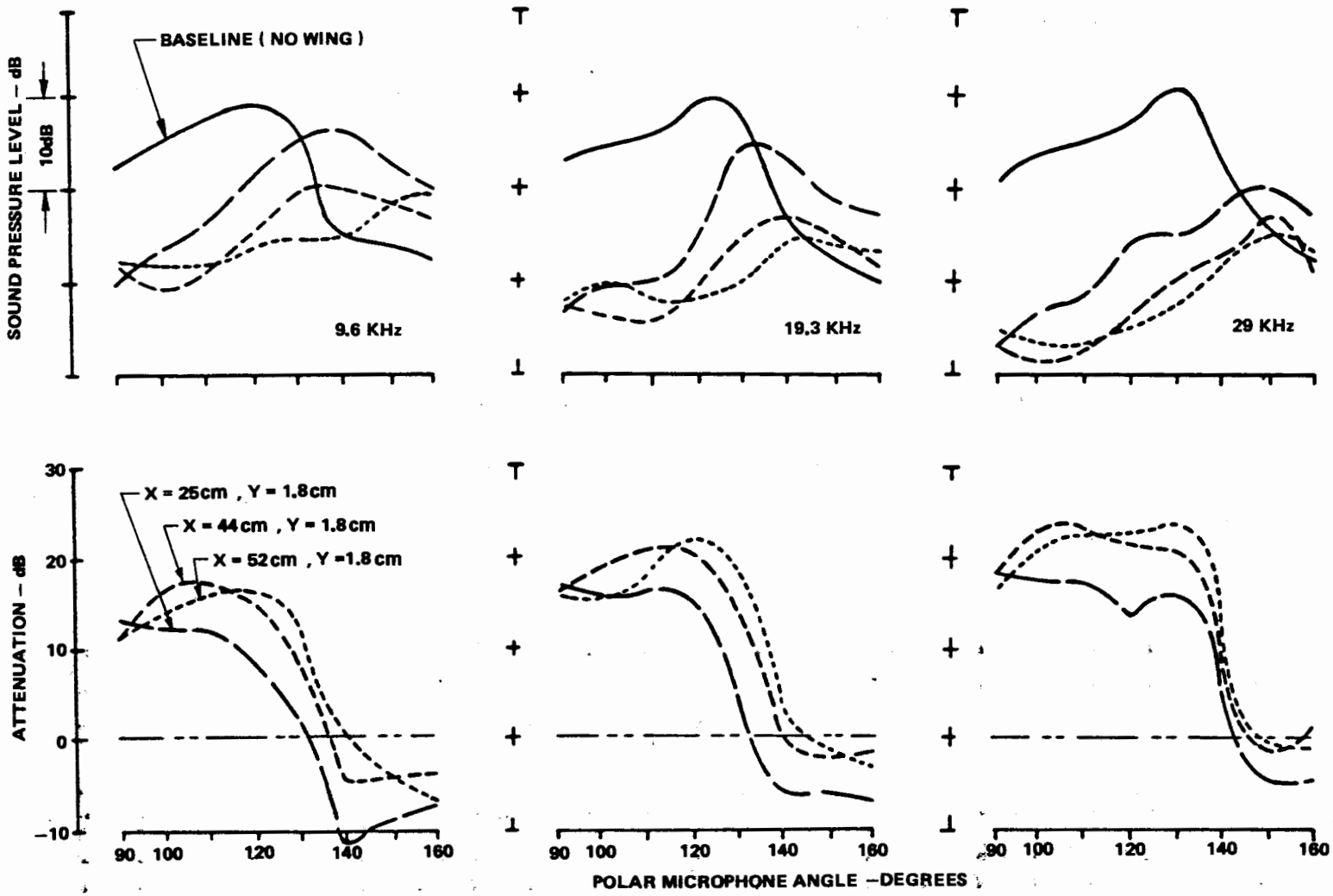

Figure 80.—Unshielded and Shielded Flyover Polar Distributions of Tone Noise From Nozzle 11 (With Thrusting Flow)

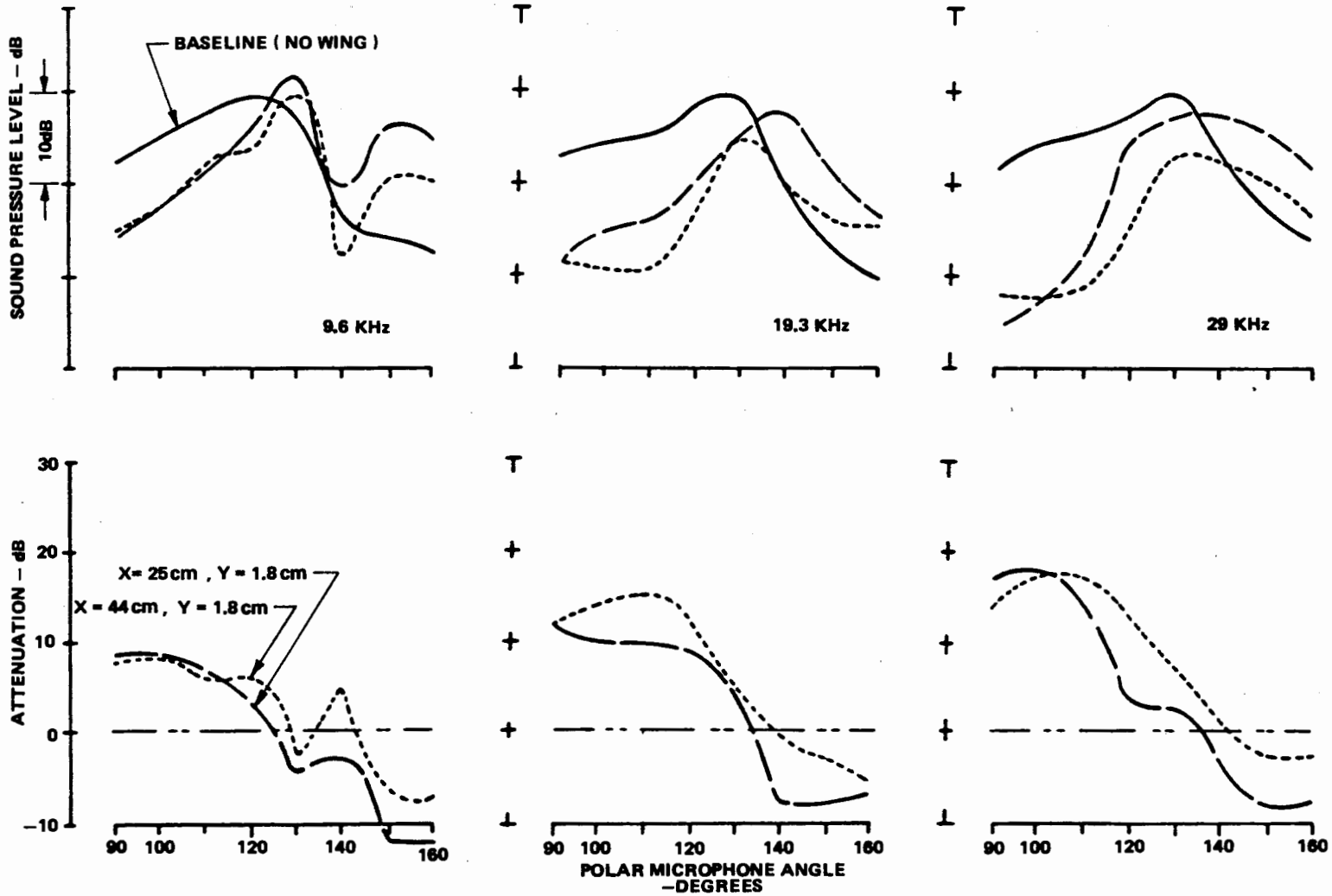

Figure 81.—Unshielded and Shielded 25° Sideline Wing-Shield Configuration Polar Distributions of Tone Noise From Nozzle 11 (With Thrusting Flow)

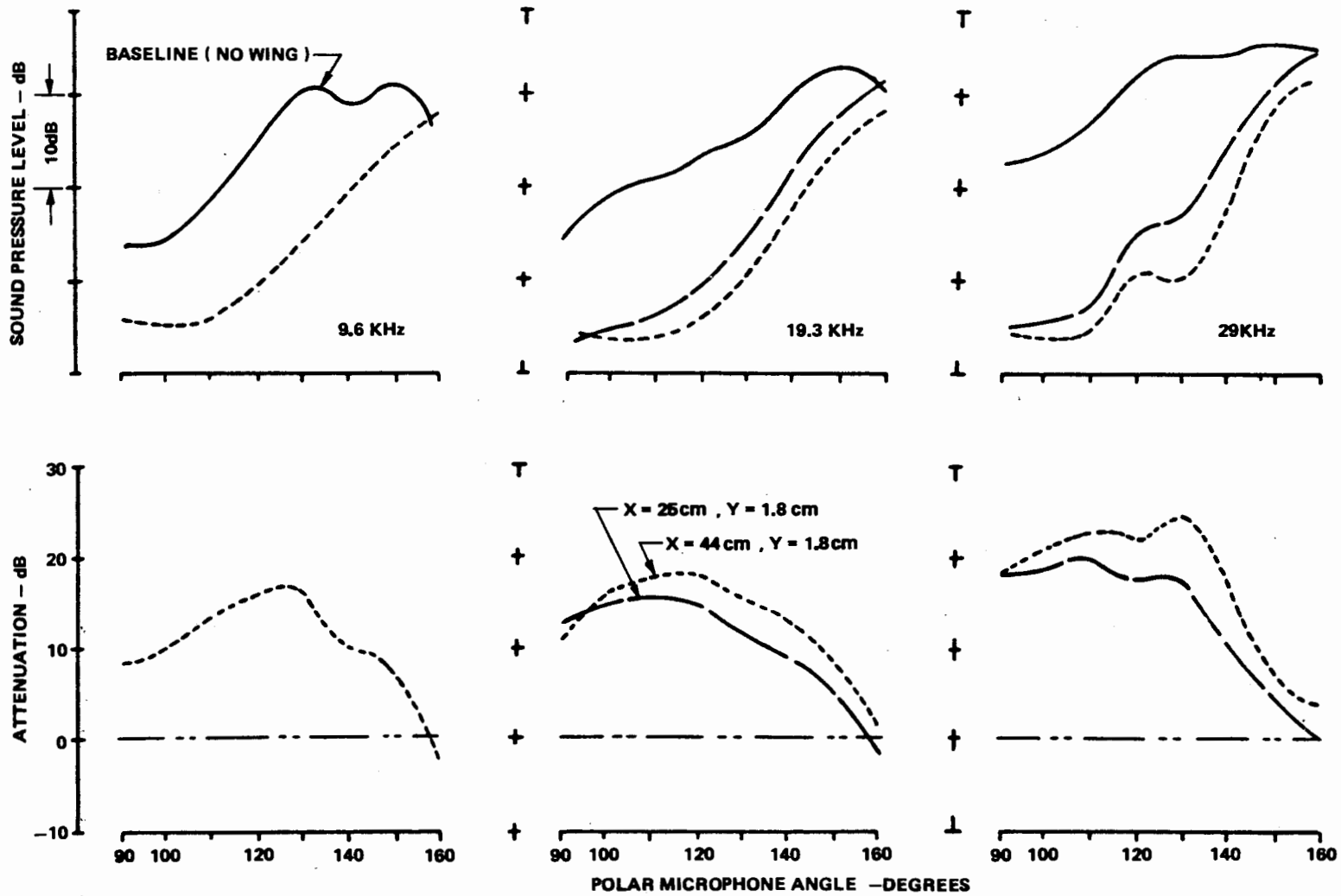

Figure 82.—Unshielded and Shielded Flyover Polar Distributions of Tone Noise From Nozzle 11 (Without Thrusting Flow)

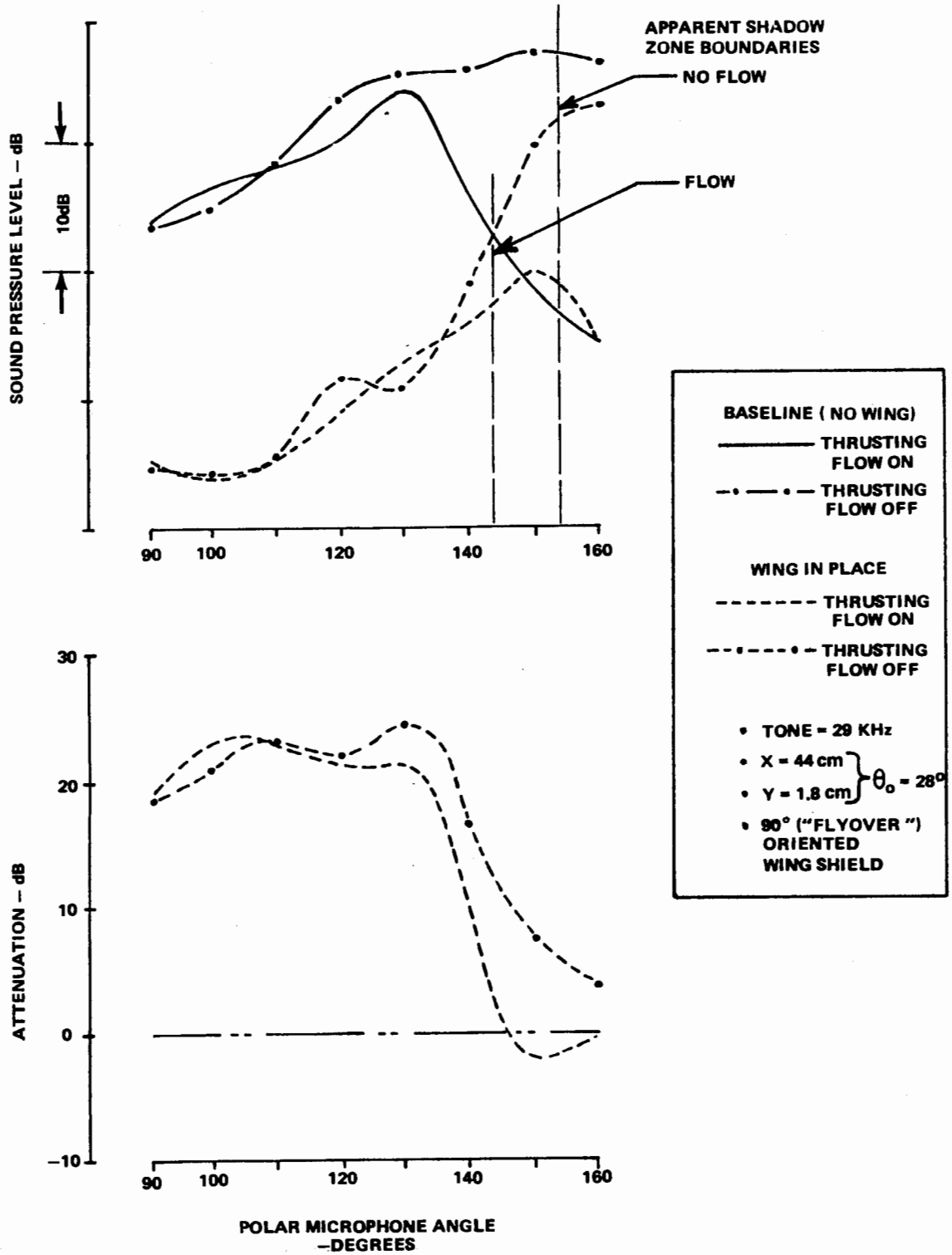

Figure 83.—Comparison of Tone Noise Polar Distribution for Nozzle 11 (With and Without Thrusting Flow)

nozzle exhaust flow region on the floor of the WIF test area. Discussions with test personnel reveal that the wire-mesh-enclosed fiberglass battens were about 95% absorptive. Reflections from these pads would be sufficient to cause the constant and identical shielding attenuations noted above.

2.3.1.4 Full-Scale JT9D Tulalip Shielding Tests

The purpose of this test was to investigate and verify predictions based on earlier model tests for the shielding effect of a wing on the far-field discharge fan, turbine, and core noise of a large, high-bypass-ratio turbofan engine. A Pratt & Whitney JT9D equipped with a coplanar exhaust nozzle system and an extensively treated inlet nozzle system was used. Figure 84 shows this engine system mounted on the test stand at the Boeing Tulalip Test Site. The extensive inlet treatment was required to suppress inlet fan noise components sufficiently so they would not interfere with assessment of wing shielding of the discharge fan noise. Figures 85 and 86 show the setup with the wing in the flyover (or 90^0) position. Figure 87 shows the dimensions of the wing and pertinent engine-to-wing parameters. Figure 88 shows the overall test arena, including the 44-m polar array of 5-m-high microphones. Figures 89a and 89b show the wing in the flyover (90^0 wing) and sideline (25^0 wing) configurations, respectively.

The various views of the test setup suggest that the test stand structure and associated hardware behind (particularly the blockhouse) and adjacent to it provided a fair potential for scattering energy to the polar array of receiving microphones. The wing in the 90^0 position would tend to reflect additional energy toward the test stand, thus enhancing the test stand's scattering potential. Also, the ground itself appears capable of diffusely scattering energy and provides yet another potential means of directing energy toward the receiving microphones other than via diffraction about the wing. Such flanking radiation via reflection off the test stand, blockhouse, etc., could be 20 dB below direct radiation (in absence of the wing). It would be hard to imagine it being much more than, say, 25 dB below direct radiation. Unfortunately, no specific data are available to directly verify this conjecture.

Table 6 shows the range of conditions examined during this test program. Each run consisted of a set of typically five to eight subruns covering engine power levels from idle (corresponding to a fan speed of ~ 1200 RPM) to full power (corresponding to a fan speed of ~ 3400 RPM). The range of the primary turbine tones was 3000 to 6200 Hz, and the range of the primary fan tone was about 1000 to 2500 Hz. The unshielded and shielded noise levels of these primary fan and turbine tones were of most interest.

Signals corresponding to microphones located 44 m from the engine nozzle at 40^0, 50^0, . . . , 150^0 and 160^0 from the engine inlet axis were processed into 20-Hz bandwidth sound pressure level (SPL) spectra (see fig. 90). The spectral "spikes" correspond to fan and turbine tones. These tones were then identified and their levels tracked as a function of run configuration and engine speed.

Typical unshielded and shielded polar distributions of T6 turbine tone noise are shown in figure 91. An arbitrary SPL scale is used because polar distributions of wing shielding attenuation are the most important. Furthermore, shielding attenuation can

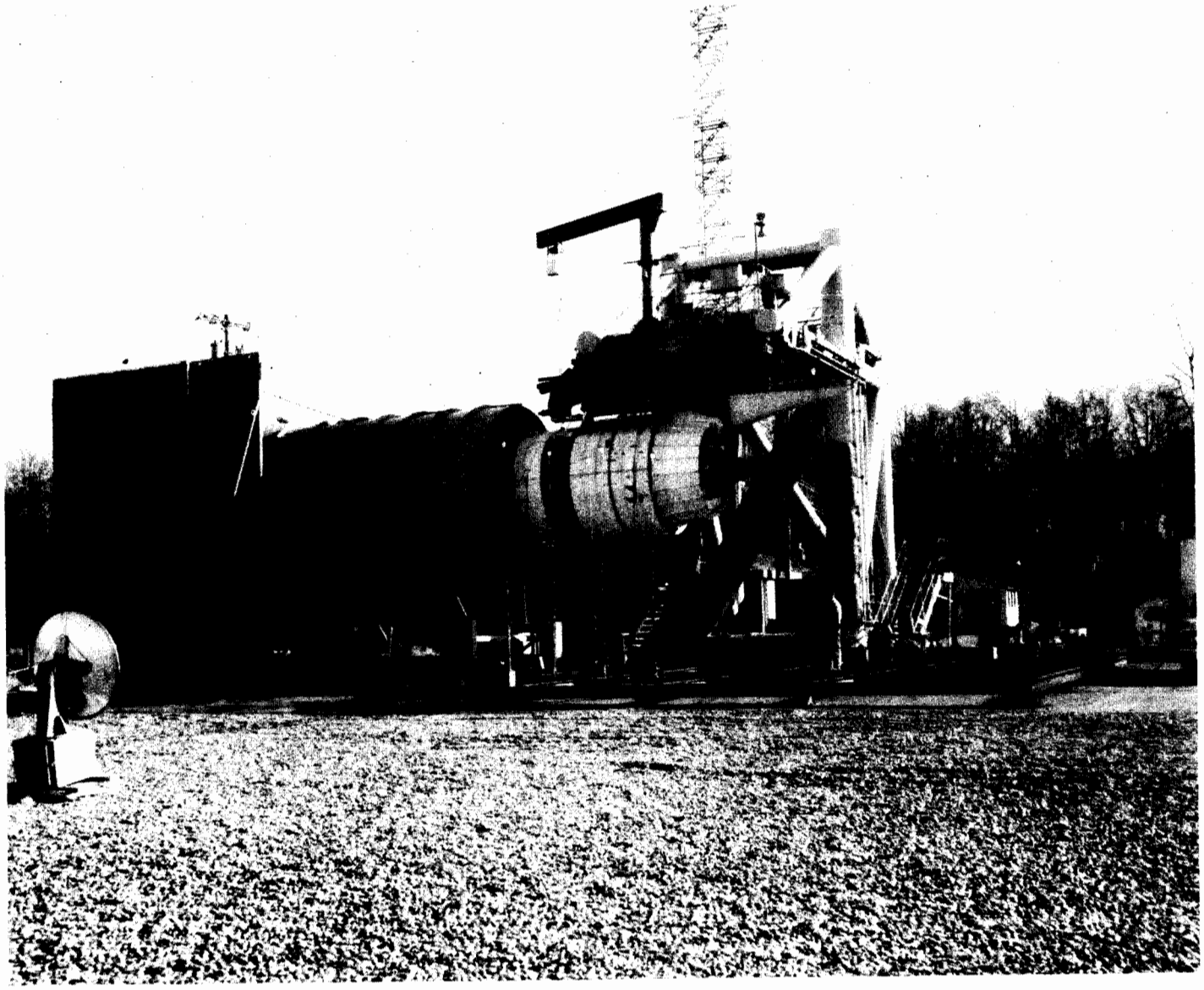

Figure 84.—Mounted Engine With Inlet Tube and Barriers—Full-Scale JT9D Tulalip Shielding Tests

Figure 85.—View of Inlet Tube and Engine From Behind 90° Wing—Full-Scale JT9D Tulalip Shielding Tests

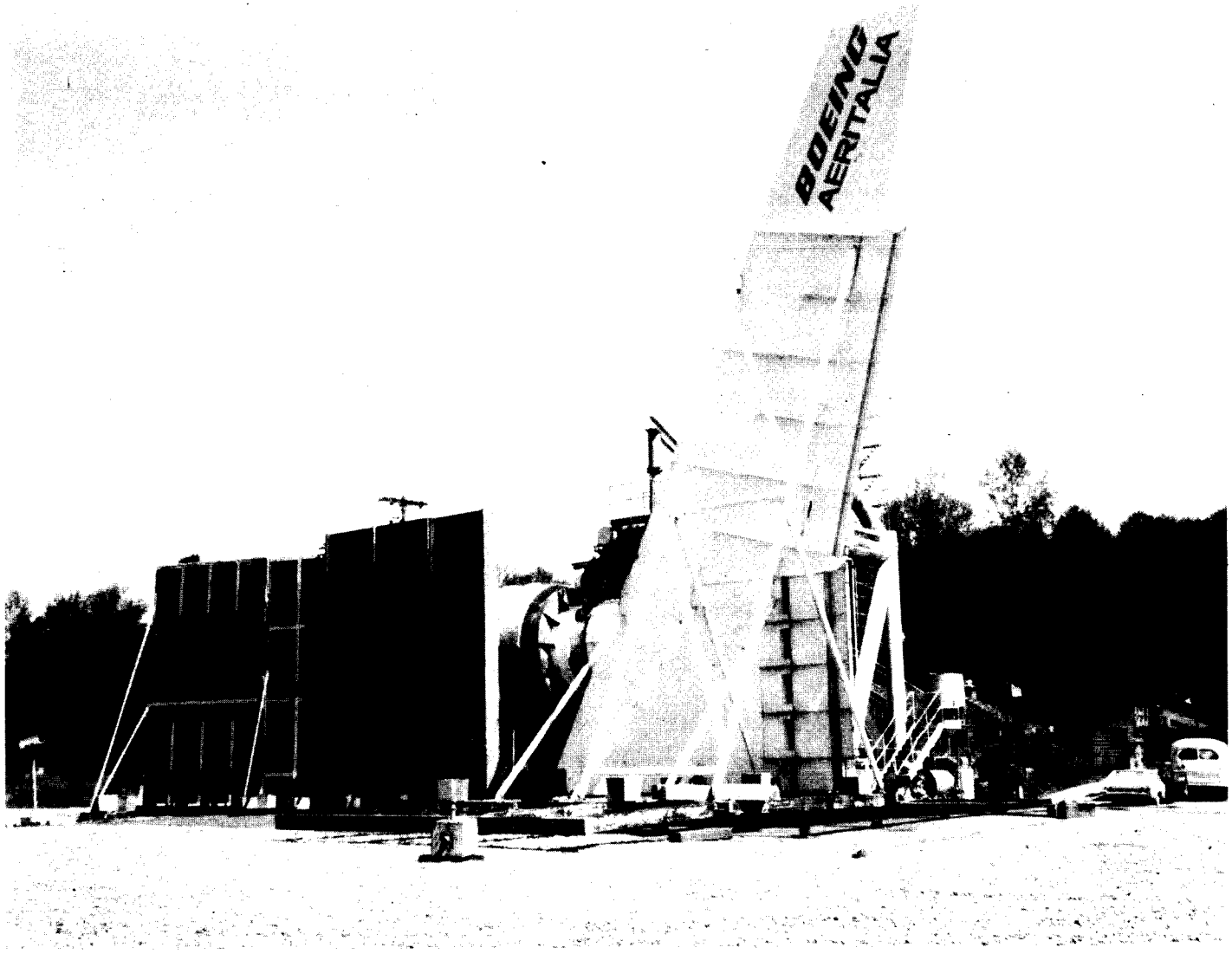

Figure 86.—Flyover (90° Wing) Configuration Setup—Full-Scale JT9D Tulalip Shielding Tests

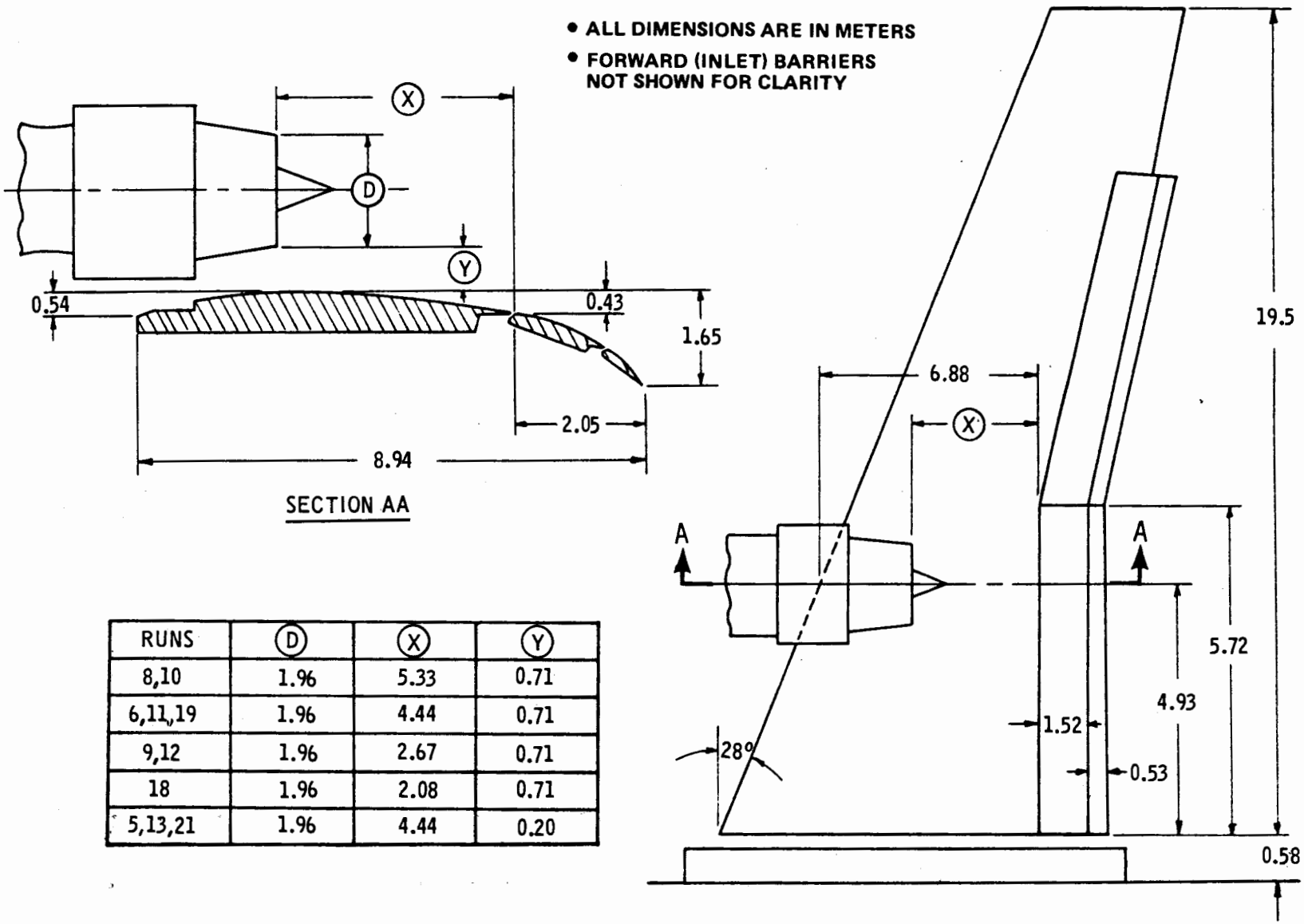

RUNS	D	X	Y
8,10	1.96	5.33	0.71
6,11,19	1.96	4.44	0.71
9,12	1.96	2.67	0.71
18	1.96	2.08	0.71
5,13,21	1.96	4.44	0.20

Figure 87.—Wing/Engine Geometry for Tulalip Shielding Tests

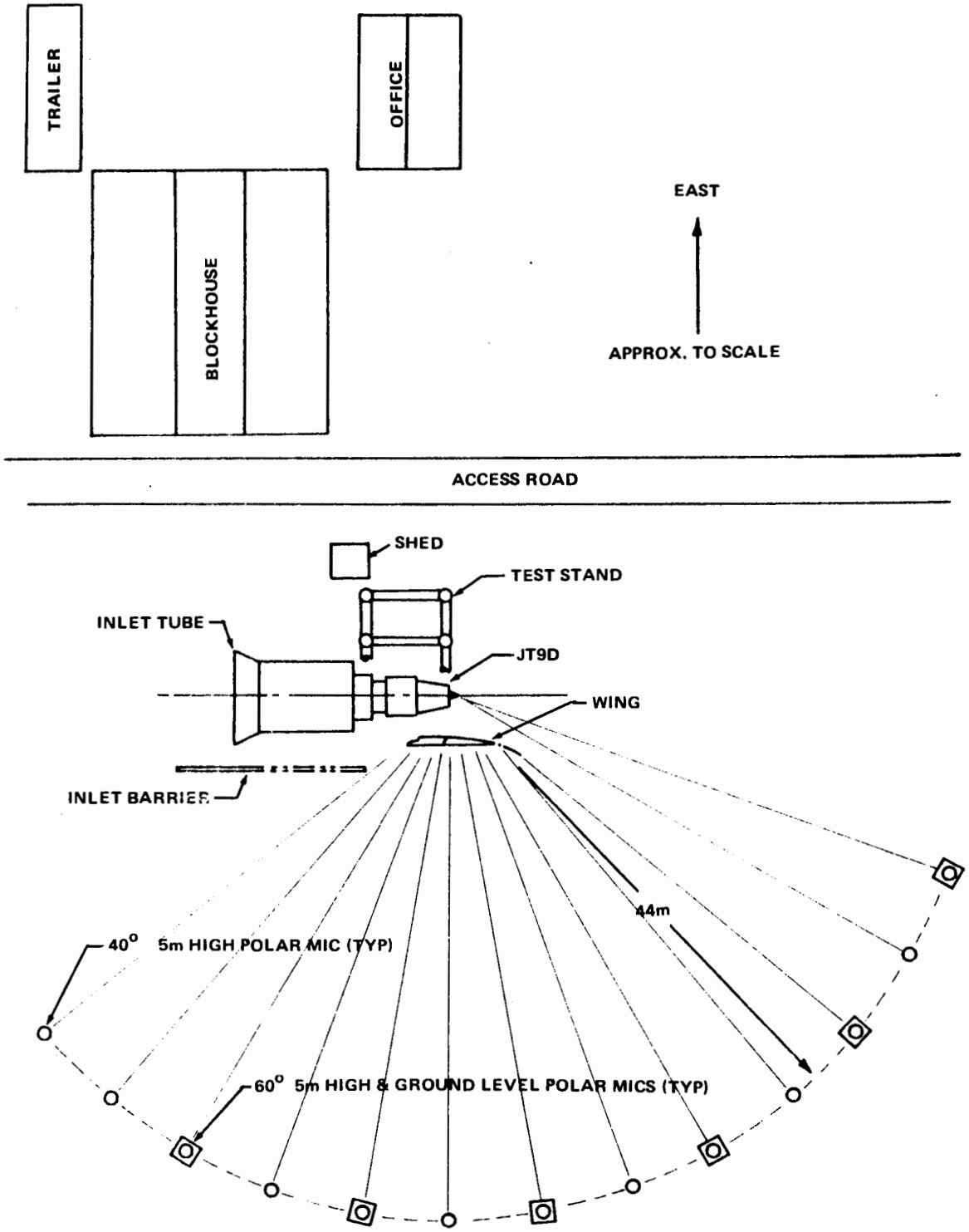

Figure 88.—Overall Arrangement for Tulalip Test Setup

Figure 89.—Tulalip Shielding Test Wing Configuration

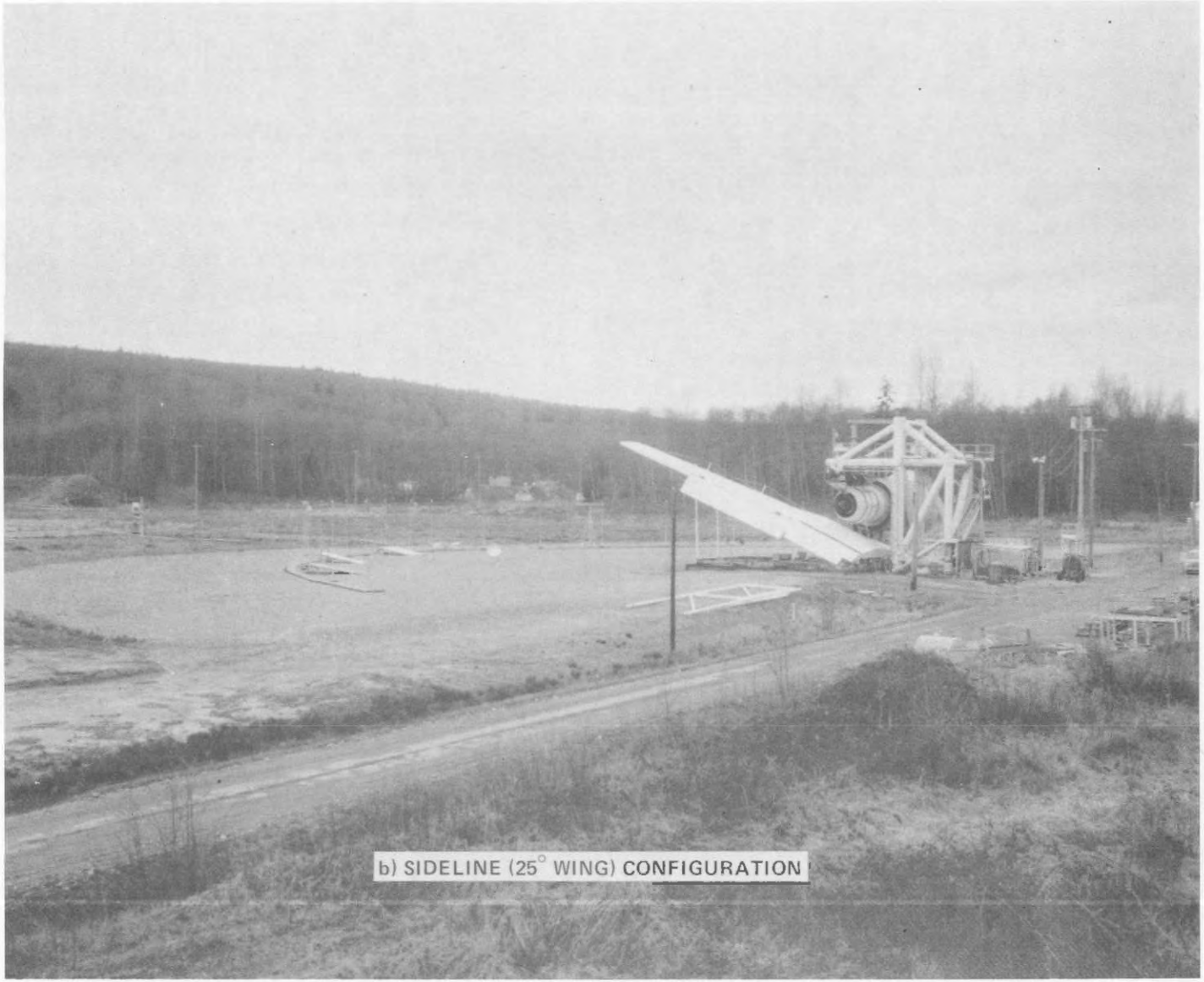

Figure 89.—(Concluded)

Table 6.—Typical JT9D Tulalip Test Conditions

RUN	X/D	Y/D	WING	EFFECT	TREATMENT
BASELINE			NONE	CORE/TURBINE NOISE WING SHIELDING	LINED INLET TUBE + 8m FORWARD BARRIER + LINED FAN DUCT
5	2.3	0.10	90°		
6	2.3	0.36			
8	2.7	0.36			
9	1.4	0.36			
13	2.3	0.10	25°		
11	2.3	0.36			
10	2.7	0.36			
12	1.4	0.36			
BASELINE			NONE	CORE/AFT FAN NOISE WING SHIELDING	LINED INLET TUBE + 8m FORWARD BARRIER + HARDWALL FAN DUCT
21	2.3	0.10	90°		
19	2.3	0.36			
18	1.1	0.36			

NOTE: D= 1.96m

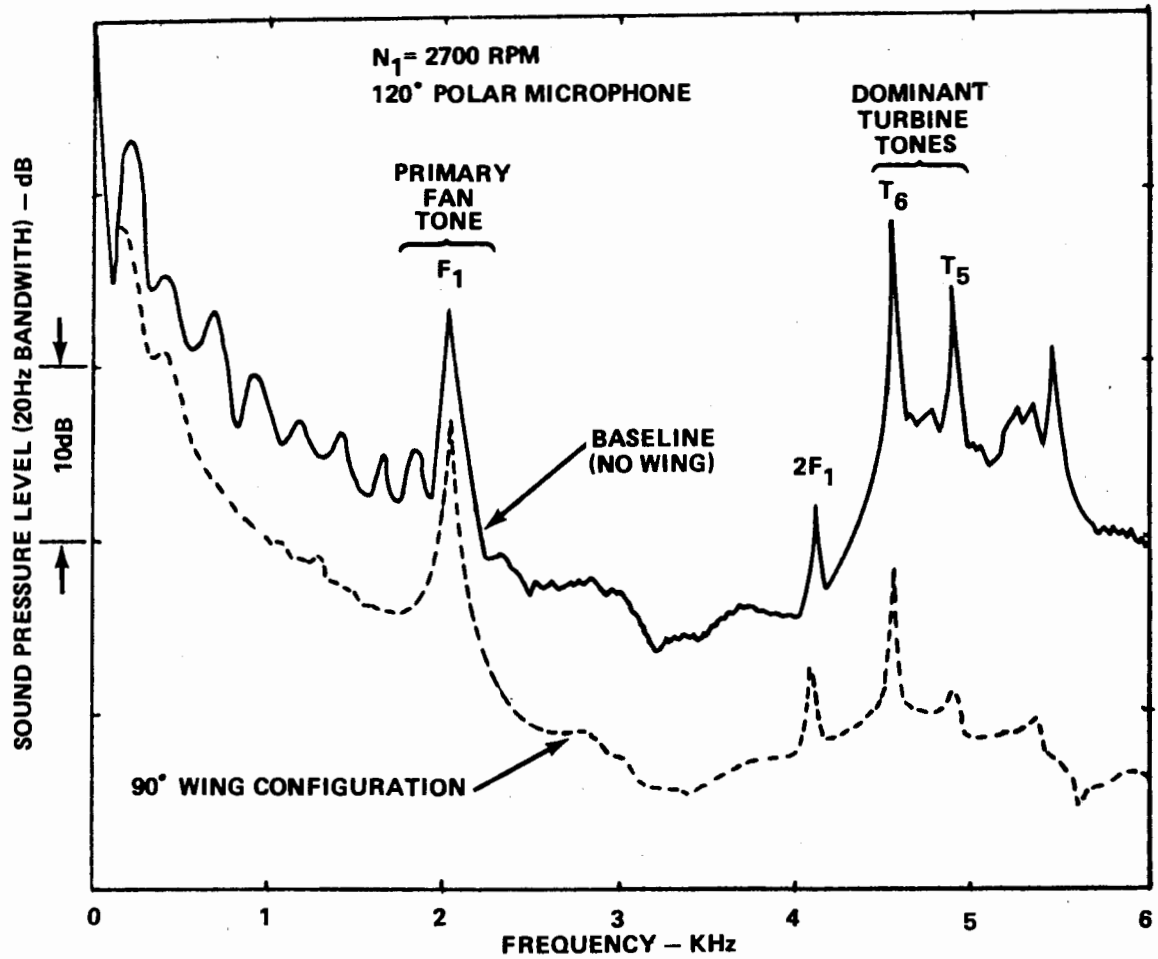

Figure 90.—Typical Narrowband Spectra From JT9D Tulalip Shielding Test

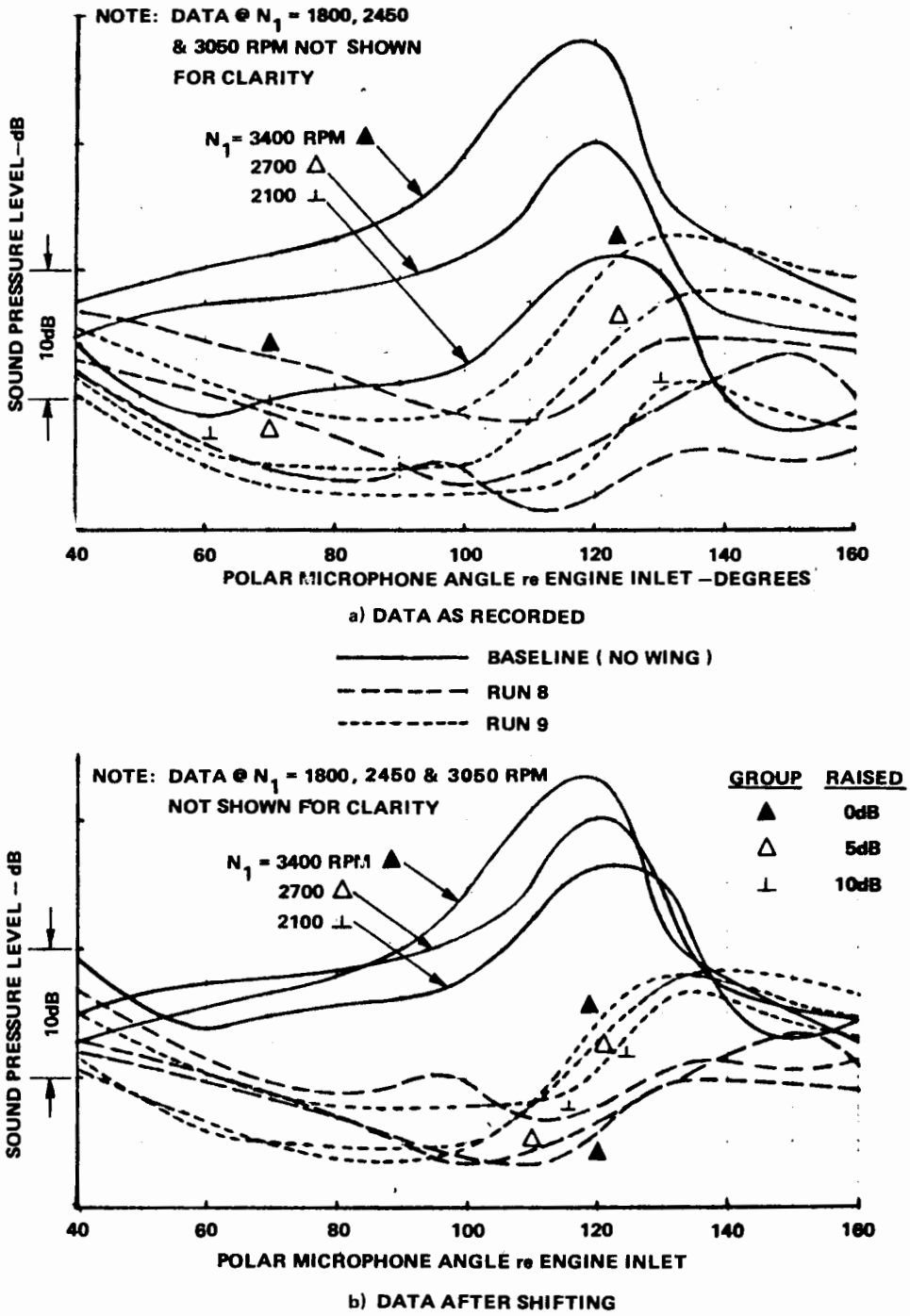

Figure 91.—Example of Recorded and Shifted Turbine (T6) Tone Data for 90° Wing Configurations

be more effectively displayed if corresponding sets of shielded and unshielded curves are shifted in level so that the average levels of all unshielded curves are equal in the sector from 130° to 140°. Such shifted curve sets are shown in the lower half of figure 91. The only variable for these curves is engine speed and, with it, tone frequency. No consistent trend with frequency can be identified in the curves.

A lack of frequency dependence, in fact, was found in the discrete tone data for all the runs listed in table 6. Hence, a mean curve corresponding to a mean frequency was developed for each run configuration in table 6. These mean frequency curves are shown in figures 92, 93, and 94. The extent of the data scatter is listed in each figure.

The following general trends are deduced from these various curves.

- To first order, the unshielded mean discharge fan and turbine tones have similar directivity, with the turbine tone being slightly more peaked.

- The effect of the wing in the flyover position on discharge fan and turbine tone noise is very nearly the same. As the engine nozzle is moved progressively further forward of the wing trailing edge and closer to the wing leading edge, shielding at high angles is increased, as would be expected from simple shielding theory.

- For the 25° (sideline) wing , data was obtained only for the turbine tones. Again as expected from simple theory, shielding at low angles is decreased while shielding at higher angles is increased as the engine nozzle is moved further forward of the wing trailing edge.

Rather interestingly, the peak shielding obtained for this 25° configuration is only very slightly less than that obtained for the 90° (flyover) wing configuration. As expected, the angular width of the shielding zone for the 25° wing is somewhat less than for the 90° wing.

A part of the Tulalip test program was also aimed at assessing wing shielding of core noise. For the JT9D, core noise is important in the 100- to 600-Hz frequency range at approach-level power settings. Jet noise tends to place an upper bound on shielding in this frequency range and becomes increasingly dominant as the power setting is increased. Shielding of true core noise can be measured only under conditions of low jet noise, hence, low power settings.

Broadband noise data for this purpose was recorded with a 46-m polar array of ground-level microphones. Attention was focused on the 125-, 250-, and 500-Hz 1/3-octave bands. Typical results for the 500-Hz band are shown in figure 95. The unshielded directivity of the noise in the three bands was similar over an N_1 speed range of 1200 to 3300 RPM and is summarized in figure 96. Directivities for speeds between these limits fall proportionately between the two curves.

Noise reductions produced by the three wing configurations (runs 18, 19, and 21) are shown in figure 97. In all cases the attenuations increase with increasing frequency and decreasing N_1 down to about 1500 RPM. Below this N_1, attenuation is essentially

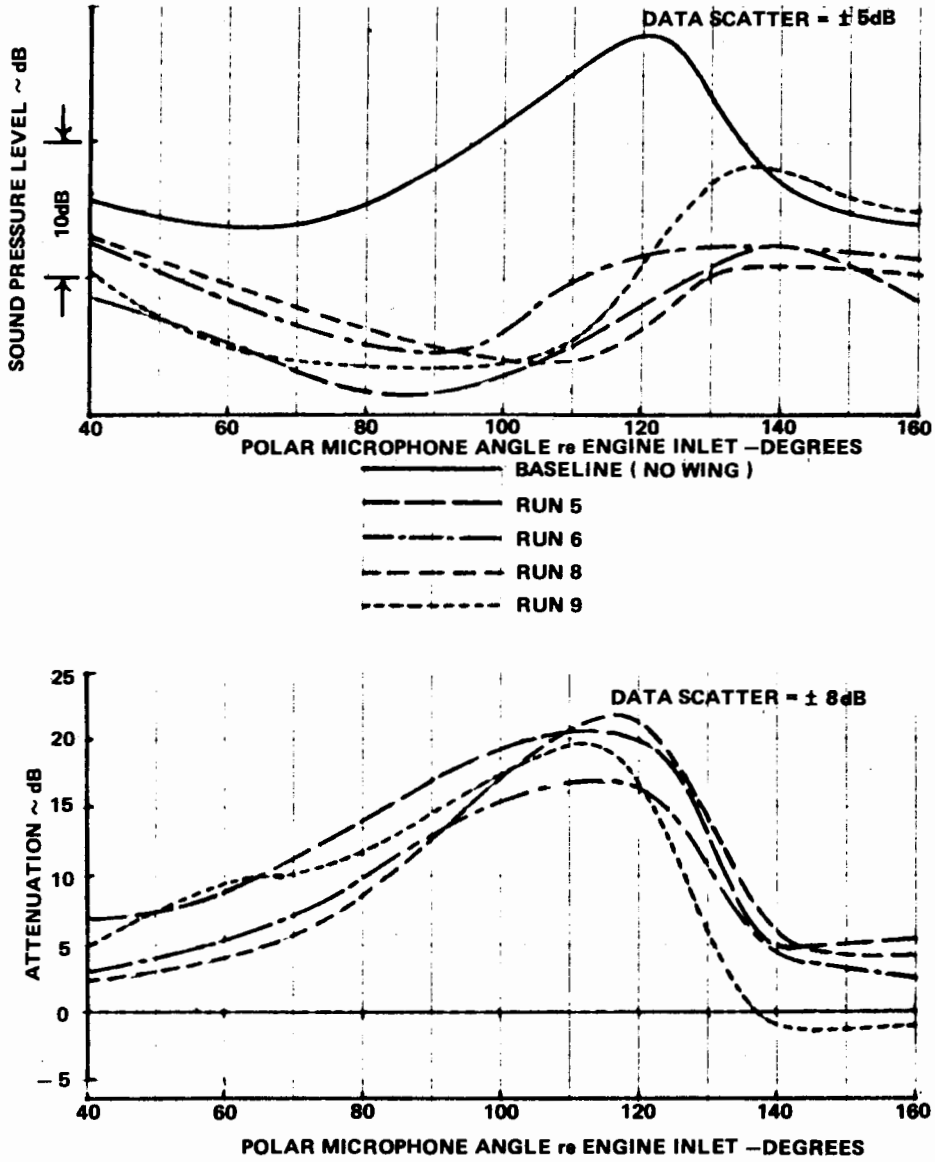

Figure 92.—Full-Scale JT9D Tulalip Shielding Test Results: Mean Shielding Effect of 90° Wing on Turbine Tone at Mean Frequency of 4.60 kHz

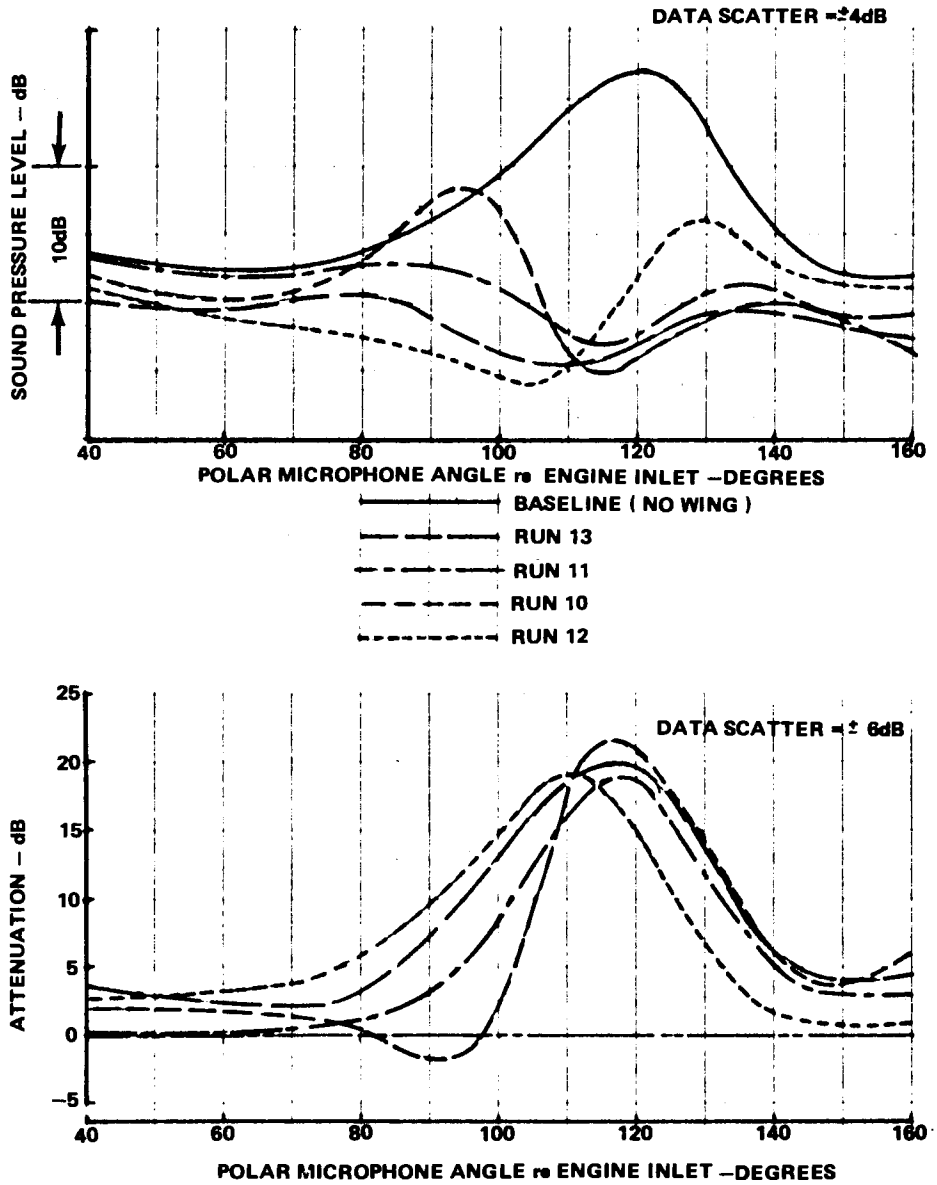

Figure 93.—Full-Scale JT9D Tulalip Shielding Test Results: Mean Shielding Effect of 25° Wing on Turbine Tone at Mean Frequency of 4.60 kHz

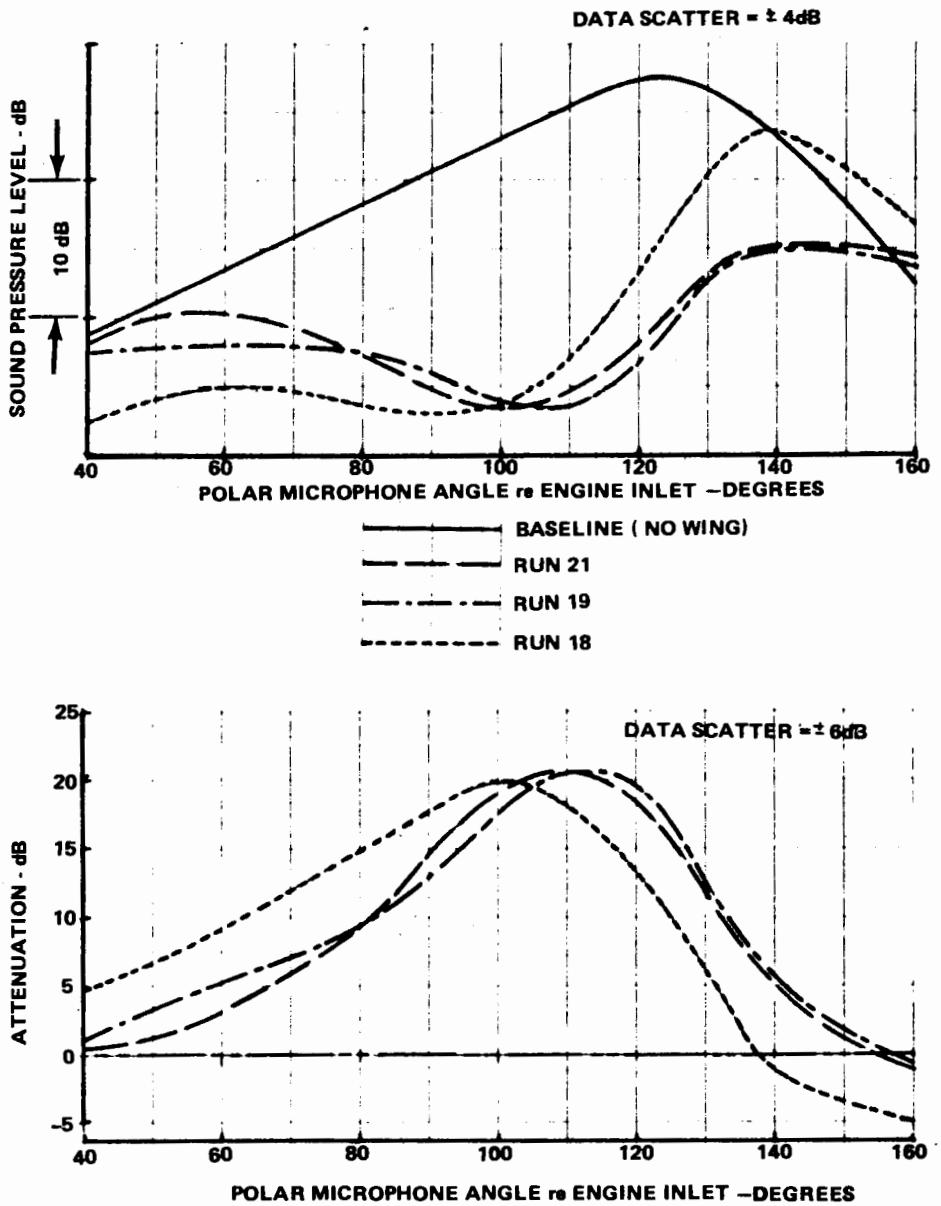

Figure 94.—Full-Scale JT9D Tulalip Shielding Test Results: Mean Shielding Effect of 90° Wing on Discharge Fan Tone at Mean Frequency of 1.66 kHz

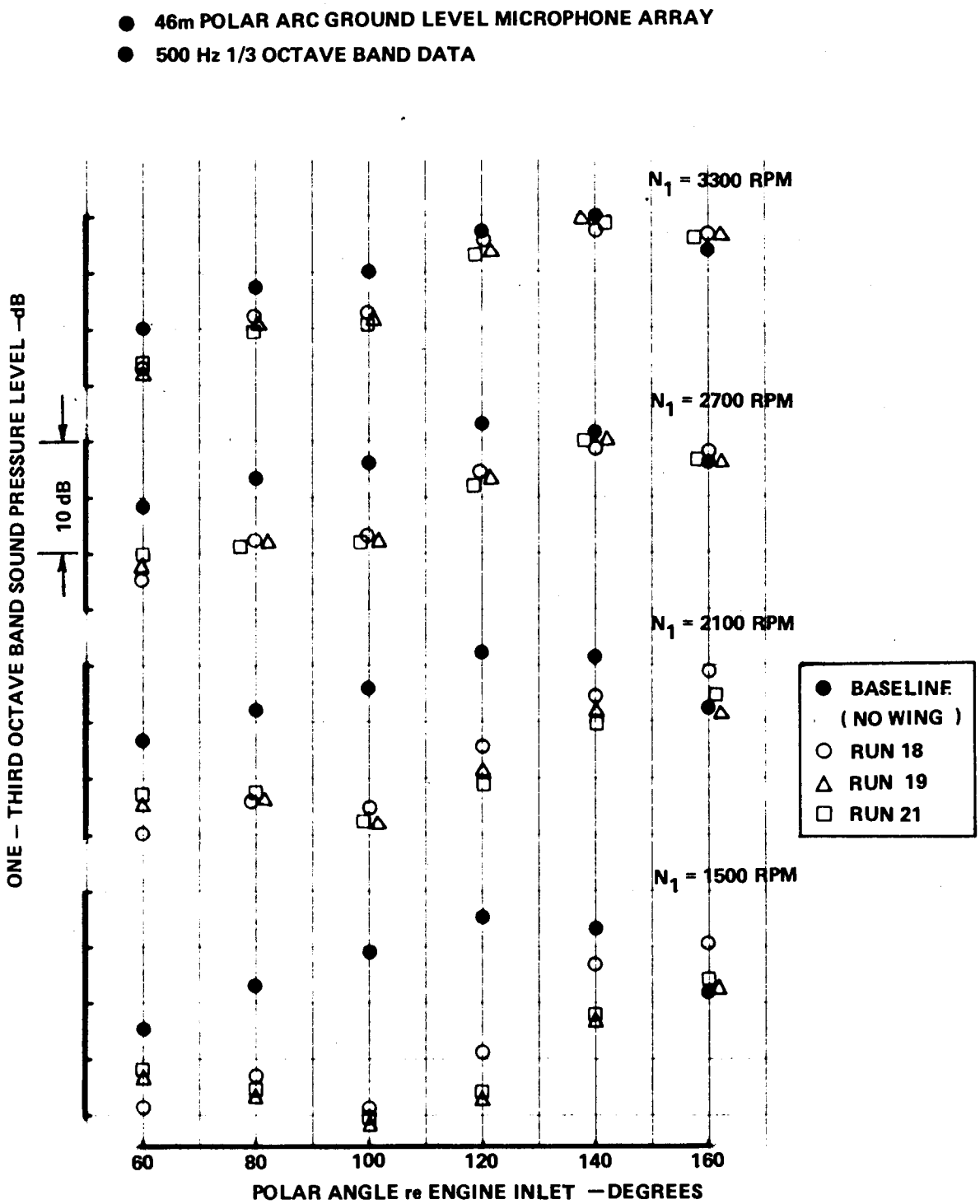

Figure 95.—Typical Full-Scale JT9D Tulalip Test Results: Broadband Core and Jet Noise

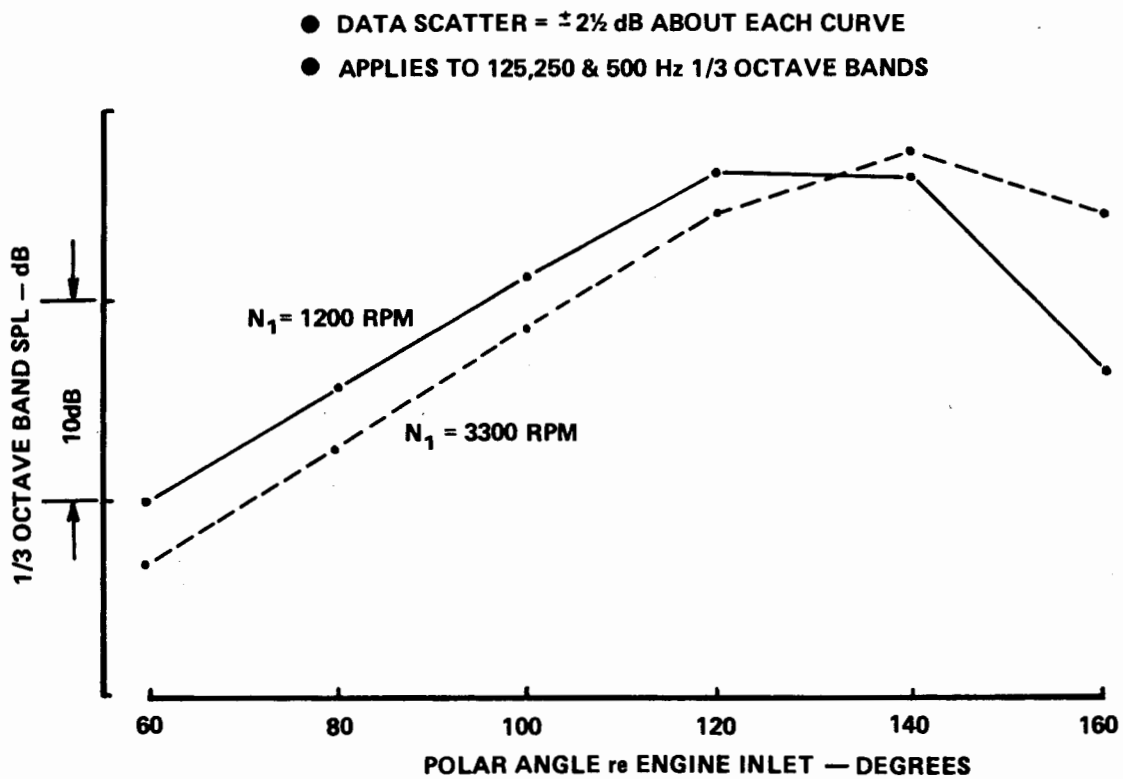

Figure 96.—Measured Average Baseline (No Wing) Directivity for Tulalip Shielding Tests

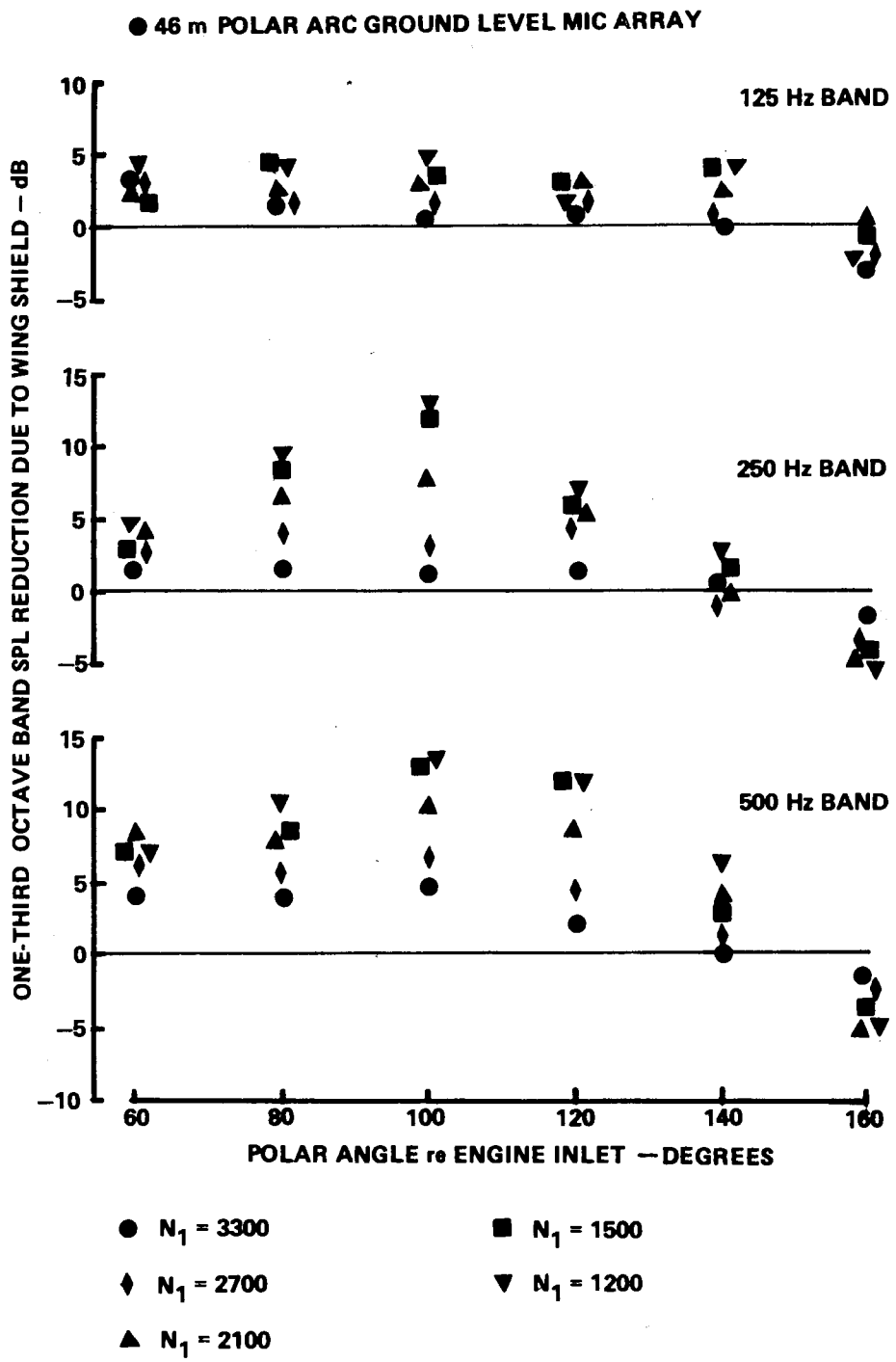

a) RUN 18

Figure 97.—Full-Scale JT9D Tulalip Shielding Test Results: Shielding Attenuation of Broadband Engine Exhaust Noise

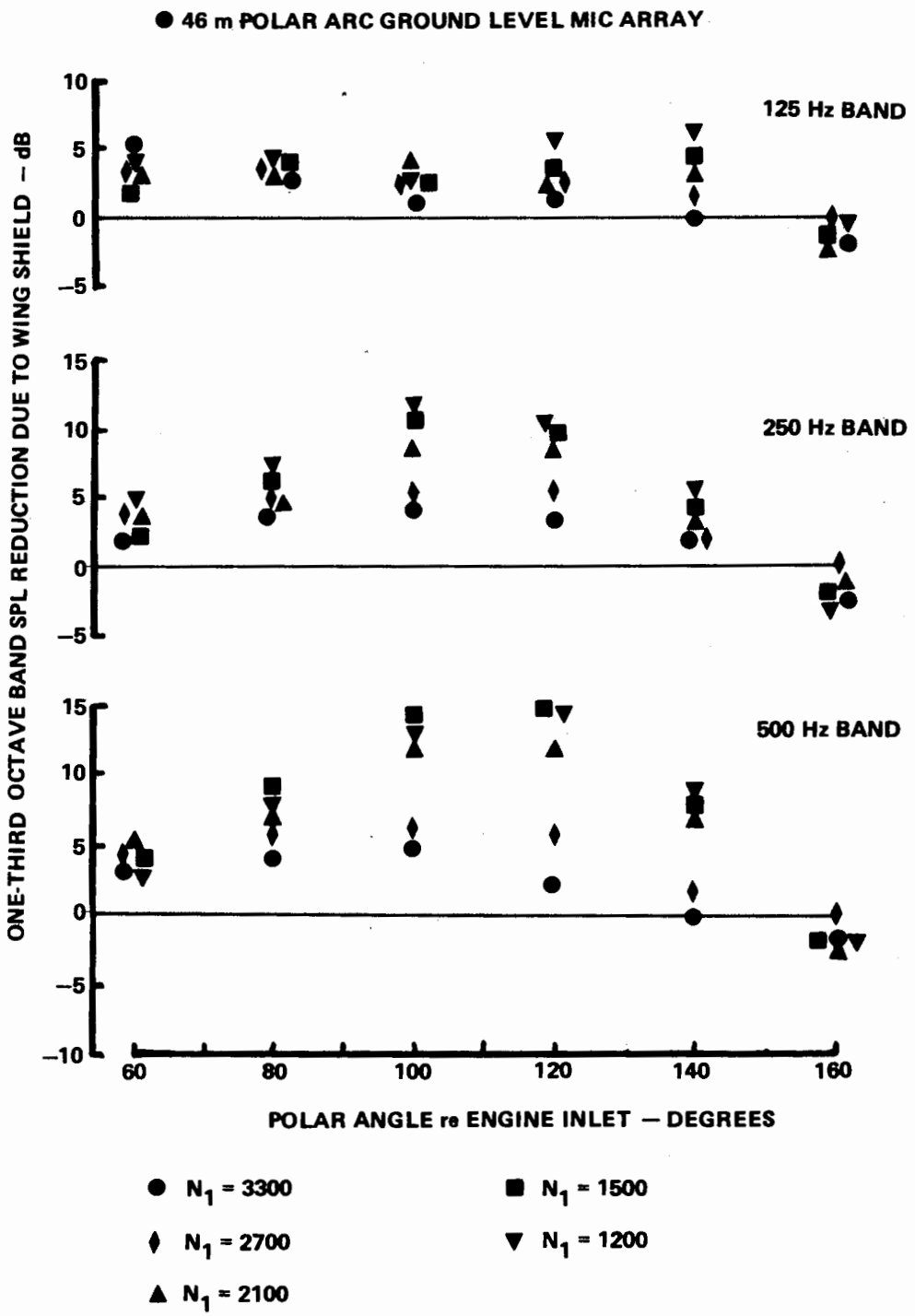

b) AVERAGE FOR RUNS 19 AND 21

Figure 97.—(Concluded)

constant. As the engine is moved further forward of the trailing edge, there is some decrease in attenuation for angles less than ~ 100° and some increase in attenuation for angles greater than ~ 100°, as might be anticipated from simple point-source-type theory.

2.3.2 AMBIENT FLOW EXPERIMENTS

In all three tests to be described in this section, either the ambient medium was in motion or the noise source was moved through an ambient medium at rest. This relative motion creates many new complexities and potential test uncertainties. These tests are hence perhaps better viewed as efforts to develop procedures for assessing the effects of motion on shielding rather than as providing assessments of the effect of motion on wing shielding.

2.3.2.1 UARL Tunnel/Powered Nacelle Shielding Test

For this test a small, powered model fan was operated in an acoustic wind tunnel and far-field noise was measured with and without a wing shield at tunnel flow velocities from 0 to 76 m/s. The purpose of the test was to explore the effect of forward velocity upon wing shielding of discharge fan and turbine tone noise. The test was conducted in September 1972.

Arrangement and a schematic of the test setup is shown in figure 98. The United Aircraft Research Laboratory Tunnel in East Hartford, Connecticut, was used for this test. The laboratory is an open flow circuit wind tunnel driven by an electrically powered fan. Air is drawn through a low-turbulence intake, exhausted via a nozzle as a jet into an anechoic room and collected on the opposite side, drawn through a series of acoustically lined bends and into the fan. The free jet test section was about 1 m in diameter by 3.7 m long. The powered nacelle used to generate discharge fan and turbine tone noise had an 18-blade, 10.2-cm tip diameter fan driven by a 29-blade turbine powered by cold compressed air. The nacelle was fitted with a coplanar, coannular fan duct. An inlet muffler lined with 21 cm of Scottfoam was used to suppress inlet fan tone noise.

The wing shield was complete with leading edge flaps and double slotted trailing edge flaps. A typical test setup with wing in place is shown in figure 99.

Noise levels of the nacelle or nacelle/wing shield combination were monitored by a sideline array of directional microphones located 2.1 m off the centerline of the tunnel flow as shown in figure 100. Use of the directive microphones (0.64-cm-diameter B&K microphones each within a 10-cm-diameter by 16-cm-deep parabolic dish reflector) was required to discriminate the noise diffracting about the wing shield from noise reflecting back from the collector of the acoustic tunnel.

The matrix of the test configurations and conditions is shown in tables 7 and 8. The data at the two nacelle speeds of 905 and 1050 RPS were averaged at each tunnel speed and each configuration. Data scatter was about ±4 dB.

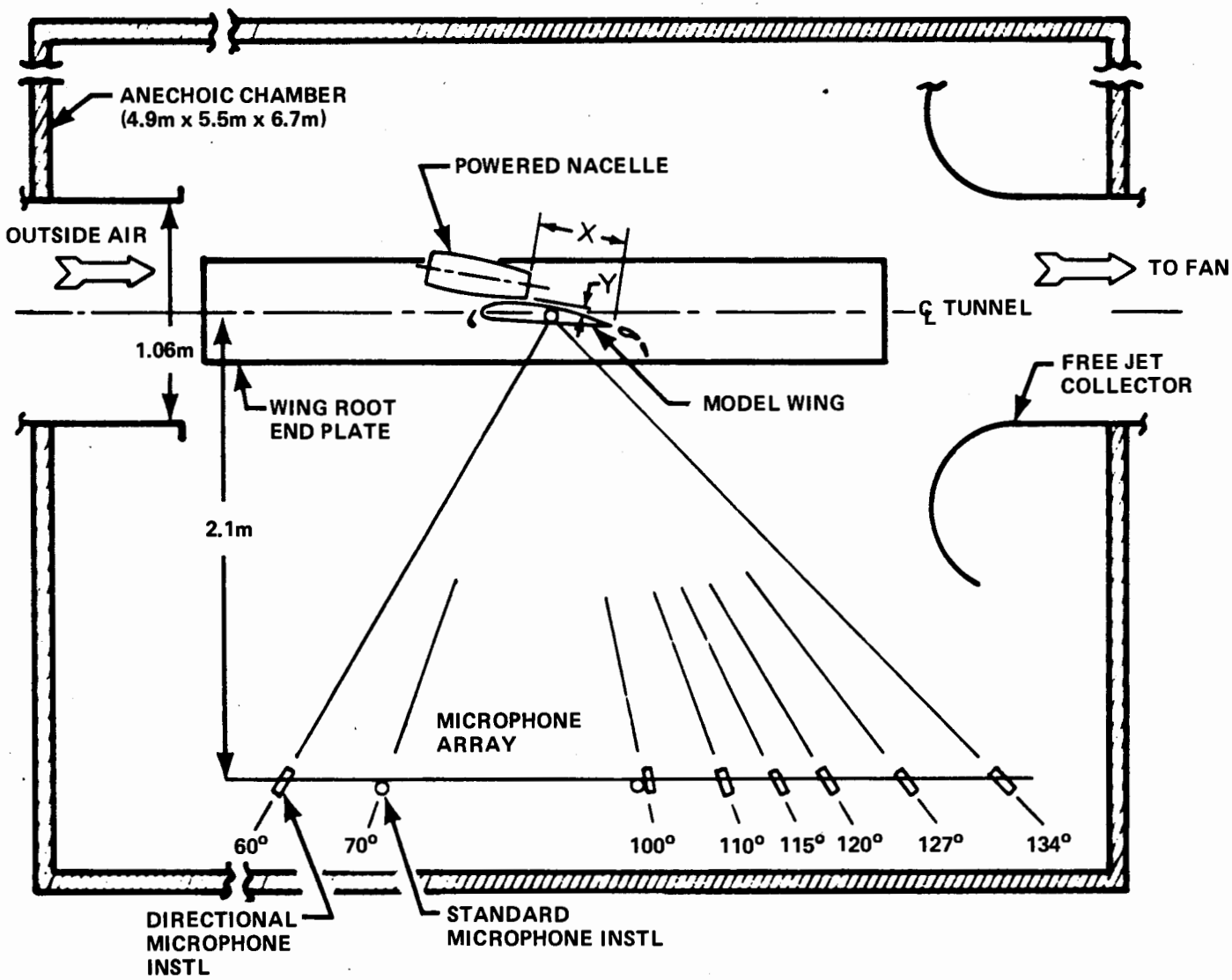

Figure 98.—Schematic of UARL Test Area

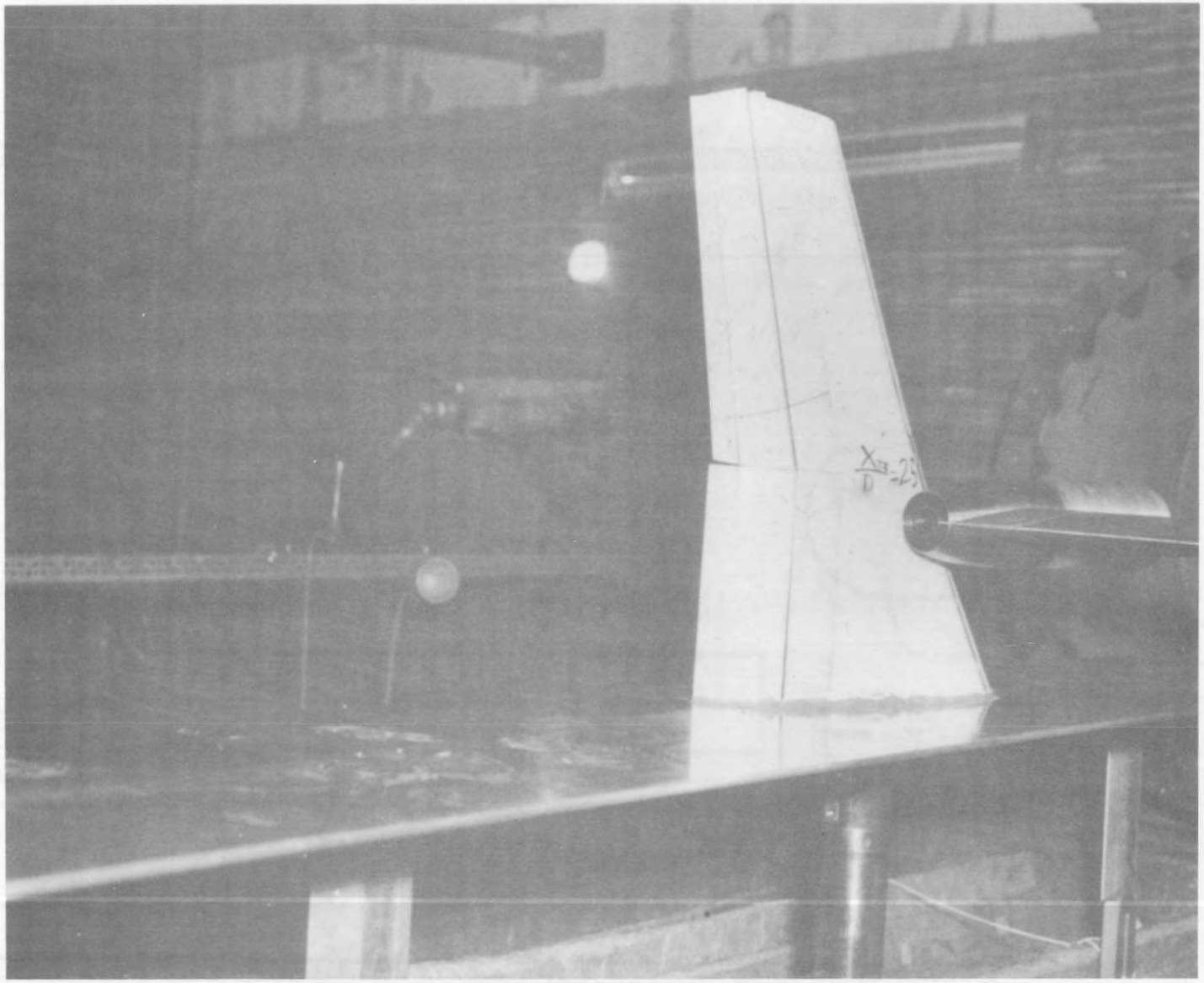

Figure 99.—Nacelle and Wing for UARL Tunnel Shielding Tests

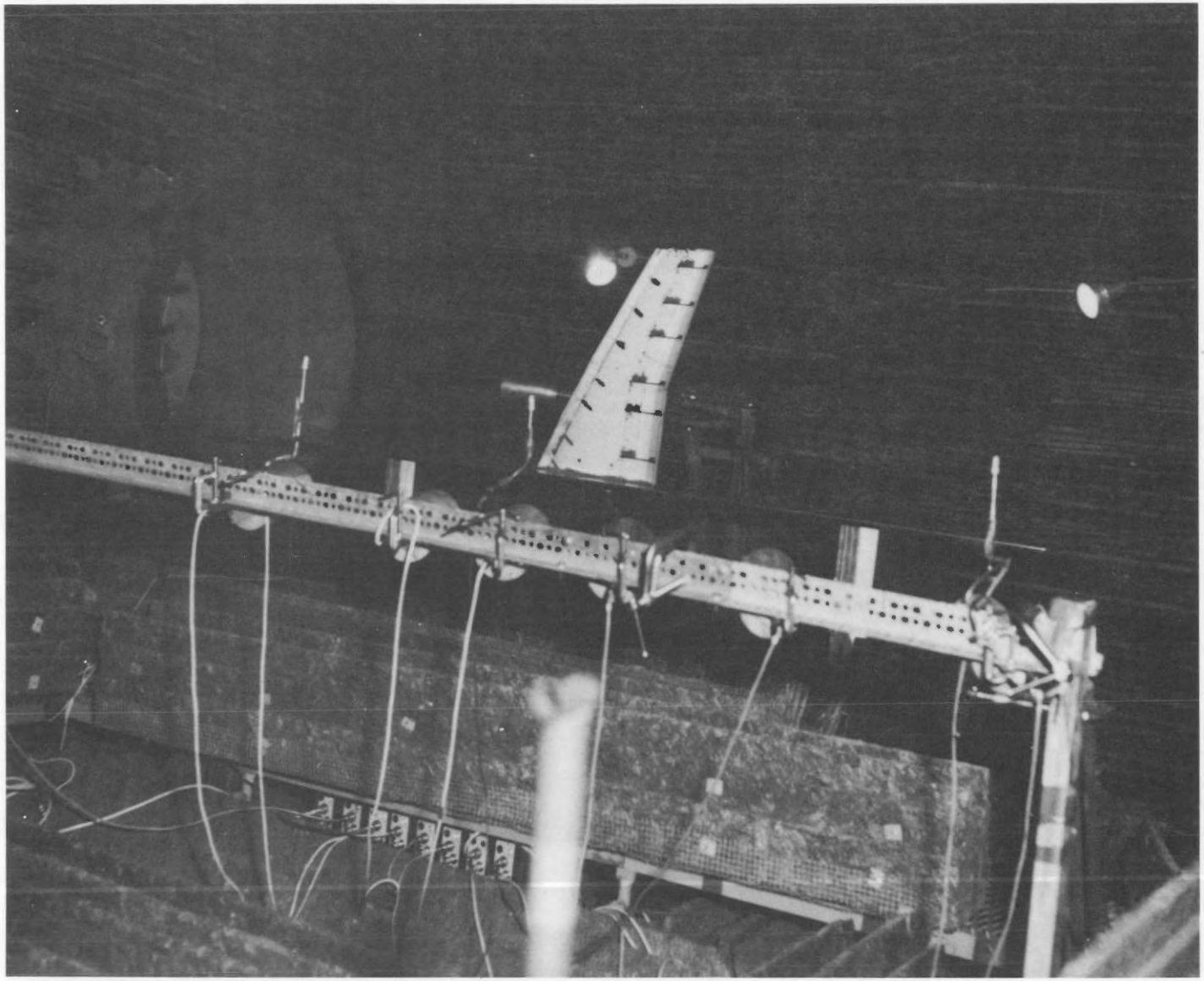

Figure 100.—Microphone Array for UARL Tunnel Shielding Tests

Table 7.—UARL Tunnel Shielding Test Configurations

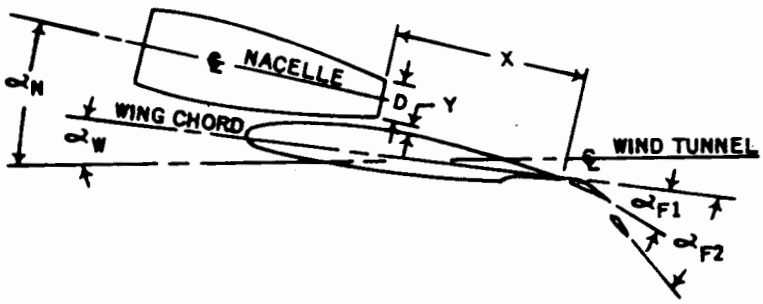

D = 7.6 cm

CONFIGURATION	X cm	Y cm	α_N	α_W	α_{F1}	α_{F2}
A	5.7	2.5	8°	8°	36°	45°
B	18	0.6	8°	6°	36°	45°
C	18	0.6	8°	8°	36°	45°
D	18	0.6	8°	8°	5°	18°
E	18	0.6	12°	8°	5°	18°

Table 8.—Tunnel and Nacelle Operating Conditions for UARL Tunnel Shielding Tests

CONFIGURATION	TUNNEL FLOW VELOCITY (m/S)	0		37		61		76	
	NACELLE SPEED—RPS	905	1050	905	1050	905	1050	905	1050
A	NO. OF DATA POINTS	2	2*	2*	2*	2*	3*	0	0
B		2	3	1	2*	3	2	0	0
C		1	1	1	1	1	1	0	0
D		2	2	2	2	2	2	2	2
E		2	2	2	2	2	2	2	2

* CONDITIONS WHERE ICE ACCUMULATIONS ON THE NOZZLE MAY HAVE COMPROMISED DATA VALIDITY

- POWERED NACELLE AVERAGE EXHAUST CONDITIONS
  - BPR = 5
  - $(M_J)_{FAN} = 0.58$ $(T_S / T_{S_0})_{FAN} = 1.0$
  - $(M_J)_{TURB} = 0.41$ $(T_S / T_{S_0})_{TURB} = 0.97$

Average results for the various shielded and unshielded configurations at *zero* tunnel flow speed are shown in figure 101. Figure 102 shows the average effect of tunnel flow velocity.

The much smaller wing shielding attenuation of turbine tone noise, compared to the attenuation of fan tone noise, is not expected from simple uniform flow theory. Theory predicts slightly greater attenuation of the turbine tone at ~ 29 kHz than of the fan tone at ~ 18 kHz. (For the JT9D Tulalip shielding tests, about the same attenuation was observed for both fan and turbine tones.)

Typical narrow-band spectra are shown in figure 103. These spectra show that when the wing is inserted, a very strong broadband hump appears, almost obscuring the turbine tone at ~ 29 kHz. This hump, as yet unexplained, could be a cause of the unexpectedly low turbine attenuation observed when the wing was inserted.

2.3.2.2 Airborne/Horn-on-Wing Shielding Test

In this test, conducted in May 1973, measurements were made of noise radiated by a horn-type loudspeaker mounted over the wing of an airborne Cessna 210 light airplane. Details of the horn location and test arrangement are shown in figures 104 and 105. The airplane was flown through the test course at an altitude of about 50 m at speeds from 27 m/s to 76 m/s. The horn was mounted in two positions with respect to the trailing edge of the wing. For each horn position a flaps-up and flaps-down (30° flaps) configuration was run, giving a total of four configuration/position combinations.

During a flyby, the three-dimensional position of the airplane was recorded by a stadiametric camera as shown in figure 106a. Measured noise levels were related to shadow angle as defined in figure 106b. Angle values were obtained from examination of the photographic records produced by the stadiametric camera. Signal/angle measurements were correlated by comparison of time marks recorded simultaneously on the camera film and on the acoustic tape recording. Noise levels were normalized to a constant (polar) distance and were obtained for the various horn positions, flap angles, and airplane flight speeds. Typical results of the test are shown in figures 107 and 108.

These figures also show results of a static test effort. The setup of this static test is shown in figure 109. For this test, a Cessna 210 wing was used together with the same horn noise source employed for the flight test. The four horn position/flap configuration combinations duplicated those used in the flight test. The input power to the horn was held constant for all static and flight tests. However, unshielded horn noise levels were measured only during the static test.

The results shown in figures 107 and 108 suggest that wing shielding attenuation decreases with increasing airplane speed, at least for the speed range covered in this test. (These results are not in agreement with the simple theory discussed in section 2.2.1.2, "Uniform Flow Effects," which for the conditions of the test would forecast some increase in shielding attenuation with increasing flight speed.) On the other hand, no consistent increase or decrease in shielding attenuation was observed in going from the lowest indicated flight speed of 27 m/s to 45 m/s. Since the zero flight speed data was obtained in a different, totally independent experiment than was the

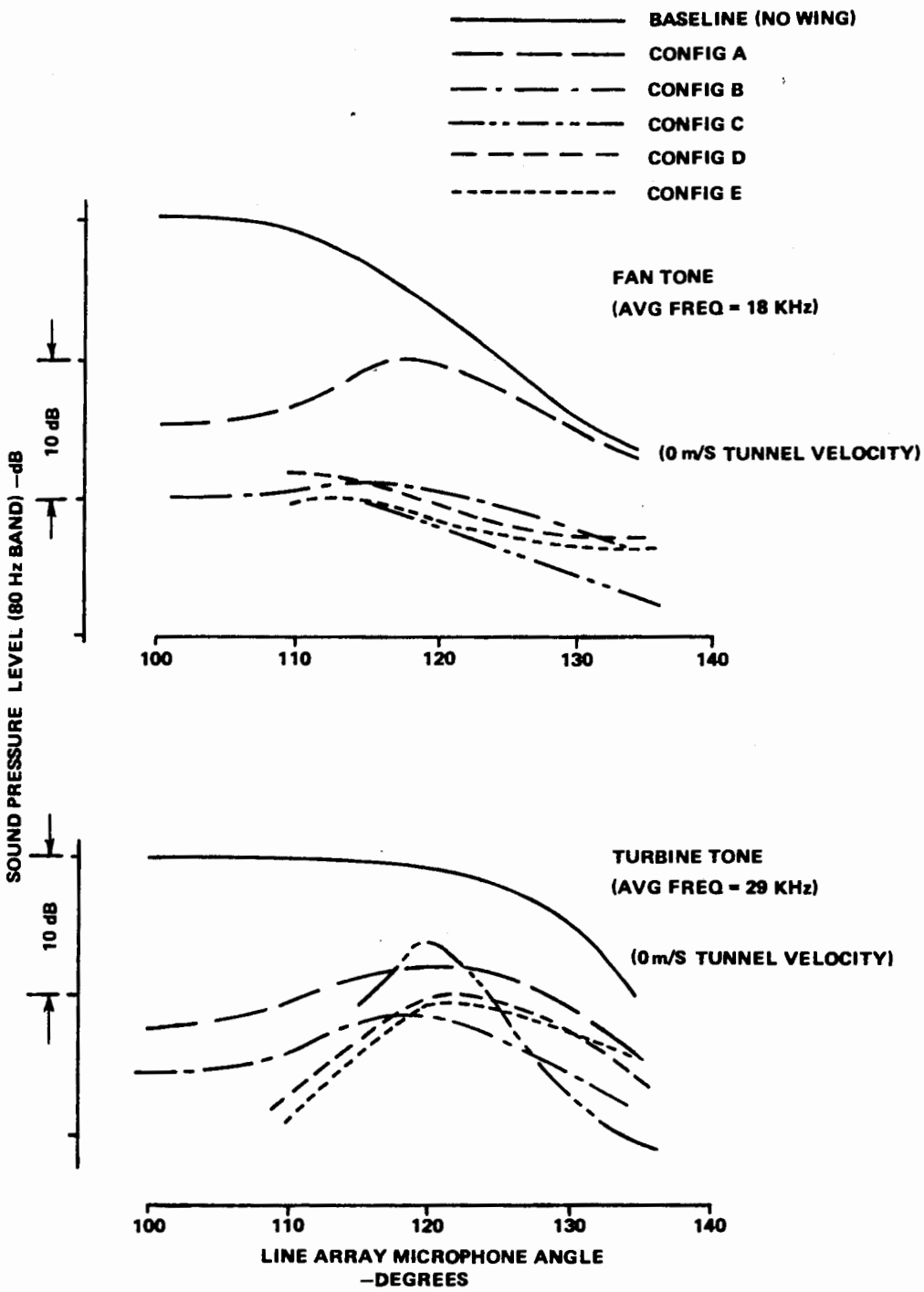

Figure 101.—Average Unshielded and Shielded Tone Noise Results at 0 m/s Tunnel Velocity (UARL Test)

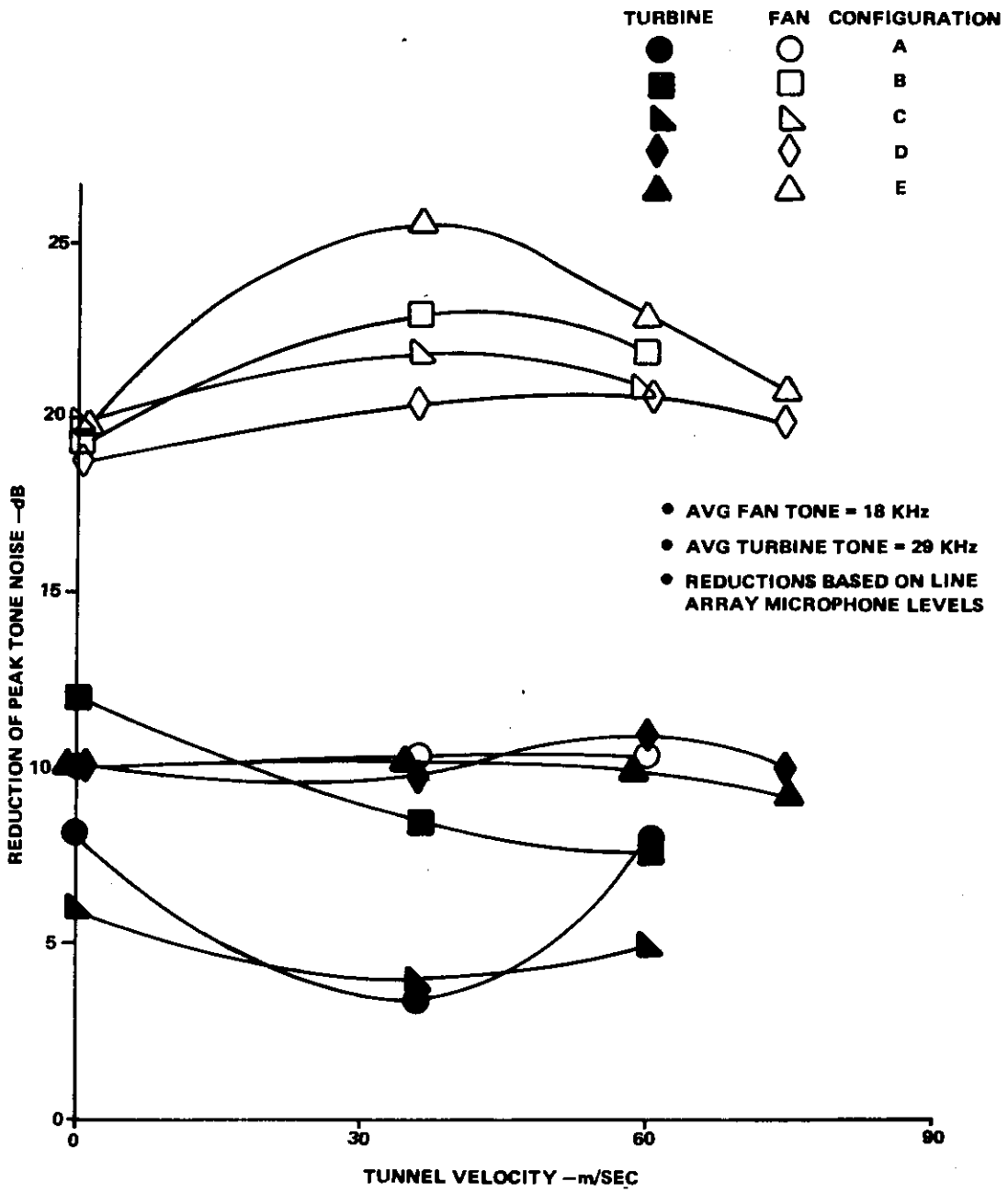

Figure 102.—Effect of Tunnel Velocity on Reduction of Tone Noise Due to Wing Shielding

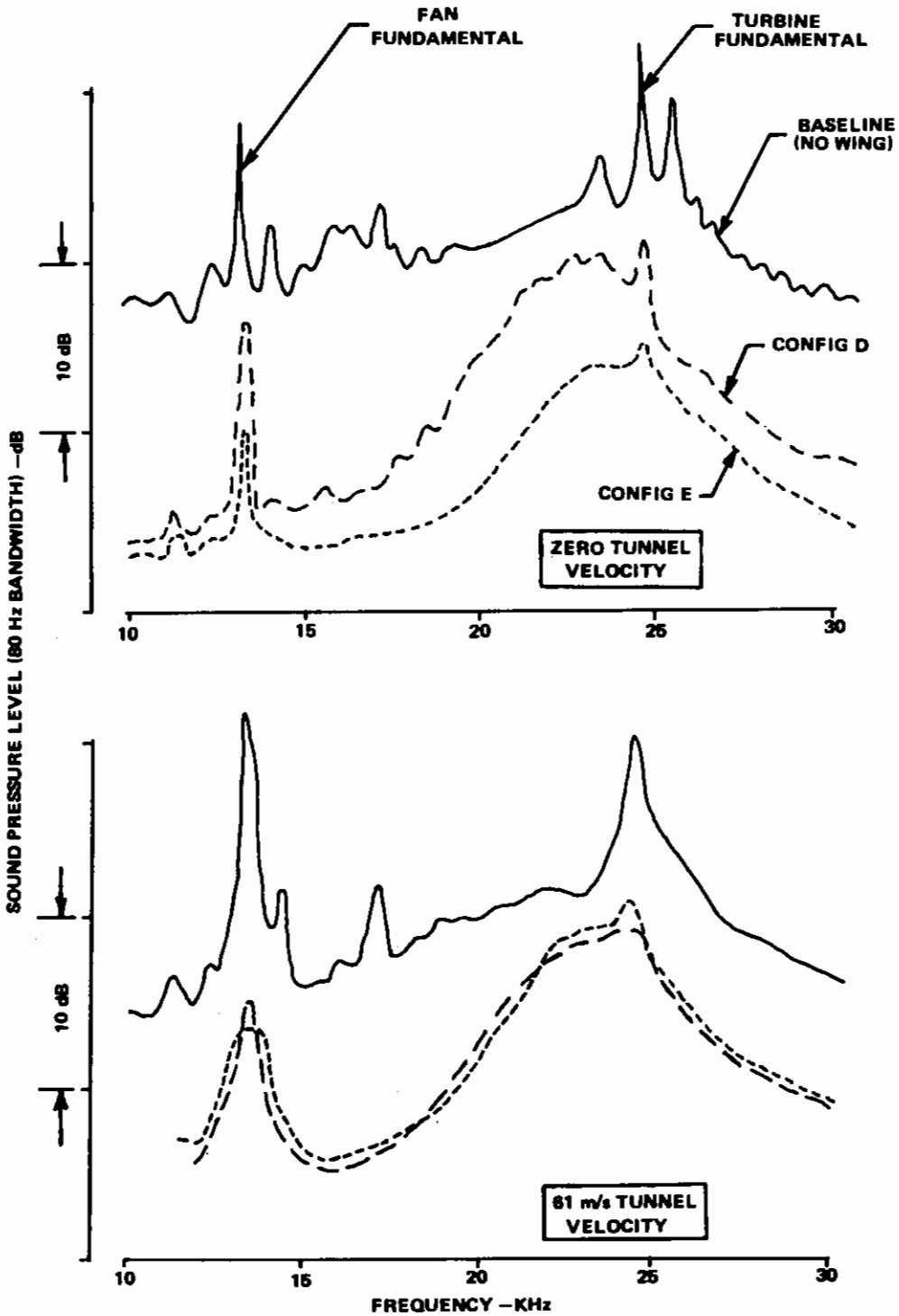

Figure 103.—Powered Nacelle Noise Spectra With and Without Wing

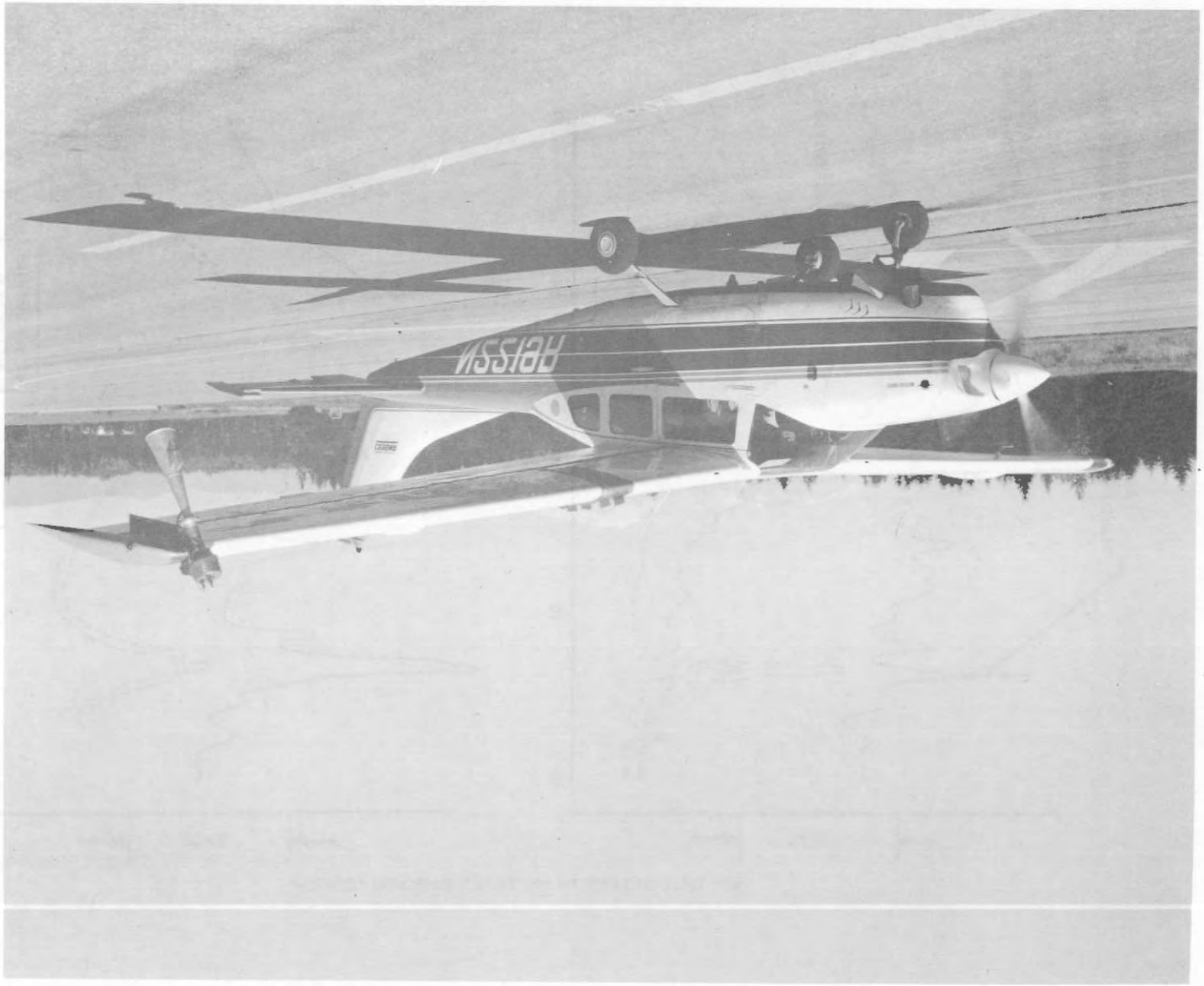

Figure 104.—Airplane With Horn Mounted Below Wing

Figure 105.—Detail of Horn Mounted Above Wing

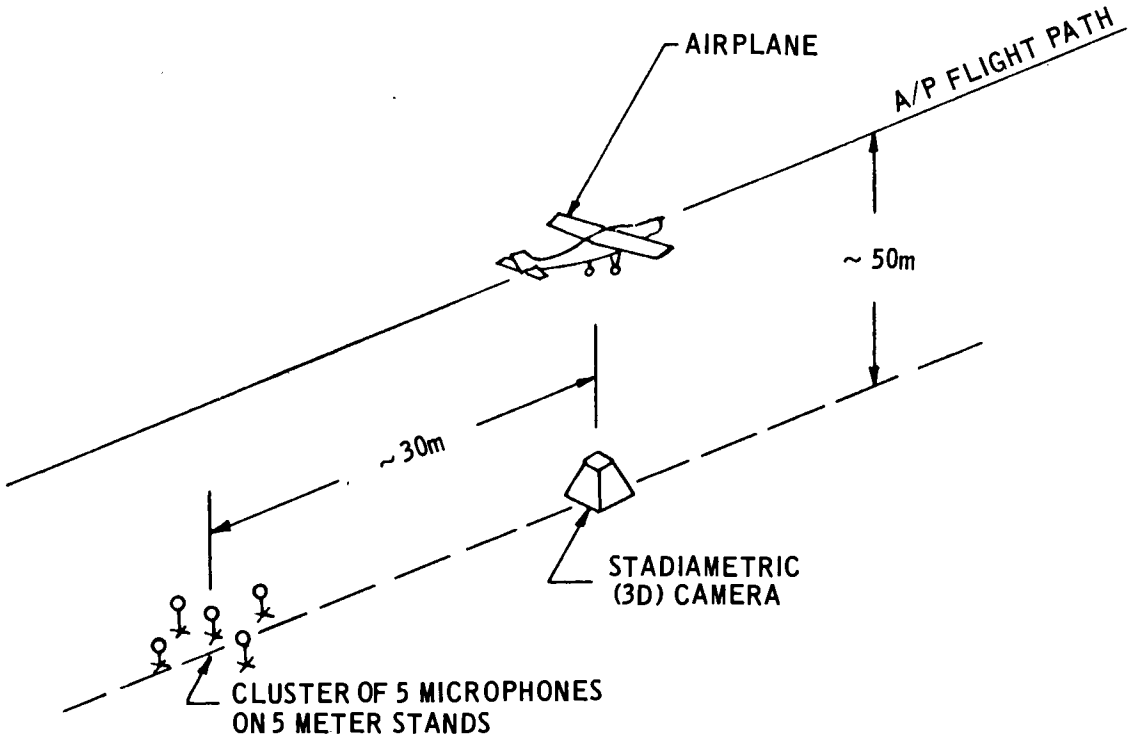

a) PERSPECTIVE SCHEMATIC OF FLIGHT TEST ARRANGEMENT

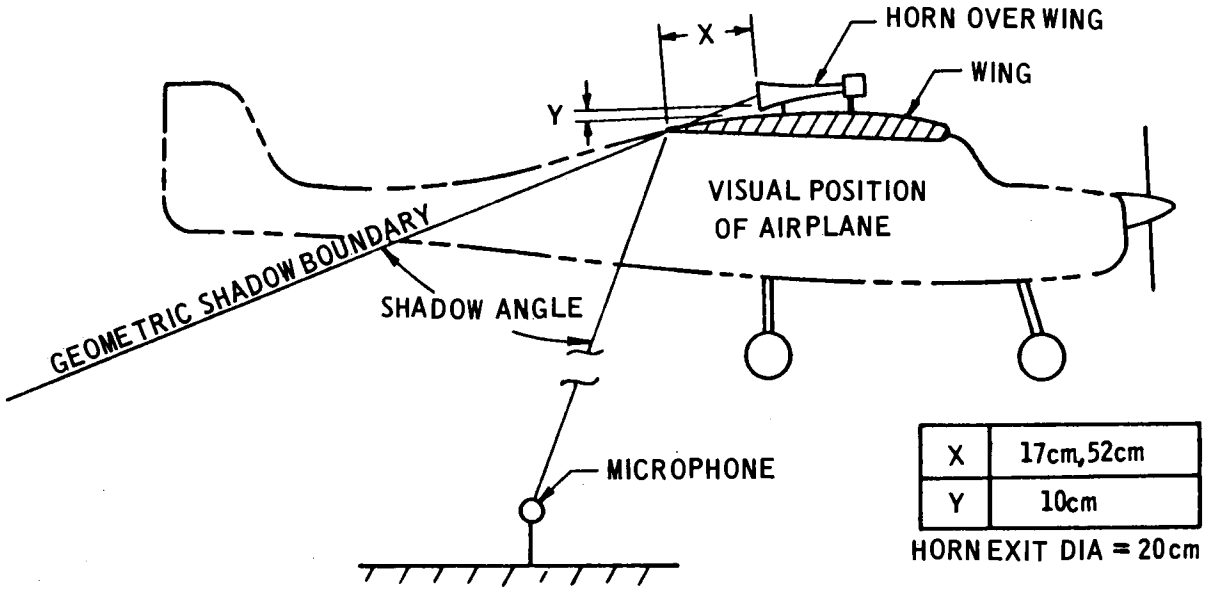

b) DEFINITION OF SHADOW ANGLE

Figure 106.—Horn-Over-Wing Flight Test Layout

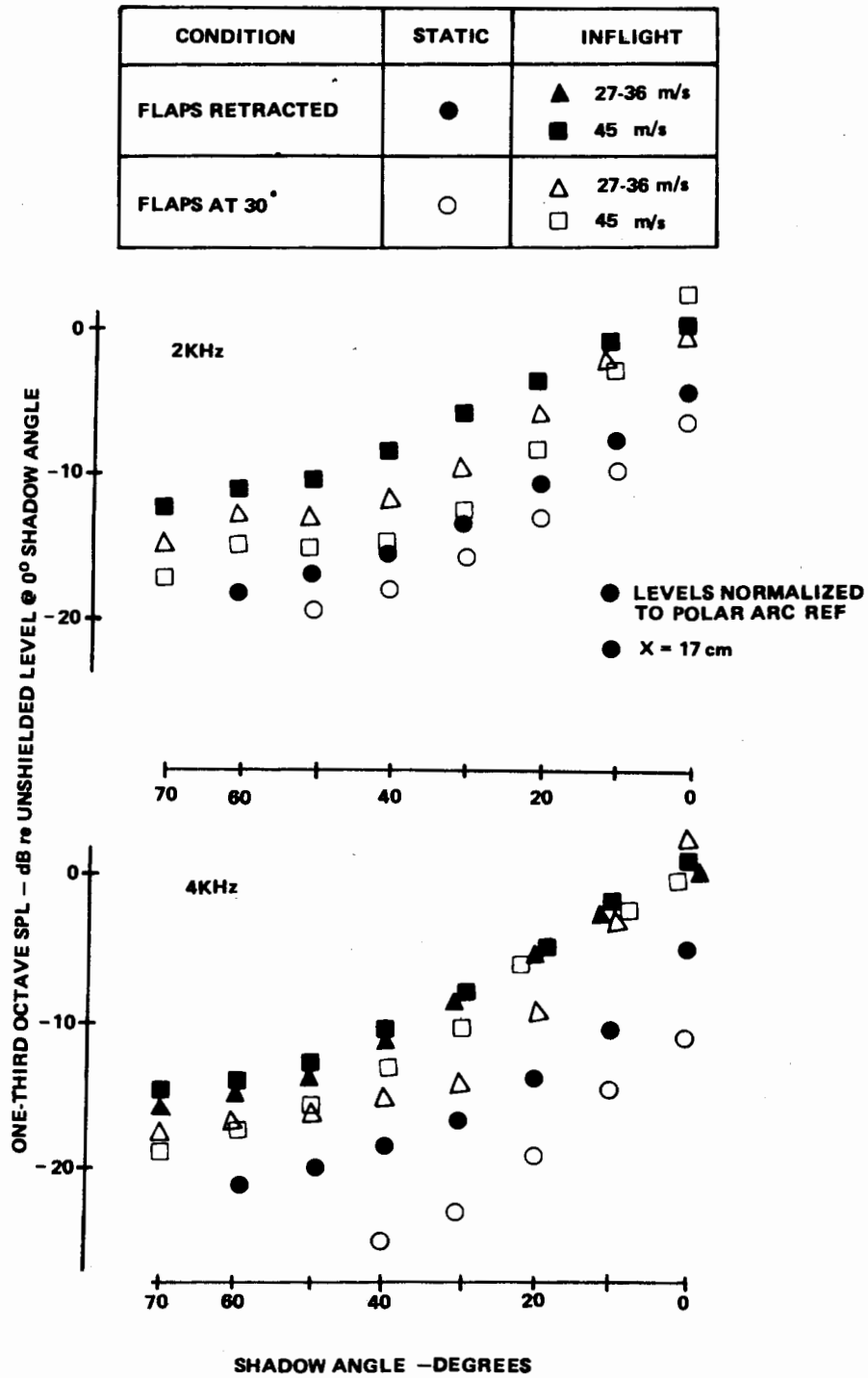

Figure 107.—Typical Results for Horn-on-Wing Shielding Test for X = 17 cm

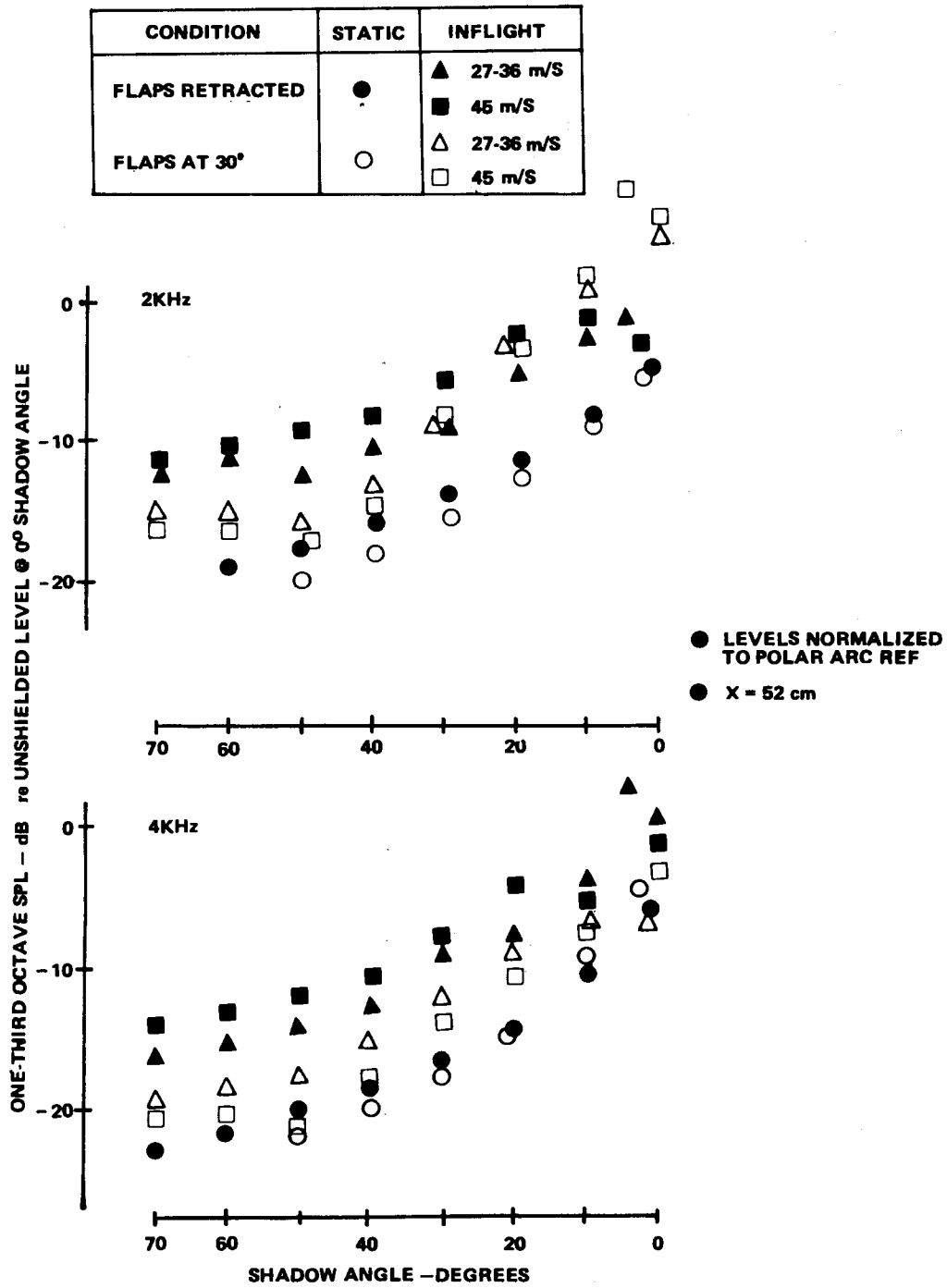

Figure 108.—Typical Results for Horn-on-Wing Shielding Test for X = 52 cm

Figure 109.—Light Airplane Static Wing Shielding Test Setup

non-zero flight speed data, the possibility arises that experimental factors rather than forward speed may be responsible for the apparent decrease in shielding attenuation with increasing flight speed.

Limited data obtained at an airplane speed of 76 m/s shows mixed behavior. For instance, with flaps retracted and the horn at either X = 17 or 52 cm at 4 kHz, a 5-dB increase in shielding attenuation (compared to the 45 m/s data) is observed at all shadow angles from 65° to 0°. However, at 2 kHz the observed shielding attenuation was almost identical to that at 45 m/s.

2.3.2.3 727-100/200 Flyby Inlet Shielding Comparison

Data for this comparison was obtained from separate level flyby tests on a 727-100 airplane conducted at Moses Lake, Washington, in September 1972 and on a 727-200 conducted at Fresno, California, in May 1971. Results of these two tests at equivalent approach power settings are shown in figures 110 and 111. At the 3-sec-before-visual-overhead instant, the spectral peak in the neighborhood of 4 kHz observed for the -200 airplane is absent in the spectrum for the -100 airplane. From flight geometry, the peak for the -200 airplane appears to be associated with inlet fan tone noise. Examination of the trailing edge flap/engine inlet geometry for the two airplanes suggests that the absence of the 4-kHz peak for the -100 airplane is due to shielding provided by the closer engine/wing spacing (by 3 m) on the -100 airplane (see fig. 112).

Table 9 lists the test conditions for the data shown in figures 110 and 111. Figure 113 shows average adjusted data for the 4 kHz 1/3-octave band. The average data has been adjusted to a constant polar distance and to zero atmospheric absorption conditions. Data scatter is ±3 dB. Data uncertainty within about 3 sec of visual overhead (equivalent to angles greater than about 30° re the engine inlet) is probably 3 dB. This uncertainty increases with increasing time before or after visual overhead (equivalent to angles less than 30°), and is primarily due to uncertainties in atmospheric conditions.

The data from the lower part of figure 113 is replotted in figure 114 along with various estimates based on simple theory developed in section 2.2. There appears to be some agreement between data and estimates. It should be noted that the estimated shielded inlet noise is for zero forward velocity. For increasing forward velocity, the shielding estimates for the inlet fan tone would be more to the right. On the other hand, wing wake scattering would tend to push the shielding curves up and back to the left with increasing airplane velocity. The uncertainty of the airplane data, particularly that for angles less than 30°, makes comparison with theory difficult.

2.4 DEVELOPMENT OF SHIELDING ESTIMATION METHOD

Methods are developed in this section for the estimation of wing and fuselage shielding of aircraft engine turbomachinery noise. Both theory and test results of sections 2.2 and 2.3 are used. Where both theory and test results are available in sufficient quantities, empirical estimation methods are developed. In areas where test data are insufficient, the methods are based strictly on theory and are considered more preliminary.

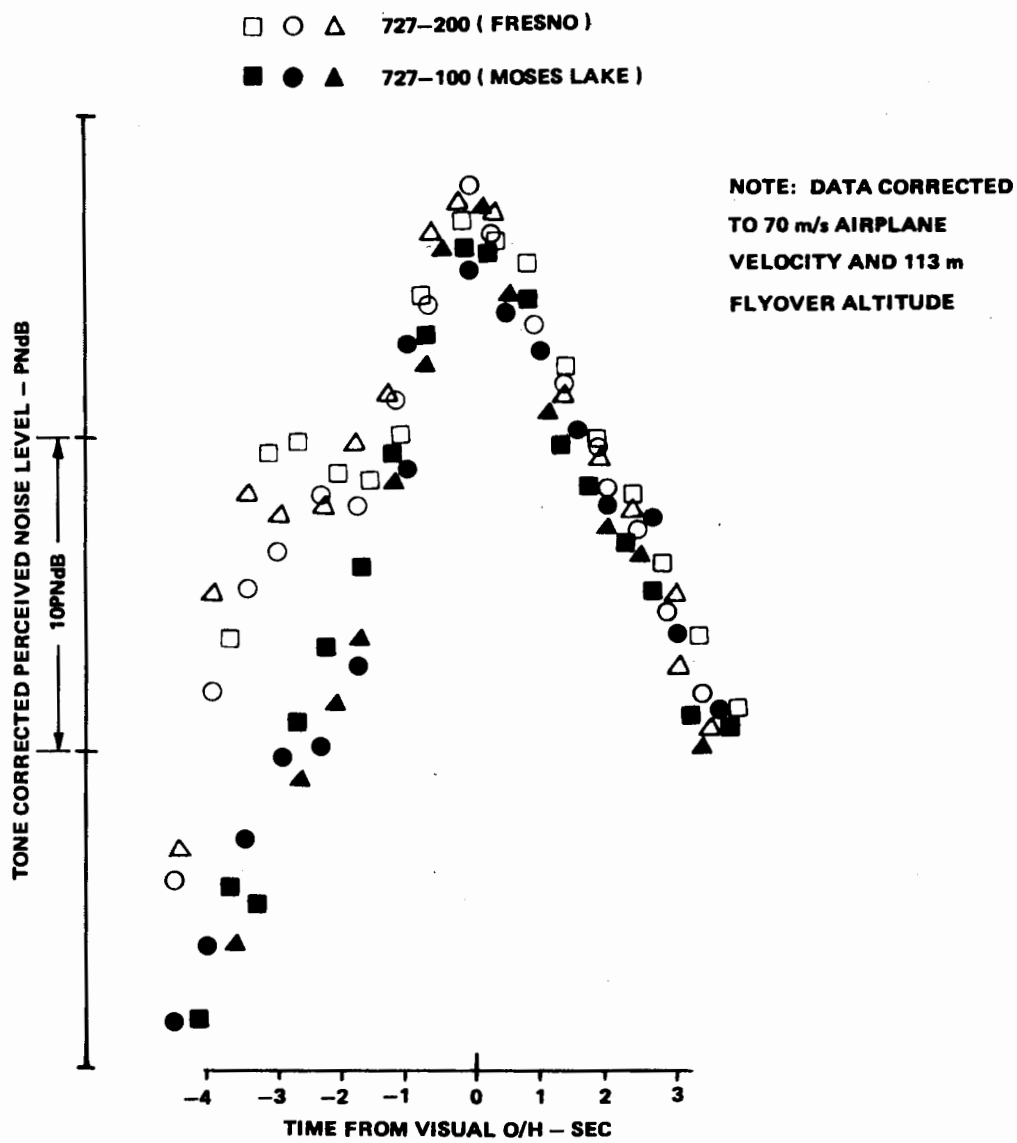

Figure 110.—Comparison of 727-100 and -200 Level Flyover Noise Levels at Approach Power and 25° Flaps

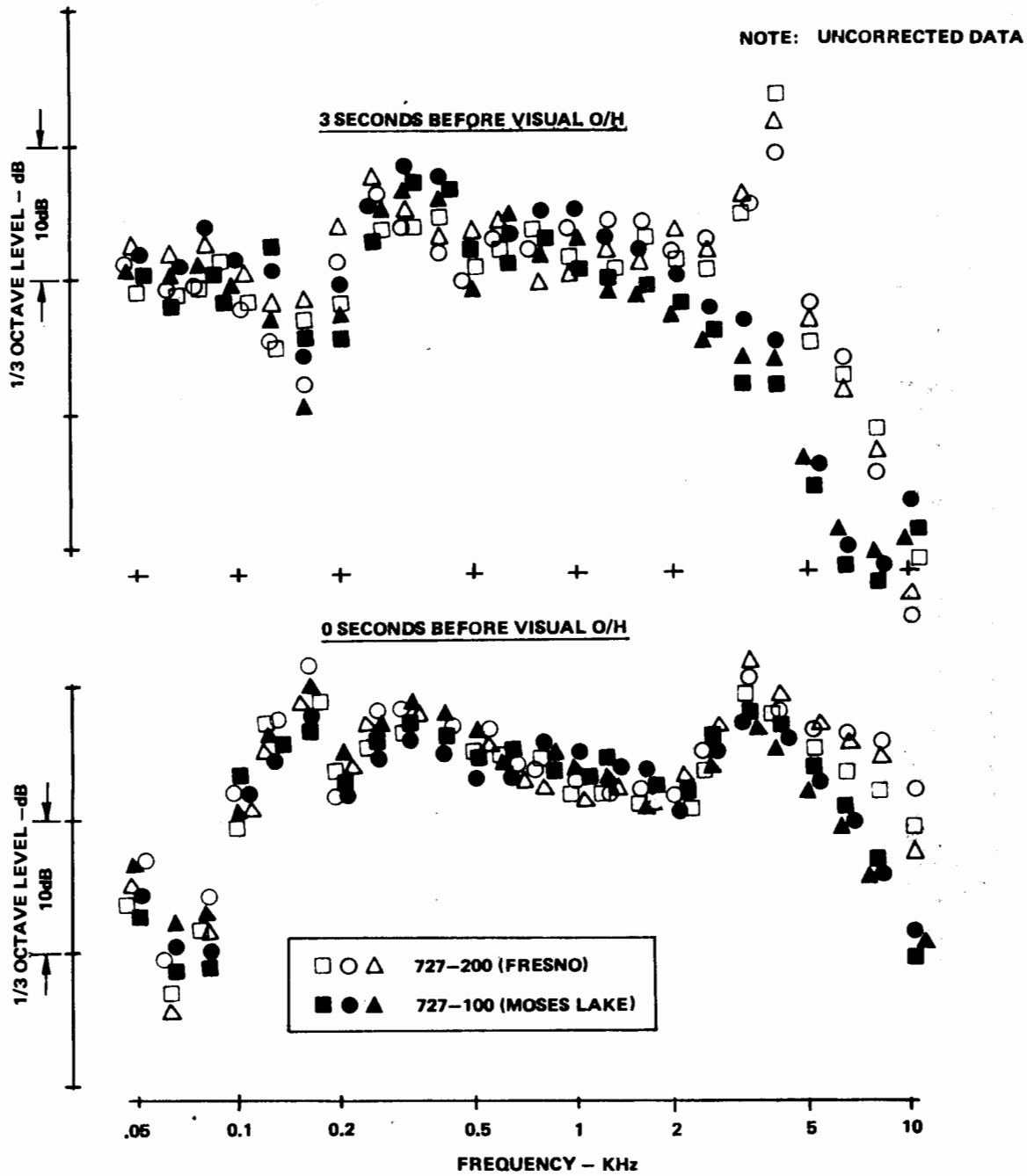

Figure 111.—Comparison of 727-100 and -200 Level Flyby Data at 25° Flaps

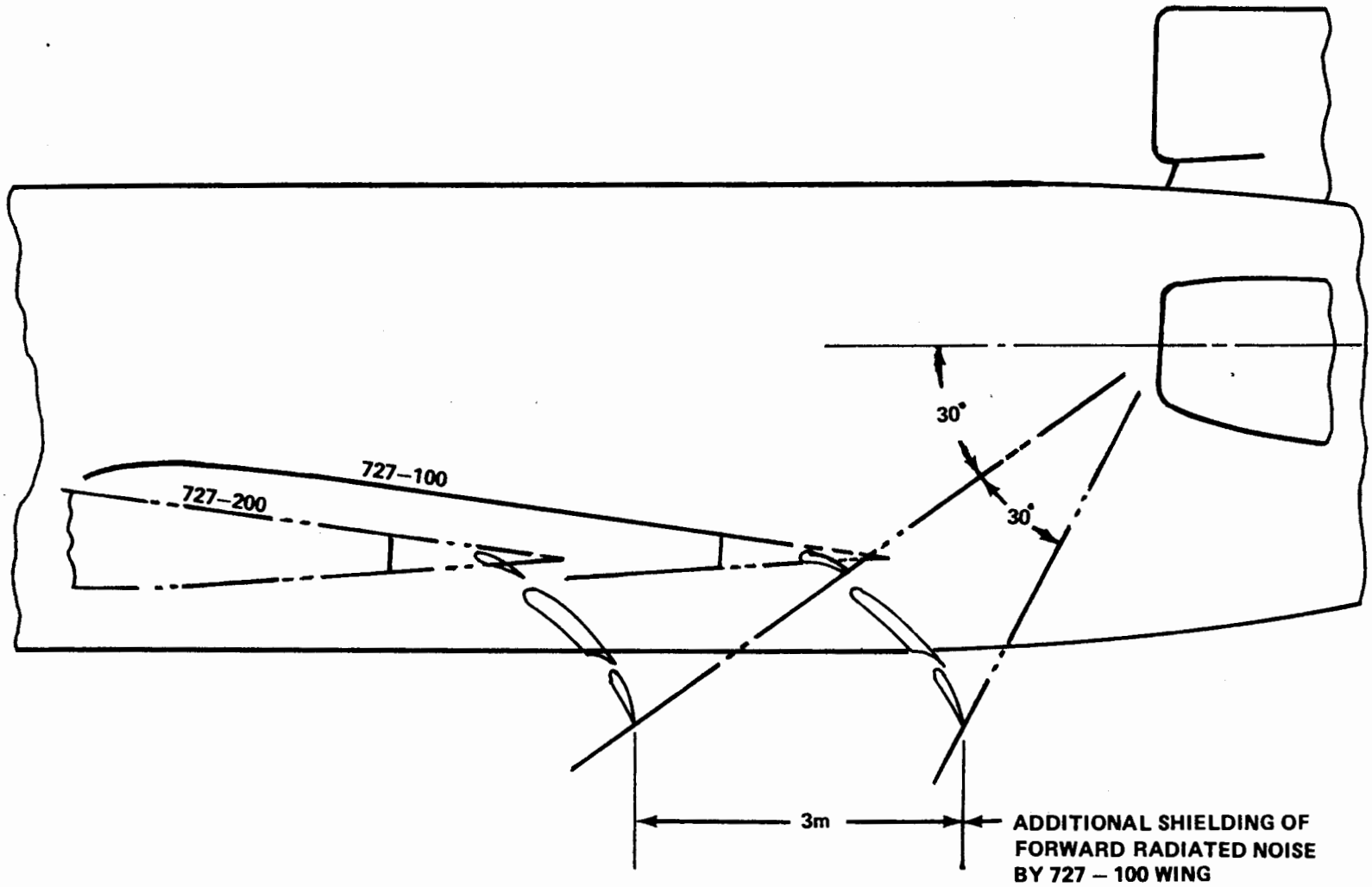

Figure 112.—727-100 and -200 Geometry Comparison

Table 9.—Mean Flyover Test Conditions for 727 Airplanes

PARAMETER	727–100 MOSES LAKE SEPT 1972	727–200 FRESNO MAY 1971	ESTIMATED ACCURACY
AIRPLANE VELOCITY (METERS/SEC)	80	80	± 5
MACH NO.	0.23	0.23	
HEIGHT AT VISUAL OVERHEAD (METERS)	110	120	± 5
RELATIVE HUMIDITY (%)	40	64	± 10
TEMPERATURE (°C)	21	14	± 10
ABSORPTION COEFFICIENT (dB/Km)	34½	28	–0.7 dB/Km PER % INCREASE IN RELATIVE HUMIDITY AND –0.5 dB/Km PER °C INCREASE IN TEMPERATURE

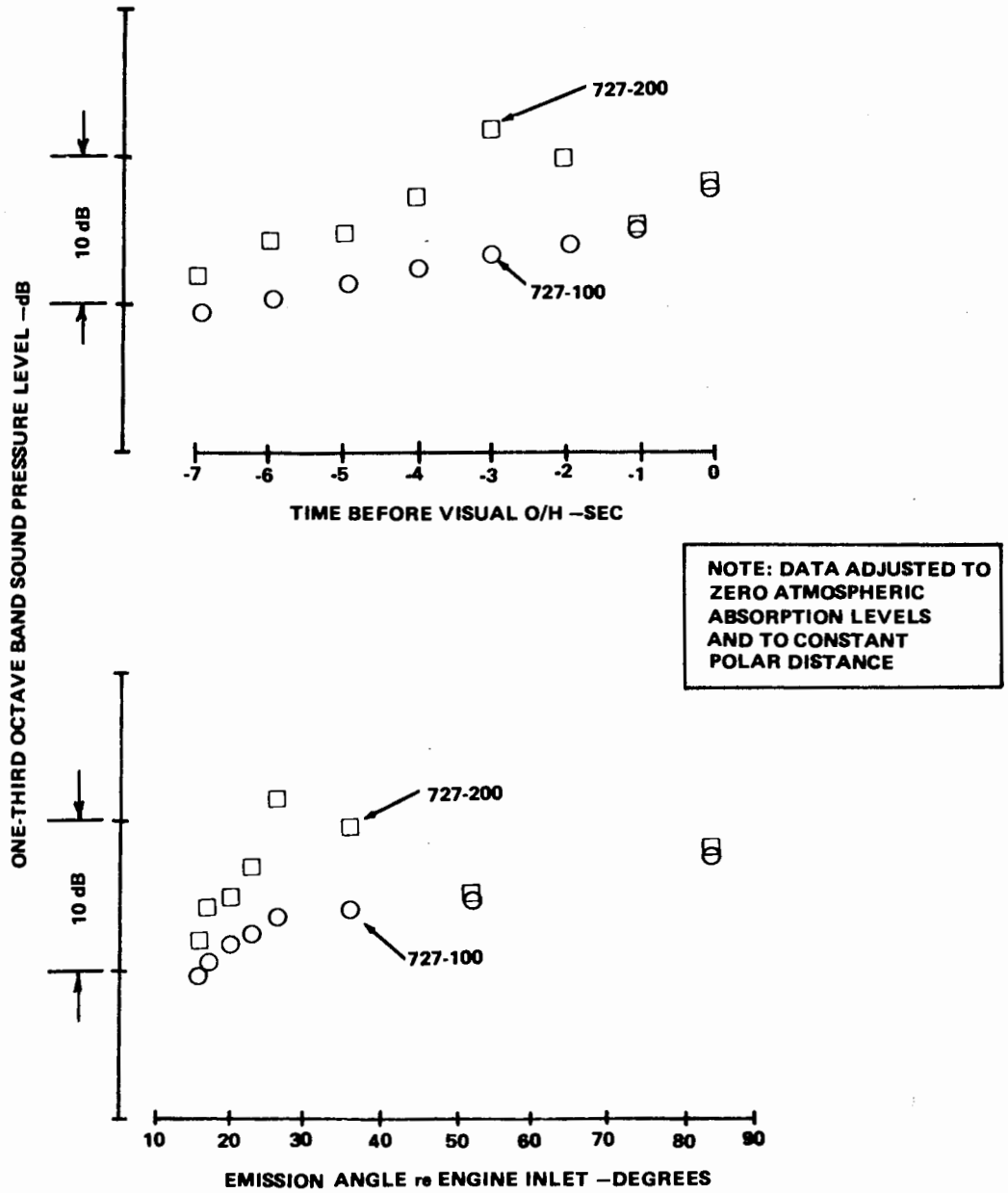

Figure 113.—Comparative Average of 4-kHz 1/3-Octave-Band Level Flyby Data for 727-100 and -200 at 25° Flaps

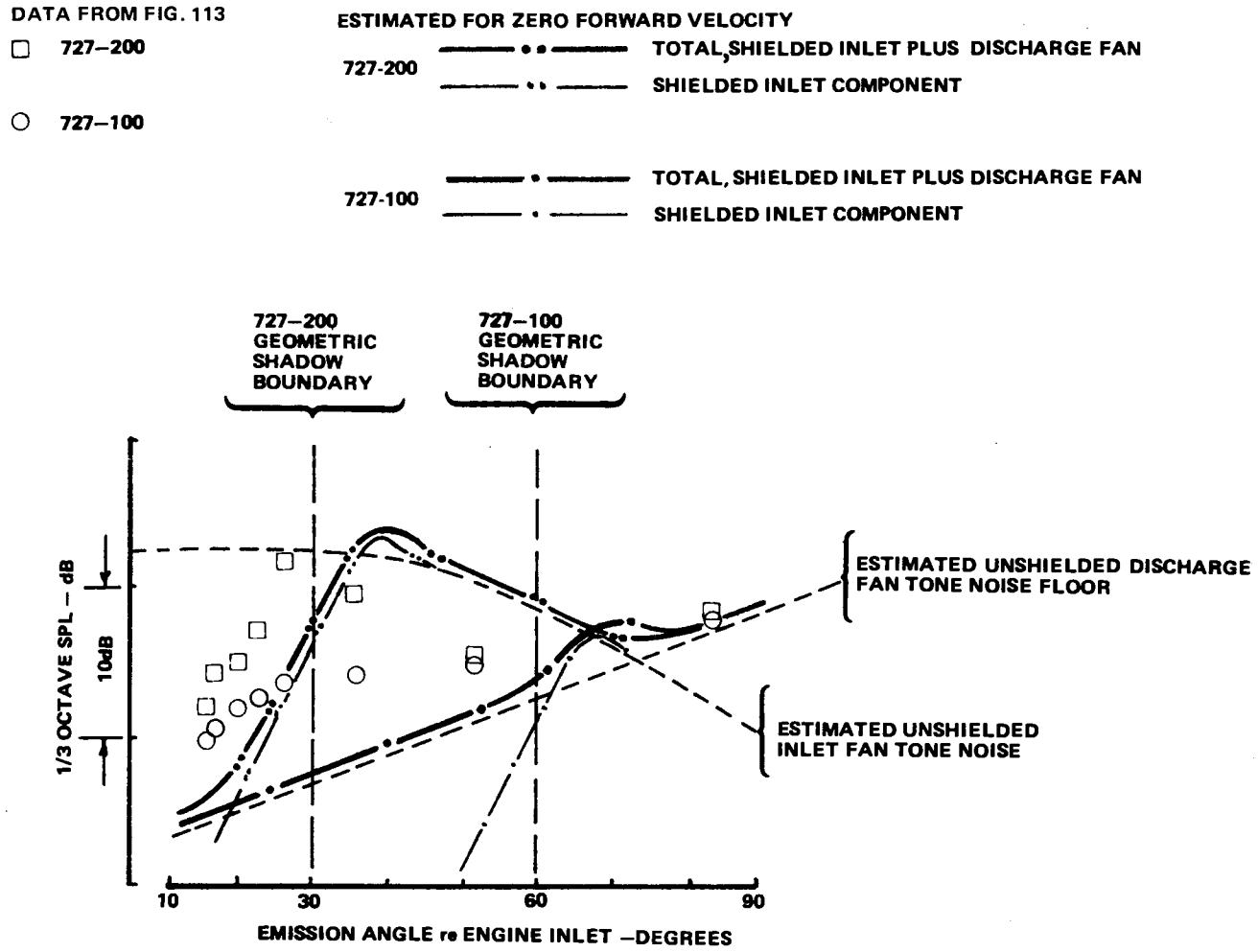

Figure 114.—Estimated and Observed Fan-Tone Flyby Noise Levels of 727-100 and -200 at 25° Flaps

Estimation methods are developed at three levels of complexity. Starting with the simplest, they are:

- Wing and fuselage shielding of compact noise sources
- Wing shielding of exhaust turbomachinery noise components
- Flight and forward velocity effects on wing shielding

First, favorable shielding comparisons are shown for diffraction theory and test results on compact noise sources "illuminating" simple rectangular planes and cylinders. Shielding test results were obtained from very basic tests using simple compact loudspeakers placed near barrier geometries ranging from semi-infinite half-planes and cylinders to complex wing/flap models. Comparison of applicable test results with simple diffraction theory for compact noise sources shielded by semi-infinite half-planes showed that:

- Superposition of simple diffraction theory solutions for each edge can describe shielding by a finite rectangular plate.
- The intensity of diffracted signals from each edge being illuminated by a directional noise source is dependent solely upon the incident signals' intensity on each respective edge.
- Complex wing/flap geometries can be simulated simply by two inclined semi-infinite half-planes.

Hence, the simple compact-source diffraction solution is established as a very basic building block for shielding calculations. In addition, the simple compact-source diffraction solution should be directly applicable for calculating shielding of inlet noise since this noise source is localized in the inlet.

Test results show that exhaust turbomachinery noise sources do not appear localized in the exhaust nozzle. The refraction properties of the exhaust jet play an important role in causing noise emanating upstream of the nozzle exhaust to have downstream apparent source locations near the wing's trailing edge. Hence, the diffraction theory for compact directional noise sources noted above is applied to exhaust TM noise by use of apparent source locations. These source locations are empirically determined. This estimation method for wing shielding of exhaust TM noise is favorably compared to test results. The method thus has direct application for exhaust fan, turbine, and core noise shielding by a wing. Except for how source locations are determined, inlet and exhaust turbomachinery noise shielding estimation methods are identical.

Finally, the small amount of noise shielding test data gathered for flight conditions or flight simulations is examined. Theoretical effects are considered, i.e., the uniform flow transformation and scattering of sound by a wake. Since there is little data for validation, the theoretical estimation methods developed for flight effects are considered preliminary and their use in estimation is optional. The major application of these strictly theoretical methods is for estimation of flight effects on wing shielding.

Throughout section 2.4, specific estimation methods are selected for use in the final procedure to calculate turbomachinery noise shielded by aircraft wing and fuselage elements during flight.

2.4.1 SHIELDING OF NOISE FROM COMPACT SOURCES

This section discusses the evaluation of data from the shielding tests conducted using a compact source in the vicinity of acoustical barriers. The source was a loudspeaker. The barriers were a flat board, a model wing, and a cylinder. No flow field existed for the tests. See section 2.3.1.1 for additional detail.

The data from these tests were used to verify both the basic theory and application of this basic theory to more complex sources, flows, and geometries. The tests are described in some detail in sections 2.3.1 and 2.3.2. Specific effects verified were the following.

- The dimensionless geometrical parameters presented in the diffraction theory can be used to scale the data.
- The source's directivity effect on the shielded sound follows that presented by a ray acoustic interpretation of diffraction theory.
- A real wing may be approximated by a collection of simple half-planes and the diffracted signal from each half-plane edge can be superimposed to estimate the sound in the wing's shadow zone.
- The bandwidth of the sound source or detection equipment "smooths out" the interference that is observed in radiation patterns for a source placed close to a barrier.

2.4.1.1 Effect of Source Directivity on Shielding

Two types of experiments–called group 1 and group 2 experiments–were conducted on compact noise sources to determine directivity effects. Common characteristics of group 1 were:

- Directional source
- Source size small with respect to barrier height (not wavelength), so that directivity rather than the noise source spatial distribution could be addressed
- Simple barrier geometry (flat board)
- Far-field measurements

The directivity of the source (an Altec driver) was varied by changing the driver orientation with respect to the barrier. However, the driver axis was always kept in a plane perpendicular to the edge. In contrast, group 2 experiments had the axis of the

driver moved out of this plane. One edge of the board was blocked with fiberglass so that the noise diffracting about only one edge could be determined.

Figure 115 gives a typical data sample. It is apparent that the total diffracted field is made up of two separate fields (incident and image).

Figure 116 shows the sound fields of sources with different directivities both with and without the barrier. Note that the diffracted sound field in the shadow region underneath the barrier is relatively independent of the unshielded sound in the same region. Rather, the shielded sound is dependent mainly on the acoustic intensity radiated toward the barrier's edge. Specifically, the shielded sound for the two different directional sources varies only 3 to 4 dB in the region for $30^0 < \theta < 90^0$, while the unshielded sound radiated in the same sector varies up to 20 dB.

On the other hand, in the light zone of the virtual image ($\theta < -\theta_0$) the diffracted sound appears closely related to the unshielded image. Due to the symmetrical behavior of the incident and the image signal, one can apply what is learned about the incident signal to the image and vice versa (a close look at all the data was made and has confirmed this interpretation).

It can therefore be concluded:

1. The sound in the shadow zone of the incident (image) signal is related to the acoustic intensity radiated in the direction of the line grazing the barrier edge.

2. The sound in the light zone of the incident (image) signal is a function of the incident (image) free-field radiation pattern.

Figure 117 shows data from the group 2 experiments on noise shielding of a compact source conducted in the Boeing Large Test Chamber as an explicit part of the current study. The test, described in section 2.3.1.1, used a small, directional (horn-type) noise source and a flat board barrier setup similar to that used as part of group 1 experiments. The major lobe of the noise source was aimed both normal (case A) and obliquely (case B) to the edge by rotating the source axis out of the plane normal to the barrier's edge.

Case A is a repeat of the configuration tested in group 1 experiments previously discussed. Case B is representative of an exhaust turbomachinery noise component where the most intense sound is radiated at angles of approximately 120^0 from the engine inlet axis. This is illustrated in figure 118.

The sound intensity at point 1 in the sketch for case B was 17 dB less than that measured for case A. The corresponding change in the shielded sound intensity throughout the shadow zone was about 17 dB (fig. 117). Hence, the sound level in the shadow zone for case B is governed by the sound intensity at point 1 even though the sound level at point 2 is appreciably higher (14 dB), reinforcing the proposition presented previously in the theory of section 2.2.1.1.; i.e.,

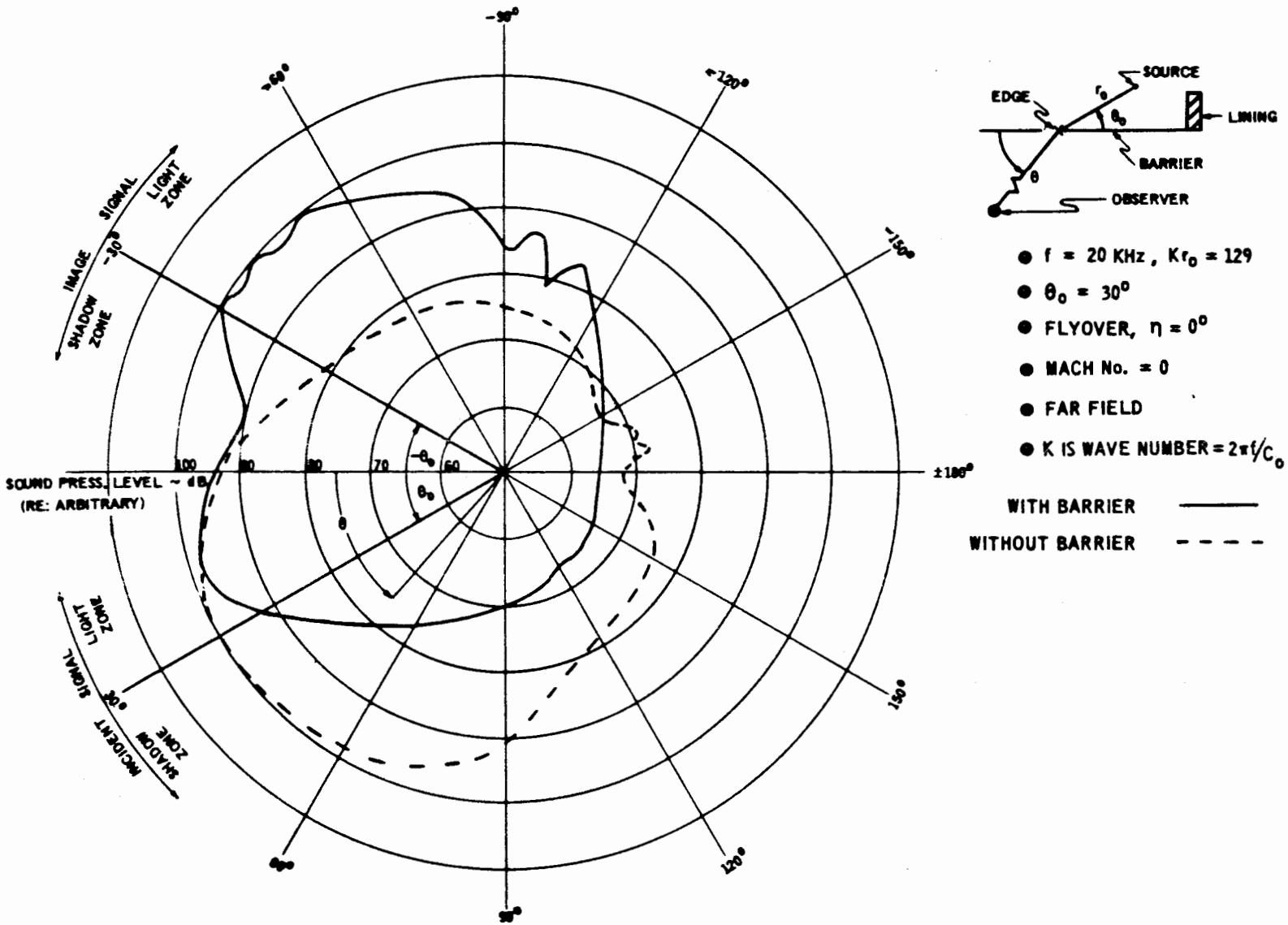

Figure 115.—Sound Field of Directional Source With and Without Acoustical Sound Barrier (Test Data, Blue Room Facility)

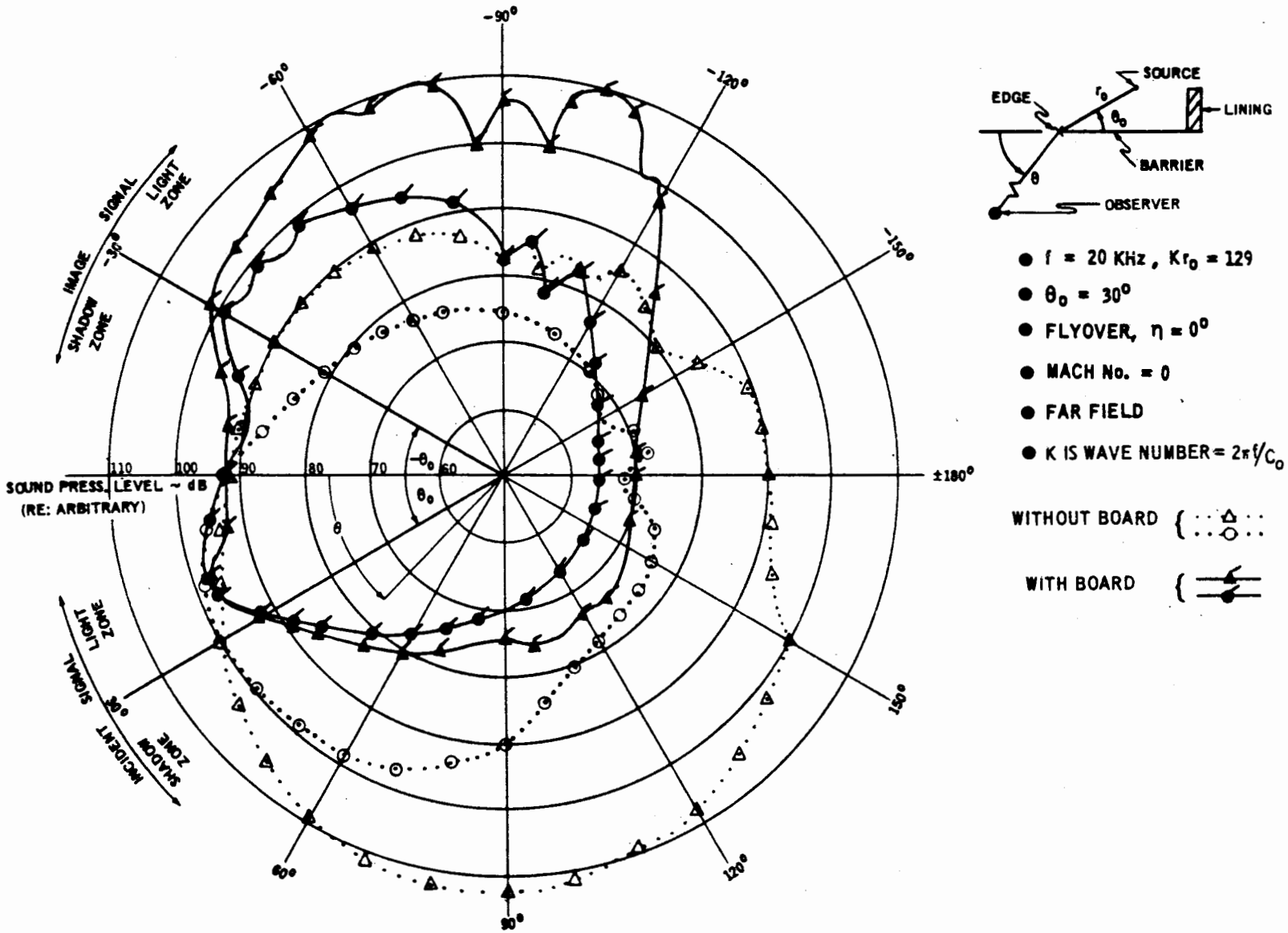

Figure 116.—Effect of Source Directivity on Sound Diffraction (Test Data, Blue Room Facility)

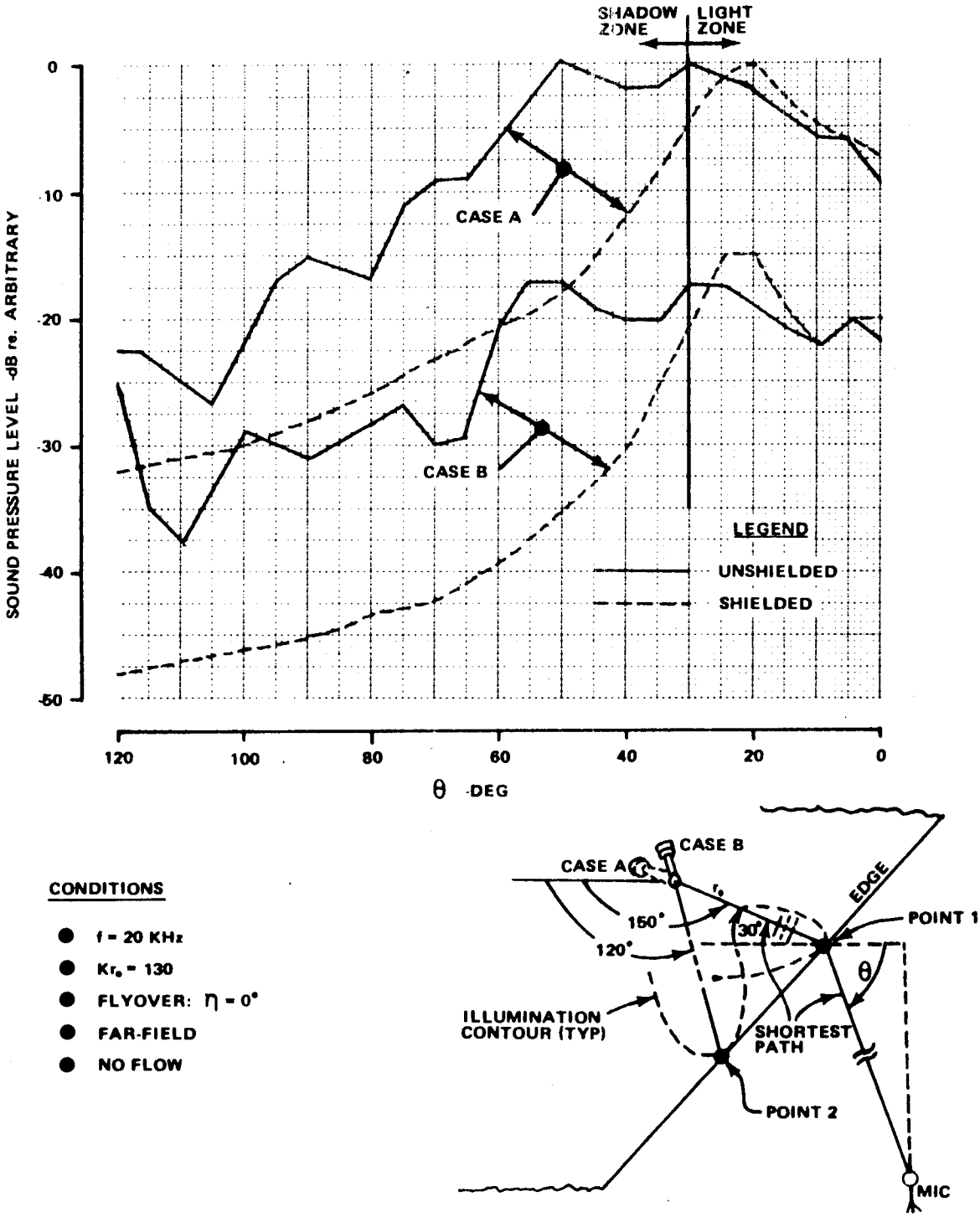

Figure 117.--Directional Source Shielding Test Results in LTC Facility

3. The sound intensity directed toward the edge via the shortest path from source to edge to observer is the proper reference intensity for calculating the diffracted sound in the shadow zone.

The above empirical observations (1, 2, and 3) substantiate the solution for the diffracted far-field sound of a directional source in the presence of a half-plane barrier presented in section 2.2.1.1 (eq. 9).

Comparison between measured and predicted diffracted far-field sound of directional sources showed good agreement for different directivities and frequencies. Figures 119 through 122 are samples of these comparisons for group 1 experiments. Note the agreement between $-80^\circ < \theta < 180^\circ$. The ripples around $\theta = -90^\circ$ are due to diffraction of the image field about the driver stand (see test setup in fig. 46) and are not accounted for in the prediction. No agreement is to be expected between $-180^\circ < \theta < -100^\circ$ because of the presence of the absorptive fiberglass.

Figure 123 shows a similar sample comparison for data from group 2 experiments in the large anechoic chamber. Note that for case B in the sample, the maximum sound intensity illuminating the edge at point 2 is greater than that at point 1, which corresponds to the shortest propagation path between source, edge, and observer.

2.4.1.2 Representation of Wing as Collection of Half-Planes

To develop an EOW noise shielding prediction procedure from the basic diffraction theory, one must account for differences between the idealized half-plane barrier and an actual wing/flap system with multiple edges and gaps between the flaps. For this purpose, configurations using a model wing/flap system as an acoustical barrier were tested as part of the group 1 experiments (see sec. 2.3.1.1).

Principle of Superposition.–Figure 124a addresses the diffraction field about a two-edge flat barrier. Measured total, individual edge diffraction fields, together with the sound field in the absence of the barrier, are shown. In area A, the total diffraction field equals the maximum of the two single-edge related fields. The principle of superposition of edge solutions does not apply for receivers above the barrier. This result is consistent with theory because the sound in area A is largely determined by the direct and image sound fields irrespective of the edge conditions. However, below the barrier surface (area B) the principle of superposition does hold since the total shielded noise appears as the sum of the leading and trailing edge components. The result is again consistent with theory because the flat board barrier tested was not acoustically compact. The distance, L, between each edge is much larger than the wavelength, i.e., $L/\lambda = 36$ at 20 kHz.

Figure 124b shows a comparison similar to that given for the flat board, except the barrier is now a model wing/flap system (see fig. 125 for detail of barrier hardware). For this case, the distance L between the leading and trailing edge is also much larger than the wavelength, i.e., $L/\lambda = 60$ at 20 kHz. Survey of the test results leads to the same conclusions about superposition for a wing/flap system as those previously listed for the flat board.

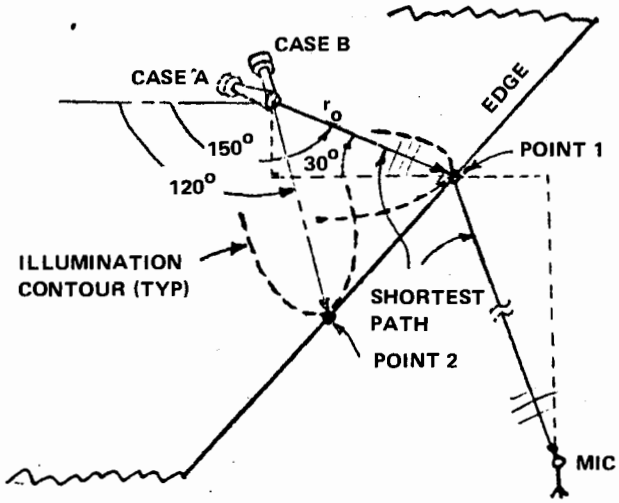

a) TEST SIMULATION OF KEY NOISE LEVELS ALONG BARRIER EDGE

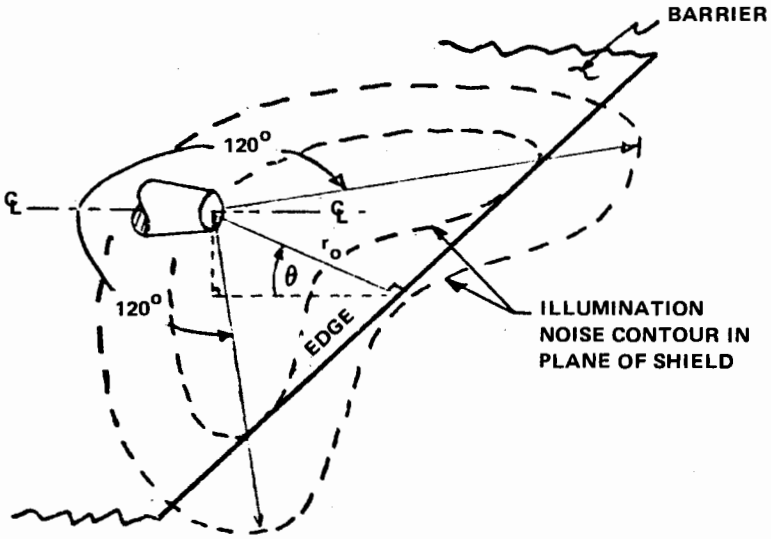

b) TYPICAL TURBOMACHINERY NOISE SOURCE DIRECTIVITY PATTERN

Figure 118.—Compact-Source Simulation of Typical Turbomachinery Noise Source

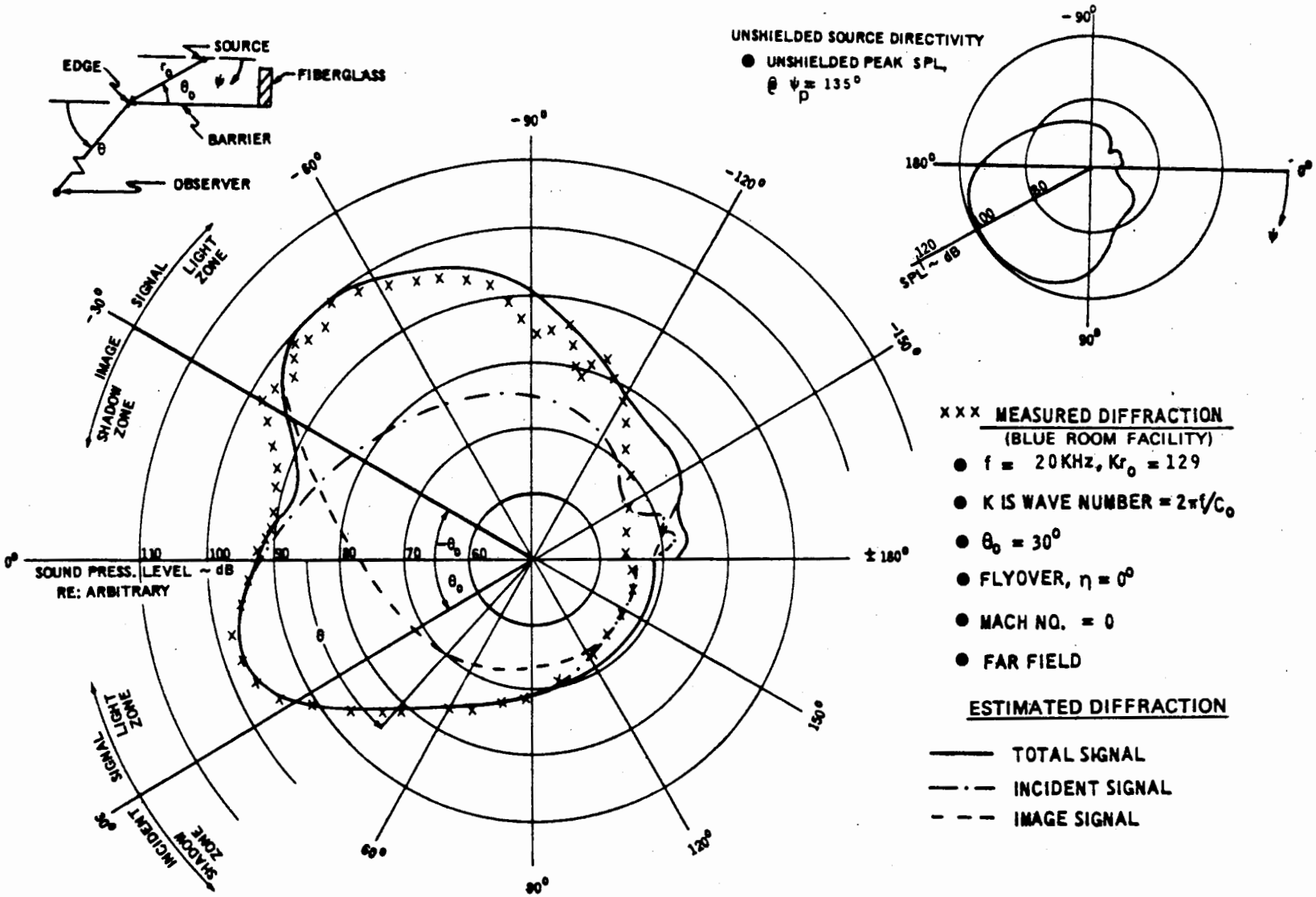

Figure 119.—Comparison of Predicted and Measured Diffraction Far Field of Directional Source (f = 20 kHz and ψ_p = 135°)

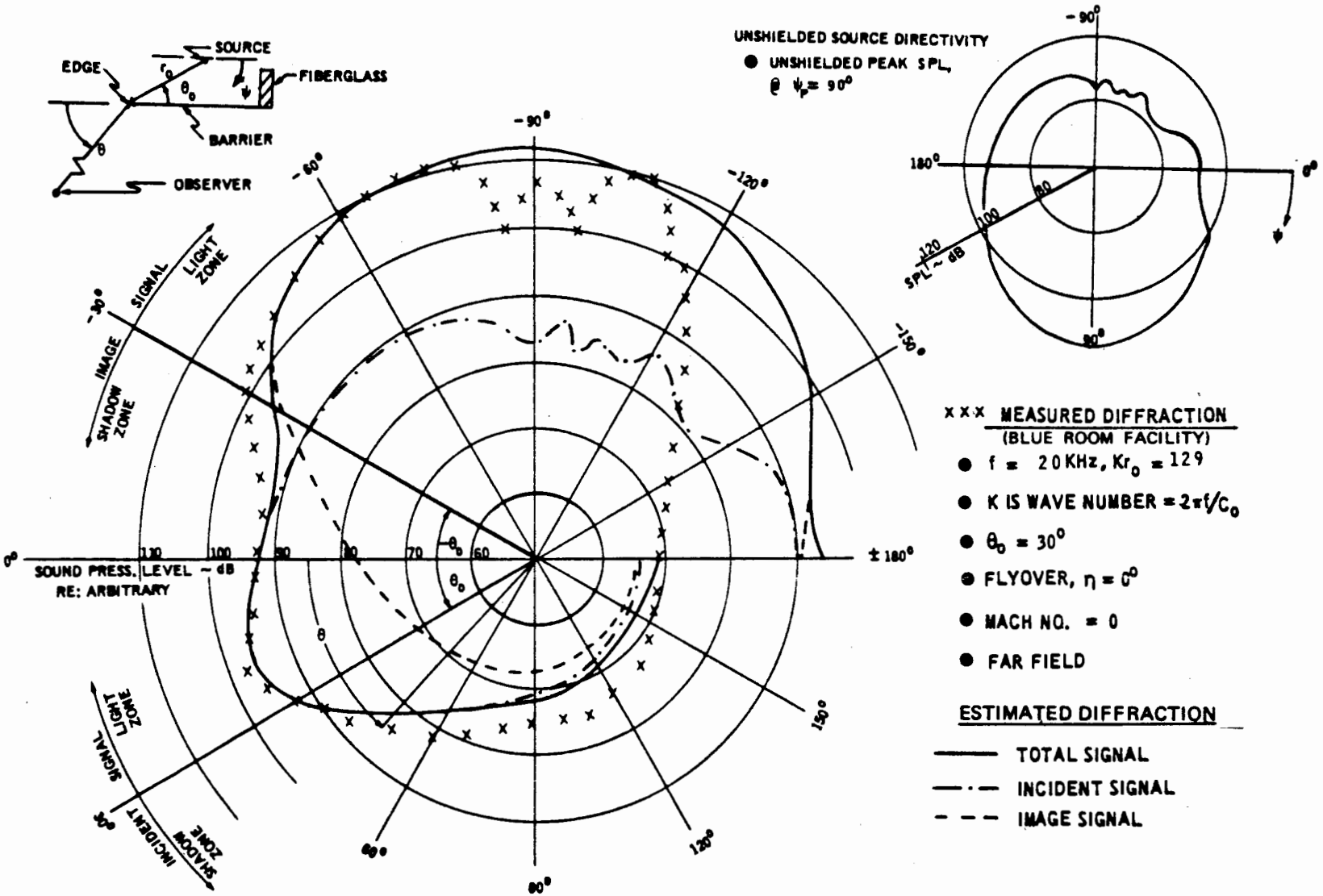

Figure 120.—Comparison of Predicted and Measured Diffraction Far Field of Directional Source ($f = 20$ kHz and $\psi_p = 90°$)

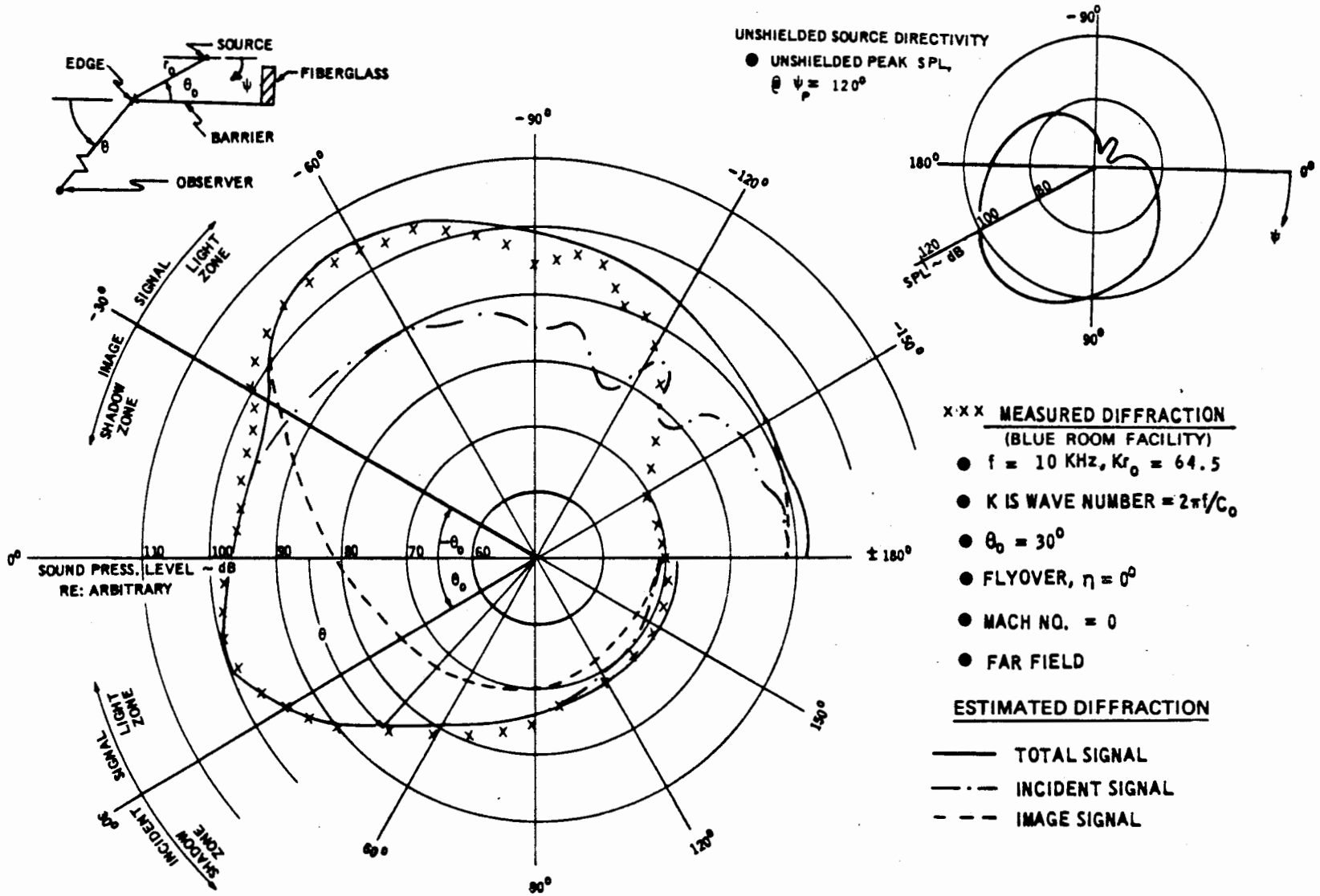

Figure 121.—Comparison of Predicted and Measured Diffraction Far Field of Directional Source ($f = 10$ kHz and $\psi_p = 120°$)

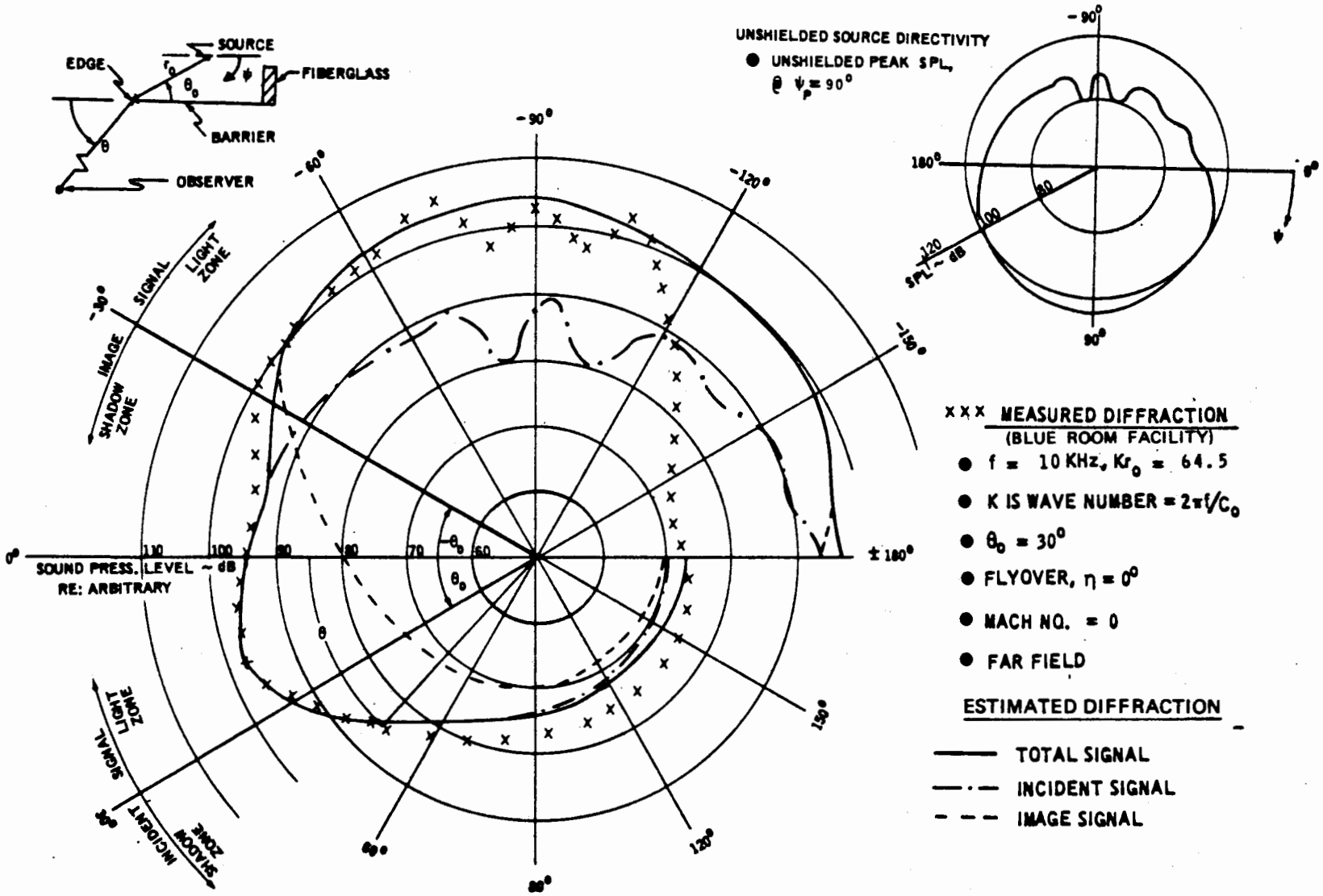

Figure 122.—Comparison of Predicted and Measured Diffraction Far Field of Directional Source ($f = 10$ kHz and $\psi_p = 90°$)

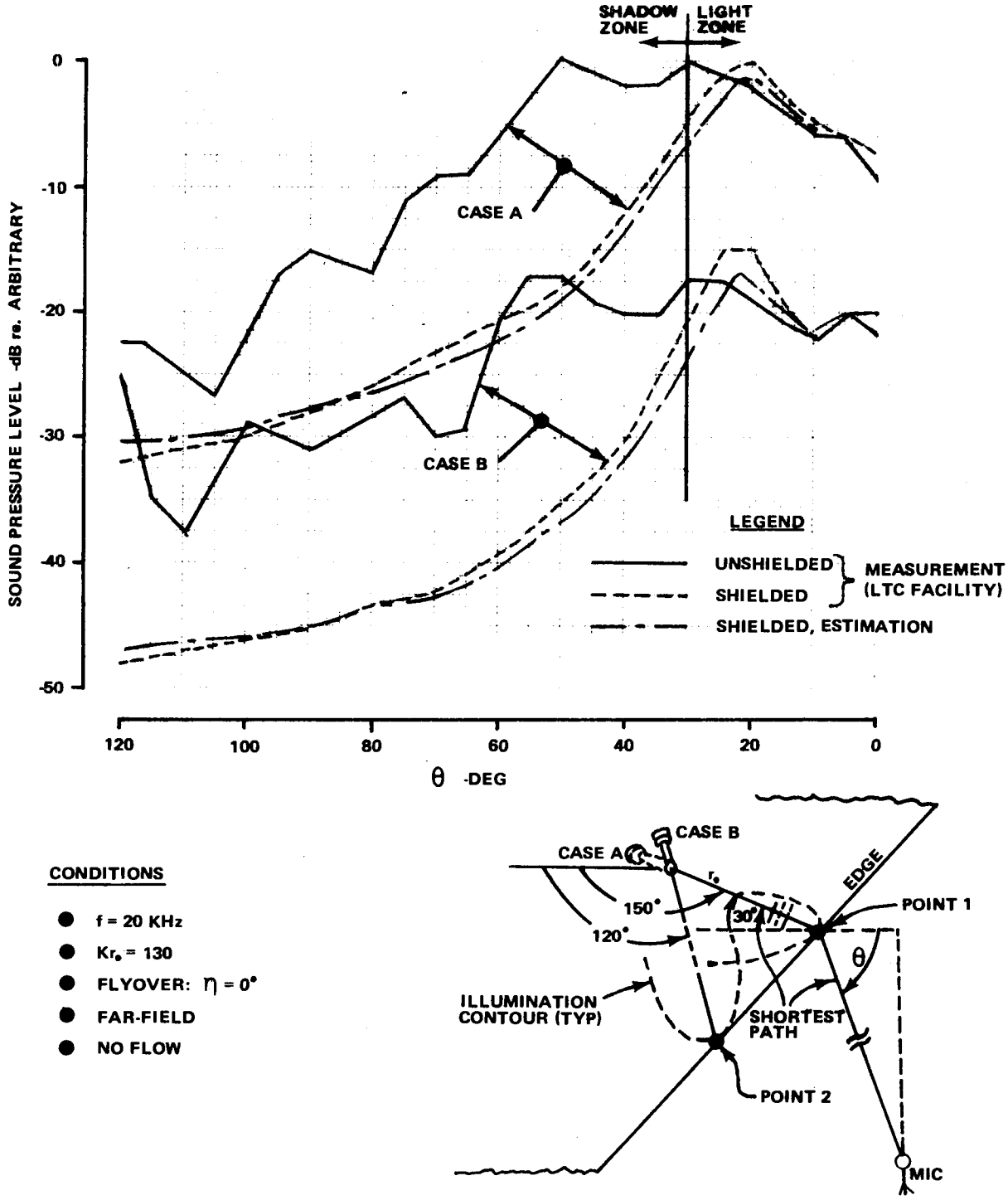

Figure 123.—Comparison of Predicted and Measured Diffraction Far Field of Directional Source

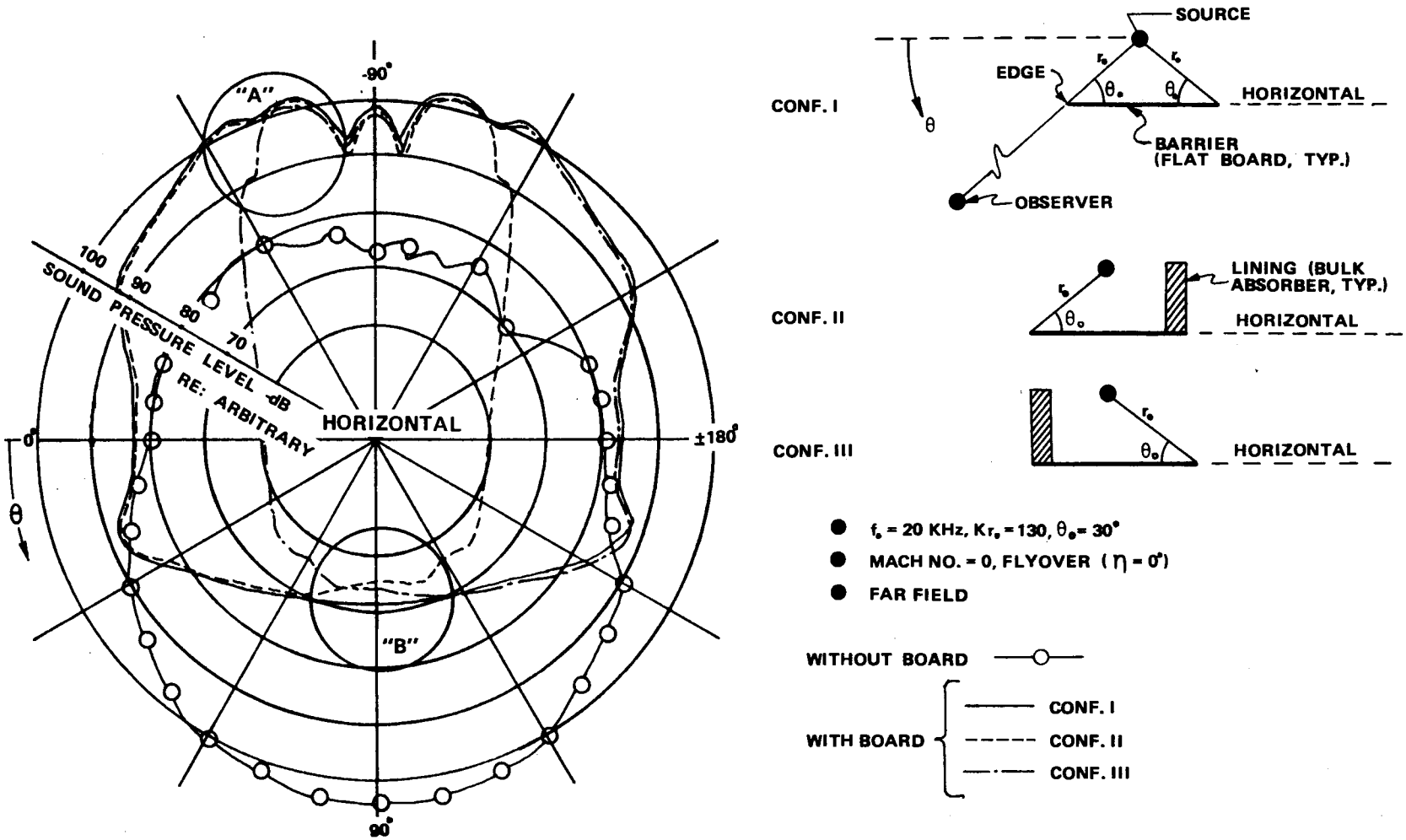

a) FOR TWO-EDGE FLAT BARRIER

Figure 124.—Superposition of Diffraction Components (Test Data, Blue Room Facility)

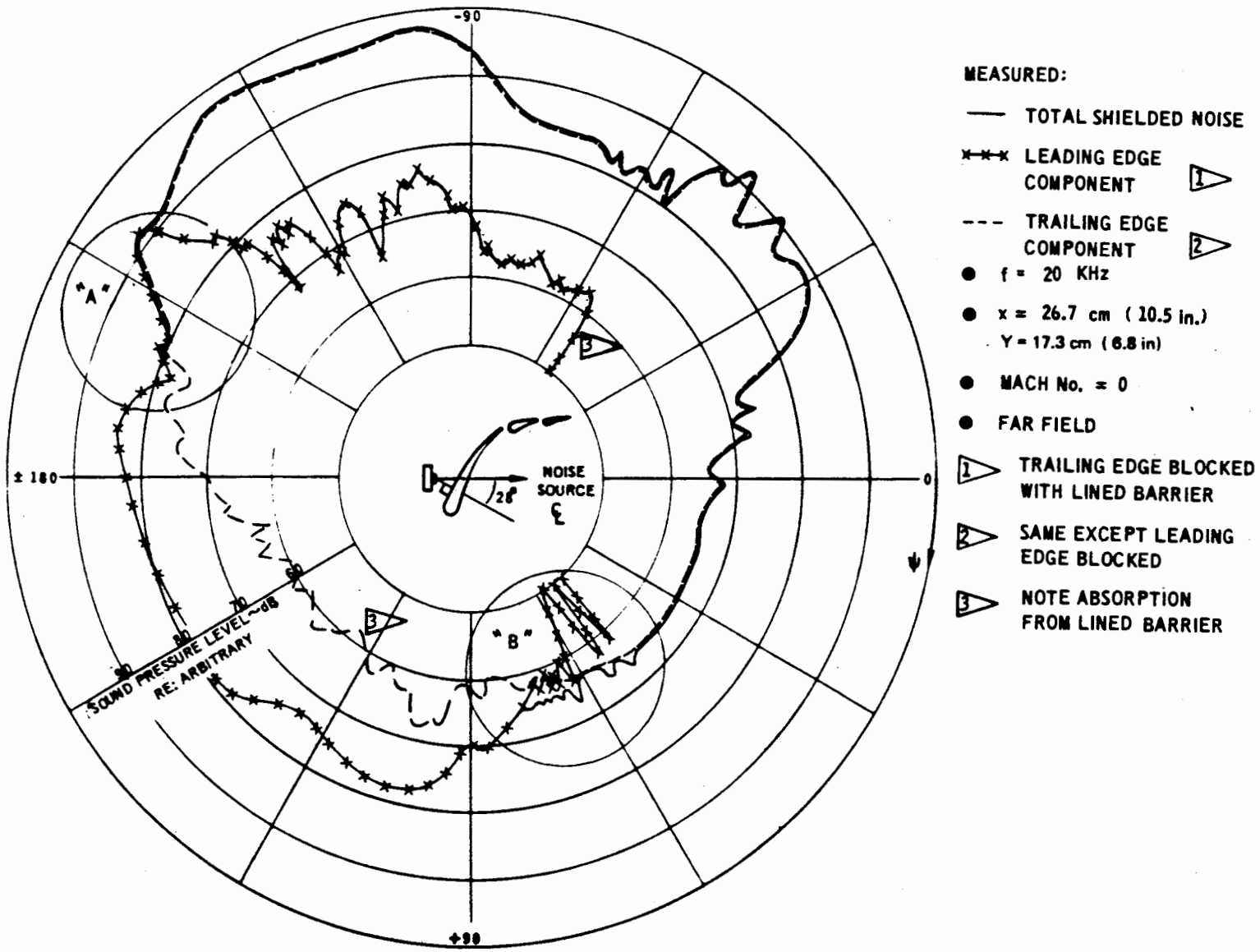

b) FOR WINGLIKE BARRIER

Figure 124.—(Concluded)

a) LEADING AND TRAILING EDGE COMPONENTS

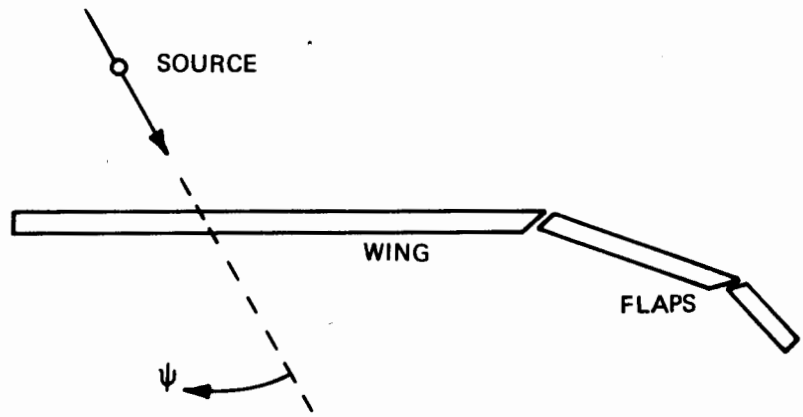

b) LEADING EDGE COMPONENTS ONLY

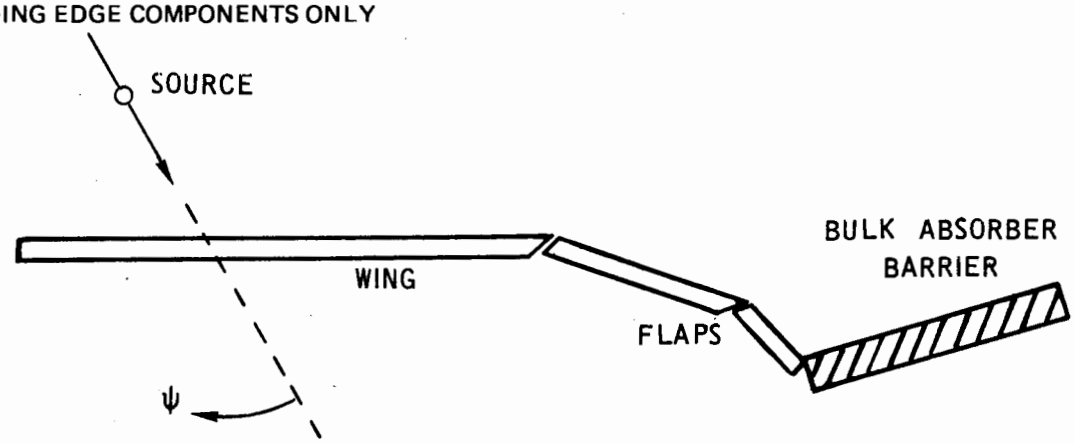

c) TRAILING EDGE COMPONENT ONLY

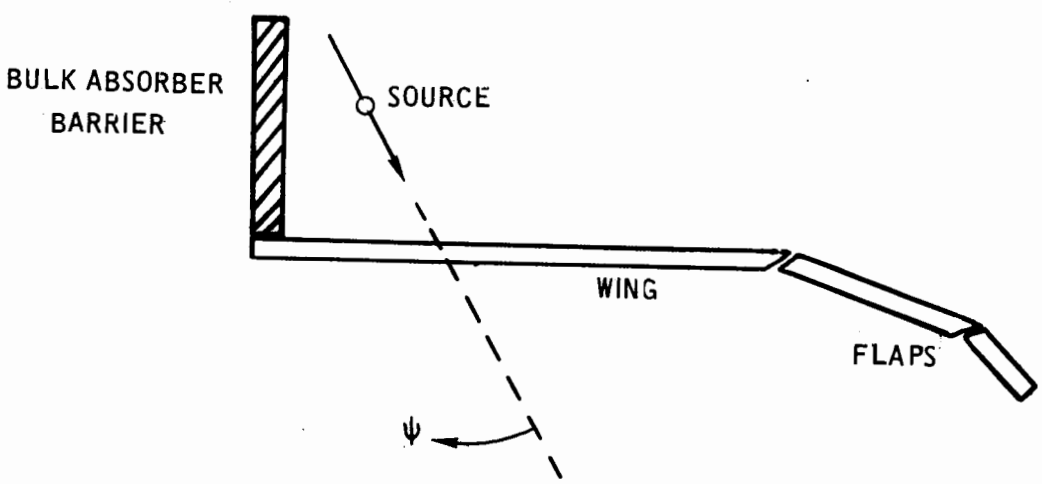

Figure 125.—Configuration Tested to Evaluate Diffraction Around Multiple Edges

Evaluation of Half-Plane Approximations.–Simplified representations are sought for the complicated geometry used in the test series on the simulated double-slotted wing/flap system, e.g., figure 125. Figure 126 shows three candidate half-plane approximations for predicting the shielded noise for this double-slotted wing/flap barrier. Predicted values for each half-plane approximation are compared to test results in figures 127, 128, and 129 for different source frequencies.

Approximation 2 fits the data best in the region above the wing. However, the best approximation in the region below the wing is approximation 1. Since the region below the wing is of primary concern to calculations of community noise levels, approximation 1 is selected for the prediction model for actual EOW installations.

Figures 130 through 133 show the measured free-field directivity, measured shielded data, and the predicted diffraction pattern using the selected half-plane approximation (No. 1). The effect of a variation in source position is shown in figures 130 and 131 for a frequency of 20 kHz. Figures 132 and 133 show the comparison for fixed-source position and different frequencies—10 and 5 kHz, respectively. The overall agreement is fairly good, reinforcing the fact that the dimensionless geometrical parameters presented in the diffraction theory can be used to scale the data. Some disagreement is shown in the deep shadow region, where the measured shielded noise is consistently higher than predicted. This is currently believed to be due to the effect of gaps, addressed briefly in the next section.

It is concluded that the half-plane diffraction theory for a directional sound source can be extended to model and estimate the community noise shielding by wing/flap barrier geometries. Figure 134 illustrates the modeling process as described below.

1. The wing/flap system is represented by two half-planes: one defined by a point on the wing surface directly beneath the source and the line corresponding to the wing's leading edge and the other defined by a point on the wing surface directly beneath the source and the line corresponding to the most aft trailing edge of the wing/flap system.

2. Reference leading and trailing edge noise levels are determined by source directivity. The total diffracted field beneath the wing is a superposition of the leading edge and trailing edge diffraction solutions corresponding to each of the half-plane approximating barriers. This approximation of a wing using half-plane theory for multiple-edge barriers is valid as long as the wing is not acoustically compact.

2.4.1.3 Effect of Flap Gaps

Figure 135 shows a typical comparison between estimations and data from group 1 experiments on wing shielding of compact sound sources. The shaded region in the figure shows disagreement between measurement and estimation. Additional measurements were made in the sector $90^0 \leq \psi \leq 140^0$ with the flap gaps sealed. Comparison of data for gaps open and gaps closed shows that the loss of shielding effectiveness is due to noise "leaking" through the gaps. Such a loss of shielding

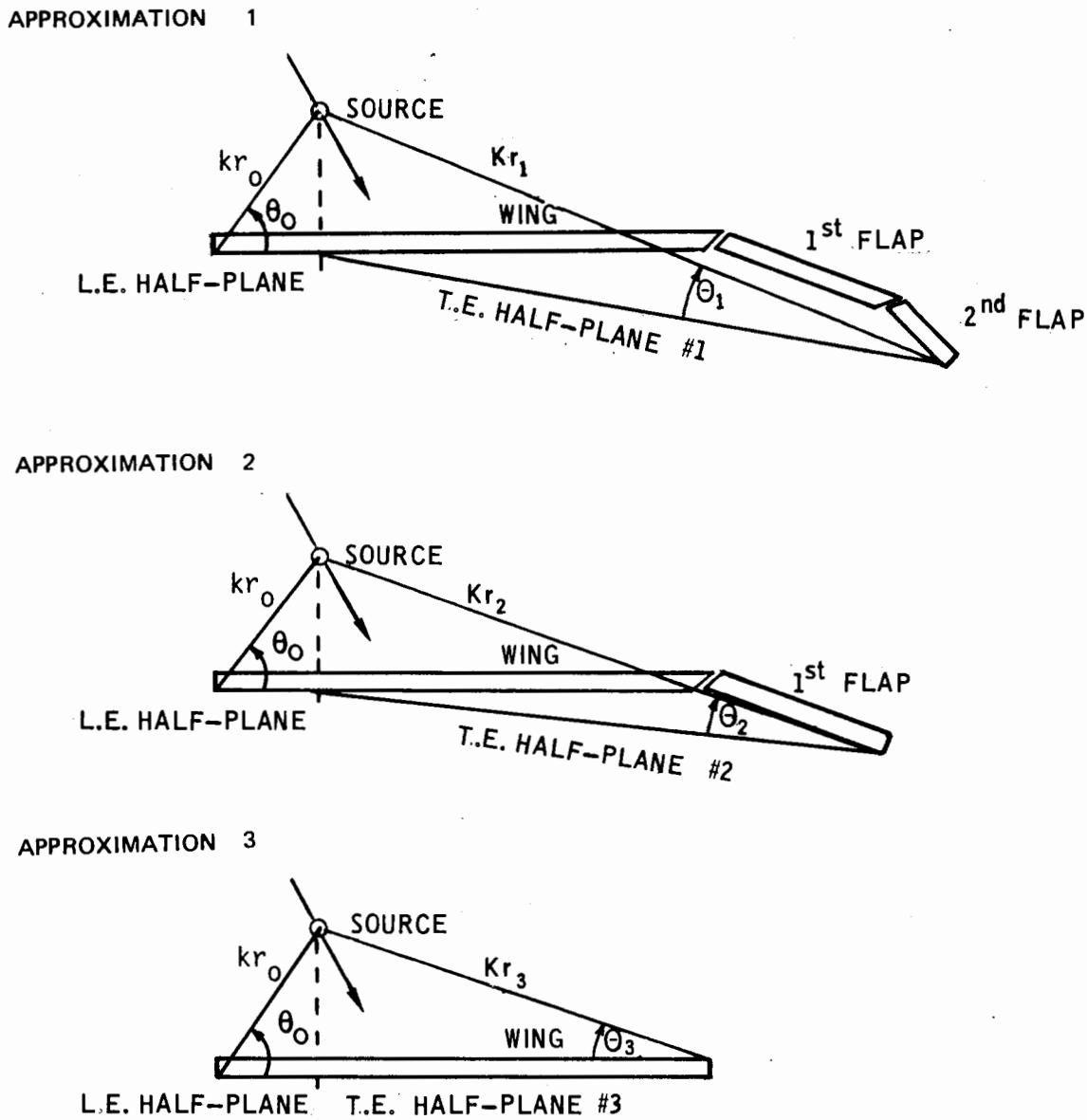

Figure 126.—Theoretical Half-Plane Evaluation Configurations

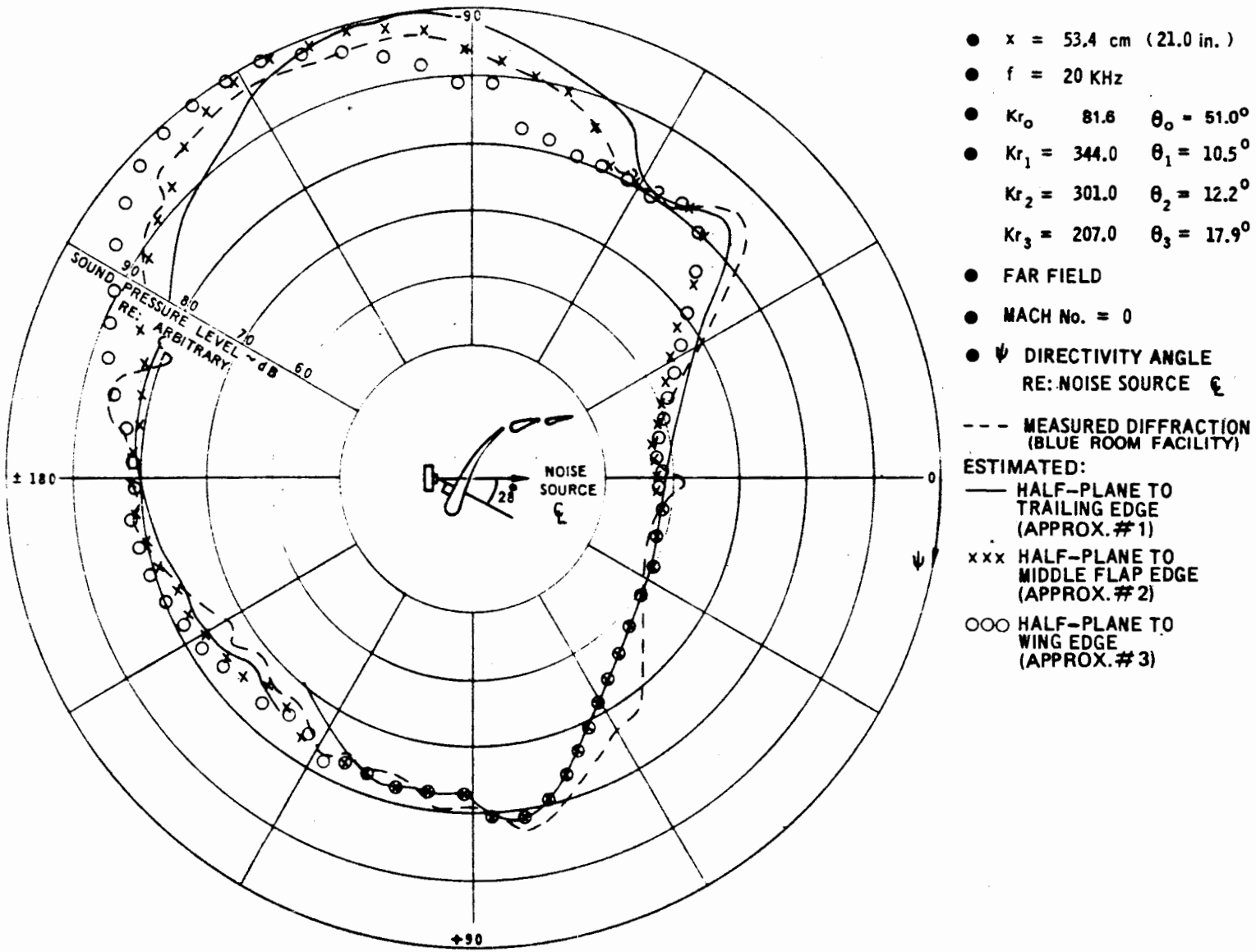

Figure 127.—Evaluation of Half-Plane Approximations, f = 20 kHz

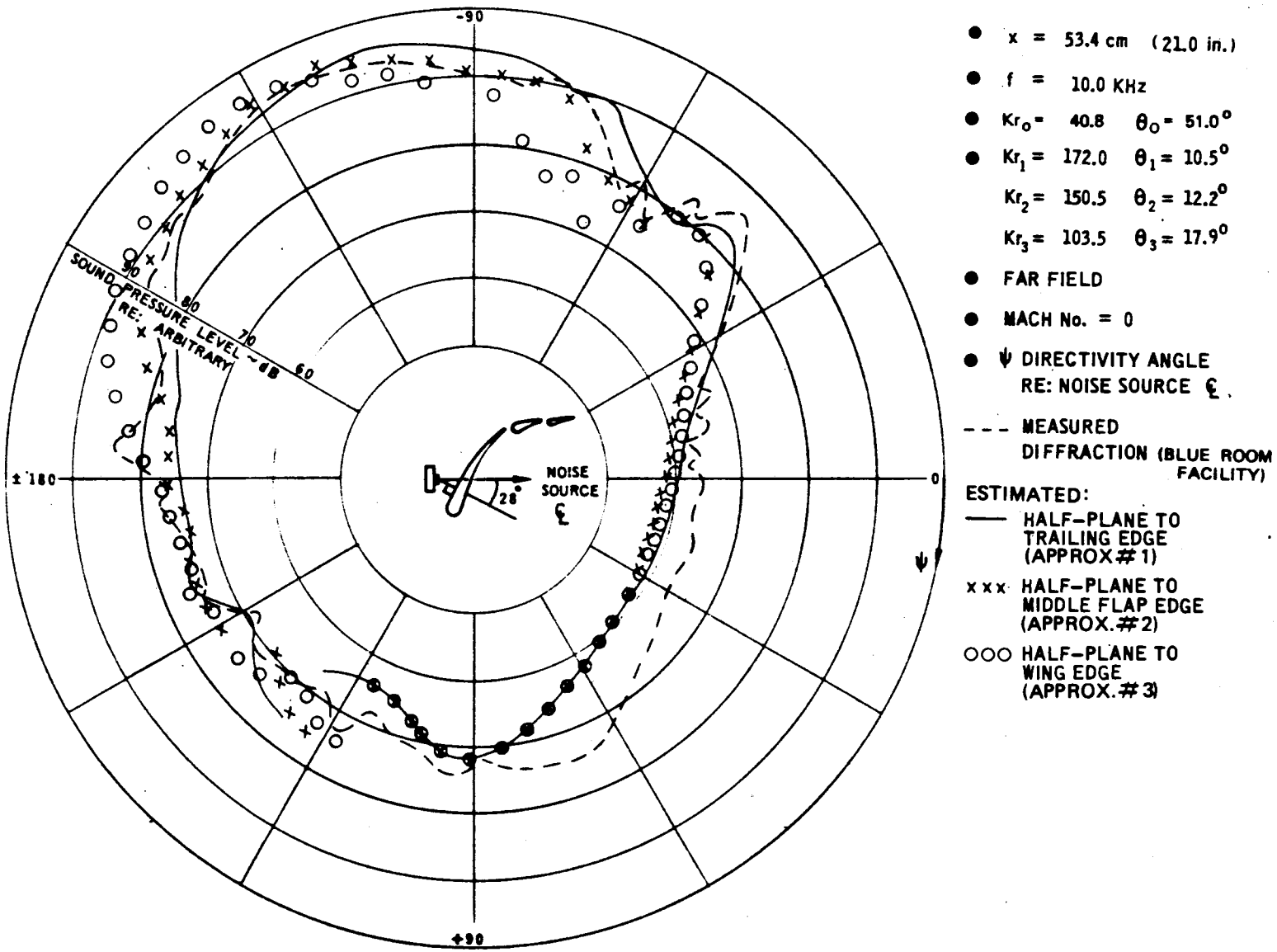

Figure 128.—Evaluation of Half-Plane Approximations, f = 10 kHz

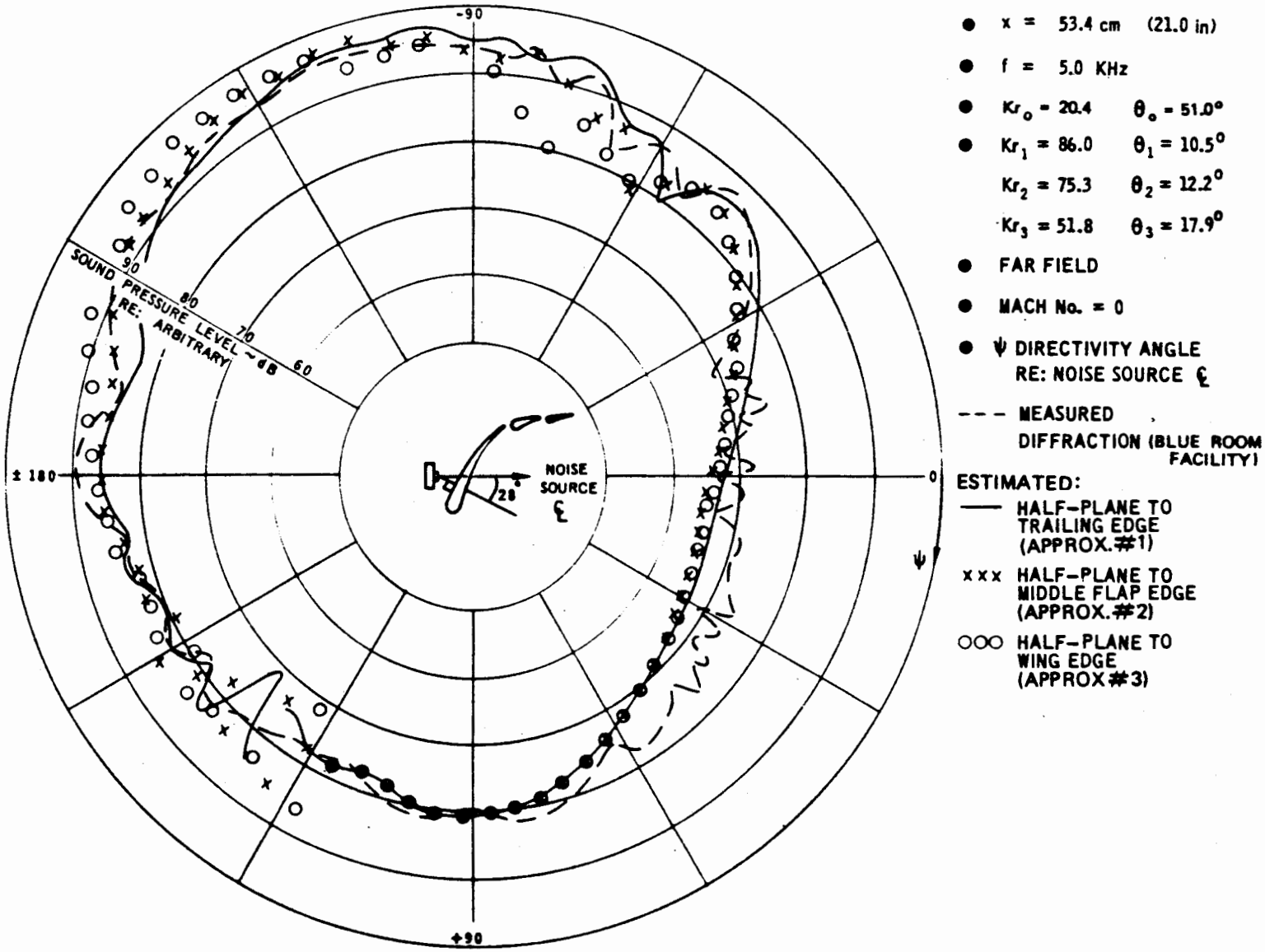

Figure 129.—Evaluation of Half-Plane Approximations, f = 5 kHz

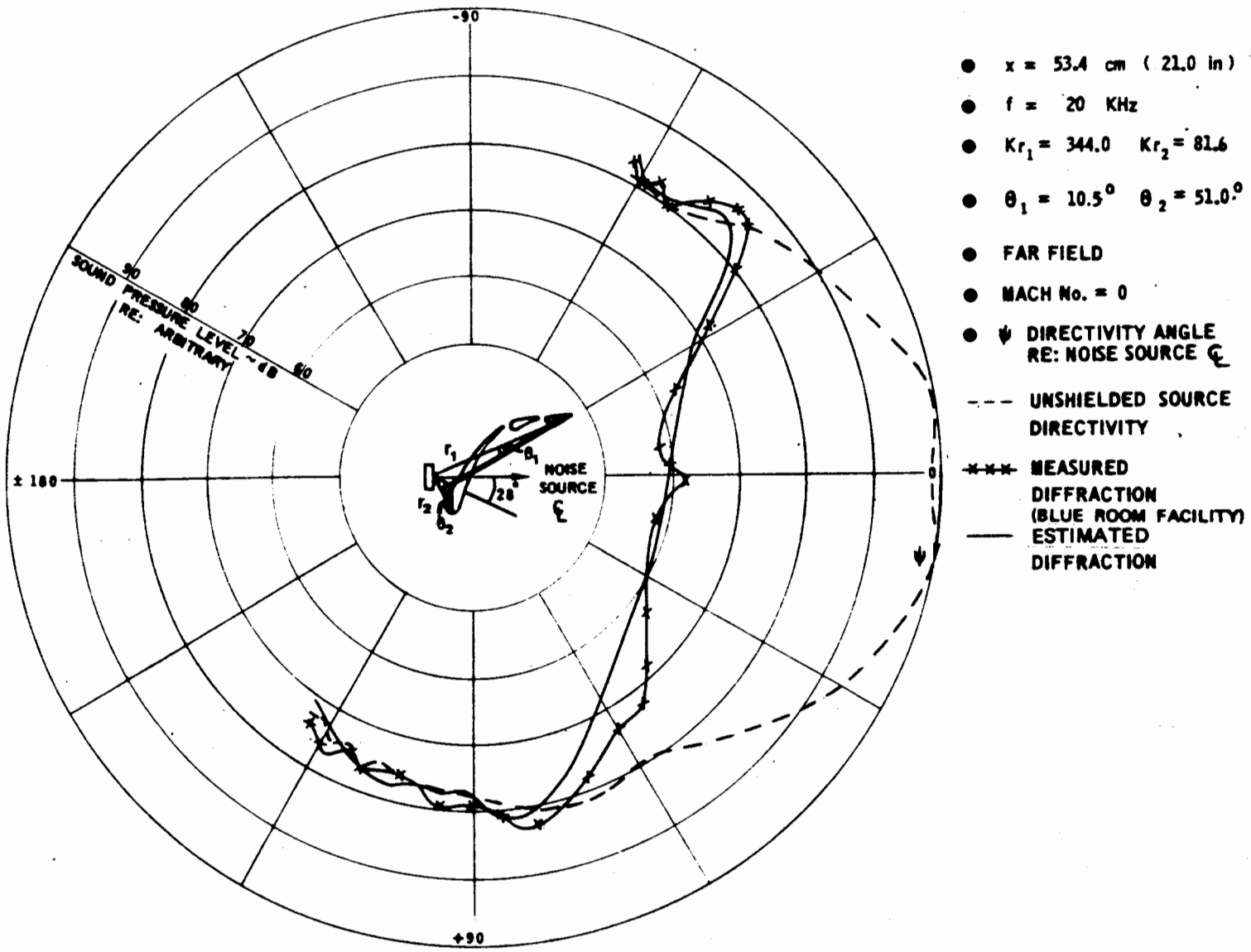

Figure 130.—Sound Diffraction About Model Wing, X = 53.4 cm, f = 20 kHz

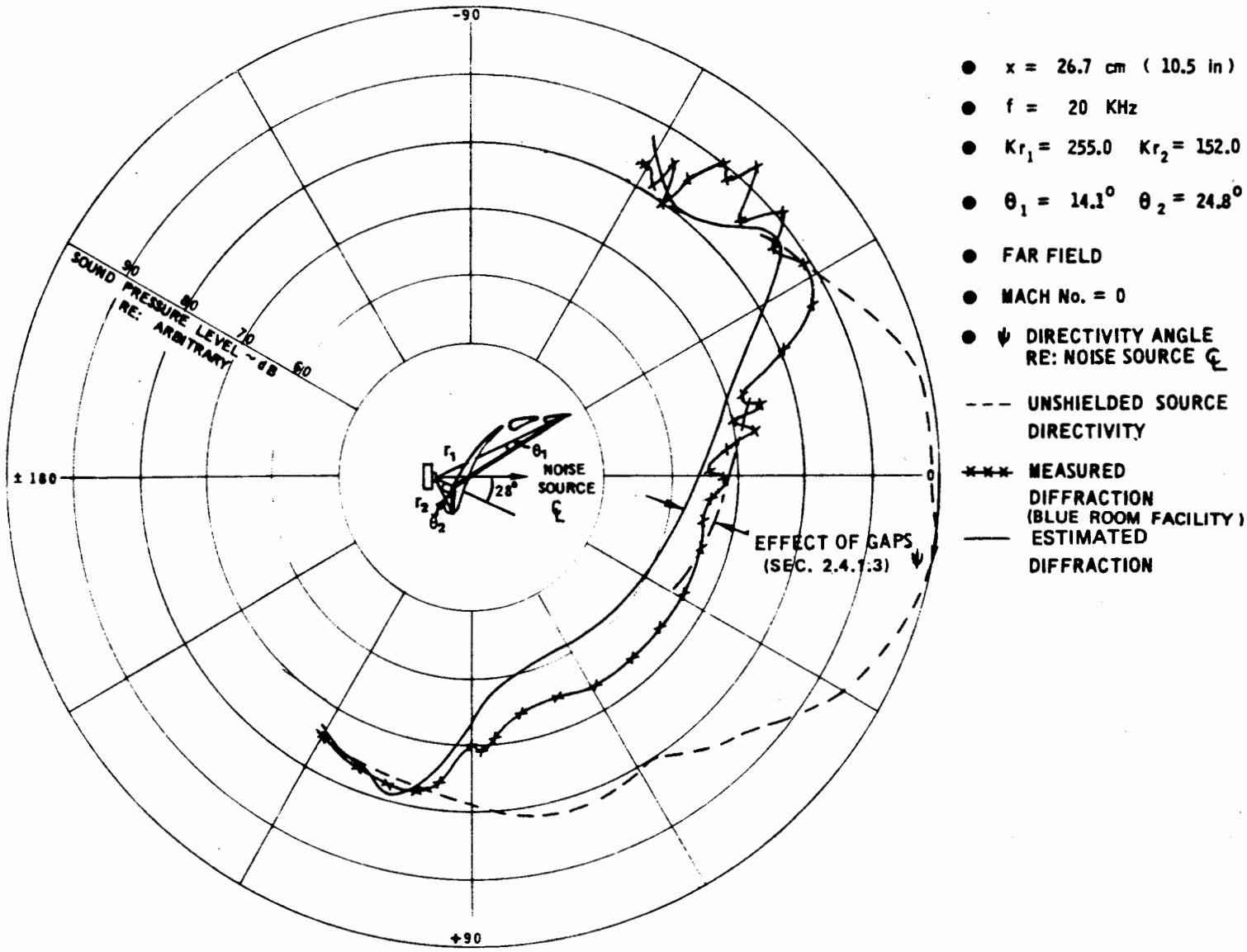

Figure 131.—Sound Diffraction About Model Wing, X = 26.7 cm, f = 20 kHz

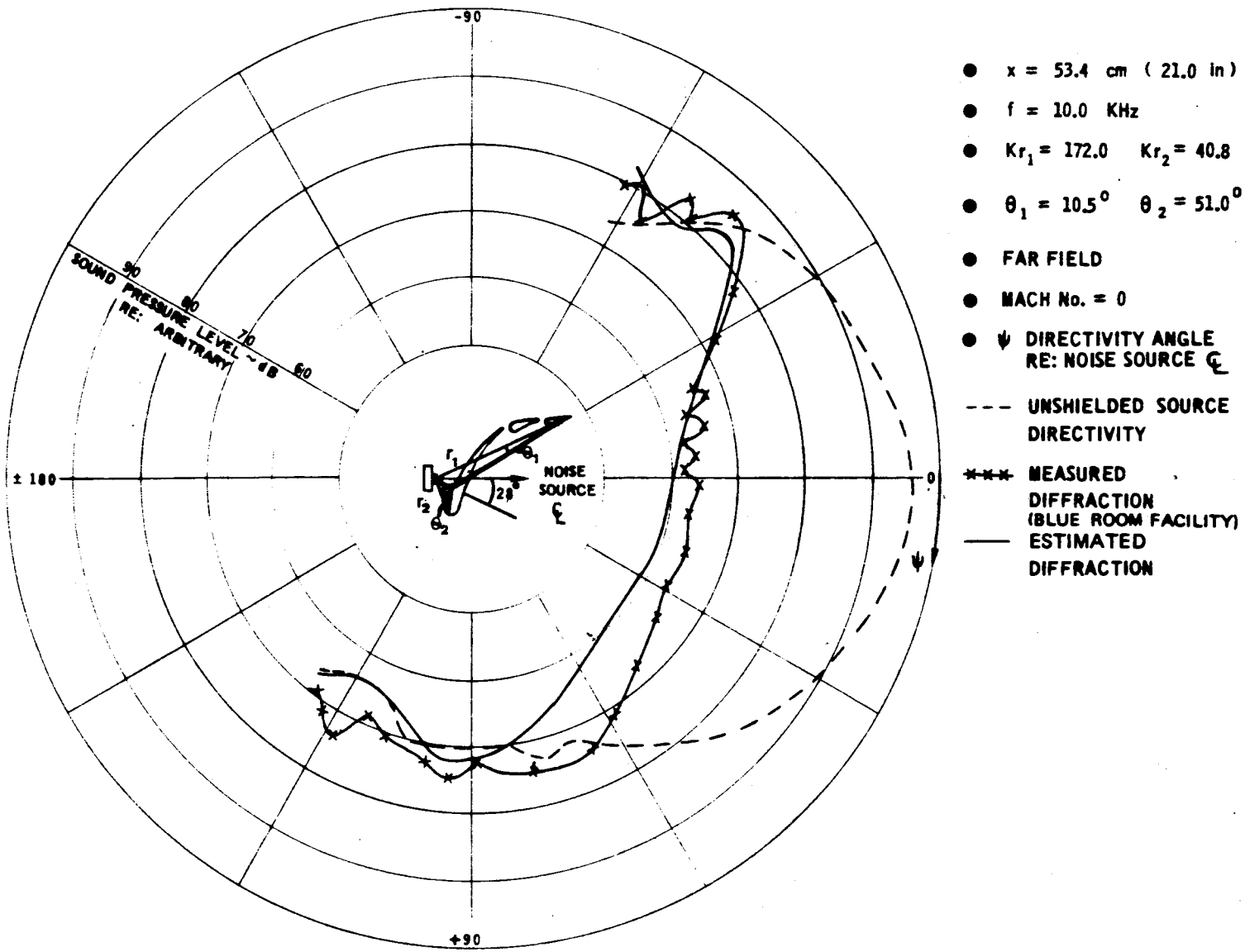

Figure 132.—Sound Diffraction About Model Wing, X = 53.4 cm, f = 10 kHz

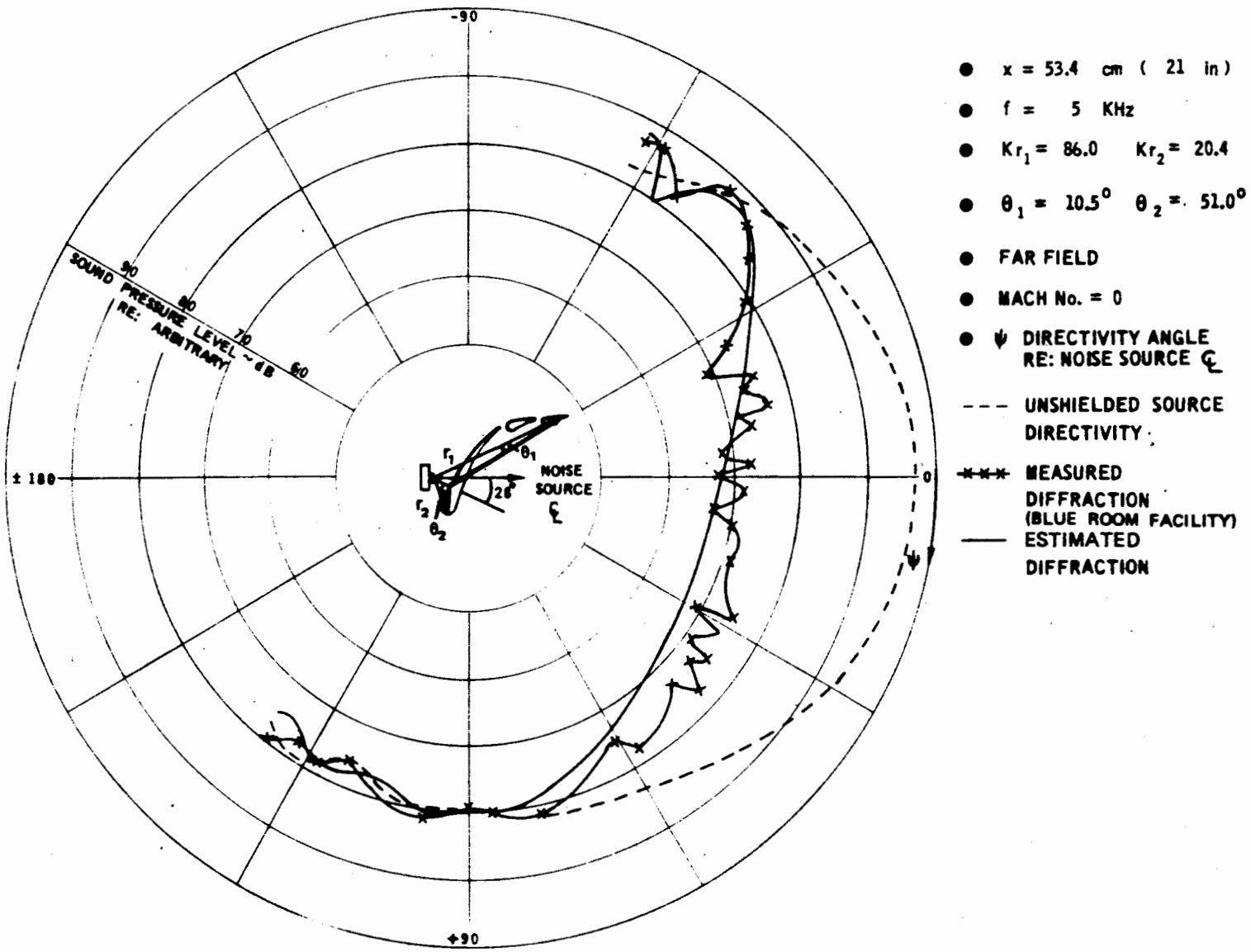

Figure 133.—Sound Diffraction About Model Wing, X = 53.4 cm, f = 5 kHz

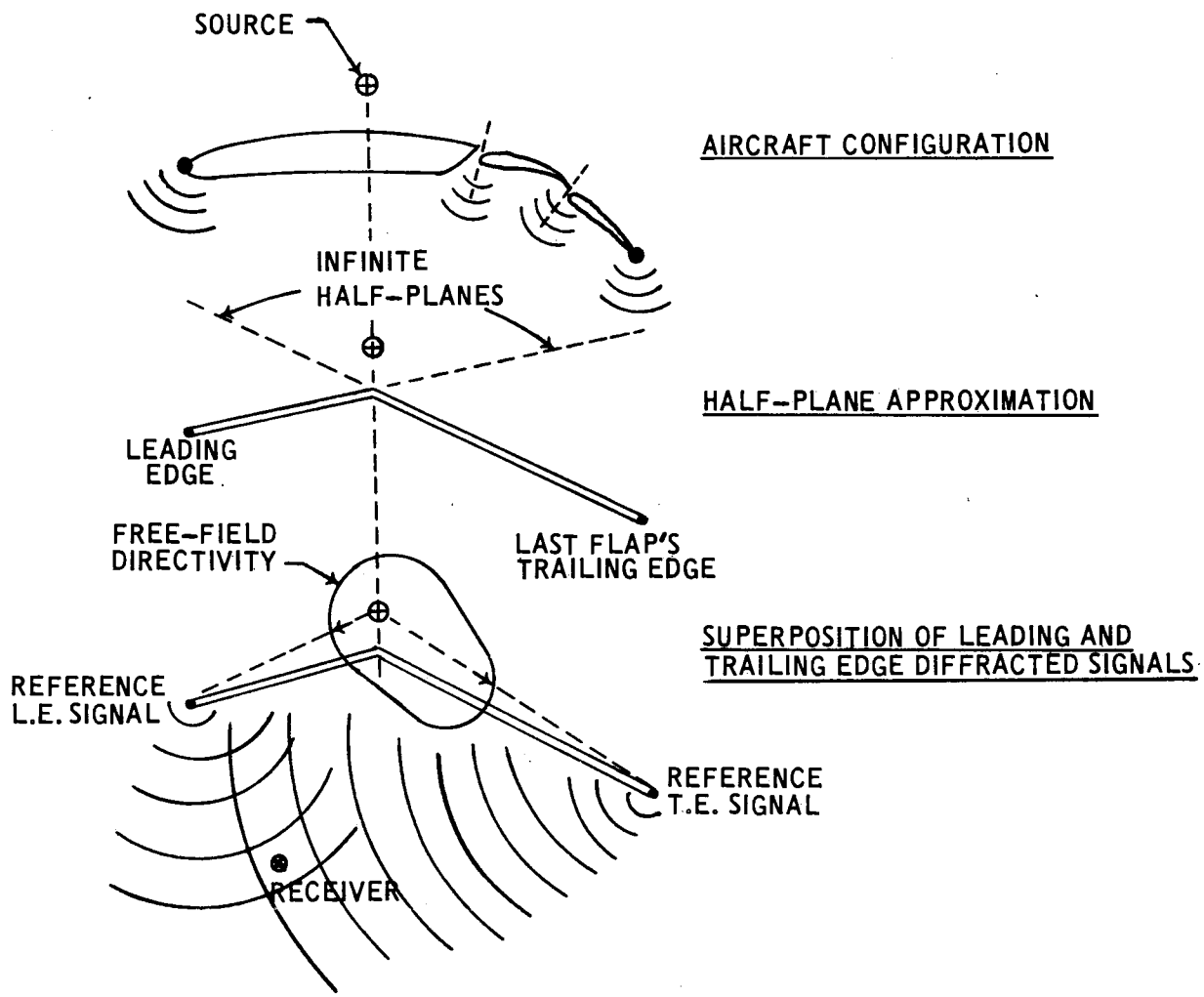

Figure 134.—Application of Half-Plane Diffraction Theory for a Directional Source Near a Wing/Flap System

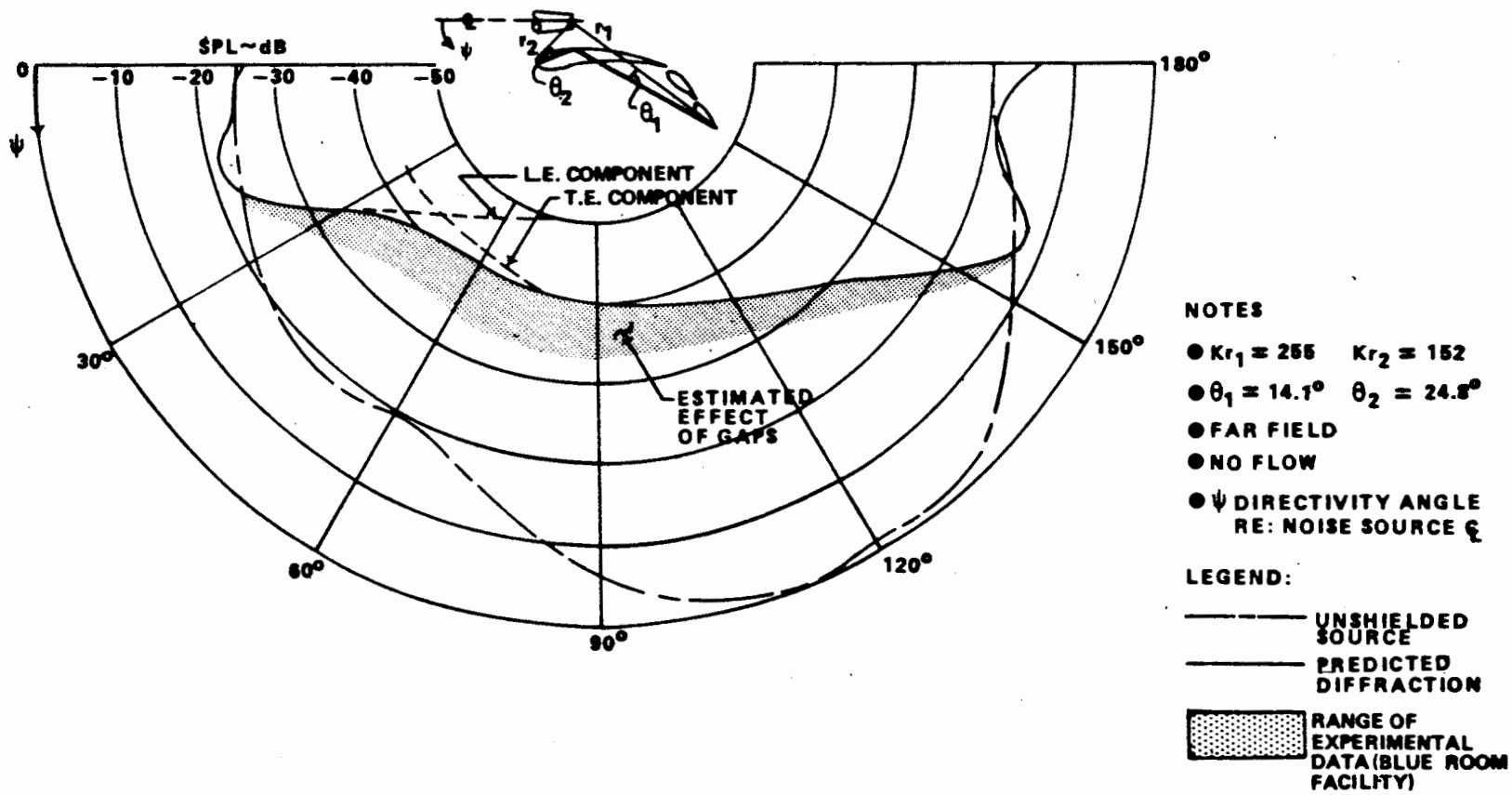

Figure 135.—Sample Sound Diffraction About Wing/Flap System

attenuation can be expected due to the test configuration geometry; i.e., the gaps are straight slots through which the noise can propagate (see fig. 136). The magnitude of the disagreement (effect of gaps) decreased as the sound source was moved further forward away from the gaps, as indicated by the open circled points for the source position in figure 136 (compare figs. 130 and 131). These tests were run statically, with no airflow about the wing. However, during flight there is flow. Also, flap gaps are usually designed with no direct line-of-sight propagation path. Flow effects were considered in a second test reported in section 2.3.1.3. Test data taken with jet flow over a model wing/flap system show that the effects of gaps are negligible, i.e., within normal acoustic data scatter, in the region below the wing. Therefore, the noise shielding loss due to gaps has not been incorporated into the final prediction procedure developed for this contract.

2.4.1.4 Shielding of Broadband Versus Narrowband Noise

Figure 137 shows a comparison of a broadband and discrete tone diffraction field from group 1 experiments on shielding of a compact sound source (see sec. 2.3.1.1). Although there is some "jitter" in the broadband measured data, it appears that the frequency averaging which occurs in the measurement for the broadband noise source has smoothed out the large interference variations that occurred in the pure tone source diffraction pattern. This substantiates the theory previously discussed in section 2.2.1.3.

2.4.1.5 Shielding by a Cylindrical Body

To evaluate noise shielding by a cylindrical body, a very simple model test was conducted in the blue room quasi-anechoic chamber as part of group 1 experiments. A loudspeaker was used as the source and an aluminum cylinder was used to represent an aircraft's fuselage (see test description in sec. 2.3.1.1).

Characteristics of this test were:

- Static, homogeneous medium
- Source size small with respect to cylinder diameter
- Omnidirectional source, at least in the region that influences the sound in the shadow zone (see fig. 138)

Note that these characteristics correspond closely to the hypothesis of the theoretical model described in section 2.2.2.1.

Figures 139 and 140 show a sample comparison between measured data and theoretical calculation. The regions of constructive and destructive interference predicted by theory agree quite well with the data. However, in the shadow zone of the cylinder, the measured noise reduction due to shielding is less (0 to 5 dB) than predicted (see also fig. 141). Possible reasons for this discrepancy are:

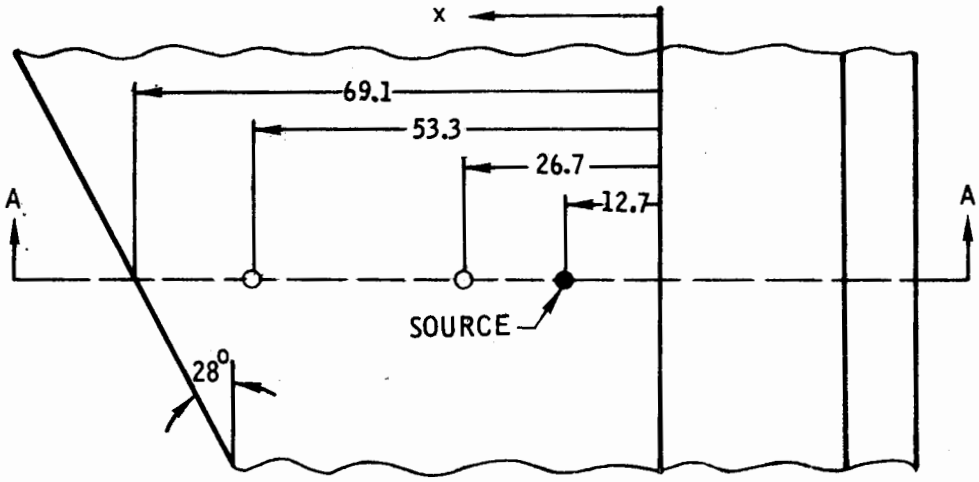

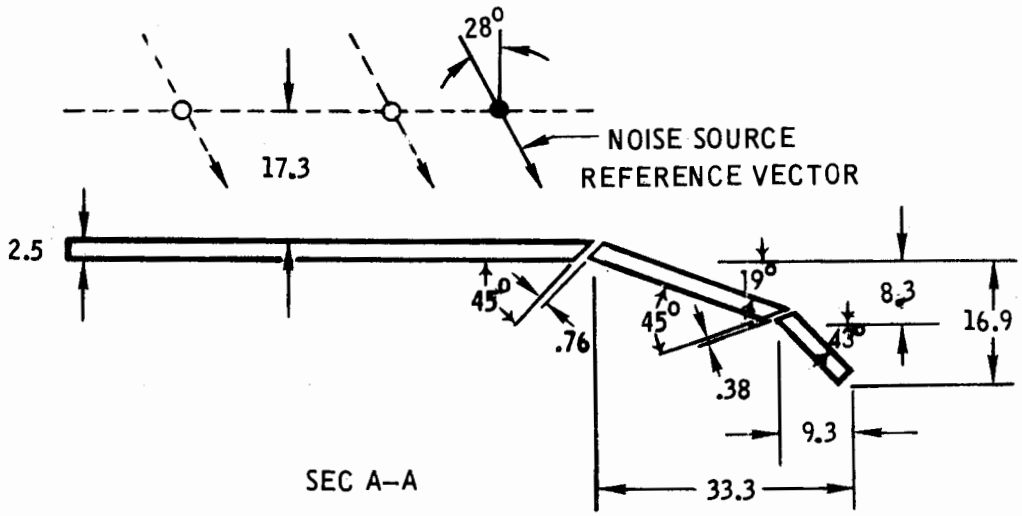

NOTES

- DIMENSIONS IN CM.
- MICROPHONE ARC IN "A–A" PLANE AT 183 CM FROM SOURCE
- SOURCE: ALTEC 3000H DRIVER

Figure 136.—Source/Wing Test Geometry

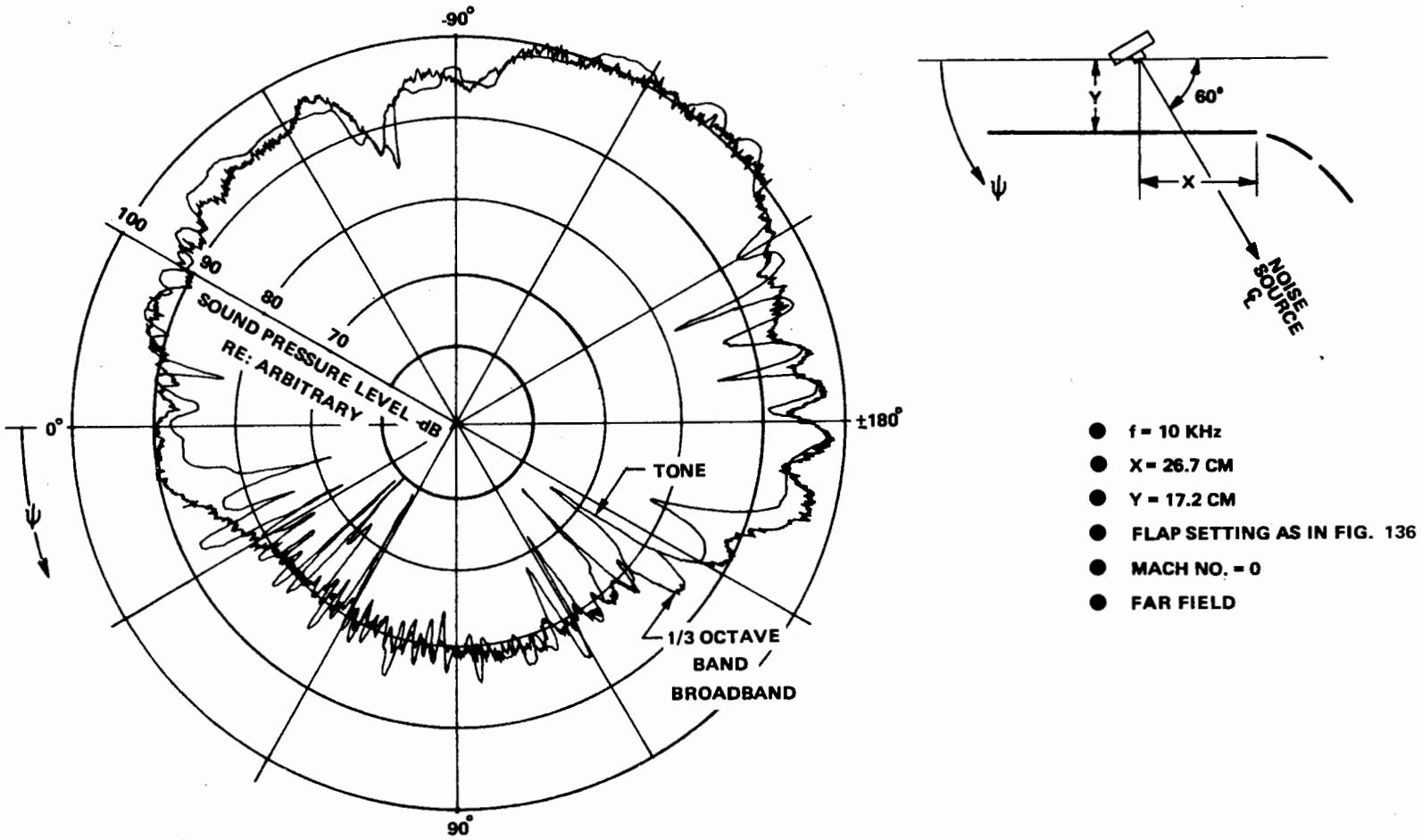

Figure 137.—Comparison of Broadband and Tone Sound Diffraction Field (Test Data, Blue Room Facility)

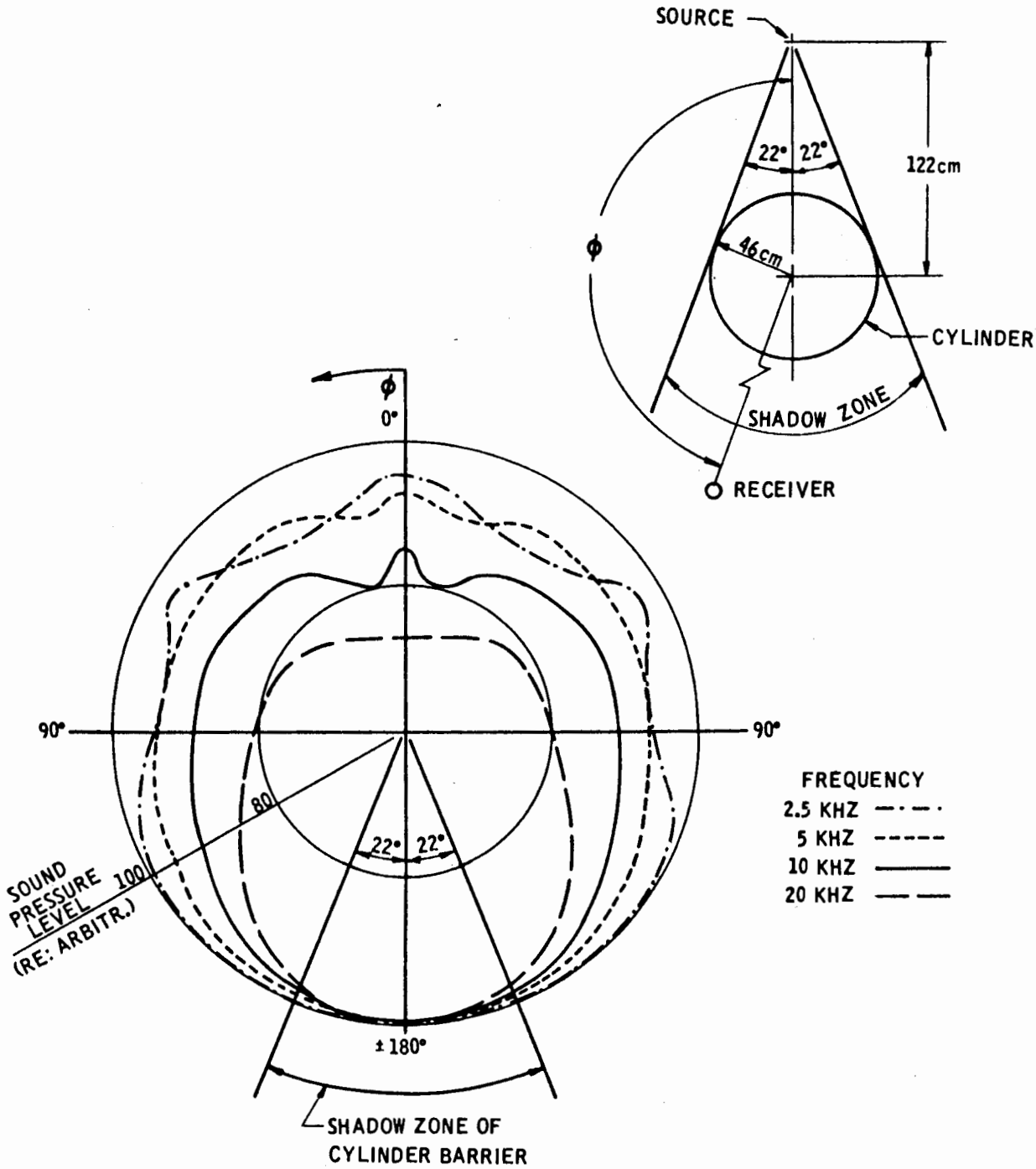

Figure 138.—Free-Field Sound Source Directivity and Cylinder Diffraction Test Geometry

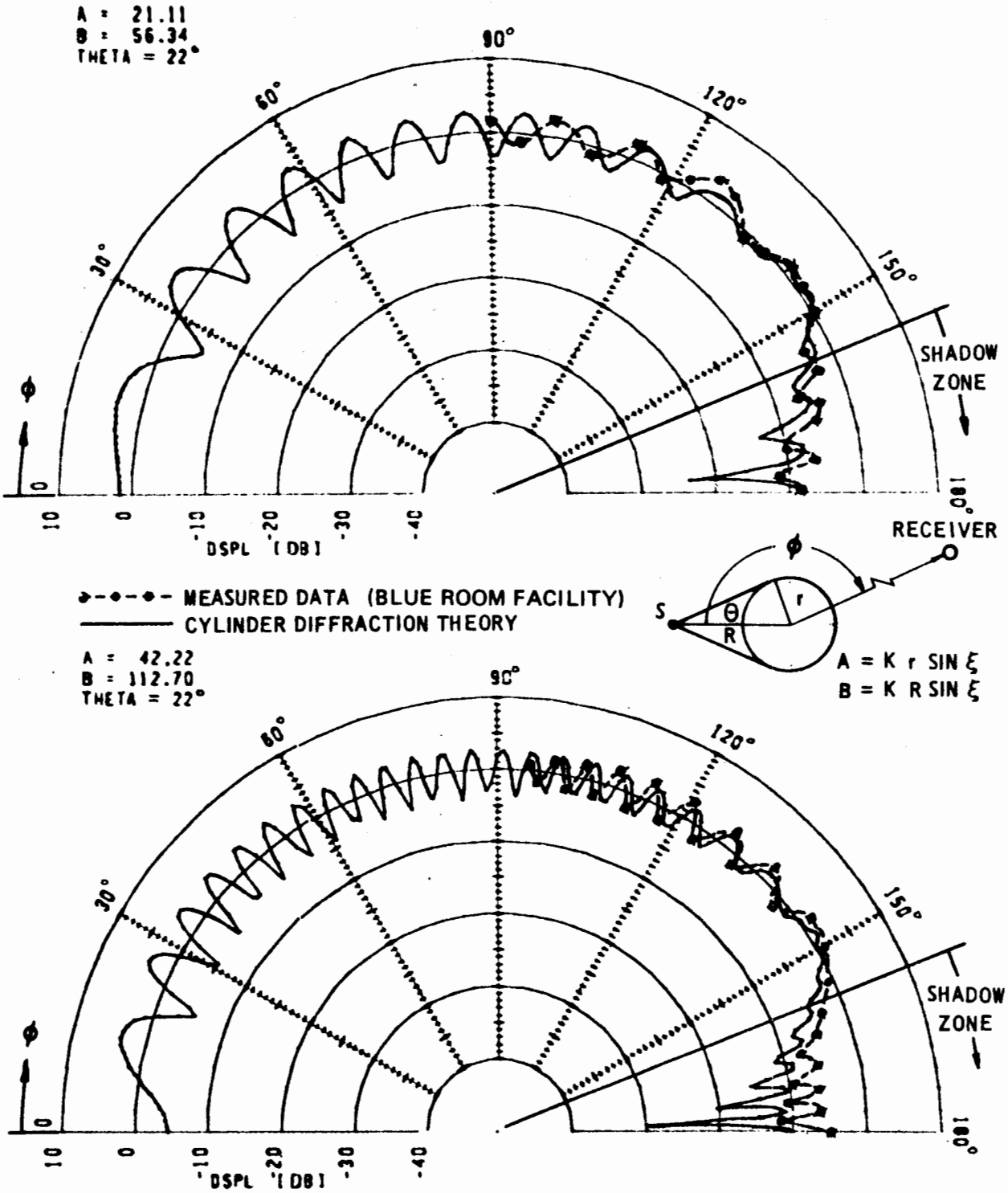

Figure 139.—Cylinder Diffraction Theory Versus Measurement (Quasi-Anechoic Chamber Test), f = 2.5 and 5 kHz

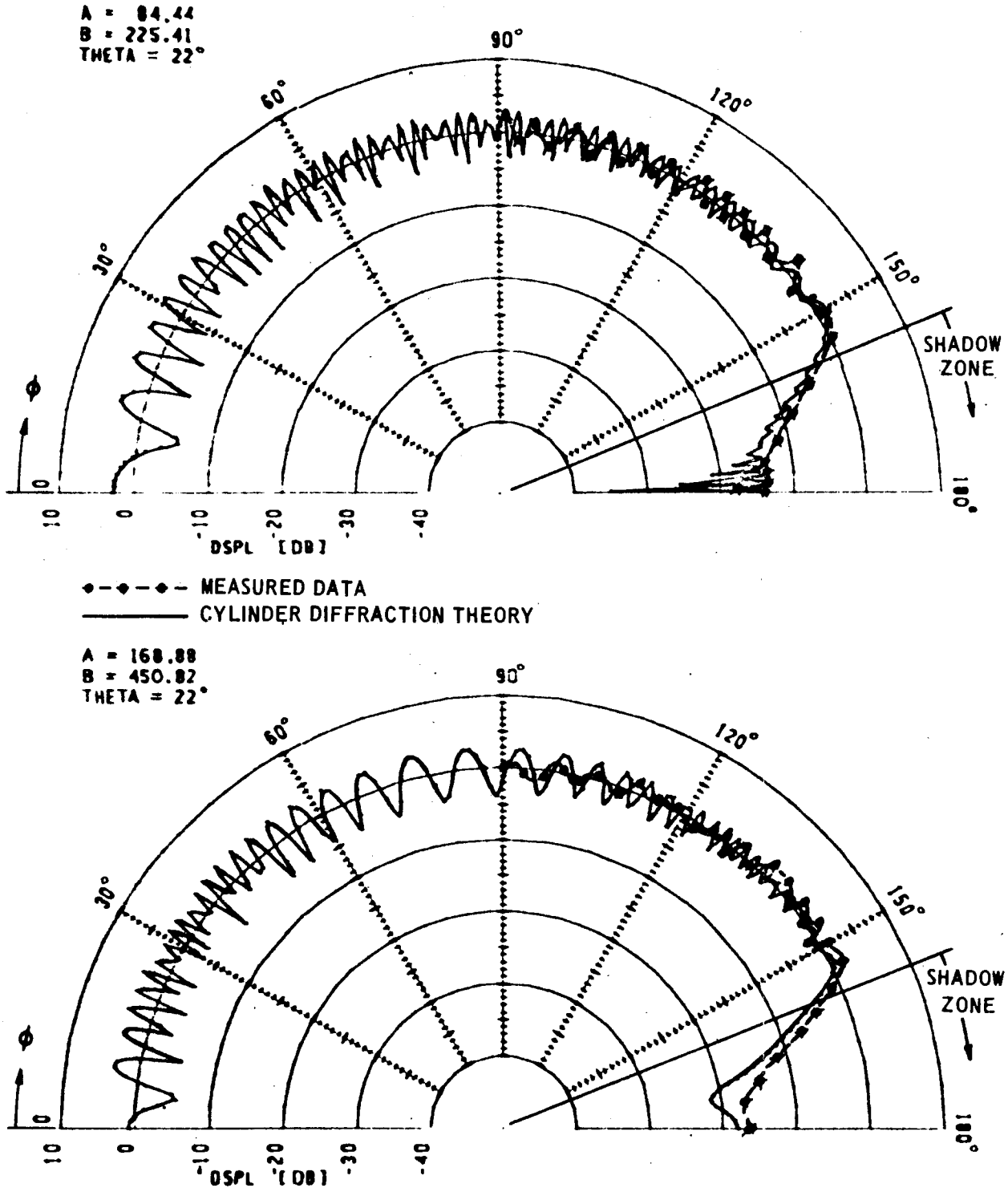

Figure 140.—Cylinder Diffraction Theory Versus Measurement (Quasi-Anechoic Chamber Test), f = 10 and 20 kHz

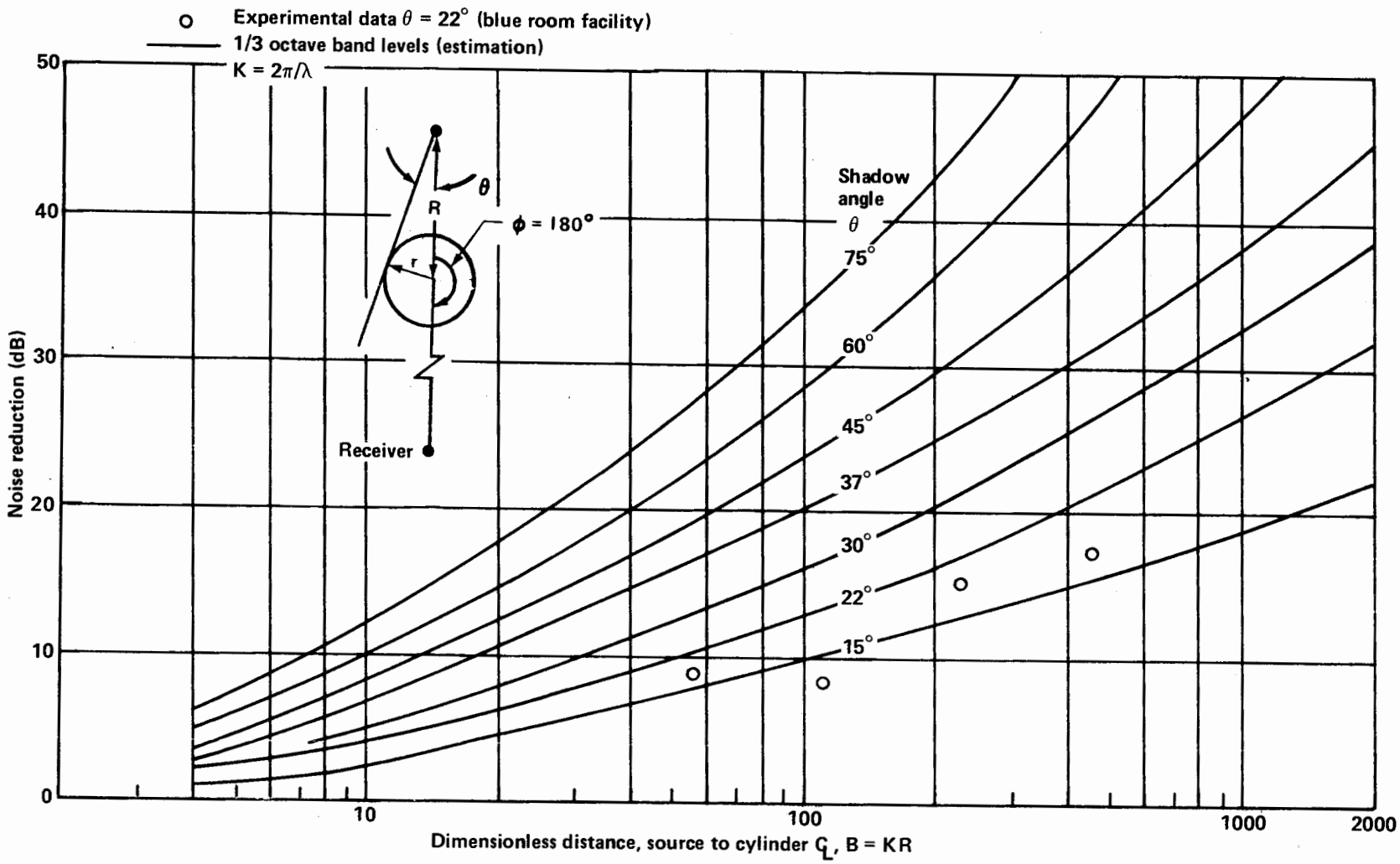

Figure 141.—Point-Source Noise Shielding From an Infinite Cylinder

- The finite length of the cylinder, i.e., acoustic waves can diffract around the top of the cylinder

- Nonperfect anechoic conditions due to location of the test apparatus in the corner of the room, i.e., flanking path acoustic waves can reflect off the floor, roof, and walls. This, in turn, limits the dynamic range of the test data. Unfortunately, room calibration data for this test are not available.

Incorporating these arguments with the measured data has substantiated the cylinder diffraction theory described in section 2.2.2.1. However, it should be emphasized that no data are available to evaluate the effects of noise source directivity, source spatial distribution, or spinning modes that occur for fan noise.

2.4.2 WING SHIELDING OF EXHAUST TURBOMACHINERY NOISE COMPONENTS

In this section we address the analysis of data from wing shielding experiments dealing with noise sources imbedded in the engine exhaust flow, excepting jet noise. The noise sources considered are fan, turbine, and core noise, which have been grouped together under the term exhaust turbomachinery (TM) noise. The origin of all these noise sources is upstream from the nozzle exhaust plane.

In the previous section, the diffraction theory for a directional compact source was verified by tests without flow. We ask the reader to recall the examples given previously in figure 15 for the diffraction theory applying to the half-plane and in figure 30 for the jet refraction theory. Figure 142 shows a theoretical prediction of TM noise shielding. Estimated trends with and without jet flow are illustrated in figure 142a. In the sketch to the right, directive/compact-source positions S and S′ are given, which produced the results shown to the left. Characteristic points (reference levels at the shadow zone boundary and the asymptotic shielded levels in the deep shadow zone) are noted by the circled points on the curves.

In figure 142b, c, and d, a breakdown of the major shielding elements considered in the estimates is shown. Sensitivity curves are provided. The major elements are:

- Dimensionless barrier height, $K\, r_0$

- Shadow boundary angle, θ_0

- Sound source's far-field directivity, $S(\psi)$

The apparent source location (r_0', θ_0') relative to the equivalent half-plane approximation for a wing edge directly relates to these elements. Changes in the elements are noted by the prime symbol. The corresponding changes in the predictions are noted by Δ_1, Δ_2, Δ_3, and $\Delta\psi$.

Comparison of figure 142 with test data given previously in figure 83 shows a striking similarity, which indicates the theory of half-plane diffraction and jet refraction can

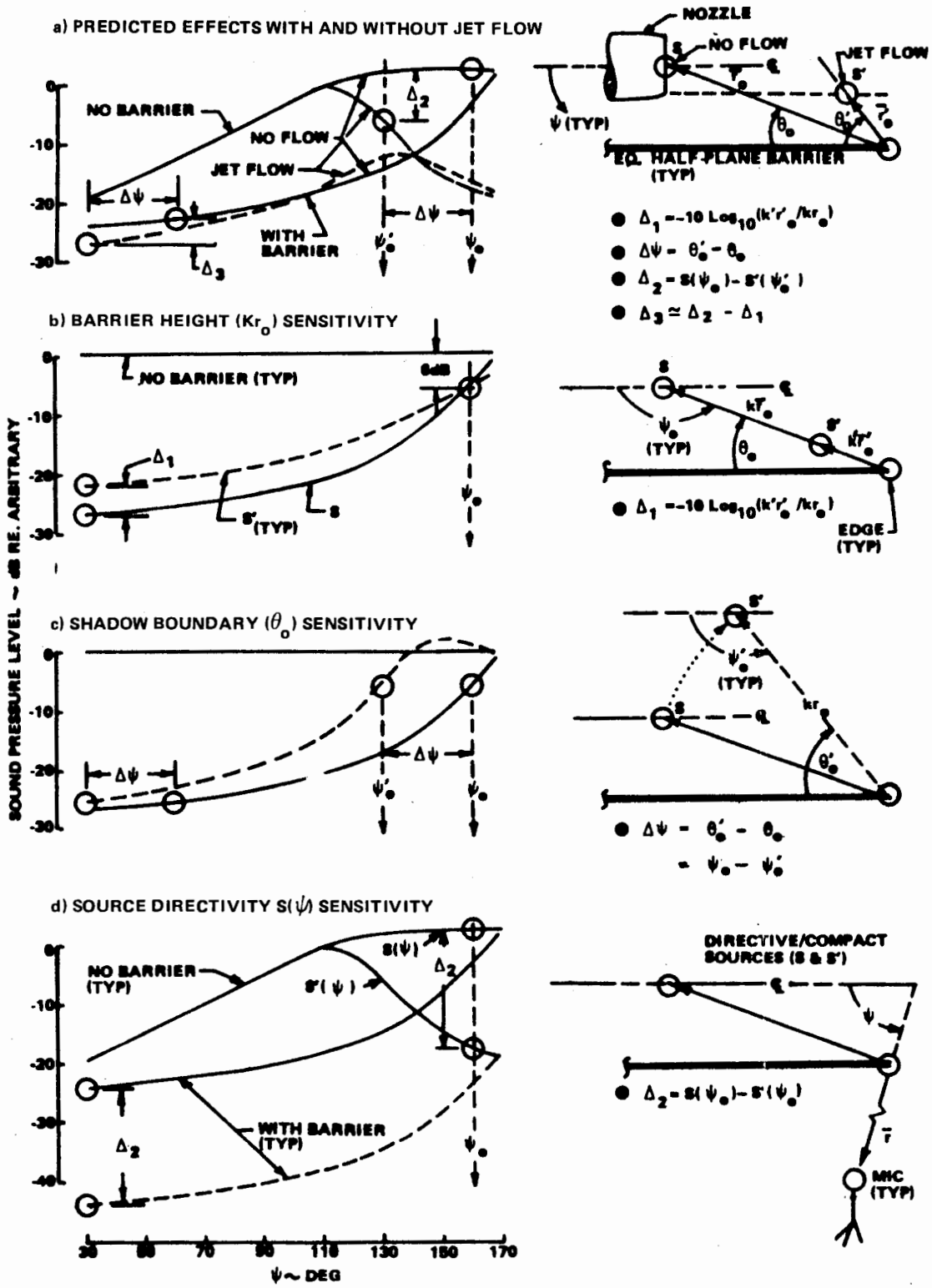

Figure 142.—Major Elements Considered Exhaust in Turbomachinery Noise Shielding Data Analysis

possibly be combined and applied to shielding cases with jet flow. Hence, we propose the extension of this theory to include cases with jet exhaust flow. This is done by use of the concept of an apparent sound emission location, not necessarily the true center of the noise source.

In the basic theory presented in sections 2.2.1.4 and 2.2.2.4, the effect of a noise source spatial distribution was evaluated. It was found that a compact-source model representative of the more complex distributed-source models could be made. In section 2.2.3, the apparent redirection of sound as it propagates through a shear layer was addressed using a simplified refraction theory. It was shown that the "apparent source" could appear at different locations when viewed from different locations outside the shear layer; i.e., $(r_0'/D, \phi_0')$ varies with $(r_0/D, \psi_0, M_0, M_J, T_S/T_{S0})$. A classic example emphasizing this fact occurs when one views a fish in an aquarium. Depending on the location of the observer, it is possible to see one, two, or three fish in the tank. Often the fish looks larger than it really is. Although this example deals with light, a similar phenomenon occurs for the case of wing shielding of TM noise components. Hence, the question to be answered is, "Where do we put the apparent source for TM noise radiating from the engine exhaust when a shielding barrier is placed in close proximity to the exit nozzles?"

By force fitting the diffraction theory of section 2.2.1.1 to the test data discussed in section 2.3.1, the apparent noise source was located for numerous test geometries and observer positions. This fitting of data was done through use of an optimization computer program that varied the position of the apparent noise source relative to the wing edges until the root-mean-square (RMS) decibel error between shielding predictions and measurements was a minimum.

The apparent noise source was found to appear quite close to the wing edges when the nozzle was brought in close proximity to the wing's upper surface. Splitting the source into two apparent sources was necessary to fit the test data, i.e., one source for the noise diffracting about the wing's leading edge and another for the noise diffracting about the wing's trailing edge. Additional apparent sources occur for the other wing edges, i.e., the root and tip, but these locations could not be discerned from the test data because the signals diffracting about these additional edges were negligible compared to those observed for the leading and trailing edges.

The location of the apparent source determined from the diffraction model was correlated with that predicted by the jet refraction theory of section 2.2.3. Correlation was fair. Hence, jet refraction appears to contain the essential elements necessary to describe the apparent source movement toward the wing edges as observed in the ensemble of test data. However, we are disturbed that the correlation is not better. The location of the apparent source is disturbingly close to the wing edges. Hence, it was necessary to assume a close location in the jet refraction model, i.e., a somewhat arbitrary location on the center of the jet shear region near the edge. Could flanking radiation due to other controlling mechanisms (either nondiffractive or refractive) be present in the data ensemble? Test site reverberation due to reflection from objects other than the wing shielding barrier is known to be present in some tests and is considered important in almost all tests. It appears that this flanking radiation could also explain apparent source movement toward barrier edges. Hence, the jet refraction

model is not unique. Unfortunately, flanking radiation cannot be quantified at this time without additional tests. Therefore, the fair correlation between apparent source locations predicted by jet refraction and those implied by shielding measurements is considered adequate to justify the use of jet refraction in the shielding estimation model. However, the refraction model was empirically adjusted so there was congruence with apparent source locations determined by a diffraction analysis of the shielding test data. The empiricisms reflect flanking radiation to the extent present in the data.

The empirically adjusted jet refraction model was then integrated with the directional/compact-source diffraction model. This integration results in the final prediction procedure for wing shielding of turbomachinery noise components. Comparisons were made using this procedure with the full-scale JT9D test data manually averaged over a range of engine operating conditions. The shielding comparisons indicate good agreement between estimation and measurement despite the large scatter (±6 dB approximately) in the *unshielded discrete tone* data. The estimated shielding attenuation changes due to variations in engine/wing geometry follow the change observed in the test data trends.

2.4.2.1 Determination of Apparent Source Location

Figure 143 shows the schematic of the optimization computer program used to determine the apparent source locations for fitting diffraction theory to wing shielding test data. The inputs to the program, indicated in the figure, are

- Engine/wing geometry as illustrated in figure 144 and the observer geometry relative to the engine

- The observed unshielded sound pressure level as a function of frequency (f) and directivity angle (ψ) relative to the engine inlet centerline

- The observed shielded sound pressure level as a function of frequency and directivity angle

- The initial guess for the apparent source coordinate, i.e., the center of the nozzle. Other guesses were also used to guarantee that the resulting optimized source position corresponded to the true optimized position and not a relative optimum.

- Associated convergence criterion and maximum step size. This information concerns only the method used to minimize the objective function and not the data presented in this report. Hence, it will not be discussed in detail.

- Selection of associated switches, indicating:

  - Assumptions used to model the source, i.e., a single point, a random-phased ring of points, or a random-phased line of points

  - The number of edge solutions considered in the shielded SPL estimates

  - The apparent source varies or is constant with frequency

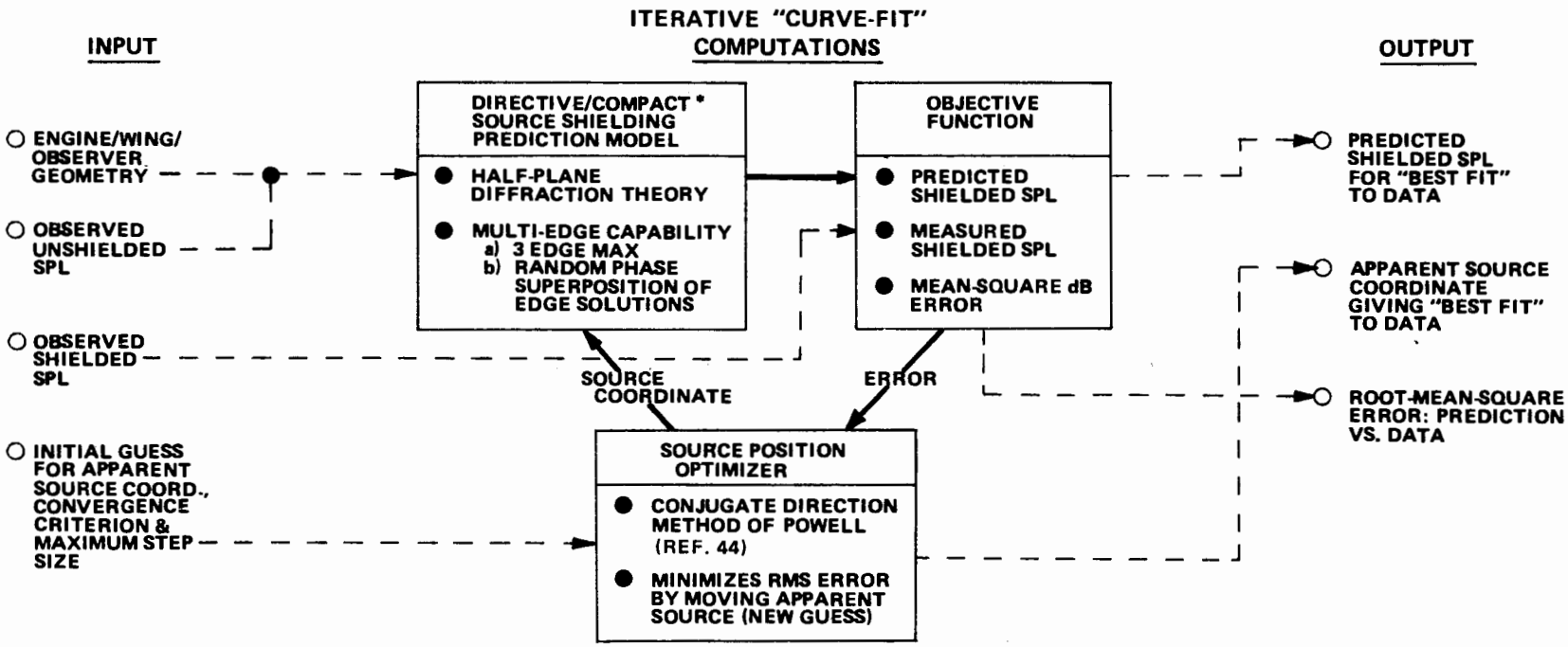

Figure 143.—Schematic of Optimization Computer Program for Determining Apparent Source Locations for Exhaust Turbomachinery Noise-Shielding Test Data

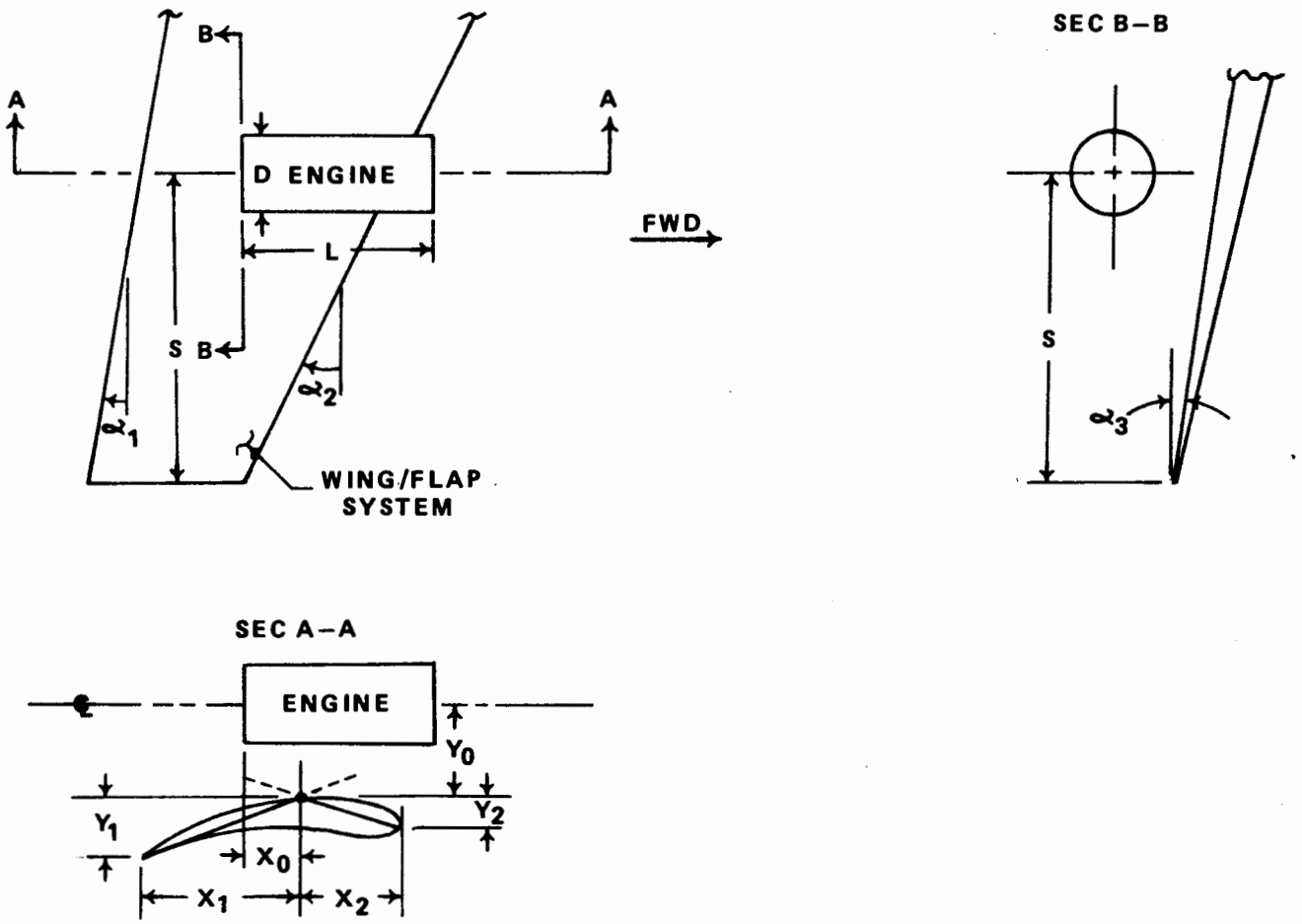

Figure 144.—Engine/Wing Geometry

The computations performed in the iterative "curve-fit" loop include the following.

- Predict the shielded SPL versus (f, ψ).

- Compute the RMS dB error between prediction and measurement, i.e., the objective function to be minimized by moving the current source.

- Compute the new apparent source position using the conjugate direction method of Powell (ref. 44). This method computes its own approximate gradients internally and a new guess for the apparent source.

The outputs of the program for the minimum RMS dB error condition are tables of:

- Predicted shielded SPL versus measured shielded SPL

- The apparent source coordinate (r_0', θ_0')

- The deviations, prediction versus measurement, and the associated RMS dB error

Figure 145 illustrates a sample use of the optimization program to determine apparent source coordinates that best predict shielded noise levels when compared with measurement. The inferred noise signals coming around the leading and trailing edges must be first deduced from the measured data. Hence, the diamond symbol is used to denote our best guess of the leading edge component, and the X symbol denotes the corresponding trailing edge component. The 3-dB designation shows where inferred leading and trailing edge components are assumed equal and are 3 dB below the measured sum. Note also that measured data is available only at 20^0 intervals in the forward arc compared to 10^0 intervals in the aft arc. Since three data points in the forward arc are insufficient for reasonable location of the leading edge apparent source, three intermediate unshielded points are assumed (inferred). The resulting theoretical compact-source diffraction model, which gives a reasonable representation of the measured shielded data, contains two apparent source locations–one for the leading edge and one for the trailing edge. The resulting data fit is quite good, except for the sector corresponding to directivity angles (ψ) greater than approximately 140^0. This was the area where curve fitting sometimes failed. This discrepancy is believed to be due to a change in the unshielded directivity pattern, which in turn is caused by the following:

- The acoustic radiation characteristics of the jet exhaust are altered by the presence of the wing.

- A scattering process occurs in the wake region behind the wing, i.e., incident sound is dispersed and modulated by inhomogeneities. This causes a loss in discreteness for the sound frequency and the sound's radiation character.

Hence, in addition to optimization for apparent source coordinates (r_0', θ_0'), an apparent source directivity shift ($\Delta\psi_S$) was also introduced in some curve fitting for improved representation.

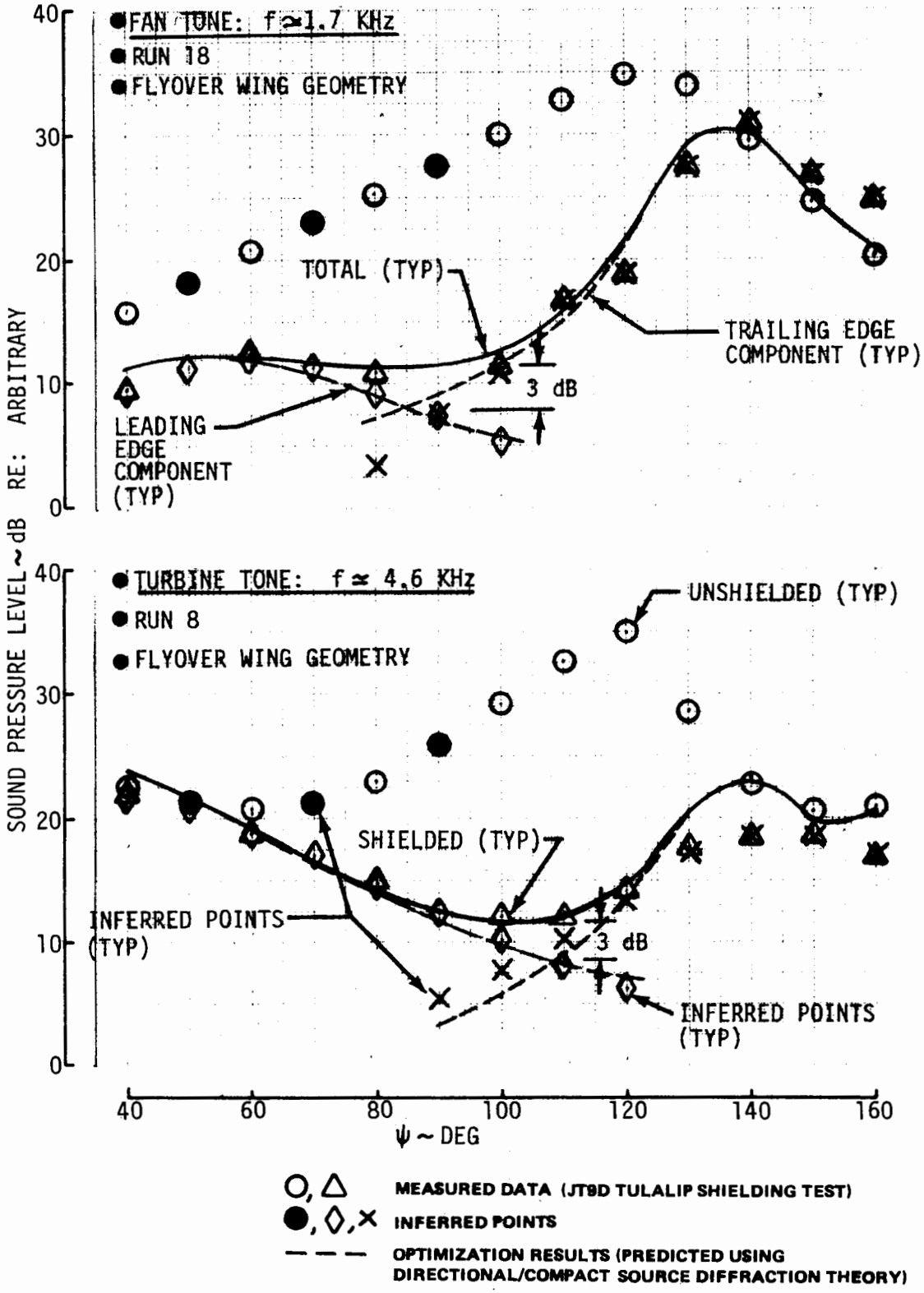

Figure 145.—Decomposition of Wing Shielding Data Into Leading and Trailing Edge Diffraction Components

Figure 146 shows similar comparisons of predictions using the optimization program with data obtained for the model test conducted in the Wall Isolation Facility (WIF). Note that the comparison is shown for three nozzle/wing geometries and that apparent source locations are listed. The curve fitting was not quite as good for this data as it was for the full-scale test data. Note that the prediction model assumes a constant apparent source location for all frequencies. Comparison of such predictions with measurement shows that the 19.3-kHz apparent source location is about right, but a better fit of shielding in the deep shadow zone would have occurred if the 9.6-kHz and the 29-kHz apparent source locations had been closer and further away from the trailing edge, respectively. This can be seen by recalling that greater attenuation occurs in the deep shadow zone at larger $K\,r_0'$, as shown earlier in figure 8. Since wave number (K) is already accounted for in the simple diffraction theory, movement of the apparent source location (r_0') could have caused better prediction of shielding over the whole frequency range. Indeed, better curve fits did result when this option was selected in the optimization process. However, no consistent trends were observed in the apparent source location for *both* the model- or full-scale test data. Hence, it was decided to hold the apparent source position constant with respect to frequency. It should be noted that the model data was suspect as to its repeatability.

Note that the compact-source diffraction model used for prediction in the comparison with measured data in figure 146 introduced an apparent source directivity shift ($\Delta\psi_S$) in addition to the usual apparent source location (r_0', θ_0'). Although this did give a better fit to the WIF measured data, the directivity shift ($\Delta\psi_S$) did not significantly reduce the prediction error when the whole ensemble of data was considered. Therefore, apparent directivity shift was not a variable incorporated into the final estimation procedure. Only apparent source location was used in the final shielding estimation procedure for exhaust turbomachinery noise.

Figure 147 compares predictions using the optimization program with model test data obtained from the WIF for fully attached flow from a D-nozzle. Although use of this data was not required for the contract, it did provide a needed data point to finalize the empiricisms required in our shielding prediction procedure. Note that the apparent source translation aft is greater for the D-nozzle with flow attachment.

Figure 148 shows the variation in apparent source location as the nozzle is moved relative to a wing/flap trailing edge at radius r_0. These are the same apparent source locations implied in the previous three figures. Results are shown for an ensemble of nozzle locations, sizes, and noise source types. Note how the apparent noise source location moves progressively closer to the trailing edge as the exhaust nozzle swings forward and downward toward the wing surface. Also note how the locus of noise source locations tightly clusters along a 45^0 to 50^0 angle from the equivalent wing half-plane. A similar chart could have been made for noise diffracting about the leading edge, but the resulting distances, r_0', were extremely small and are suspected of being controlled by flanking radiation.

Figure 149 shows the shift in apparent source coordinates relative to exhaust nozzle coordinates plotted as a function of the cotangent of the directivity angle ψ_0 grazing the

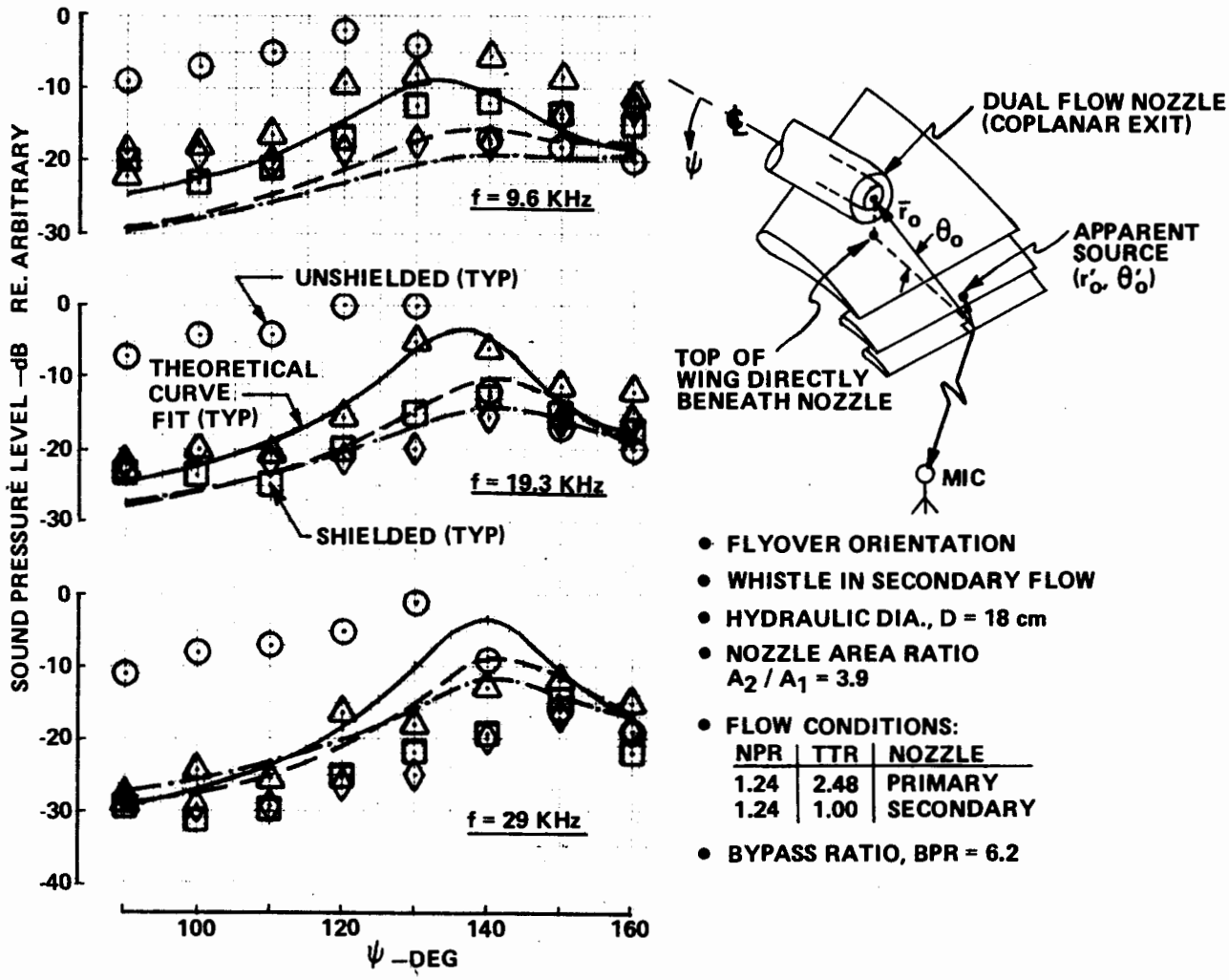

SYM	TEST GEOMETRY r_o / D	θ_o– DEG	SYM	CURVE FIT PARAMETERS r'_o / r_o	$(\theta'_o - \theta_o)$ –DEG	$\Delta\psi_s$–DEG 1
△	3.24	10	——	.494	20.1	6.6
□	4.22	7.8	- - -	.294	21.2	5.9
◇	4.57	7.2	—·—	.090	21.7	4.0

1 DIRECTIVITY SHIFT APPLIED TO THE UNSHIELDED DATA TO COMPENSATE FOR THE CROSS-OVER INDICATED IN SHIELDED DATA

Figure 146.—Comparison of Optimization Prediction With Shielding Model Test (WIF)

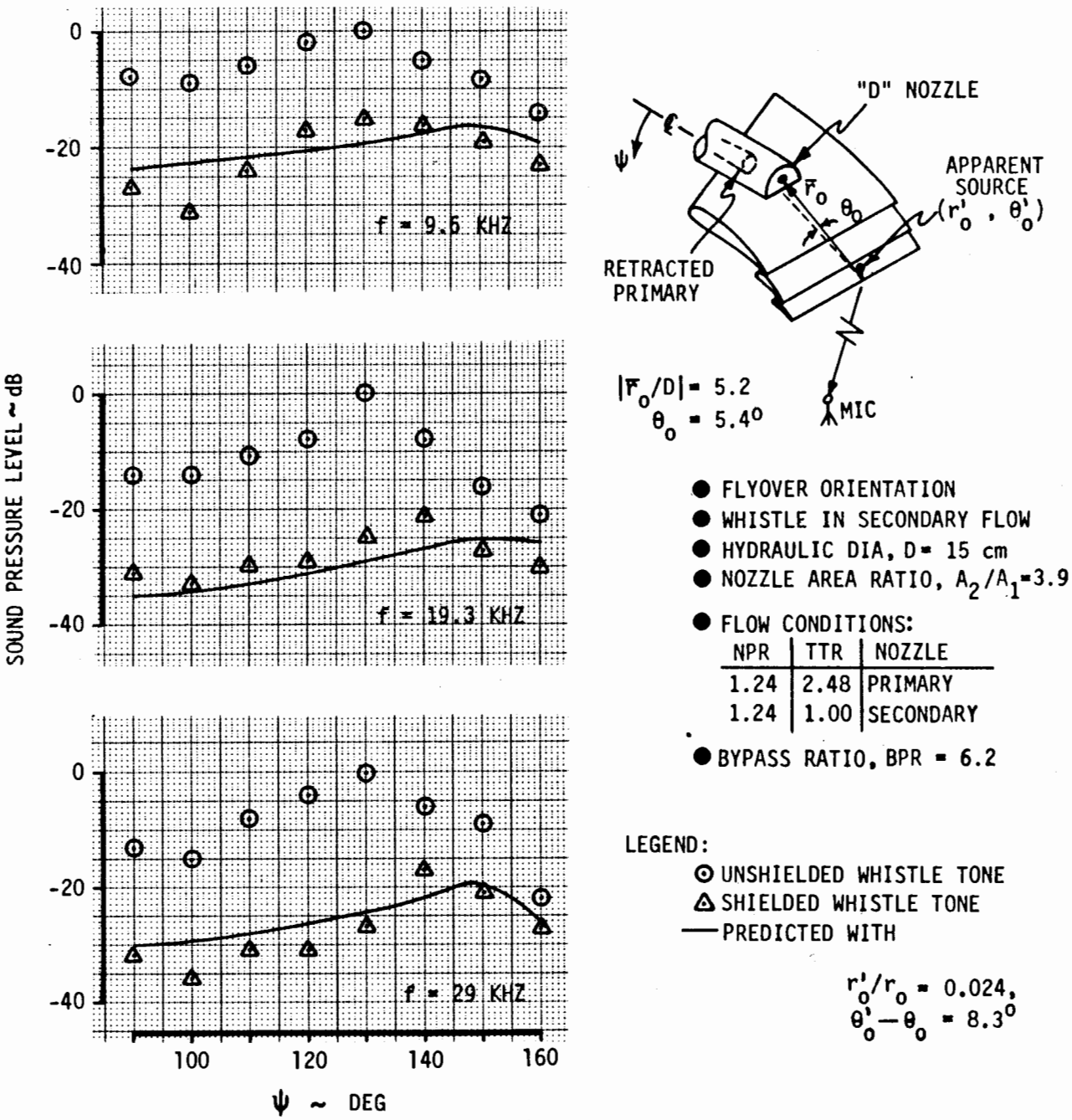

Figure 147.—D-Nozzle Wing Shielding Results and Optimized Prediction

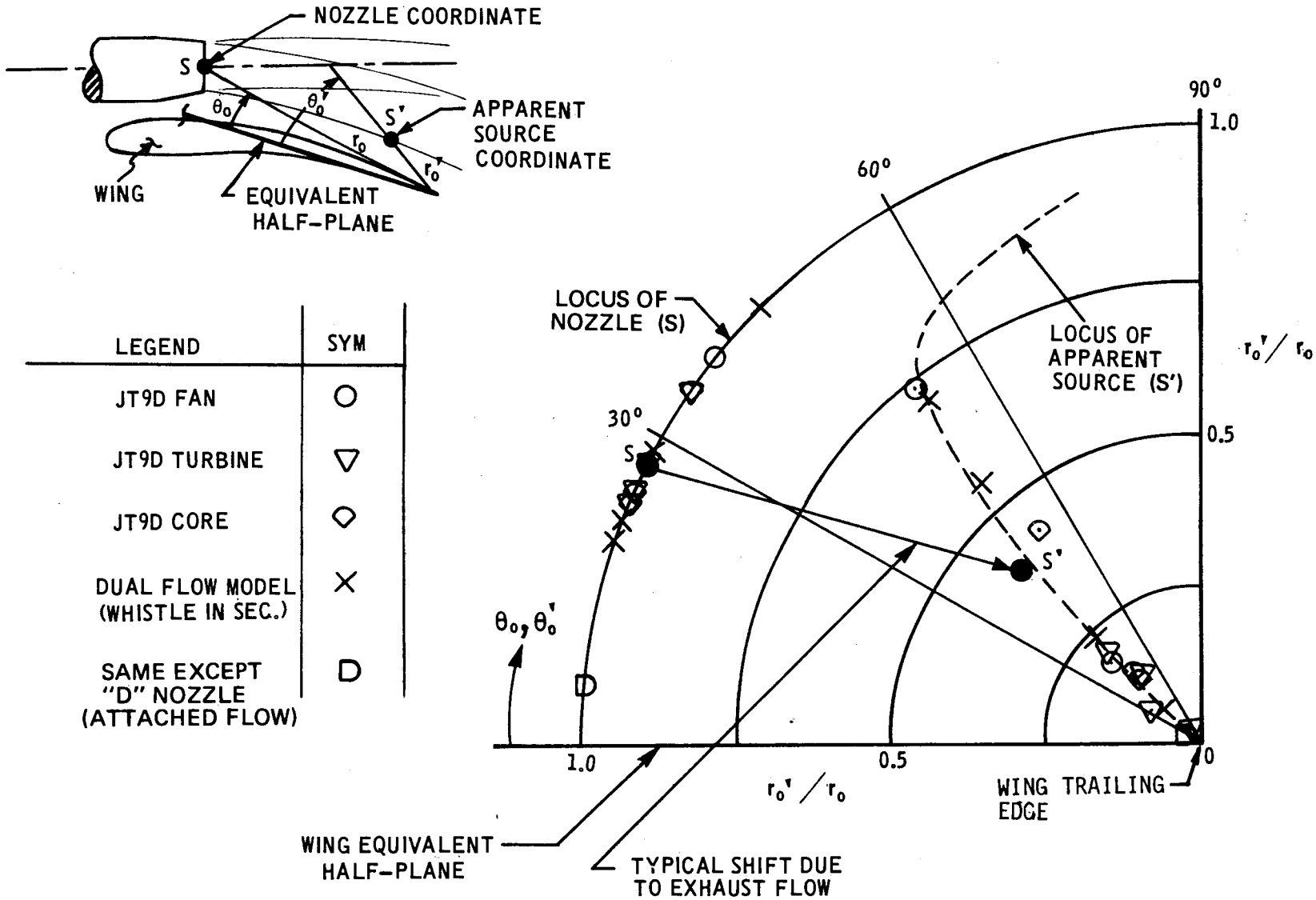

Figure 148.—Apparent Source Location in Exhaust Flow (Trailing Edge)

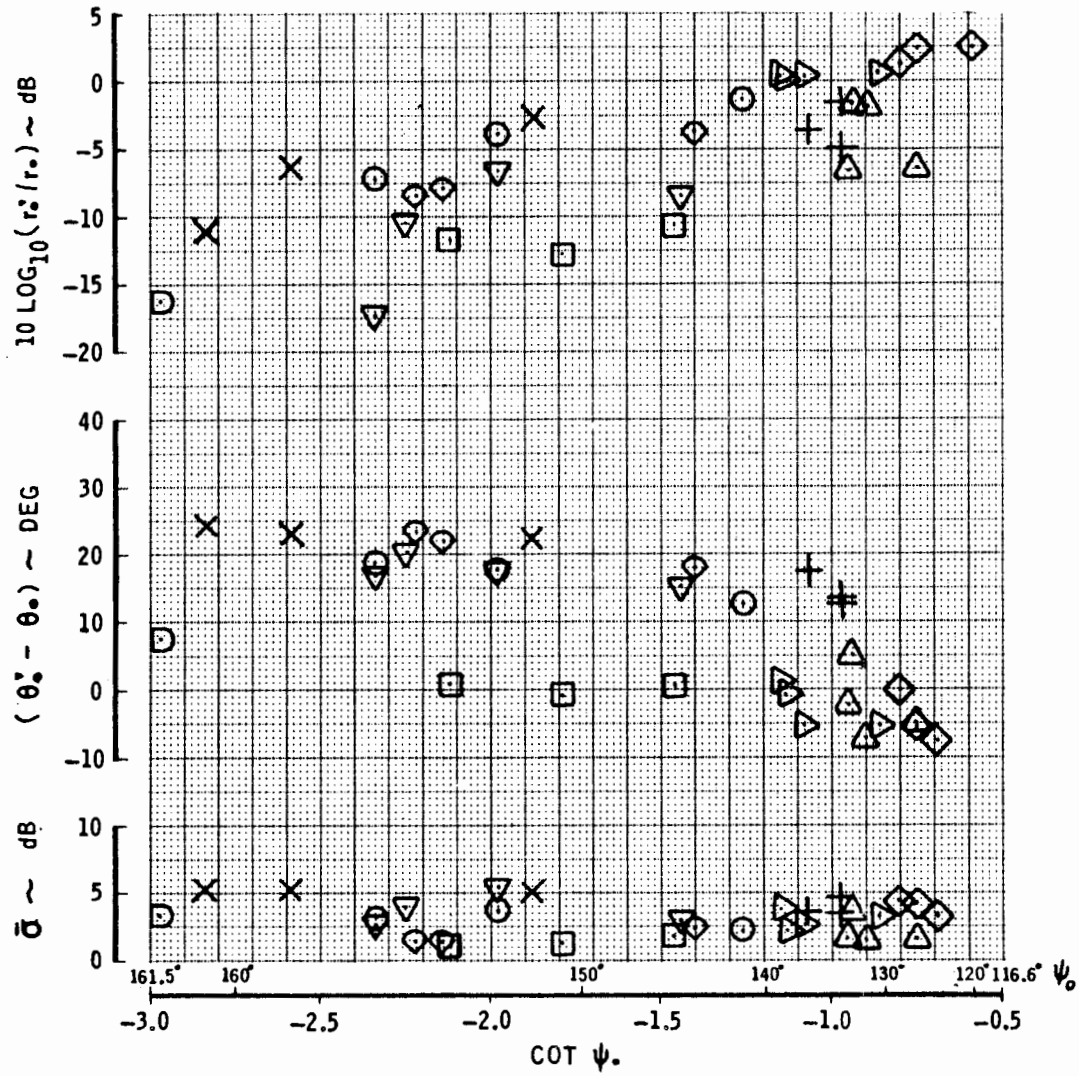

SYMBOL	DATA SOURCE	NE	WING GEOM
○	JT9D FAN TONE	1	FLYOVER
▽	JT9D TURBINE TONE	1	FLYOVER
△	JT9D TURBINE TONE	1	25° WING
▷	JT9D TURBINE TONE	3	25° WING
×	DUAL FLOW MODEL WHISTLE IN SECONDARY	1	FLYOVER
D	SAME EXCEPT "D" NOZZLE	1	FLYOVER
+	DUAL FLOW MODEL WHISTLE IN SECONDARY	3	25° WING
□	MODEL FAN RIG (1 FT. DIA.)	1	FLYOVER
◇	MODEL FAN RIG (1 FT. DIA.)	3	25° WING
▽	JT9D CORE NOISE	2	FLYOVER

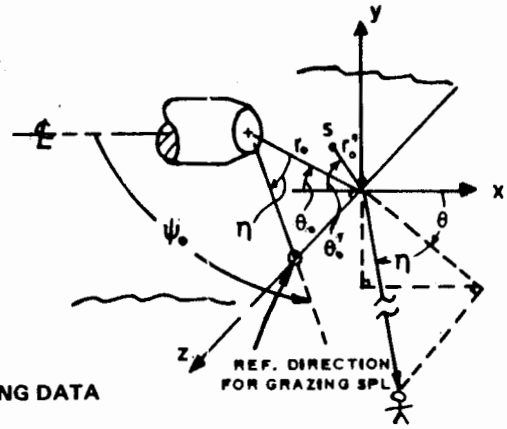

NUMBER OF EDGES CONSIDERED IN FITTING SHIELDING DATA

$\bar{\sigma}$ = STANDARD DEVIATION

Figure 149.—Wing Shielding Optimization Results for Apparent Source Position (Directional/Point-Source Analysis)

wing's trailing edge. When plotted in this form, $10 \log_{10}(r_0'/r_0)$ can be related directly to the shielding attenuation in the deep shadow zone behind the barrier. The variable $(\theta_0' - \theta_0)$ shows the corresponding decrease in the angular size of the shadow zone. Note the similarity in the apparent source coordinates in figure 149 as determined empirically by diffraction theory when compared to the corresponding variables predicted by jet refraction theory as shown in figures 31 and 32. This similarity has led us to consider jet refraction theory as an estimation method of apparent source locations for exhaust turbomachinery noise components. If jet refraction theory would predict the same source coordinates as the empirically determined diffraction apparent source coordinates, there would be some expectation that jet refraction could be used to estimate noise source coordinates for engine exhaust conditions beyond the limited scope of the existing shielding test data.

Note in figure 149 that $10 \log_{10}(r_0'/r_0)$ and $(\theta_0' - \theta_0)$ for the shielding test conducted in the model fan rig room do not seem to agree with the rest of the data. The SPL data for this test is strongly suspected of being contaminated by flanking radiation (see sec. 2.3.1.1). Hence, we have not used this data to develop our estimation procedure. The remaining test data seem to follow trends expected for refraction theory (sec. 2.3.3).

2.4.2.2 Correlation of Apparent Source Location With Jet Refraction

The jet refraction theory presented in section 2.3.3 was used to compute apparent source coordinates relative to the wing edges for the average flow conditions used in the WIF model test and the full-scale JT9D test at the Tulalip facility. These coordinates were correlated with those obtained from analysis of the wing shielding SPL data using diffraction theory. Figure 150 shows this correlation in terms of the variables that impact wing shielding attenuation, i.e.,

- $10 \log_{10}(r_0'/r_0)$ corresponds to the loss of attenuation in the deep shadow zone.

- $(\psi_0 - \psi_0')$ corresponds to the angular change in the direction acoustic waves leave the jet exhaust relative to the case with no flow. For flyover wing geometries, $(\psi_0 - \psi_0')$ approximately equals $(\theta_0' - \theta_0)$ defined previously in figure 149.

It can be seen that a fair correlation exists. The values of $10 \log_{10}(r_0'/r_0)$ predicted by refraction appear on the average approximately 5 dB less than those obtained from analysis of measured data. The predicted angular change $(\psi_0 - \psi_0')$ appears to be offset by an angle (γ) approximately equal to 13° for the full-scale test data and tends to follow a different slope (α) than that indicated for an ideal correlation. The angular offset (γ) suggests that local ambient flow is being induced between the wing and the jet exhaust for the engine/wing geometry tested. The theory indicates that for an ambient flow condition of about Mach 0.1, the shadow zone boundary would appear at angles (ψ_0') about 13° larger than for the case where the ambient flow is zero. Unfortunately, the necessary flow data are not available to provide a more quantitative explanation. A qualitative understanding can be gained if the theory is reviewed noting the distinctions given for the effects of convection, i.e., θ_0 and θ_0' in section 2.2.1.2 and θ_0' and ϕ_0' in section 2.2.3.2. The discrepancy of 5 dB in the values predicted for $10 \log_{10}(r_0'/r_0)$ suggests that another mechanism could be contaminating the SPL shielding data, i.e., possibly flanking radiation, to be discussed in section 2.4.2.4.

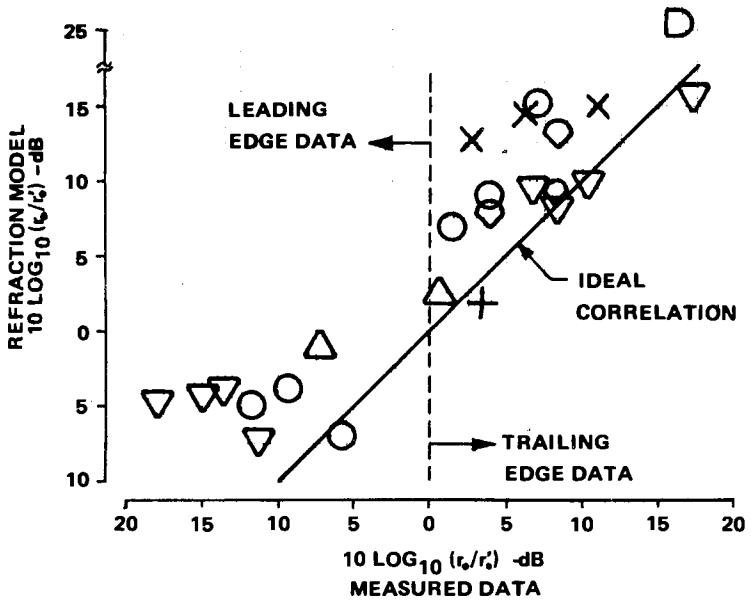

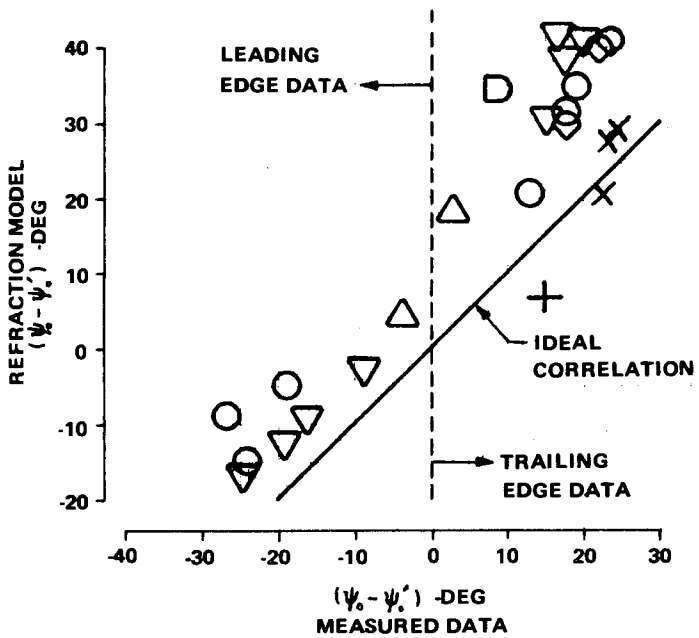

NOTES

- (r_o, r_o') ARE DISTANCES FROM WING EDGE TO NOZZLE & APPARENT SOURCE, RESPECTIVELY
- (ψ_o, ψ_o') ARE DIRECTIVITY ANGLES (RELATIVE TO INLET CENTERLINE) GRAZING WING EDGE FOR NOZZLE & APPARENT SOURCE, RESPECTIVELY
- NO EMPIRICISMS INCLUDED IN PREDICTIONS FOR REFRACTION MODEL I.E. $(\alpha, \beta, \gamma) = (1, 1, 0)$
- MEASURED DATA ARE RESULTS FROM FITTING DIFFRACTION MODEL TO WING SHIELDING DATA

SYM	DATA SOURCE	WING GEOMETRY
⊙	JT9D FAN TONE	FLYOVER
▽,△	JT9D TURBINE TONE	FLYOVER, 25° WING
⊙	JT9D CORE NOISE	FLYOVER
×,+	DUAL FLOW MODEL WHISTLE IN SEC	FLYOVER, 25° WING
D	SAME EXCEPT D NOZZLE	FLYOVER

Figure 150.—Correlation of Apparent Source Location With Refraction Model (No Empiricisms)

2.4.2.3 Empirical Adjustments

Assuming that the shielded SPL data obtained by test is controlled by both jet refraction and wing diffraction, empirical adjustments are necessary to bring the simplified theoretical models in line with the test data. We have verified the diffraction theory for directive sources in section 2.4.1 and have noted how the directive radiation pattern is set up for a real engine (sec. 2.2.3). For the model tests conducted in the Wall Isolation Facility with the flow turned off, diffraction theory predicted the shielded whistle tones quite well with the source located at the center of the nozzle exit plane. Again, assuming the noise source is at the nozzle, large discrepancies occurred between diffraction theory predictions and test data when the exhaust flow was turned on.

Hence, it seems appropriate to empirically modify the theory that attempts to account for the effect of flow, i.e., the jet refraction model. To work this problem correctly, the impact of jet flow on sound radiation in the near field needs to be determined. Unfortunately, the formulation of this problem is difficult when barriers are placed near a jet and such formulation is beyond the scope of the current effort. To circumvent this difficulty, we propose to:

- Use the far-field radiation pattern of the unshielded noise component as input to the diffraction model.

- Empirically adjust the apparent source positions predicted by the simplified jet refraction model to match those obtained in section 2.4.2.1, where simple diffraction theory was used to obtain apparent source locations by analysis of far-field shielding data.

This adjusting has been done through use of the empirical parameters (α, β, γ). Figure 151 defines the apparent source location for the simplified flyover case. Angle $\Delta\psi_P$ shows the grazing incidence direction as predicted by jet refraction theory. Line N-P represents the shortest path direction from the nozzle to edge to observer. Line P-P′ represents the direction acoustic waves leave the jet exhaust (from the apparent source). With these definitions, the angle $\Delta\psi$ can be represented as some fraction α of the grazing incidence angle $\Delta\psi_P$ prediction by jet refraction displaced by a constant angle γ. Hence,

$$\Delta\psi = \alpha\,(\Delta\psi_P - \gamma)$$

The quantities α and γ are to be determined so that $\Delta\psi$ closely agrees with the "measured" angles ($\psi_O - \psi_O'$)

$$(\psi_O - \psi_O') = \Delta\psi = \alpha\,(\Delta\psi - \gamma) \tag{68}$$

Hence, this is the apparent angular change in the direction sound leaves the jet relative to the case without flow.

The apparent source in figure 151 is then found by determining the intercept of this direction for wave propagation relative to the wing edge with a plane offset by a

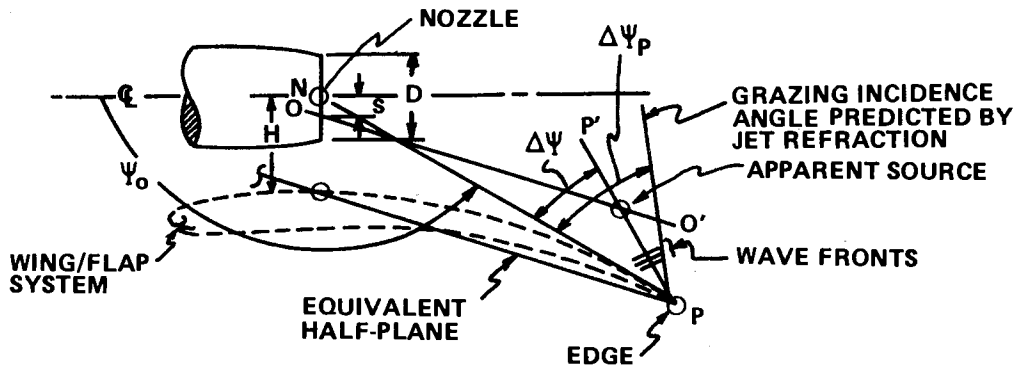

NOTES

1) LINE N–P REPRESENTS DIRECTION FOR SHORTEST PATH FROM NOZZLE TO EDGE TO OBSERVER
2) LINE P – P' REPRESENTS DIRECTION ACOUSTIC WAVES LEAVE THE JET EXHAUST
3) LINE O – O' IS THE INTERSECTION OF TWO PLANES: ONE PLANE IS PARALLEL TO H.P. AND DISPLACED A DISTANCE S FROM NOZZLE. THE OTHER PLANE IS NORMAL TO H.P. AND CONTAINS THE ENGINE CENTERLINE

Figure 151.—Apparent Source Location for Wing Trailing Edge (Flyover Case)

distance S from the nozzle center. This plane is to be parallel to the equivalent half-plane representing the wing edge being considered. The distance S is computed by the formula

$$S = \beta D/2 \tag{69}$$

where

D = is the exhaust nozzle hydraulic diameter, computed by taking four times the discharge area divided by the perimeter around the nozzle's exit plane

β = empirical parameter determined so that the resulting values of r_0'/r_0 agree well with corresponding "measured" values

The results of the analysis to determine empirical parameters (α, β, and γ) are shown in figure 152. The plotted data points represent the adjustments that make the predicted apparent source coordinates exactly match those obtained in section 2.4.2.1. To these data points we have "faired" a set of similar curves corresponding to each source of data, i.e., whistle, fan, turbine tones, or core noise. We propose that these faired curves be used instead of the data points so that interpolations/extrapolations will have smooth transitions. This permits us to consider other wing geometries besides those tested. Note that the angle γ has a constant value of 13° for full-scale and D-nozzle model data, and a value of -16° for dual-flow model data.

Figure 153 shows the correlation of apparent source positions predicted by this modified refraction model with those obtained from fitting wing shielding data with diffraction theory (sec. 2.4.2.1). The correlation now shows an excellent agreement for the angular shift ($\psi_0 - \psi_0'$) and a good agreement for the loss in maximum shielding attenuation "due to jet flow," i.e., $10 \log_{10}(r_0'/r_0)$. The data show that the leading edge has the largest scatter and indicate that our uncertainty in predictions will be greater for noise diffracting around the wing's leading edge.

Hence, the final estimation procedure for shielding of exhaust turbomachinery noise components uses apparent source coordinates defined by an empirically modified jet refraction theory. For a two-dimensional *static* case with no wing sweep angle, the apparent source coordinate (r_0', θ_0') relative to the edge is defined as follows:

$$\psi_0' = \psi_0 - \alpha\,(\Delta\psi_P - \gamma) \tag{70}$$

$$\theta_0' = \theta_0 + \alpha\,(\Delta\psi_P - \gamma) \tag{71}$$

$$r_0' = (r_0 \sin\theta_0 - 0.5\,\beta\,D)/\sin\theta_0' \tag{72}$$

where $\Delta\psi_P$ is predicted by the jet refraction theory of section 2.2.3.2. The more complicated three-dimensional case with wing sweep angle is actually programmed for computer computations. This three-dimensional geometry is illustrated and solved vectorially in figure 33 of the jet refraction theory section.

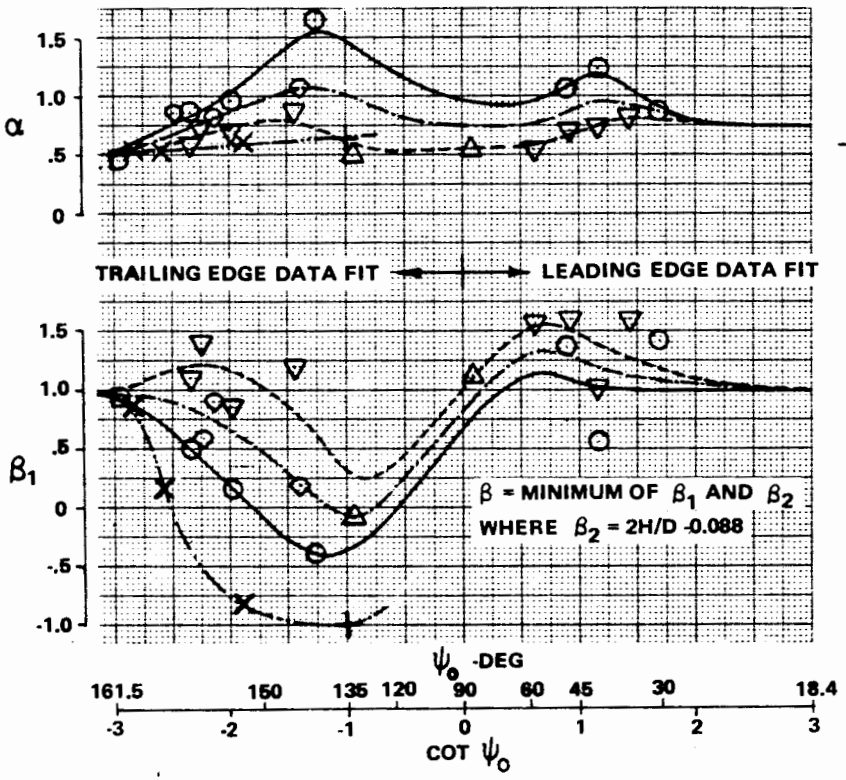

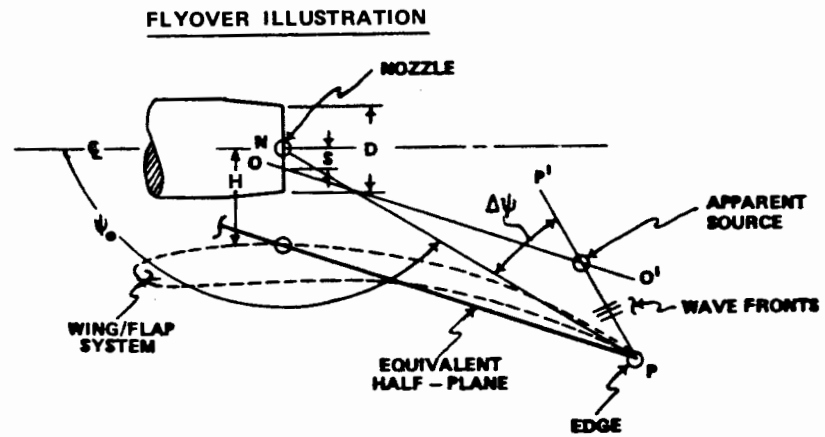

NOTES

1) LINE N-P REPRESENTS DIRECTION FOR SHORTEST PATH FROM NOZZLE TO EDGE TO OBSERVER
2) LINE P-P' REPRESENTS DIRECTION ACOUSTIC WAVES LEAVE THE JET EXHAUST
3) LINE O-O' IS THE INTERSECTION OF TWO PLANES: ONE PLANE IS PARALLEL TO H.P. AND DISPLACED A DISTANCE S FROM NOZZLE. THE OTHER PLANE IS NORMAL TO H.P. AND CONTAINS THE ENGINE CENTERLINE
4) $\Delta\psi = \alpha(\Delta\psi_p - \gamma)$ & $S = \beta D/2$
   WHERE (α, β, γ) ARE EMPIRICAL ADJUSTMENTS.
   $\Delta\psi_p$ IS DETERMINED BY JET REFRACTION THEORY.
   γ = 13° FOR FULL SCALE & "D" NOZZLE DATA
   = -16° FOR DUAL FLOW MODEL DATA

LEGEND	SYM	DATA SOURCE	WING GEOM
———	○	JT9D FAN TONE	FLYOVER
- - - - - -	▽,△	JT9D TURBINE TONE	FLYOVER, 25° WING
—·—·—	◇	JT9D CORE NOISE	FLYOVER
··—··—	X,+	DUAL FLOW MODEL WHISTLE IN SEC.	FLYOVER, 25° WING
	D	SAME EXCEPT "D" NOZZLE (ATTACHED FLOW)	FLYOVER

Figure 152.—Empirical Adjustments to Jet Refraction Theory for Apparent Source Position

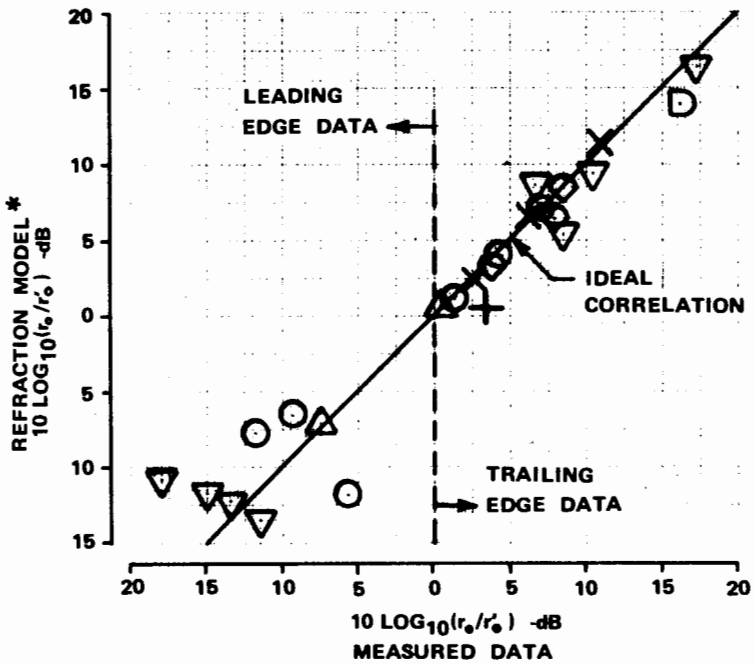

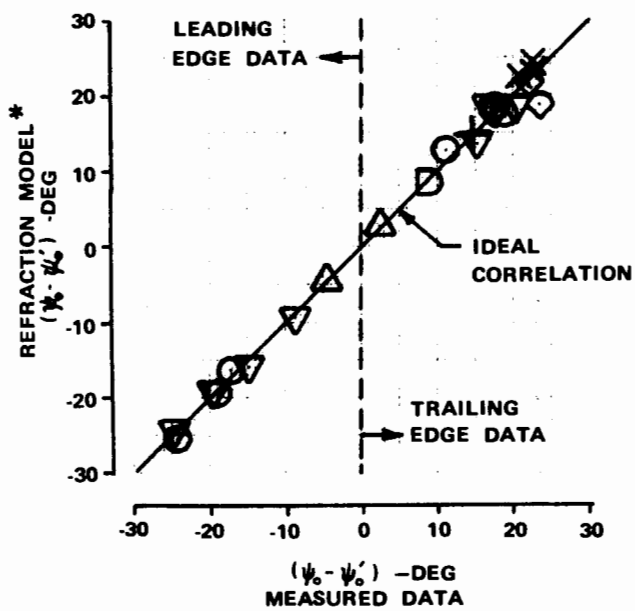

NOTES

- (r_o, r'_o) ARE DISTANCES FROM WING EDGE TO NOZZLE & APPARENT SOURCE, RESPECTIVELY
- (ψ_o, ψ'_o) ARE DIRECTIVITY ANGLES (RELATIVE TO INLET CENTERLINE) GRAZING WING EDGE FOR NOZZLE & APPARENT SOURCE, RESPECTIVELY
- MEASURED DATA ARE RESULTS FROM FITTING DIFFRACTION MODEL TO WING SHIELDING DATA

* EMPIRICISMS (α, β, γ) FROM FIG. 152 ARE INCLUDED IN REFRACTION MODEL

SYM	DATA SOURCE	WING GEOMETRY
○	JT9D FAN TONE	FLYOVER
▽,△	JT9D TURBINE TONE	FLYOVER, 25° WING
◇	JT9D CORE NOISE	FLYOVER
×,+	DUAL FLOW MODEL WHISTLE IN SECONDARY	FLYOVER, 25° WING
D	SAME EXCEPT D NOZZLE	FLYOVER

Figure 153.—Correlation of Apparent Source Location With Refraction Model (Empiricisms Included)

This empirically modified refraction model has been integrated with the diffraction model of section 2.2.1 to form our wing shielding estimation procedure for exhaust TM noise components. Figures 154, 155, and 156 illustrate the application of the empirically corrected method for estimation of JT9D wing shielding data. Figures 154 and 155 show the data scatter observed in the full-scale test. The directivity curves and average test conditions given in the figures were input to the procedure. The prediction agrees fairly well with the test data.

Figure 156 shows a comparison of estimations with test data manually averaged over the range of the engine operating conditions tested. It should be noted that these data were not directly used to determine the apparent source positions. Rather, the individual test data at each engine/wing geometry and each frequency were used to determine the source positions, as discussed in section 2.4.2.1. Changes in shielding are shown as the engine/wing geometry is changed. Again, the trends predicted by the procedure and those observed in the data agree fairly well. This indicates that the smoothing done in the empirical adjustments of figure 152 does not significantly degrade the prediction accuracy.

2.4.2.4 Possible Importance of Flanking Radiation

An important product of the data analyses described in section 2.4.2.1 was the definition of model- or full-scale fan tone, turbine tone, and core noise equivalent point-source locations which, in order to fit the available data, were very often extremely close to the barrier edges. An assumption underlying the optimization program developed to determine such locations was that the noise penetrating into the shadow zone is primarily the result of diffraction about the edges of the shield barriers. A candidate explanation for the validity of the resulting locations was developed by appeal to refraction considerations. However, such locations could also result if the assumption that noise reaching the shadow zone is in fact *not* primarily due to refraction through flow and diffraction about the edges of the shield barrier but, rather, is controlled by other mechanisms.

As an example, consider data obtained for the simulated semi-infinite half-plane barrier/small horn noise source (fig. 46) obtained during the group 2 tests and conducted in the model fan rig room (section 2.3.1.1). Such data are shown in figure 157, along with an estimate based on the simple point-source theory developed in section 2.2. For this estimate the assumption is made that radiation from the Altec loudspeaker horn can be modeled as a point source located at the exit plane of the noise source. As can be seen, the estimate predicts noticeably more shielding attenuation than, in fact, is achieved.

The required location for the equivalent point source to fit the test data and the resulting shielding prediction were found using the optimization program discussed in section 2.4.2.1 and shown schematically in figure 143. The required equivalent source location is significantly closer to the edge of the barrier than to the exit plane of the loudspeaker. The resulting predictions of noise levels in the shadow zone are in good agreement with the data when this so-called "equivalent source location" is used. However, this is a misnomer because no physical process exists to justify this movement

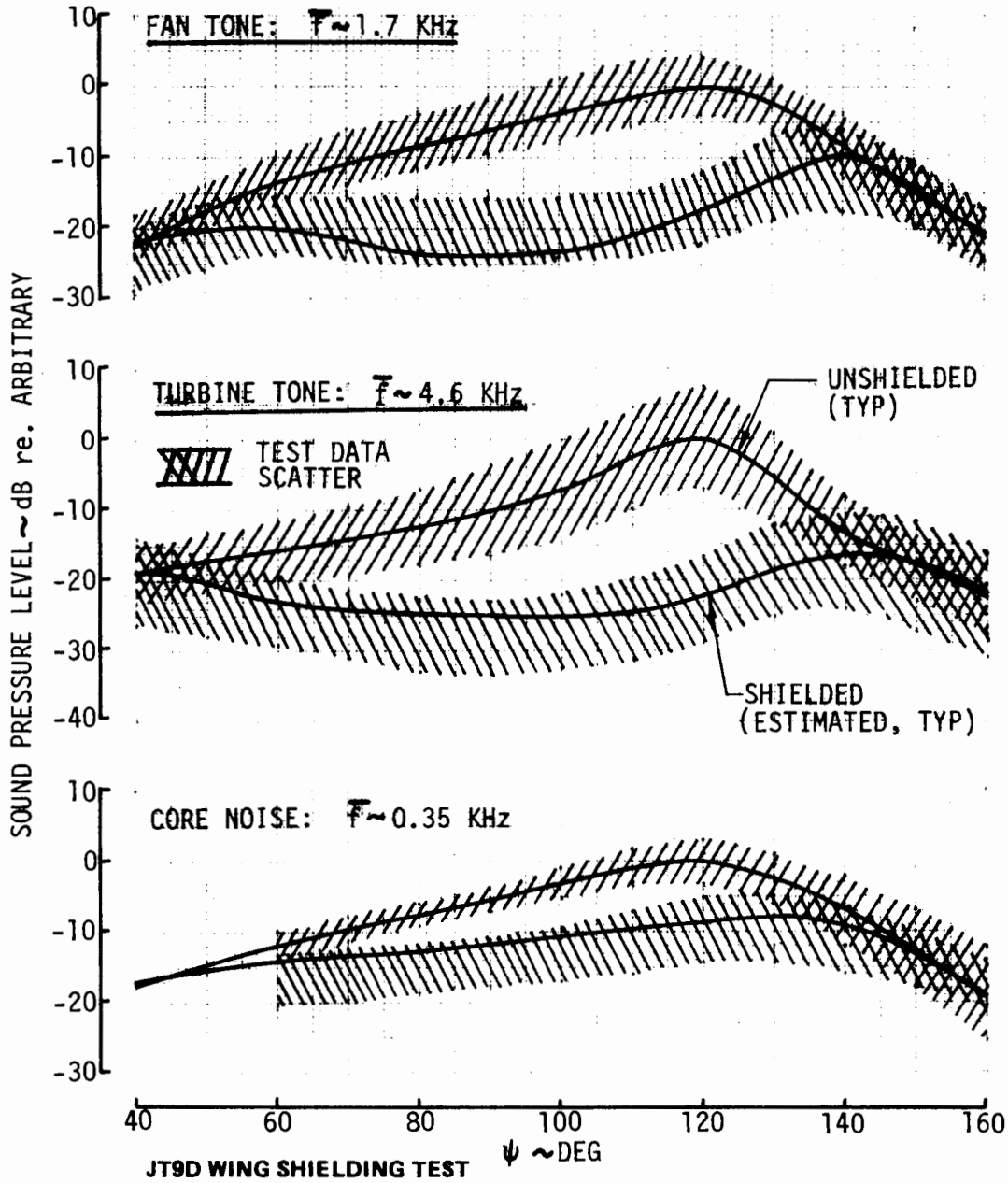

JT9D WING SHIELDING TEST

- **AVG FLOW CONDITIONS:**
  $M_o = 0$, $M_{j1} = 0.46$, $M_{j2} = 0.82$
  BPR ≈ 5, $T_{S1}/T_{S0} = 2.55$, $T_{S2}/T_{S0} = 1.06$
- **AVG ENGINE/WING GEOMETRY:** D = 1.96m, S/D = 8.1,
  $\alpha_1 = 0°$, $\alpha_2 = 28°$, $\alpha_3 = 0°$
  $X_o/D = 0$, $X_1/D = 3.1$, $X_2/D = 1.5$
  $Y_o/D = 0.75$, $Y_1/D = 0.84$, $Y_2/D = 0.28$
- **SIDELINE MICROPHONE ARRAY AT 45.7m FROM ENGINE ℄**

Figure 154.—Turbomachinery Noise Shielding Model Performance (Flyover Wing Geometry)

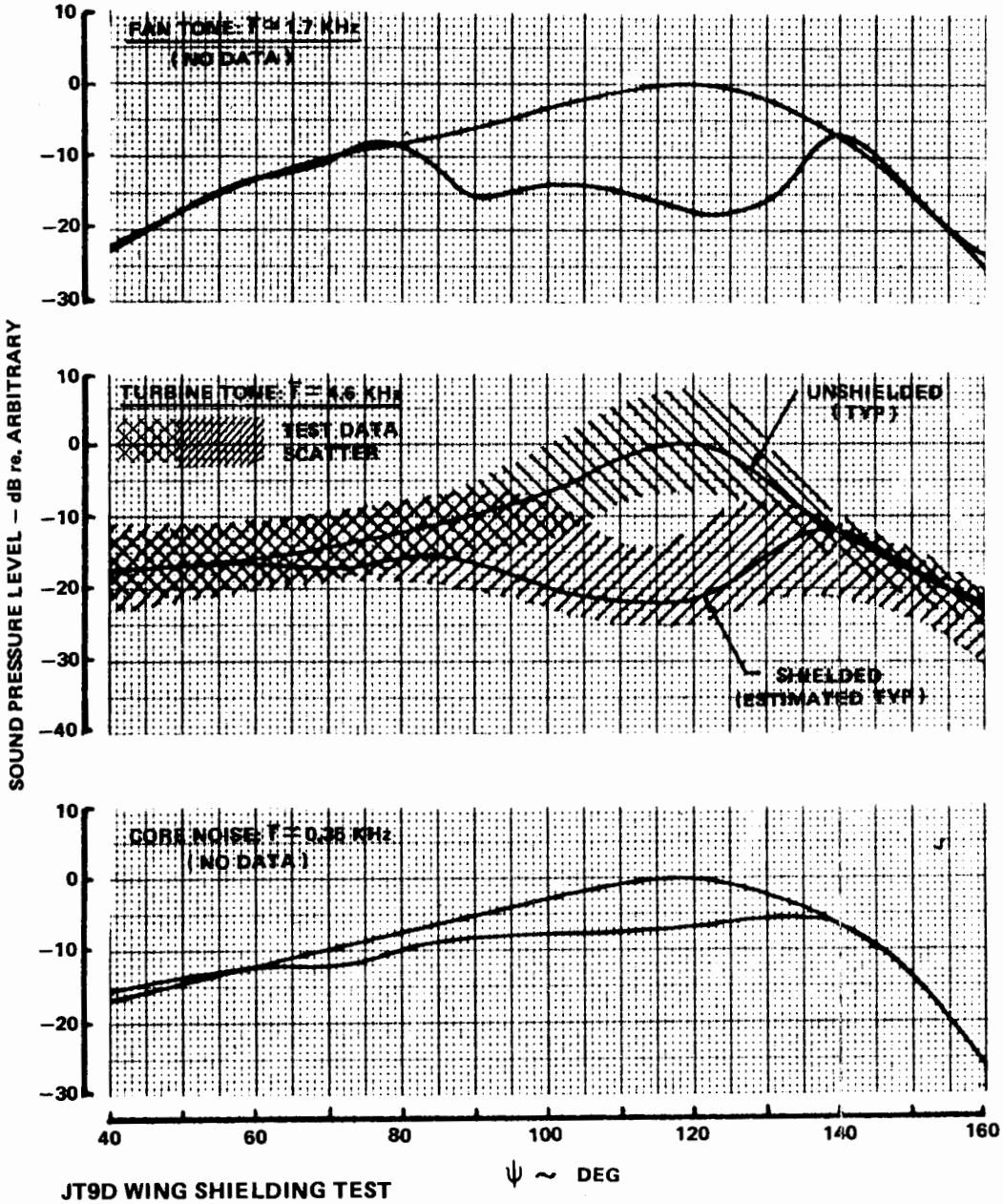

JT9D WING SHIELDING TEST

- **AVERAGE FLOW CONDITIONS:** $M_o = 0$, $M_{j1} = 0.46$, $M_{j2} = 0.82$; BPR ≃ 5, $T_{s1}/T_{so} = 2.55$, $T_{s2}/T_{so} = 1.05$
- **AVERAGE ENGINE / WING GEOMETRY:** D = 1.96m, S/D = 8.1,
  $\alpha_1 = 10°$, $\alpha_2 = 28°$, $\alpha_3 = 0°$
  $X_o/D = 0$, $X_1/D = 3.1$, $X_2/D = 1.5$
  $Y_o/D = 0.75$, $Y_1/D = 0.84$, $Y_2/D = 0.28$
- **SIDELINE MICROPHONE ARRAY AT 45.7m FROM ENGINE ℄**

Figure 155.—Turbomachinery Noise Shielding Model Performance (25° Wing Geometry)

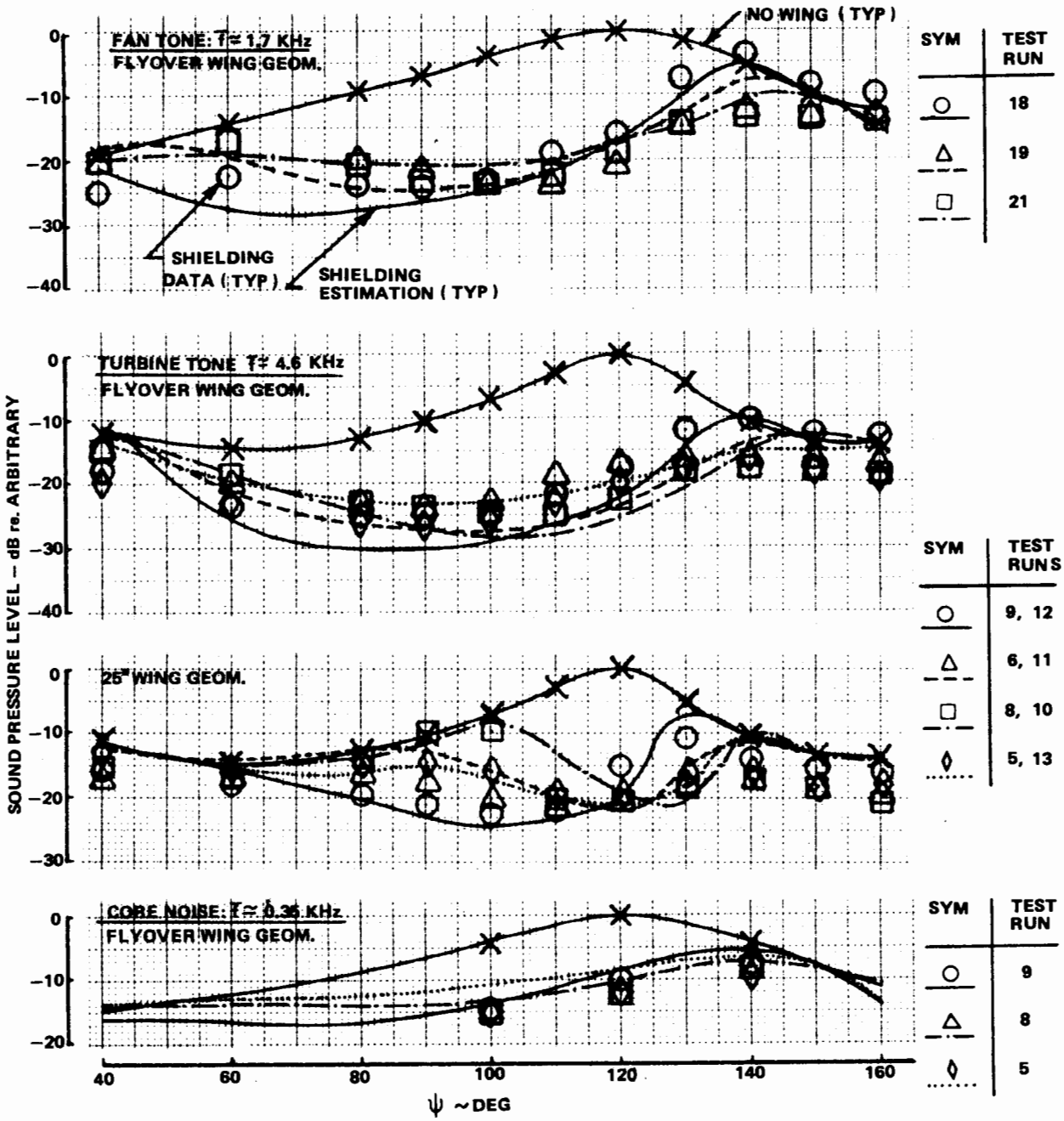

- JT9D FULL SCALE TEST (TULALIP FACILITY)
- SPL DATA AVERAGE OVER DIFFERENT FLOW CONDITIONS
- AVERAGE FLOW CONDITIONS: $M_o = 0$, $M_{j1} = 0.46$, $M_{j2} = 0.82$

  BPR ≃ 5, $T_{s1} / T_{so} = 2.55$, $T_{s2} / T_{so} = 1.05$
- POLAR ARC MICROPHONE ARRAY (R = 45.7 m)

Figure 156.—Turbomachinery Noise Shielding: Prediction Versus Measurement

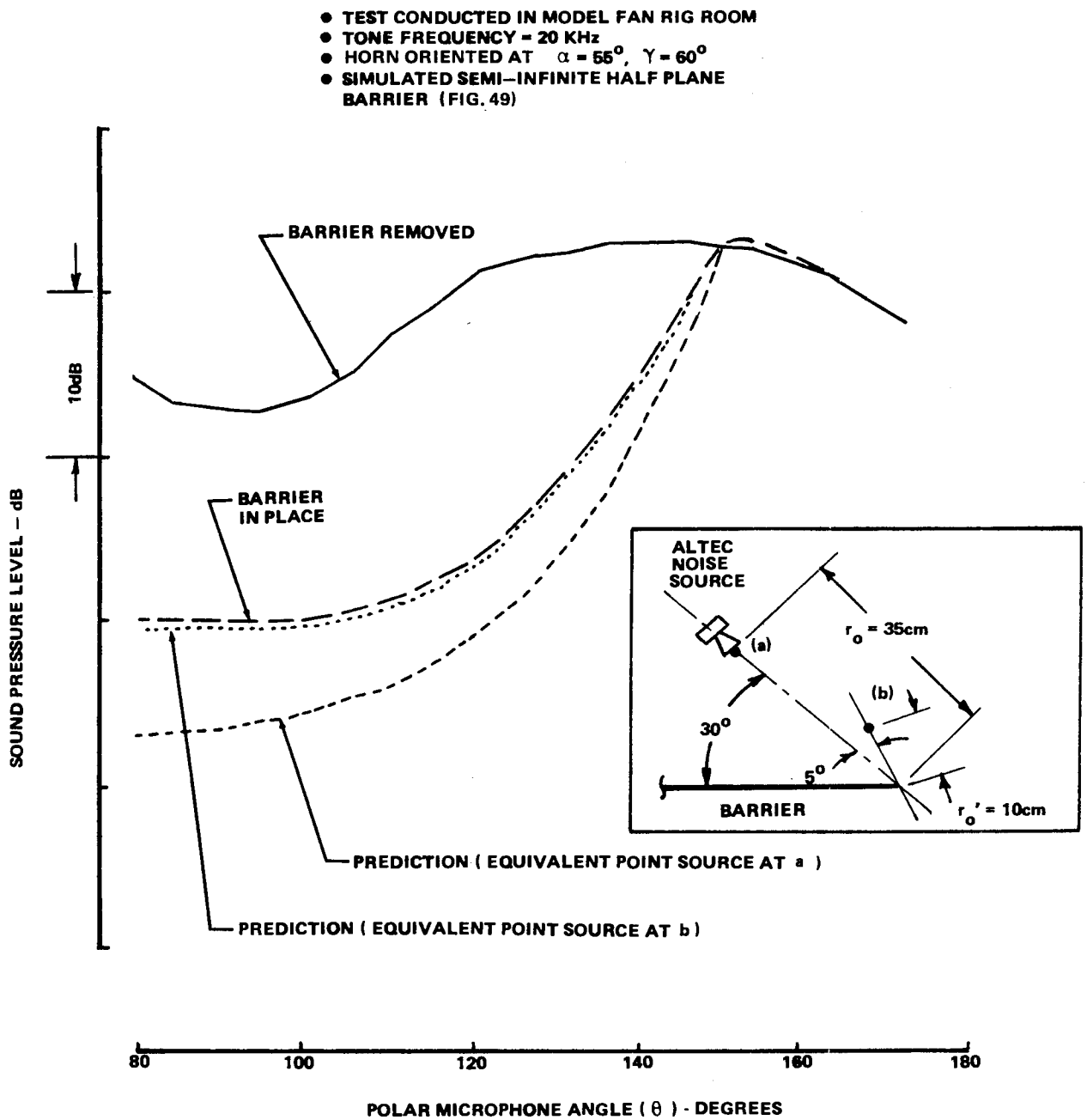

Figure 157.—Comparison of Estimated and Actual Shielding as Measured in Model Fan Rig Room

of the source. Some process other than edge diffraction is governing the observed sound field in the shadow zone.

The same barrier and essentially the same noise source combination were also tested in the Large Test Chamber (LTC) as a part of the group 2 test program (fig. 52). Resulting data are shown in figure 158. An estimate based on an equivalent point source located at the exit plane of the Altec noise source is also shown. In this case agreement between prediction and measurement is good.

Since the barrier and noise source involved in both these tests were essentially the same, differences in measured shielding effectiveness can be credited to differences in the two test rooms. The excellent agreement between LTC test data and prediction, coupled with informal assessments of 40-dB-down reverberant levels in the LTC, strongly suggests that noise reaching the shadow zone of the simulated semi-infinite half-plane barrier was diffraction controlled when tested in the LTC. On the other hand, the much smaller size of the model fan rig test room coupled with assessments of room wall absorptions of 95% to 98% would suggest 20- to 25-dB-down reverberant levels in this test room. Flanking radiation can cause the deep, shadow zone levels measured in the fan rig room test to exceed the levels detected during the LTC tests.

Based on the example cited, it is concluded that equivalent noise source locations appearing close to barrier edges can result (using the optimization program of sec. 2.4.2.1) from failure to account for radiation penetrating the shadow of a barrier due to mechanisms other than diffraction about the barrier's edges. Radiation reaching the shadow zone of a barrier due to mechanisms other than diffraction has already been referred to as "flanking radiation." Two causes of such radiation are

- Reflection off and/or scattering from structures in the vicinity of the noise source/shield combination. This appears to have been the case for the example cited.

- Scattering by atmospheric irregularities and turbulence. Experimental data shows that this mechanism appears to place an upper limit on outdoor shielding of about 24 dB or less (refs. 45 through 48).

The probability of flanking radiation being a significant or dominant contributor to shadow zone noise levels increases with continuing decreases in the diffracted signal strength (relative to the peak unshielded level) in the shadow zone. This appears to have been the case for the cited example.

The cited group 2 test example is the only one performed at Boeing where flanking radiation is clearly demonstrated. However, by association, shielding data taken during the model fan rig test program (sec. 2.4.2.2) can be expected to be contaminated (dominated) by flanking radiation in deep shadow regions since these data were taken in the same test room as the cited group 2 test data. Beyond this, we can only suspect that other Boeing shielding tests were contaminated by flanking radiation because similar patterns can be discerned.

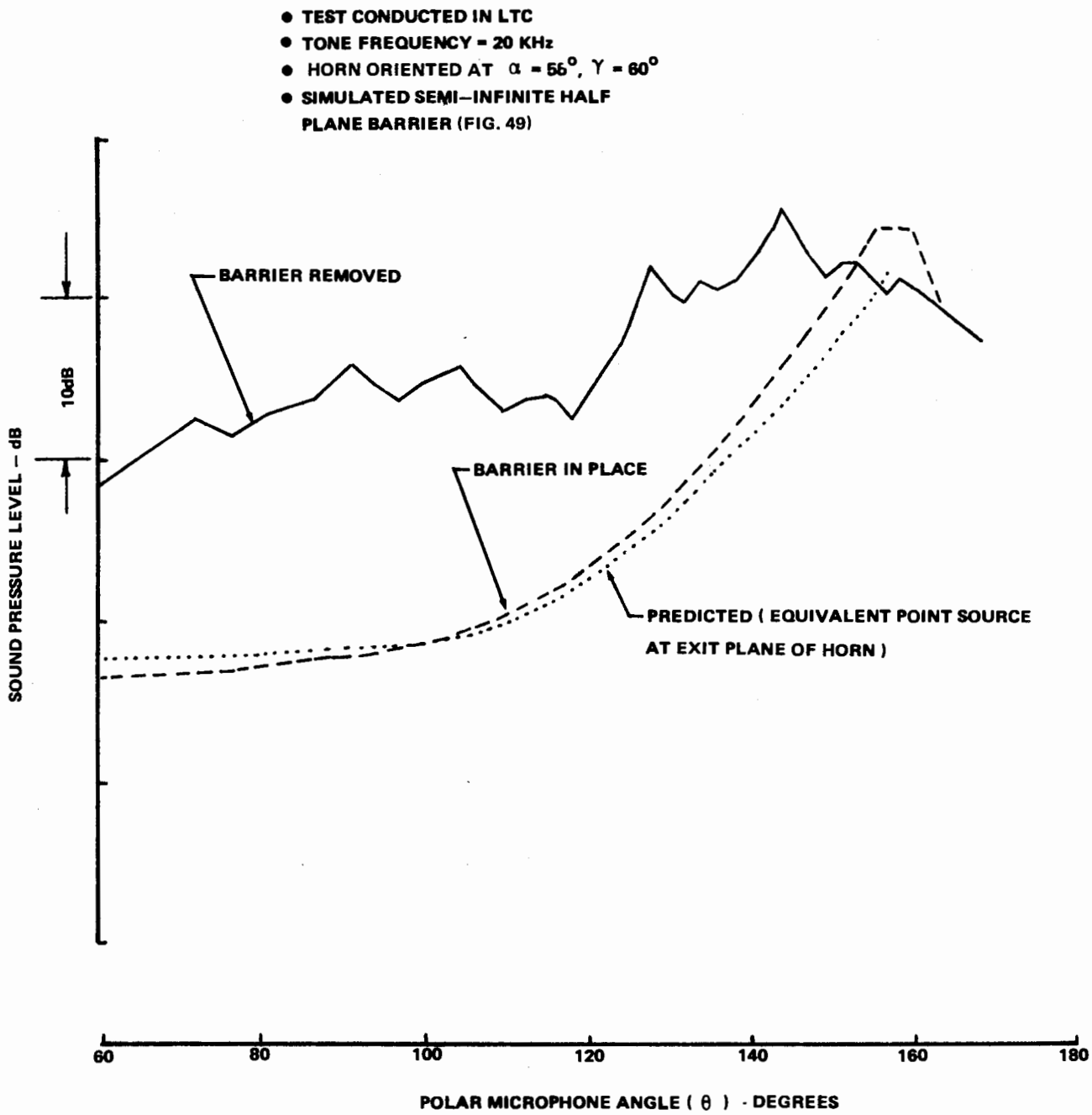

Figure 158.—Comparison of Estimated and Actual Shielding as Measured in LTC

For instance, the possibility of flanking radiation was pointed out in the Wall Isolation Facility tests (fig. 69). Reflections from pads below the wing shield/nozzle combination could be responsible for the nearly identical deep shadow zone shielding levels of a 90° wing barrier with and without thrusting flow (fig. 83). In the case of the full-scale JT9D Tulalip shielding test program (sec. 2.3.1.4), the observed maximum shielding attenuation for discrete tones was always 20 to 23 dB, independent of the fan or turbine tone frequency, position of the engine, or whether the wing was at 90° or 25°. These results suggest dominating flanking radiation in the deep shadow zone due to atmospheric, ground, or test stand scattering. The arrangement of the test setup (fig. 88) also suggests that the blockhouse, etc., could reflect significant energy into the shallow shadow zone at the leading edge of the wing.

With regard to the analyses developed in the previous three sections, the importance of flanking radiation is that it could lead to equivalent source locations appearing very close to barrier edges. Needless to say, with the present data base, identification of the flanking path contribution would be difficult, although in the future such a data analysis could be attempted. It is equally clear that the present data base is not really adequate for resolving the critical matter of what effect nozzle exhaust flow has on the propagation of internally generated noise out of the nozzle and hence out of the flow. An experimental program modeled after the Wall Isolation Facility shielding test program, but performed in a carefully controlled and monitored facility such as the LTC, would go a long way toward resolving this matter of nozzle exhaust flow effects.

In the absence of a quantitative assessment of flanking radiation, the method for estimating static shielding of exhaust TM noise components developed in section 2.4.2.3 is to be used. No explicit method for predicting flanking radiation is incorporated. However, if flanking radiation is important for the test data used in the formulation of the method of section 2.4.2.3, it is implicitly accounted for by the use of empirical source locations shown in figure 152.

2.4.2.5 Application to Shielding of Inlet Noise

Our attention now turns to consideration of the noise emitted from the engine's inlet. No strong shear gradient is present as for the case of exhaust noise components. Hence, flow refraction effects should be negligible. It is expected that diffraction theory by itself should work fairly well for wing shielding predictions of inlet noise.

Boeing possesses 727 airplane flight test data somewhat related to inlet fan noise shielding by a wing and fuselage, but this data is insufficient for a prediction procedure development. The only static test data available to our knowledge specifically addressing inlet noise shielding is that published by Hellstrom (ref. 5). His test data is for a flat barrier shield rather than a wing. Hellstrom made use of half-plane diffraction theory for a simple point source placed at the center of the inlet plane to analyze his data. He found that the theory worked quite well. This is not surprising because the radiation pattern for inlet turbomachinery noise is almost omnidirectional for directivity angles (ψ) less than approximately 70° relative to the engine's inlet centerline.

If we consider Hellstrom's results in conjunction with our test data dealing with a directive/compact source for a model wing without flow (sec. 2.4.1), it appears that the prediction model discussed previously in section 2.4.2.3 can be extended to include inlet noise by simply deleting the jet refraction effects. This would place the noise source location at the center of the inlet. This is what we propose to do for inlet noise shielding estimation until additional test data become available.

2.4.3 FLIGHT AND FORWARD VELOCITY EFFECTS ON WING SHIELDING

This section assesses collective shielding data trends for the three experiments described in section 2.3.2 wherein either the noise source/shield or the ambient medium was in motion. These data trends are compared with anticipated shielding trends based on flight effects theory presented in section 2.2.1.2 ("Uniform Flow Effects") and 2.2.4.2 ("Wing Wake Scattering").

2.4.3.1 General Assessment

As a result of these efforts it appears:

- Shielding effectiveness of a wing is *not* systematically dependent upon ambient flow or forward velocity up to the test data limit of about 75 m/s. However, the existing test data base is so limited that more testing is required to validate this apparent result.

- Test data trends could be consistent with the predicted combined effects of wing wake scattering and uniform flow diffraction theory. It is difficult to separate the effect of each because they tend to be opposite. However, scattering would have to be comparable to uniform flow effects in order to account for the observed flight effects.

- Accounting for the opposite effects of wing wake scattering and uniform flow hypothesized above requires rather strong scattering. However, the importance of wing wake scattering is difficult to assess because not only is little acoustic data available, but the near-wake turbulence properties necessary for scattering calculation are also scarce.

- Effects of uniform flow on measured shielding do not seem as dominant as predicted by the uniform flow diffraction theory of section 2.2.1.2. With increasing ambient flow velocity, the theory generally predicts

  - Increasing shielding effectiveness for noise emanating from the wing/flap system's trailing edge

  - Decreasing shielding effectiveness for noise emanating from the wing's leading edge

Based on these assessments, we propose the inclusion of uniform flow effects for optional use in an expanded version of the estimation method developed in section 2.4.2.

However, we do not recommend that the uniform flow option be generally used with the computerized estimation procedure to be discussed in section 4.0. This is because, taken alone, uniform flow effects on diffraction appear to decrease leading edge and increase trailing edge shielding attenuation much more than that observed. The joint accounting for both uniform flow and wing wake scattering is probably necessary, but near-wing wake turbulence is insufficiently known to warrant computerized estimation (only a manual procedure is provided for estimation of wing wake scattering).

2.4.3.2 Data Evaluation

Data for the three experiments in which either the noise source/shield or the ambient medium was in motion were previously presented and discussed briefly in section 2.3.2.1 (UARL tunnel/powered nacelle shielding test), section 2.3.2.2 (airborne/horn-on-wing shielding test), and section 2.3.2.3 (727-100 and -200 airplane flyby inlet shielding comparison). Review of the data suggests

- In the case of the UARL tunnel tests, the rate of change of fan tone shielding effectiveness is positive for tunnel velocities from 0 to 45 m/s but is negative for tunnel velocities from 45 to 75 m/s. At 75 m/s, the shielding effectiveness of the wing is nearly the same as at 0 m/s (fig. 102). Turbine tone data is considered to be suspect, as was noted in the discussion in section 2.3.2.1.

- In the case of the airborne/horn-on-wing tests, the static shielding is significantly greater than that measured during flight. However, there is some question as to whether the comparison of static and flight data is appropriate. Increases in flight speed from 27 to 75 m/s produce shielding changes of up to 5 dB but with no consistent pattern discernible. A troublesome character of the *static* data is its inconsistency with the directive/compact-source theory substantiated in section 2.4.1. The data indicate that increasing the distance of the source from the edge of the wing leads to either no change or a reduction in shielding effectiveness (see figs. 107 and 108). Directive/compact-source theory would predict increasing shielding effectiveness with increasing distance from the barrier edge.

- Important unshielded data is lacking in the case of the 727-100 and -200 airplane comparison. Surprisingly, static fan noise level estimates accounting for shielding tend to agree with the flyby measurements. Conclusions are not firm, however, because unshielded data is lacking and the shallow angles result in greater uncertainty due to the greater importance of atmospheric inhomogeneities (see fig. 114).

Subject to the limitations of the data from the three tests, no systematic dependence upon ambient flow velocity or airplane velocity appears to be exhibited. The extent of the data is, however, extremely limited. Hence, these tests are better viewed as efforts to develop test techniques for determining flight effects on shielding rather than to provide definitive data to make a quantitative assessment of the effects that were originally sought. More testing is clearly needed before the effect of ambient flow velocity or airplane velocity on wing shielding can be reasonably demonstrated. A test plan for such tests, reflecting consideration of problems encountered in the tests of section 2.3.2, has been formulated and is presented in appendix B of the volume II report.

2.4.3.3 Implications of Flight Effects Theory

We have established that our shielding test data does not show a strong dependence on flight speed. Could this be consistent with the uniform flow effects and wing wake scattering theories presented in sections 2.2.1.2 and 2.2.4.2?

According to the theory of section 2.2.1.2, the effect of uniform flow on the diffracted field is to reduce the amount of energy diffracting about the trailing edge of a barrier and to increase that diffracting about the leading edge. The trailing edge diffracted field is generally the dominant field. The theory predicts that these effects should increase with increasing ambient flow velocity or airplane velocity.

For an ideal, omnidirectional/compact source, the effect of flow does not appear to be terribly strong. For example (referring to fig. 18), a flow speed of 270 m/s (Mach 0.8) decreases the diffracted levels in the deep shadow zone of a trailing edge case about 9 dB yet increases the diffracted levels in the deep shadow zone of a leading edge case. Note for this example the apparent change in the shadow boundary with flow.

When this uniform flow theory is combined with directive/compact-source diffraction theory, the effect of flow can be significantly greater. This can occur when the shadow zone boundary intersects the unshielded noise radiation curve at a steep part of the curve. As suggested above, changes in flow speed affect the apparent shadow zone boundary location. This, in turn, causes the predicted shielded noise to "fair" into the unshielded curve at a different location. The steepness of the unshielded noise directivity curve in the region near the shadow zones with and without flow makes the predicted effect of flow to appear significantly greater than that for the omnidirectional source.

When the uniform flow theory is combined with the analytical model for prediction of static TM noise shielding (sec. 2.4.2), the effect of flow is estimated to be significant. For example, figure 159 shows estimates using this combined model for the UARL/powered nacelle test geometry. Comparison with actual UARL data, shown in figure 160, suggests that the theory is suspect. However, wing wake scattering effects remain to be considered.

The scattering theory discussed in section 2.2.4.2 gives a possible explanation for the discrepancy shown in figure 160. Acoustic scattering in the wing wake can increase the amount of noise penetrating into the shadow zone of the wing's trailing edge. This scattered sound increases with tunnel velocity because the energy scattered is directly dependent on the turbulence intensity in the wake. The turbulence in turn increases with tunnel flow speed and the wing's profile drag. Hence, the absolute level of the scattered sound field depends not only on the ambient flow but also on the wing's drag characteristics. Unfortunately, the critical drag parameters for the model wing/flap systems tested are not known. Despite this limitation, further examination of the theory in section 2.2.4.2 can provide an additional insight.

Examples of the scattered sound field are shown in figures 38, 39, and 40 of section 2.2.4.2. The scattering angle (θ in fig. 37) for a flyover-type situation is

- ESTIMATES GENERATED BY CONTRACT PREDICTION PROGRAM (APPENDIX A)
- FAN TONE = 18 KHz
- GEOMETRY IS PER FIGURE 101 WITH X = 18 cm, Y = 0.6 cm, $\alpha_N = 8°$

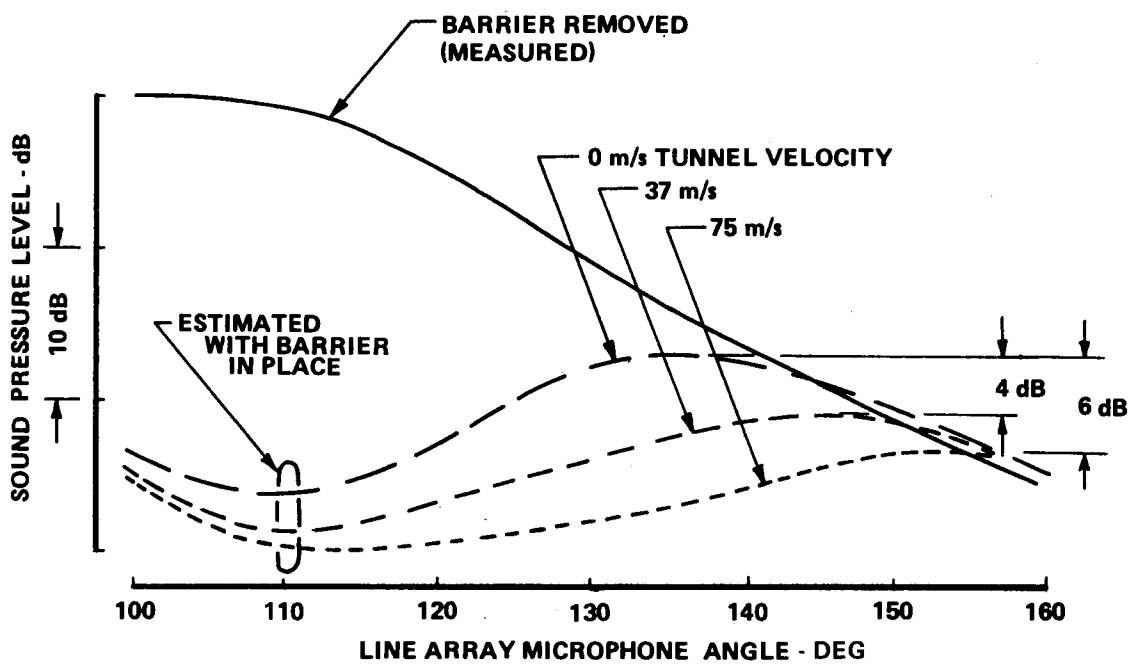

Figure 159.—Predicted Effect of UARL Tunnel Velocity on Shielding Effectiveness of Model Wing Barrier

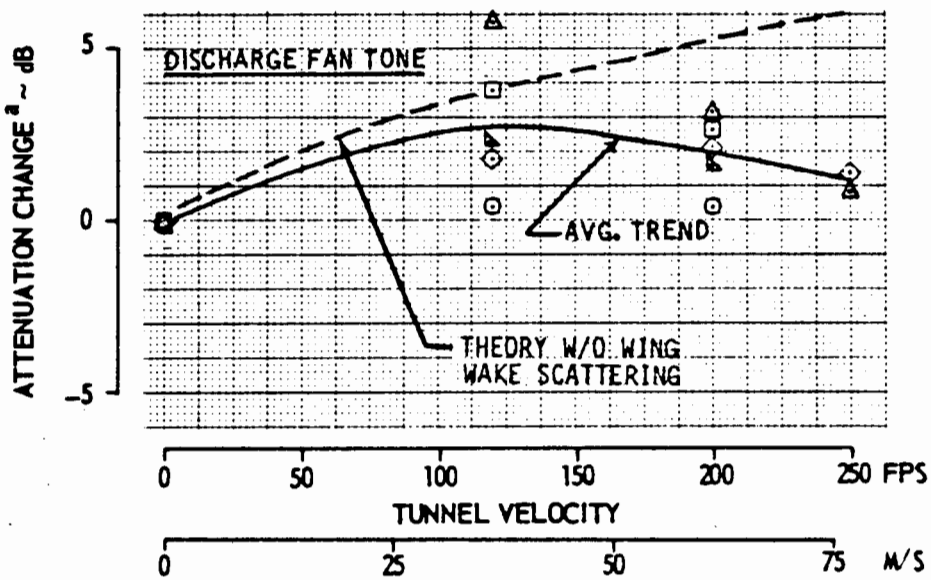

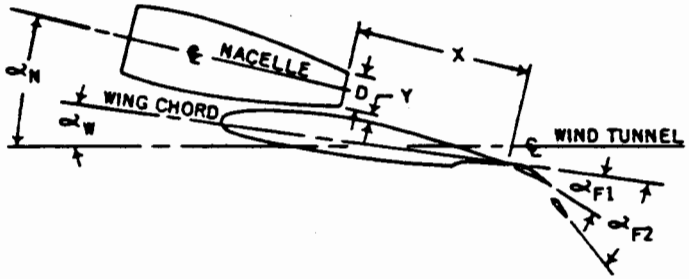

TEST CONFIGURATIONS

SYM	X/D	Y/D	α_N	α_W	α_{F1}	α_{F2}
○	0.9	0.33	8°	8°	36°	45°
□	2.5	0.08	↓	6°	↓	↓
▷	↓	↓	↓	8°	↓	↓
◇	↓	↓	↓	↓	5°	18°
△	↓	↓	12°	↓	↓	↓

NOTES

a. ATTENUATION = MAX. SPL| NO WING − MAX. SPL| WITH WING

b. UARL MODEL TEST

c. POWERED NACELLE:
BPR = 5, D = 7.6cm

d. AVERAGE EXHAUST CONDITIONS:
FAN: $M_j = 0.58$, $T_s/T_{so} = 1.0$
TURBINE: $M_j = 0.41$, $T_s/T_{so} = 0.97$

Figure 160.—Effect of Tunnel Flow on Wing Shielding Attenuation

essentially equivalent to the shadow zone angle ($\theta - \theta_0$) (relative to the apparent sound source grazing incidence angle). For high-drag coefficients, the predicted scattered field for shadow angles less than 30° can approach the strength of the incident noise field on the edge of the barrier. Thus, the wing wake scattered noise field could approach or exceed the diffracted field in just the angular sector where uniform flow effects are predicted to be greatest. Such a situation could clearly result in shielding effectiveness that increases only slowly, or perhaps even decreases, with increasing ambient flow velocity.

This last point was examined further. Another look was given to the 727-100 and -200 airplane flight test data (sec. 2.3.2.3) in conjunction with the uniform flow (sec. 2.2.1.2) and scattering (sec. 2.2.4.2) theories. Wing wake scattering estimates were completed using the nominal wing profile drag coefficient for the flight test conditions. Wing shielding estimates using diffraction theory that also included uniform flow effects were made for both aircraft configurations illustrated in figure 161. The estimates for each configuration were subtracted from one another to put them in a form directly comparable with the data showing the change in SPL as the wing is moved relative to the pod engines. These estimates are shown in figure 162.

The estimated shielding based on diffraction theory alone failed to match the test data. Inclusion of the wake effects brought the estimates in alignment with the data. Assumptions for the estimates were:

- Unshielded inlet noise was omnidirectional.
- Center engine's inlet noise contribution was significantly less than that for the pod engines.
- Exit fan noise contribution to the shielding effects was negligible.

These assumptions were reasonable in the region where wing shielding attenuation was observed.

It is concluded that the combined effects of uniform flow on diffraction and wing wake scattering *could* result in the type of behavior observed for the tests discussed in section 2.3.2. However, little progress can be made unless a reasonably reliable estimation procedure for one of the two effects can be developed. At present, neither theory provides such a reliable method.

2.4.3.4 Inclusion of Flight Effects in Shielding Estimation Model

The method for estimating static TM noise shielding developed in sections 2.4.1, 2.4.2, and 2.4.3 is shown schematically in figure 163a. Based on the discussion of the previous section, figure 163b shows a desirable expansion of this method to explicitly attempt to account for forward velocity effects, i.e., uniform flow and wing wake scattering effects. The method shown in figure 163c has been computerized and integrated with the airplane flyby noise estimation program developed for NASA under contract NAS2-6969. (The TM noise shielding estimation routines that have been programmed

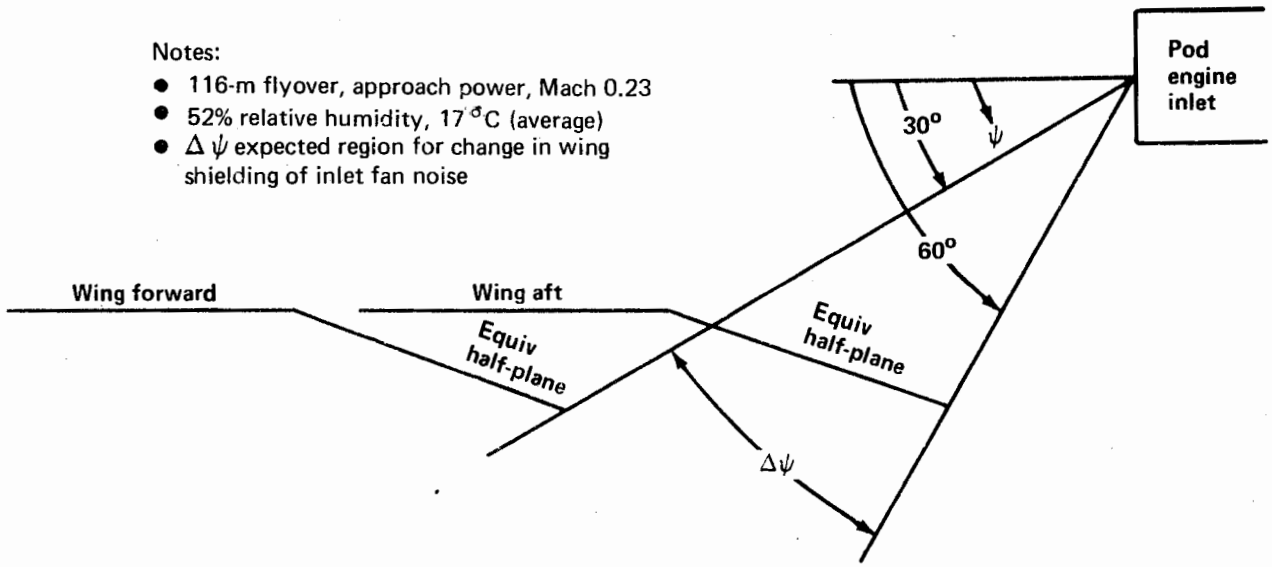

Figure 161.—727-100 and -200 Aircraft Engine/Wing Geometry

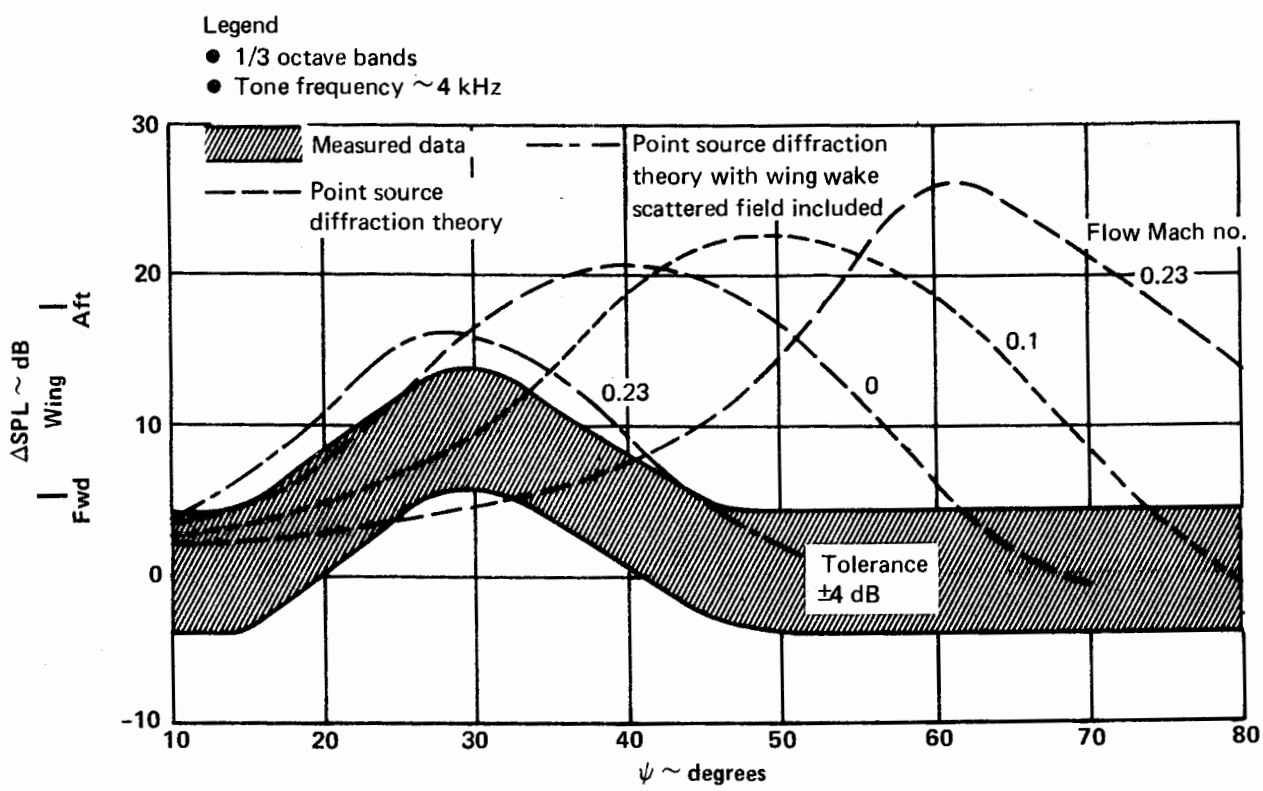

Figure 162.—Flight Test Results and Estimates

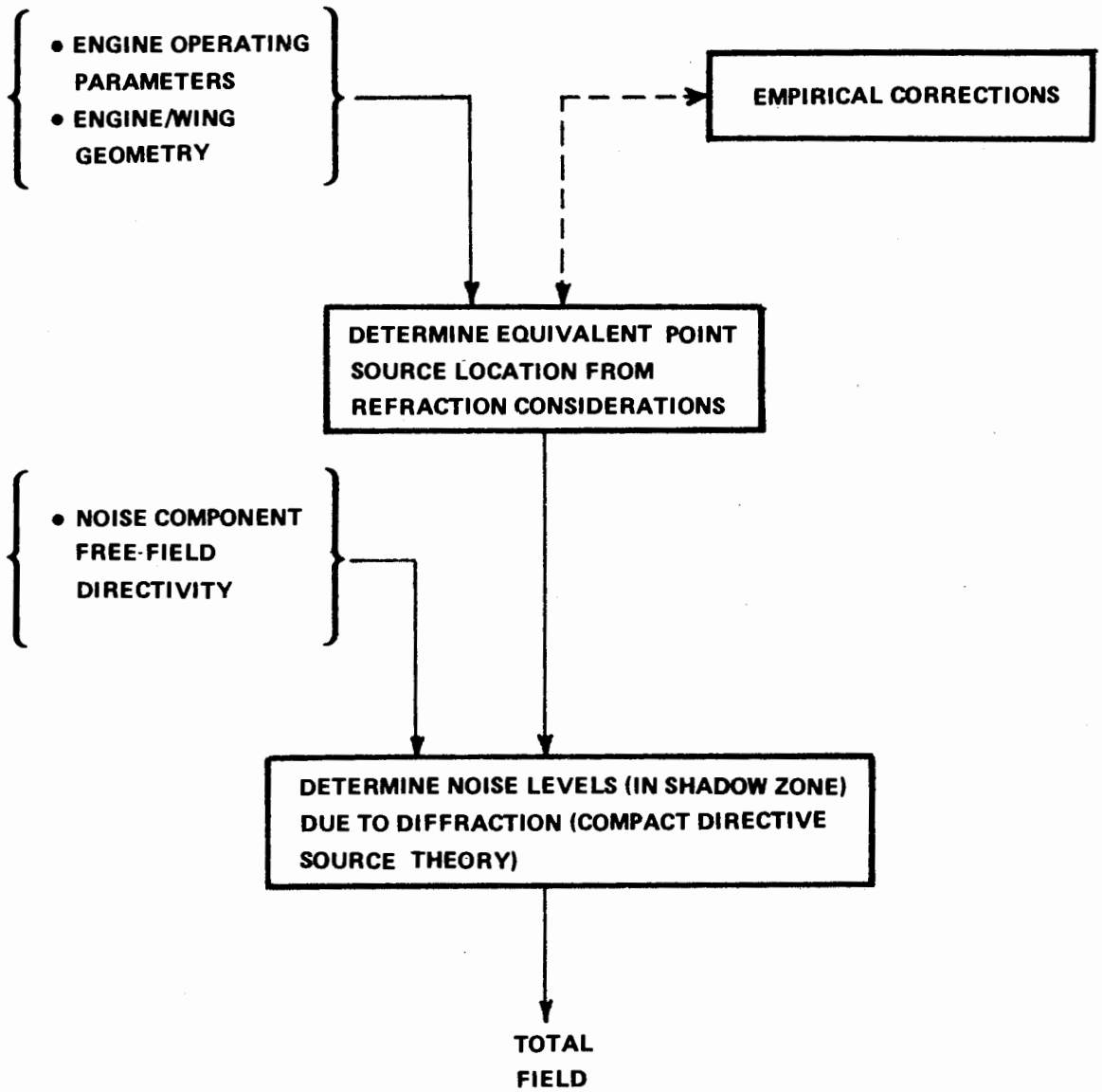

a) STATIC METHOD BASED UPON SECTION 2.2 STATIC THEORY AND SECTION 2.4.1/2.4.2 ANALYSIS OF DATA

Figure 163.—Schematic of Turbomachinery Noise Estimation Methods

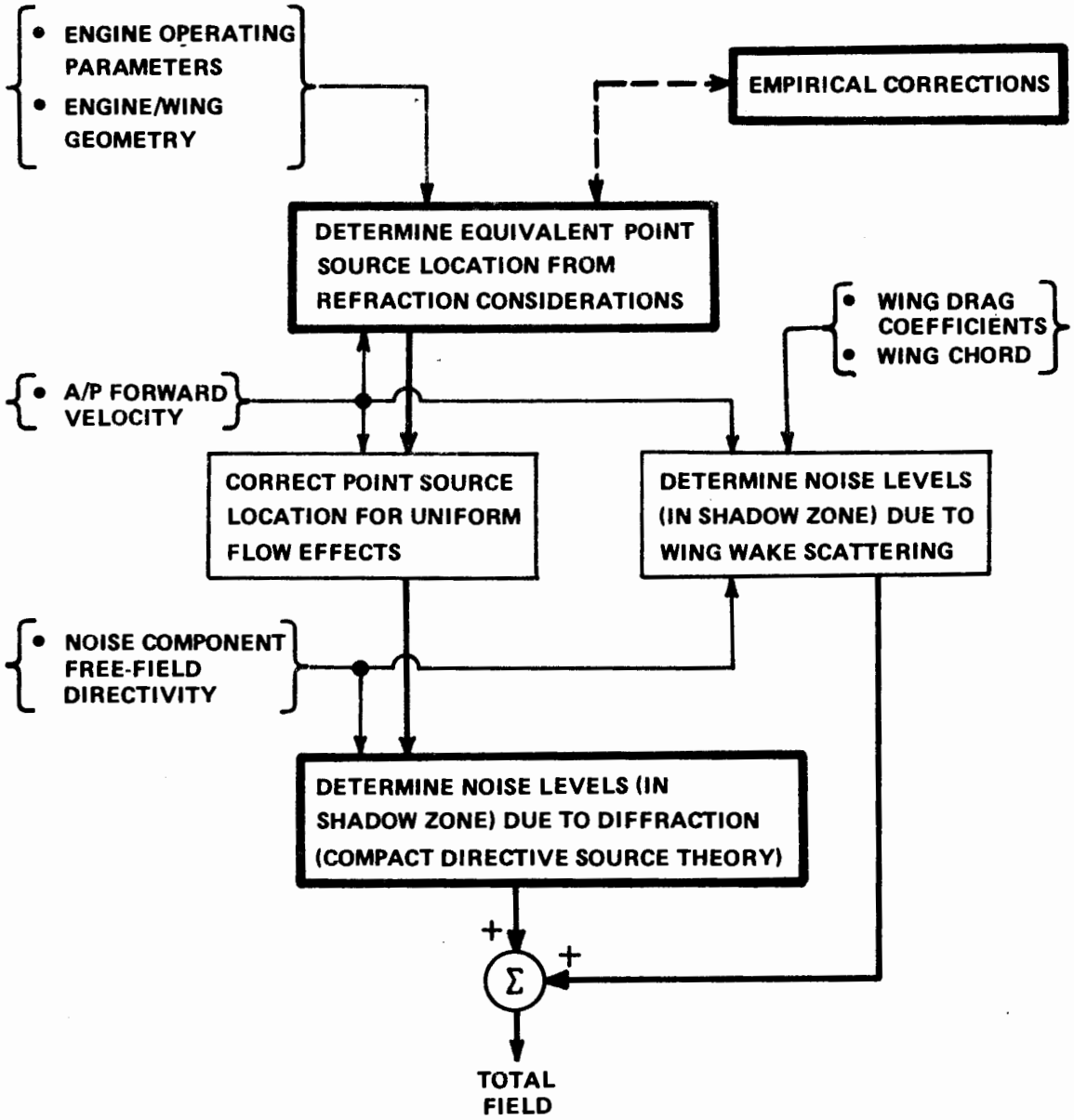

b) IDEALLY EXPANDED METHOD INCORPORATING MAIN FORWARD VELOCITY EFFECTS DISCUSSED IN SECTION 2.2

Figure 163.—(Continued)

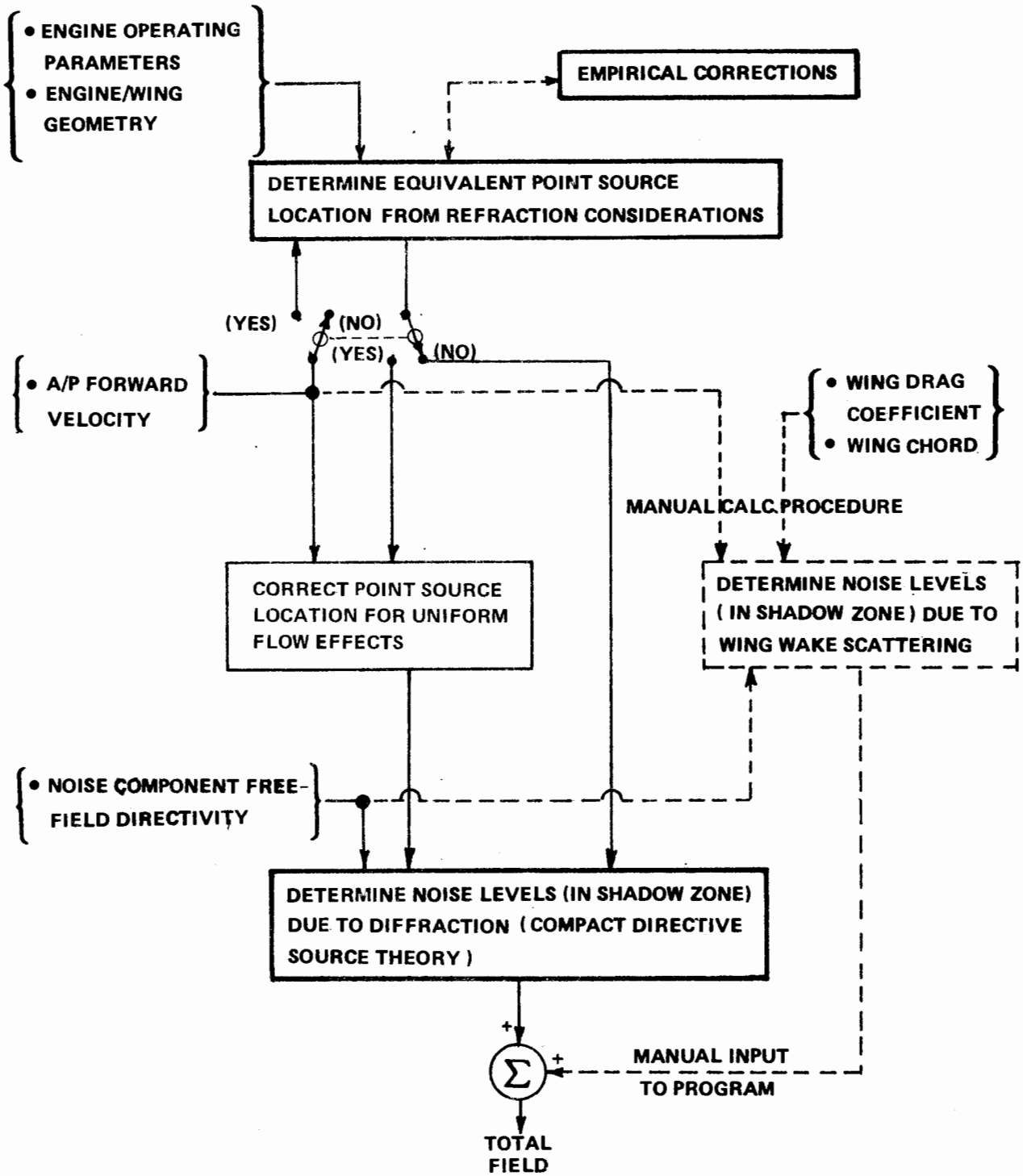

c) COMPUTERIZED METHOD
- MANUAL INPUT FOR WING WAKE SCATTERING

ESTIMATES TOTAL FIELD
- OPTIONAL INCLUSION OF FLIGHT EFFECTS

Figure 163.—(Concluded)

are discussed in secs. 4.2.1 and 4.2.2.) As can be seen, only uniform flow effects are included. (A manual procedure for estimating wing wake scattering has been developed and is discussed in sec. 4.3.2.) We believe that wing wake scattering theory is still too preliminary (sec. 2.2.4.2) to warrant integration into a complex computer prediction system at this time.

Figure 163c also shows a program option to either bypass or use the uniform flow effects correction. Figure 164 illustrates JT9D wing-shielded noise levels calculated both with and without inclusion of uniform flow effects. The curves are for a wing/engine combination of the type tested at Tulalip (sec. 2.3.1.4). As can be seen, the uniform flow effect significantly increases the trailing edge shielding effectiveness of the wing.

At first glance, the changes shown in figure 164 seem too large. When viewed in light of the test data scatter observed in both the static and flight effects tests (secs. 2.3.2 and 2.4.2.3), the changes do not appear so unreasonable. The angular sector where the large changes occur is the shallow angle region where the theory as well as the test data are suspect. Unfortunately, when wing shielding is used, this region becomes very important in determining the effective perceived noise level. For conservative reasons, it is tentatively proposed to use the computerized shielding estimation package without the uniform flow effects included in the calculation.

In conclusion, the matter of flight effects on shielding of TM noise components must be considered to be in its infancy of understanding. More testing and analysis is clearly needed. Based on insight gained from the tests conducted and the theory presented in section 2.2, a plan for such tests has been formulated and is presented in appendix B of the volume II report.

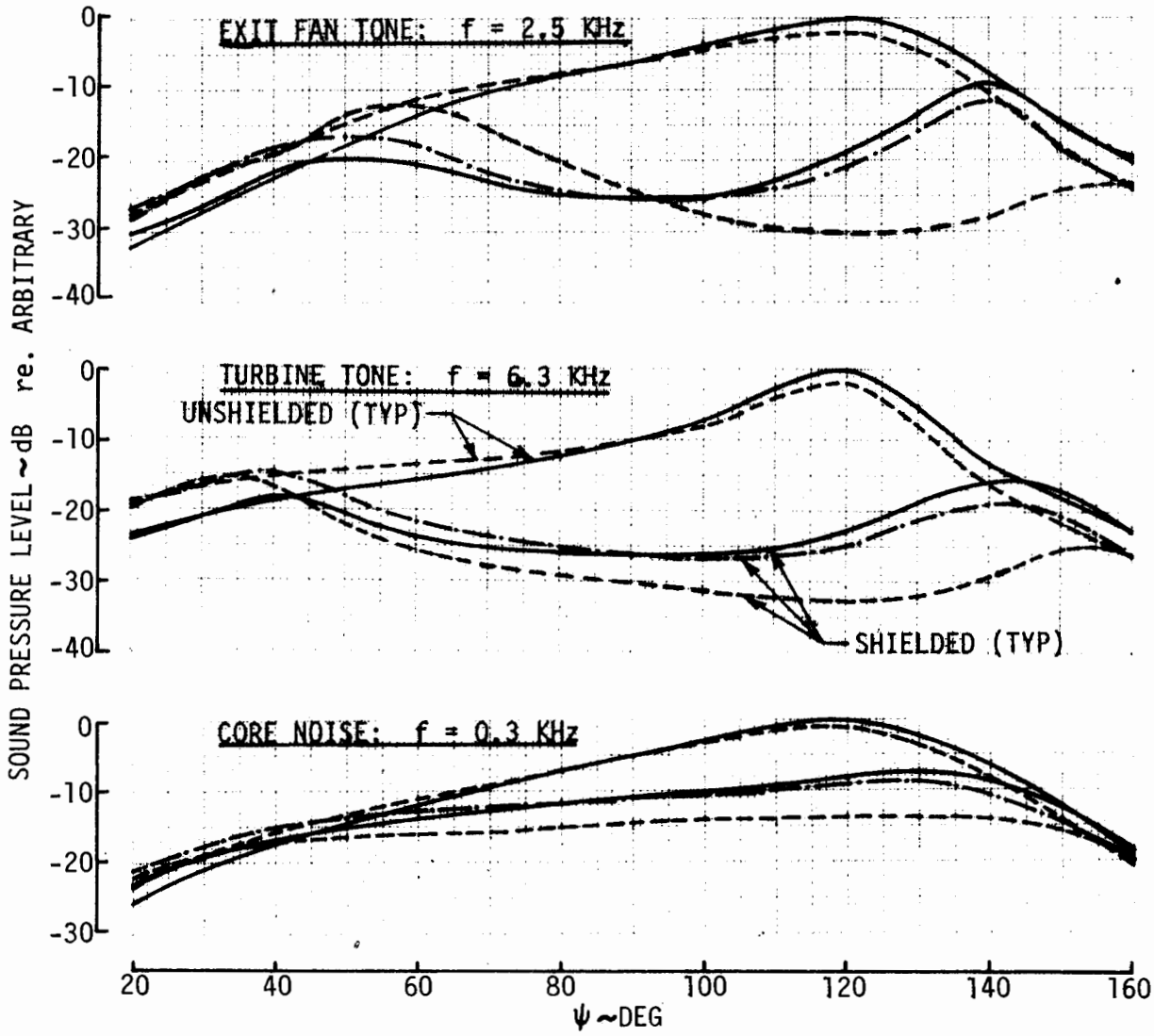

	A/P MACH #	DOPPLER EFFECT	SHIELDING FLT. EFFECT	ENGINE RPM
- - - -	0.25	Yes	Yes	Const.
—·—	0.25	Yes	No	Const.
———	0.25	No	No	Const.

- FLYOVER NOISE ESTIMATES, CPA = 45.7 M
- EXHAUST CONDITIONS AND ENGINE/WING GEOMETRY SAME AS AVERAGES QUOTED FOR JT9D STATIC SHIELDING TEST
- WING WAKE SCATTERING LIMIT NOT INCLUDED IN ESTIMATES

Figure 164.—Estimated Turbomachinery Noise Shielding in Flight

3.0 INFLUENCE OF WING ON JET EXHAUST NOISE

The principal source of jet engine exhaust noise is the free jet mixing layer. In contrast to the noise components discussed in the previous sections, the mixing-layer-generated noise occurs outside the engine in a volume extending aft from the nozzle exit plane. Jet mixing layer noise is typically broadband. The higher frequency components are generated near the nozzle, with lower frequency components generated progressively further downstream.

This section discusses the effects of an engine-over-wing installation when the wing/flap system is in close proximity to the jet engine exhaust. A potential exists for reducing community noise through shielding of the jet exhaust mixing layer noise by the wing/flap system. But the engine jet exhaust flow interacts with the wing/flap system, causing a low-frequency interaction noise that could limit the benefits of the jet exhaust mixing layer shielding. These two aspects of the wing's influence on jet exhaust noise are briefly examined below. This is followed by a discussion of Boeing/Aeritalia experiments on jet noise shielding by winglike structures. Finally, estimation methods are developed for both jet exhaust noise shielding and the noise generated by interaction of the jet with the wing/flap system.

3.1 JET NOISE SHIELDING AND JET/EDGE INTERACTION NOISE

This section briefly considers the nature of jet exhaust mixing layer noise shielded by a wing in close proximity to the exhaust jet, as well as the additional low-frequency noise generated by the interaction of the exhaust jet with the shielding structure.

3.1.1 JET EXHAUST NOISE SHIELDING

Based on the results of section 2.0, it might be anticipated that the effect of the wing/flap system as a shield for jet exhaust mixing layer noise would be to reduce the noise reaching the geometric shadow zone. This is similar to the classical shielding obtained by erecting a barrier between a noise source and an observer. But the noise generation mechanisms are different for a jet mixing layer in close proximity to the wing/flap system. The main difference is that the jet mixing layer constitutes a distributed noise source that extends beyond the wing/flap system "barrier." This increases the analytical complexity compared to that for the usually assumed "point" source of simple source/barrier analysis.

Several experimental investigations have been conducted to study the shielding capability of an engine-over-wing configuration. They are discussed in section 3.2, but a typical result is shown here for a scale model (fig. 165). For the configuration tested at frequencies above 8 kHz, the shielded jet noise is on the order of 7 dB lower than the jet-alone noise. An empirical prediction method for jet noise shielding is presented later in section 3.3.

Figure 165 also shows a substantial noise increase at lower frequencies. This increase is attributed to the jet exhaust flow interaction with the trailing edge of the wing/flap system. The nature of this interaction is briefly discussed in the next section.

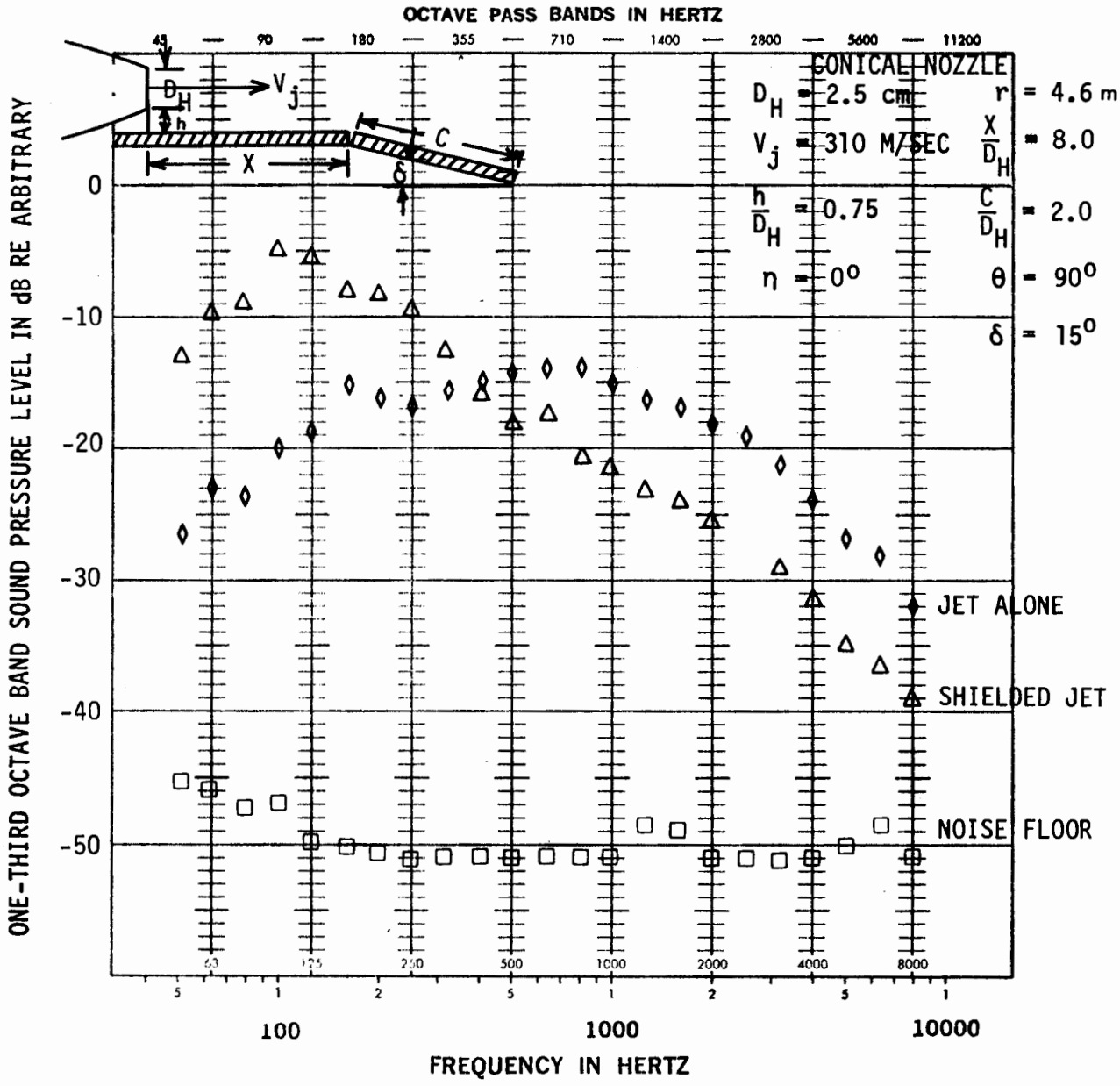

Figure 165.—Jet Exhaust Flow Shielding and Interaction

3.1.2 JET/EDGE INTERACTION NOISE

When a turbulent fluid such as an engine exhaust jet flows over an edge such as the trailing edge of a wing/flap system, a large increase in low-frequency noise is generated (e.g., refs. 45 through 48). The phenomenon is attributed to the scattering of the turbulent flow quadrupole noise sources by the edge (ref. 17). And, at sufficiently low flow speeds, this could be the dominant sound source since the edge-scattered noise intensity is proportional to the fifth power of the flow velocity. As mentioned in the previous section, the substantial low-frequency noise increase shown in figure 165 is due to this noise generation mechanism. In section 3.4, a semiempirical estimation equation is derived for jet/edge interaction noise.

3.2 EXPERIMENTS

This section describes various experimental investigations performed by the Boeing/Aeritalia companies that relate to jet noise shielding and jet/edge interaction noise. The jet noise shielding experimental results are used to confirm, with independent data, the empirical shielding estimation equation (ref. 50) described in section 3.3. The jet/edge interaction experimental results were used in the formulation of the jet/edge interaction estimation equation derived in section 3.4.

3.2.1 COLD PIPE FLOW SHIELDING/INTERACTION TEST

In 1972 tests were performed at Boeing to gain an understanding of the nature of exhaust jet noise shielding by a wing/flap system as well as to study the phenomenon of the noise generated by the interaction of a jet exhaust with the wing/flap system's trailing edge. The test used cold exhaust flow from a 2.5-cm pipe over a simple, nominal size 81- by 30-cm wing/flap system. Photographs of the test setup in the Boeing Quiet Air Facility are shown in figures 166 and 167. A schematic drawing defining the test parameters is shown in figure 168. The test parameters used to achieve the test objectives are tabulated in table 10.

Table 10.—Range of Parameters for Cold Pipe Flow Test

Pipe diameter (D_H)	2.5 cm
Exit Mach no. (M_J)	0.5, 0.75, 0.90
Shield length (X/D_H)	0, 2, 4, 6, 8
Pipe centerline height above shield (H/D_H)	2, 4, 6
Flap chord (C/D_H)	0.75, 1.5, 3
Flap angle (Φ)	15°, 30°, 60°
Polar microphone angle (θ)	90°-180°, $\Delta\theta$ =10°
Shield tilt angle (ψ)	30°, 60°, 90°

Typical test results showing the effect of shield length (X/D_H) are given in figure 169a for X/D_H = 4 and in figure 169b for X/D_H = 8. As expected, at the higher frequencies the shield effectiveness increases with increased shield length. But increased shield length increases the low-frequency far-field noise that is due to the interaction between

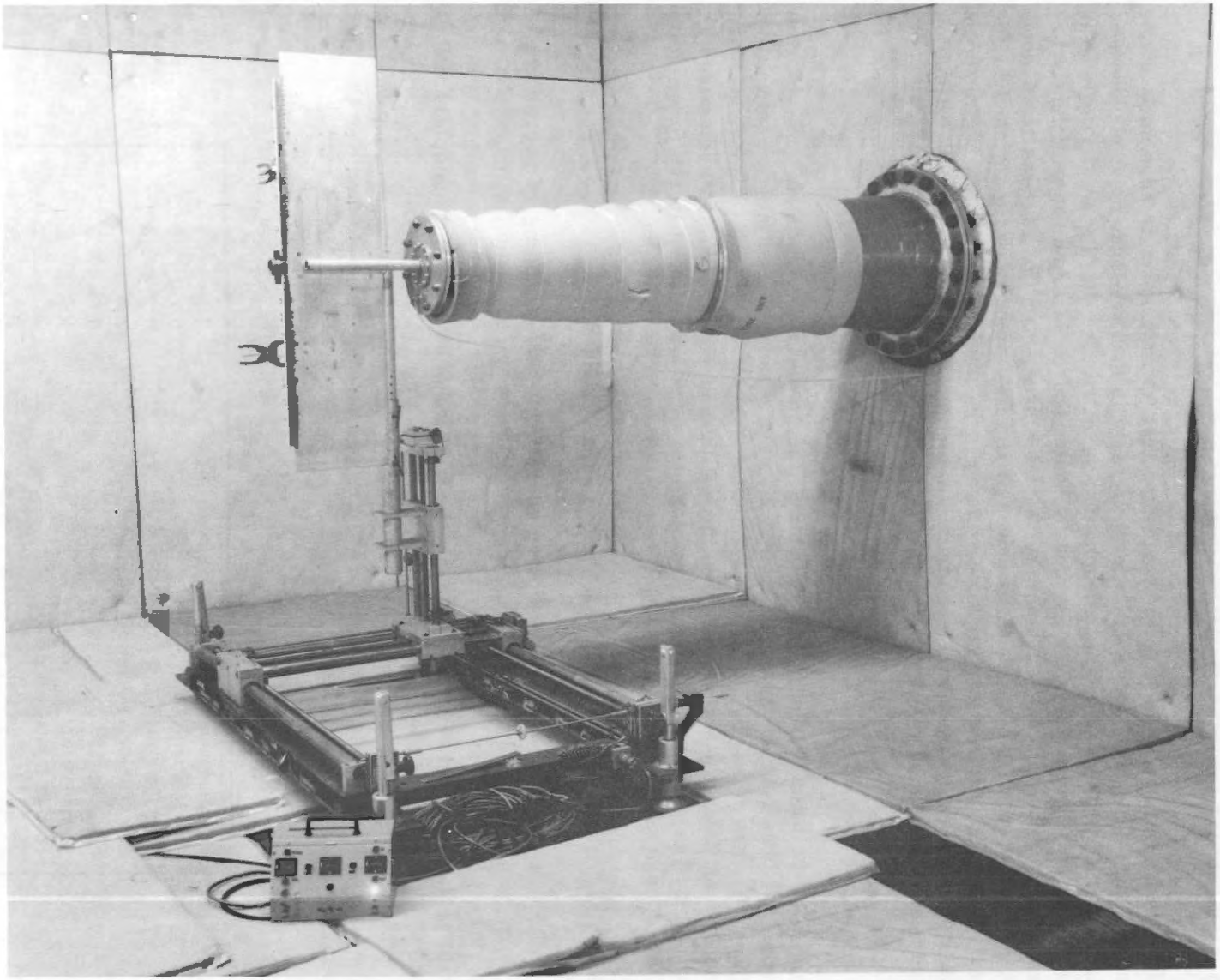

Figure 166.—Cold Pipe Flow Test Setup

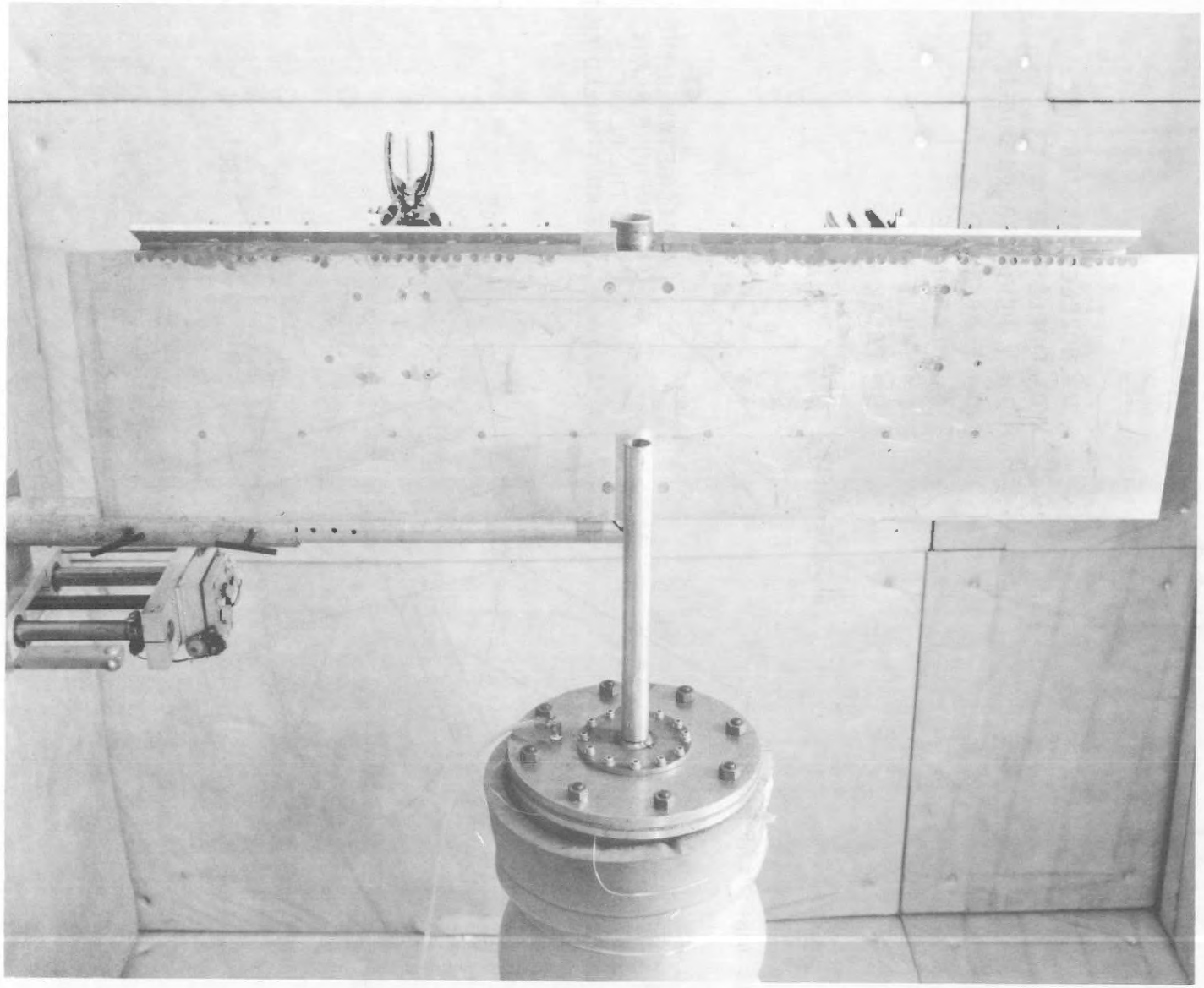

Figure 167.—Cold Pipe Flow Test—Closeup View

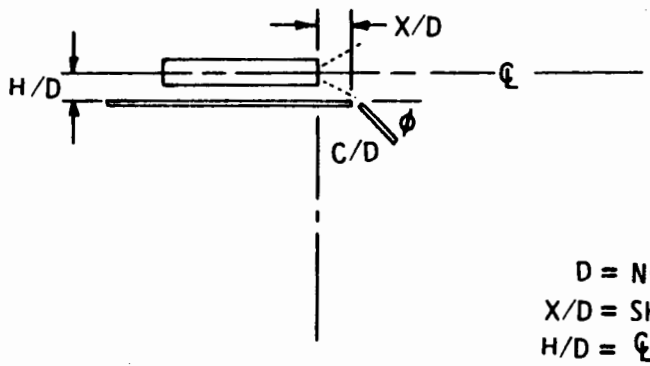

D = NOZZLE DIAMETER PIPE
X/D = SHIELD LENGTH
H/D = ℄ HEIGHT ABOVE SHIELD
C/D = FLAP CHORD
ϕ = FLAP ANGLE
ψ = SHIELD TILT
θ = POLAR ANGLE

a) SIDE VIEW

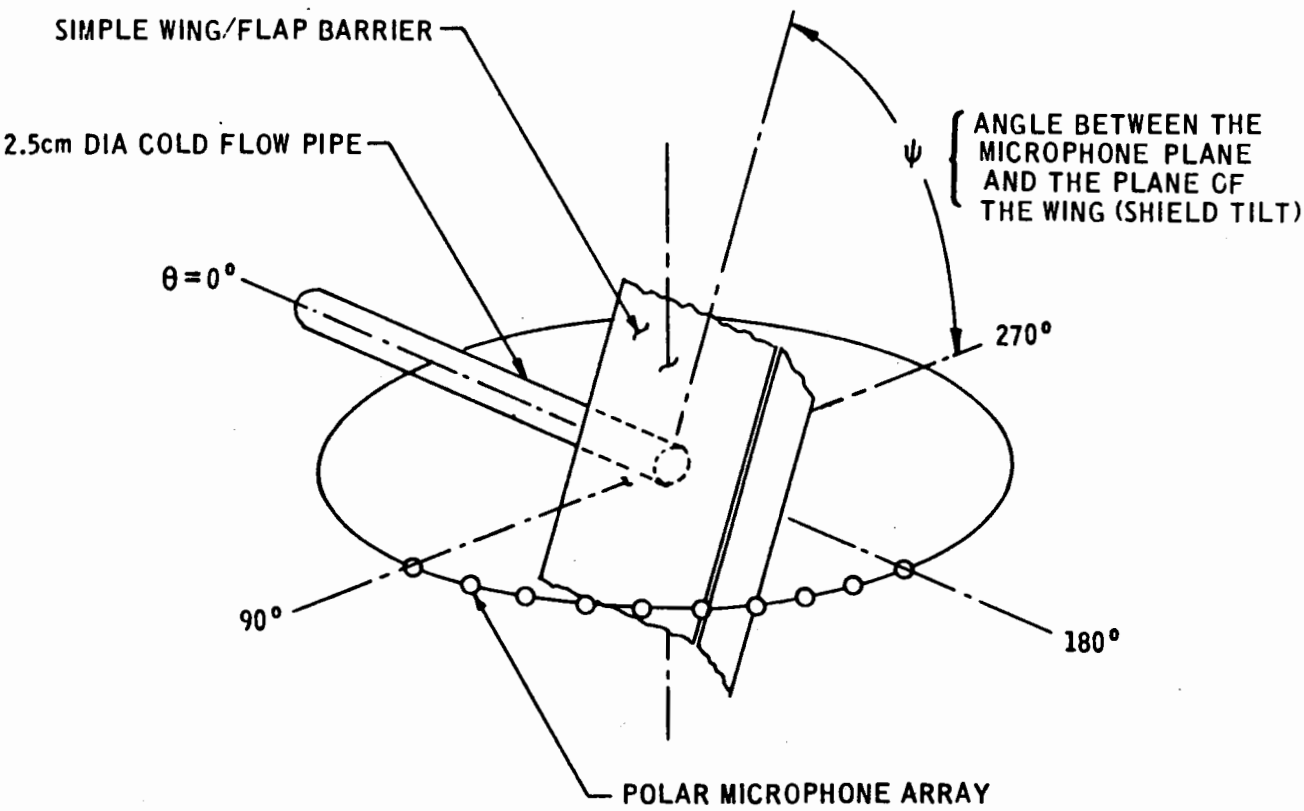

b) PERSPECTIVE

Figure 168.—Schematic of Cold Pipe Flow Test

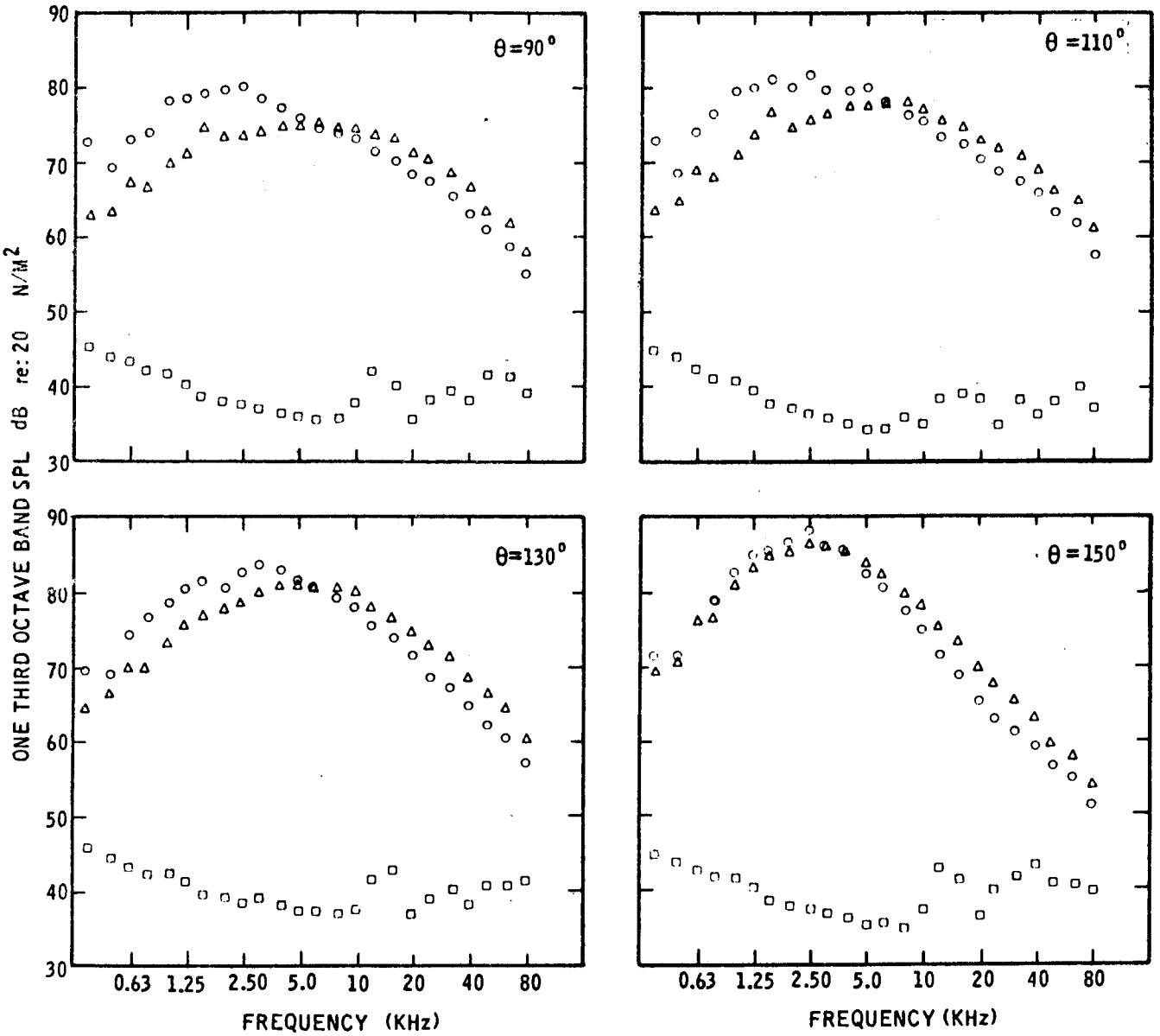

SYMBOL	CONFIGURATION	X/D	H/D	C/D	ϕ	ψ	M
○	WITH SHIELD	4	0.75	2	15	90	0.9
△	WITHOUT SHIELD	NOT APP					↓
□	NOISE FLOOR	NOT APP					

a) X/D = 4

Figure 169.—Typical Cold Pipe Flow Test Results

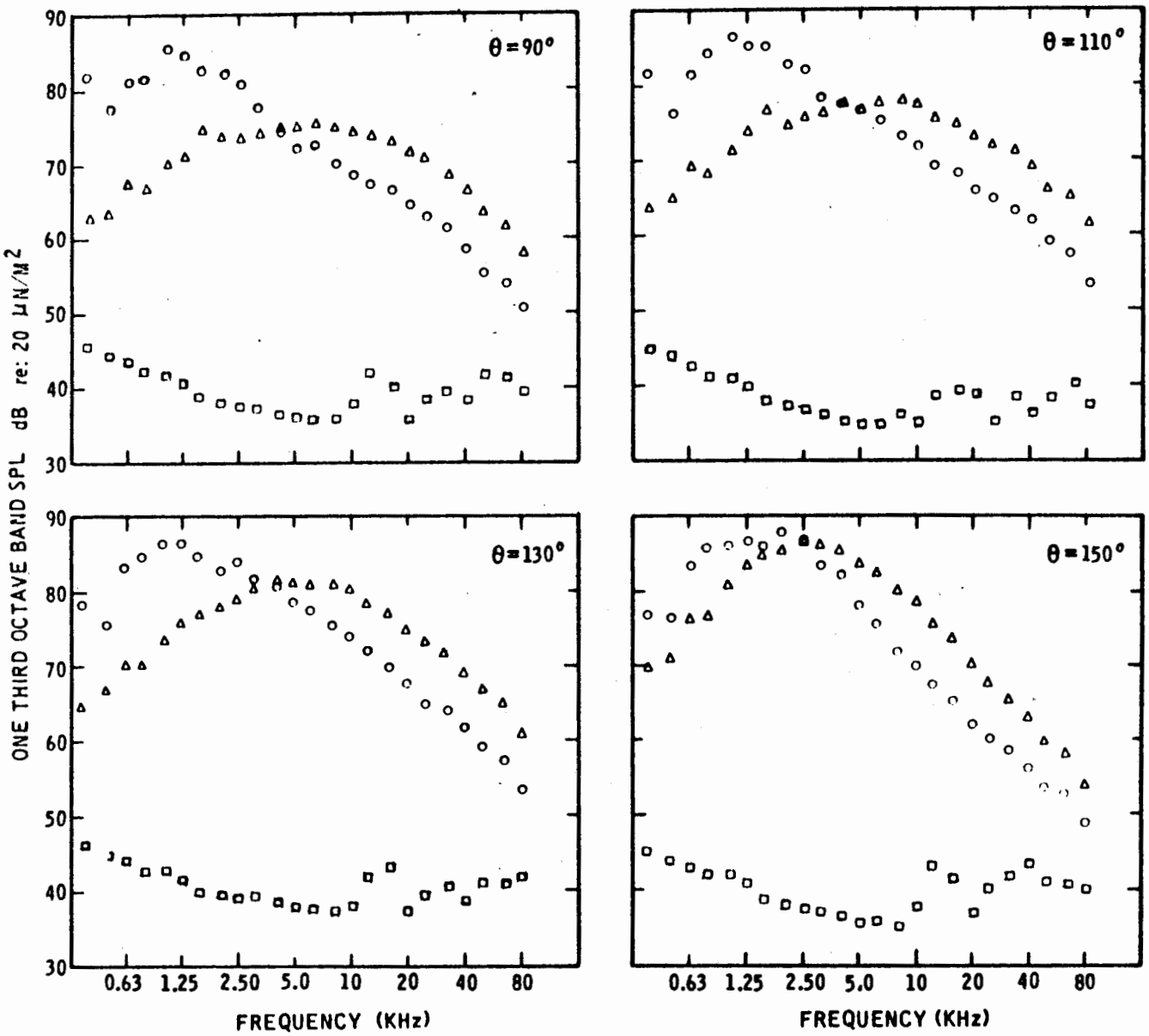

SYMBOL	CONFIGURATION	X/D	H/D	C/D	ϕ	ψ	M_J
○	WITH SHIELD	8	0.75	2	15	90	0.9
△	WITHOUT SHIELD	NOT APP					↓
□	NOISE FLOOR	NOT APP					

b) X/D = 8

Figure 169.—(Concluded)

the exhaust flow and wing/flap system trailing edge. The effect of nozzle placement parameters (X/D_H and h/D_H) with respect to the wing/flap shield surface is discussed in section 3.3 with regard to jet noise shielding estimation and, in section 3.4, the nozzle placement effect is discussed with regard to jet/edge interaction noise estimation.

Results from this test are directly used to determine the effect of nozzle placement when the jet exhaust does not completely interact with (i.e., impinge on) the shield trailing edge.

3.2.2 WALL ISOLATION FACILITY SHIELDING TEST

Boeing/Aeritalia conducted tests in 1972 to investigate the jet noise suppression benefits attainable from the shielding effect of an engine-over-wing configuration. Four types of dual-flow high-bypass-ratio nozzles were used, with their dimensions as shown in figure 170. Each nozzle was run at the operating conditions shown in table 11.

Table 11.—Nozzle Operating Conditions

Primary		Secondary	
Pressure ratio	Total temp.	Pressure ratio	Total temp.
1.2	753°K	1.2	289°K
1.36	843°K	1.4	289°K
1.6	843°K	1.6	289°K

Figure 171 shows the test setup at the Wall Isolation Facility (WIF) while figures 172 and 173 show a closeup of the shield/nozzle relationship and a schematic of the nozzle/shield detail, respectively. Two shield orientations were used: a "flyover" configuration with the wing oriented at 90° and a "sideline" configuration with the wing oriented at 25°.

Typical test results are exhibited in figures 174a and b for a fixed shield length X/D_H = 2.87 and varying nozzle heights above the shield surface. The trend of increased shielding attenuation with decreased nozzle height above the shield can be discerned at times (fig. 174a). This follows the results of diffraction theory and is discussed in more detail in section 3.3.

Also, the test results show an increase of jet/edge interaction noise with a decrease in nozzle height above the shield. This effect is considered in section 3.4.

Results from this test were used to confirm the jet noise shielding estimation equation of section 3.3 and to help establish the frequency scaling for jet/edge interaction noise of section 3.4.

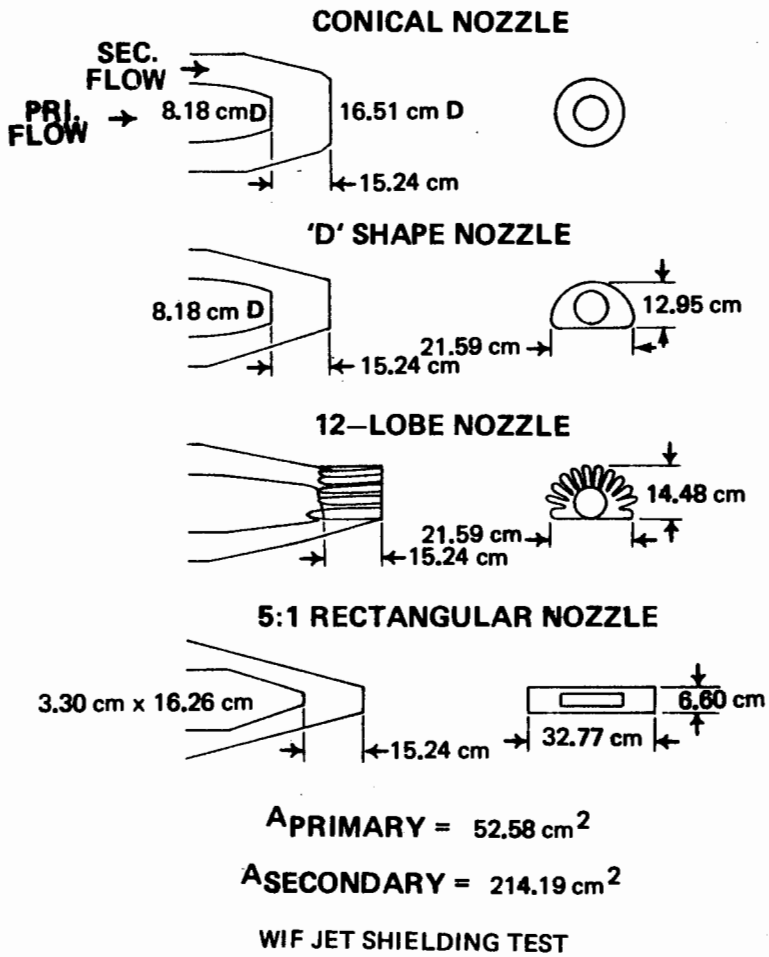

Figure 170.—Nozzle Types and Dimensions

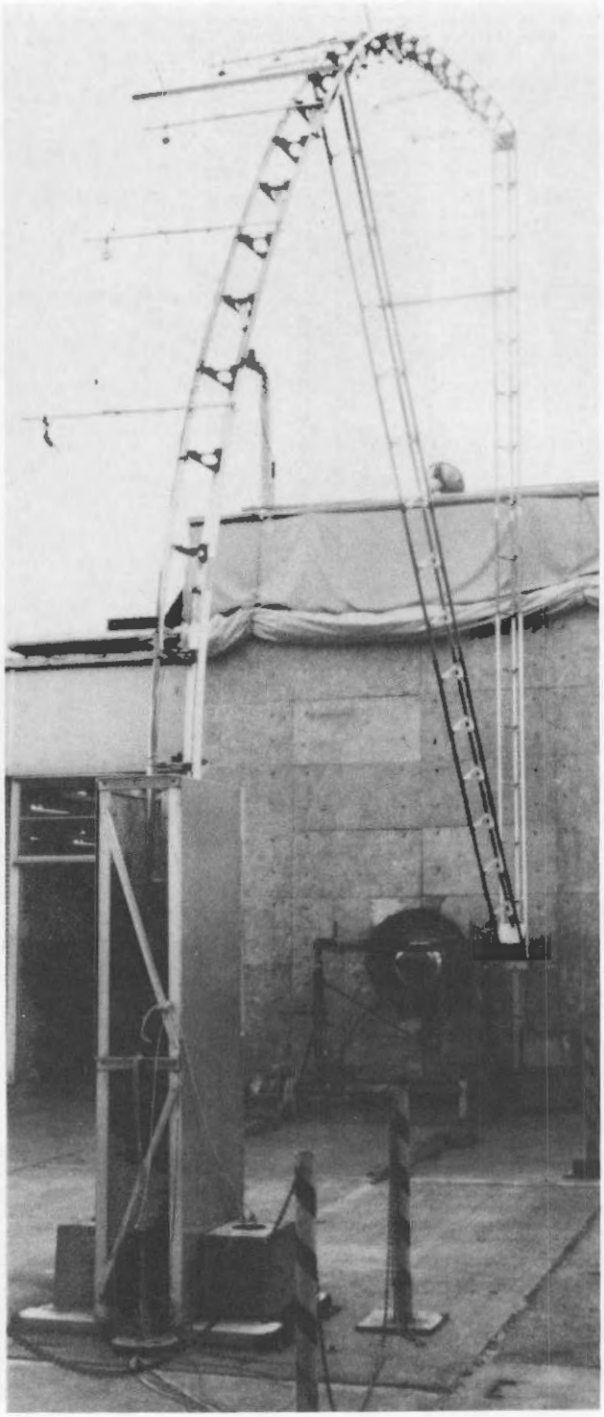

Figure 171.—Wall Isolation Facility (WIF) Jet Shielding Test Setup

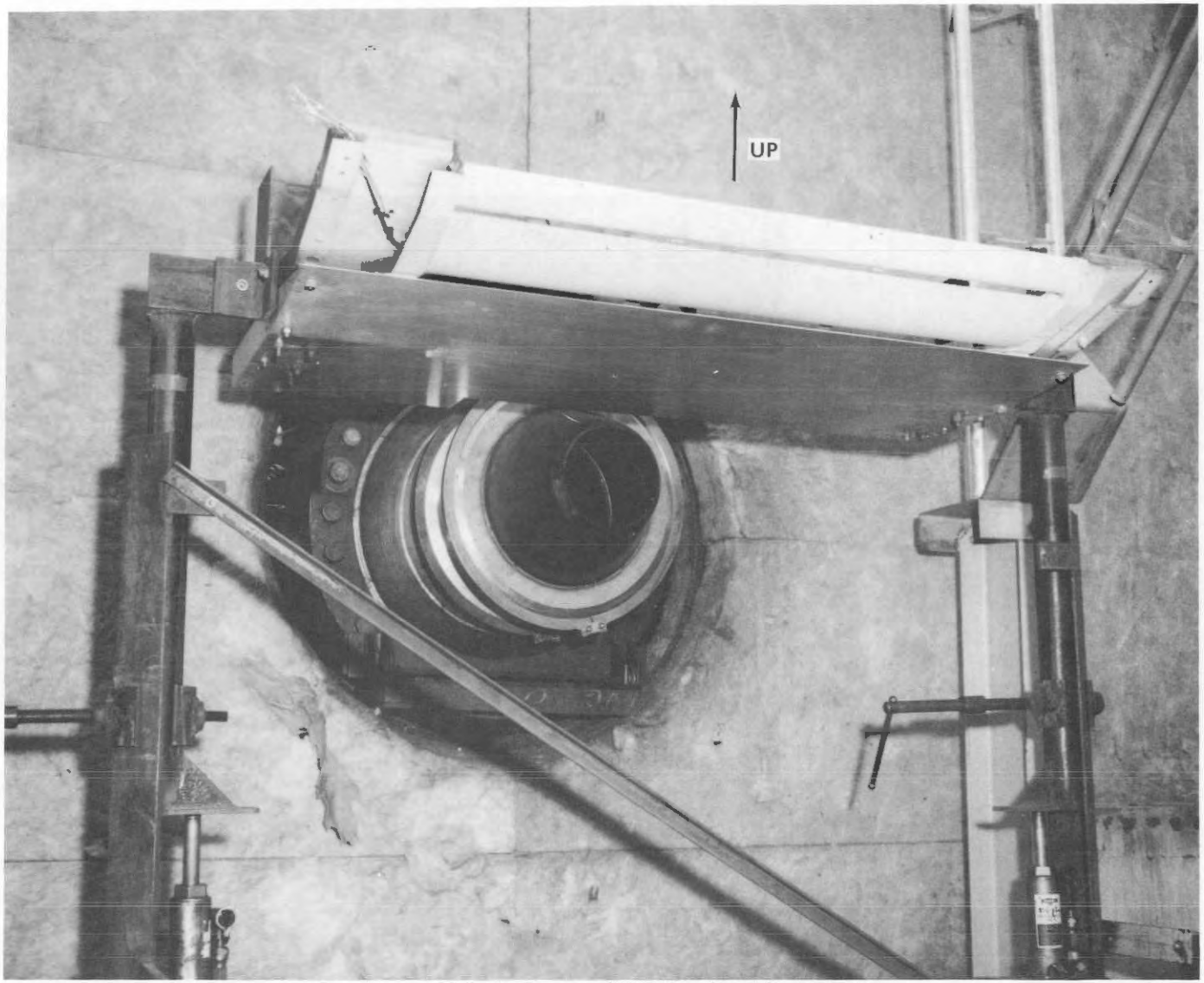

Figure 172.—Nozzle/Shield Closeup (WIF Jet Shielding Test)

NOTE: $D_{EQ} = \left\{ 4/\pi \times (\text{SECONDARY EXHAUST AREA}) \right\}^{1/2}$

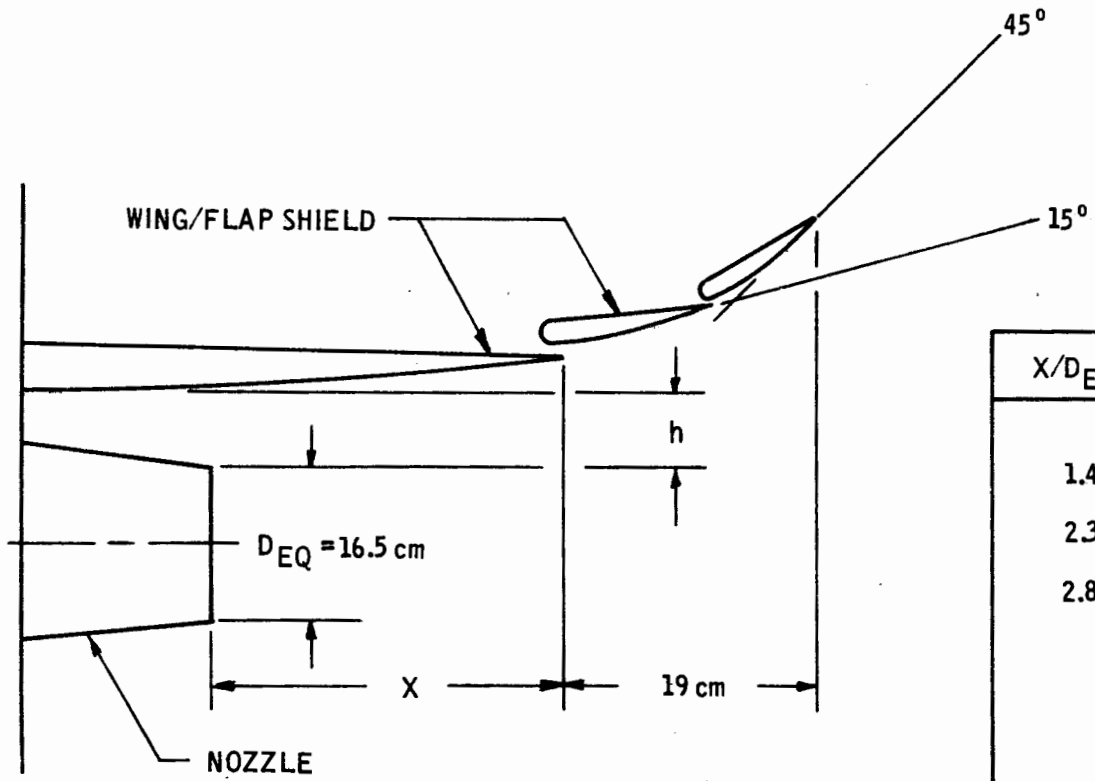

X/D_{EQ}	h/D_{EQ}
1.41	0
2.34	0.1
2.87	0.2
	0.5
	1.0

WIF JET SHIELDING TEST

Figure 173.—Nozzle/Shield Schematic (WIF Jet Shielding Test)

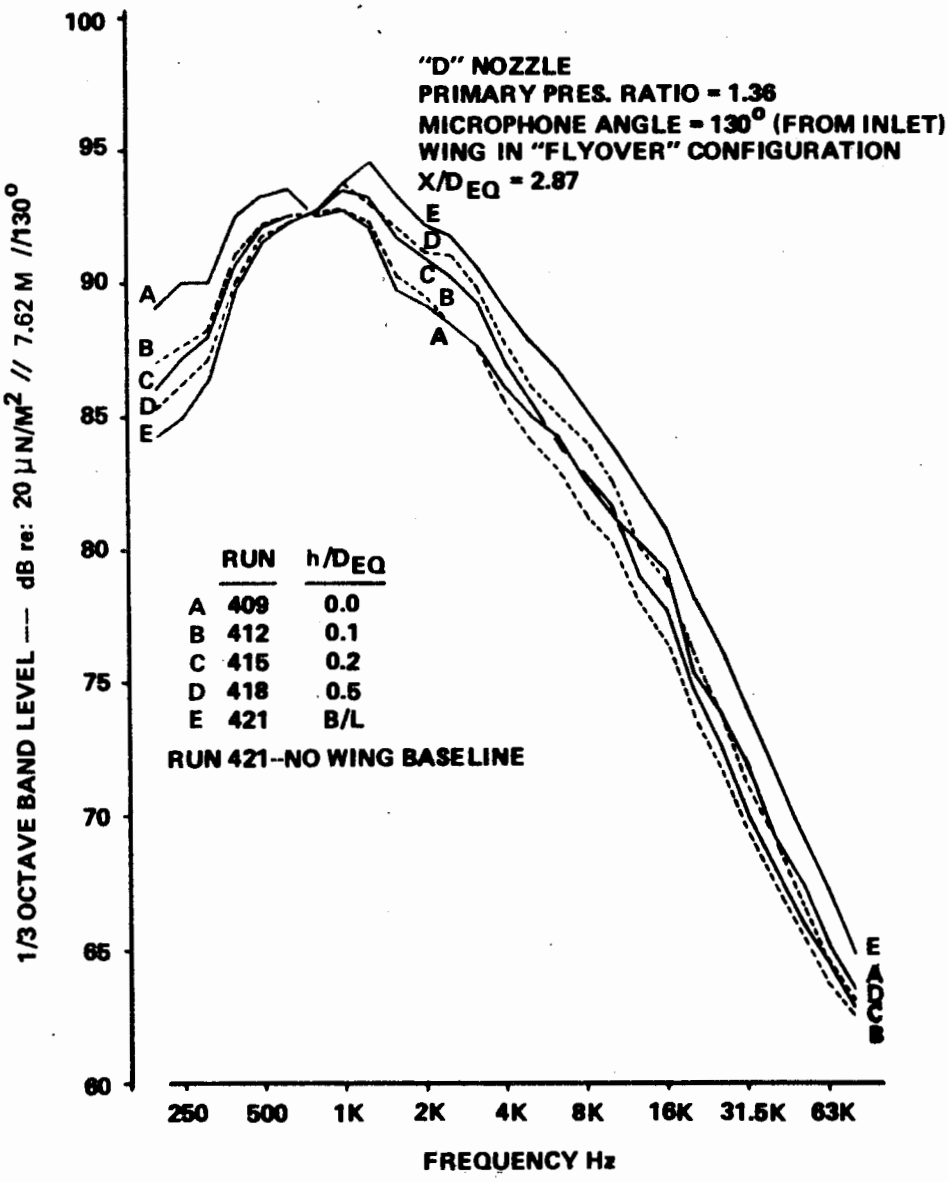

a) 1/3-OCTAVE-BAND SPECTRA

Figure 174.—W/F Jet Shielding Test Results

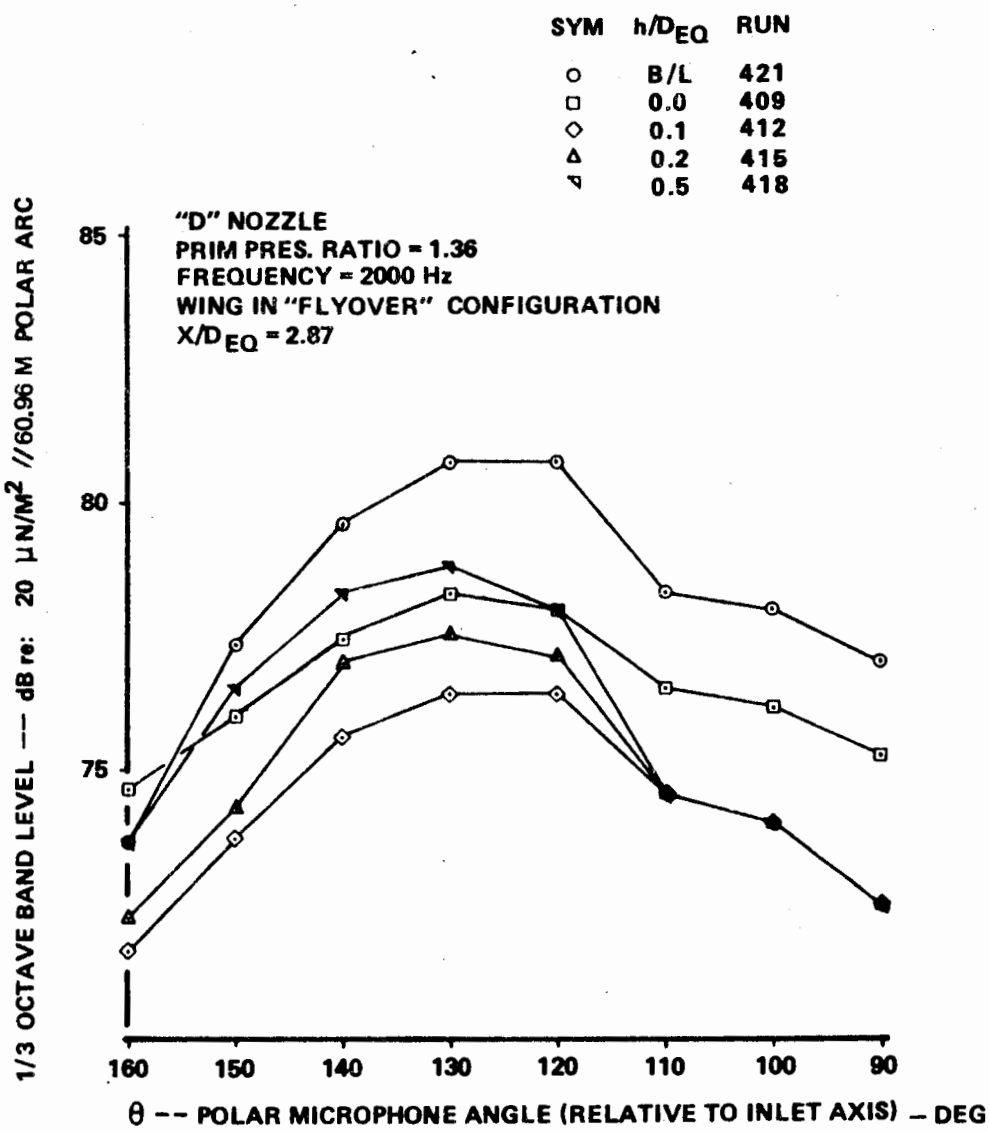

b) DIRECTIVITY

Figure 174.—(Concluded)

3.2.3 SST MODEL JET SHIELDING TEST

This Boeing test, carried out in 1966 in support of the supersonic transport program, was conducted in the Annex D Flow Facility. Two high-exhaust-velocity, hot single-flow nozzles shown in figure 175 were mounted in the test rig as shown in figures 176 and 177. The test setup dimensions and parameters varied are illustrated in figure 178. The purpose of the test was to determine the jet noise attenuation provided by various-sized, flat, rectangular plates placed near the jet. Figure 179 illustrates typical results.

The shielding results from this experiment were used as verification data for the jet noise shielding estimation equation of section 3.3.

3.2.4 WALL ISOLATION FACILITY TEST (JET/EDGE INTERACTION NOISE)

This experiment used the Boeing Wall Isolation Facility (WIF) to demonstrate the effect of forward velocity on the generation of jet/edge interaction noise (ref. 49). The test schematic is shown in figure 180. As seen, the far-field noise was monitored by a 3-m-radius polar array of microphones. Two "primary" nozzle arrangements were used to simulate the engine nozzle: a cold single-flow, 7.8-cm-diameter round nozzle and a cold single-flow D-nozzle of 7.8 cm effective diameter, shown in figure 181. A 36-cm-diameter round nozzle provided a large free jet and was used to simulate the effect of ambient flow velocity. This large nozzle was placed concentric about either primary nozzle and is shown in figure 181 with the primary D-nozzle. The D-nozzle was in contact with the wing surface for all tests, but the round nozzle was also tested at distances of 0.8, 1.6, and 2.1 cm between the nozzle lip and shield surface. The primary nozzles were operated at flow speeds of 183, 244, and 305 m/s while the concentric nozzle used to simulate ambient flow was operated at flow speeds up to 60 m/s.

A wing/body shield is shown in figure 182, and a schematic drawing with dimensions is shown in figure 183. Tests were run at flap angle settings of 0°, 5°, and 10°.

Typical test results are shown in figure 184 for the D-nozzle configuration. The simulated ambient flow effect on jet/edge interaction noise from this experiment was used in the development of the jet/edge interaction noise prediction procedure discussed in section 3.4.

3.2.5 QUIET AIR FACILITY TEST (JET/EDGE INTERACTION)

Tests were conducted at Boeing in the Quiet Air Facility (QAF) to study the characteristics of noise generated at the edge of a plate with turbulent flow passing over one side. The three basic test setups were a slot nozzle, a D-nozzle, and a variable divergent rectangular nozzle, shown respectively in figures 185, 186, and 187. Dimensional details of these nozzles are shown respectively in figures 188, 189, and 190.

Typical results for the jet/edge noise spectra of the D-nozzle with a 30.4-cm plate are shown in figure 191 for various radiation angles. The D-nozzle was also tested in a configuration with a 15.2-cm plate, and these results were used in section 3.4 to determine the shield length effect on jet/edge interaction noise.

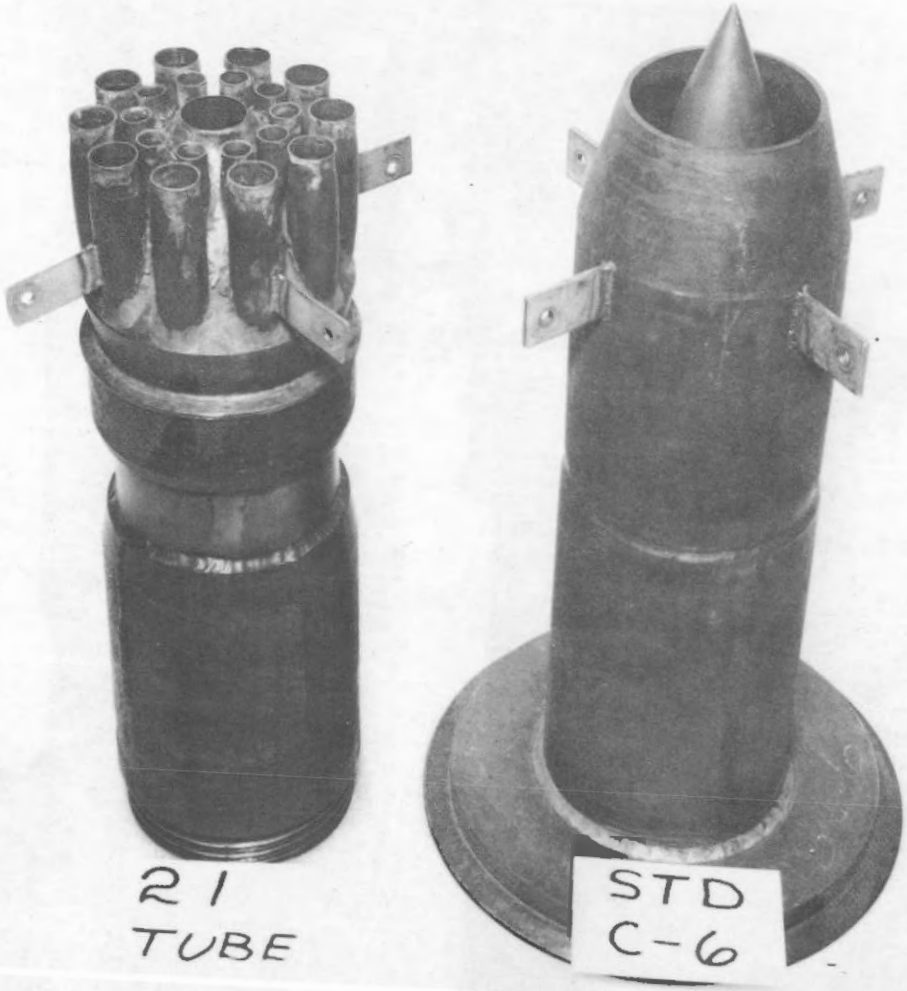

Figure 175.—SST Jet Shielding Exhaust Nozzles

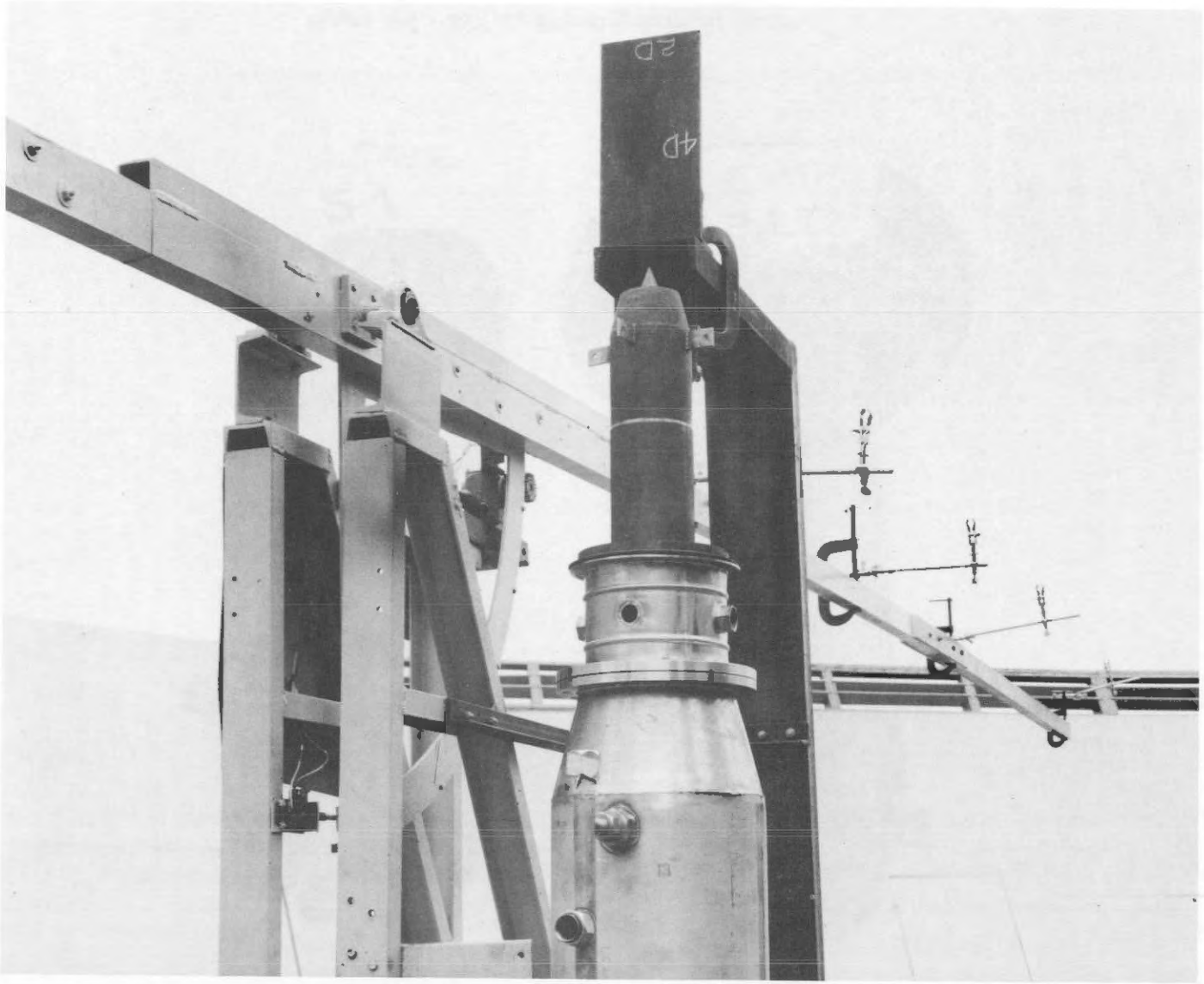

Figure 176.—Test Setup With Standard C-6 Nozzle (SST Jet Shielding Test)

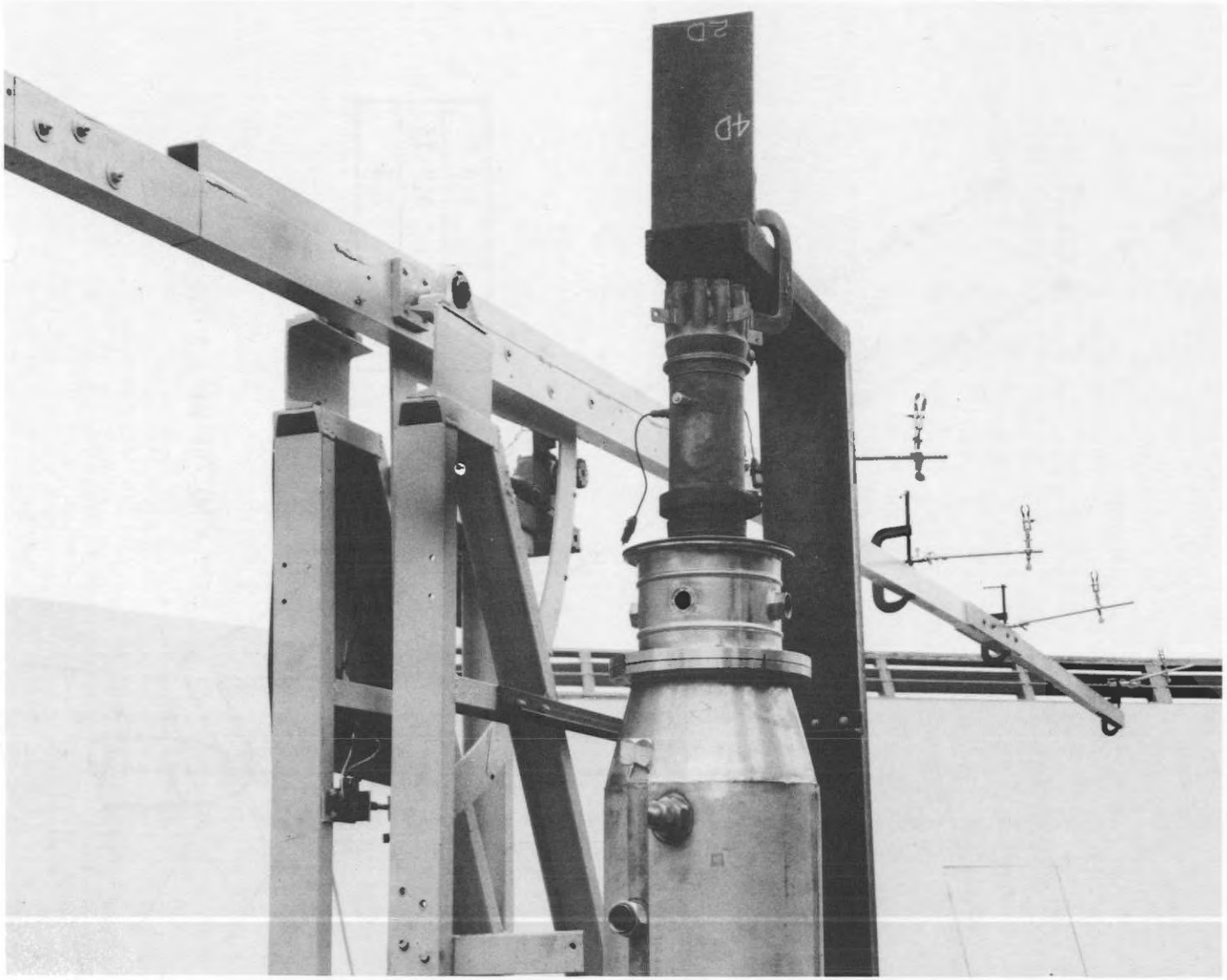

Figure 177.—Test Setup With 21-Tube Nozzle (SST Jet Shielding Test)

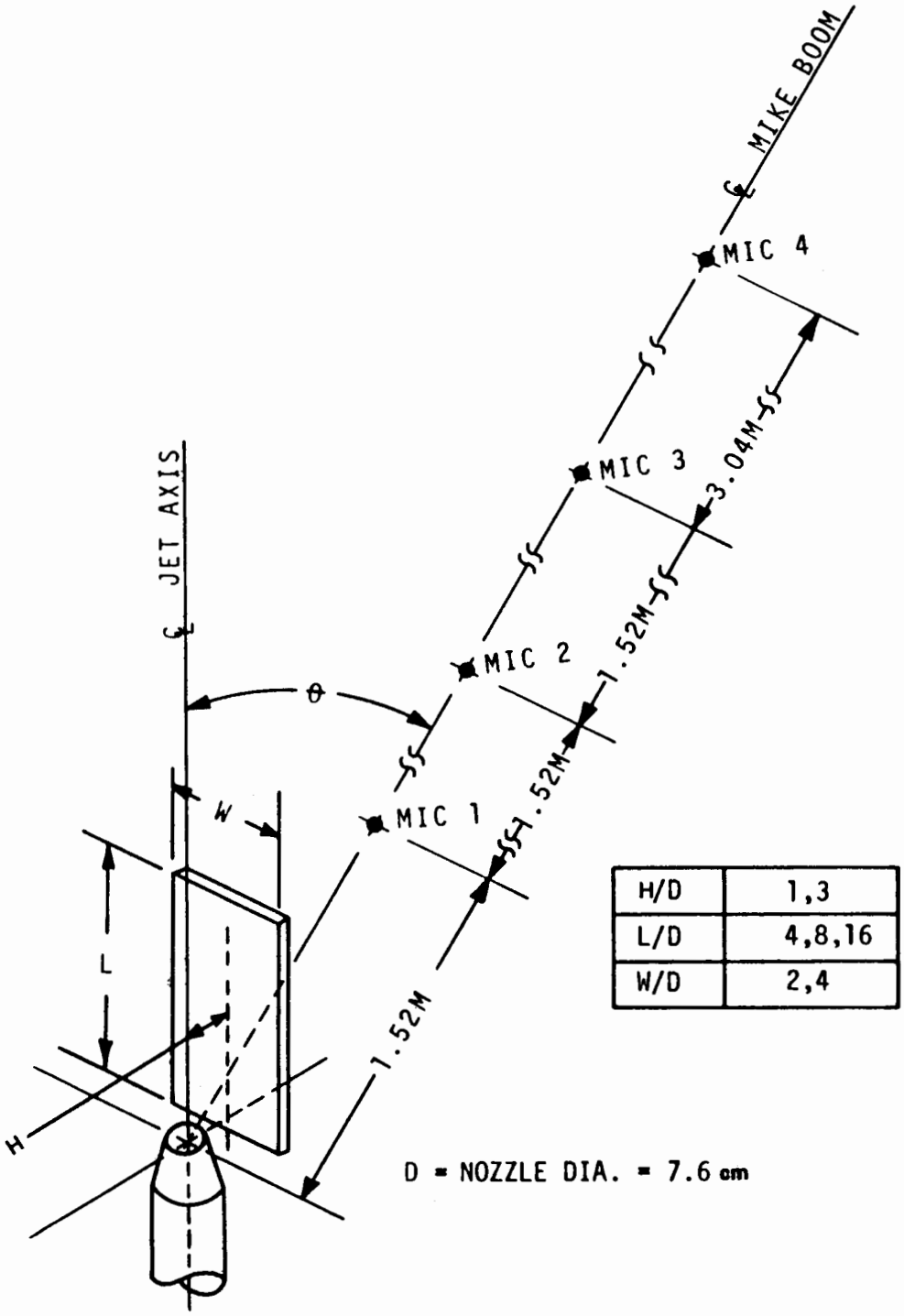

H/D	1,3
L/D	4,8,16
W/D	2,4

Figure 178.—SST Jet Shielding Test Setup Schematic

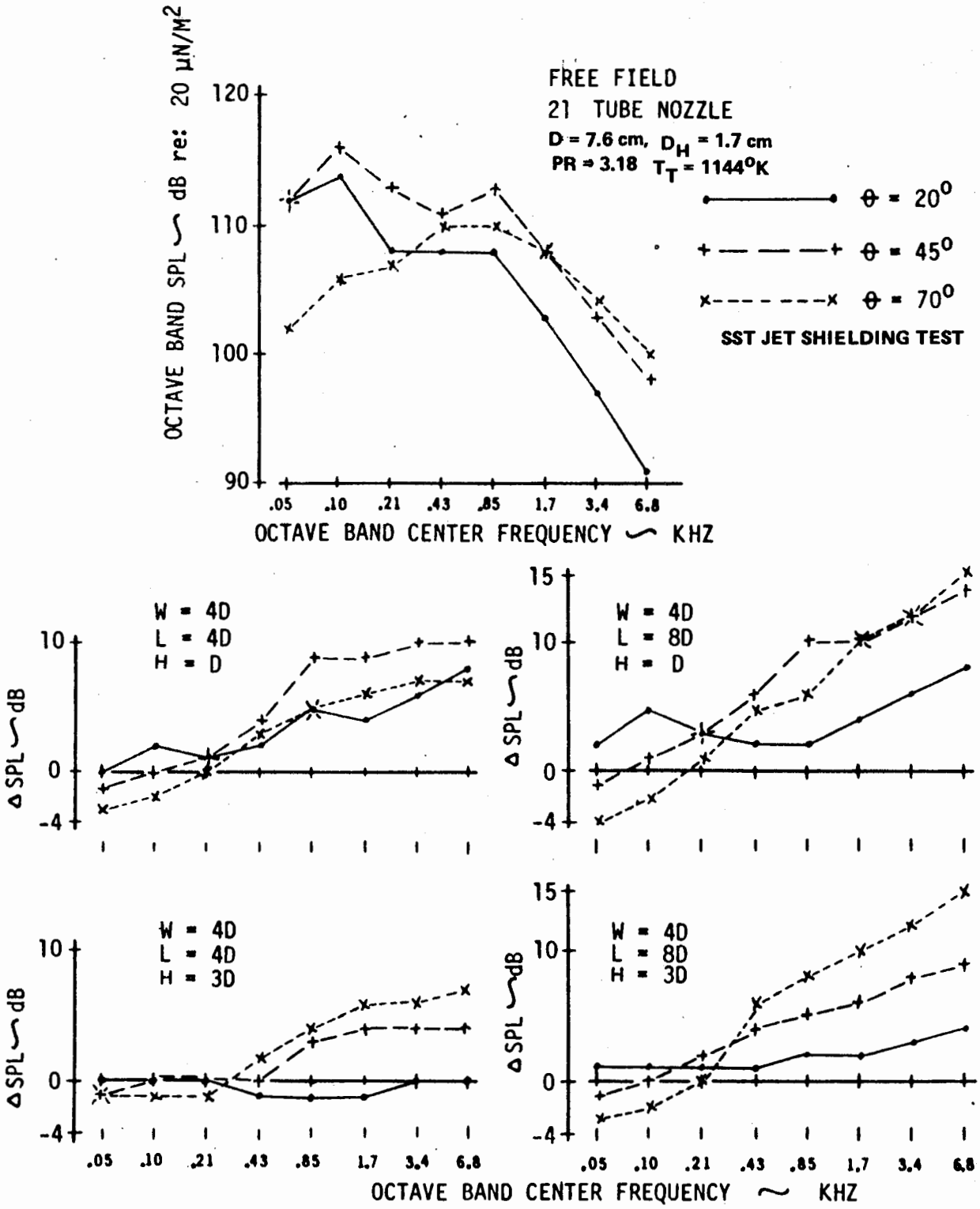

Figure 179.—Effect of Rectangular Panel Shields on Far-Field Radiated Noise of Hot, Single-Flow, 21-Tube Nozzle

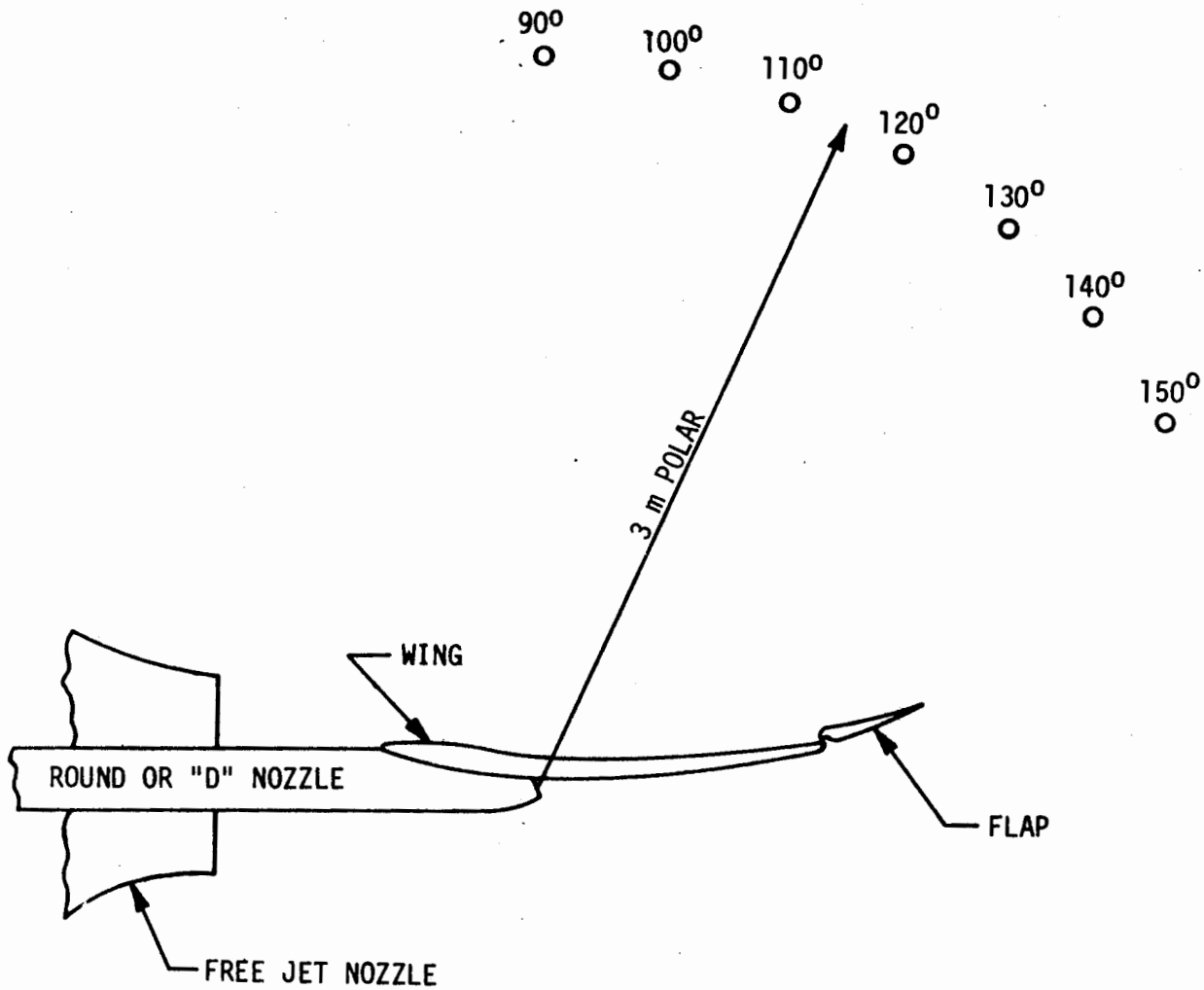

Figure 180.—WIF Jet/Edge Interaction Test Schematic—Elevation

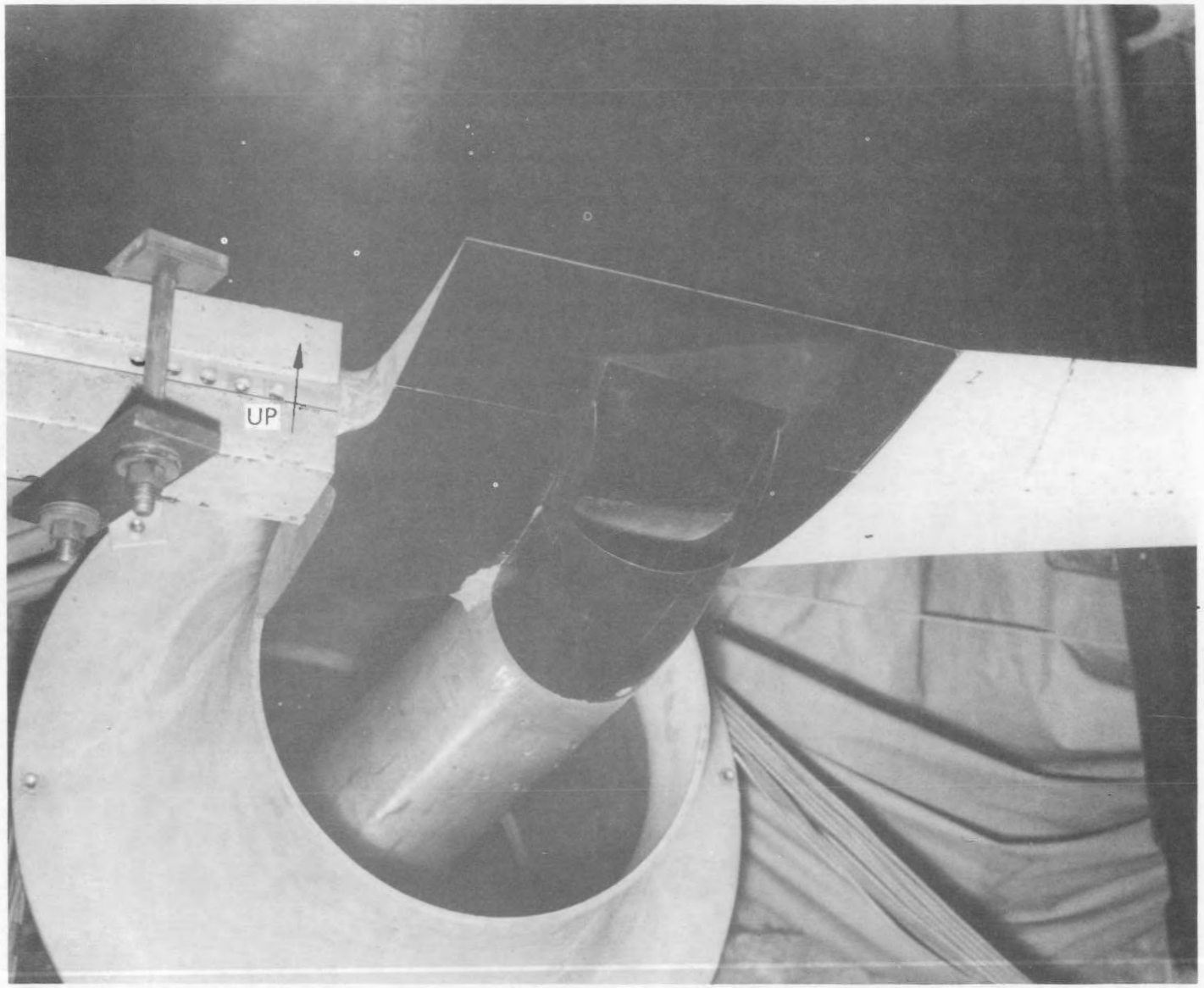

Figure 181.—D-Nozzle Forward Velocity Test (WIF Jet/Edge Interaction Test)

Figure 182.—Wing/Body Shield (WIF Jet/Edge Interaction Test)

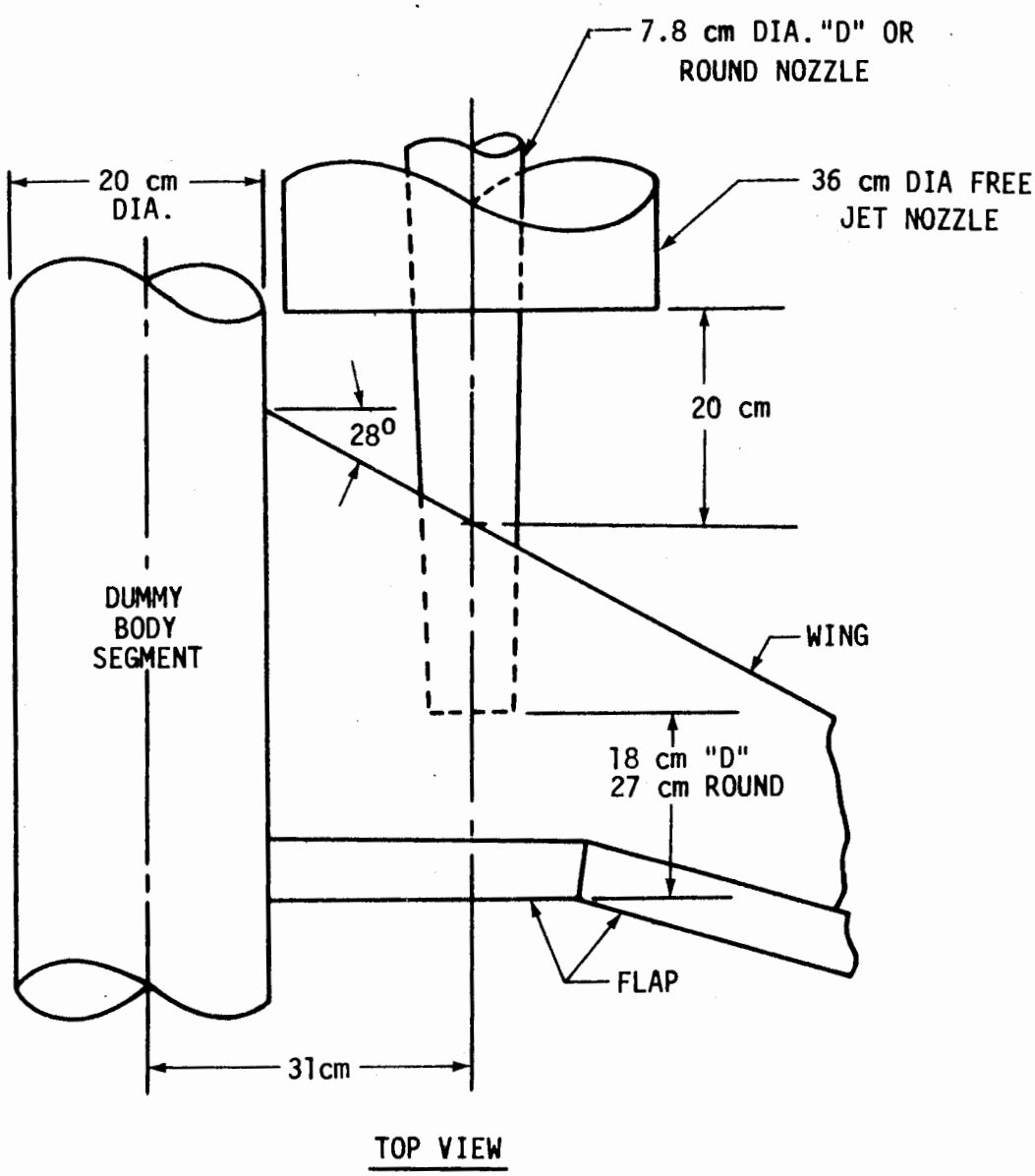

Figure 183.—Wing/Body Shield Schematic (WIF Jet/Edge Interaction Test)

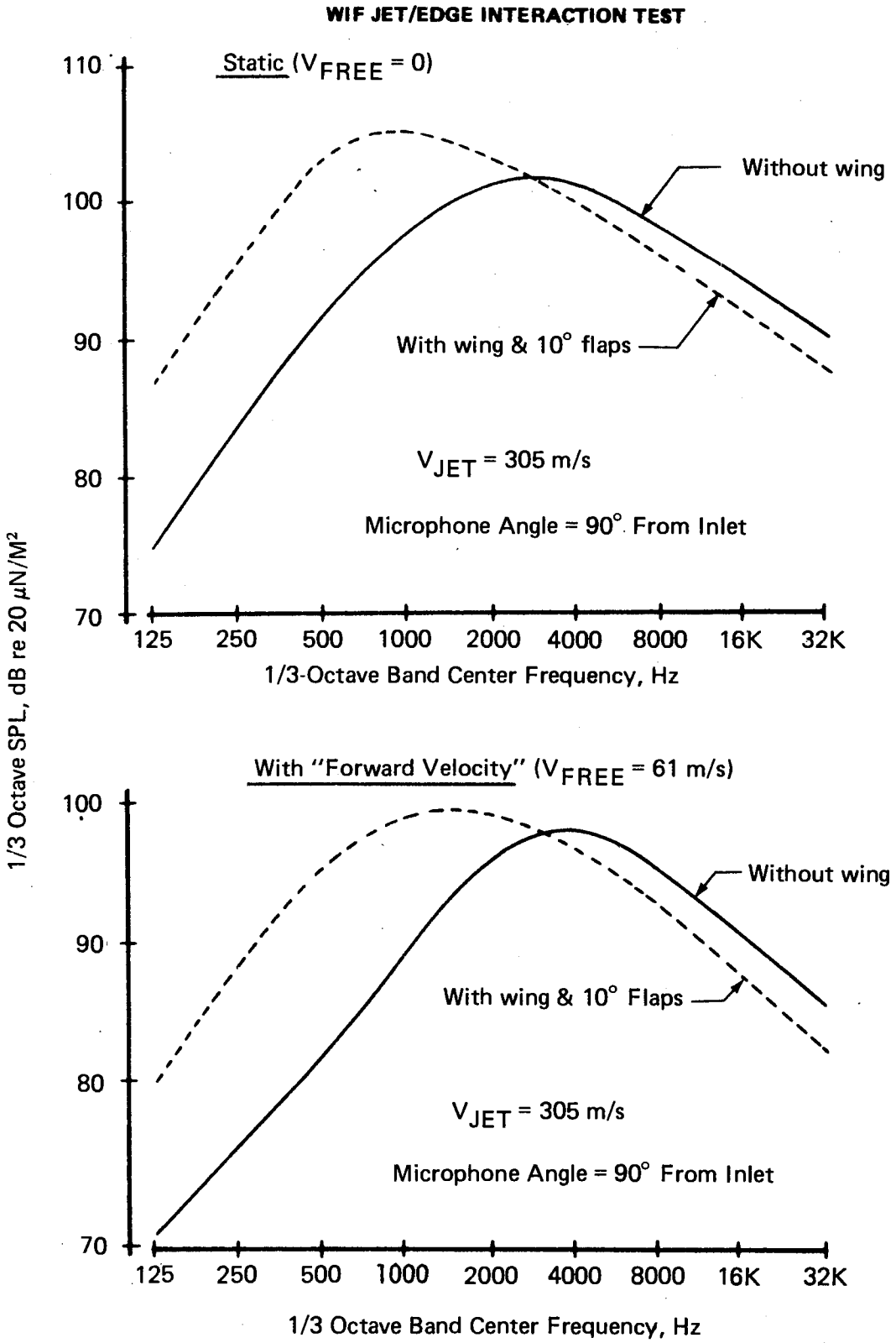

Figure 184.—Far-Field Noise of D-Nozzle Rig

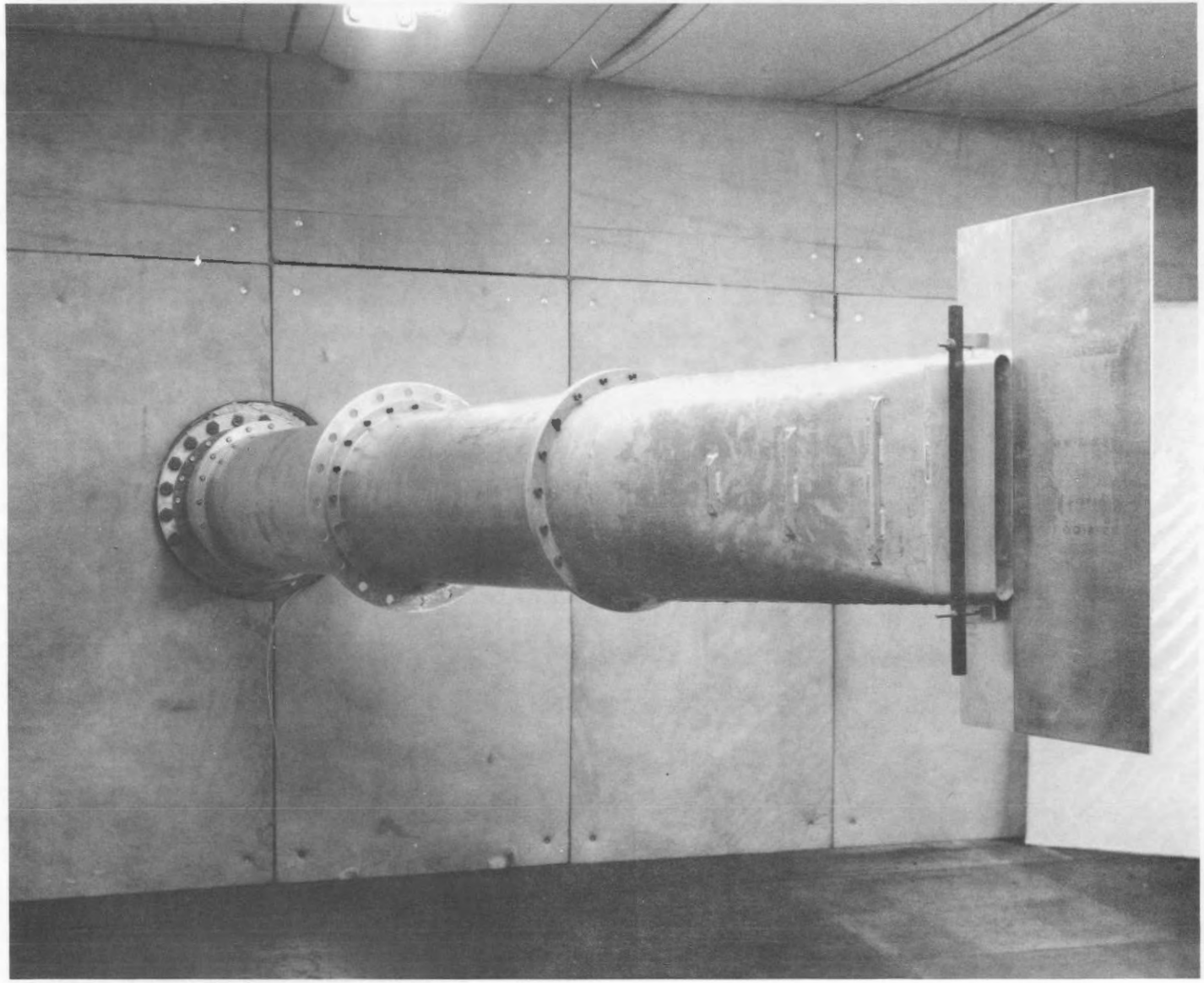

Figure 185.—Slot Nozzle With 30.4-cm Plate (QAF Jet/Edge Interaction Test)

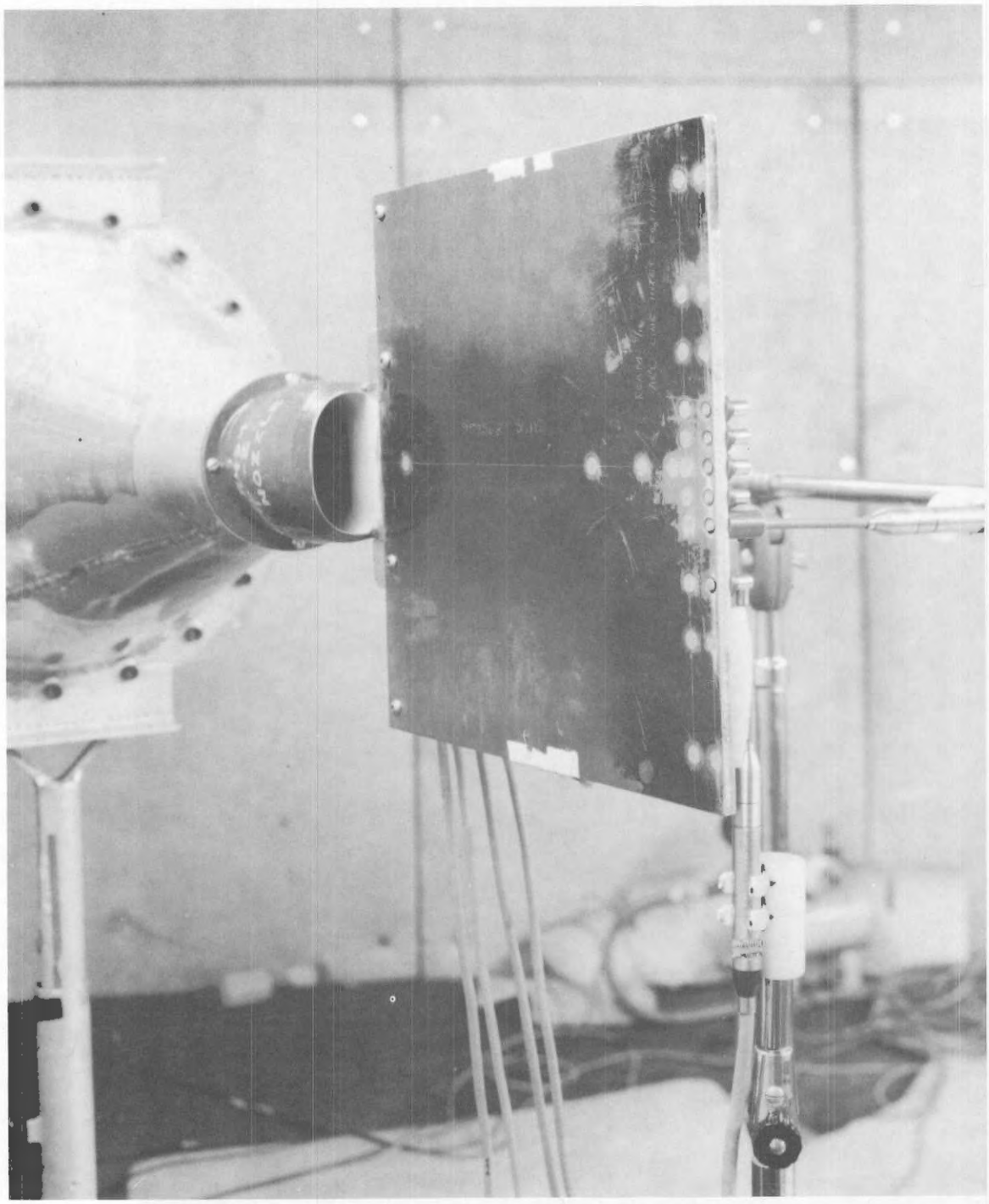

Figure 186.—D-Nozzle With 30.4-cm Plate (QAF Jet/Edge Interaction Test)

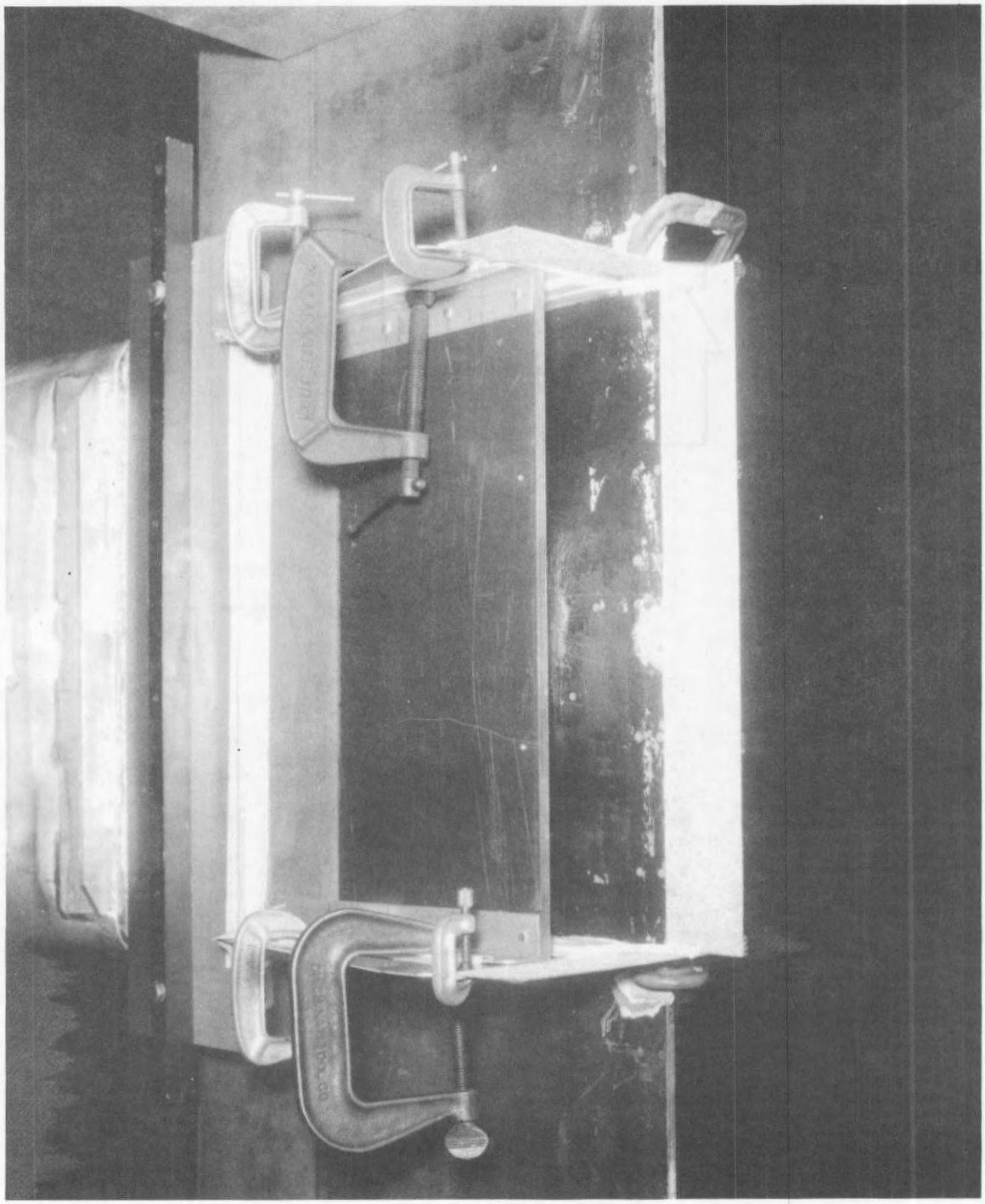

Figure 187.—Variable Divergent Rectangular Nozzle (QAF Jet/Edge Interaction Test)

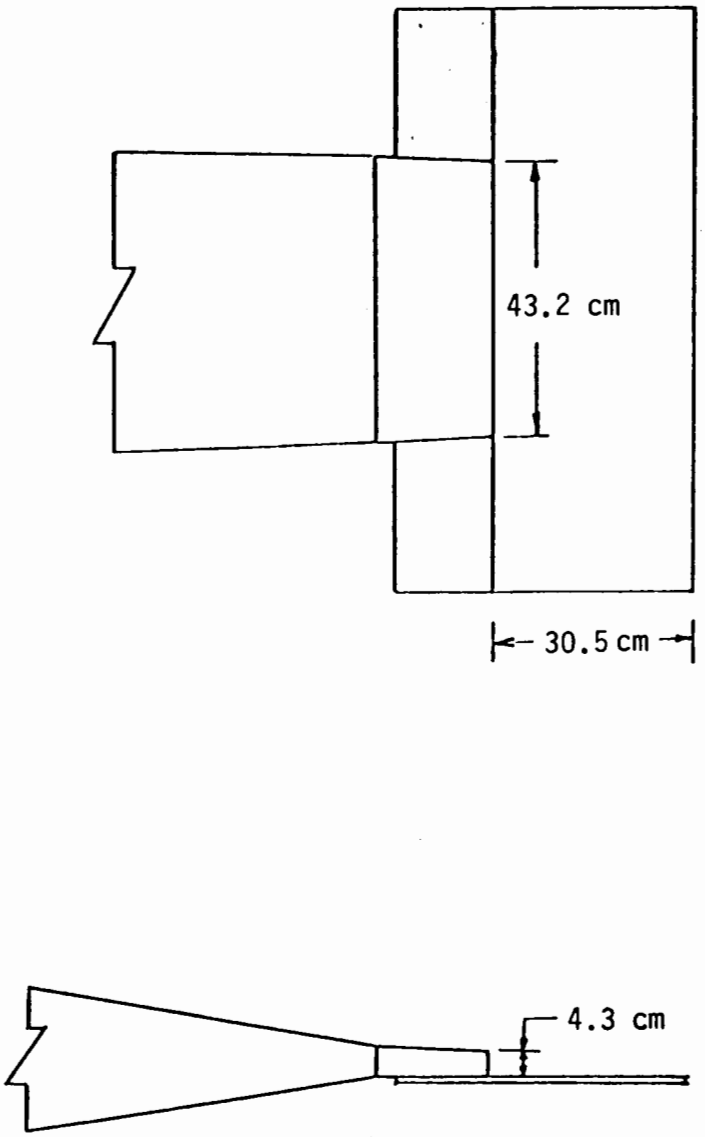

QAF JET/EDGE INTERACTION TEST

Figure 188.—Slot Nozzle With 30.5-cm Plate

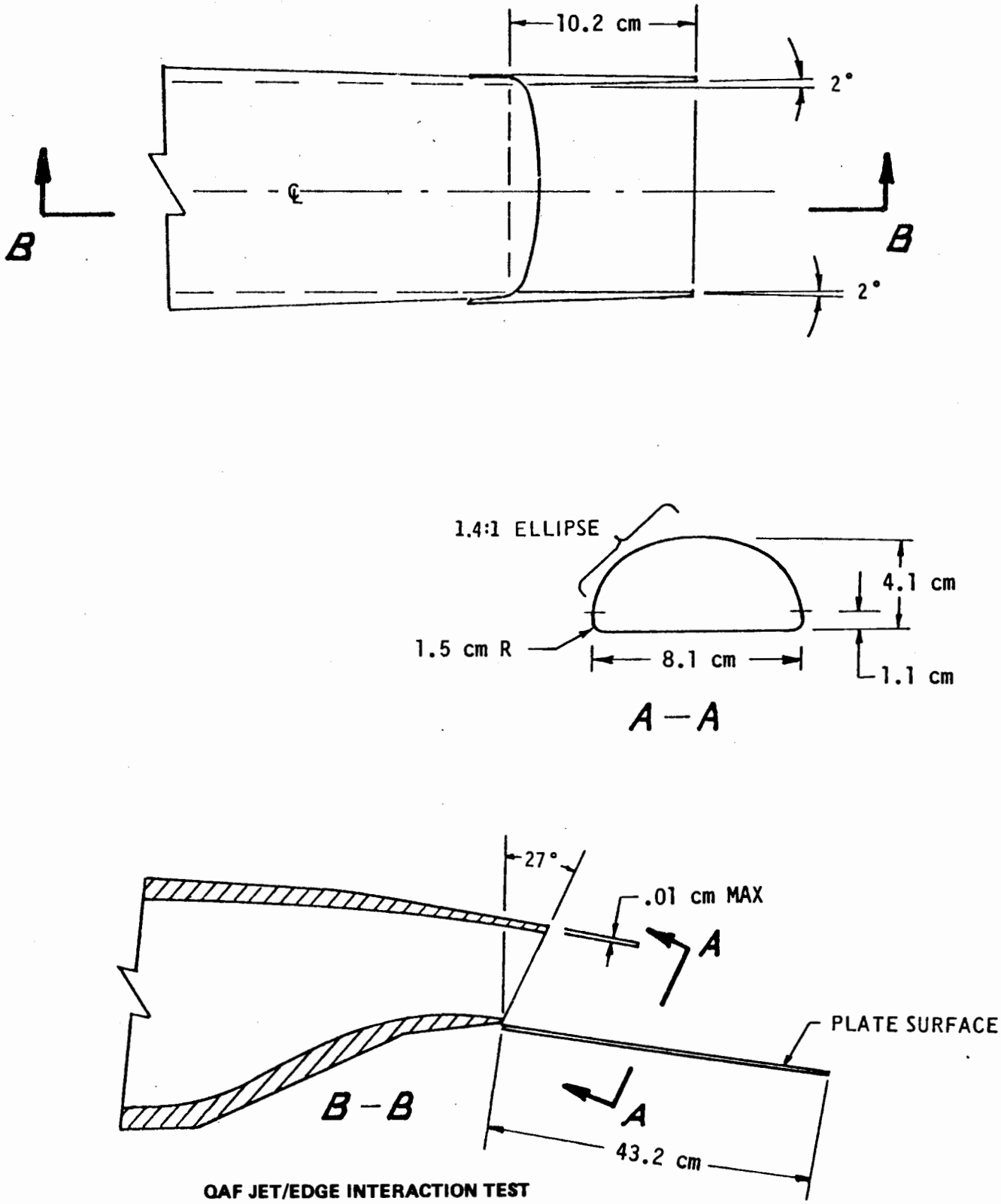

Figure 189.—D-Nozzle for Jet/Edge Noise Test

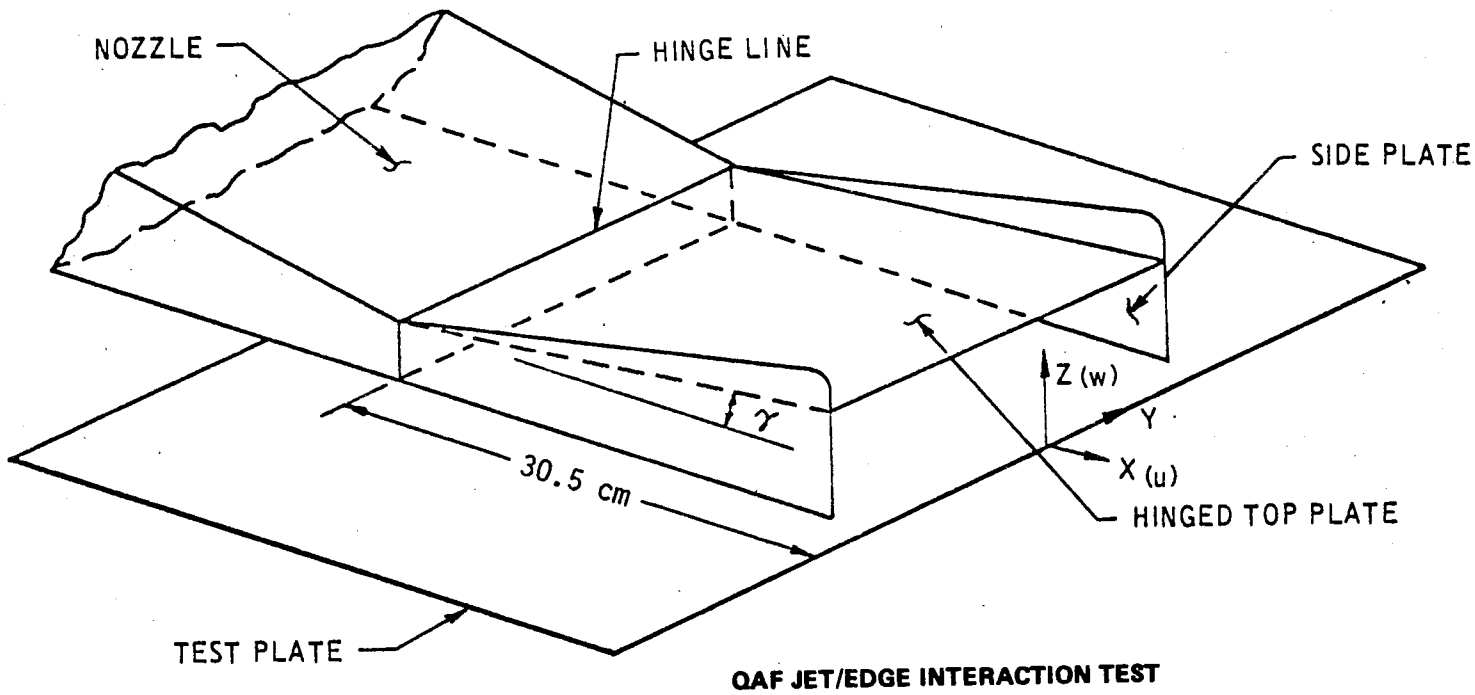

Figure 190.—Variable Divergent Rectangular Nozzle—Side Plates and Hinged Top Plate

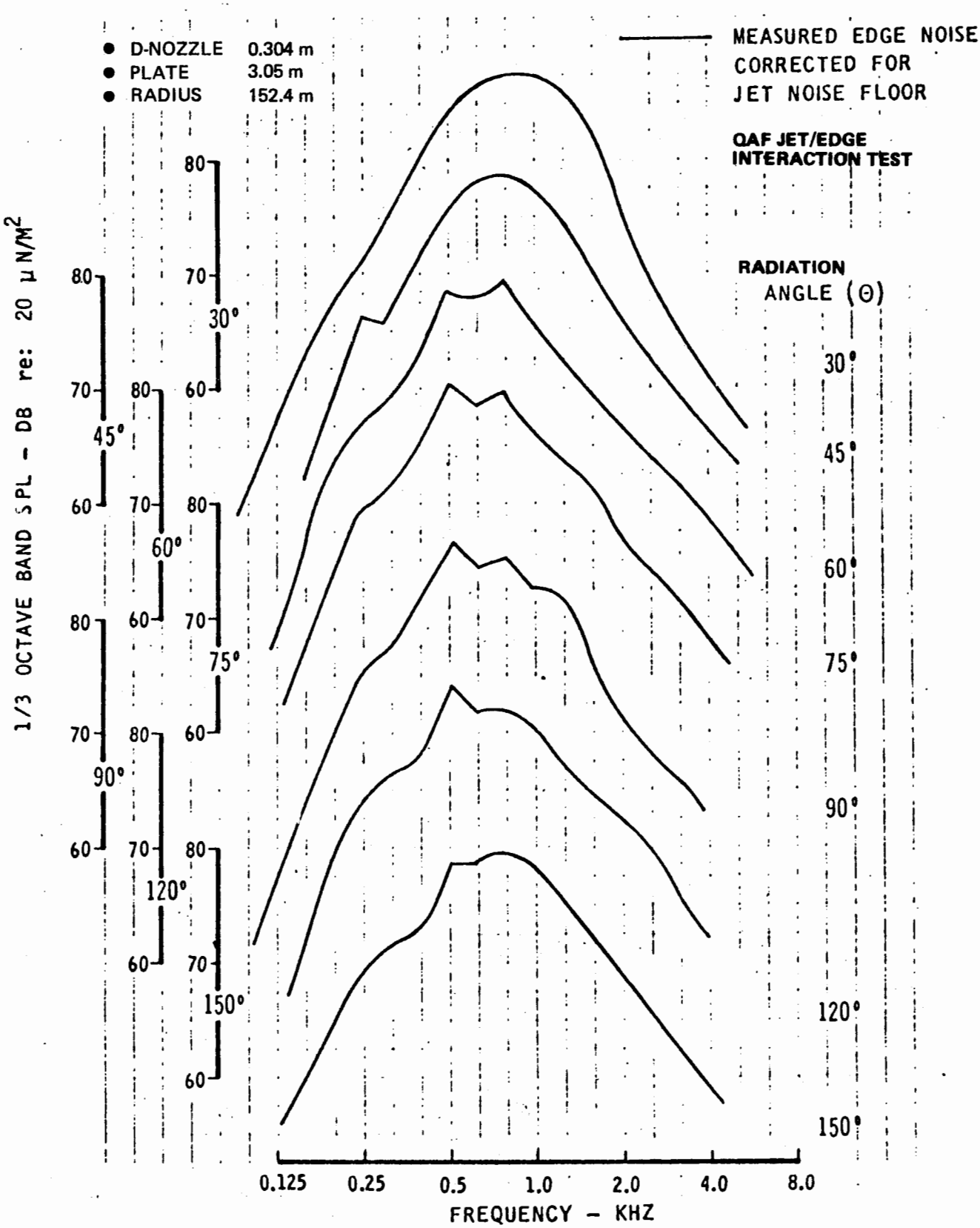

Figure 191.—Edge Noise Spectra as a Function of Radiation Angle

3.3 JET NOISE SHIELDING ESTIMATION

The study of jet noise shielding for an engine-over-wing configuration was undertaken to develop an estimation procedure from available experimental data and empirical studies. Jet noise shielding model test data have been obtained from Boeing/Aeritalia tests described in sections 3.2.2 and 3.2.3 for a variety of nozzle-shield configurations and jet flow conditions. In addition, evaluation of the empirical jet noise shielding estimation method proposed by U. von Glahn et al. in reference 50 has been completed. A comparison was made of the empirical correlation technique presented by von Glahn et al. (refs. 50 and 51) and the Boeing/Aeritalia data, which include subsonic and supersonic hot flow over a broad range of shield lengths, frequency, and nozzle heights above the shielding surface. The measured shielding attenuation was compared with that estimated by the correlation method of reference 50. Although there is considerable data scatter, the jet noise shielding attenuation appears to increase with increasing frequency and shield length.

In general, the data are within ±2.5 dB of the estimation curve (ref. 50). Further tests taken under more stringently controlled conditions are required to evaluate the effects of wing/flap geometry and engine height above the wing. For the interim period, the proposed method of estimating jet noise shielding is considered to be acceptable.

3.3.1 EMPIRICAL ESTIMATION EQUATIONS

The work of reference 50 considers the noise reductions observed when a cold-flow model jet is placed near a shielding surface. A correlation method is developed to collapse the acoustic data and is proposed as a technique for estimating jet noise shielding. The correlation parameter used in reference 50 is defined as

$$Z = \left\{ \frac{1}{1 + 0.033 \left(\frac{\theta}{180^\circ - \theta}\right)^4} \right\} \left\{ \frac{f\, L\, a_\infty^2}{g\, D_H\, V_J\, 10^6} \right\} \left\{ 1 + (4.5)\, 10^9 \left(\frac{g\, D_H}{a_\infty^2}\right)^2 \right\}$$

where

a_∞ = ambient speed of sound

g = 9.8 m/s^2

f = geometric mean frequency for constant-percentage-band filters

and the other symbols are illustrated in the following sketch.

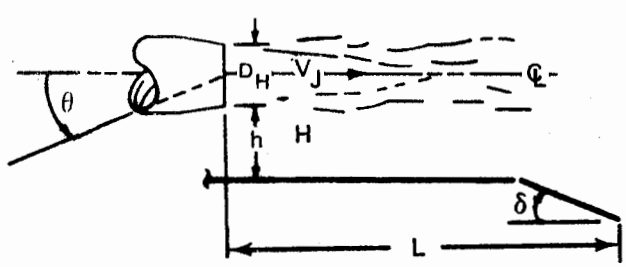

The jet noise shielding attenuation is also found to be weakly dependent on variations in the shield configurations, i.e., wing only, wing with flap (gaps closed), and wing with flaps (gaps open). Three estimation expressions for jet noise shielding are given in reference 50 and are listed as follows:

$$SPL = 10 \log (1 + 0.6\, z) \quad \text{Wing alone} \tag{73}$$

$$= 10 \log (1 + 1.4\, z^{.85}) \quad \text{Wing with flap (gap closed)} \tag{74}$$

$$= 10 \log (1 + z^{.925}) \quad \text{Wing with flap (gap open)} \tag{75}$$

These equations are plotted in figure 192 along with the data scatter band associated with the test data of reference 50. A close look at the data from references 50 and 51 shows that the data scatter for equation (73) encompasses that of equations (74) and (75). The 90% confidence band for all the data is approximately ±2.5 dB about the curve for equation (73). Since the curves for equations (74) and (75) lie within this scatter band, one cannot propose their use as a realistic refinement for predictions.

3.3.2 DATA/ESTIMATION EQUATION COMPARISON

The test data for the configurations shown in figure 193 were obtained from the Boeing/Aeritalia tests described in sections 3.2.2 and 3.2.3. The frequency range considered in each test was 2 to 64 kHz. Although these data have been analyzed in full-octave and/or 1/3-octave bands, the filter bandwidth appears to have no effect on jet noise shielding. Data are shown at the following frequencies: 2, 4, 8, 16, 32, and 64 kHz.

In general, the Boeing/Aeritalia data shown in figure 194 indicate an increase in shielding attenuation with increasing frequency, which is consistent with theoretical considerations. However, the D-nozzle data appear to indicate a loss in shielding attenuation above a certain frequency. This apparently opposite trend is attributed to equipment noise floor and/or the presence of a high-frequency noise source due to the turbulent shear layer on the shielding surface.

The Boeing/Aeritalia data (fig. 194) indicate that the jet noise shielding is also weakly dependent on the nozzle-height-to-shield-length ratio, H/L. For the data shown in figure 194, the values of H/L varied from 0.03 to 6. Diffraction theory suggests that a variation in shielding should occur; i.e., more shielding can be realized for smaller values of H/L provided no flow attachment occurs. Unfortunately, the quality of the available data is too poor to determine the functional dependence with H/L. Additional testing needs to be done under stringently controlled conditions to investigate the effect of H/L variations.

Since the majority of the data lie within ±2.5 dB about the curve for equation (73) (fig. 192) and equations (74) and (75) lie within this same data scatter band, equation (73) is proposed for estimates of jet noise shielding. Refinements to this empirical equation are desired, but can be accomplished only by additional testing. It seems appropriate that the additional testing address parametric variations of H/L.

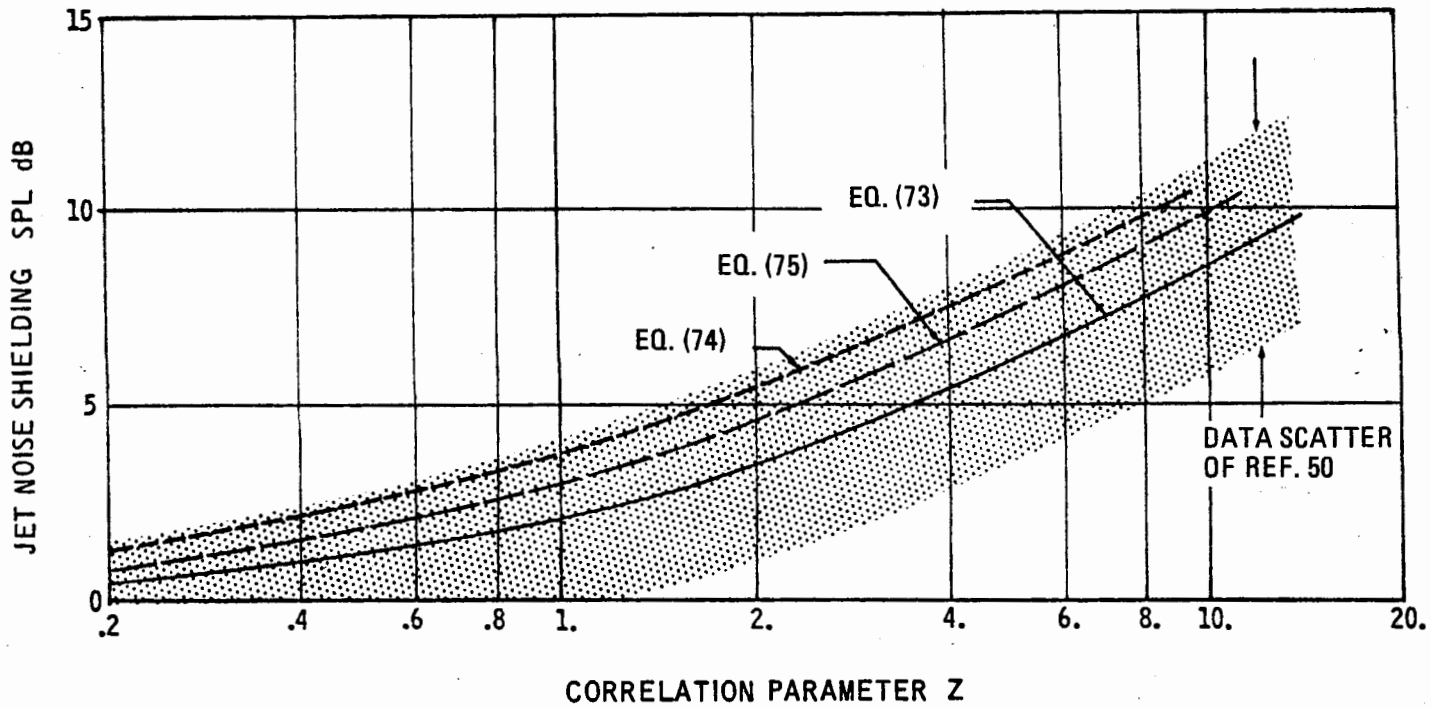

Figure 192.—Estimation Equation Comparison

TEST CONFIGURATION 1 – ROUND CONVERGENT NOZZLE

DATE: 1973

H/D_H = .625, 1.0
L/D_H = 2.5
D_H = 7.62 cm
Vj = 304.8 m/s
T_T = 289°K

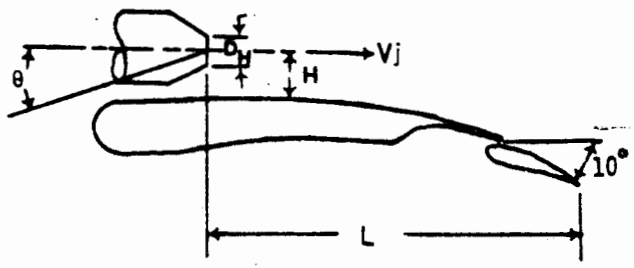

TEST CONFIGURATION 2 – "D" NOZZLE

BPR = 7
T_{T_1} = 839°K
T_{T_2} = 289°K
V_{j_1} = 376 m/s
V_{j_2} = 230 m/s

H/D_H = .14, .26, .38, .74
L/D_H = 4.2
D_H = 13.7 cm (HYDRAULIC DIAMETER)
Vj = 248.7 m/s (MIXED FLOW)
DATE: 1972

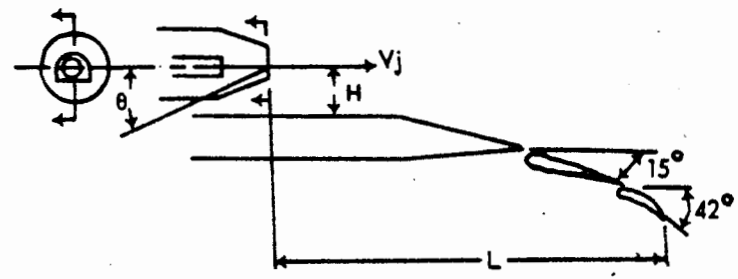

TEST CONFIGURATION 3 – ROUND CONVERGENT PLUG NOZZLE

H/D_H = 3
L/D_H = 5, 9, 17
D_H = 7.62 cm
Vj = 807.7 m/s
T_T = 1144°K
DATE: 1966

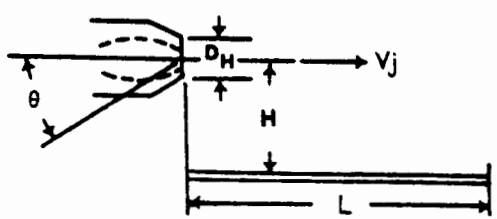

TEST CONFIGURATION 4 – 21 TUBE SUPPRESSOR NOZZLE

H/D_H = 13.7
L/D_H = 22.9, 41.2, 77.9
D_H = 1.66 cm (HYDRAULIC DIAMETER)
Vj = 807.7 m/s
T_T = 1144°K
DATE: 1966

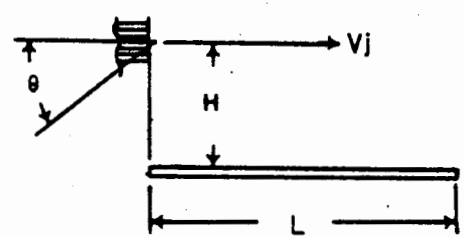

Figure 193.—Model Jet Noise Shielding Configurations

$$\Delta SPL = 10 \log \left(1 + .6\, z\right)$$

$$z = \left\{\frac{1}{1+.033\left(\frac{\theta}{180^\circ-\theta}\right)^4}\right\}\left\{\frac{f L a_\infty^2}{g D_H V_j \cdot 10^6}\right\}\left\{1+\left(4.5\right)10^9\left(\frac{g D_H}{a_\infty^2}\right)^2\right\}$$

a_∞ = AMBIENT SPEED OF SOUND ~340 m/s
f = 1/3 OB SPECTRUM FREQUENCY ~ Hz
g = 9.8 m/s²

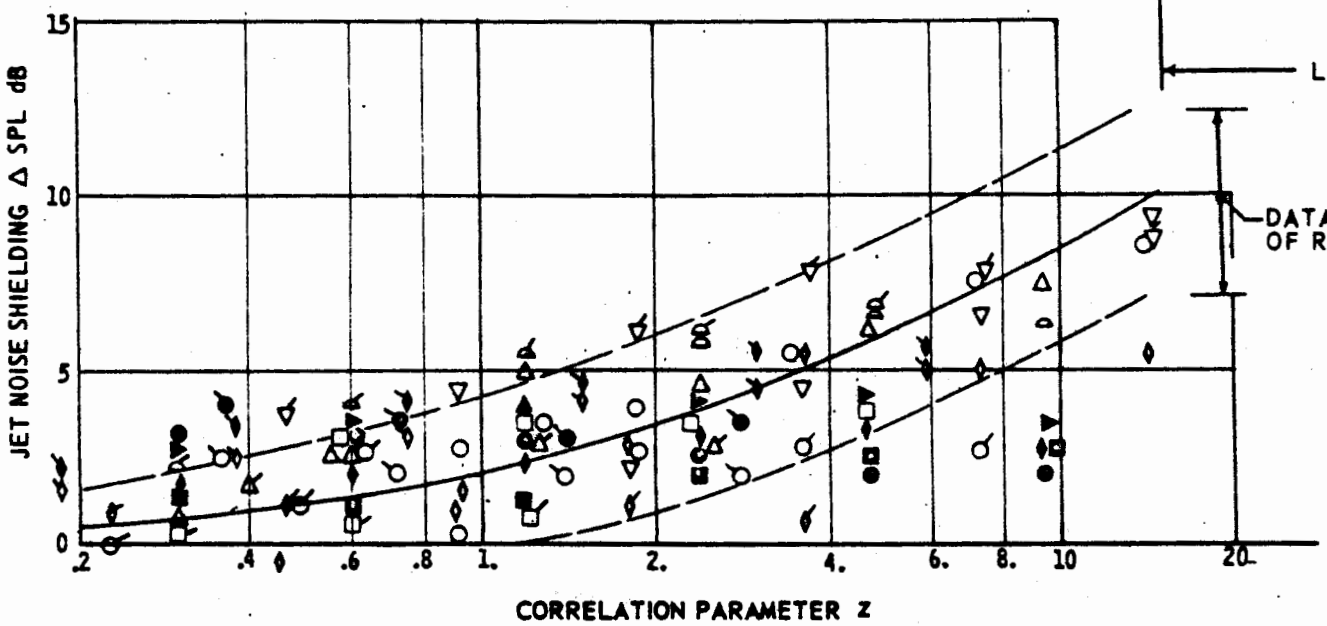

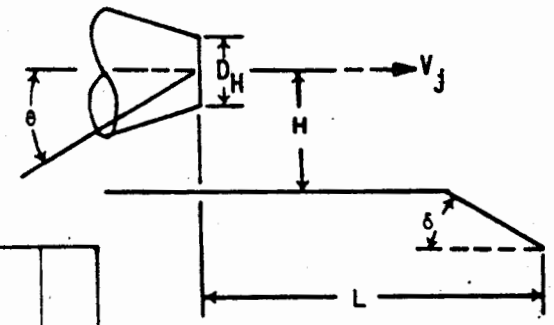

TEST CONFIGURATIONS (SEE FIG. 193)

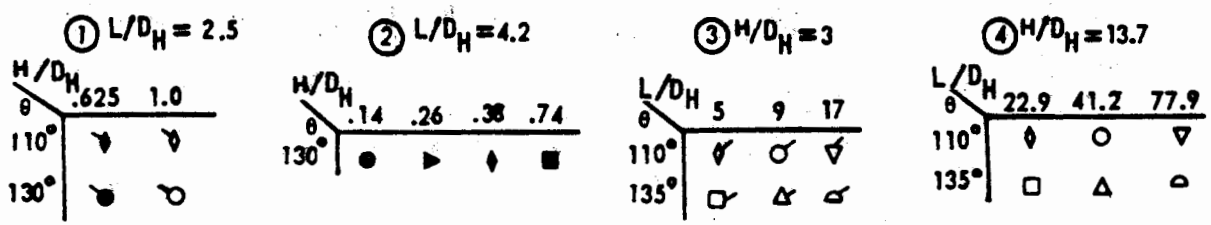

Figure 194.—Jet Noise Shielding Data Correlation

3.4 JET/EDGE INTERACTION NOISE ESTIMATION

The concept of augmented lift, achieved by deflecting the engine jet exhaust downward over a wing/flap system, has the potential of reducing community noise because of the shielding effect of an engine-over-wing installation. However, the jet/edge noise generated by the interaction of the engine jet exhaust flow with the wing/flap system could limit the benefits of shielding. In this section, a semiempirical estimation equation is obtained for jet/edge interaction noise, which includes the effect of nozzle placement relative to the shielding surface and the effect of airplane flight speed.

To formulate a practical basis for estimation, the jet/edge noise radiated due to the interaction of the jet exhaust with the wing/flap surfaces is treated as a problem of diffraction at the edge of a rigid half-plane. Ffowcs-Williams and Hall (ref. 17) and Crighton and Leppington (refs. 15 and 16) treat the diffraction problem within the Lighthill formulation of aerodynamic sound by dealing with a volume distribution of quadrupoles near the edge. On the other hand, Chase's formulation (refs. 13 and 14) explicitly relates the sound radiated from subsonic turbulent flow at the edge of a rigid half-plane to a wave-vector/frequency spectral density model of hydrodynamic pressure. This treatment, which circumvents the difficulty of requiring knowledge of Lighthill volume sources in favor of a model of hydrodynamically driven surface pressure sources, is used to obtain the estimation prediction equation herein.

The geometric effects of incomplete interaction when the jet exhaust does not fully impinge upon the surface, and the position of the trailing edge relative to the exhaust jet potential core, are empirically treated from a limited amount of data from Boeing/Aeritalia tests and reference 52. From these data, the decrease of the turbulence characteristic frequency with distance along a jet is used to define an empirical Strouhal number relation for the frequency scaling of the interaction noise, which includes the length of the shielding surface.

Flight effects have been considered by von Glahn et al. (ref. 53) and Bhat and Gallo-Rosso (ref. 49). They found that jet/edge interaction noise is increasingly reduced with increasing ambient flow speed and can be taken to have a fifth power dependence on relative jet velocity (ref. 49). The effect of ambient flow is introduced into this analysis through the stretching of the jet potential core and the dependence of the jet turbulence intensity on relative jet velocity. In appendix H of volume II, a study of the resulting flight math model for the jet/edge interaction noise confirms the fifth power relative velocity dependence if, as in reference 49, the shield is shorter than the jet potential core. Otherwise, if the shield length always remains longer than the potential core, the study shows a dependence of the interaction noise on the product of jet velocity squared and relative velocity cubed. No experimental data are available for this case.

3.4.1 THEORETICAL BASIS

The theoretical analysis of Chase (refs. 13 and 14) has been found to be the most useful for formulation of an estimation method for the jet/edge noise radiated from jet engine exhaust flow interaction with a wing/flap system. The central result of his analysis is given by the relation between the power spectral density $\phi_P(\underset{\sim}{r}, \omega)$ of radiated pressure and the wave-vector/frequency power spectral density $P(\underset{\sim}{k}, \omega)$ of surface pressure:

$$\phi_P(\underset{\sim}{r}, \omega) \cong \frac{1}{\pi} \frac{b}{r^2} \frac{u}{a_\infty} |\cos \eta| \sin^2 \frac{\theta}{2} \int dk_1 \, P(\underset{\sim}{k}, \omega) \tag{76}$$

where the edge geometry and coordinates are defined in figure 195.

When an appropriate model for $P(\underset{\sim}{k}, \omega)$ is assumed (e.g., turbulent boundary layer or jet flow over an edge), equation (76) gives the spectral density of radiated pressure for the assumed turbulent flow over the edge. For the purpose of devising an estimation method, Chase's assumed jet exhaust model for the wave-vector spectrum of surface pressure was generalized a posteriori. Thereby, a subsequent fit of empirical acoustic data was facilitated. The result is the spectral density of radiated pressure given by (cf. eq. 26, ref. 14):

$$\phi_P(\underset{\sim}{r}, \omega) \sim \rho_J^2 \; u \, v^4 \frac{b \, \Delta}{a_\infty \, r^2} \frac{1}{\omega} |\cos \eta| \sin^2 \frac{\theta}{2} \; \frac{(1 + F)^\nu (\omega/\omega_o)^\mu}{[1 + F(\omega/\omega_o)^\gamma]^\nu} \tag{77}$$

It is shown in appendix G of volume II that the spectrum shape factor F in equation (77) is the ratio of the low-frequency to high-frequency falloff from the spectrum peak. In terms of the empirically determined exponents μ, γ, and ν, F is defined by

$$F = \frac{\mu}{\gamma \, \nu - \mu} \tag{78}$$

3.4.2 EFFECT OF FORWARD VELOCITY

It is convenient at this point to introduce the effect of ambient flow on the jet/edge interaction noise spectral density given by equation (77). The relevant term affected by ambient flow is $(u \, v^4)$, the product of convection velocity (u) with jet turbulence velocity (v) to the fourth power. The convection velocity (u) is defined by the phase of the longitudinal (streamwise) cross-spectral density of surface pressure. It is assumed to scale with the jet convection velocity (V_c) taken relative to the nozzle; i.e., $u \sim V_c$. In a jet the turbulence velocity scales with relative velocity; i.e., $v \sim V_R$. Thus, $u \, v^4 \sim V_c \, V_R^4$.

A practical simplification is obtained by replacing the streamwise (along-the-surface) component of jet convection velocity by the average value; i.e.,

$$V_c = \left[\frac{1 + \frac{V_a}{V_J} \cos \alpha}{2} \right] V_J$$

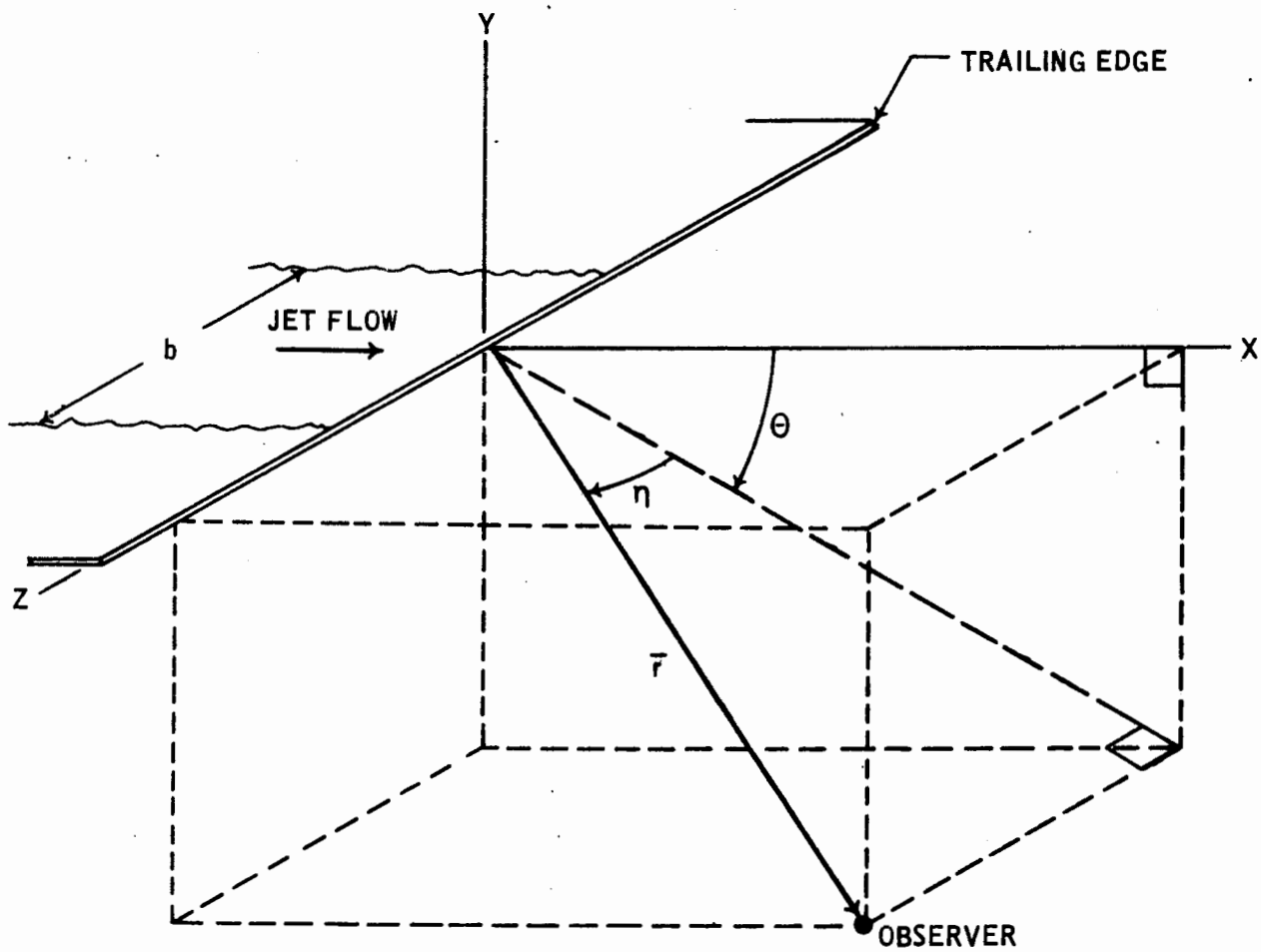

Figure 195.—Jet/Edge Interaction Geometry and Coordinates

is replaced by

$$V_c = \left[\frac{\tilde{V}_c}{V_J}\right] V_J$$

If $[\tilde{V}_c/V_J] = 0.625$ is taken as a weighted average, there occurs no more than a 1.5-dB difference between noise estimates using the exact value of V_c and the weighted average value $V_c = 0.625\ V_J$ over the ambient flow speed range from zero to 75% of the jet velocity.[1] Hence, within experimental accuracy, the effect of ambient flow on jet/edge interaction noise in this range correlates with relative velocity only and exhibits no other explicit dependence on airplane speed.

On this basis, equation (77) is rewritten in a form that includes the effect of airplane speed:

$$\phi_P(\underset{\sim}{r}, \omega) \sim \rho_J^2\ V_J\ V_R^4\ \frac{b\,\Delta}{a_\infty\ r^2}\ \frac{1}{\omega}\ |\cos\eta|\ \sin^2\frac{\theta}{2}\ \frac{(1+F)^\nu\ (\omega/\omega_o)^\mu}{\left[1 + F\ (\omega/\omega_o)^\gamma\right]^\nu} \tag{79}$$

Flight effects other than those considered in obtaining the jet/edge interaction noise spectral density given by equation (79) will be deferred until section 3.4.4, where they arise in the discussion of incomplete interaction and the position of the trailing edge relative to the jet potential-core length. For these cases, the effect considered is due to stretching of the jet potential core.

3.4.3 SEMIEMPIRICAL ESTIMATION PROCEDURE

Experimental verification of theoretical results and a method for predicting jet/edge interaction noise are provided by an expression for normalized sound pressure level. This is obtained from equation (79) which, upon noting that the product ($b\,\Delta L$) scales with the nozzle exhaust area (A_J), may be written in the normalized form

$$\frac{\omega\ \phi_P(\underset{\sim}{r}, \omega)}{\Gamma\ \dfrac{\rho_J^2\ V_J\ V_R^4\ A_J}{a_\infty\ r^2}\ |\cos\eta|\ \sin^2\dfrac{\theta}{2}} = \frac{(1+F)^\nu\ (\omega/\omega_o)^\mu}{\left[1 + F\ (\omega/\omega_o)^\gamma\right]^\nu} \tag{80}$$

where Γ is a normalizing constant. In terms of 1/3-octave-band sound pressure level measurements, the normalized SPL from equation (80) is given by

$$S(f/f_o) = (SPL + 6.3) - 10\log\frac{\rho_J^2\ V_J\ V_R^4\ A_J}{a_\infty\ r^2} - 10\log|\cos\eta|\ \sin^2\frac{\theta}{2} - 10\log\frac{\Gamma}{p_{ref}^2} \tag{81}$$

[1]Typical values of V_a/V_J for a 747 on approach are less than 1/2; for the YC-14, less than 1/3. For the ambient flow speed range from zero to 50% of jet velocity, the difference is less than 1 dB.

where

$$S(f/f_o) = 10 \log \frac{(1 + F)^{\nu} (f/f_o)^{\mu}}{\left[1 + F (f/f_o)^{\gamma}\right]^{\nu}} \tag{82}$$

and

$$SPL + 6.3 = 10 \log \frac{\omega \bar{\phi}_p (r, \omega)}{p_{ref}^2} \tag{83}$$

Note that $\bar{\phi}_p$ is the mean power spectral density in the bandwidth $\Delta\omega$ for calculation of the SPL.

Equation (81) implies scaling relations that can be experimentally verified. According to equation (81), measured values of SPL taken under varying conditions (e.g., V_J, V_R, A_J, θ, etc.) should collapse to a single expression for normalized sound pressure level when suitably scaled. Figure 196, obtained from reference 49, illustrates the data collapse over a wide range of configurations from single- and dual-flow, round and D-shaped nozzles of various diameters, with free and forced mixing, at different jet velocities and shield lengths. Figure 196 is also used to empirically establish the spectral shape for the following jet/edge interaction noise estimation procedure.

3.4.3.1 Estimation Procedure

1. Calculate Peak SPL

   From equation (82), $S(1) = 0$ at $f/f_o = 1$. The condition for this to be a maximum value, such that peak SPL occurs at the frequency f_o, is established in appendix G of volume II. A dimensionally convenient expression for peak SPL at $S(1) = 0$ is thereby obtained from equation (81) in the form

$$\text{peak SPL} = 10 \log \left\{ \left(\frac{\rho_J}{\rho_o}\right)^2 \left(\frac{V_J V_R^4}{V_o^5}\right) \left(\frac{A_J}{r^2}\right) \left(\frac{a_o}{a_\infty}\right) \frac{|\cos \eta| \sin^2 \frac{\theta}{2}}{|\cos \eta_o| \sin^2 \frac{\theta_o}{2}} \right\} + N \tag{84}$$

   The empirical constant N is determined from tests at fixed values of the observation angles (η_o, θ_o), jet density (ρ_o), and ambient sound speed (a_o). The reference velocity (V_o) is 0.3048 m/s (1 fps).

2. Determine Spectrum Shape

   The 1/3-octave-band sound pressure level is obtained upon adding the normalized sound pressure level to the peak SPL

$$SPL = \text{peak SPL} + S (f/f_o) \tag{85}$$

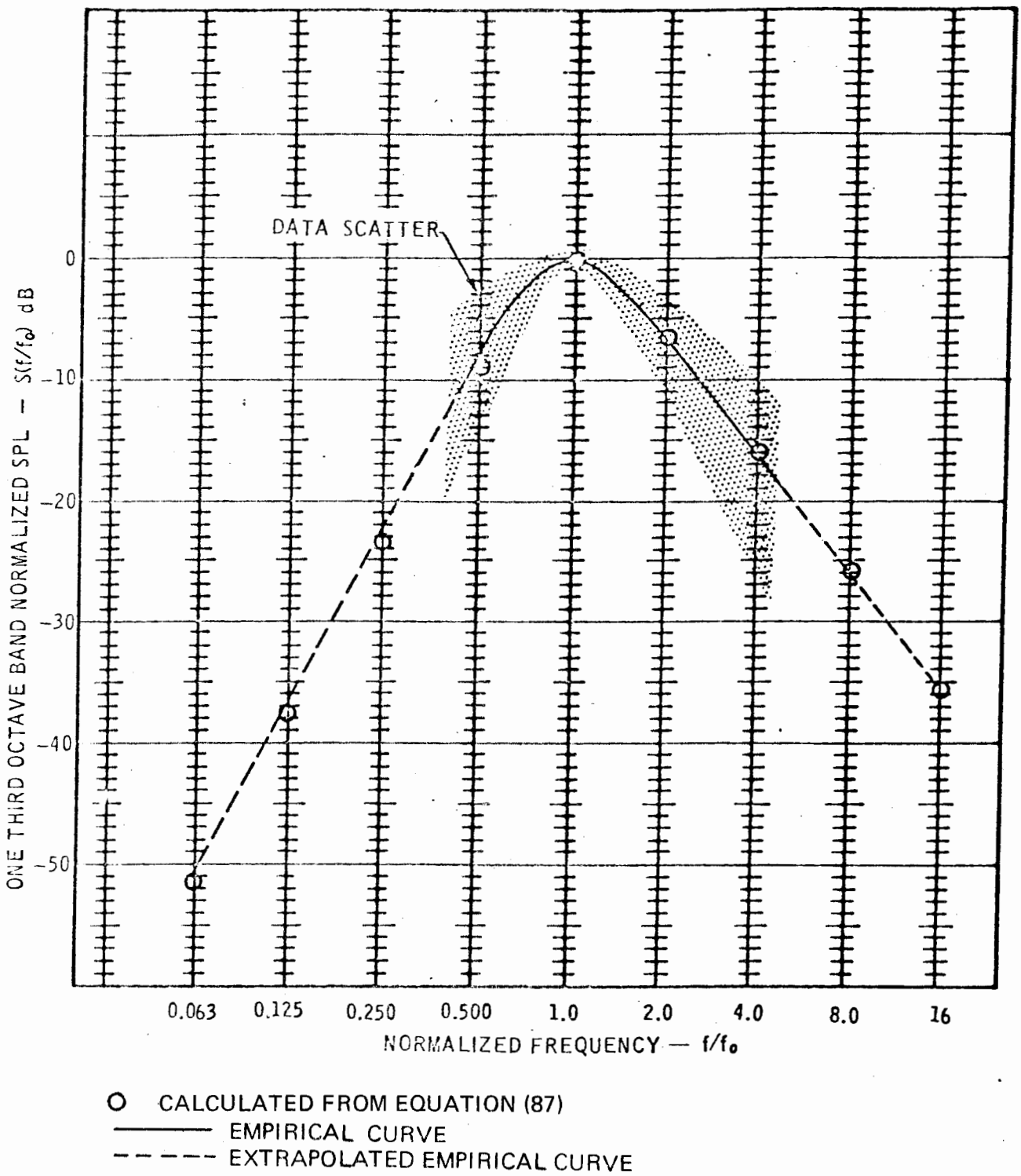

Figure 196.—Jet/Edge Interaction Normalized Sound Pressure Level (Ref. 49)

where $S(f/f_0)$ is calculated from equation (82) when μ, γ, and ν have been empirically determined.

3. Locate Spectrum

The frequency (f_0) at which the spectral peak occurs can be found from the characteristic Strouhal number

$$f_o = S_t \frac{V_J}{D_H} \tag{86}$$

where D_H is the nozzle hydraulic diameter and S_t the Strouhal number as determined in section 3.4.5.

3.4.3.2 Evaluation of Empirical Constants

The empirical constants required in the estimation procedure are determined using the data presented by Bhat and Gallo-Rosso (ref. 49). The data are presented in figures 196 and 197. As previously discussed, figure 196 is a plot of the normalized sound pressure level, equation (82), from which the exponents μ, γ, and ν are evaluated. Figure 197 is a plot of equation (84) at test conditions ($\rho_J = \rho_0$, $a_\infty = a_0$, $\eta = \eta_0$, and $\theta = \theta_0$) from which the empirical constant N is evaluated.

To evaluate the exponents (μ, γ, and ν), it is shown (app. G of vol. II) that the spectrum shape factor (F) given by equation (78) is the ratio of the low-frequency ($f/f_0 << 1$) to high-frequency ($f/f_0 >> 1$) spectral falloff from the peak. Thus, from figure 196, the high-frequency falloff of 31.7 dB/decade gives ($\gamma\nu - \mu = 3.2$), while the low-frequency falloff of 48.3 dB/decade gives $\mu = 4.8$. Therefore, $\gamma\nu = 8$ and, from equation (78), F = 1.5.

To complete the empirical evaluation of the exponents, another condition is required. This is obtained from the low-frequency limit (eq. G-2 of app. G, vol. II) and the data point S(0.063) = -51 dB at $f/f_0 = 0.063$, viz.,

$$-51 = 10\,\nu \log 2.5 + 48 \log (0.063)$$

when F = 1.5 and $\mu = 4.8$, as previously determined. Solving for ν gives $\nu = 1.67$ for a straight-line fit of slope 48 dB/decade through the data point (-51, 0.063). Similarly, the high-frequency limit (eq. G-3 of app. G, vol. II) and the data point S(16) = -36 dB at $f/f_0 = 16$ gives $\nu = 1.14$ for a straight-line fit of slope -32 dB/decade through the data point (-36, 16).

Because the values of ν differ in the high- and low-frequency limit straight-line fits, an iterative procedure is called for to find a best-fit value of ν. A reasonable first choice is to take the average value $\nu = 1.4$. Since $\gamma\nu = 8$, the value $\gamma = 5.7$ is obtained. Substituting these values into equation (82) results in the equation for the normalized sound pressure level:

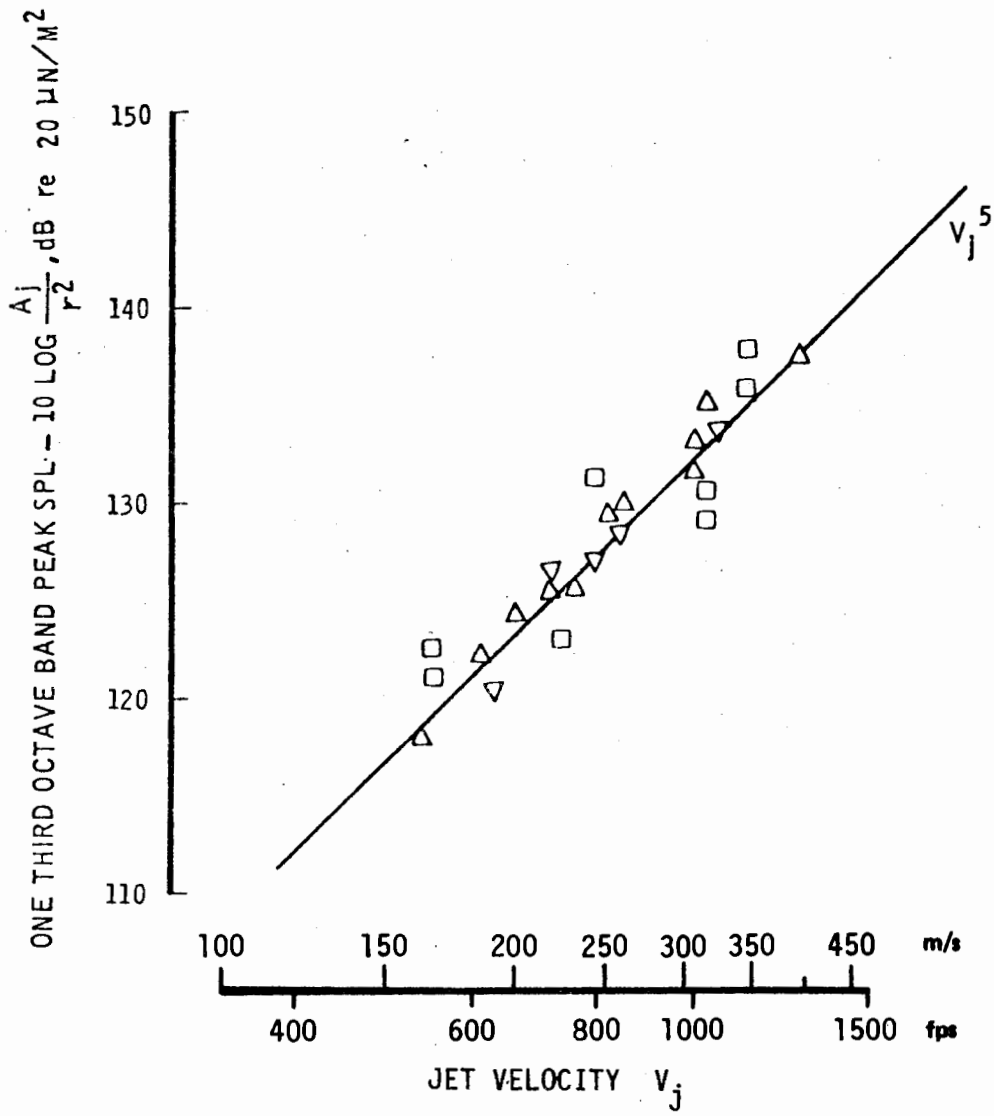

△ SINGLE FLOW "D" NOZZLE
▽ DUAL FLOW "D" NOZZLE
□ DUAL FLOW AXISYMMETRIC NOZZLE

$\eta_o = 0°$
$\Theta_o = 90°$
$\rho_o = 1.225\ Kg/m^3\ (0.0765\ lb_m/ft^3)$
$a_o = 340$ m/s (1116 fps)
$V_a = 0$

Figure 197.—Jet/Edge Interaction 1/3-Octave-Band Peak SPL Scaling (Ref. 49)

$$S(f/f_o) = 10 \log \left\{ \frac{3.61\,(f/f_o)^{4.8}}{\left[1 + 1.5\,(f/f_o)^{5.7}\right]^{1.4}} \right\} \tag{87}$$

Values of $S(f/f_o)$ calculated from equation (87) are shown in figure 196 as circled points. They are an excellent fit to the empirical curve.

The remaining empirical constant to be evaluated is N in equation (84). With $\rho_J = \rho_o$, $a_\infty = a_o$, $\eta = \eta_o$, $\theta = \theta_o$, and $V_o = 1$ fps, equation (84) gives

$$N = \text{peak SPL} - 10 \log \left[V_J\, V_R^4\, \frac{A_J}{r^2} \right]$$

Figure 197 is a plot of the above expression under static test conditions ($V_a = 0$) such that $V_J\ V_R^4 = V_J^5$. The data plotted exhibit the anticipated velocity to the fifth power dependency and yield the value N = -18 for fixed test conditions ($\eta_o = 0^o$, $\theta_o = 90^o$, $\rho_o = 1.225$ kg/m^3 (0.0765 lbm/ft^3), and $a_o = 340$ m/s (1116 fps)).

Combining equations (84), (85), and (87) together with the numerical value

$$N - 10 \log |\cos \eta_o| \sin^2 \frac{\theta_o}{2} = -15$$

for $\eta_o = 0^o$, $\theta_o = 90^o$ yields the following prediction equation for jet/edge interaction noise:

$$\begin{aligned} SPL = {} & 10 \log \left[\left(\frac{\rho_J}{\rho_o}\right)^2 \left(\frac{V_J\, V_R^4}{V_o^5}\right) \left(\frac{A_J}{r^2}\right) \left(\frac{a_o}{a_\infty}\right) |\cos \eta| \sin^2 \frac{\theta}{2} \right] \\ & + 10 \log \left\{ \frac{3.61\,(f/f_o)^{4.8}}{\left[1 + 1.5\,(f/f_o)^{5.7}\right]^{1.4}} \right\} - 15, \quad \text{dB re. } 20\ \mu N/m^2 \end{aligned} \tag{88}$$

Equation (88) defines the 1/3-octave-band sound pressure level for jet/edge interaction noise without modifying the data for the effect of nozzle placement relative to the shield surface. The data used in formulating equation (88) is limited to low-aspect-ratio (less than 1:5) nozzles lying on shield surfaces of length less than about four nozzle hydraulic diameters (ref. 49). As discussed in the following section, the maximum sound pressure level occurs when the shield length equals the jet potential-core length for a nozzle lying on the shield surface. Nevertheless, equation (88) forms the basis for jet/edge interaction noise without modification of the data used in its formulation because it is considered a representative average of a large number of configurations. Consequently, equation (88) is taken to define the maximum sound pressure level for a nozzle lying on a shield surface of length equal to the jet potential-core length. To this basis, corrections for geometric configurations are applied according to the results of the next section. Equation (88) should be refined if more complete data become available from tests in which the shield surface length relative to the jet potential-core length is a controlled parameter.

3.4.4 CORRECTION FOR NOZZLE PLACEMENT

Two cases of nozzle placement with respect to the shield surface are considered: (1) the geometric effect of shield length and nozzle height above the shield surface and (2) for a nozzle lying on the surface, the effect of the position of the shield's trailing edge relative to the exhaust jet potential-core length. These two cases are then combined to give the complete correction for nozzle placement, which is to be added to equation (88) derived in the preceding section.

3.4.4.1 Nozzle Off the Surface, h > 0

The geometric effect of shield length and nozzle height above the shield surface on jet/edge interaction noise is schematically shown in figure 198. There, it is seen that an interaction height (d) may be defined from the relation

$$\frac{d}{L} = \frac{h}{L} - \tan\beta$$

The stretched potential-core length L_c of the jet, due to ambient flow velocity, is given by

$$\frac{L_c}{L_{c_o}} = \frac{V_J}{V_R}$$

Thus,

$$\tan\beta = \frac{V_R}{V_J} \quad \frac{D_H/2}{L_{c_o}} = \frac{V_R}{V_J} \tan\beta_o$$

and the interaction height (d) becomes

$$\frac{d}{L} = \frac{h}{L} - \frac{V_R}{V_J} \tan\beta_o \tag{89}$$

Boeing tests described in section 3.2.1, which used the exhaust flow from a 1-in.-diameter circular pipe, have shown that at a fixed frequency $f \approx f_0$ (1250 Hz), $\Delta SPL = SPL_{edge + jet} - SPL_{jet}$ varies with the ratio h/L. It is reasonable to expect similar behavior for nozzle flow. Accordingly, these results are used herein. Table 12 gives the values of ΔSPL for the various combinations of h/D_H and L/D_H tested.

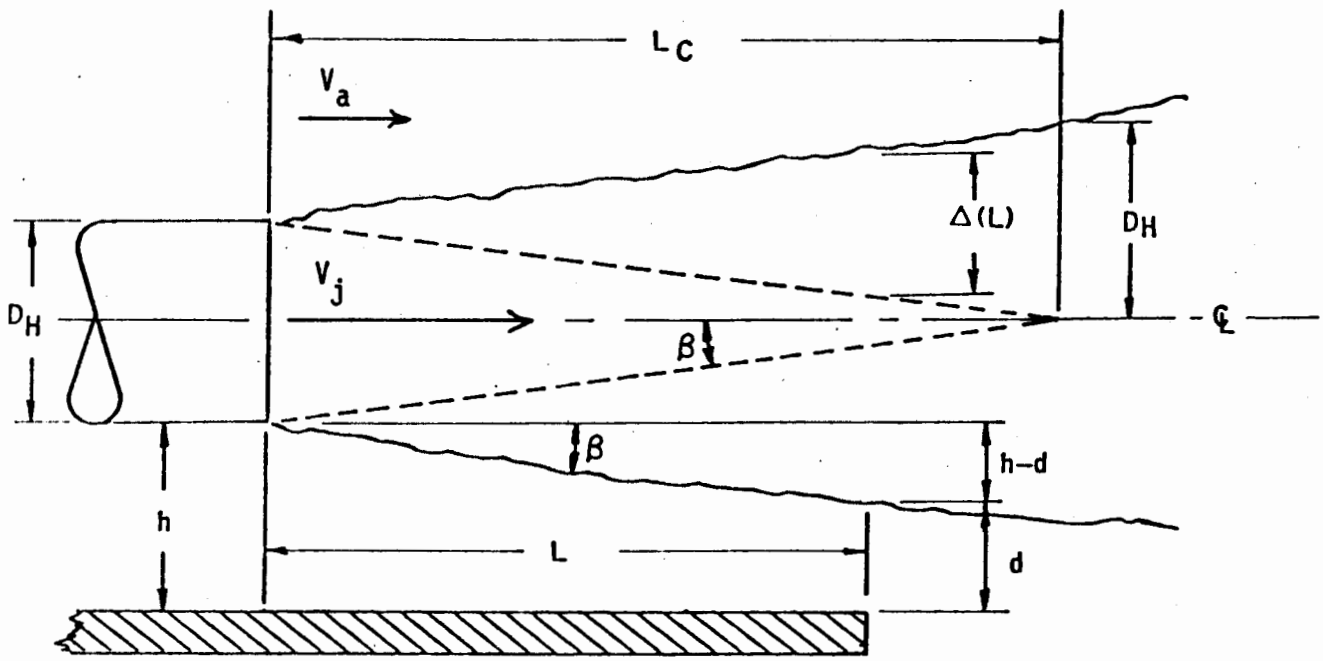

Figure 198.—Jet/Edge Interaction Schematic Showing Effect of Nozzle Placement

Table 12.—"Observed" Jet/Edge Interaction Noise (ΔSPL) as a Function of Nozzle/Shield Geometry

L/D_H	h/D_H		
	3/4	3/2	3
	ΔSPL		
2	3	1	0
4	7.6	3.5	0
8	13.6	8.4	2.4

From the data of table 12, average values of ΔSPL versus h/L were calculated and plotted on semilog paper as shown in figure 199. The equation of the straight line plotted through the data of figure 199 is

$$\Delta SPL = 20 \exp\left[-5\frac{h}{L}\right] \tag{90}$$

The effect of interaction height (d) is introduced by writing equation (90) in the equivalent form

$$\Delta SPL = 20 \exp\left[-5\frac{V_R}{V_J}\tan\beta_o\right] \exp\left[-5\left(\frac{h}{L} - \frac{V_R}{V_J}\tan\beta_o\right)\right] \tag{91}$$

From equation (91) and the assumption that the interaction noise is a maximum when the interaction height $d \leqslant 0$, the maximum interaction sound pressure level is seen to occur when $0 \leqslant h/L < 0.1$, if the condition $(V_R/V_J)\tan\beta_o = 0.1$ is assumed for the case without ambient flow. Consequently, the condition of no ambient flow gives the maximum ΔSPL when there is complete interaction as

$$\Delta SPL = \left\{20 \exp(-0.5)\right\} \exp\left[-5\left(\frac{h}{L} - 0.1\right)\right] ; \ \frac{h}{L} \geqslant 0.1 \tag{92}$$

with the redefinition that the nozzle is considered to lie on the shield surface when $h/L < 0.1$.

These results are generalized to include ambient flow effects by expressing ΔSPL in terms of an incomplete interaction parameter Z which is a function of d/L, the ratio of interaction height to shield length:

$$\Delta SPL = C\, Z\left(\frac{d}{L}\right); \ 0 < Z \leqslant 1 \tag{93}$$

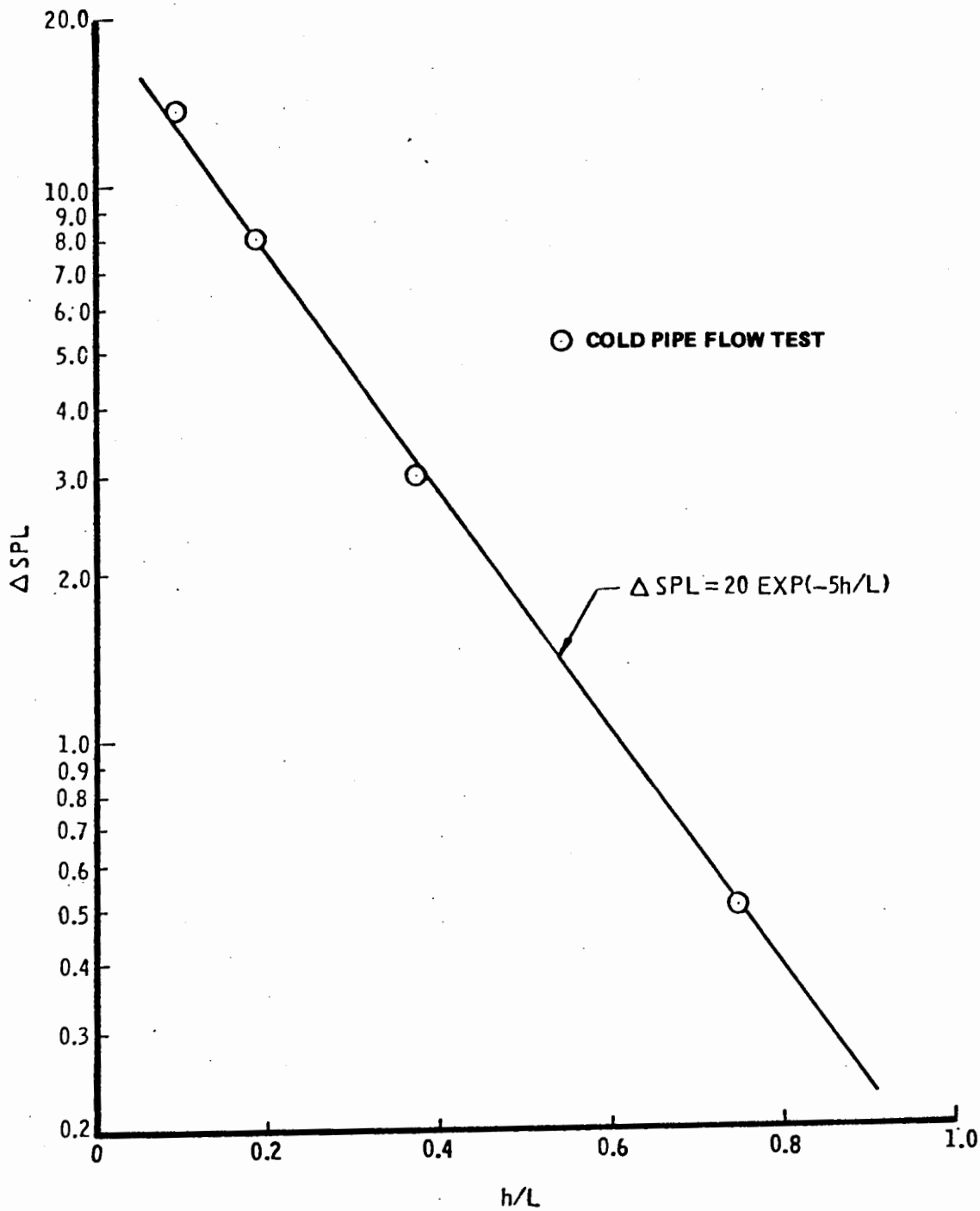

Figure 199.—Effect of Nozzle Placement (Incomplete Interaction) on Jet/Edge Interaction Noise

where

$$Z(d/L) = \exp\left[-b\frac{d}{L}\right] = \exp\left[-b\left(\frac{h}{L} - \frac{V_R}{V_J}\tan\beta_o\right)\right] \tag{94}$$

$$C = C_o \exp\left[-b\frac{V_R}{V_J}\tan\beta_o\right] \tag{95}$$

with $h/L \geqslant (V_R/V_J)\tan\beta_o$, $C_o = 20$, and $b = 5$ from equation (92). It should be clear that the limited amount of data is extended to include the effect of flight speed so that equation (93) reduces to equation (92) when $(V_R/V_J)\tan\beta_o = 0.1$. More experimental justification is required than that currently available. With this understanding, equation (93) provides the means to determine the correction for incomplete interaction including ambient flow effects.

In order to apply equation (93) to obtain the correction for incomplete interaction, consider the following identity:

$$\begin{aligned} SPL_{edge+jet} - \max SPL_{edge+jet} &\equiv (SPL_{edge+jet} - SPL_{jet}) \\ &\quad - (\max SPL_{edge+jet} - SPL_{jet}) \\ &\equiv \Delta SPL - \max \Delta SPL \end{aligned}$$

or

$$SPL_{edge+jet} - \max SPL_{edge+jet} = -C\,(1 - Z) \tag{96}$$

from equation (93). Finally, the jet noise source is subtracted via

$$\begin{aligned} SPL_{edge} - SPL_{jet} &= SPL_{edge+jet} - SPL_{jet} \\ &\quad + 10\log\left[1 - 10^{-0.1\,(SPL_{edge+jet} - SPL_{jet})}\right] \end{aligned}$$

or

$$\begin{aligned} SPL_{edge} - \max SPL_{edge} &= (SPL_{edge+jet} - \max SPL_{edge+jet}) \\ &\quad + 10\log\left[\frac{1 - 10^{-0.1\,\Delta SPL}}{1 - 10^{-0.1\,\max \Delta SPL}}\right] \end{aligned}$$

to obtain, when equations (93) and (94) are substituted,

$$SPL_{edge} - \max SPL_{edge} = -C(1 - Z) + 10 \log \left[\frac{1 - 10^{-0.1\,C\,Z}}{1 - 10^{-0.1\,C}} \right] \tag{97}$$

Equation (97), in terms of the incomplete interaction parameter Z and the interaction constant C, is a general form for the desired incomplete interaction correction when ΔSPL is given by the expression of equation (93). From the limited data of table 12 the parameter Z was found to decay exponentially with h/L, and the empirical constants C_0 and b in equations (94) and (95) were evaluated as $C_0 = 20$ and $b = 5$.

In summary, equation (97)–with Z and C given by equations (94) and (95), respectively–provides the correction for incomplete interaction between the jet exhaust and the shield surface. It considers the incomplete interaction as a primarily geometric effect and accounts for ambient flow in terms of its stretching effect on the potential core.

3.4.4.2 Nozzle On the Surface, h=0

Boeing/Aeritalia tests (sec. 3.2.5) using a D-nozzle ($D_H = 5.1$ cm) lying on the shield surface show an approximately 4-dB increase in trailing edge noise per doubling of shield length ($L/D_H = 3$ and $L/D_H = 6$). In these tests the jet potential core was about six hydraulic diameters in length, and the noted level differences may be attributed to the shield's trailing edge lying within the jet potential-core region when $L/D_H = 3$ and lying just at the end of the jet potential core when $L/D_H = 6$. Additional data from Hayden (ref. 52) is presented in figure 200, which shows trailing edge noise from an aspect-ratio-10 slot-nozzle/plate system. For this nozzle, $L/D_H \approx 0.5\,L/H$ (H is nozzle height, see fig. 200) so the abscissa on figure 200 is just twice the ratio of plate length L to hydraulic diameter D_H. In this figure, the two circled points are the relative values at $L/D_H = 3$ and $L/D_H = 6$ from the Boeing/Aeritalia D-nozzle tests. For want of more complete data, it is proposed to simplify these results by assuming a 3-dB increase per doubling of shield length for $L/D_H < L_c/D_H$ and a 3-dB falloff per doubling for $L/D_H \geq L_c/D_H$ since the maximum level occurs when the shield length equals the jet potential-core length. Introducing the potential-core stretching effect due to ambient flow, these results can be expressed by

$$SPL_{edge} - \max SPL_{edge} = -10 \left| \log \left(\frac{L_{c_0}}{L} \frac{V_J}{V_R} \right) \right| \tag{98}$$

for $0 \leq h/L < (V_R/V_J) \tan \beta_0$, because the nozzle is considered to lie on the surface in this range of h/L (the interaction height $d \leq 0$).

Equation (98) is the required correction to account for the position of the shield trailing edge relative to the length of the stretched jet potential core. It gives a 3-dB falloff per halving or doubling of the shield length with respect to the jet potential-core length.

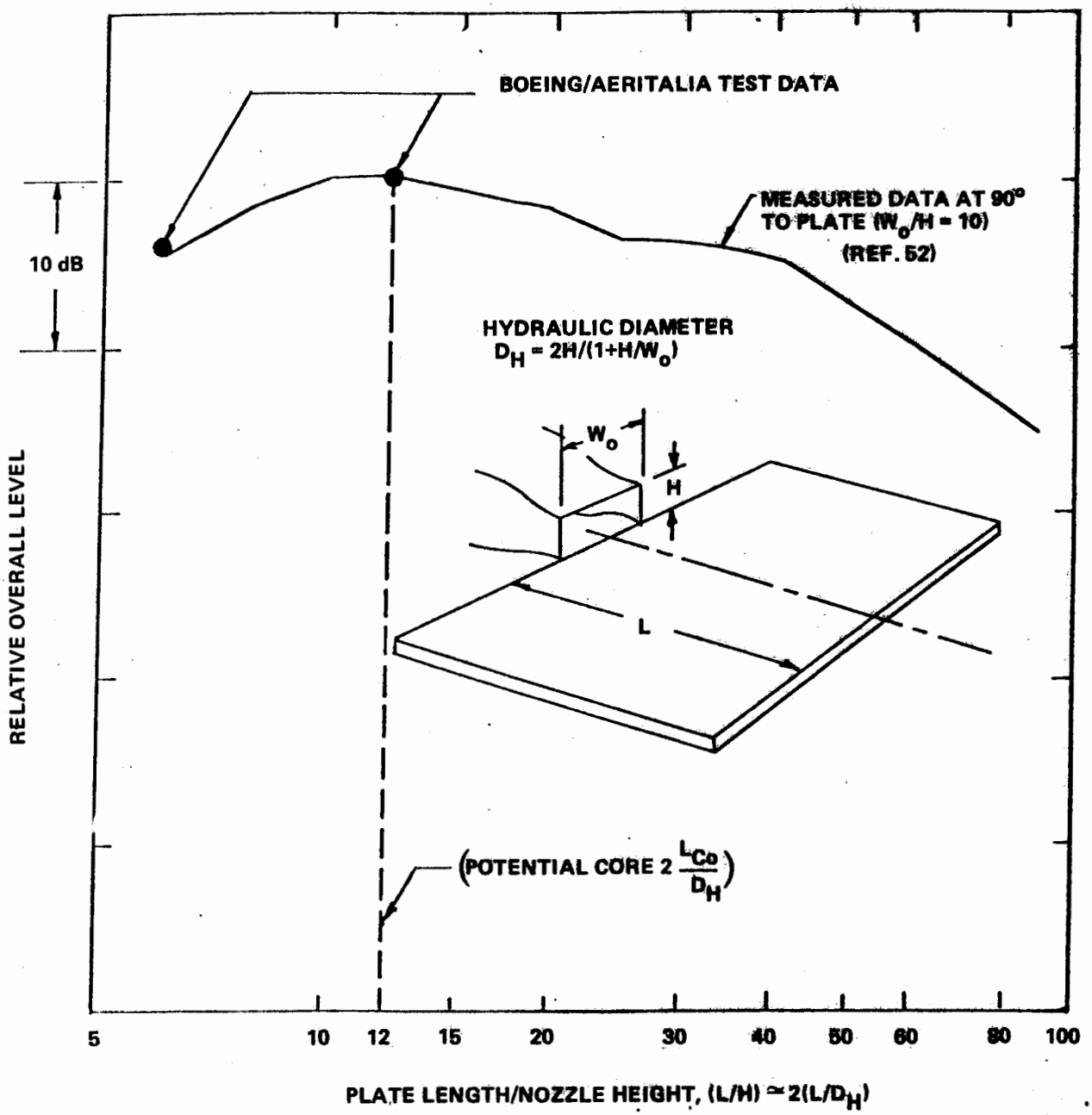

Figure 200.—Effect of Nozzle Placement (Trailing Edge Position Relative to Potential Core Length) on Jet/Edge Interaction Overall SPL

3.4.4.3 Combined Correction for Nozzle Placement

The previous results are combined to give the correction $K = SPL_{edge} - \max SPL_{edge}$ for the effects of nozzle placement on jet/edge interaction noise.

1. For $0 \leqslant \frac{h}{L} < \frac{V_R}{V_J} \tan \beta_o$

$$K = -10 \left| \log \left(\frac{L_{c_o}}{L} \frac{V_J}{V_R} \right) \right| \tag{99}$$

2. For $\frac{h}{L} \geqslant \frac{V_R}{V_J} \tan \beta_o$

$$K = -10 \left| \log \left(\frac{L_{c_o}}{L} \frac{V_J}{V_R} \right) \right| - C(1 - Z) + 10 \log \left[\frac{1 - 10^{-0.1CZ}}{1 - 10^{-0.1C}} \right] \tag{100}$$

with

$$Z = \exp \left[-5 \left(\frac{h}{L} - \frac{V_R}{V_J} \tan \beta_o \right) \right]$$

$$C = 20 \exp \left[-5 \frac{V_R}{V_J} \tan \beta_o \right]$$

The values of β_o and L_{co} to be used when calculating K depend on the nozzle configuration; e.g., for a convergent round nozzle, $\tan \beta_o \approx 0.1$ and $L_{co} \approx 5$ D.

The geometric effects correction K given by either equation (99) or (100), as specified by the value of h/L, is added to equation (88) for maximum jet/edge interaction noise. This completes the calculation of the 1/3-octave-band sound pressure level for jet/edge interaction noise except for the specification of the frequency f_o at peak SPL, which is determined in the following section.

3.4.5 STROUHAL NUMBER

The frequency (f_o) at which the spectrum peaks can be determined from the characteristic Strouhal number based on the nozzle hydraulic diameter. It turns out that f_o depends on the length of shield surface. An explanation of how f_o varies with shield length follows from the assumptions: (1) the boundary layer development on the shield surface may be disregarded and (2) the wall jet may be modeled as a free jet

mixing layer. In a free jet mixing layer, a turbulence characteristic frequency can be estimated from

$$\omega \sim \frac{V_R}{\Delta(L)}$$

where $\Delta(L)$ is a transverse mixing layer dimension at the shield length L. From similar triangles (fig. 198),

$$\frac{\Delta(L)}{D_H} = \frac{L}{L_c}$$

From potential-core stretching due to ambient flow, $L_c = L_{co}\,(V_J/V_R)$. The characteristic frequency ω is independent of relative velocity and varies inversely with the shield length; i.e., $\omega \sim V_J/L$. A result is subsumed from these factors to give the Strouhal number in the form

$$S_t = \frac{f_o\, D_H}{V_J} = \frac{k}{\frac{L}{D_H} + a} \tag{101}$$

where k and a are constants (a is a dimensionless virtual origin of the jet). To obtain equation (101), it was tacitly assumed that f_o is proportional to the jet turbulence characteristic frequency at the shield edge. Figure 201 shows Boeing/Aeritalia data from D-nozzle tests. A plot of equation (101) with k = 1.8 and a = 3 is also shown, and supports the argument that f_o varies inversely with the shield length. Thus, for jet/edge interaction noise estimation, the characteristic frequency (f_o) at peak SPL is calculated from

$$\frac{f_o\, D_H}{V_J} = \frac{1.8}{\frac{L}{D_H} + 3} \tag{102}$$

3.4.6 SUMMARY OF ESTIMATION EQUATION

For convenience, the estimation equations are collected and summarized in this section. To equation (88) for maximum jet/edge interaction noise is added the nozzle placement effect correction K from equations (99) and (100). With the frequency (f_o) at peak SPL given by equation (102), the resulting expressions for estimating jet/edge interaction 1/3-octave-band sound pressure level are

VELOCITY-V_j		BOEING / AERITALIA TEST DATA
SYM	m/s.	
▽	76.2	"D" – SHAPE NOZZLE
△	152.4	D_H = 5.1 cm
◊	228.6	
□	304.8	
○	376.4	D_H = 13.78 cm
x	AVG	L/D_H = 2.7

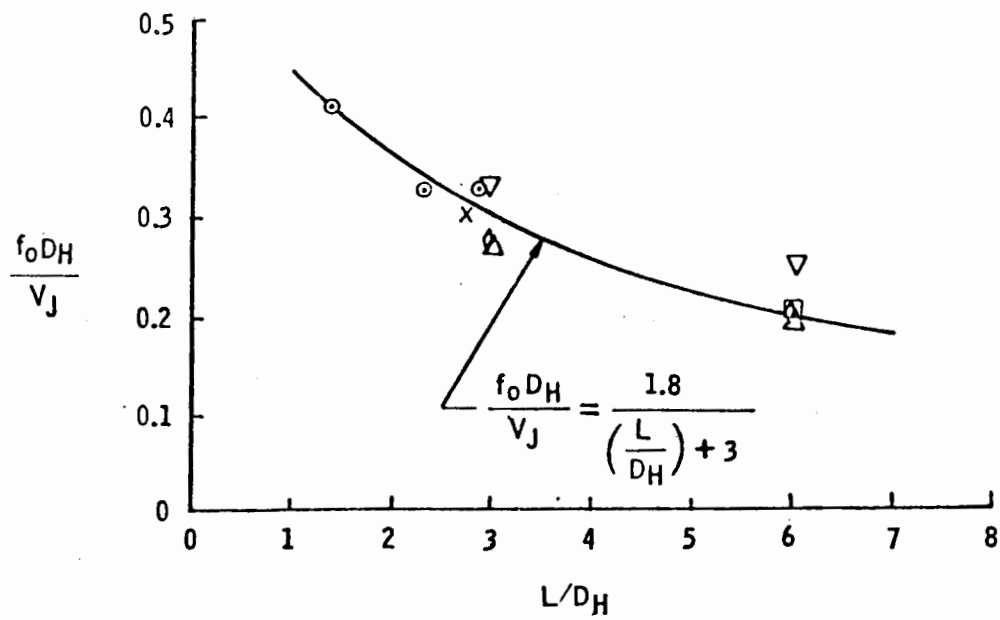

Figure 201.—Characteristic Frequency, f_o, as a Function of Shield Length, L, for Jet/Edge Interaction Noise

$$SPL = 10 \log \left\{ \left(\frac{\rho_J}{\rho_o}\right)^2 \left(\frac{V_J V_R^4}{V_o^5}\right) \left(\frac{A_J}{r^2}\right) \left(\frac{a_o}{a_\infty}\right) |\cos \eta| \sin^2 \frac{\theta}{2} \right\}$$

$$+ 10 \log \left\{ \frac{3.61 \, (f/f_o)^{4.8}}{\left[1 + 1.5 \, (f/f_o)^{5.7}\right]^{1.4}} \right\} - 15 + K, \text{ dB re. } 20 \, \mu N/m^2 \tag{103}$$

with the reference values

ρ_o = 1.225 kg/m^3 (0.0765 lbm/ft^3)

a_o = 340 m/s (1116 fps)

V_o = 0.3048 m/s (1 fps)

The frequency f_o at which the spectrum peaks is given by

$$f_o = \frac{1.8}{\frac{L}{D_H} + 3} \left(\frac{V_J}{D_H}\right) \tag{104}$$

For a given nozzle with known β_o and L_{co} (e.g., $\tan \beta_o = 0.1$ and $L_{co}/D_H = 5$ for a round convergent nozzle), the nozzle placement correction K is given by

1. For $0 \leqslant \frac{h}{L} < \frac{V_R}{V_J} \tan \beta_o$

$$K = -10 \left| \log \left(\frac{L_{c_o}}{L} \frac{V_J}{V_R} \right) \right| \tag{105}$$

2. For $\frac{h}{L} \geqslant \frac{V_R}{V_J} \tan \beta_o$

$$K = -10 \left| \log \left(\frac{L_{c_o}}{L} \frac{V_J}{V_R} \right) \right| - C(1 - Z) + 10 \log \left[\frac{1 - 10^{-0.1CZ}}{1 - 10^{-0.1C}} \right] \tag{106}$$

with

$$Z = \exp \left[-5 \left(\frac{h}{L} - \frac{V_R}{V_J} \tan \beta_o \right) \right]$$

$$C = 20 \exp \left[-5 \frac{V_R}{V_J} \tan \beta_o \right] \tag{107}$$

In the next section equations (103) through (107) are used to calculate jet/edge interaction noise for a convergent round nozzle/wing configuration tested by von Glahn, Groesbeck, and Reshotko (ref. 50).

3.4.7 DATA/ESTIMATION EQUATION COMPARISON

Independent jet/edge interaction noise data are available from von Glahn et al. (ref. 50) to compare with the estimation equation of section 3.4.6. They compared the interaction noise from a 2-in. convergent round nozzle/wing system measured in two different acoustic arenas. The test conditions are specified in figure 202, which presents the test results. Two cases of nozzle height above the wing are shown. At $h/L = 0.042$, the nozzle is considered to be on the shield and complete interaction occurs. At $h/L = 0.17$, the nozzle is above the shield and incomplete interaction occurs. The shield length-to-diameter ratio $L/D_H = 5.25$ was the same for both nozzle heights.

The solid curves of figure 202 were calculated for the specified test conditions from the estimation equations (103) through (107) with $V_R/V_J = 1$ for zero ambient flow, and $\tan \beta_0 = 0.1$ and $L_{c0}/D_H = 5$. The jet density and ambient sound speed were taken at the reference values $\rho_0 = 1.225$ kg/m^3 (0.0765 lbm/ft^3) and $a_0 = 340$ m/s (1116 fps), respectively.

The comparison between estimated and measured jet/edge interaction noise spectra is only fair. However, in making the comparison, it should be noted that von Glahn et al. (ref. 50) distinguish two noise sources in their measured data. The source peaking at lower frequency was identified as jet/edge interaction noise and the source peaking at the higher frequency was identified as "scrubbing" noise of the jet flow on the surface. On the other hand, the data of Bhat and Gallo-Rosso (ref. 49), which was used to define the spectral shape in the estimation method, does not exhibit a dual-noise-source behavior. If the dual-noise-source hypothesis is accepted, the estimation method would appear to give a median result. It is interesting to note that reducing the estimated level 3 dB and shifting 2/3 octave down in frequency gives an excellent comparison with the low-frequency noise source that is purported to be jet/edge interaction noise by von Glahn et al. (ref. 50).

3.4.8 CONCLUSIONS

Jet/edge interaction noise is readily calculated from equations (103) through (107) of section 3.4.6. Estimated spectra compare favorably with the measurements of von Glahn et al. (ref. 50), which had not been used to formulate the estimation equations. The question of the existence of dual sources, which appear in the measurements of von Glahn et al. (ref. 50) but not in those described by Bhat and Gallo-Rosso (ref. 49), should be resolved in order to more accurately describe the spectral shape.

The numerical values used in the nozzle placement effect correction and the Strouhal number dependence on shield length were obtained from a very limited amount of available data. Additional tests are needed that vary the length of shield relative to the jet potential-core length as well as the nozzle height above the shield.

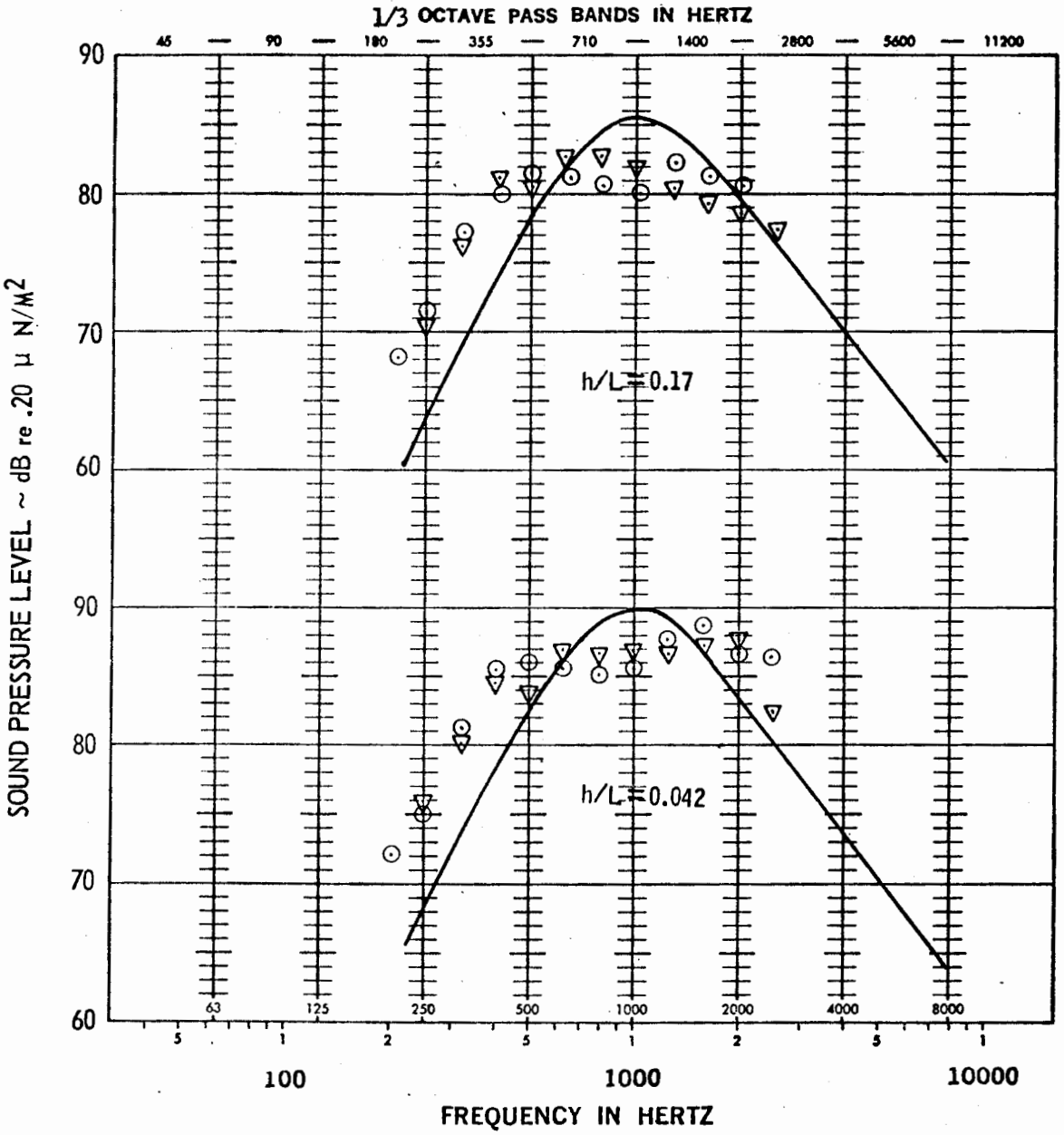

LEGEND:

——— PRESENT ESTIMATES

○ ARENA 1 TEST

▽ ARENA 2 TEST

NOTES:

1) JET NOISE REMOVED FROM DATA

2) $M_j = 0.80$, $T_s / T_{so} = 0.89$

3) D = 5.1 cm, L/D = 5.25

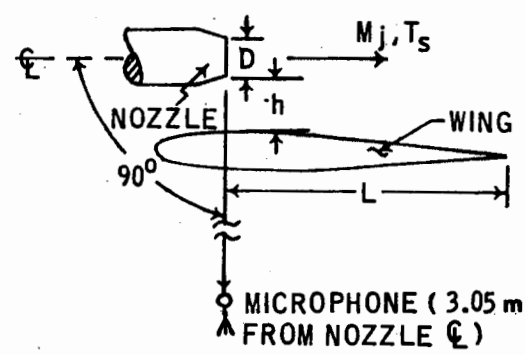

Figure 202.—Jet/Edge Interaction Noise (Estimation Versus NASA Data) (Ref. 50)

The conjecture of section 3.4.5 that the Strouhal number is independent of relative velocity should be experimentally verified. The relative velocity to the fifth power scaling indicated by the estimation equations for shields shorter than the jet potential-core length (cf., app. H in vol. II) is confirmed by the tests of Bhat and Gallo-Rosso (ref. 49).

4.0 SUMMARY OF ESTIMATION PROCEDURES

This section summarizes procedures for estimation of wing and fuselage shielding of jet aircraft noise in the community. These estimation methods are the result of the analysis in the preceding two sections. Some of these procedures are of such quality to merit computerization for community noise predictions, while others are not. Those meriting computerization have been programmed and are discussed below in section 4.2. The computer program user's guide is contained in volume II as appendix A. The other procedures, however, are presented as manual estimation methods because the effects they attempt to predict are significant and important at times.

4.1 SCOPE OF ESTIMATION PROCEDURES

The noise shielding estimation procedures developed herein fall in two categories:

- New computerized procedures that have been added to the "old" NAS2-6969 contract computer software
- Manual procedures

The computerized procedures deal with the estimation of:

- Wing shielding attenuation of noise generated inside the engine, i.e., turbomachinery (TM) noise
- Effect of a wing on noise generated outside the engine, i.e., jet noise and jet/edge interaction noise

The manual procedures deal with estimating:

- Turbomachinery noise shielding attenuation provided by a fuselage
- Noise propagating into the shadow zone under the wing due to the presence of a wake behind the wing.

In each of these procedures, an attempt is made to account for the effects of the following variables on the community noise observed under the airplane's flightpath:

- Engine/airframe/observer geometry
- Engine cycle
- Flight speed
- Directivity and spectrum shape of individual noise components

Human response measures in perceived noise level (PNL) versus time and effective perceived noise level (EPNL) are calculated. Figure 203 shows the computation sequence performed by the new computer software. This figure is the same as that shown on page 10 of reference 2 except where we have noted new additions.

The user of the new computer program (app. A in vol. II) may obtain at his option the following outputs in addition to those noted in the preceding paragraph.

- Individual noise component behavior, i.e.,
  - One-third or full-octave-band SPL spectra versus time
  - Configuration corrections, which can now include shielding
  - SPL spectra emitted toward the observer at index conditions (spectra normalized to a distance of 1-m radius without propagation effects between airplane and observer)
  - PNL versus time
  - EPNL
- Empiricisms used in wing shielding computations, i.e., parameters (α, β, γ) of figure 152 and the directivity curve for the unshielded noise
- Engine/wing geometry
- Aircraft/observer geometry versus time
- Noise extrapolation corrections for sound propagation between airplane and observer, i.e.,
  - Spherical divergence
  - Atmospheric absorption
  - Extra ground attenuation
  - Ground reflection

Also, the results from the manual estimation procedures can be input to the new computer program via a measured SPL data and measured configuration correction input method available in the new software. Actually, this capability already existed in the old software and was maintained in the new software. In fact, all the capabilities of the old software are still available. The users of the old program may use the new program without any changes in their input data cards. Unless the user specifically requests shielding computations, the new program functions exactly like the old program and gives the same answers. Figure 204 shows the interface between the new software additions and the old program that permits such functioning.

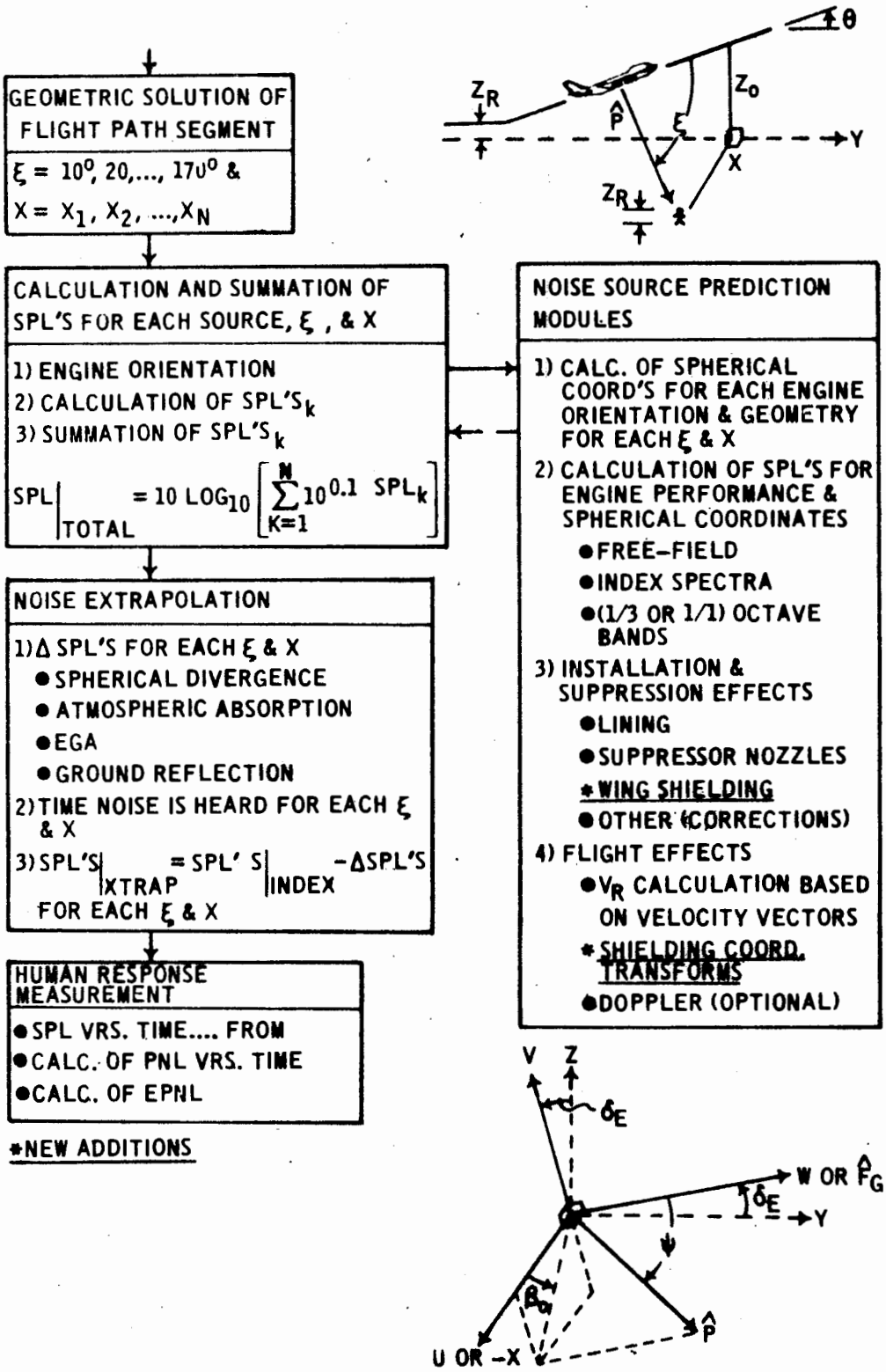

Figure 203.—Computation Sequence

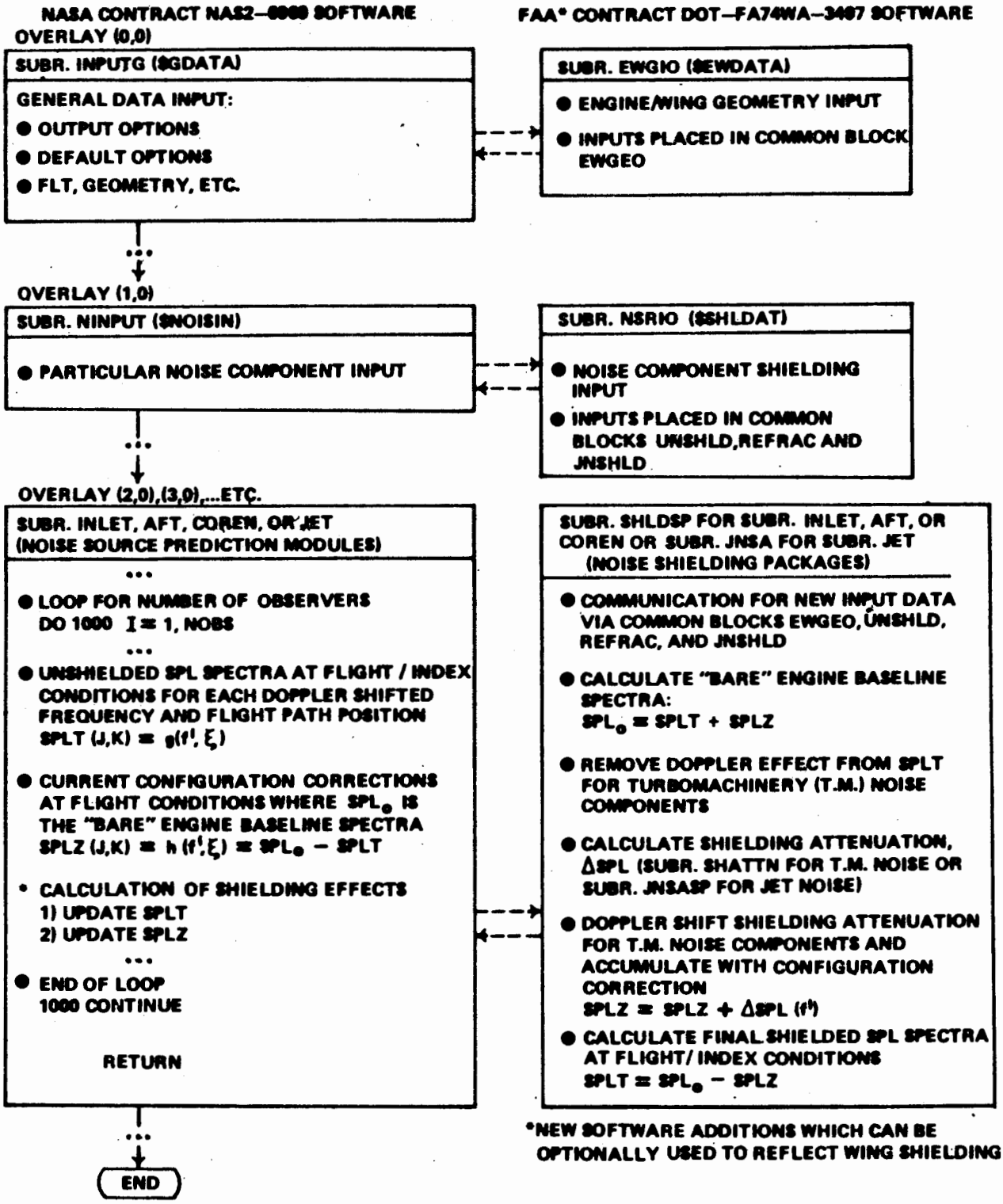

Figure 204.—Interface Between New and Old Software

Figure 205 illustrates the scope of the work done to develop the noise shielding prediction procedures, emphasizing those noise components that offer the greatest noise reduction potential, i.e., TM noise. Similar steps were taken for jet noise shielding. It was found that without the use of suppressor nozzles or forced mixers, jet noise shielding doesn't have as large a noise reduction potential. Also, jet noise is in a realm apart from TM noise. This is because the noise source has a large spatial distribution that varies with frequency, nozzle geometry, and engine cycle. A purely theoretical treatment for jet noise shielding is beyond present capabilities. Hence, the procedures presented here for jet noise are strictly empirical based on von Glahn's and Boeing/Aeritalia data. The effects of flight and wing edges other than the trailing edge are believed to have a negligible effect on shielding attenuations for jet noise. The data base available is insufficient to conclude otherwise. Thus, no special effort was made to include these additional factors in the jet noise shielding estimation procedure.

The estimation procedure for jet/edge interaction noise generation is based on theory. A major part of the procedure required empirical evaluation of constants and of cases when the jet exhaust was only partially interacting with the wing. This empirical evaluation used Boeing/Aeritalia data. Comparisons of predicted jet/edge interaction noise with independent NASA data were favorable. The effect of flight on jet/edge interaction noise is significant, and these effects have been included in the estimation procedure.

In section 4.4, a representative sample illustrates use of the new computer program. Plots of part of the predicted results for this sample are shown in the "Summary" of this document.

4.2 COMPUTERIZED PROCEDURES

This section describes the methods that have been included in the new software, which represents a revision of that developed under NASA contract NAS2-6969. The procedures estimate the sound attenuations due to placement of a wing/flap system near a jet engine for TM noise (inlet fan or compressor, exit fan, turbine, and core noise) and jet noise components. The estimation capability for a new noise source–jet/edge interaction noise–is included in the new program.

The majority of the mathematics concerning TM noise shielding are already presented in sections 2.2.1, 2.2.3, and 2.4.2.3. It is felt that a detailed presentation of equations computerized for these noise components would be a tremendous burden on the reader; e.g. five coordinate systems are used to relate the engine/wing/observer geometry to the effects of jet refraction, uniform flow, and diffraction. The geometry and vector solutions are already illustrated graphically in the sections noted. For this reason it is felt that computerized procedures can best be described through use of flow charts showing the basic computations performed by the major subroutines. Detail equations can then be found by reference to the computer listing in conjunction with the engineering sections cited in the flow charts. The computer listing is given in the third volume of this report. The new code contains a generous amount of comment cards indicating what calculations are being performed.

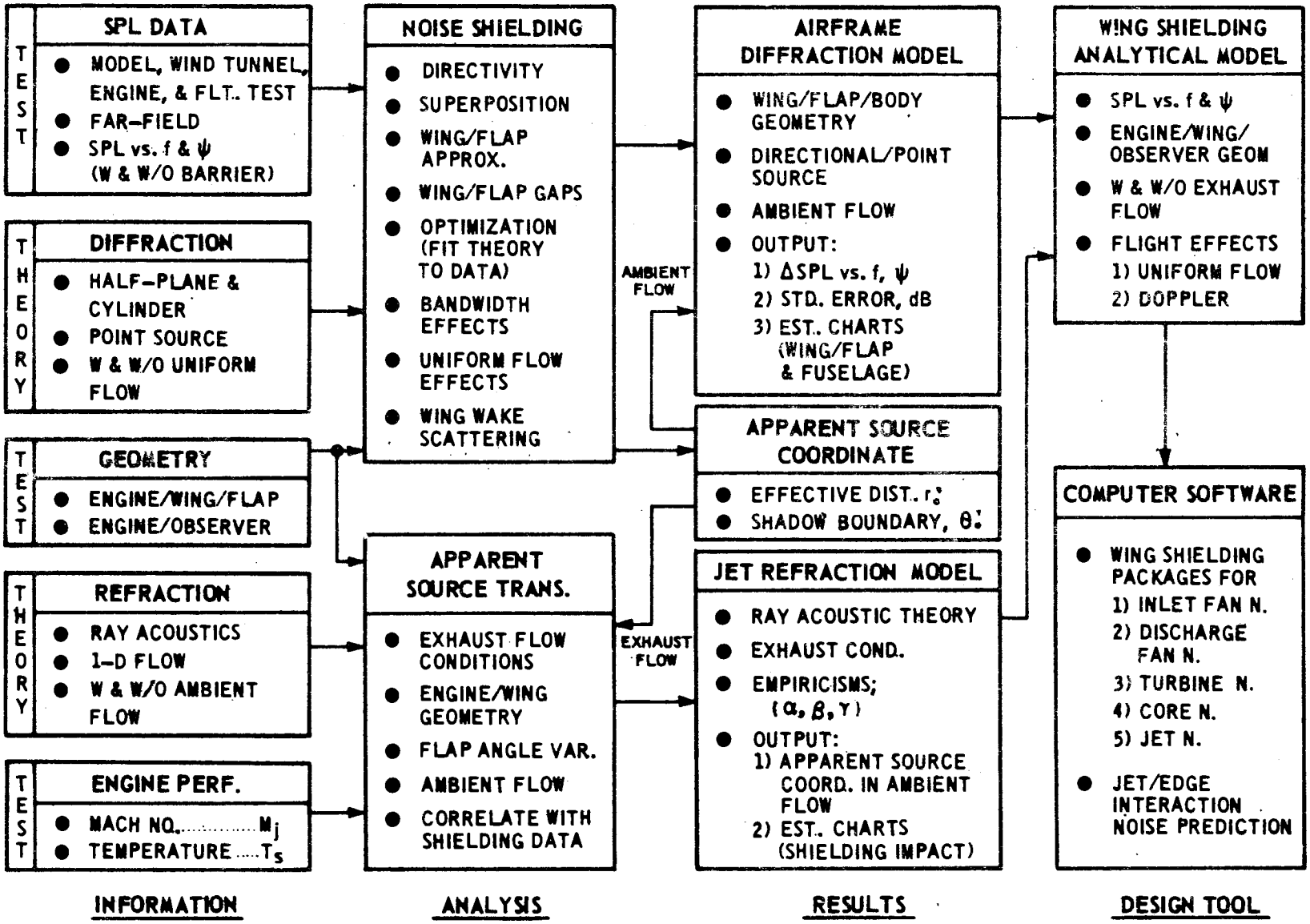

Figure 205.—Airframe Shielding Model Development

On the other hand, the equations dealing with jet noise shielding and estimation of jet/edge interaction noise are not nearly so complex, i.e., we only have to consider one wing edge. Those applying to jet noise are also more subject to change. For these reasons we have included in section 4.2.3 the specific details that were computerized.

4.2.1 WING SHIELDING OF DISCHARGE TURBOMACHINERY NOISE COMPONENTS

4.2.1.1 Application

This procedure updates the estimated sound pressure level spectra and configuration corrections per NAS2-6969 contract software to include the effects of wing shielding.

4.2.1.2 Conditions

The conditions for the attenuations correspond to those used to estimate the unshielded noise spectra, i.e., index conditions (ref. 2).

4.2.1.3 Required Data

Engine/wing geometry:

α_1, α_2, α_3, X_0/D, X_1/D, X_2/D, Y_0/D, Y_1/D, Y_2/D, S/D, D	See figure 144

Noise component parameters:

M_J	Exhaust flow Mach number
T_s/T_{so}	Exhaust flow static temperature ratio, with T_{so} being the ambient temperature in absolute units (^{0}K or ^{0}R)
(α, β) vs. cot ψ_0 and γ	Empirical adjustment curves for the jet refraction portion of the estimation procedure. See figure 152 for default curves built into the new program or use $(\alpha, \beta, \gamma) = (1, 1, 0)$ for a purely theoretical calculation.
USPL vs. ψ	Empirical sound pressure level directivity curve based on static tests (dB). If desired, this input is used to override the predicted unshielded SPL spectra versus ψ resulting from the NAS2-6969 contract procedures. Thus, the user may estimate shielding attenuations based on his own data. Default curves built into the new program for this input are shown in figure 206 for whichever noise component is being considered.

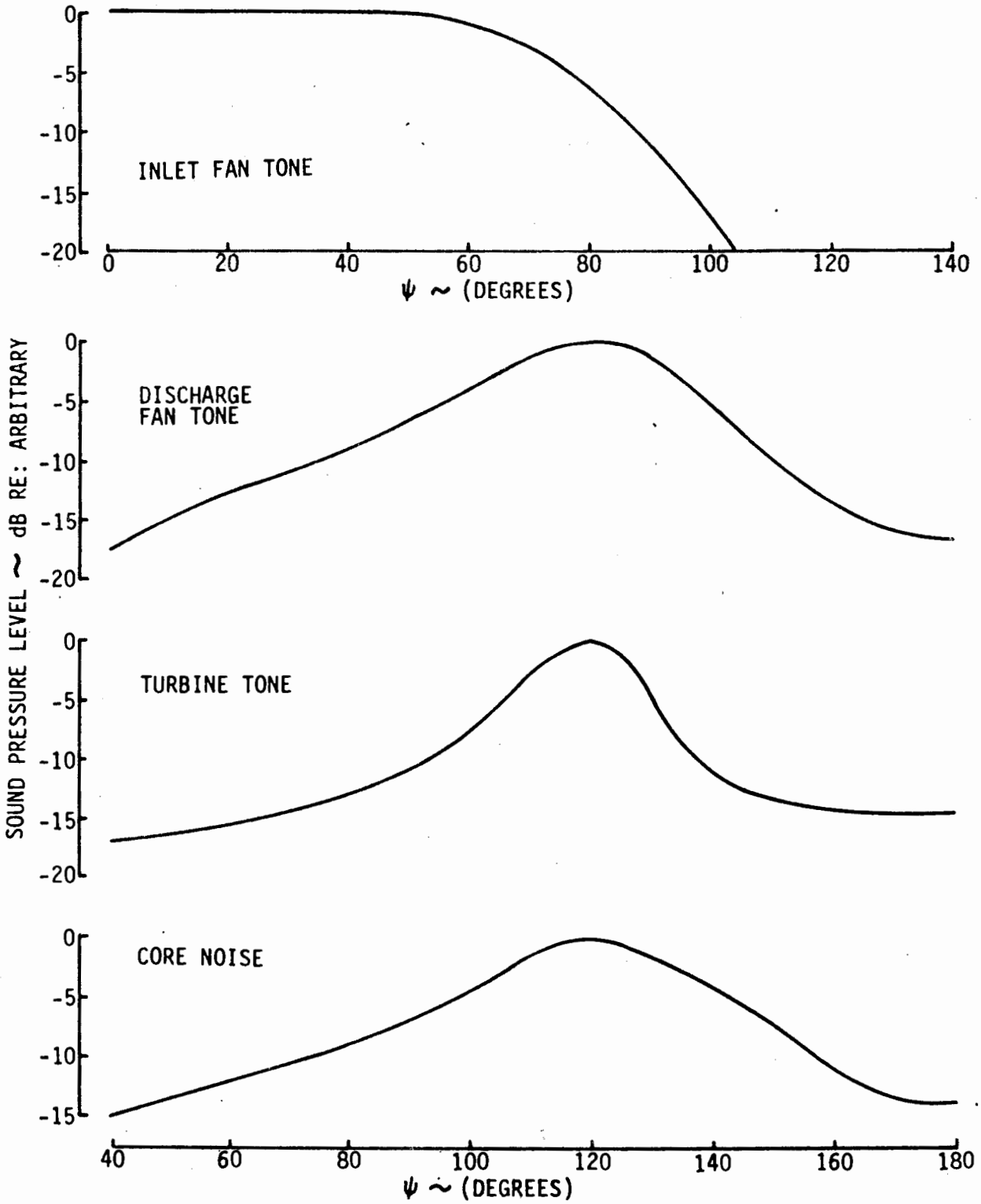

Figure 206.—Unshielded SPL Directivity Curves for High-Bypass-Ratio Turbofans

Additional data required, but available in original NAS2-6969 software:

M_0	Aircraft Mach number
C_z	Ambient speed of sound at aircraft altitude Z_0 in figure 6 of reference 2 (m/s or fps)
f	1/3- or full-octave band geometric mean frequencies (Hz)
BW	Filter bandwidth in decades: BW = 0.1 for 1/3-octave bands = 0.3 for full-octave bands
SF	Doppler shift, i.e., $(1 - M_0 \cos \xi)$ with ξ being the angle between the flightpath and sound propagation path to the observer
ψ	Actual directivity angle relative to the engine inlet centerline to be used in the calculations (deg)
SPLT vs. (f, ψ)	Predicted unshielded SPL spectra versus ψ at flight, index conditions based on NAS2-6969 procedures (dB). This may or may not be used in the calculation of shielding attenuations at the user's option.
SPLZ vs. (f, ψ)	Estimated configuration corrections that do not include wing shielding at the index conditions used for SPLT above (dB)
δ_E	Engine inclination angle relative to the horizon (deg)
(X, Y, Z_N)	Aircraft coordinates relative to each observer positioned on sidelines to the airplane's flight track (m or ft). See figure 6 of reference 2.

Switches for options selected (see app. A in vol. II for detailed description):

ISFE	Flight effects indicator for wing shielding calculations. Part of $GDATA input.
IES	Number of wings to be considered, i.e., - Just the wing on near side of airplane or - Both wings on near and far side of airplane. Part of $EWDATA input.
IWED	Types of wing edges to be considered. Part of $SHLDAT input.

4.2.1.4 Calculation

Figure 207 shows some of the computation steps taken in the interface subroutine SHLDSP of the new software. The input spectra to the routine are those estimated by the original NAS2-6969 contract software. These spectra are at flight conditions; i.e.,

START

- INPUT via COMMON BLOCKS (Sec. 4.2.1.3)

- DOPPLER SHIFTS;
  $\Delta L = 10 \log_{10}(SF)$ .....1/3 OCTAVES

  $\Delta B = 0.1 \Delta L / BW$ .....FREQUENCY INDEX

- BARE ENGINE REFERENCE SPECTRA AT FLT. CONDITIONS;
  $SPL_0 = SPLT + SPLZ$

- REMOVE FLT. EFFECT FROM SPLT
  $USPL_J$ = (TABLE-LOOK-UP ON $SPLT_J$ AT $J = J - \Delta B$)
  $+ n \Delta L$
  where n = 4, 4, 2 for fan,turbine,core,noise,resp.

- CALC. SHIELDING ATTENUATION SPECTRUM FOR SOURCE/WING OBSERVER STATIONARY RELATIVE TO ONE ANOTHER, ΔSPL_J → SUBR. SHATTN

- DOPPLER SHIFT SHIELDING ATTENUATION;
  ΔSPL_J = (TABLE-LOOK-UP ON ΔSPL_J AT $J = J + \Delta B$)

- UPDATE CONFIGURATION CORRECTIONS TO INCLUDE SHIELDING;
  $SPLZ = SPLZ + \Delta SPL_J$

- UPDATE INDEX SPECTRA TO INCLUDE SHIELDING;
  $SPLT = SPL_0 - SPLZ$

- OUTPUT; SPLT AND SPLZ SPECTRA WHICH NOW INCLUDE WING SHIELDING EFFECTS

- RETURN TO CALLING PROGRAM

Figure 207.—Wing Shielding Package (Subroutine SHLDSP)

the source is moving through a stationary atmosphere with the observer at rest in the atmosphere. Before the shielding computations are performed, the spectra must be converted to laboratory conditions like those in a wind tunnel; i.e., source and observer are stationary relative to each other, but both are in a uniform flow medium. This is done by removing the Doppler shift and level change originally included when the unshielded spectra were estimated. The user may select the uniform flow Mach number of the laboratory conditions to be zero or M_0 for shielding calculations using the input switch ISFE.

At this point the unshielded spectra are input to the wing shielding calculation subroutine SHATTN. This program is the main computation routine for shielding. Subroutine SHATTN returns the shielding attenuation spectra $\Delta SPL(f, \psi)$ at the laboratory conditions. The attenuation spectra are then Doppler shifted and added to the original configuration correction spectra, SPLZ. The new correction spectra are then subtracted from the "bare engine" reference spectra, resulting in the final shielded SPL spectra at index conditions.

Attention now turns to the discussion of computations performed in subroutine SHATTN. Figure 208 shows the macro flow chart for this routine. Basic calculation steps are indicated, along with the sections of this report where the mathematics with illustrations can be found. The major looping and transfers to the next level of subroutines that perform the calculation tasks are also noted. For detailed computations performed in each of the tasks, one must see the listing for the subroutines noted in the figure, which have been generously commented for this purpose.

The first task (secs. 2.2.1.1 and 2.4.1.2) performed by subroutine EEGEOM concerns the engine/edge geometry, i.e., those terms important in the shielding calculation that are constant with respect to airplane/observer geometry and frequency variations. This task has subtasks:

- Determine the set of unit vectors $(\hat{X}, \hat{Y}, \hat{Z})$ defining a right-handed coordinate system fixed to each wing edge.
- Compute key engine orientation angles (α, δ) from unit vectors $(\hat{X}, \hat{Y}, \hat{Z})$ relative to the engine inlet centerline vector $(\hat{S})$ for the fifth task, wing edge diffraction, below.
- Calculate the unit vector for ambient flow parallel to the half-plane approximating each wing edge.
- Determine the nozzle coordinate (r_0, θ_0) relative to each wing edge.

The second task (secs. 2.2.1.1 and 2.4.1.2) performed by subroutine EOGEOM deals with the edge/observer geometry, i.e., the terms that vary with respect to the edge being considered and the airplane/observer geometry. Three coordinate systems are related to one another for the calculation of direction angles used in the diffraction section:

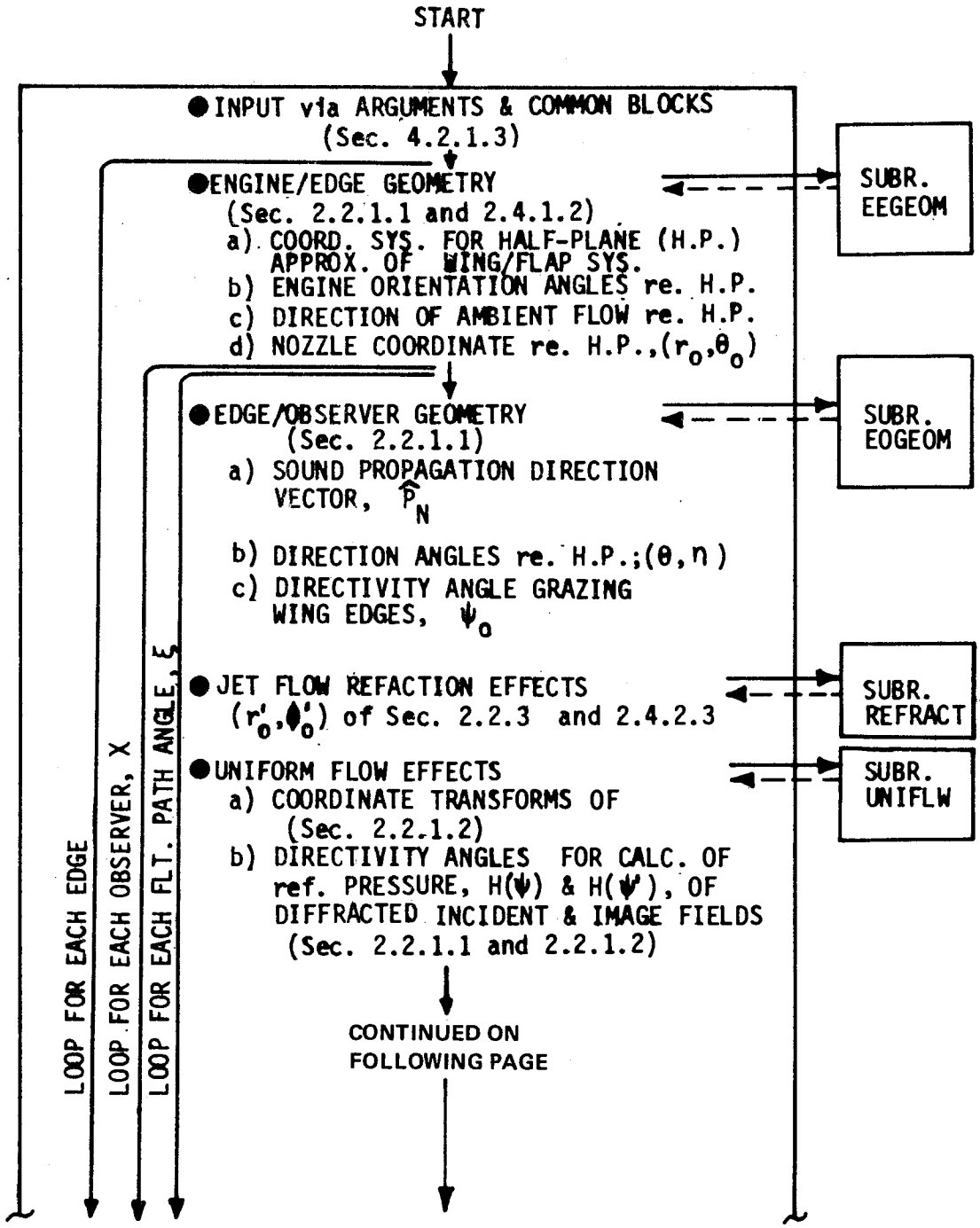

Figure 208.—Wing Shielding Calculation Module (Subroutine SHATTN)

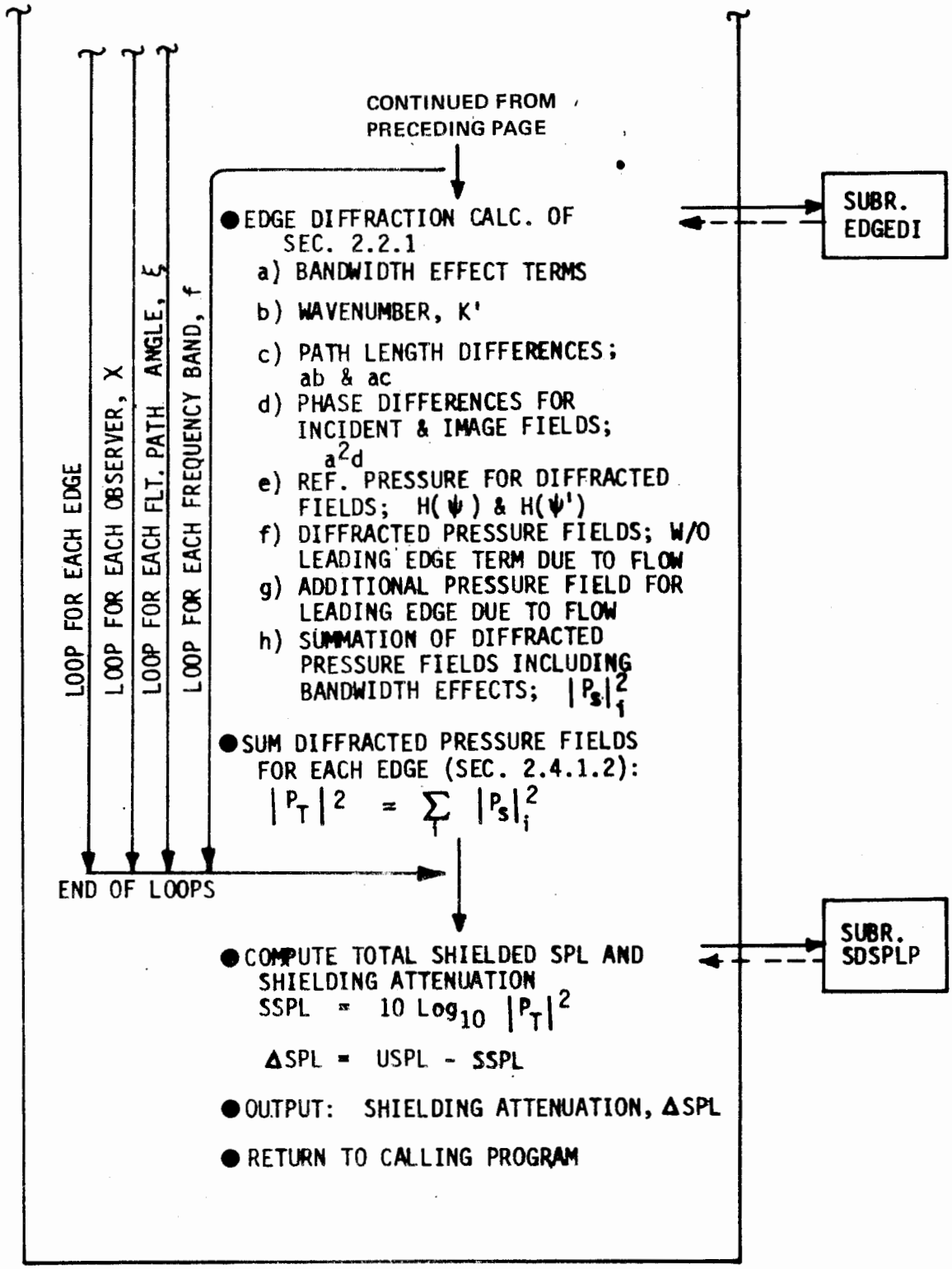

Figure 208.—(Concluded)

- Coordinate system of figure 6 of reference 2

- Coordinate system fixed to the engine

- Coordinate system fixed to the edge being considered.

The sound propagation direction vector, $\hat{P}_N$, is calculated and related to the wing edge. The direction angles (θ, η, and ψ_0) are calculated. This completes the geometry calculations that ignore the effects of flow.

The third task (secs. 2.2.3 and 2.4.2.3) pertains to the effects of jet flow and determines an apparent source position (r_0', ϕ_0') relative to each wing edge. The computations involved in this step, performed by subroutine REFRACT, are the following.

- Approximate the three-dimensional problem by the two-dimensional equivalent given in sections 2.2.3.2 and 2.2.3.3.

- Compute the direction of sound leaving the jet relative to the case without jet flow, i.e., results in $\Delta\psi_P$.

- Apply empiricism (α and γ of sec. 2.4.2.3) to predicted angular change.

- Relate the corrected angular change back to the three-dimensional problem and compute the apparent source location using vector techniques (sec. 2.2.3.3) and empiricism (β of sec. 2.4.2.3).

The fourth task (sec. 2.2.1.2) concerns the effects of ambient flow on wing shielding. Subroutine UNIFLW performs this task. In this routine, the following calculations are made.

- Solve the three-dimensional coordinate transformation that accounts for uniform flow. The apparent source and observer position vectors are changed by this transformation.

- Determine the reference pressure functions, $H(\psi)$ and $H(\psi')$, for the directional/compact-source diffraction equation (9). This is done by specifying the directivity angles to enter a table look-up interpolation on the unshielded SPL directivity curve.

The fifth task (sec. 2.2.1) deals with the calculation of wing edge diffraction. Subroutine EDGEDI performs the computations. In this routine, all the effects in the diffraction theory for the half-plane are integrated. The effects are:

- Filter bandwidth

- Wave number

- Path length and phase differences between incident and image diffracted fields

- Directivity via the functions $H(\psi)$ and $H(\psi')$

- Additional noise emanating from the leading edge due to flow

- Multiple edges, i.e., random-phase superposition (sec. 2.4.1.2) of edge solutions resulting in the shielded pressure spectra for each observer (X) and flightpath position (ξ).

The last computation task pertains to the final shielding attenuation calculation. Subroutine SDSPLP is used for this task. The total shielded pressure spectra are converted to sound pressure level. The shielded SPL spectra are compared with the unshielded spectra used to perform the shielding calculation, i.e., the predicted spectra USPL determined from SPLT in subroutine SHLDSP or the input directivity curve selected by the user. The shielded SPL spectra are subtracted from the unshielded SPL spectra, resulting in the estimated wing shielding attenuation ΔSPL. This is the result returned to subroutine SHLDSP.

Subroutine SHLDSP uses the wing shielding attenuations to update the estimated unshielded spectra (SPLT) and the configuration corrections (SPLZ) to include wing shielding effects. These updated spectra are returned to the particular TM noise source prediction module being used, i.e., subroutines INLET, AFT, or COREN.

4.2.2 WING SHIELDING OF INLET TURBOMACHINERY NOISE COMPONENTS

The application and conditions specified in section 4.2.1 also apply for this noise component; hence, they will not be repeated here.

4.2.2.1 Required Data

Engine/wing geometry (fig. 144):

Same as section 4.2.1.3, except L/D is also required.

Noise component parameters:

None required, except USPL versus ψ as stated previously in section 4.2.1.3.

Additional data available in original NAS2-6969 software:

Same as section 4.2.1.3.

Switches for options selected:

Same as section 4.2.1.3.

4.2.2.2 Calculations

The subroutines used for inlet TM noise component shielding calculations are the same as those used for the discharge TM noise components (sec. 4.2.1.4). One routine is not called and the reference no-flow condition is different, as explained in the exceptions below.

- The call to subroutine REFRACT is bypassed because the engine exhaust flow region is remote relative to the inlet flow region; i.e., no jet refraction effects are included.

- The reference no-flow condition has the location of the source at the center of the engine's inlet plane instead of at the center of the nozzle exit plane.

4.2.3 WING SHIELDING OF JET NOISE

Presented in this section is the computerized procedure for the estimation of engine-over-wing jet noise shielding attenuation. The procedure, based on the empirical formulation of section 3.3, has been included in the coding of subroutine JNSA (fig. 204). In section 4.2.3.3, the procedure is defined for application to three different types of engines: turbojets, single-flow-nozzle turbofans, and coannular-flow-nozzle turbofans.

4.2.3.1 Required Data

f	Geometric mean frequencies (Hz)
C_z	Ambient speed of sound at aircraft altitude Z_0 (m/s or fps)
(X, Y, Z_N)	Aircraft coordinates (m or ft)
δ_E	Engine inclination angle (deg)

For the primary jet case:

D_1	Hydraulic diameter of nozzle (m or ft)
V_1	Velocity of jet exhaust relative to nozzle (m/s or fps)
L_1/D_1	Dimensionless shield length measured in direction parallel to engine exhaust axis from the nozzle exit plane
SPL_1	Predicted primary-jet noise spectrum at index conditions (dB re: 20 $\mu N/m^2$)

For the secondary jet case:

D_2	Hydraulic diameter of nozzle (m or ft)

V_2	Velocity of jet exhaust relative to nozzle (m/s or fps)
L_2D_2	Dimensionless shield length measured in direction parallel to engine exhaust axis from the nozzle exit plane
SPL_2	Predicted bulk-flow jet noise spectrum at index conditions (dB re: 20 $\mu N/m^2$)

4.2.3.2 Calculation

For the primary jet case:

1. The reference correlation term is

$$Z_o = (6.0)\ 10^{-7} \left(\frac{L_1}{D_1}\right) \left(\frac{f\, C_z^{\,2}}{g_c\, V_1}\right) \left[1 + (4.5)\ 10^9 \left(\frac{g_c\, D_1}{C_z^2}\right)^2\right] \tag{108}$$

where g_c = 9.807 m/s^2 (32.174 ft/s^2)

Repeat the following calculations through line 4 for each aircraft position relative to the observer.

2. Calculate the direction angles:

$$\theta = \cos^{-1}\left[(-Y \cos\delta_E - Z_N \sin\delta_E)/\sqrt{Y^2 + Z_N^2}\ \right] \tag{109}$$

$$\eta = \sin^{-1}\left[X/(X^2 + Y^2 + Z_N^2\ )^{.5}\right] \tag{110}$$

3. Calculate the directivity effect:

$$Z = Z_o \cos\eta / \left[1 + 0.033\ \left(\frac{\theta}{180° - \theta}\right)^4\right] \tag{111}$$

4. Calculate the jet noise shielding attenuation:

$$\Delta SPL = 10 \log_{10} (1 + Z) \tag{112}$$

This attenuation is subtracted from the unshielded primary-jet noise spectrum, SPL_1, to get the shielded jet noise spectrum, $SSPL_1$.

For the secondary jet case:

The calculation for the sound pressure level attenuation of the bulk-flow noise spectrum follows the same methods as outlined above for the primary jet, except D_2, V_2, L_2/D_2 replace D_1, V_1, L_1/D_1. The resulting attenuation is subtracted from the unshielded bulk-flow noise spectrum, SPL_2, to get the shielded bulk-flow jet noise spectrum, $SSPL_2$.

4.2.3.3 Estimation Procedure

For turbojets:

Use the procedure of section 4.2.3.2 for the primary-jet case to calculate the turbojet noise shielding attenuation.

For single-flow-nozzle turbofans:

1. Calculate the mixed flow velocity:

$$V_M = [V_1 (T_{TM} - T_{T2}) - V_2 (T_{TM} - T_{T1})] / (T_{T1} - T_{T2}) \tag{113}$$

where

$$T_{TM} = (\dot{M}_1 T_{T1} + \dot{M}_2 T_{T2}) / (\dot{M}_1 + \dot{M}_2) \tag{114}$$

and

(T_{T1}, T_{T2})	=	total temperature (°K or °R) of primary and secondary jets, respectively
$(\dot{M}_1, \dot{M}_2)$	=	mass flows (kg/s or lbm/s) of primary and secondary jets, respectively

2. Let $V_1 = V_M$

   D_1 = single-flow-nozzle diameter

3. Use the procedure of section 4.2.3.2 for the primary-jet case to calculate the single-flow-nozzle turbofan noise shielding attenuation.

For coannular-flow-nozzle turbofans:

1. Add the predicted primary flow (SPL_1) and the predicted bulk-flow (SPL_2) jet noise spectra on an energy basis:

$$SPL_T = 10 \log_{10} \left[10^{.1\, SPL_1} + 10^{.1\, SPL_2} \right] \tag{115}$$

2. Calculate the shielded primary- and bulk-flow jet noise spectra, $SSPL_1$ and $SSPL_2$, using the procedures of section 4.2.3.2 for turbojets and single-flow-nozzle turbofans, respectively.

3. Add the two shielded spectra, $SSPL_1$, and $SSPL_2$, on an energy basis:

$$SSPL_T = 10 \log_{10} \left[10^{.1\ SSPL_1} + 10^{.1\ SSPL_2} \right] \tag{116}$$

4. Calculate the coannular-flow-nozzle turbofan shielding attenuation:

$$\Delta SPL = SPL_T - SSPL_T \tag{117}$$

4.2.4 JET/EDGE INTERACTION NOISE

Presented here is the computerized procedure for the estimation of jet/edge interaction noise spectra for an engine-over-wing configuration. The procedure has been coded in subroutine JEINT, which is interfaced with the original NAS2-6969 software as an additional noise source prediction module (see sec. 4.3.12 of app. A, vol. II). The procedure is based on the semiempirical formulation of section 3.4 except that instead of equation (97), the variation in the jet/edge interaction noise with the ratio of nozzle height to shield length (h/L) is defined by

$$\Delta SPL_{edge} = SPL_{edge} - \max SPL_{edge} = -24 \log_{10} \left[\frac{h/L}{(V_R/V_J) \tan \beta} \right]$$

This equation actually was obtained prior to equation (97) by antilogarithmic subtraction of the jet noise directly from the data of table 12 and fitting the straight line as shown in figure 209. On the other hand, equation (97) was obtained by antilogarithmic subtraction of the jet noise from the exponential fit (eq. 96) to the data of table 12. Differences between these two data reduction techniques are within the experimental accuracy and need not be considered further. At values of $h/L > 0.8$, the straight-line fit does not follow the data, as can be seen by the data point at ($h/L = 1.5$, $t/t_0 = 15$) on figure 209. But, at these high values of h/L, the data and the corresponding values from either data reduction technique are considerably below the free jet noise level and can be ignored. Consequently, the straight-line fit of figure 209 was used in the computerized procedure.

4.2.4.1 Required Data

(X, Y, Z_N)	Aircraft coordinates relative to the observer at retarded time (m or ft)
C_z	Ambient speed of sound at aircraft altitude Z_0 (m/s or fps)
P_z	Ambient pressure at aircraft altitude Z_0 (atm or psfa)

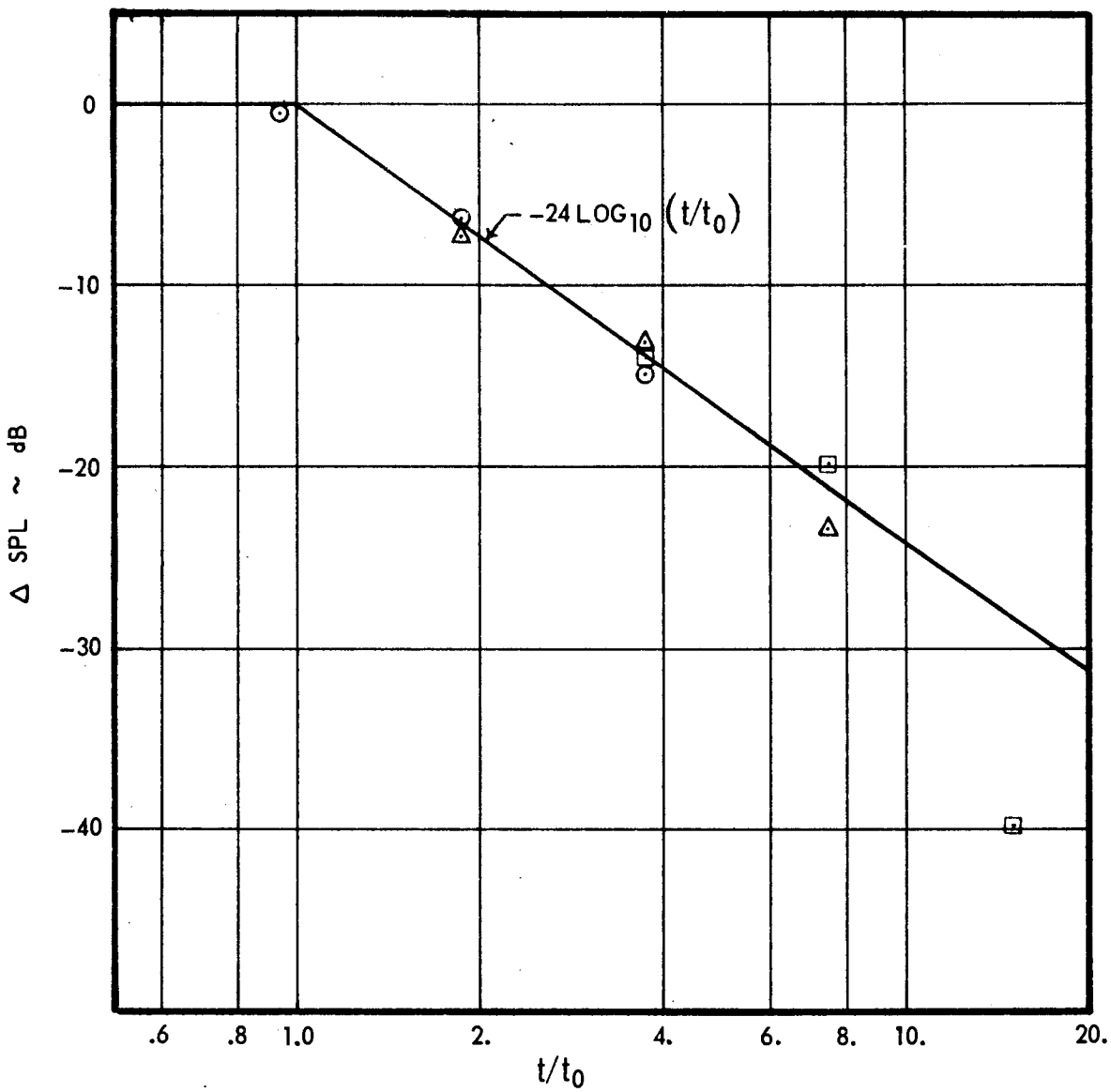

LEGEND:

⊙ L/D = 8
△ L/D = 4
⊡ L/D = 2
} D = 2.54 cm

$t_0 = 0.1$, $V_j = 310$ m/s
$T_T = 288°K$, $V_o = 0$ m/s

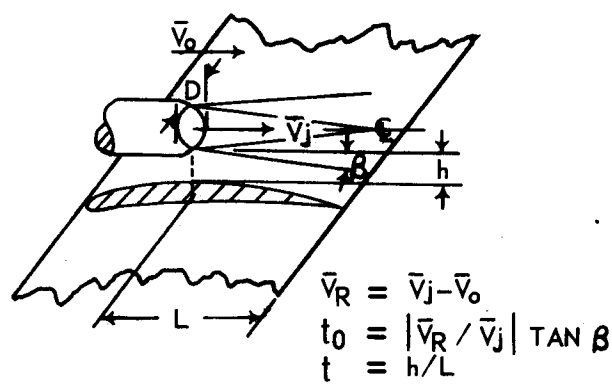

Figure 209.—Effect of h/L Geometry Variation on Jet/Edge Interaction Noise

GRAD	Aircraft climb gradient, i.e., tan θ
BW	Filter bandwidth in octaves: BW = 1 for full-octave-band SPL = 1/3 for 1/3-octave-band SPL Default value is 1/3.
M_O	Aircraft Mach number
SF	Doppler shift factor ($1 - M_O \cos \xi$)
f	Geometric mean frequencies for SPL spectra (Hz)
M_J	Jet Mach number
T_S/T_{SO}	Jet static temperature ratio where T_{SO}=288.2 °K (518.7 °R)
D	Hydraulic diameter of jet nozzle (m or ft); i.e., D equals 4 times discharge area divided by nozzle perimeter
A/D^2	Dimensionless discharge area. Default value for round nozzle is ($\pi/4$) or 0.785.
h/D	Dimensionless nozzle lip height above the wing surface. Default value is 0.
L/D	Dimensionless distance between nozzle exit to the wing/flap system's trailing edge measured along the wing/flap surface
L_C/D	Dimensionless jet-core length. Default value for round nozzle is 5.
β	Jet spreading angle (deg). Default value for round nozzle is 5.7°. *Restriction:* $\beta > 0^0$
δ_E	Nominal flap angle or, for the case with the flaps being retracted, the wing's angle of attack relative to the horizontal (deg). Default value is 0.
N	Number of jet engines. Default value is 1.

4.2 4.2 Calculation

Jet speed of sound:

$$C_J = C_O \, (T_S/T_{SO})^{.5} \tag{118}$$

where C_O = 340.3 m/s (1116.4 fps)

Jet velocity:

$$V_J = M_J \, C_J \tag{119}$$

Ambient velocity:

$$V_O = M_O \, C_Z \tag{120}$$

Relative jet velocity:

$$V_R = |\bar{V}_J - \bar{V}_o|$$

$$= \left[V_J^2 - 2V_J V_o \cos(\delta_E - \theta) + V_o^2\right]^{.5} \tag{121}$$

Characteristic frequency:

$$f_o = (V_J/D)\ 1.8/[3 + (L/D)] \tag{122}$$

Characteristic reference sound level:

$$SL_o = 10 \log_{10}\left[\frac{V_J V_R^4}{V_{ref}^5} \left(\frac{P_z}{P_{so}}\right)^2 \left(\frac{T_{so}}{T_s}\right)^2 \left(\frac{C_o}{C_z}\right)\left(\frac{A}{r_o^2}\right) BW\ N\right]$$

$$- 10 \left| \log_{10}\left[\left(\frac{L_c}{L}\right)\left(\frac{V_J}{V_R}\right)\right]\right| - 4.6\ dB \tag{123}$$

where

V_{ref} = 0.3048 m/s (1 fps)

P_{so} = 1 atm (2116 psfa)

r_o^2 = 1 m^2 (10.76 ft^2)

Let

$$t = (h/D)/(L/D) \tag{124}$$

$$t_o = (V_R/V_J) \tan \beta \tag{125}$$

If $(t > t_o)$, **then** $SL_o = SL_o - 24 \log_{10} (t/t_o)$ (126)

1. **Repeat the following calculations through line 3 for each observer coordinate.**

   Direction angles:

$$\theta_o = \cos^{-1}\left[\left(Y \cos \delta_E + Z_N \sin \delta_E\right)/\left(Y^2 + Z_N^2\right)^{.5}\right] \tag{127}$$

$$\eta = \cos^{-1}\left[\left(Y^2 + Z_N^2\right)/\left(X^2 + Y^2 + Z_N^2\right)\right]^{.5} \tag{128}$$

Directivity correction:

$$Q = |\cos \eta| \sin^2(0.5\, \theta_o)/(SF)^3 \tag{129}$$

If $(Q < \epsilon)$, then set $Q = \epsilon$, where $\epsilon = 10^{-10}$.

$$DC = 10 \log_{10} (Q) \tag{130}$$

2. Repeat the following calculations through line 3 for each filter band frequency.

Normalized Dopper-shifted frequency:

$$f_N = f\,(SF)/f_o \tag{131}$$

Spectrum shape correction:

$$SSC = 10 \log_{10} \left\{ f_N^{4.8} / \left[1 + 1.5\, (f_N)^{5.7} \right]^{1.4} \right\} \tag{132}$$

3. Final sound pressure level calculation:

$$SPL = SL_o + DC + SSC$$

in dB re: 20 $\mu N/m^2$ at free field, index (r = 1 m) conditions.

4.3 MANUAL PROCEDURES

This section presents manual estimation procedures. These procedures can be used to calculate:

- Engine noise shielding provided by a fuselage
- Sound scattering due to wing wake turbulence

The procedures are preliminary based on the theory presented in sections 2.2.2 and 2.2.4 of this report.

Estimates provided by these procedures may be included in computerized predictions of community noise. The new computer program will accept such estimates if the user will specify them as "measured" configuration correction or "measured" SPL spectra input. See appendix A of volume II (secs. 4.3.1 and 4.3.11) for additional detail.

4.3.1 FUSELAGE SHIELDING

The fuselage shielding prediction procedure presented here is strictly theoretical (see sec. 2.2.2). Available data substantiate the theory (sec. 2.4.1.5), but are inadequate to develop a semiempirical method. These data were obtained from a simple test (see sec. 2.3.1.1) whose conditions correspond closely to the hypothesis of the theory.

Unfortunately, the method has not been verified for an actual engine-over-fuselage installation. Hence, the user should use it mainly for trade studies, recognizing that the noise reductions predicted are maximums.

Two forms of the prediction procedure are provided:

- Determination of the far-field sound anywhere about a fuselage
- Quick estimation of the far-field sound reduction in the deep shadow of the fuselage (flyover case)

The first method has more general application because it can be used to estimate the effects of fuselage reflections in addition to shielding. The second method is based on the first and is provided for those interested in only flyover noise reduction potential.

4.3.1.1 Observer at Arbitrary Location (Method l)

Inputs (see fig. 23):

- f Sound source frequency (Hz)
- C_o Ambient speed of sound (m/s or fps)
- r Fuselage radius (m or ft)
- R Source distance from fuselage's centerline (m or ft)
- ξ Observer angle with respect to fuselage centerline (deg)
- ϕ Angle between source and observer lines where the two lines intersect at the center of the fuselage (deg). This angle is measured in the plane normal to the fuselage centerline.
- M_o Ambient flow Mach number

Calculation:

1. Wave number:

$$K = 2\pi f/C_o \tag{133}$$

2. Flow transform on wave number:

$$K' = K/\sqrt{1 - M_o^2} \tag{134}$$

3. Flow transform on observer angle:

$$\xi' = \cos^{-1}\left[(\cos\xi + M_o)/(1 + M_o\cos\xi)\right] \tag{135}$$

4. Two-dimensional equivalent model terms:

$$b = K' R \sin\xi' \tag{136}$$

$$\theta = \sin^{-1}(r/R) \tag{137}$$

5. Interpolation on data curves:

   See appendix D of the volume II report for data curves. Enter table D-1 of the appendix to find which figures to use. Interpolate or extrapolate with respect to the variables (log b, θ, ϕ) for regions where the curves do not oscillate wildly. If the values of (b, θ, ϕ) correspond to a region with oscillations, interpolation/extrapolation using the discrete tone curves (solid line) cannot be done. Consider use of the 1/3-octave-band curves (dashed line) because they are considerably smoother than those for discrete tones.

4.3.1.2 Observer Located Directly Beneath Flightpath (Method 2)

Inputs:

The inputs are the same as in section 4.3.1.1, except ϕ is assumed to be $\pm 180^0$.

Calculation:

The calculation is the same as in section 4.3.1.1, except for step 5. A nomogram is provided (fig. 210) where (b, θ) and the noise reduction (NR) are the variables. This nomogram was derived from the figures in appendix D of the volume II report using the 1/3-octave-band curves.

4.3.1.3 Example Calculation

Inputs:

ϕ = $\pm 180^0$

f = 1000 Hz

r = 2.09 m (6.87 ft)

R = 3.46 m (11.37 ft)

ξ = 90^0

M_0 = 0.3

C_0 = 340.2 m/s (1116 fps)

Calculations:

$K = 2\pi f/C_0 = 18.5\ m^{-1}\ (5.63\ ft^{-1})$

$K' = K/\sqrt{1 - M_0^2} = 19.4\ m^{-1}\ (5.9\ ft^{-1})$

$\xi' = \cos^{-1}\left[(\cos\xi + M_0)/(1 + M_0 \cos\xi)\right] = 72.5^0$

$b = K'\ R \sin\xi' = 64$

$\theta = \sin^{-1}(r/R) = 37.2^0$

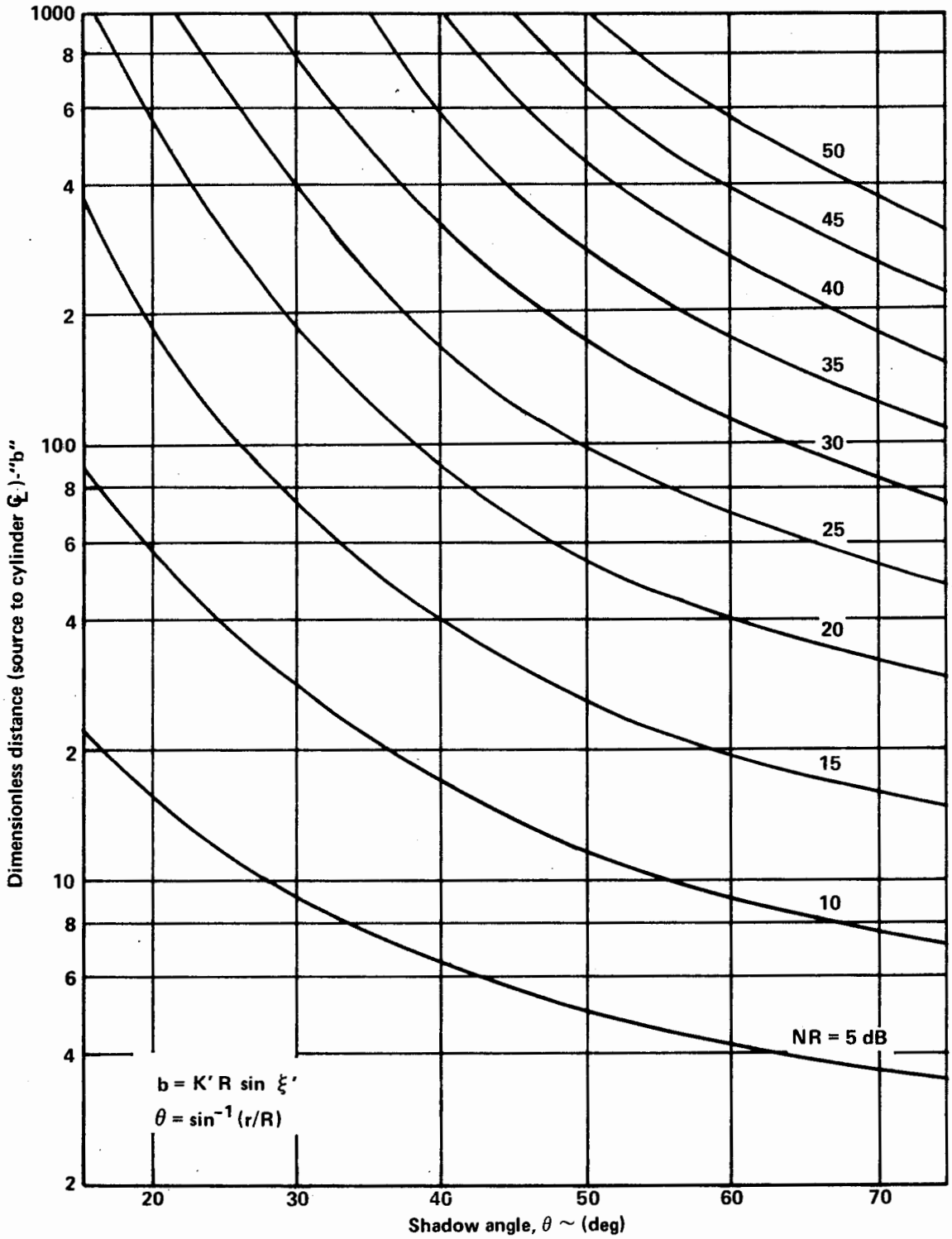

Figure 210.—Nomograph of Noise Reduction Underneath the Airplane Flightpath ($\phi = \pm 180°$)

Method 1–Observer At Any Angle ϕ:

See table D-1 in appendix D, volume II, for the figures to be used for data, e.g., figures D-5 and D-8. Interpolate with respect to (log b, θ) from the ***dashed*** line curves given for (b, θ) equal to (40, 30°), (160, 30°), (40, 45°), and (160, 45°). Figure 211 shows the result of the interpolation.

Method 2–Observer Directly Under Flightpath

Enter figure 210 with the above values of (b, θ) equal to (64, 37.2°) and read the noise reduction: NR = 16.5 dB.

4.3.1.4 Extension of Methods to Include Distributed Sources

Approximate the distributed source with a cluster of point sources. Repeat the calculations described previously in section 4.3.1.1 for each point source. The noise reduction is given by:

$$NR = 10 \log_{10} \left[\sum_{J=1}^{N} \left| p_{SJ} \right|^2 \Big/ \sum_{J=1}^{N} \left| p_{OJ} \right|^2 \right] \tag{138}$$

with p_{SJ} and p_{OJ} being the shielded and unshielded sound pressures related to the Jth point source.

Note:

Consider the case of an engine's inlet being approximated by a ring of point sources. The points placed out of the plane containing the fuselage and engine axis make the observer location underneath the airplane's flightpath to occur at angles ϕ not equal to 180°. Hence, the nomogram in figure 210 is not adequate. Only the table look-up method can be used, i.e., section 4.3.1.1.

4.3.2 WING WAKE SCATTERING

This prediction procedure can be used to estimate the amount of sound scattered into the wing shadow zone by turbulence in the near-wing-wake region. The effects of refraction by a wing wake are considered insignificant compared to scattering. Scattering can establish a limit on wing shielding attenuation of engine-generated noise. The procedure presented below estimates this limit for noise in the shadow zone of a wing.

The procedure is based on the theory presented in section 2.2.4. No test data are available to verify the method.

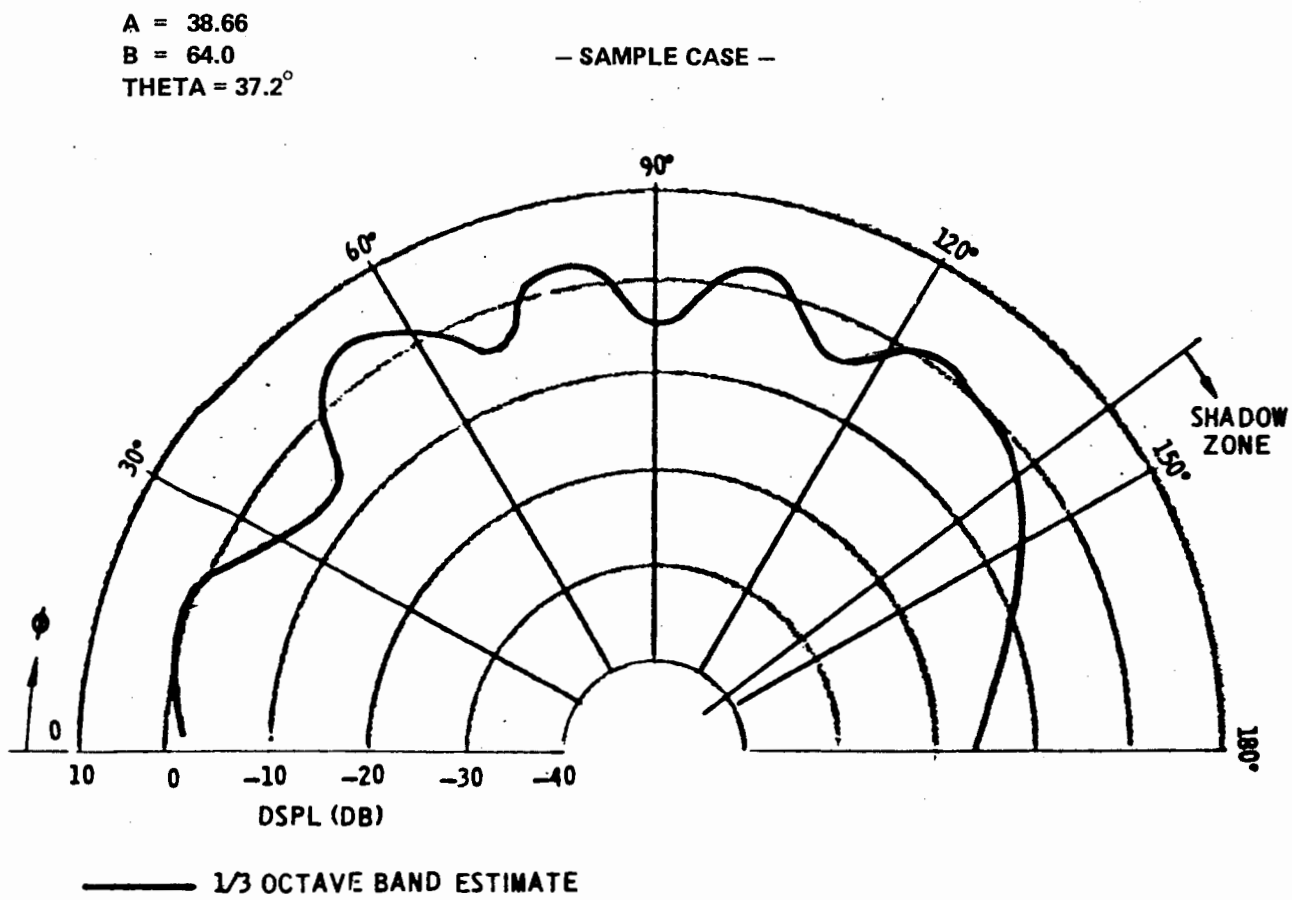

Figure 211.—Interpolated Noise Diffraction About a Fuselage

4.3.2.1 Input Data (see fig. 37)

$SPL(\psi_o')$	Reference far-field sound pressure level for sound energy incident to the near wake of a wing/flap system (dB). This corresponds roughly to the peak level for the sound diffracting around the wing's trailing edge.
C_o	Local speed of sound (m/s or fps)
C	Wing chord (m or ft)
C_D	Wing profile drag coefficient
f	Sound source frequency (Hz)
θ	Scattering angle relative to the incident sound direction (deg)
M_o	Aircraft Mach number

4.3.2.2 Calculation

1. Characteristic eddy scale:

$$\ell = \ell_o \sqrt{C_D/C_{Do}} \tag{139}$$

where the reference conditions (ℓ_o, C_{Do}) are (0.15 C, 0.2).

2. Strouhal number:

$$S = f\,\ell/C_o \tag{140}$$

3. Relative turbulence intensity:

$$\bar{u}^2/U_o^2 = \left(\bar{u}^2/U_o^2\right)_{ref} C_D/C_{Do} \tag{141}$$

with the reference turbulence intensity

$$\left(\bar{u}^2/U_o^2\right)_{ref} = 9.5 \times 10^{-3}$$

4. Differential scattering cross-section characteristic level:

$$L_o = 10 \log_{10}(d\sigma_S/d\Omega) \tag{142}$$

from the curves plotted as functions of θ and S in figures 41 and 42.

5. Relative overall scattered intensity:

$$F_o = 1.27\pi\, M_o^2 \left(\bar{u}^2/U_o^2\right) \tag{143}$$

6. **Relative scattered sound intensity level:**

$$\Delta SPL = 10 \log_{10}(q_s/q_I)$$

$$= \text{minimum of } (0, FL_o) \tag{144}$$

where

$$FL_o = 10 \log_{10}(F_o) + L_o \tag{145}$$

7. **Scattered sound pressure level in direction θ:**

$$SPL(\theta) = SPL(\psi_o') + \Delta SPL \text{ in dB} \tag{146}$$

4.3.2.3 Example Calculation

Inputs:

$SPL(\psi_o')$	= 100 dB re: 20 $\mu N/m^2$
C_o	= 340.2 m/s (1116 fps)
C	= 6.1 m (20 ft)
C_D	= 0.032
f	= 3.16 kHz
θ	= 45°
M_o	= 0.27

Calculations:

1. ℓ_o = 0.15 C = 0.91 m (3 ft)

   ℓ = $\ell_o \sqrt{C_D/C_{Do}}$ = 0.37 m (1.2 ft)

2. S = $f\,\ell/C_o$ = 3.4

3. $\bar{u}^2/U_o^2$ = $\left(\bar{u}^2/U_o^2\right)_{ref} C_D/C_{Do}$ = (1.52) 10^{-3}

4. L_o = +13 dB from figures 41 or 42 for (θ, S) = (45°, 3.4)

5. F_o = $1.27\pi M_o^2 \; (\bar{u}^2/U_o^2)$ = (4.42) 10^{-4}

6. FL_o = $10 \log_{10}(F_o) + L_o$ = −20.5 dB

   ΔSPL = minimum of (0, FL_o) = −20.5 dB

7. $SPL(\theta)$ = $SPL(\psi_o') + \Delta SPL$ = 79.5 dB re. 20 $\mu N/m^2$

4.4 EXAMPLE CASE

This section presents a practical community noise prediction problem for an EOW configured aircraft. This problem has been solved using the new computer software described in appendix A of the volume II report. Portions of the predicted results for this example have been illustrated in the "Summary" of this document. Sample input data and computer printout for the problem are given in sections 5.2 and 5.3 of volume II, appendix A. Additional detail is provided here to assist the user of the new computer software in solving his own problem.

4.4.1 STATEMENT OF PROBLEM

We wish to compare the community noise of an engine-over-wing (EOW) configured aircraft at takeoff conditions relative to that of a conventional engine-under-wing (EUW) configured aircraft. It is anticipated that the noise emanating from the engine's inlet may limit the noise reduction potential of an EOW-configured aircraft. Hence we will consider the inlet to have peripheral lining treatment for the EOW case.

4.4.2 INPUT DATA (See specific data input sample in user's guide, appendix A of volume II, for complete list.)

1. Homogeneous atmospheric conditions:

   - Pressure = 1 atm (14.7 psia)
   - Temperature = 298.2 °K (536.7 °R)
   - Relative humidity = 70%

2. Aircraft/observer geometry:

   - Level flight at altitude = 304.8 m (1000 ft)
   - Two observer locations relative to flight track = 0, 648.6 m (0, 2128 ft)

3. Aircraft Mach number = 0.29

4. Noise components considered:

   - Inlet fan noise
   - Exit fan noise
   - Turbine noise
   - Core noise
   - Jet noise
   - Jet/edge interaction noise

5. Engine type:

   - Typical high-bypass-ratio turbofan (BPR = 5)
   - Coplanar exit nozzles

6. Engine operating conditions:

   Takeoff power (see sec. 4.2 of app. A, vol. II, for specific inputs of mass flows, velocities, temperatures, Mach numbers, etc., for particular noise component input on $NOISIN data cards)

7. Configuration corrections:

- Double-layer lining, peripheral treatment for inlet length-to-diameter ratio of approximately 1
- Wing shielding with the geometry of figure 144 specified by

α_1	=	10^0	α_2	=	28^0	α_3	=	3^0
X_0/D	=	0	X_1/D	=	3.1	X_2/D	=	1.5
Y_0/D	=	0.75	Y_1/D	=	0.84	Y_2/D	=	0.28
S/D	=	8.1	L/D	=	4	D	=	1.96 m (6.42 ft)

8. Flight effects:

- Doppler shift is applied.
- Two estimates are to be made:
  - Prediction based on static model
  - Prediction based on extending the static model to flight using transforms of the uniform flow theory in sections 2.2.1.2 and 2.2.3
- Wing wake scattering is not included.
- The combined effects of scattering and uniform flow perhaps cause actual noise levels to be somewhere between the two estimated extremes (sec. 2.4.3). However, we recommend use of a conservative noise shielding estimate (no inclusion of uniform flow and scattering effects) until there is further test clarification of ambient flow effects.

4.4.3 RESULTS

Table 13 tabulates results estimated for the example with the observer positioned directly under the airplane's flightpath. A similar table can be made for the other observer position to the side of the airplane's flight track. For the suppressed noise estimates, some of the numbers appear as pairs. These are conservative and optimistic estimates of the shielding attenuation in flight. Figure 212 shows the results plotted for the total noise observed. Similar plots can be made for each noise component.

A breakdown of the effective perceived noise level into noise component contributions is shown in figure 213. Results of noise estimates for a typical landing approach are also shown; however, input for this case is not illustrated. The community noise reductions for this configuration are approximately (9, 5, 6.5)±1.5 EPNdB at takeoff, sideline, and approach, respectively. The plotted results also show which noise components would have to be reduced further to obtain more community noise suppression:

- Inlet fan noise
- Exit fan noise that propagates forward around the wing's leading edge
- Core noise

Table 13.—Estimated Flyover Test Results

Description	EPNL (EPNdB)	PNL (PNdB)		
		T_1	T_2	T_3
A. UNSUPPRESSED (EUW)				
1. Total	108.7	108.0	113.1	104.3
2. Inlet Fan	98.5	105.5	79.3	53.8
3. Exit Fan	105.8	100.2	111.2	101.2
4. Turbine	89.9	85.5	96.4	79.3
5. Core	96.3	96.2	99.3	93.7
6. Jet	84.6	78.2	86.4	85.7
B. SUPPRESSED (EOW)				
1. Total	101.1/ 98.6	105.8/105.7	95.5/ 92.3	103.0/ 92.1
2. Inlet Fan	96.2/ 96.1	103.3/103.2	74.5/ 74.3	51.8/ 51.7
3. Exit Fan	94.2/ 88.8	94.2/ 98.2	90.2/ 83.8	99.8/ 81.5
4. Turbine	76.0/ 70.8	78.3/ 73.7	75.3/ 70.1	76.7/ 69.2
5. Core	92.5/ 89.8	97.9/ 90.7	90.7/ 86.9	91.8/ 86.3
6. Jet	82.5	72.7	81.8	84.7
7. Jet/Edge Interaction	74.1	77.1	65.8	51.7
C. SUPPRESSION				
1. Total	7.6/ 10.1	2.2/ 2.3	17.2/ 20.8	1.3/ 12.2
2. Inlet Fan	2.3/ 2.4	2.2/ 2.3	4.8/ 5.0	2.0/ 2.1
3. Exit Fan	11.6/ 17.0	6.0/ 2.0	21.0/ 27.4	1.4/ 19.7
4. Turbine	12.9/ 19.1	7.2/ 11.8	21.1/ 26.3	2.6/ 10.1
5. Core	3.8/ 6.5	-1.7/ 5.5	8.6/ 12.4	1.9/ 7.4
6. Jet	2.1	5.5	4.6	1.0

Notes

1. (T_1, T_2, T_3) = (-0.7, 2.0, 5.0) sec. relative to visual overhead for the time the noise is observed. These times correspond to emission angles ψ = (60, 110, 140) degrees relative to the engine inlet centerline.

2. Detailed 1/3 octave band SPL and configuration correction spectra for each noise component can be obtained by simply running the computer sample given in Appendix A of the Volume II report.

3. Numbers shown as pairs xx/yy are with input variable ISFE of $GDATA parameters equal to (1, 0), respectively. This corresponds to inclusion and exclusion of flight effects in the shielding calculation.

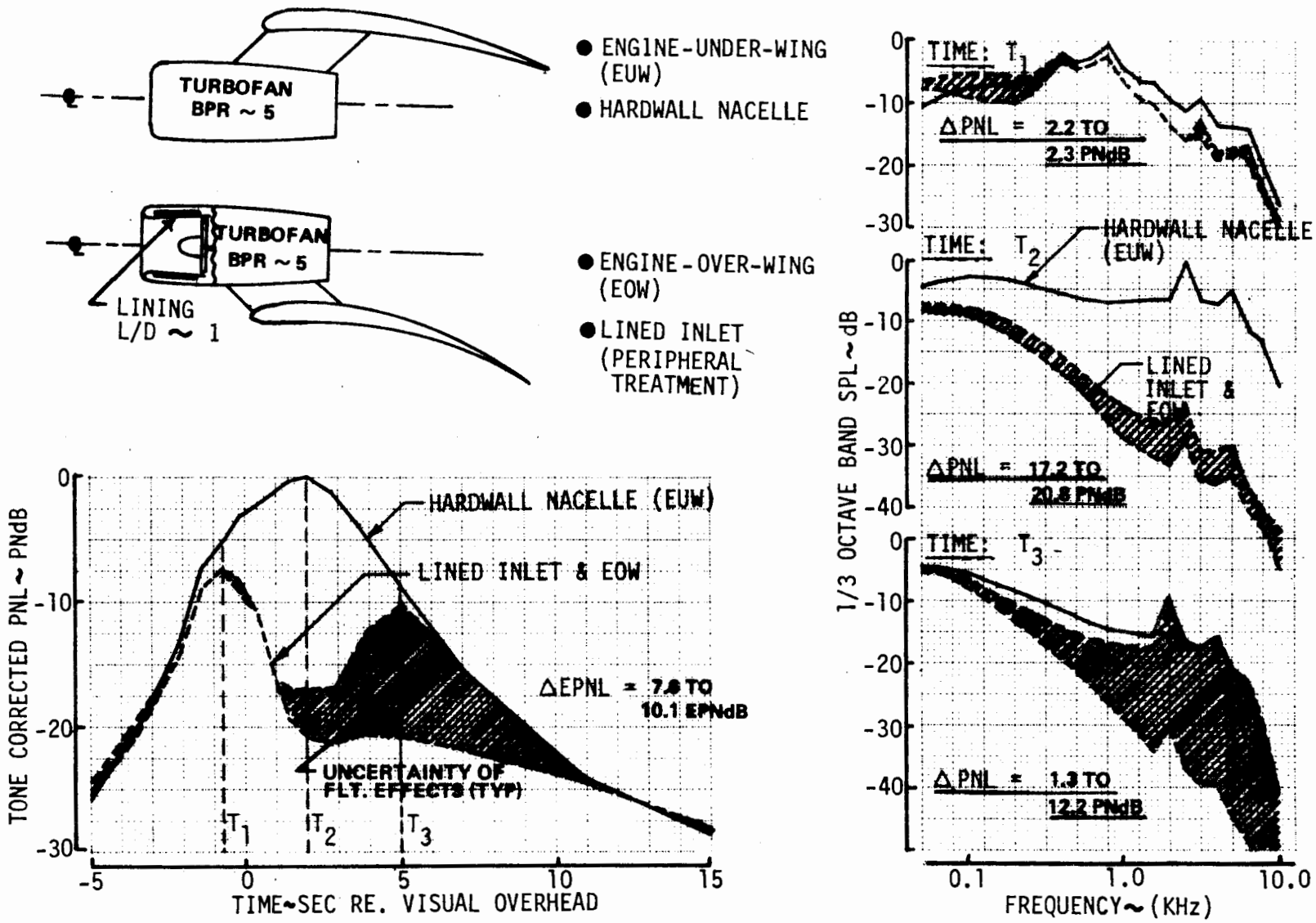

Figure 212.— Example Noise Estimation Capability (Takeoff)

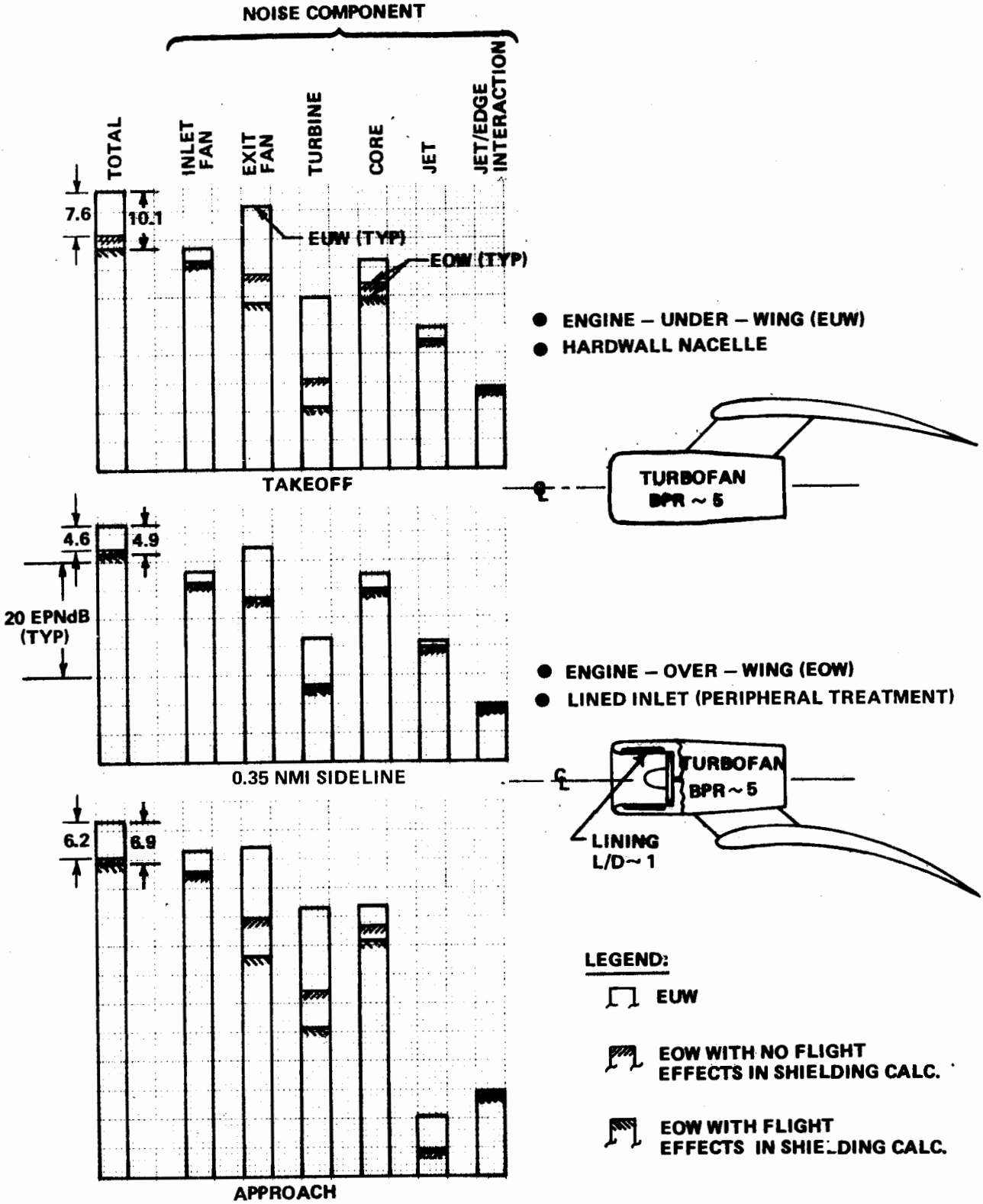

Figure 213.—Example of Aircraft Configuration Noise Reduction

5.0 CONCLUSIONS

5.1 NOISE REDUCTION POTENTIAL FOR THE ENGINE-OVER-WING CONFIGURATION

Analyses based on the computerized model presented in this report forecast that significant reductions can be achieved with engine-over-wing (EOW) configured airplanes as compared to current engine-under-wing (EUW) airplanes. For instance, an EOW aircraft powered by typical high-bypass turbofan engines (as JT9D, CF6-50, RB.211, etc.) with carefully treated inlets should achieve community noise levels 5 to 10 EPNdB lower than comparable EUW aircraft. Such reductions require a balanced application of inlet lining treatment to suppress inlet turbomachinery (TM) noise and wing shielding to suppress exhaust TM, core, and jet noise components. Typical component noise reductions are shown in table 14. The table shows uncertainty as to the full effect of airplane velocity on wing shielding effectiveness. This can be resolved only by further testing and analysis.

5.2 COMPUTERIZED MODEL FOR TURBOMACHINERY NOISE SHIELDING

The computerized model for TM noise shielding estimation was systematically developed from simple to progressively more complex representations. The theory of shielding provided by a semi-infinite half-plane for omnidirectional sources was used as a very basic building block. This is generalized in a series of steps, each step being developed and assessed with the aid of appropriate test data, and hence treated as an assumption in the development of the next step. The major steps of generalization in order of development were:

- Effect of source directivity
- Effect of multiedged nature of wing barriers
- Effect of noncompact noise sources and sound sources involving thrusting flow
- Effect of ambient flow and/or airplane forward velocity

The method used to account for source directivity shows excellent agreement with test data (involving no-flow noise sources). It predicts that the noise level in the shadow zone is set by the noise levels incident upon the barrier edge positions for the shortest propagation path between source, edge, and observer.

The method for describing the multiedged effects of the airplane wing shows good agreement with test data (involving no-flow noise sources). It predicts that the noise in the shadow zone is the sum of the diffracted noise contributions from each wing edge, primarily the leading edge and trailing edge, treated independently of all other edges.

The method for modeling noncompact noise sources, as those associated with inlet TM noise components, shows reasonable agreement with the very limited non-Boeing data

Table 14.—Typical Estimated Community Noise Reduction for EOW Versus EUW Configured Airplane

COMPONENTS (IN DESCENDING ORDER OF IMPORTANCE WHEN UNSUPPRESSED)	TYPICAL ESTIMATED REDUCTIONS (EPNdB) ①		
	TAKEOFF	0.35 NMI SIDELINE	APPROACH
EXIT FAN	14½ ± 3 ②	9 ± 3	15½ ± 3
INLET FAN ③	2½	2	3½
CORE	5 ± 1½	3 ± 1½	5 ± 1½
TURBINE	16 ± 3	8½ ± 3	17½ ± 3
JET	2	1	5½
JET/EDGE INTERACTION ④	–	–	–
TOTAL	9 ± 1½	5 ± 1½	6½ ± 1½

NOTES:

① SEE SECTION 4.4.3 FOR CONFIGURATION DETAILS

② VARIABILITY SHOWN INDICATES UNCERTAINTY IN THE EFFECT OF FORWARD VELOCITY UPON TM NOISE WING SHIELDING EFFECTIVENESS

③ ASSUMES MINIMAL INLET TREATMENT EMPLOYED FOR EUW CONFIGURED AIRPLANE

④ JET/EDGE INTERACTION NOISE IS TYPICALLY NOT PRESENT FOR EUW CONFIGURATIONS, BUT WILL BE UNAVOIDABLE IN EOW CONFIGURATIONS PROVIDING SIGNIFICANT EXHAUST NOISE SHIELDING.

base. An equivalent compact/directive noise source, having the same far-field directivity behavior as the physical noise source, is assumed to be located at the center of the engine inlet plane.

The model for noise sources associated with thrusting flow, as for the exhaust TM noise components, uses equivalent compact/directive noise sources (one for each important wing edge) which need not be located at the center of the nozzle exhaust plane. The directivity of each equivalent source is taken to be the same as the far-field directivity of the physical noise source considered. Equivalent source locations are determined, resulting in estimations that closely agree with appropriate test data.

The coordinate transformations used to represent airplane forward velocity (and/or ambient flow) effects on TM noise components are based on a priori extension of uniform flow theory developed by Candel. This a priori extended theory predicts:

- A rather large increase in shielding effectiveness for noise diffracting about the wing trailing edge

- A decrease in shielding effectiveness for noise diffracting about the wing leading edge

Rather limited test data suggest that the effect of forward velocity (ambient flow) causes more moderate shielding attenuation changes. This may occur because the theory for flight effects may be incomplete. Wing wake scattering could be the most important missing item. A manual estimation procedure is provided so that the results can be input to the computerized TM noise shielding prediction model.

5.3 OBSERVATIONS FROM FULL-SCALE ENGINE NOISE SHIELDING TEST

The full-scale JT9D Tulalip shielding data, which is a principal basis for empirical aspects of the computerized model for discharge TM noise components, suggests that:

1. The lowest shielded fan and turbine tone noise levels occur for deep shadow zone positions ($80^0 \leq \psi \leq 100^0$) and are consistently 20 to 23 dB below the highest unshielded noise levels (which correspond to $\psi \sim 120^0$). This is true quite independent of frequency in the range of 1.5 to 4.6 kHz and independent of the engine/wing geometries investigated.

2. The peak shielded noise levels occur close to either the trailing edge shadow boundary or the leading edge shadow boundary. These peak levels are sensitive to engine/wing geometry and are very important contributors to EPNL.

5.4 APPARENT TURBOMACHINERY NOISE LOCATION IN JET FLOW

Using compact-source half-plane diffraction theory, the apparent source location must be close to the wing trailing edge in order to simulate measured shielding results for exhaust TM noise. These apparent source locations are 1/4 to 1/20th of the nozzle

distance from the wing edge. In comparison, in the absence of thrusting flow, noise emanating from a nozzle appears to originate from the nozzle exit plane. Simple theory for the refraction of sound propagating out of a hot, high speed flow into a colder, lower speed (ambient) flow can and is used to account in part for equivalent source locations appearing close to wing edges. Comparison of apparent source locations predicted by this jet refraction theory with those implied by shielding tests showed significant similarity. Hence, apparent source locations are calculated by an empirically adjusted jet refraction model. The model is not unique. Axially distributed sources such as a line noise source may result in a better representation. However, a single-source representation was chosen for simplicity and because it gave reasonably good results.

5.5 POSSIBLE IMPORTANCE OF FLANKING RADIATION

Achievement of only a 23-dB shielding maximum in the JT9D full-scale test could be due to flanking radiation. Flanking radiation arises due to reflection and scattering of sound from objects other than the wing. These objects may be "hard" surfaces (test stand structure, trees, buildings, walls, ground, etc.) or "soft" surfaces such as turbulence in the jet, wing wake, and atmosphere. Flanking radiation probably contributes to the sound observed in the deep shadow zone in addition to that due to diffraction about wings. Hence the "true" apparent sources for the portion of sound diffracting about the wing may not be as close as estimated by the jet refraction portion of the procedure. This could cause shielding predictions to be suspect for engine cycles radically different from a high-bypass-ratio turbofan (BPR = 5). The flanking radiation and hence deep shadow zone noise levels could be unique to the test sites. Flanking radiation levels could be different on an airborne EOW airplane. The relative importance of diffracted versus flanking sound will not be known until more carefully controlled tests are conducted in anechoic chambers using full EOW airplane models simulating not only all shielding structures but also reflecting structures such as fuselage, fin, and stabilizer. Finally, wind tunnel tests using these models need to be completed to assess ambient flow effects on shielding. Careful control of reverberation and flanking path effects need to be considered in the tunnel tests. A special pulse technique is required to overcome these problems. Until this type of testing is done, the estimation method herein probably accounts for the combined effects of wing diffraction, flanking, and flight effects in a conservative manner.

5.6 JET NOISE SHIELDING MODEL

The computerized jet noise shielding model is based on empirical methods developed at NASA and independently checked against Boeing/Aeritalia data. Good agreement between the model and the independent data is observed. Additional Boeing/Aeritalia work shows that wing shielding effectiveness of jet noise is independent of airplane velocity (or ambient flow speed) for takeoff or approach speeds. This feature is incorporated in the computerized model.

5.7 JET/EDGE INTERACTION NOISE MODEL

The computerized jet/edge interaction noise model is based upon theory developed by Chase and semiempirical results using test data of Bhat and Gallo-Rosso, and von

Glahn et al. Additional elements for the effect of forward velocity and corrections for nozzle placement have been developed and incorporated in the model. The model has been checked against independent data from tests conducted by von Glahn et al. A favorable comparison resulted. The model predicts a reduction in jet/edge interaction noise with increasing forward velocity. Based on model predictions, it is concluded that jet/edge interaction noise will likely not present a community noise problem for EOW configurations. However, more low-frequency noise will result from the presence of jet/edge interaction noise. This could cause:

- Distinctive differences in an EOW community noise signature when compared to EUW
- Increased low-frequency cabin noise
- Increased regions of structure susceptible to sonic fatigue

6.0 RECOMMENDATIONS

1. The estimation methods presented in this report for wing and body shielding of jet engine noise components should be reliable for trade studies involving engines with bypass ratios of about 5, airplane Mach numbers not greatly in excess of 0.25, and engine/wing geometries not greatly different than those considered during tests described in this report. Hence, we recommend that this procedure be used for trade studies only.

2. Use of these prediction models for optimization studies should be undertaken only in conjunction with a concurrent test verification program. Failure to support such predicted optimization with tests will entail unreasonable risk.

   Configurations involving attached flow should be analyzed with conservatism. The computerized prediction model has been adjusted to give results consistent with measured data for a dual-flow D-shaped nozzle. Further test assessment of EOW systems with attached flow is required.

3. Further study is required to determine the importance of flanking paths due to the test site and how these contribute to the shadow zone noise levels. Although the semiempirical noise shielding estimation model assumes all sound enters the shadow zone by diffraction about an edge, this is not consistent with the actual test data base. The following flanking path mechanisms were probably important during static tests:

   - Reflection from hard objects at the test site other than wing structure
   - Sound scattering from a rock surface ground plane
   - Sound scattering due to atmospheric turbulence

   The relative importance of each must be carefully assessed in any further testing if improvement is to be achieved in the accuracy of wing shielding estimations.

4. Although unwanted reflecting objects were present during many tests, airplane reflecting structures such as the fuselage, vertical fin, and horizontal stabilizer were not simulated. Hence, any future testing to determine shielding from an airplane configuration should simulate the whole configuration. This is relatively easy in model tests, but may be more difficult in full-scale tests.

5. The flight effects procedures for wing shielding of turbomachinery noise components have not been clearly resolved. The test program defined in appendix B of the volume II report would provide most of the needed data. It proposes use of a special pulse technique to overcome problems of reverberation and flanking path radiation. The test is designed to separate the relative motion effects of ambient flow from the effects of sound scattering due to turbulence in the wing wake.

6. Once sound scattering by the turbulent wing wake is known to be an important contributor to noise levels in the shadow zone, there must be further testing of near-wing-wake turbulence to determine intensity and corresponding effects on shadow zone noise levels. Testing should be conducted to accurately measure this turbulence as a function of the wing's profile drag. Measurements should include:

   - Turbulence intensity
   - Turbulence scale
   - Mean velocity profile behind the airfoil section

   A variety of typical airfoil sections including configurations with flaps should be used for the experiment. The experiment should address the effects of variations in the angle of attack and the Reynolds number based on the wing chord. Of particular interest is the range of Reynolds number greater than 4.0×10^6.

7. With the present data base, specification of the flanking-path contribution is difficult, although in the future such a data analysis could be attempted. The present data base is not really adequate for resolving the effect of nozzle exhaust flow on the propagation of noise from within the nozzle out through the flow. An experimental program modeled after the Wall Isolation Facility shielding test program, but performed in an anechoic facility such as the Boeing Large Test Chamber, would go a long way toward resolving this matter of nozzle exhaust flow effects.

8. There is a need for further testing on fuselage shielding. In addition to a need for basic static data, information is needed to determine the effects of boundary layer, distributed sources, and ambient flow effects on shadow zone noise levels.

9. Further testing is needed on jet/edge interaction noise. The numerical values used in the nozzle placement effect correction and the Strouhal number dependence on shield length were obtained from a very limited amount of available data. Specifically, additional tests are needed that vary the length of shield relative to the jet potential-core length as well as the nozzle height above the shield.

10. The conjecture of section 3.4.5 that jet/edge interaction noise Strouhal number is independent of relative velocity should be experimentally verified. The relative velocity to the fifth power scaling relation indicated for shields shorter than the jet potential-core length (cf., app. H of vol. II) is confirmed by the tests of Bhat and Gallo-Rosso. However, the scaling relationship, i.e., $V_J^2 V_R^3$, indicated for shields longer than the jet potential core has no substantiating test data. Additional tests should be conducted to verify this theory where data is lacking.

REFERENCES

1. DOT/FAA, *Federal Aviation Regulations,* Vol. III, Part 36, Appendix B, December 1969.

2. D. G. Dunn and N. A. Peart; *Aircraft Noise Source and Contour Estimation,* NASA CR114649, July 1973.

3. K. C. Crowley, M. A. Jaeger, and D. F. Meldrum, *Aircraft Noise Source and Contour Computer Programs User's Guide*, NASA CR114650, July 1973.

4. A. DiBlasi et al., "Noise Shielding Effects for Engine-Over-Wing Installations," AIAA paper 75-474, March 1975.

5. G. Hellstrom, "Noise Shielding Aircraft Configurations, A Comparison Between Predicted and Experimental Results," ICAS paper 74-58, 25-30 August 1974.

6. A. Sommerfeld, *Optics, Lectures on Theoretical Physics,* Vol. IV, Academic Press, Inc., 1954.

7. P. C. Clemmow, "A Method for the Exact Solution of a Class of Two-Dimensional Diffraction Problems," *Proceedings of the Royal Society,* A205, 1951, pp. 286-308.

8. B. Noble, *Methods Based on the Wiener-Hopf Technique for the Solution of Partial Differential Equations,* Pegamon Press, 1966.

9. P. M. Morse and K. U. Ingard, *Theoretical Acoustics,* McGraw-Hill Book Co., Inc., New York, 1968.

10. J. J. Bowman, T. B. A. Senior, and P. L. E. Uslenghi, *Electromagnetic and Acoustic Scattering by Simple Shapes,* North Holland Publishing Co., 1969.

11. J. J. Adamczyk, "Analytical Investigations of Compressibility and Three Dimensionality on the Unsteady Response of an Airfoil in a Fluctuating Flow Field," AIAA paper 73-683, 16-18 July 1973.

12. S. M. Candel, "Diffraction of a Plane Wave by a Half-Plane in a Subsonic and Supersonic Medium," *JASA*, Vol. 54, October 1973, pp. 1008-1016.

13. D. M. Chase, "Sound Radiated by Turbulent Flow Off a Rigid Half-Plane as Obtained From a Wavevector Spectrum of Hydrodynamic Pressure," *JASA,* Vol. 52, 1972, pp. 1011-1023.

14. D. M. Chase, "Noise Radiated From an Edge in Turbulent Flow According to a Model of Hydrodynamic Pressure: Comparison With a Jet Flow Experiment," AIAA paper 74-570, 17-19 June 1974.

15. D. G. Crighton and F. G. Leppington, "Scattering of Aerodynamic Noise by a Semi-Infinite Compliant Plate," *J. Fluid Mechanics,* Vol. 43, 1970, pp. 721-736.

16. D. G. Crighton and F. G. Leppington, "On the Scattering of Aerodynamic Noise," *J. Fluid Mechanics*, Vol. 46, 1971, pp. 577-597.

17. J. E. Ffowcs-Williams and L. H. Hall, "Aerodynamic Sound Generated by Turbulent Flow in the Vicinity of a Scattering Half-Plane," *J. Fluid Mechanics*, Vol. 40, 1970, pp. 657-670.

18. D. S. Jones, "Diffraction Theory–A Brief Introductory Review," *J. Sound and Vibration*, Vol. 20, 8 February 1972.

19. D. S. Jones, "Aerodynamic Sound Due to a Source Near a Half-Plane," *J. Inst. Math. Applics.*, Vol. 9, 1972, pp. 114-122.

20. K. L. Chandiramani, "Diffraction of Evanescent Waves, With Applications to Aerodynamically Scattered Sound and Radiation From Unbaffled Plates," *JASA*, Vol. 55, January 1974, pp. 19-29.

21. J. C. Cooke, *Notes on the Diffraction of Sound*, ARC-CP-1192, London Aeronautical Res. Council, 1971.

22. H. Levine, "Diffraction Radiation," Imperial College of Science and Technology, Dept. of Mathematics, London, England, May 1972.

23. J. W. S. Rayleigh, *Theory of Sound* (reprinted by Dover Publications, 1974), Vol. 2, p. 133, 1878.

24. J. W. Miles, "On the Reflection of Sound at an Interface of Relative Motion," *JASA*, Vol. 29, No. 2, 1951, pp. 226-228.

25. H. S. Ribner, "Reflection, Transmission, and Amplification of Sound by a Moving Medium," *JASA*, Vol. 29, No. 4, 1957, pp. 435-441.

26. C. Yeh, "A Further Note on the Reflection and Transmission of Sound Waves by a Moving Fluid Layer," *JASA*, Vol. 43, No. 6, 1968, pp. 1454-1455.

27. L. K. Schubert, "Numerical Study of Sound Refraction by a Jet Flow; I. Ray Acoustics and II. Wave Acoustics," *JASA*, Vol. 51, 1972, pp. 439-463.

28. H. Y. Lu, "Acoustic Far Field of a Point Source in Cylindrical and Planar Parallel Flowing Fluid Layers," AIAA paper 75-500, March 1975.

29. G. F. Butler, T. A. Holbeche, and P. Fethney, "Some Experimental Observations of the Refraction of Sound by Rotating Flow," *AGARD Conference Proceedings No. 131*, paper 9, Brussels, Belgium, 19-21 September 1973.

30. M. J. Lighthill, "On the Energy Scattered From the Interaction of Turbulence With Sound or Shock Waves," *Proceedings of the Cambridge Philosophical Society*, Vol. 49, 1953, pp. 531-551.

31. G. K. Batchelor, "Wave-Scattering Due to Turbulence," Symposium on Naval Hydrodynamics, National Academy of Sciences, Pub. 515, 1957, pp. 409-430.

32. V. I. Tatarski, *Wave Propagation in a Turbulent Medium,* Dover Publications, Inc., New York, 1961.

33. A. L. Monin, "Characteristics of the Scattering of Sound in a Turbulent Atmosphere," *Soviet Physics-Acoustics*, Vol. 39, 1962, pp. 1125-1132.

34. A. A. Townsend, "Measurements in the Turbulent Wake of a Cylinder," *Proceedings of the Royal Society*, A190, 1947, pp. 551-561.

35. M. L. Uberoi and P. Freymuth, "Spectra of Turbulence in Wakes Behind Circular Cylinders," *Physics of Fluids,* Vol. 12, 1969, pp. 1359-1363.

36. L. T. Clark, *The Generation of Aerodynamic Sound by 65 Series Airfoils Immersed in a Subsonic Flow as a Function of Airfoil Camber, Incidence, and Wake Flow Parameters*, Boeing document D6-25357 (Proprietary), June 1970.

37. M. Abramowitz and I. A. Segan, *Handbook of Mathematical Functions*, Fifth Edition, Dover Publications, Inc., New York, May 1968.

38. J. B. Keller, "Geometrical Theory of Diffraction," *J. Optical Society of America*, Vol. 52, No. 2, February 1962, pp. 116-130.

39. IBM Corp., "Scientific Subroutine Package," IBM Application Program H20-0166-5, 1968, pp. 215, 216, and 371.

40. W. Baerg and W. H. Schwarz, "Measurements of the Scattering of Sound From Turbulence," *JASA,* Vol. 39, 1966, pp. 1125-1132.

41. M. J. Rudd, "A Note on the Scattering of Sound in Jets and the Wind," *J. Sound and Vibration*, Vol. 26, 1973, pp. 551-560.

42. I. H. Abbott and A. E. von Doenhoff, *Theory of Wing Sections,* Dover Publications, New York, 1959.

43. W. Baerg and W. H. Schwarz, "Pulse Technique for Measuring the Scattering of Sound From Turbulence," *JASA*, Vol. 40, 1966, pp. 133-137.

44. M. J. D. Powell, "An Efficient Method for Finding the Minimum of a Function of Several Variables Without Calculating Derivatives," *Computing Journal*, Vol. 7, 1964, p. 155.

45. L. L. Beranek (ed), *Noise and Vibration Control*, McGraw-Hill, 1971, pp. 174-180.

46. E. J. Rathe, "Note on Two Common Problems of Sound Propagation," *J. Sound and Vibration,* Vol. 10, 1969, pp. 470-479.

47. F. Fleischer, "Zur Anwendung von Schallschirmen," *Larmbekampfung,* Vol. 14 (6), 1970, pp. 131-136.

48. W. E. Scholes, "Noise Reduction by a Barrier," paper 70/67 presented at British Acoustical Society Meeting, Newcastle on Tyne, April 1970.

49. W. V. Bhat and D. Gallo-Rosso, "Effect of Forward Speed on Jet Wing/Flap Interaction Noise," AIAA paper 75-475, March 1975.

50. U. von Glahn, D. Groesbeck, and M. Reshotko, "Geometry Considerations for Jet Noise Shielding With CTOL Engine-Over-The-Wing Concept, AIAA paper 74-568, June 1974.

51. U. von Glahn and D. Groesbeck, "Influence of Mixer Nozzle Velocity Decay Characteristics on CTOL-OTW Jet Noise Shielding," AIAA paper 75-97, January 1975.

52. R. E. Hayden, *Noise From Interaction of Flow With Rigid Surfaces: A Review of Current Status of Prediction Techniques,* NASA CR2126, October 1972.

53. U. von Glahn, J. Goodykoontz, and J. Wagner, "*Nozzle Geometry and Forward Velocity Effects on Noise for CTOL Engine-Over-The-Wing Concept*, NASA TMX-71453, October 1973.

BIBLIOGRAPHY

1. M. Abramowitz and I. A. Segan, *Handbook of Mathematical Functions,* Fifth Edition, Dover Publications, Inc., New York, May 1968.

2. J. J. Adamczyk, "Analytical Investigations of Compressibility and Three Dimensionality on the Unsteady Response of an Airfoil in a Fluctuating Flow Field," AIAA paper 73-683, 16-18 July 1973.

3. J. Atvars, L. K. Schubert, E. Grande, and H. S. Ribner, "Refraction of Sound by Jet Flow or Jet Temperature," AIAA paper 65-82, May 1965.

4. W. Baerg and W. H. Schwarz, "Measurements of the Scattering of Sound From Turbulence," *JASA*, Vol. 39, 1966, pp. 1125-1132.

5. G. K. Batchelor, "Wave-Scattering Due to Turbulence," Symposium on Naval Hydrodynamics, National Academy of Sciences, Pub. 515, 1957, pp. 409-430.

6. R. J. Beckemeyer, "On the Effect of Thin Shear Layers With Flow and Density Gradients on Small Disturbances in Inviscid, Compressible Flows," *J. Sound and Vibration,* Vol. 31, 22 November 1973, pp. 251-256.

7. W. V. Bhat and D. Gallo-Rosso, "Effect of Forward Speed on Jet Wing/Flap Interaction Noise," AIAA paper 75-475, March 1975.

8. D. I. Blokhintsev, *Acoustics of a Nonhomogeneous Moving Medium,* NACA TM1399, 1946.

9. J. J. Bowman, T. B. A. Senior, and P. L. E. Uslenghi, *Electromagnetic and Acoustic Scattering by Simple Shapes,* North Holland Publishing Co., 1969.

10. G. F. Butler, T. A. Holbeche, and P. Fethney, "Some Experimental Observations of the Refraction of Sound by Rotating Flow," *AGARD Conference Proceedings No. 131*, paper 9, Brussels, Belgium, 19-21 September 1973.

11. S. M. Candel, "Diffraction of a Plane Wave by a Half-Plane in a Subsonic and Supersonic Medium," *JASA,* Vol. 54, October 1973, pp. 1008-1016.

12. D. Censor, "Propagation and Scattering of Sound Waves in Moving Media," *Israel Journal of Technology,* Vol. 9, No. 1-2, 1971.

13. K. L. Chandiramani, "Diffraction of Evanescent Waves, With Applications to Aerodynamically Scattered Sound and Radiation From Unbaffled Plates," *JASA*, Vol. 55, January 1974, pp. 19-29.

14. D. M. Chase, "Sound Radiated by Turbulent Flow Off a Rigid Half-Plane as Obtained From a Wavevector Spectrum of Hydrodynamic Pressure," *JASA,* Vol. 52, 1972, pp. 1011-1023.

15. D. M. Chase, "Noise Radiated From an Edge in Turbulent Flow According to a Model of Hydrodynamic Pressure: Comparison With a Jet-Flow Experiment," AIAA paper 74-570, 17-19 June 1974.

16. D. Chestnutt, D. J. Maglieri, and R. E. Hayden, "Flap Noise Generation and Control," *Proceedings of the NASA STOL Tech. Conference*, NASA SP-320, 1972, pp. 413-426.

17. L. T. Clark, *The Generation of Aerodynamic Sound by 65 Series Airfoils Immersed in a Subsonic Flow as a Function of Airfoil Camber, Incidence, and Wake Flow Parameters*, Boeing document D6-25357 (Proprietary), June 1970.

18. P. C. Clemmow, "A Method for the Exact Solution of a Class of Two-Dimensional Diffraction Problems," *Proceedings of the Royal Society*, A205, 1951, pp. 286-308.

19. T. W. Cole and E. A. Rathbun, *Small Scale Acoustic Investigation of Hybrid High Lift Systems Combining Upper Surface Blowing With the Internal Blown Flap*, NASA CR114757, 1974.

20. J. C. Cooke, *Notes on the Diffraction of Sound*, ARC-CP-1192, London Aeronautical Res. Council, 1971.

21. S. J. Cowan and R. W. Crouch, "Transmission of Sound Through a Two-Dimensional Shielding Jet," AIAA paper 73-1002, October 1973.

22. D. G. Crighton and F. G. Leppington, "Scattering of Aerodynamic Noise by a Semi-Infinite Compliant Plate," *J. Fluid Mechanics*, Vol. 43, 1970, pp. 721-736.

23. D. G. Crighton and F. G. Leppington, "On the Scattering of Aerodynamic Noise," *J. Fluid Mechanics*, Vol. 46, 1971, pp. 577-597.

24. A. DiBlasi et al., "Noise Shielding Effects for Engine-Over-Wing Installations," AIAA paper 75-474, March 1975.

25. R. G. Dorsch, "Externally Blown Flap Noise Research," SAE paper 740468, 1974.

26. R. G. Dorsch, P. L. Lasagna, D. J. Maglieri, and W. A. Olsen, *Flap Noise-Aircraft Engine Noise Reduction*, NASA SP-311, 1972.

27. R. Dorsch and M. Reshotko, "EBF Noise Tests With Engine Under-the-Wing and Over-the-Wing Configurations," *Proceedings of the NASA STOL Tech. Conference*, NASA SP-320, 1972, pp. 455-473.

28. R. Dorsch, M. Reshotko, and W. Olsen, *Flap Noise Measurements for STOL Configurations Using External Upper Surface Blowing*, NASA TMX-68167, 1972.

29. D. G. Dunn and N. A. Peart, *Aircraft Noise Source and Contour Estimation*, NASA CR114649, July 1973.

30. M. D. Falarski, K. Aoyagi, and D. G. Koenig, *Acoustic Characteristics of a Large-Scale Wind-Tunnel Model of an Upper-Surface Blown Flap Transport Having Two Engines,* NASA TMX-62319, 1973.

31. J. E. Ffowcs-Williams and L. H. Hall, "Aerodynamic Sound Generation by Turbulent Flow in the Vicinity of a Scattering Half-Plane," *J. Fluid Mechanics,* Vol. 40, 1970, pp. 657-670.

32. M. R. Fink, "Mechanism of Externally Blown Flap Noise," AIAA paper 73-1029, October 1973.

33. E. Grande, *Refraction of Sound by Jet Flow and Jet Temperature, Extension of Temperature Range Parameters and Development of Theory,* NASA CR840, August 1967.

34. C. M. Harris, *Handbook of Noise Control,* Chap. 3, Sec. 4, McGraw-Hill Book Co., 1957.

35. R. E. Hayden, *Noise From Interaction of Flow With Rigid Surfaces: A Review of Current Status of Prediction Techniques,* NASA CR2126, October 1972.

36. R. E. Hayden, T. D. Scharton, Y. Kadman, J. Wilby, and M. J. Rudd, *A Preliminary Evaluation of Noise Reduction Potential for the Upper Surface Blown Flap,* NASA CR112246, 1972.

37. R. E. Hayden, "Fundamental Aspects of Noise Reduction From Powered-Lift Devices," SAE paper 730376, 1973.

38. G. Hellstrom, "Noise Shielding Aircraft Configurations, A Comparison Between Predicted and Experimental Results," ICAS paper 74-58, 25-30 August 1974.

39. IBM Corp., "Scientific Subroutine Package," IBM Application Program H20-0166-5, 1968, p. 371.

40. R. W. Jeffery and T. A. Holbeche, "An Experimental Investigation of Noise Shielding Effects for a Delta-Winged Aircraft In Flight Wind Tunnel, and Anechoic Room," RAE TM Aero 1621, February 1975.

41. D. S. Jones, "Diffraction Theory–A Brief Introductory Review," *J. Sound and Vibration*, Vol. 20, 8 January 1972.

42. D. S. Jones, "Aerodynamic Sound Due to a Source Near a Half-Plane," *J. Inst. Math. Applics.,* Vol. 9, 1972, pp. 114-122.

43. J. B. Keller, "Geometrical Theory of Diffraction," *J. Optical Society of America,* Vol. 52, No. 2, February 1962, pp. 116-130.

44. A. Krasil'shchikova, "Diffraction of an Acoustic Wave by a Stationary Plate," *Revue Roumaine des Sciences Techniques, Serie de Mecanique Appliquee,* Vol. 17, No. 3, 1972, pp. 521-530.

45. J. Laufer, R. E. Kaplan, and W. T. Chu, "On Noise Produced by Subsonic Jets," *Vol. 1 Proceedings,* D.O.T. Second Interagency Symposium on University Research in Transportation Noise, NCSU, Raleigh, North Carolina, June 1974.

46. H. Levine, "Diffraction Radiation," Imperial College of Science and Technology, Dept. of Mathematics, London, England, May 1972.

47. M. J. Lighthill, "On the Energy Scattered From the Interaction of Turbulence With Sound or Shock Waves," *Proceedings of the Cambridge Philosophical Society,* Vol. 49, 1953, pp. 531-551.

48. H. Y. Lu, "Acoustic Far Field of a Point Source in Cylindrical and Planar Parallel Flowing Fluid Layers," AIAA paper 75-500, March 1975.

49. G. R. MacGregor and C. D. Simcox, "The Location of Acoustic Sources in Jet Flows by Means of the Wall Isolation Technique," AIAA paper 73-1041, 15-17 October 1973.

50. L. Maestrello, *On the Relationship Between Acoustic Energy Density Flux Near the Jet Axis and Far Field Acoustic Intensity,* NASA TND-7269, October 1973.

51. D. J. Maglieri and H. H. Hubbard, "Preliminary Measurements of the Noise Characteristics of Some Jet-Augmented-Flap Configurations," NASA memo 12-4-58L, 1959.

52. R. Mani, "Diffusion of Radiation Patterns Due to Scattering by Random Inhomogeneities," *J. Sound and Vibration,* Vol. 17, 8 July 1971.

53. R. Mani, "Refraction of Acoustic Duct Waveguide Modes by Exhaust Jets," *Quarterly of Applied Mathematics,* Vol. 30, January 1973, pp. 501-520.

54. J. W. Miles, "On the Reflection of Sound at an Interface of Relative Motion," *JASA,* Vol. 29, No. 2, 1951, pp. 226-228.

55. A. L. Monin, "Characteristics of the Scattering of Sound in a Turbulent Atmosphere," *Soviet Physics-Acoustics,* Vol. 39, 1962, pp. 1125-1132.

56. P. M. Morse and K. U. Ingard, *Theoretical Acoustics,* McGraw-Hill Book Co., Inc., New York, 1968.

57. B. Noble, *Methods Based on the Wiener-Hopf Technique for the Solution of Partial Differential Equations,* Pegamon Press, 1966.

58. R. B. Oetting, "Preliminary Wind Tunnel Noise Measurements of a Semi-Span Wing With an Upper-Surface Blown Flap," AIAA paper 74-191, January-February 1974.

59. R. C. Potter, *An Investigation to Locate the Acoustic Sources in a High Speed Jet Exhaust Stream,* NASA CR101105, February 1968.

60. V. W. Ramsey, *Acoustic Scattering From an Aircraft Trailing Vortex,* PhD Thesis, Stanford Univ., California, 1973.

61. J. W. S. Rayleigh, *Theory of Sound* (reprinted by Dover Publications, 1947), Vol. 2, p. 133, 1878.

62. G. Reethof and J. M. Seiner, "Measurements of the Axial Variation of the Source Strength Intensity in an Axisymmetric Subsonic Jet," *Vol. 1 Proceedings,* D.O.T. Second Interagency Symposium on University Research in Transportation Noise, NCSU, Raleigh, North Carolina, June 1974.

63. M. Reshotko, J. H. Goodykoontz, and R. G. Dorsch, *Engine-Over-the-Wing Noise Research,* NASA TMX-68246, 1973.

64. H. S. Ribner, "Reflection, Transmission, and Amplification of Sound by a Moving Medium," *JASA,* Vol. 29 No. 4, 1957, pp. 435-441.

65. E. G. Richardson, "The Transmission of Sound Through a Wake," *Proceedings of the Physical Society,* Vol. 76, 1960, pp. 25-32.

66. M. J. Rudd, "A Note on the Scattering of Sound in Jets and the Wind," *J. Sound and Vibration,* Vol. 26, 1973, pp. 551-560.

67. T. D. Scharton and B. P. Pinkel, "Reduction of Noise Generated by Flow of Fluid Over a Flat Plate," 84th Meeting of the Acoustical Society of America, Miami Beach, Florida, November-December 1972.

68. D. Schmidt, "Experimental Investigations on the Scattering of Sound in a Turbulent Stream," Max Planck Inst. for Stromungsforschung, Gottingen, W. Germany, 1962.

69. L. K. Schubert, "Numerical Study of Sound Refraction by a Jet Flow. I. Ray Acoustics," *JASA,* Vol. 51, 1972, pp. 439-446.

70. L. K. Schubert, "Numerical Study of Sound Refraction by a Jet Flow. II. Wave Acoustics," *JASA,* Vol. 51, 1972.

71. T. E. Siddon, "Some Observations on Source Detection Methods With Application to Jet Noise," *Vol. 1 Proceedings,* D.O.T. Second Interagency Symposium on University Research in Transportation Noise, NCSU, Raleigh, North Carolina, June 1974.

72. C. C. Smith, Jr., A. E. Phelps, III, and W. L. Copeland, *Wind Tunnel Investigation of a Large Scale Semi-Span Model With an Upswept Wing and an Upper Surface Blown Jet Flap,* NASA TND-7526, 1974.

73. A. Sommerfeld, *Optics, Lectures on Theoretical Physics,* Vol. IV, Academic Press, Inc., 1954.

74. G. G. Steinmetz and J. J. Singh, *Reflection and Transmission of Acoustic Waves From a Moving Layer,* NASA TND-6673, March 1972.

75. J. Taillet, *Description and Implementation of a Method for Characterizing Noise Sources in Jets,* NASA-TT-F-14851, April 1973.

76. V. I. Tatarski, *Wave Propagation in a Turbulent Medium,* Dover Publications, Inc., New York, 1961.

77. A. A. Townsend, "Measurements in the Turbulent Wake of a Cylinder," *Proceedings of the Royal Society,* A190, 1947, pp. 551-561.

78. M. L. Uberoi and P. Freymuth, "Spectra of Turbulence in Wakes Behind Circular Cylinders," *Physics of Fluids,* Vol. 12, 1969, pp. 1359-1363.

79. U. von Glahn, J. Goodykoontz, and J. Wagner, *Nozzle Geometry and Forward Velocity Effects on Noise for CTOL Engine-Over-the-Wing Concept,* NASA TMX-71453, 1973.

80. U. von Glahn, D. Groesbeck, and M. Reshotko, "Geometry Considerations for Jet Noise Shielding With CTOL Engine-Over-the-Wing Concept," AIAA paper 74-568, 17-19 June 1974.

81. U. von Glahn and D. Groesbeck, "Influence of Mixer Nozzle Velocity Decay Characteristics in CTOL-OTW Jet Noise Shielding," AIAA paper 75-97, January 1975.

82. U. von Glahn, M. Reshotko, and R. Dorsch, *Acoustic Results Obtained With Upper-Surface-Blowing Lift Augmentation Systems,* NASA TMX-68159, 1972.

83. W. L. Waites and Y. T. Chin, *Small Scale Wind Tunnel Model Investigation of Hybrid High Lift Systems Combining Upper Surface Blowing With the Internal Blown Flap,* NASA CR114758, 1974.

84. A. R. Wenzel and J. B. Keller, "Propagation of Acoustic Waves in a Turbulent Medium," *JASA,* Vol. 50, September 1971.

85. L. N. Wilson, *Application of Crossed Beam Technology to Direct Measurement of Sound Sources in Turbulent Jets, Part I–Final Report,* NASA CR129018, February 1970.

86. C. Yeh, "A Further Note on the Reflection and Transmission of Sound Waves by a Moving Fluid Layer," *JASA,* Vol. 43, No. 6, 1968, pp. 1454-1455.

GPO 907-590